OCS Study
BOEM 2014-771

Current-Topography Interaction and Its Influence on Water Quality and Contaminant Transport over Shelf-Edge Banks

U.S. Department of the Interior
Bureau of Ocean Energy Management
Gulf of Mexico OCS Region

OCS Study
BOEM 2014-771

Current-topography Interaction and Its Influence on Water Quality and Contaminant Transport over Shelf-Edge Banks

Authors

William J. Teague
Hemantha W. Wijesekera
Ewa Jarosz

Prepared under BOEM Contract
M10PG00038
by
Naval Research Laboratory
Stennis Space Center
Mississippi 39522

Published by

U.S. Department of the Interior
Bureau of Ocean Energy Management
Gulf of Mexico OCS Region

New Orleans, LA
July 2014

DISCLAIMER

This report was prepared under contract between the Bureau of Ocean Energy Management (BOEM) and the Naval Research Laboratory. This report has been technically reviewed by BOEM and it has been approved for publication. Approval does not necessarily signify that the contents reflect the views and policies of BOEM, nor does mention of trade names or commercial products constitute endorsement or recommendation for use.

REPORT AVAILABILITY

To download a PDF file of this Gulf of Mexico OCS Region report, go to the US Department of the Interior, Bureau of Ocean Energy Management, Environmental Studies Program Information System website and search on OCS Study BOEM 2014-771.

This report can be viewed at select Federal Depository Libraries. It can also be obtained from the National Technical Information Service; the contact information is below.

U.S. Department of Commerce
National Technical Information Service
5301 Shawnee Rd.
Springfield, Virginia 22312
Phone: (703) 605-6000, 1(800)553-6847
Fax: (703) 605-6900
Website: http://www.ntis.gov/

CITATION

Teague, W.J., H. W. Wijesekera, and E. Jarosz. 2014. Current-topography interaction and its influence on water quality and contaminant transport over shelf-edge banks. U.S. Dept. of the Interior, Bureau of Ocean Energy Management, Gulf of Mexico OCS Region, New Orleans, LA. OCS Study BOEM 2014-771. 280 pp.

Contents

Acknowledgements

We extend thanks the captain, crew, and marine technician of the R/V *Pelican* and crew of the R/V *Manta* for their assistance. The measurements were made in cooperation with the Flower Garden Banks National Marine Sanctuary, administered by the National Oceanic and Atmospheric Administration (NOAA). Support provided by Alexis Lugo-Fernandez of BOEM and Emma Hickerson of NOAA were greatly appreciated. We thank Andrew Quaid and Justin Brodersen of the Naval Research Laboratory, and Mark Hulbert and Steve Sova of NVision Solutions Inc., for their technical support in instrument preparations and successful mooring deployments.

1. Introduction

This work is a component of a major collaborative study between the Naval Research Laboratory (NRL) and the Bureau of Ocean Energy Management (BOEM; begun under the Minerals Management Service). The study coordinated the use of novel and complementary sampling platforms and methods to address inter-related scientific questions about the dynamics and bio-optical properties of the Flower Garden Banks National Marine Sanctuary (FGBNMS). Other collaborators included the National Oceanic and Atmospheric Administration (NOAA) and the Office of Naval Research (ONR). The collective work has two main objectives: (1) To obtain quantitative understanding of turbulence and sub-mesoscale processes over the East Flower Garden Bank and (2) To examine the importance of these topographic-induced processes on shelf edge circulation on longer (e.g., seasonal) time scales.

The first objective is addressed by a project of NRL entitled “Mixing over Rough Topography” (MORT). The MORT program was highly successful and was led by Hemantha Wijesekera, William Teague, and Ewa Jarosz at NRL, in collaboration with James Moum at Oregon State University, Mark Moline at California Polytechnic State University, and Michael Gregg at the University of Washington. The second objective is addressed by the NRL team in collaboration with BOEM, in the project referred to as “Currents over Banks” (COB) and with Emma Hickerson at NOAA’s FGBNMS. The problems to be addressed concern the relationships between bio-optical and physical properties at a variety of space and time scales. The large dynamical range called for collaborative use of several sampling platforms. The MORT project used moorings, autonomous platforms (remus), towed underway surveys, vertical profilers, and dye releases over an 18-day intensive observational period during May and June 2011 and leveraged the longer time-scale observational program in COB.

The MORT-COB effort addressed the structure and dynamics of circulation over the East Flower Garden Bank for time scales varying from days to months in relation to mixing, surface and bottom boundary layers, mesoscale features, and biological and optical features. This proposed work required mainly moorings consisting of bottom-mounted acoustic Doppler current profilers (ADCPs), temperature-conductivity strings, and pressure sensors deployed for a period of about one year starting in December 2010. Apart from the mooring-based survey, several 2- to 3-day surveys of turbulence and optical profiling were conducted during mooring deployments and recovery. In addition, a small-scale survey was conducted during the spawning period of corals in August 2011 using the NOAA-supported small research vessel, R/V *Manta*.

1.1 About This Document

This document provides a summary of the work performed for understanding of processes at the Flower Garden Banks (FGB). The analyses culminated in eight papers, consisting of six refereed journal papers and two conference reports. Two of the journal papers have been published at the time of this report and the other four papers have been submitted and are under review. Copies of each of the journal papers and reports are contained in Appendices A–H attached to this report. Each paper is cited and is described in the Results, section 5.0. Main conclusions, organized by paper and corresponding appendix, are provided in the Conclusions, section 6.0.

The current and hydrographic variability and possible relationships to wind and eddy forcing are discussed in Appendix A. Furthermore, Appendix A provides the background of the low frequency variability observed from the moorings for the five other journal papers. The surface wave effects on the high-frequency current flows are discussed in Appendix B. Form and frictional drags are discussed in Appendix C. Turbulence is discussed in Appendix D. Near inertial currents are described over the mooring period in Appendix E. Turbulence and its relationship to hydraulic control are provided in Appendix F. Some results of a bio-physical modeling effort in the Gulf of Mexico using the Navy Coastal Ocean Model are given in Appendix G. Finally, coral and larvae stochastic plume forecasts focused on the FGB are provided in Appendix H.

2. Background

The FGB are a series of topographic banks formed by coral reefs located on the Texas-Louisiana continental shelf in the northwestern Gulf of Mexico. They are part of a marine sanctuary designated as the Flower Garden Banks National Marine Sanctuary (FGBNMS), managed by NOAA. The footprint of the banks ranges from about 2 km^2 to 100 km^2 and the tops rise to within about 18 m of the sea surface from water depths of 100–150 m. The role of the banks and their interactions in modifying the circulation and transport of materials is poorly understood. The banks are large enough to alter the circulation on the outer shelf.

Hydrodynamic processes on the reefs impact the dispersion and material transport of dissolved and particulate nutrients and of planktonic material (Wolanski et al., 1989). The extent that bottom sediments can be driven by strong current events and ultimately deposit contaminants onto low relief features of the banks is not known. The dynamics of current and topography interactions in controlling the dispersion of the biological organisms and inorganic materials on the reefs and among the reefs are not well understood but may play a key role in reef habitat. Better understanding of the hydrodynamic processes that control material transport on reefs can provide marine managers information they need to more successfully manage coral reefs as natural resources.

It has also been recognized that the small-scale roughness properties of the seafloor are critical in determining important mixing processes. Numerical modeling studies show that turbulent transports have an important function in circulation, and on bio-optical, chemical, and sedimentary property distributions on the continental shelf (e.g., Durski et al., 2004; Durski and Allen, 2005; Gan, 2002; Kurapov et al. 2005; Wijesekera et al., 2003). Both model sensitivity studies and model-data comparisons emphasize the importance of obtaining a more realistic parameterization for turbulent mixing in the water column. To better characterize the reef environment, we need to understand the role of turbulent processes and higher frequency currents within the background lower-frequency current flows.

3. Objectives

1. Produce a three-dimensional view of the flow fields around a selected bank and to extend those results to flow over other banks in the region;
2. Increase our understanding of the effects of topography and water stratification on circulation around the banks and the resulting energy subsidy to reef communities;
3. Assess pathways for potential oil and gas impacts on bank communities from adjacent shunting and surface discharge activities;
4. Examine oceanic response over topographic bank (surface waves, bottom stresses, currents) to extreme, episodic atmospheric wind events, such as severe storms;
5. Expand understanding of non-hydrostatic processes over the reefs; and
6. Expand understanding of diapycnal mixing over rough bottom topography and processes responsible for generating turbulence; and
7. Understand lateral mixing process, topography induced wakes, and the resulting lateral eddy diffusivities.

4. Approach

This observational effort was possible only now, because of the recent advancement of oceanographic instrumentation and NRL capabilities. Measurements were made at varieties of spatial and temporal scales for understanding of dynamics over rough topography on the continental shelf in the Flower Gardens region. The processes that were examined over the East Flower Garden Bank (EFGB) are not limited to this particular bank; they can be applicable to other banks in the Flower Gardens and, in general, to other world ocean shelves. The field experiment used both long and short-term moorings, autonomous platforms (remus), a vertical microstructure profiler (VMP), and a towed undulating profiler (ScanFish) in coordination with a dye release experiment. For the long-term, low-frequency measurements, five bottom-mounted ADCP moorings and four temperature/salinity string moorings were deployed in December, 2010 at the EFGB for approximately one year and will provide coverage for all four seasons. These moorings were recovered during 18 days of intensive observations in June 2011 from the R/V *Pelican*. They were replaced by five new ADCP moorings and three string moorings. Because of time constraints, the fourth string mooring could not be redeployed. Final recovery of the long-term moorings was made using the R/V *Pelican* in December 2011. The FGBNMS vessel *Manta* was used for additional measurements during the June experiment with focus primarily on VMP and ship-mounted ADCP measurements. Standard CTD stations were conducted during the cruises.

This field work required close coordination with the managers of the FGBNMS to determine sharing and contribution of resources by the FGBNMS, timing of the field work, and specific study site selection. NRL consulted and complied with restrictions and methods imposed by FGBNMS regulations.

4.1 Eulerian Framework Measurements

***Long-term moorings**:* Five moorings containing ADCPs in NRL's Barny mounts were deployed at depths between 47 m and 127 m and sampled every 12 or 15 minutes over a period of one year. One mooring was deployed on top of the bank and the other four surrounded the bank. Near-full water column current profiles were obtained. Each mooring also included a wave-tide gauge or a high frequency pressure sensor which could provide valuable measurements of surface waves during winter and tropical storms (Teague et al., 2007; Wang et al. 2005). String moorings with several temperature and conductivity sensors were deployed within about 200 m of the four ADCP mooring surrounding the bank. These moorings were deployed in December 2010, recovered and redeployed during June 2011, and finally recovered in December 2011. A detailed description of the mooring observations can be found in Appendix A and in Teague et al. (2013).

***Short-Term Moored Measurement:** a)* Five ADCP moorings in Barny mounts were deployed only during the June cruise to sample every minute to provide high resolution currents over the cruise period.; *b)* Two thermistor and conductivity string moorings were deployed next to the bank and *c)* High-resolution pressure sensors were deployed in the Barnys to evaluate pressure drag (collaboration with Oregon State University group). Details of the short-term mooring observations can be found in Appendices B and D, and in Wijesekera et al. (2013).

***Underway Ship Measurements (June cruise):** a)* ScanFish measurements of T, C, and Inherent Optical Properties (IOP); *b)* Profiling microstructure measurements of high-resolution T,C, and velocity shear*; c)* Ship-mounted ADCP, ship meteorological measurements, and underway water flow-through system; *d)* Vertical profiles of acoustic backscatter measured with an 120 kHz echosounder. Vertical displacements of scattering layers show internal wave amplitude and length (provided that phase speeds are slow compared to ship speed) and may also show smaller-scale overturning structures. Echosounder pulses may scatter from turbulent density fluctuations in addition to biological material, yielding a qualitative measure of the intensity of turbulent fluctuations. These measurements are more fully described in Appendix D.

***Autonomous Measurements**:* A REMUS-AUV (collaboration with Mark Moline of California Polytechnic State University through ONR funding) provides high-resolution temperature, conductivity, pressure, and fluorescence data. These measurements are described in Appendix D.

4.2 Lagrangian Framework Measurements

Two dye experiments were conducted using Fluorescein Dye: (1) dye was released to the west of the bank and (2) dye was released to the east side of the bank. The dye was tracked by combining ScanFish and REMUS mounted fluorescence detecting fluorometers. The combined sampling method did very well. The dye dispersion provides a detailed view of the flow and the spatial variability of diapycnal and lateral mixing over the bank. During the second dye release, the dye was tracked almost to the West Flower Garden Bank (WFGB). In addition, CTD profiles were collected to examine hydrographic, irradiance (par), oxygen, and transmission of light levels across the bank. The dye patches revealed finescale to mesoscale features and are used to quantify horizontal (isopycnal) and vertical (diapycnal) diffusion. The dye measurements are described in Appendix D.

4.3 Model

The NRL Oceanography Division has implemented a 1/25º horizontal-resolution numerical ocean model for the Gulf of Mexico (GOM). The model domain encompasses the entire GOM extending from 18º to 31º north and from 77º to 98º west and includes Mexican and other waters. The physical formulation is based on the Naval Coastal Ocean Model (NCOM) configured with a 40 level σ-z vertical structure: 19 terrain-following σ (sigma) levels at the top of the water column, and 21 z (depth) levels at the bottom. The terrain-following levels, reaching from the surface to about 137 m, allow higher vertical resolutions for resolving mixed layer-shallow waters, while the z-levels are used in the stratified ocean. The ocean bathymetry is constructed from the NRL 2-minute database with the coastline set at a depth of 2 m. The physical model is one-way coupled to a 13-component ecosystem (biogeochemical) model that includes nutrients, two classes of plankton, oxygen, and carbon dioxide. The current configuration is tailored, but not limited to, real-time prediction; providing nowcasts (current state of the ocean) and up to 120-hour forecasts for the region. In this configuration, the model receives (initial) boundary information from the operational 1/8º Global NCOM, and it is forced by three-hourly 1/2º momentum and heat fluxes from the Naval Operational Global Prediction System (NOGAPS). The NCOMGOM model assimilates daily surface/subsurface temperature and salinity generated by the Modular Ocean Data Assimilation System (MODAS), which regresses satellite derived sea surface temperature and sea surface height data to obtain T&S synthetic profiles. The model was initialized on January 1, 2009 from the operational 1/8º Global NCOM physical state, the World Ocean Atlas 2005, and Carbon Dioxide Information Analysis Center biogeochemical fields. Results from the real-time NCOMGOM nowcasting-forecasting ocean modeling system are compared and evaluated against in-situ and remotely sensed observations, which include bio-optical products processed by the NRL Ocean Color Section. Google Earth/Ocean is used as a platform for viewing the model results interactively and dynamically in real-time.

NCOMGOM was configured at a 1-km high-resolution nest for the Flower Garden Banks. MORT-COB conductivity, temperature and depth (CTD) data were compared with model output. In general, the model reproduces the vertical temperature gradient well, but it is slightly cold biased and does not capture the small scale structure clearly present in the observations. Near-bottom temperatures measured at the moorings were also compared with near-bottom temperatures from the model. The overall trend in bottom temperature was captured by the model. Model derived temperature and salinity are shown for the time period of 2000 through 2010. These results are described in Appendix G.

In another separate modeling effort, a GOM regional model of NCOM at 1km and 3km resolutions was used to demonstrate simplified coral and larvae stochastic plume forecasts using passive tracers. The method for this demonstration uses continuous source terms and includes the uncertainty on the dispersion depth as well as the estimated errors on the water velocities through an extended forecast range ocean model ensemble (60 days). The resulting maps from the system provide likely areas where possible existent larvae and suspended coral might be dispersed in the water column as well as the sources of water arriving at the Marine Sanctuary along specific schedules. This model can be used to assess the fate of larvae spawning events as well as for the identification of water sources present in the Marine Sanctuary during the most sensitive periods. This work is described in Appendix H.

5. Results

Detailed analyses of the observations were conducted and results are provided in journal papers and reports. Each analysis is briefly described below and full text versions of the documents are found in Appendices A through H.

1. Teague, W. J., H. W. Wijesekera, E. Jarosz, D. B. Fribance, A. Lugo-Fernandez, and Z. R. Hallock, 2013. Current and hydrographic conditions at the East Flower Garden Bank in 2011, Continental Shelf Research, 63, pp. 43–58, DOI information: 10.1016/j.csr.2013.04.039.

This paper sets the scene for the other analyses performed using the long-term mooring data and for the other EFGB papers. Four acoustic Doppler current profiler (ADCP) moorings and four temperature/salinity strings were deployed around the EFGB with an additional ADCP on top of the bank for about one year. The currents from the long-term moorings were described, as well as the long-term temperature and salinity measurements. Currents were generally eastward over the bank in the upper water column. Eddy events occasionally reversed the eastward flow for a few days. Currents in the lower water column tended to align with the bank's bathymetry and mostly were directed offshore at the southern edge of the bank. Wind and eddy events moved both shelf and off-shelf waters over the bank including waters from as deep as 200 m through upwelling and/or mixing processes. Mixed layers changed by as much as 50 m in a couple of days. Inertial currents occurred throughout the year and were often much larger than the tidal currents. Commonly, the inertial currents were strong enough to reverse the predominantly eastward current flow on time scales of less than a day. Westward propagating cyclonic eddies (often associated with anticyclonic eddies) likely connect biological activities of the EFGB with the West Flower Garden Bank. Banks such as the EFGB, with large aspect ratios and heights, strongly alter circulation and enhance exchange processes at the shelf break. See Appendix A.

2. Wijesekera, H. W., D. W. Wang, W.J. Teague, E. Jarosz, E. Rogers, D. B. Fribance, and J. N. Moum, 2013. Surface wave effects on high-frequency currents over a shelf edge bank, Journal of Physical Oceanography, V43, 1627–1647, DOI: 10.1175/JPO-D-12-0197.1.

The long-term ADCPs and vertical strings of temperature, conductivity, and pressure sensors, deployed on and around the EFGB, were used to examine surface wave effects on high-frequency flows over the bank and to quantify spatial and temporal characteristic of these high-frequency flows. The EFGB, about 5 km wide and 10 km long, consists of steep slopes on southern and eastern sides that rise from water depths over 100 m to within 20 m of the surface. Three-dimensional flows with frequencies ranging from 0.2 to 2 cycles per hour were observed in the mixed layer when wind speed and Stokes drift at the surface were large. These motions were stronger over the bank than outside the perimeter. The squared vertical velocity, w^2, was strongest near the surface and decayed exponentially with depth, and the e-folding length of w^2 is twice larger than that of Stokes drift. The two-hour averaged w^2 in the mixed layer, scaled by the squared friction velocity, was largest when the turbulent Langmuir number was less than unity and the mixed layer was shallow. It is suggested that Langmuir circulation is responsible for the generation of vertical flows in the mixed layer, and that the increase in kinetic energy over the bank is due to enhancement of Stokes drift by wave focusing. The lack of agreement with open-ocean Langmuir scaling arguments is likely due to the enhanced kinetic energy by wave focusing. See Appendix B.

3. Wijesekera, H. W., E. Jarosz, W. J. Teague, D. W. Wang, D. B. Fribance, J. N. Moum, and S. J. Warner, 2014. Measurements of form and frictional drags over a rough topographic bank, Journal of Physical Oceanography, submitted.

Pressure differences across the topography generate a form drag, which opposes the flow in the water column, and viscous and pressure forces acting on roughness elements of the topographic surface generate a frictional drag on the bottom. Form drag and bottom roughness lengths were estimated over the EFGB in the GOM by combining an array of bottom pressure measurements, and profiles of velocity and turbulent kinetic dissipation rates. The EFGB is a coral bank about 6 km wide and 10 km long located at the shelf edge and rises from 100 m water depth to about 18 m below the sea surface. The average frictional drag coefficient over the entire bank was estimated as 0.006 using roughness lengths that ranged from 0.001 cm for relatively smooth portions of the bank to 1–10 cm for very rough portions over the corals. The measured form drag over the bank showed multiple time-scale variability. Diurnal tides and low-frequency motions with periods ranging from 4 to 17 days generated form drags of about 2000 N m^{-1} - 3000 N m^{-1} with average drag coefficients between 0.03 and 0.22, which are a factor of 5–35 times larger than the average frictional drag coefficient. Both linear wave drag and quadratic drag laws have similarities with the observed form drag. The form drag is an important flow retardation mechanism even in the presence of the large frictional drag associated with coral reefs, and requires parameterization. See Appendix C.

4. Jarosz E., H. W. Wijesekera, W. J. Teague, D. B. Fribance, and M. A. Moline, 2014. Observations on stratified flow over a bank at low Froude numbers, Journal of Geophysical Research, submitted.

In June 2011, a nine-day oceanographic survey was conducted over the EFGB. Current, temperature, conductivity, and microstructure measurements were collected to characterize flow evolution, turbulence and mixing over the surveyed bank. During the experiment, the flow was highly-stratified, subcritical with the Froude number below 0.4, hydrostatic, and non-linear with rotational effects being not negligible. Observations also showed that flow structure, turbulence, and mixing were highly dependent on the direction and strength of currents; thus, they varied spatially and temporarily. Responses resulting from interactions between the free-stream flow and the obstacle were significantly different on the upstream and lee sides of the bank. Blocking and diverging of the flow just below the bank height was observed on the upstream side. On the lee side, a wake with imbedded vortices developed. Moreover, turbulence was amplified over the bank top and on its lee side. Turbulent dissipation rates were as high as 10^{-6} W kg^{-1} resulting in measured rates of energy dissipation and mixing by turbulence per unit width as high as 40 W m^{-1}. Mixing on the lee side was also elevated with eddy diffusivities reaching 10^{-3} m^2 s^{-1} that were above a typical value of 10^{-5} m^2 s^{-1} commonly found for continental shelves with slowly varying topography. On the upstream side, estimated eddy diffusivities were close to that for the flat bottom shelves, i.e., they were generally less than $0.5 \cdot 10^{-4}$ m^2 s^{-1}. See Appendix D.

5. Teague, W. J., H. W. Wijesekera, E. Jarosz, A. Lugo-Fernandez, and Z. R. Hallock, 2014. Wavelet analysis of near-inertial currents at the East Flower Garden Bank, Continental Shelf Research, submitted.

Near-inertial currents (NICs) often dominate the mean circulation at the EFGB. The bank is about 6 km wide in the east-west direction and rises to within about 20 m from the surface. NICs near the EFGB are described using current data from five acoustic Doppler current profilers that were moored at the edges of the bank and on top of the bank for about a year. A wavelet analysis was used to better describe the nonstationarity of the NICs. NICs were strongest during spring and summer because of their near-resonant response with sea breeze and the shallowness of the mixed layer, and exhibited a first-baroclinic-mode vertical structure. NICS were generally larger near the surface and extended to the bottom on the west side of the EFGB but only to within about 20 m of the bottom on the eastern side of the bank. NIC ellipses were nearly circular and rotated clockwise above the top of the EFGB but became flatter and aligned with the bathymetry with increasing depth; occasionally, on the eastern side of the bank, the NIC vectors rotated counter-clockwise due to probable effects of lee vortices arising from the mean flow interacting with the bank. Both downward and upward energy propagations were observed below the mixed layer, but most energy input by the wind at the surface was likely transferred downward through divergence of the meridional flow against the coastal boundary. The inertial currents were at times more energetic that the mean flow, and often accounted for more than 50% of the total current energy. See Appendix E.

6. Gregg, M. C. and J. M. Klymak, 2014. Mode-2 hydraulic control of flow over a small ridge on a continental shelf, Journal of Geophysical Research, submitted.

Some of the most intense turbulence in the ocean has been found in hydraulic jumps found in the lee of sills where low internal modes are hydraulically controlled. Observations on the outer Texas-Louisiana continental shelf and modeling demonstrate hydraulic control of internal mode-2 over a 20-m-high ridge on the 100-m-deep continental shelf. Flow perturbations produced by the hydraulic response dominated the water column and included large vertical displacements in the weakly stratified surface layer overlaying the ridge. The mode-2 response differed in form from a hydraulic jump but produced turbulence one to two decades more intense than the local background. See Appendix F.

7. deRada, S., R. A. Arnone, and S. Anderson, 2009. Bio-physical ocean modeling in the Gulf of Mexico, Oceans 2009, MTS/IEEE Biloxi–Marine Technology for Our Future: Global and Local Challenges, E-ISBN: 978-0-933957-38-1.

The Navy Coastal Ocean Model (NCOM) was configured at 4 km horizontal resolution with a 40-layer σ/z vertical structure to conduct a 30+ year (1979–2011) reanalysis in the Gulf of Mexico. An inner 1-km nest (with the same vertical structure) for the FGBMS was also configured as a downscale to the 4 km model. The models are forced by NASA’s Modern Era Retrospective-analysis for Research and Applications atmospheric fluxes, and by open boundary conditions prescribed from Global NCOM which starts in 1998–a daily climatology was constructed for use in years before 1998. Similarly, a daily temperature and salinity synthetic field was constructed through the Modular Ocean Data Assimilation

System to constrain the model by time-space relaxation. The objective is to examine and quantify oceanic temperature variability in the GOM and to evaluate the model skill before conducting long-term forecasting simulations. The model is validated in multiple ways. Ten SST time series of model compared with NDBC in-situ observations across the GOM (black dots) illustrate the model's relative skill from year 2000 to 2010. The model does not assimilate these observations. Further validation of the model compared with observations was provided with MORT conductivity, temperature, and depth data taken at the EFGB. Model simulations agree well with the MORT observations and suggest that the model has excellent skill l in hindcasting temperature measurements. See Appendix G.

8. Coelho, E., G. Peggion, P. Hogan, P. Thoppil, C. Rowley, 2014. Long range stochastic plume simulations in the Gulf of Mexico, contribution 044/3-34, 2014 Gulf of Mexico Oil Spill and Ecosystem Science Conference, Mobile, AL, USA.

Simplified coral and larvae stochastic plume forecasts were applied to the FGNMS using passive tracers. The demonstration uses continuous source terms and includes the uncertainty on the dispersion depth and the estimated errors on the water velocities through an extended forecast range ocean model ensemble (60 days) in development by other related projects. The resulting maps from the system provide likely areas where possible existent larvae and suspended coral might be dispersed in the water column as well as the sources of water arriving to the FGBNMS along specific schedules. This report is supplied in Appendix H.

6. Conclusions

Full conclusions are provided in the text for each paper and report in the appendices. Some of the main conclusions are summarized below. The conclusions are organized by paper or report and the corresponding appendix.

6.1 From Appendix A: Currents and Hydrographic Conditions

- A two-layer current system is found in the vicinity of the EFGB.
- Currents at the bank were generally eastward but were sometimes reversed by eddies.
- Currents followed bathymetry around the EFGB in the lower water column.
- Near bottom currents at southwestern and southeastern corners of the bank were mostly directed offshore.
- Offshore currents in the lower water column were sometimes larger that east-west currents in the upper water column.
- The region just south of the EFGB could be a region of convergence for the deep offshore current flow.
- Integral time scales for along-shelf flows ranged from a week to more than two weeks.
- Integral time scales for cross-shelf flows generally ranged from three to five days.
- Main tide constituents were M2, K1, and O1, but tidal currents were weak (2–5 cm/s).
- Inertial currents were significant and strongest during summer.
- Inertial currents sometimes reversed the eastward flow.
- Inertial currents were enhanced by sea-breeze effects and exceeded 20 cm/s.
- Some correlations between currents and winds were found.

- Generally, eastward flow over the EFGB is the southern limb and return flow of the cyclonic gyre on the Louisiana-Texas shelf.
- Storm events are effective in driving shelf water over the bank.
- Mixed layers ranged from 10 m and shallower to deeper than 80 m.
- Mixed layers ranged between 20 m and 40 m over much of the year.
- Mixed layers were deepest (60 m to 80 m) during December and January.
- Mixed layers can shallow from 80 m to 20 m in less than two days.
- Westward tracking eddies and southward deep current flows may be a major conduit for shelf water exchange between the FGB and the rest of the GOM.
- Northward deep currents at the southern edge of the EFGB can transport deep ocean water onto the bank and the shelf.
- Much of the cross-shelf exchange is likely to occur in the lower water column and near the bottom.
- Upwelling in response to storms can transport cooler deeper waters onto the EFGB.

6.2 From Appendix B: Surface Wave Effects

- High-frequency, three-dimensional flows with frequencies ranging from 0.2 to 2 (Nyquist frequency) cycles per hour were found in the mixed layer when wind speed and Stokes drift were large. It is suggested that Stokes drift and mean flow interactions such as Langmuir circulation are responsible for generating significant velocity fluctuations.

- Stokes drift over the bank was estimated from two-dimensional directional wave spectra from a 600 kHz ADCP. The estimated Stokes drift at the surface (U_{S0}) varied with the wind speed and is about 0.6% of the wind speed for winds greater than 10 m s^{-1}.

- Vertical velocity fluctuations showed upward and downward motions with similar magnitudes. The probability distribution of velocity fluctuations departs from the Gaussian distribution especially at the tail ends of the distribution.

- Squared vertical velocity (w^2) was strongest near the surface and decayed exponentially with depth, and the associated e-folding length is a factor of two larger than the e-folding length associated with Stokes drift.

- The squared two-hour and mixed-layer averaged vertical velocity, normalized by the squared friction velocity varied from 0.1 to 60, and was strongest when the turbulent Langmuir number was less than unity and the mixed layer was shallow.

- Although vertical velocity is likely to be a function of Stokes drift, frictional velocity, and mixed layer depth, a unique scaling for profiles of vertical velocity was not found. However, Stokes drift scaling provides a better representation of vertical velocity in the mixed layer, when effects of the mixed layer depth and the penetration depth of the vertical velocity are included.

- Largest velocity variances were found over the EFGB (at M5), located nearly 3 km north of the peak of the bank. It is suggested based on a wave refraction-diffraction model

(REF/DIF1) that the increase in kinetic energy over the bank is due to enhancement of Stokes drift by topography-induced waves focusing.

- The lack of agreement with open-ocean parameterizations of vertical kinetic energy over the bank is likely due to the enhancement of kinetic energy resulting from localized focusing of surface waves.
- Wave-driven velocity fluctuations play an important role in mixing and vertical transports and, in addition, can strongly impact coral habitats over the EFGB.
- Velocity fluctuations over the EFGB are closely related to surface wave conditions that can have strong localized variability due to wave focusing over the bank.
- The scaling of wave-induced mixed-layer currents over a shelf edge bank differs from the open ocean.
- Further studies are needed for the generalization of wave-driven mixing processes in the coastal environment.

6.3 From Appendix C: Form and Frictional Drags

- Nearly six-month-long bottom-pressure records (June–December 2011) showed significant semi-diurnal (M_2) tide, diurnal (K_1 and O_1) tides, synoptic scale (4–6 day), and 10–17 day variability over and around the bank.
- Based on the pressure spectra, tidal elevations of M_2, K_1, and O_1 were 0.27 m, 0.78 m, and 0.72 m, respectively.
- Barotropic tidal currents were small (K_1, O_1 speeds < 5 cm s^{-1}) compared to inertial currents that were over 15 cm s^{-1}. M_2 tidal currents were less than 3 cm s^{-1}, and the depth-averaged sub-tidal currents were about 4–9 cm s^{-1}.
- The estimated form drag from bottom pressure anomalies across the bank showed variability on multiple time scales.
- The form drag resulting from diurnal tidal motions and 4–17 day oscillations had magnitudes of about 2000 N m^{-1} to 3000 N m^{-1}. This is the first direct estimate of form drag at subtidal bands from pressure measurements.
- Coefficients of the time-averaged bulk drag (C_D) ranged from 0.03 to 0.22, which was a factor of 5-35 larger than the averaged-frictional drag coefficient.
- The enumerated power per unit length at sub-tidal motions was about 73 W m^{-1}. The total power over the EFGB was ~ 0.3 MW.
- Physical parameters describing the dynamics of flows over the EFGB have a range of values representing a highly non-linear, hydrostatic flow regime with upstream blocking.

- Both linear wave drag and quadratic drag laws had similarities with the observed form drag, but no unique parameterization was found.
- These measurements of the velocity and dissipation over the bank provide the first estimates of frictional drag coefficients and roughness lengths over the EFGB. Over the top of the bank, the bottom roughness lengths encompass those expected for a smooth bottom with z_0 of 0.001 cm as well as higher roughness values over corals. Given that the coral coverage is not continuous, a range of values representing smooth to relatively rough regimes was expected.
- The bottom roughness range was from 0.001 cm (smooth bottom) to 68 cm, with mean and median values of 3.6 cm and 0.24 cm, respectively. Nearly 1/3 of the roughness estimates were greater than 1 cm. This is the first measurement of bottom roughness over the EFGB.
- The mean and median of the frictional drag coefficient were about $6x10^{-3}$ and $3x10^{-3}$, respectively. This is the first measurement of the frictional drag coefficient over the EFGB.
- Large roughness elements can impact the hydraulic flow control and coral reef ecology.
- Locations with coral coverage have increased drag, leading to more turbulence and mixing at these locations relative to regions without corals.
- Turbulence will increase the delivery of nutrients and particulates to the corals. Additionally, it helps to disperse larvae during spawning events, generating a positive feedback cycle that sustains the health of the coral community.
- The magnitude of the bottom stress over the bank can modify the separation of flow, lee wave structure and strength of the form drag; it is a factor to consider in the parameterization of the form drag in numerical models.
- Consequently, our observations and analysis of the hydrographic, velocity, microstructure and pressure measurements suggest that the EFGB is a “hot spot” of mixing on the shelf of GOM.
- The analysis further demonstrates that the form drag resulting from low-frequency currents over an isolated bank on the continental shelf is an important physical process that must be parameterized to represent a wide range of flow states.

6.4 From Appendix D: Stratified Flow at Low Froude Numbers

- Measured currents during an intensive two-week field experiment in June 2011 were a combination of the sub-tidal, inertial, tidal, and higher frequency motions with a maximum speed of about 50 cm s^{-1}.

- During June 2011, the waters at the EFGB were highly stratified throughout the entire water column, with the depth mean buoyancy frequency of 0.016 s^{-1} and 0.018 s^{-1} for the eastward and westward mean flow phases, respectively.

- During June 2011, the mixed surface and bottom boundary layers were generally less than 4 m thick.

- The flow conditions over the EFGB were classified as subcritical when transects were sampled since all estimated Froude numbers (F_o) were less 0.4.

- Flow dynamics over the bank were also hydrostatic and non-linear, and rotational effects were not negligible during June 2011.

- Observations clearly showed that flow structure and mixing were highly dependent on the direction and strength of the currents in the EFGB region, and varied spatially and temporarily.

- Responses resulting from interactions between the free-stream flow and the bank were significantly different on the upstream and lee sides of the EFGB.

- Blocking and diverging of the flow was observed on the upstream side of the EFGB, for both mean eastward and westward current phases.

- On the downstream side of the bank, a wake developed and was consistent with low Froude numbers.

- Current observations and estimated relative vorticities implied that eddies developed on the lee side of the bank.

- Turbulence was amplified over the EFGB top and on its lee side.

- Estimated TKE dissipation rates from current shear observations were as high as 10^{-6} W kg^{-1} resulting in measured rates of energy dissipation and mixing by turbulence per unit width over the bank as high as 40 W m^{-1}.

- Even for such weak flow conditions, mixing on the downstream side was also enhanced by a few orders of magnitude above the typical shelf value of 10^{-5} m^2 s^{-1}, and the eddy diffusivity there was as high as 10^{-3} m^2 s^{-1}.

- On the upstream side, its estimated values were close to that for continental shelf with gradually varying bathymetry and it was generally less than $0.5 \cdot 10^{-4}$ m^2 s^{-1}.

- Turbulence and mixing are expected to be more elevated during the more extreme but commonly observed currents in the EFGB region than turbulence and mixing observed during June 2011.

6.5 From Appendix E: Near Inertial Currents

- Near inertial currents (NICs) at the EFGB occur in bursts throughout the year but are most concentrated during the spring and summer where they are enhanced by sea-breeze effects.

- The bank tends to modify NIC characteristics below the top of the EFGB.

- NICs can occasionally reverse the predominantly eastward mean flow on short time scales.

- Typically, the vertical structure of the NICs followed a first-baroclinic mode with a 180° phase shift between upper and lower layers but was more complicated when waters were weakly stratified.

- NICs were generally stronger at the surface but sometimes were largest at mid-depth.

- Barotropic tidal currents were small and generally less than the NICs at the EFGB.

- Above the bank, NICs were highly coherent.

- Below the top of the bank, the NIC ellipses tended to align with the bathymetry and become more rectilinear while flowing around the bank.

- CCW rotation of the ellipse vector was common on the lee or eastern side of the bank below the top.

- NICs were often a significant part of the total current and could account for more than 50% of the total current energy throughout the water column.

- NICs are likely to be partially responsible for enhanced mixing of physical, biological, and geological properties.

- Characteristics of the near-inertial currents observed at the EFGB are expected to be similar at the other banks.

- In combination with the mean currents and passing eddies, in the vicinity of the banks, NICs probably play a significant role in the transport and mixing of physical and biochemical properties around the numerous banks with greater mixing levels than over most of the continental shelf.

- NICs may have a pronounced effect on the ecosystem of the GOM shelf region.

- NICs are most intense during spring and summer, the period of most active biological activity, such as the mass coral spawning event that happens annually 7–10 days after the full moon, typically in the month of August.

6.6 From Appendix F: Mode-2 Hydraulic Control

- Using measurements made during November 2011, when stratification was weak, flow across a 20-m-high ridge (EFGB) on a 100-m-deep continental shelf was critical to internal mode-2 for three hours while the water column flowed westward with maximum speeds somewhat less than 0.2 m s^{-1}. The water column was weakly stratified to 60 m, and internal mode-1 was never close to being controlled.

- During mode-2 control, the interface was depressed over the EFGB crest, and overlying isopycnals were elevated throughout the weakly stratified surface layer.

- When control was lost, the displacements propagated eastward, possibly as a bore along the interface that was related to large overturns that were observed in the surface layer. These overturns carried fluid with high chlorophyll concentrations upward from the interface into most of the surface layer.

- Average dissipation rates below the interface and over the ridge were 10^{-8} to 10^{-7} W kg^{-1}, one to two decades larger than nearby background levels. Corresponding diapycnal diffusivities were 10^{-4} to 10^{-3} m^2 s^{-1}.

- Observed and modeled dissipation rates and diapycnal diffusivities rose by one to two decades over EFGB.
- Control of mode-2, and perhaps higher modes, can affect mixing over rough bottoms nearly as much as does mode-1 control.
- Control can be simulated numerically, raising the prospect of being able to predict the dominant mixing once accurate energy balances are developed for the diverse set of hydraulic controls being found.
- The large responses observed in the surface layer over a ridge occupying only the bottom 20% of the water column demonstrate that mixed layer studies over continental shelves cannot be conducted without considering the effect of relatively small bottom roughness.

6.7 From Appendix G: Bio-Physical Model

- A real-time Gulf of Mexico Modeling System (GOMMS) capable of forecasting biological, optical, and physical properties up to 120 hours has been developed.
- The major added value of the GOM Ocean Model over that of Global Navy Coastal Ocean Model (NCOM) is the addition of the optical and ecosystem models which are validated against ocean-color observations, namely chlorophyll from satellite.

- This new capability couples the Navy’s state of the art physical model (NCOM) with a 9- and a 13-component ecological model that can provide coastal managers and researchers advanced knowledge of bio-physical processes in both the coastal zone and the open ocean.

- This new modeling capability will help predict the influence that large mesoscale processes, such as the Loop Current and the Warm Core rings, have on localized coastal environments, estuaries, and embayment areas like Tampa, Florida; Mobile, Alabama; and Houston, Texas.
- "Bio-Optical-Physical Ocean Weather Forecasting" is a new capability and falls behind present capabilities of Meteorological Weather Forecasting.
- The lower-resolution model bathymetry captures the general shape of the EFGB and WFGB.
- In general, the model reproduces the vertical temperature gradient well observed during MORT-COB, but it is slightly cold biased and does not capture the small scale structure clearly present in the observations.
- The overall trend in bottom temperatures measured at the MORT-COB moorings was captured by the model.
- The GOMMS model simulated reanalysis results suggests good skill in hindcasting temperature measurements and could provide a baseline before attempting extended projections.

6.8 From Appendix H: Stochastic Plume Forecasting

- Maps from the Navy Coastal Model (NCOM) can suggest likely areas where larvae and suspended coral might be dispersed in the water column and the sources of water arriving to the FGBNMS along specific schedules.
- This demonstration presented a methodology that allows assessment of the fate of larvae spawning events as well as the identification of water sources that will be present in the FGBNMS during the most sensitive periods for the several habitats in the region and could be used for efficient planning of monitoring tasks and mitigation in the case of accidents at sea.

7. References

Durski, S.M., S.M. Glenn, and D.B. Haidvogel, 2004. Vertical mixing schemes in the coastal ocean: Comparison of the level 2.5 Mellor-Yamada scheme with an enhanced version of the K profile parameterization, Journal of Geophysical Research 109: doi: 10.1029/2002JC001702. issn: 0148-0227.

Durski, S.M. and J.S. Allen, 2005. Finite amplitude evolution of instabilities associated with the coastal upwelling front, Journal of Physical Oceanography, 37(4), 837–854.

Gan J. and J.S. Allen, 2002. A modeling study of shelf circulation off northern California in the region of the Coastal Ocean Dynamics Experiment: response to relaxation of upwelling winds, Journal of Geophysical Research, 107, C9, 3123, doi:10.1029/2000JC000768.

Kurapov, A.L., J.S. Allen, G.D. Egbert, R.N. Miller, P.M. Kosro, M. Levine, and T. Boyd, 2005. Distant effect of assimilation of moored currents into a model of coastal wind-driven circulation off Oregon, Journal of Geophysical Research, 110, C02022, doi:10.1029/2003JC002195.

Teague, W.J., E. Jarosz, D.W. Wang, and D.A. Mitchell, 2007. Observed oceanic response over the upper continental slope and outer shelf during Hurricane Ivan, Journal of Physical Oceanography, V37(9), 2181–2206.

Teague, W.J., H.W. Wijesekera, E. Jarosz, D.B. Fribance, A. Lugo-Fernandez, and Z.R. Hallock, 2013. Current and hydrographic conditions at the East Flower Garden Bank in 2011, Continental Shelf Research, 63, pp. 43–58, DOI information: 10.1016/j.csr.2013.04.039, 2013.

Wang, D.W., D. A. Mitchell, W. J. Teague, E. Jarosz, and M.S. Hulbert, 2005. Extreme waves under Hurricane Ivan, Science, Vol 309, 896.

Wijesekera, H.W., J.S. Allen, and P.A. Newberger, 2003. Modeling study of turbulent mixing over the continental shelf: comparison of turbulent closure schemes, Journal of Geophysical Research, 108(C3), 3103, doi:10.1029/2001JC001234.

Wijesekera, H.W., D. Wang, W.J. Teague, E. Jarosz, E. Rogers, D.B. Fribance, and J.N. Moum, 2013. Surface wave effects on high-frequency currents over a shelf edge bank, Journal of Physical Oceanography, V43, 1627-1647, DOI: 10.1175/JPO-D-12-0197.1.

Wolanski, E., D. Burrage, and B. King, 1989. Trapping and dispersion of coral eggs around Bowden Reef, Great Barrier Reef, following mass coral spawning, Continental Shelf Research, 9(5), 479–496.

APPENDIX A

Current and Hydrographic Conditions at the East Flower Garden Bank in 2011

Current and Hydrographic Conditions at the East Flower Garden Bank in 2011

W.J. Teague[1 *], H.W. Wijesekera[1], E. Jarosz[1], D.B. Fribance[2], A. Lugo- Fernández[3],
and Z.R. Hallock[4]
[1]Naval Research Laboratory, Stennis Space Center, MS, 39529, USA
[2]NRC Postdoctoral Research Associate, Naval Research Laboratory, Stennis Space Center, MS, 39529, USA
[3]Bureau of Ocean Energy Management, New Orleans, LA, 70123, USA
[4]QinetiQ North America, Slidell, LA,70461, USA

Journal Citation:
Teague, W.J., H.W. Wijesekera, E. Jarosz, D.B. Fribance, A. Lugo-Fernandez, and Z.R. Hallock, 2013. Current and hydrographic conditions at the East Flower Garden Bank in 2011, Continental Shelf Research, 63, pp. 43-58, DOI information: 10.1016/j.csr.2013.04.039.

Abstract

The East Flower Garden Bank (EFGB), part of the Flower Garden Banks National Marine Sanctuary, is located in the northwestern Gulf of Mexico, about 185 km southeast of Galveston, Texas. With a width of about 5 km, the steep-sided bank rises from water depths of over 100 m to within less than 20 m of the surface. Four acoustic Doppler current profiler (ADCP) moorings and four temperature/salinity strings were deployed around the EFGB with an additional ADCP on top of the bank for about one year. The main objective was to understand the ocean processes over the EFGB and to examine the importance of the topographically induced processes on shelf edge circulation on longer (e.g. days to seasonal) time scales. Currents were generally eastward over the bank in the upper water column. Eddy events occasionally reversed the eastward flow for a few days. Currents in the lower water column tended to align with the bank's bathymetry and mostly were directed offshore at the southern edge of the bank. Wind and eddy events moved both shelf and off-shelf waters over the bank including waters from as deep as 200 m through upwelling and/or mixing processes. Mixed layers changed by as much as 50 m in a couple of days. Inertial currents occurred throughout the year and were often much larger than the tidal currents. Commonly, the inertial currents were strong enough to reverse the predominantly eastward current flow on time scales of less than a day. Westward propagating cyclonic eddies (often associated with anticyclonic eddies) likely connect biological activities of the EFGB with the West Flower Garden Bank. Banks such as the EFGB, with large aspect ratios and heights, strongly alter circulation and enhance exchange processes at the shelf break.

Keywords: East Flower Garden Bank; Current; Mixed-layer depth; Temperature/salinity; ADCP; Northwestern Gulf of Mexico; (27-28N; 93-94W)

---

[*] Corresponding Author: W.J. Teague; William.Teague@nrlssc.navy.mil; phone: 228-688-4734

1. Introduction

The general circulation of the outer Texas-Louisiana shelf has been broadly described by several investigations (Cochrane and Kelly, 1986; Cho et al., 1998; Nowlin et al., 1998; Nowlin et al., 2005). The low-frequency flow at the shelf edge was found to be generally towards the east or northeast. This flow balances the generally westward flow on the inner shelf and is the southern limb of the cyclonic gyre in the northwestern Gulf of Mexico (Cochrane and Kelly, 1986). Currents on the inner-shelf are coherent with the low-frequency, alongshelf winds (Jarosz and Murray, 2005; Cochrane and Kelly, 1986). It has been suggested that the currents in the northwestern Gulf of Mexico near the shelf edge are driven by the winds (Sturges and Blaha, 1976; Blaha and Sturges, 1981), buoyancy forces, and mesoscale eddies generated directly and indirectly by rings detached from the Loop Current (LC) (Hamilton, 1992; Hamilton et al., 2002; Nowlin et al., 2005). Eastward currents at the shelf edge are thought to result from an integrated effect of anticyclonic eddies impinging on the shelf (Cochrane and Kelly, 1986; Hamilton, 1992; Hamilton et al., 2002; Nowlin et al., 2005). There could be large cross-isobath currents due to eddies. These eddy driven cross-isobath flows may even dominate the exchange across the shelf break (Nowlin et al., 2005). Oey (1995) proposed that the flow at the shelf edge was additionally modulated by the wind stress curl. Observations of temperature and salinity show that interaction of eddies with the shelf edge can advect warmer and saltier water onto the shelf while moving cooler and fresher shelf water offshore (Nowlin et al., 1998).

The Flower Garden Banks are located on the outer shelf in the northwestern Gulf of Mexico. They are far enough off the Louisiana coast in order not to be directly influenced by Mississippi and Atchafalaya Rivers runoff (Rezak et al., 1990), although some low-salinity (30-31 psu) water has been observed near the surface and just above the coral heads at high river discharge periods (Dodge and Lang, 1983; Nowlin et al., 1998; Deslarzes and Lugo-Fernández, 2007). Flow appears to have at least two layers much of the year. Using current meter data from two moorings located about 5 km northeast and 11 km west of the East Flower Garden Bank (EFGB), respectively, McGrail (1983) and Halper et al. (1988) found that there is usually strong eastward flow at mid-depth (about 50 m). On the other hand, Beard (1984) observed westward flow nearby from current data during the March-May time period. Halper et al. (1988) observed eastward flow at the beginning of winter but soon observed a north-south sloshing with little along shelf eastward flow. Using historical data, Sahl (1984) found that the near bottom flow was mainly offshore. Inertial oscillations associated with the passage of hurricanes (Price, 1976; Brooks, 1983) and atmospheric cold fronts (Chen et al., 1996; Halper et al., 1988; Daddido et al., 1978) have been observed. Mid-depth currents in excess of 60 cm/s and inertial currents with amplitudes in excess of 20 cm/s were found (Halper et al., 1988). The inertial oscillations can generate the largest percentage of the variance for periods between 3 and 40 hours and are generally on the order of magnitude of tidal variance (Chen et al., 1996). Currents near the bottom just to the northeast of the EFGB were observed to oscillate in the north-south direction with mean flows towards the south-southeast (Halper et al., 1988). No correlation was found between the oscillations and the passage of cold fronts. In addition, changes in the general current patterns between summer and winter could not be explained by changes in the wind fields. Tidal amplitudes are small at the Flower Garden Banks (DiMarco and Reid, 1998). Hence, the currents near the shelf edge at the EFGB are complicated and are not well understood.

Characterizing the flow near the shelf edge is important for determining the exchange mechanisms between the deep ocean and the shelf. Rough bathymetric features at the edge of the shelf may impact the structure and dynamics of the circulation (Moum and Nash, 2000). The purpose of this paper is to describe the low-frequency currents at the EFGB corresponding to periods of semi-diurnal tidal frequencies and longer. Long-term measurements from December 2010 to December 2011 of current velocity, temperature, and salinity from the EFGB (Figure 1) are analyzed to obtain a quantitative understanding of submesoscale processes over the EFGB and to examine the importance of topographically induced processes on shelf edge circulation on longer (days to months) time scales. The topics discussed in this paper are mainly the current and hydrographic variability and possible relationships to wind and eddy forcing. Section 2 provides some background information on the Flower Garden Banks. Section 3 provides a description of the data and instrumentation. Basic statistics of the currents are given in Section 4. A description of the current flow over and around the bank is provided in Section 5. Temperature and salinity observations from the string moorings are described and related to water mass movements and mixed layer depths in Section 6. Finally, a summary of the results is presented in Section 7.

2. Flower Garden Banks Background

A series of topographic banks formed containing coral communities and coral reefs referred to as the Flower Gardens are part of a marine sanctuary designated as the Flower Garden Banks National Marine Sanctuary (FGBNMS), and are managed by the National Oceanic and Atmospheric Administration (NOAA). They are located on the Texas-Louisiana continental shelf in the northwestern Gulf of Mexico (see http://flowergarden.noaa.gov). These banks are the northernmost coral reefs in the continental United States. The footprint of the banks range from 2 km^2 to over 100 km^2 and the tops rise to within about 20 m of the sea surface from water depths of 100-150 m. The East Flower Garden Bank is part of the FGBNMS and is located about 192 km southeast of Galveston, Texas (Figure 1). The pear-shaped EFGB is about 5 km wide and 8 km in length. Slopes are steep on the eastern and southern sides of the bank and gentle on the western and northern sides. The shallowest depth on this bank is 18 m. The surrounding waters depths are about 100 m to the west and north and about 120 m to the east and south. The EFGB is located about 20 km east of the similarly-sized West Flower Garden Bank (WFGB).

The EFGB is home to a wide array of marine life, including numerous species of rays, sharks, sea turtles and marine mammals, over 170 species of fish and approximately 300 species of reef invertebrates (Gittings, 1998). The salt dome underlying the bank has furnished the framework for coral reef development, as well as providing a reservoir for oil and gas resources. Within a four-mile radius of the Flower Garden Banks, there are currently ten oil production platforms and there is one gas production platform within the East Sanctuary boundary. Maintaining this natural habitat is very important to the ecology of the Gulf of Mexico.

The role of the FGBs and their interactions in modifying the circulation and transport of materials is not well understood. These banks are large enough to alter the circulation on the outer shelf. Hydrodynamic processes on the reefs impact the dispersion and material transport of dissolved and particulate nutrients and of planktonic material (Wolanski et al., 1989). The extent to which bottom sediments can be resuspended and driven by strong current events and ultimately deposit contaminants onto low relief features of the banks is not known. The dynamics of current and topography interactions in controlling the dispersion of biological organisms and inorganic materials on the reefs and between the reefs are not well understood but may play a key role in reef habitat. Better understanding of the hydrodynamic processes that control material transport on reefs can provide marine managers with information necessary for the successful management of coral reefs as natural resources.

3. Data

Five ADCP moorings and four string moorings containing temperature, conductivity, and pressure (TCP) sensors were deployed around and on top of the EFGB (Figure 1) for a one-year period. Locations of the ADCP moorings M1-M5 and string moorings S1-S4, and bathymetry are shown in Figure 1. Note that M1, M2 and M4 were deployed near the same depths on the shelf (100 m – 110 m); M3 was deployed at a depth of about 127 m, while M5 was located near the top of the bank, just to the north of the peak of the bank, at a depth of 47 m. M1-M4 were deployed just outside of the EFGB boundaries (within a couple of hundred meters). The deployment cruise was conducted from December 7 to 13, 2010 and utilized the R/V Pelican, out of Cocodrie, Louisiana, approximately 350 km from the EFGB. The deployment period for these moorings was six months because of anticipated biological fouling and corrosive processes, particularly for instruments located at the shallower depths. Hence two deployments were required for the year-long measurement period. All of the moorings were successfully recovered during a Pelican cruise conducted from 26 May to 16 June of 2011. The data were downloaded, instruments were serviced and all five of the ADCP moorings and three of the four string moorings were redeployed for another six months with only a gap of 1 to 4 days in the data. The string mooring at S1 was not redeployed due to logistical problems. Finally, all of the moorings were recovered during a Pelican cruise that was conducted from December 6 to 12 of 2011.

The ADCPs were deployed on the bottom in trawl-resistant bottom mounts that utilized dome-shaped mounting pods, called Barnys because of their barnacle-like shape (Perkins et al., 2000). Barnys are highly resistant to trawling but trawling was not a problem next to the EFGB. However the Barny's donut structure is conducive to the moorings lying flat on the bottom and hence an optimum beam orientation. The orientation is verified with an attitude sensor prior to final release of the mooring on the bottom. The Barny mounts were equipped with RD Instruments Workhorse ADCPs operating at 300 kHz (M1-M4) or at 600 kHz (M5), Sea-Bird Electronics Model 26 wave/tide gauges, and EdgeTech acoustic releases for location and recovery. During the June turnaround cruise, wave/tide gauges for M2, M4, and M5 were replaced with high-frequency pressure sensors (ppods; Moum and Nash, 2008). Ppods will be used to measure the pressure drop across the EFGB in response to the flows over the bank and topographic form drag will be estimated in a future study. The ADCPs (transducer heads situated about 0.5 m off the bottom) recorded current profiles at 2 m vertical resolution at each mooring except for a resolution of 4 m at M3 every 12 or 15 minutes with an accuracy of 0.5% of the water velocity over nearly the full water column. Inherent to the ADCP design, side-lobe interference with the main lobes of the acoustic beams prevented determination of the velocity within about 5 to 10 m from the surface (depending on the water depth). The ADCP data records were complete (approximately 6-month records for each deployment period) with the exception of the data at M5 which recorded only 41 days of data at the start of the first half of the deployment but recorded a full record for the second half of the deployment. Very little editing was required for the current data. Water temperatures were recorded within the Barny with an accuracy of 0.01°C. The ppod and wave/tide gauge data will not be discussed here. For some of the analyses, high-frequency fluctuations (including tidal and inertial) were removed from the data by applying a low-pass filter with a 40 h half-amplitude point or cutoff frequency. The usual naming conventions are utilized: U positive towards the east and V positive towards the north. Table 1 provides a summary of the Barny mooring positions, time periods, sampling intervals, water depths, and instrument types.

Four TCP string mooring were deployed within about 200 m of Barny moorings at M1-M4 during the first half of the deployment and three were redeployed at M2-M4 during the second half of the mooring period. Each string contained eight to twelve sensors that recorded temperature and conductivity. Some of these also recorded pressure. The large majority of the instruments were Sea-Bird Electronics MicroCats (SBE37). Some In-Situ Aqua Trolls that recorded temperature, conductivity, and pressure were interspersed on each of the string moorings. The MicroCats sampled every 6 minutes with an accuracy of ±0.002°C and 3 µS/cm. The Aqua Trolls sampled every 12 minutes with lower accuracies of ±0.1°C and ±0.5% of reading + 1 µS/cm. The string data were low-pass filtered (0.5 h) and resampled at 15 min intervals. Several of the conductivity sensors failed towards the ends of the deployments due to biofouling. Records that ended prematurely but when between good records, located above and below, were vertically interpolated. TCP sensor types, nominal depths, and length of good data record from the beginning are listed in Table 2.

Meteorological wind observations were collected half-hourly at the southern edge of the EFGB at National Data Buoy Center Station 42047, and at Station 42046 located approximately 37 km west of the EFGB. Winds at 42046 were used when 42047 was out of service which was about half of the year-long mooring period. The data at the two buoys were quite similar during concurrent recording periods. Winds are shown as a vector stick plot and as a time series plot of speed in Figure 2. Wind velocities were smoothed using a 12-h running mean for both the speed and stick plot, but were subsampled every 6 hours for the stick plot. For January through May and September through December winds were dominated by north-south changes in direction caused by passage of numerous atmospheric fronts. From May through August winds were primarily from the southwest, south and southeast with strongest winds from the southeast. Winds during the deployment period were typical for this area (Cochrane and Kelly, 1986; Gutierrez de Velasco and Winant, 1996; Walker and Hammack, 2000). Note the persistent northerly episode between days 240 and 255. Figure 3 shows the clockwise (CW) rotary autospectrum of the wind data for each season: winter (January-March), etc. A significant peak in the diurnal frequency is present for the summer (July-September); low-frequency energy is lower for the summer than for the other seasons. Counterclockwise spectra (not shown) contain no peaks. The diurnal peak may be associated with a modulation of the wind field by sea breeze. Zhang et al. (2009) suggested that sea breeze can have effects as far as 300 km from the coast.

4. Statistics

Basic statistics for each ADCP mooring were computed for each half of the deployment period (mid-December 2010 through early June 2011 referred to as winter-spring, and early June 2011 through early December 2011 referred to as summer-fall) from the low-pass filtered data. Statistics for the top, several mid-level, and bottom velocity bins are shown in Table 3. The standard error listed here is defined as the standard deviation divided by the square root of the number of degrees of freedom, which is estimated as the sample period divided by the integral time scale. The integral time scale is defined as the discrete integral of the time-lagged autocorrelation function from zero lag to the first zero crossing after demeaning and detrending the time series.

Integral time scales during winter-spring for the U velocity component (omitting M5 due to the short record) generally were about one to two weeks in the upper water column and less than a week in the lower water column and near the bottom except for at M1 where time scales were longer throughout the water column. Periods of stronger eastward flow that occurred during the winter-spring period were less interrupted by the bank at M1 due to its location on the north side of the bank, and resulted in these longer time scales. Time scales for the V component were generally less than a week but were sometimes longer near the bottom for V than for U. Integral time scales during the summer-fall period for the U component were generally longer than for winter-spring near the surface (10 to 20 days) and somewhat shorter, from 2 to 5 days, near the bottom. Shorter time scales, mostly less than 5 days, for the V component throughout the water column were similar to those in the winter-spring period. The shorter time scales for the V component were related to the on and off shelf flows along the topography, perhaps influenced by shelf waves. The longer time scales for the U component corresponded primarily to periods of strong east-west velocity in the upper water column. Similar integral time scales were found in the northeastern Gulf of Mexico (Teague et al., 2006; Carnes et al., 2008) and for the alongshelf currents in the northwestern Gulf of Mexico (Nowlin et al., 2005).

East-west velocity components were generally larger than the north-south components. The maximum current speed observed over the entire deployment was 59 cm/s (at M3 near the surface) directed towards the east-northeast. The maximum current speed observed on top of the bank was 46 cm/s (near the surface) during both deployment periods. Average east-west velocity components generally decreased with depth while average north-south components often increased with depth. For moorings located off the bank, the maximum southward current velocity of -27 cm/s occurred near the bottom at M3. Standard deviations of U and V generally were of the same order or greatly exceeded the mean values. Hence, the means were often not well defined.

Mean eddy kinetic energy (EKE) off the bank for the winter-spring period ranged from a low of about 10 cm^2/s^2 near the bottom at M4 to a high of 73 cm^2/s^2 near the surface at M2, while on top of the bank at M5 mean EKE ranged from 26 to 78 cm^2/s^2. During summer-fall mean EKE off the bank ranged from 5 cm^2/s^2 near the bottom at M2 to 127 cm^2/s^2 at M3 while EKE ranged from 68 to 133 cm^2/s^2 on top of the bank at M5. Mean kinetic energy (MKE) off the bank for winter-spring ranged from less than 1 cm^2/s^2 at M4 to106 cm^2/s^2 at M2. On top of the bank at M5 (short record) MKE ranged from 98 cm^2/s^2 to 210 cm^2/s^2. MKE off the bank for summer-fall ranged from less than 1 cm^2/s^2 at M4 to 25 cm^2/s^2 at M2, while on top of the bank MKE ranged from 16 to 24 cm^2/s^2. EKE was dominant during summer-fall period while MKE was more dominant during winter-spring due to stronger east-west mean flows. The observed EKE's are similar to those observed near the shelf break in the northeastern Gulf of Mexico but the MKE's are generally more than twice as large as those observed in the northeastern Gulf (Teague et al., 2006; Carnes et al., 2008). The larger MKE values observed here are due to the dominant eastward flows.

Compass rose plots are shown for near surface and near-bottom velocities in Figure 4. Compass rose plots provide an angle histogram of the distribution of current speed and direction along the sixteen compass points (every 22.5 degrees). The length of each bin reflects the percentage of the number of observations in that direction and the color bar indicates the magnitude of the current speed distribution. For the winter-spring period the roses for the near surface currents (M1-M4; M5 not shown due to the short record) show eastward flow with the large majority of the flow between NE and SE and at least some currents in all directions. At mid-depths (excluding M5) currents began to align with the bathymetry (not shown). Roses for near the bottom show the currents aligning with the bathymetry, primarily offshore at M2 and M3 but a significant percentage of currents are also directed onshore. For the summer-fall period currents near the surface are also mostly eastward but were more evenly distributed in all directions. Deep currents for the summer-fall period are distributed similarly to the winter-spring period. However, the full record for M5 shows primarily eastward flow with some reversals.

For further illustration, progressive vector diagrams (pvds) were computed for two layers for both deployment periods (Figure 5; note that the pvd for M5 for the winter-spring period is only for the first 41 days). Velocities were averaged from approximately 80 m depth to near the surface for the top layer and from about 80 m to near bottom for the bottom layer, except for at M5 where the layer depth was 40 m. The pvd for the winter-spring period shows the predominately eastward flow in the top layer (red lines) and flow more aligned with the bathymetry in the bottom layer (blue lines). Compass rose plots show that although the bulk of the bottom layer flow was directed offshore, there are periods when it was onshore. The pvds indicate that the cumulative deep flows were strongest at M1 and M3. More off-shelf flow was found at M3 than at M2. At M4 the bottom layer flowed back toward the bank and then probably along the bathymetry. The kinks in the pvds occurring about midway in the winter-spring period, primarily in the upper layer, may be indicative of eddy processes over the bank. In addition, the pvds for the upper layer show mainly eastward flow until late in the summer-fall period, when the currents turned clockwise, suggesting a stronger eddy event.

5. Currents

Temporal means and principal variability ellipses (which express the variability about the means) were computed for each ADCP, for the entire period of the experiment. Ellipse parameters are presented as profiles of mean current speed and direction along with profiles of ellipse major/minor axes and ellipse orientation, as functions of depth in Figure 6. An ellipse centered on the tip of the vector representing the mean current velocity, reflects the area that is within one standard deviation of the mean. Higher variabilities, indicated by the major axes of the ellipses, are generally in the direction of the mean flows. Speeds of the means were similar and generally decreased with depth. At M3 there was a local speed minimum of about 2 cm/s near 70 m depth and a maximum of about 4 cm/s near 100 m depth. Directions of the means shallower than 70 m were nearly eastward. The variability ellipse axes generally decreased linearly with depth with major to minor axis ratios of about 2 to 1. Near the surface, ellipse orientations were essentially east-west. Below about 40 m orientations for M1 and M3 rotated CCW with depth from E-W to about SW-NE; for M2 and M4 orientations rotated CW to about NW-SE. The near-bottom ellipse orientations for M1-M4 are thus aligned with local bathymetry. Orientations for M5 remained close to zero (E-W), being confined to the upper 50 m. The major axes are essentially standard deviations of speed along an axis in the orientation direction, and provide a rough measure of uncertainty for the mean profiles. Hence, deeper than about 70 m, mean speeds were significantly lower than the major axis profiles and corresponding directions (of the means) were more unreliable.

Monthly averages of U and V component profiles are presented in Figure 7. The U component dominated except for October – December where V components had similar magnitudes to U components. Lowest velocities occurred in March. Sometimes there were fairly constant velocity layers near the surface. Layers of near constant velocity also occurred near the bottom. Velocity-shear gradient layers that extended from near the surface to near the bottom occurred in February and March, and between the surface and bottom layers when present. Subsurface velocity minima and maxima occurred throughout the water column. U components were eastward in the upper water column except for October and November. V components were generally small in both directions except for during October to December where the V components were directed mainly southward and were similar in magnitude to the U component. Cross-shelf exchange could have occurred during this time period. Largest average velocities were not confined to the top of the bank.

Sections of low-passed filtered (40h) U and V velocity components as a function of time and depth are shown for each of the Barny moorings in Figure 8a (U component) and in 8b (V component). Eastward flows along the shelfbreak dominated the circulation pattern. There were periods of westward flow during March (days 60-80), October (days 270-300), and November (days 310-330). The westward flows can perhaps be attributed either to small cyclonic eddies that were generated from processes associated with a nearby LC Ring or by storm events. Vorticity computed between currents at M2, M3, and M4 (Figure 9) displayed large positive peaks (near days 60, 280, and 330) for westward-flow time periods and are suggestive of cyclonic eddies. Sea-surface heights (SSHs) from altimetry suggested that the LC extended well into the northern Gulf during October 2011. However, temporal resolution of the altimetry tracks of about 10 days and spatial resolutions of the tracks of about 7 km along track and tens of km between tracks were not adequate in resolution to resolve eddies with diameters on the order of 10 km.

SSHs and sea-surface temperatures are assimilated by NRL’s Intra-Americas Sea Nowcast/Forecast System (IASNFS) (Ko et al., 2008). Hence, the model can provide a reasonable broad picture of the eddy field. Currents and temperature at 50 m depth from this model are shown in Figure 10 for October 18, 2011 (day 290). The LC extended well into the Gulf of Mexico (edge is shown in Figure 10 at about 26°N and 88°W) with a detached anticyclonic warm core ring near 25°N and 92°W. There are a series of anticyclones and cyclones depicted by the model between the LC and the detached warm ring. The model resolved a small cyclonic eddy depicted south of the EFGB and north of the warm ring (approximately at 27.7°N and 93.5°). The horizontal scale of the eddy was on the order of 50 to 75 km. The eddy remained in the vicinity of the bank for about two weeks. The IASNFS was used here to provide a perspective on the larger scale circulation at the time and to suggest what processes impacted those around and on the EFGB. A very similar pattern of cyclonic and anticyclonic eddies were also revealed in SSH data (posted at http://www.esl.lsu.edu). The cyclonic eddy appeared larger in the SSH data than in the model depictions. The main advantage of the model is that the current patterns are revealed.

The 3 major tidal components in this region are M2, K1, and O1 (DiMarco and Reid, 1998) which have periods of 12.42, 23.93, and 25.82 hours, respectively. Our measurements revealed amplitudes of these tides ranging between 3 and 5 cm/s, similar to the findings of DiMarco and Reid (1998). The inertial period at the EFGB is approximately 25.58 h which is near the O1 period. Intense inertial oscillations were found from April through August (days 90 to 230) (Figure 11). Amplitudes of the inertial oscillations were often larger than tidal amplitudes and exceeded 15 cm/s. Inertial amplitudes could be modified by diurnal tides, depending on the phase difference. However the amplified inertial amplitudes occurred mainly during summer months and were likely associated with a near-resonant response to sea breeze (Zhang et al., 2009, Jarosz et al., 2007) as evidenced by the peak during summer in the CW rotary wind autospectrum (Figure 3). The generally observed eastward flow was reversed towards the west during this period when the amplitudes of the inertial oscillations exceeded the background eastward flow. Since the reversals may only last a few hours, they were not resolved in the plot of the filtered velocity sections (Figure 8). The direction of the V component of velocity, reflective of on-shelf and off-shelf flow, was greatly affected by the inertial oscillations, as reversals in V occurred throughout the entire deployment period.

The contribution of the inertial, diurnal tide, and higher frequency kinetic energies (referred to as HFE) is shown by the ratio of HFE to total current kinetic energy in Figure 12. The HFE is computed from the square of the total currents minus the 40-hr low-passed currents. The HFE ranged from about 20% to 40% of the total energy in the upper 40 m to about 30% to 80% of the total energy in the lower water column, and was often near maximum close to the bottom. Interestingly, the ratio of HFE to total kinetic energy was largest at moorings M2 and M4. The lower ratio in the upper water column may be reflective of the more dominant wind driven circulation while the higher ratio in the lower water column may indicate relatively stronger inertial and diurnal tide contributions. The presence of the bank likely drives this distribution of energy.

Current vector stick plots for near bottom levels at M1–M5 were computed from the 40-h low-passed data (subsampled every 12 h) and are shown in Figure 13. Visual inspection of these plots suggests the presence of continental shelf waves at M1–M4. Shelf waves have frequencies less than the local inertial frequency and wavelengths much greater than the water depth. They have been observed through analyses of pressure and current records (Mooers and Smith, 1968; Cutchin and Smith, 1973; Gill and Schumann, 1974; McGrail and Carnes, 1983; Halper et al., 1988). Current fluctuations due to shelf waves can be comparable to or larger than fluctuations due to tides (Kubota, et al., 1981). Some of the forcing mechanisms for the generation of shelf waves include tropical cyclones, winds, atmospheric pressure fluctuations and tides. The spectrum for the V component of velocity for M3 near the bottom is shown in Figure 14. The semi-diurnal tide and diurnal tide /near inertial bands are clearly represented by sharp peaks in the spectrum. In addition, there are two broader peaks, at 60 and 96 hours, which may be related to the shelf waves. The largest non-tidal peak (96 hours) occurs in the V component, the component directed cross-shelf. Correspondingly there is a broad peak in the spectra for the U component of the winds between 48 and 120 hours (spectra not shown) suggesting that the shelf waves are forced by the local winds. The low-frequency current oscillations due to the shelf waves can cause sediment resuspension and contribute to cross-shelf transport of fine sediment. Further analyses of these possible shelf waves are not presented here.

Coherences were computed between the currents over their full depth range and east-west (EW) and north-south (NS) wind stresses (not shown). The V current components were marginally coherent with the wind stress. The U current components, however, were influenced by the winds over the bank. The winds highly impacted (multiple coherences up to 66%) currents in the upper 20 m near frequencies associated with periods of a week to ten days, which is suggestive of some wind effects on the surface currents associated with frontal passages. Results from coherence analyses also show that the EW current fluctuations at these periods of about a week to ten days were significantly coherent with the NS wind stress but not so with the EW wind stress, suggesting that the current fluctuations are influenced by the cross-shelf wind-stress component. These results may seem contrary to results presented by Cochrane and Kelly (1986). They suggest that the currents in general west of 92.5° W are influenced primarily by the alongshore component of the wind stress but are more weakly influenced east of 92.5° W. However, their coherency spectra also shows that the cross-shelf wind stress is significant with both the alongshore and cross-shelf currents at periods of about ten days in agreement with our results.

To investigate large-scale features of the currents and to explore the extent to which the velocities at different depths are correlated an empirical orthogonal function (EOF) analysis was conducted. The larger scale correlated modes of motion over and around the bank are extracted in order to provide a simpler picture of the dominant current variability. At each ADCP location an EOF analysis was done on U(z,t) and V(z,t) (functions of depth (z) and time (t)). To compute EOFs for both velocity components simultaneously, U and V were further concatenated to form a single array (at each ADCP location): UV=[U(z,t),V(z,t)], which was then analyzed as a scalar array. This method is described by Preisendorfer (1988) and Kaihatu et al. (1998). The method yields a set of eigenfunctions (EOFs; functions of z, mode) and principal components (PCs; functions of t, mode). The resulting eigenfunctions were separated into U and V parts and speed and orientation profiles formed for each mode; as with principal ellipses, an orientation of θ is equivalent to $\theta+180^{\circ}$. The eigenfuctions were dimensionalized by multiplication by the square root of the eigenvalue. These then yield magnitudes and orientations of the fluctuations associated with each mode. Modes 1 and 2 accounted for at least 70% of total variance; M5 was significantly higher since the data were limited to the upper ~50 m where depth dependence was minimal. Mode 1 accounted for at least 53% of all variance and was clearly dominant compared to Mode 2 whose maximum was about 20%.

Shallower than about 50 m mode 1 magnitudes were at their largest and indicated that velocities in this depth interval were vertically correlated (the M5 profiles fell off above 50 m, due to the proximity of the bottom), and may indicate a frictional (Ekman) layer. Orientations above 50 m were ~E-W, as for the principal ellipses. Below 50 m, profile magnitudes for M2 and M4 fell off more rapidly than for M1 and M3, indicating lower vertical correlations with shallower depths for M2 and M4; this difference was likely due to the greater rotation with depth, from E-W, required for deep velocities to be aligned with the constraint of local bathymetry at these locations. The orientation profile for M1, rotated slightly with depth to about WSW-ENE; for M3, it rotated further to about SW- NE. At all locations, mode 1 PCs were highly correlated (at least 0.97) with the depth-averaged eastward (U) velocity. A second EOF analysis was done using velocity anomalies about vertical averages at each location, to better isolate baroclinic variability. The results were not quite as robust (explained variances for mode 1 are about 40%-45%). The mode 1 eigenfunction magnitude profiles for M1-M4 nearly overlay each other and ranged from maxima of about 5 cm/s near surface and bottom, with zero crossings near 55 m; for M5, the profile was similar, but shallower. Orientations profiles for this case were also mainly E-W. Correlation coefficients between mode 1 PC series for M1-M4 showed agreement, which was due mainly to the shallower E-W variability. The lowest value (0.63) was for M3 and M2, located near the southern edge of the bank. The largest value (0.91) was for M1 and M4, located north and east of the bank, respectively.

6. Temperature and Salinity

Temperature sections, smoothed over 6 hours, are shown in Figure 15. The vertical striping near the diurnal tidal frequency throughout the records could have been enhanced by the inertial oscillations. Salinity measurements were quite noisy and high-resolution salinity sections are not shown. String sensors were subject to heavy biofouling noted during their recovery. Conductivity measurements were most affected and there were numerous spikes and drifts in the calculated salinity. However, low-resolution salinity time series are shown in Figure 16b. Here the salinity was filtered with a median filter that was one-day long and then a single point was plotted for each day. The median filter effectively eliminated borderline wild points and should provide a more realistic salinity. The temperature time series were correspondingly filtered for comparison with the salinity time series and are shown in Figure 16a. There was little stratification in the water column from the beginning of the deployment to about day 90 (March 31). Temperature range over the water column was only about 3°C while the salinity range was generally less than 1 psu and sometimes much less (S4, day 40, about 0.2 psu). Stratification gradually increased from day 90 to day 250 (March 31 to September 7) where temperature ranged about 12°C over the water column, and then decreased back to the range observed during beginning of the deployment (in December 2010 and 2011). Drifts in salinity may have occurred for some of the instruments after day 200 (July 19). However, similar patterns of decreasing salinity occurred at each of the string moorings, suggesting that at least the trend of decreasing salinity may be real. In addition, the decreasing salinity trend appeared mostly in the lower water column where biofouling was not as much of an issue as in the upper water column.

Temperature over the entire year ranged from about 16° to 30°C while salinity ranged from about 34 psu to almost 37 psu. Salinity values were typically greater than 36 psu, reflective of salinities off the shelf and south of the bank. The observed annual temperature range agrees with historical data, e.g., Lugo-Fernández (1998); but the salinity range observed is smaller than at other times, see Deslarzes and Lugo-Fernández (2007) and references therein. However, salinities within a few meters of the surface were not measured. Historically, the low salinity events tend to have salinities of 30-33 psu that occur near summer maxima in surface temperature but associated with a temperature drop (Deslarzes and Lugo-Fernández, 2007).

Two periods in which salinities were significantly lower than usual in the upper water column occurred approximately between days 90 and 120 (March 31 and April 30) and days 150 and 200 (May 30 and July 19). During the first event, the salinities decreased to about 35 psu and during the second event they decreased to about 34 psu. The two low salinity events were associated with warmer water in the top part of the water column (Figure 15). The generation mechanism for this type of event could possibly be entrainment of shelf water by an eddy at the shelf edge. In addition, a relatively low temperature range of about 2°C throughout the water column was observed between days 40 and 60 (February 9 and March 1) (Figures 15 and 16a). The salinity time series (Figure 16b) show a few salinities lower that 36 ppt during this time period. The cooler and less saline water was likely transported by southwestward currents (Figure 8) over the bank by eddy activity since the winds were mostly out of the south (Figure 2).

Bottom temperatures acquired from the ADCPs in the Barny moorings are shown in Figure 17. Similar patterns in temperature fluctuations were found between the moorings. Records for M1-M4 show similar low-frequency variations; of these, the largest differences were exhibited by M3, which was deployed closer to the shelf break and 25-30 m deeper than the other 3. The record from M5 was from shallower than 50 m and shows an overall higher temperature and more variability than the deeper records. Interestingly, a sudden temperature drop of about 6°C (29°C to 23°C) occurred over two days (days 236 to 238) at M5 located on top of the bank. Drops of 2 to 3°C also occurred at about the same time at each of the other moorings. A second drop in temperature closely followed. Temperatures at M5 fell to 22°C at day 246 and near the same time fell 3 to 4°C at M3 and M4, with low temperatures of 14°C and 15°C recorded at M3 and M4, respectively. Temperature at M2 fell less than a degree. At approximately day 250, the temperature at M5 increased by about 7°C (21°C to 28°C) over a period of about four days (days 246 to 250) which is also evident to a lesser degree at each of the other moorings. A similar, but less extreme, temperature fluctuation began at day 260.

These drops in temperature were evident in the temperature sections (Figure 15) over most of the water column. From the temperature section for S3-D2 (Figure 15), colder water from approximately 75 m depth rose 30 m to about 45 m depth (days 236-238). The temperature time series (Figure 16a) also showed these drops in temperatures at each of the string moorings. In particular, significant drops in temperature occurred at S3 and S4 where anomalous temperatures of 14° and 15°, respectively, were also observed near the bottom. Corresponding drops in salinity to about 35.5 psu (Figure 16b) were found in conjunction with the temperature drops.

There is evidence that the temperature and salinity drops were wind related. At M3, between depths of about 60 m and the bottom, relatively strong southwestward currents (Figure 8) were observed for several days around day 250, aligned with the topography of the bank.

These currents may have been in response to a storm event that lasted about a week and winds peaked at about 27 kts (14 m/s; Figure 2 near day 250). Hence, less saline shelf water over the EFGB was likely driven from the inner shelf by winds. Movement of low salinity pools of water off the inner shelf by strong north winds have been described in detail and referred to as “squirts” by Walker et al. (1996). The cooler waters observed here near the bottom at the EFGB must have originated in deeper water off the shelf and were likely due to upwelling or vigorous mixing induced by the strong event of southwestward winds that rotated to southeastward during the event. Climatological temperature profiles (Boyer et al., 2009), and temperature sections just south of the EFGB by McGrail and Carnes (1983) and Nowlin and Parker (1974) show that the 14° waters are typically found at 200 m water depth. Therefore, water at depths of at least 200 m can be mixed into the upper water column and hence affect the upper portions of the EFGB.

For calculation of mixed-layer depth (MLD), the temperature profiles from the string moorings, each consisting of about ten observations over the water column, were interpolated to one-meter intervals. Temperatures were not extrapolated to the surface. The MLD was then set at the depth level where the temperature changed by at least 0.25° C from the shallowest temperature measurement. Upon visual inspection of typical individual temperature profiles, this criterion provided reasonable MLDs over the entire data set. To reduce the higher frequency variability, the MLDs were smoothed over about a day. The average MLD over all the strings was also computed and a five-day boxcar average was applied to reduce the daily variability. The MLDs are shown in Figure 18 for each of the string moorings, along with their composite five-day average. MLDs ranged from about 60 to 80 m from mid-December 2010 until February 2011 and then MLDs rapidly decreased to less than 20 m over a period of about two days. This large change in MLD was associated with the cyclonic eddy discussed in Section 5. The MLD increased to over 50 m as the eddy moved out and decreased to 20 to 40 m until mid-October where it gradually increased to 60 to 80 m toward the end of the deployment period in December 2011. The mixed layer was deepest during the months of December and January) and ranged from about 60 to 80 m in depth. MLDs ranged between 20 and 40 m for much of the year (March to October). November appeared to be a transition month (at least for 2011) where the MLD increased to depths greater than 60 m. Fluctuations in the MLD of 10 to 20 m at periods of about a week were likely related to atmospheric frontal passages. This seasonal cycle of the mixed layer at the FGB is similar to that reported by McGrail (1983). Deepening of the MLD occurred from December to February and then rapidly decreased. This trend in MLD during this time period may be related to reduced solar heating and increased wind mixing and has been observed in the data from Kara et al. (2003) and Monterey and Levitus (1997).

7. Summary

The EFGB interrupted the along shelf current flow and resulted in a two-layer current system in the vicinity of the bank. Currents at the EFGB were generally eastward throughout the year in the upper part of the water column above the sill of the bank but were reversed for periods from a day to a week or more by cyclonic eddies impinging on the edge of the shelf. These cyclonic eddies may have originated as LC frontal eddies that were transferred to warm core rings upon separation. The currents were reversed to westward flow in the upper water column from a few days to several weeks during March (days 60-80), October (days 270-300), and November (days 310-330). The bank impacted the flow in the lower water column and the flow followed the bathymetry. Near-bottom currents at the southwestern (M2) and southeastern (M3) corners of the bank were mostly directed offshore throughout the year in southeastward and southwestward directions, respectively, following the bathymetry. Average southward or offshore currents in the lower layer of the water column were sometimes comparable or larger than the east-west currents in the upper water column. The maximum observed offshore (onshore) velocity was 27 cm/s (20 cm/s). The region just south of the EFGB could be an area of convergence for the deep offshore flow. Integral time scales for the cross-shelf flows generally ranged from 3 to 5 days throughout the water column while the time scales for the along-shelf flows were longer and ranged from about a week to more than two weeks.

The main tidal components were M2, K1, and O1 but tidal currents were weak at the EFGB. However, inertial currents (periods near the O1 tide) were often significant and could reverse the generally eastward low-frequency surface flows for a few hours when these background currents were weak. The inertial currents are enhanced during summer when in phase with wind modulations due to sea-breeze effects and can easily exceed 20 cm/s. Since the radius of the bank is only about 4 km, a 10 cm/s current can move matter from the top of the bank to off the bank in about half a day. Nevertheless, these westward-induced short-term currents are not persistent enough for direct westward advection of particle off the bank to other banks.

Some correlations with the winds were found. However, the generally eastward current flow over the EFGB was not correlated with EW wind stress but likely is the southern limb and return flow of the cyclonic gyre on the Louisiana-Texas shelf that is driven by westward winds on its northern limb (Cochrane and Kelly, 1986). A significant southward component of the flow through much of the water column was caused by a storm event in September. During this event, the correlation of the southward flowing currents with winds blowing from the north was high and lower salinity shelf waters were driven from the inner shelf to over the EFGB. Interestingly, EW current fluctuations at periods of about a week to ten days were significantly coherent with the NS wind stress (cross-shelf wind-stress component) but not so with the EW wind stress.

Mixed layers often extended to the bottom on top of the bank and ranged from as shallow as 10 m to deeper than 80 m just off the bank. Mixed-layer depths changed rapidly and were observed to shallow from about 80 m to 20 m in less than two days due to an eddy passage that transported cooler shelf water over the bank. Mixed layers were deepest (60 to 80 m) during December and January and generally ranged between 20 and 40 m for much of the year. November was the transition month for the seasonal deepening of the mixed layer.

The southward deep flows at the southern edge of the EFGB in conjunction with the well-known westward motion of LC warm core eddies, and associated cyclonic and anticyclonic eddies, may be a major conduit for shelf water exchange between the Flower Gardens and rest of the Gulf. Conversely, the less-frequent northward deep flows at the southern edge of the bank can transport deep ocean water onto the shelf and Flower Gardens. Offshore flows at the EFGB were largest in the October to December time period for 2011. Much of the cross-shelf exchange is likely to occur in the lower-water column and near the bottom. Eddies don’t necessarily have to pass directly over the bank to transfer particulates that reside on the bank since they can entrain the offshore flow. Upwelling in response to storms can also transport cooler deeper waters onto the shelf. One such event was observed during a high wind period during September where 14°C water was upwelled from depths exceeding 200 m onto the shelf. In addition, shelf waves may contribute to the shoreward and offshore flows near the bottom. Numerous other banks in the Flower Garden Sanctuary can then be affected, as well as other regions in the Gulf of Mexico and in the Atlantic Ocean through eddies and the LC connectivity as shown herein and by Lugo-Fernández et al. (2001) and Lugo-Fernández (2006). Similar processes should also be common at the WFGB, similarly located at the shelf edge. Upper layer currents generally did not reverse towards the west for long enough periods to connect the EFGB with the WFGB. However, connections between the EFGB to the WFGB can be made through the train of westward propagating eddies, as discussed by Lugo-Fernández et al. (2001) using surface drifters. The WFGB can also connect with the EFGB through the generally eastward upper-layer flows. Connectivity between the banks is expected to be higher during LC ring passages.

Acknowledgements

This work was sponsored by the Bureau of Ocean Energy Management (BOEM; formerly Minerals Management Service) in the project referred to as “Currents Over Banks (COB)” through Interagency Agreement No. M10PG00038 and by the Office of Naval Research in a Naval Research Laboratory (NRL) project referred to as “Mixing Over Rough Topography (MORT)”. The measurements were made in cooperation with the Flower Garden Banks National Marine Sanctuary (administered by the National Oceanic and Atmospheric Administration (NOAA)). Thanks are extended to our mooring team of Mark Hulbert, Andrew Quaid, and Justin Brodersen of NRL, and to Steve Sova of QinetiQ.

References

Beard, D.W., 1984. Wind-induced circulation on the outer continental shelf of Texas, Spring 1982. M.S. thesis, Department of Oceanography, Texas A&M University, College Station, Texas, 128 pp.

Boyer, T.P., Antonov J.I., Baranova, O.K., Garcia, H.E., Johnson, D.R., Locarnini, R.A., Mishonov, A.V., O’Brien, T.D., Seidov, D., Smolyar, I.V., Zweng, M.M., 2009. World Ocean Database 2009, S. Levitus (ed.), NOAA Atlas NESDIS 66, U.S. Gov. Printing Office, Wash., D.C., 206 pp.

Brooks, D.A., 1983. The wake of Hurricane Allen in the western Gulf of Mexico. Journal of Physical Oceanography 13, 117-129.

Blaha, J., Sturges, W., 1981. Evidence for wind-forced circulation in the Gulf of Mexico. Journal of Marine Research 39 (4), 711-734.

Carnes, M.R., Teague, W.J., Jarosz, E., 2008. Low-frequency current variability observed at the shelfbreak in the northeastern Gulf of Mexico: November 2004-May 2005. Continental Shelf Research 28 (3), 399-423, DOI: 10.1016/j.csr.2007.10.005.

Chen, C., Reid, R.O., Nowlin, W.D., Jr., 1996. Near-inertial oscillations over the Texas-Louisiana shelf, Journal of Geophysical Research 101, 3509-3524.

Cho, K., Reid, R.O., Nowlin, W.D., Jr., 1998. Objectively mapped steam function fields on the Texas-Louisiana shelf based on 32 months of moored current meter data. Journal of Geophysical Research 103 (C5), 10,377-10,390.

Cochrane, J.D., Kelly, F.J., 1986. Low-frequency circulation on the Texas-Louisiana continental shelf. Journal of Geophysical Research 91, 10645-10659.

Cutchin, D.L., Smith, R.L., 1973. Continental shelf waves: Low-frequency variation in sea level and currents over the Oregon continental shelf. Journal of Physical Oceanography 3, 73-82.

Daddido, E., Wiseman, W.J., Murray, S.P., 1978. Inertial currents over the inner shelf near 30 N. Journal of Physical Oceanography 8, 728-733.

Deslarzes, K.J.P., Lugo-Fernández, A., 2007. Influence of terrigenous runoff on offshore coral reefs: An example from the Flower Garden Banks, Gulf of Mexico. In: Aronson R.B. (Ed.), Geological approaches to coral reef ecology: placing the current crises in historical context. Springer Verlag, pp. 126-160.

DiMarco, S.F., Reid, R.O., 1998. Characterization of the Principal Tidal Current Constituents on the Texas-Louisiana Shelf. Journal of Geophysical Research 103, 3093-3109.

Dodge, R.E., Lang, J.C., 1983. Environmental correlates of hermatypic coral (Montastrea annularis) growth on the East Flower Gardens Bank, northwest Gulf of Mexico. Limnology and Oceanography 28, 228-240.

Gill, A.E., Schumann, E.H., 1974. The generation of long shelf waves by the wind. Journal of Physical Oceanography 4, 83-90.

Gittings, S.R., 1998. Reef community stability on the Flower Garden Banks, northwest Gulf of Mexico. Gulf of Mexico Science 16, 161-169.

Gutierrez de Velasco, G., Winant, C.D., 1996. Seasonal patterns of wind stress and wind stress curl over the Gulf of Mexico. Journal of Geophysical Research 101, 18,127-18140.

Halper, F.B., McGrail, D.W., Merrell, W.J., Jr., 1988. Seasonal variability in the currents on the outer Texas-Louisiana shelf. Estuarine, Coastal and Shelf Science 26, 33-50.

Hamilton, P., 1992. Lower continental slope cyclonic eddies in the central Gulf of Mexico. Journal of Geophysical Research 97, 2185-2200.

Hamilton, P., Berger, T.J., Johnson, W., 2002. On the structure and motions of cyclones in the northern Gulf of Mexico. Journal of Geophysical Research 107 (C12), Art. No. 3208.

Jarosz, E., Murray, S.P., 2005. Velocity and transport characteristics of the Louisiana-Texas coastal current. Circulation in the Gulf of Mexico: Observations and Models, Geophysical Monograph Series 161, American Geophysical Union, 10.1029/161GM11.

Jarosz, E., Hallock Z.R., Teague, W.J., 2007. Near-Inertial Currents in the DeSoto Canyon Region. Continental Shelf Research 27, 2407-2426.

Kaihatu, J.M., Handler, R.A., Marmorino, G.O., Shay, L.K., 1998. Empirical orthogonal function analysis of ocean surface currents using complex and real-vector methods. Journal of Atmospheric and Oceanic Technology 15, 927-941.

Kara, A. B., Rochford, P.A., Hurlburt, H.E., 2003. Mixed layer depth variability over the global ocean. Journal of Geophysical Research 108, 3079, doi:10.1029/2000JC000736.

Ko, D.S., Martin, P.J., Rowley, C.D., Preller, R.H., 2008. A real-time coastal ocean prediction experiment for MREA04. Journal of Marine Systems 69, Issues 1-2, 17-28, http://dx.doi.org/10.1016/j.jmarsys.2007.02.022.

Kubota, M., Nakata, K., Nakamura, Y., 1981. Continental shelf waves off the Fukushima Coast Part I: Observations. Journal of the Oceanographical Society of Japan 37, 267-278.

Lugo-Fernández, A., 1998. Ecological implications of hydrography and circulation to the Flower Garden Banks, northwest Gulf of Mexico. Gulf of Mexico Science 16:144-160.

Lugo-Fernández, A., 2006. Travel times of passive drifters from the western Caribbean to the Gulf of Mexico and Florida-Bahamas. Gulf of Mexico Science 24, 61-67.

Lugo-Fernández, A., Deslarzes, K.J.P., Price, J.M., Boland, G.S., Morin, M.V., 2001. Inferring probable dispersal of Flower Garden Banks coral larvae (Gulf of Mexico) using observed and simulated drifter trajectories. Continental Shelf Research 21, 47-67.

McGrail, D.W., Carnes, M., 1983. Shelfedge dynamics and the nepheloid layer in the northwestern Gulf of Mexico. SEPM Special Publication 33, 251-264.

McGrail, D.W., 1983. Flow, boundary layers, and suspended sediment at the Flower Garden Banks. In: Rezak, R., Bright, T.J, McGrail, D.W. (Eds.), Reefs and banks of the northwestern Gulf of Mexico: their geological, biological, and physical dynamics. Final Report, Technical Report No. 83-1-T., U.S. Department of the Interior, Minerals Management Service, Gulf of Mexico OCS Regional Office, New Orleans, LA, pp 141-230

Monterey, G., Levitus, S., 1997. Seasonal variability of mixed layer depth for the world ocean, NOAA Atlas NESDIS 14, 100 pp., U.S. Govt. Print. Off., Washington, D.C., 1997.

Moum, J.N., Nash, J.D., 2000. Topographically induced drag and mixing at a small bank on the continental shelf. Journal of Physical Oceanography 30, 2049-2054.

Moum, J.N., Nash, J.D., 2008. Seafloor pressure measurements of nonlinear internal waves. Journal of Physical Oceanography 38, 481-491.

Mooers, C.N.K., Smith, R.L., 1968. Continental shelf waves off Oregon. Journal of Geophysical Research 73, 549-557.

Nowlin, W.D., Jr., Parker, C.A., 1974. Effects of a cold-air outbreak on shelf waters of the Gulf of Mexico, Journal of Physical Oceanography 4, 467-486.

Nowlin, W.D., Jr., Jochens, A.E., Reid, R.O., DiMarco, S.F., 1998. Texas-Louisiana Shelf Circulation and Transport Process Study: Synthesis Report, LATEX A. OCS Study MMS 98-0035 and MMS 98-0036, vols. I and II, U.S. Department of the Interior, Minerals Management Service, Gulf of Mexico OCS Region, New Orleans, Louisiana.

Nowlin, W.D., Jr., Jochens, A.E., DiMarco, S.F., Reid, R.O., Howard, M.K., 2005. Low-frequency circulation over the Texas-Louisiana continental shelf. Circulation in the Gulf of Mexico: Observations and Models, Geophysical Monograph Series 161, American Geophysical Union, 10.1029/161GM17.

Oey, L.-Y., 1995. Eddy and wind-forced shelf circulation. Journal of Geophysical Research 100, 8621-8637.

Perkins, H., De Strobel, F., Gauldesi, L., 2000. The barny sentinel trawl-resistant ADCP bottom mount: design, testing, and application. IEEE Journal of Oceanic Engineering 25, 430–436.

Price, J.F., 1976. Several aspects of the response of shelf waters to a cold front passage. Memoires Societe des Sciences de Liege, 6e series X, 201-208.

Preisendorfer, R.W., 1988. Principal Component Analysis in Meteorology and Oceanography. Elsevier, 425 pp.

Rezak, R., Gittings, S.R., Bright, T.J., 1990. Biotic assemblages and ecological controls on reefs and banks of the northwest Gulf of Mexico. American Zoologist, 30, 23-35.

Sahl, L.E., 1984. Suspended sediment on the upper Texas continental shelf. Ph.D Dissertation, Department of Oceanography, Texas A&M University, College Station, Texas, 184 pp.

Sturges, W., Blaha, J.P., 1976. A western boundary current in the Gulf of Mexico. Science 192, 367-369.

Teague, W.J., Jarosz, E., Carnes, M.R., Mitchell, D.A., Hogan, P.J., 2006. Low-frequency current variability observed at the shelfbreak in the northeastern Gulf of Mexico: May-October 2004. Continental Shelf Research 26, 2559-2582.

Walker, N.D., Huh, O.K., L.J., Rouse, Jr., and Murray, S.P., 1996. Evolution and structure of a coastal squirt off the Mississippi River delta: Northern Gulf of Mexico. Journal of Geophysical Research 101, C9, 20,643-20,655.

Walker, N. D., and Hammack, A.B., 2000. Impacts of winter storms on circulation and sediment transport: Atchafalaya–Vermillion Bay Region, Louisiana, U.S.A., Journal of Coastal Research., 16, 996–1010.

Wolanski, E., Burrage, D., King, B., 1989. Trapping and dispersion of coral eggs around Bowden Reef, Great Barrier Reef, following mass coral spawning. Continental Shelf Research 9, 479–496.

Zhang, X., DiMarco, S.F., Smith IV, D.C., Howard, M.K., Jochens, A.E., Hetland, R.D., 2009. Near-Resonant Ocean Response to Sea Breeze on a Stratified Continental Shelf, Journal of Physical Oceanography 39, 2137-2155.

Figures and Tables

Table 1. ADCP Mooring Summary.
Columns correspond to Mooring number, Latitude, Longitude, start day and end day in 2010-2011, sampling interval in minutes (dt), depths (in m) of top velocity bin (z1) and bottom velocity bin(zn), and bin interval (dz), water depth in m, and ADCP frequency.

	LAT	LON	St day 2010/2011	End day 2011	dt min	z1 m	zn m	dz m	Depth m	Type
M1-D1	27.975	-93.632	342	152	12	12	98	2	101	300kHz
M1-D2	27.971	-93.630	153	342	15	8	91	2	98	300kHz
M2-D1	27.906	-93.640	343	151	12	12	102	2	106	300kHz
M2-D2	27.907	-93.640	152	342	15	11	100	2	105	300kHz
M3-D1	27.896	-93.569	343	151	12	12	120	4	127	300kHz
M3-D2	27.896	-93.569	152	342	15	16	116	4	127	300kHz
M4-D1	27.952	-93.581	343	151	12	12	102	2	106	300kHz
M4-D2	27.952	-93.581	152	342	15	11	101	2	106	300kHz
M5-D1	27.935	-93.600	343	19	12	6	43	2	47	600kHz
M5-D2	27.935	-93.600	152	342	15	6	43	2	47	600kHz

Table 2. String Mooring Summary.
Columns correspond to String Mooring number, Latitude, Longitude, start day and end day in 2010-2011, top instrument level (top-z) and near-bottom instrument level (bot-z) in m, water depth in m, number of instruments (no), and Type of instruments (and number of) (MC – SeaBird MicroCat); AT—In-Situ Aqua Trolls).

	LAT	LON	St day 2010/2011	End day 2011	top-z m	bot-z m	Depth m	no	Type
S1-D1	27.974	-93.634	343	153	7	101	102	11	8MC, 3AT
S2-D1	27.905	-93.643	344	161	11	107	108	12	8MC, 4AT
S2-D2	27.905	-93.643	162	342	8	106	107	10	8MC, 2AT
S3-D1	27.895	-93.570	346	158	12	128	129	13	9MC, 4AT
S3-D2	27.895	-93.570	161	341	10	128	129	13	9MC, 4AT
S4-D1	27.951	-93.577	344	158	12	104	106	10	8MC, 2AT
S4-D2	27.951	-93.577	162	341	12	106	107	11	8MC, 3AT

Table 3. Basic statistics over the winter-spring (D1) and summer-fall (D2) periods for selected depth levels. Columns correspond to mooring, measurement depth z, average current component $\overline{U}$, standard deviation σ_u, standard errors SE_u, minimum u value U_{min}, maximum u value U_{max}, and similarly for V, maximum speed S_{max}, direction of the maximum speed D_{max}, integral time scales IT_u and IT_v, mean kinetic energy MKE and mean eddy kinetic energy EKE. Units are cgs.

	z	$\overline{U}$	σ_U	SE_U	U_{min}	U_{max}	$\overline{V}$	σ_V	SE_V	V_{min}	V_{max}	S_{max}	D_{max}	IT_U	IT_V	MKE	EKE
M1-D1	12	13.76	10.49	2.35	−18.11	41.49	1.11	5.05	0.76	−12.47	23.06	41.5	91.02	8.59	3.9	95.35	67.73
M1-D1	20	13.13	10.02	2.46	−18.21	37.54	0.47	5	0.77	−14.29	21.55	37.54	90.92	10.34	4.08	86.37	62.67
M1-D1	40	12.04	9.25	2.85	−12.76	35.32	0.47	4.39	0.69	−14.25	17.16	35.36	93.11	16.25	4.22	72.65	52.39
M1-D1	60	9.83	9.23	3.01	−16.89	32.86	1.43	3.99	0.62	−10.21	15.39	32.95	94.37	18.18	4.13	49.38	50.59
M1-D1	80	5.72	7.75	2.18	−16.5	25.77	2.24	3.67	0.41	−8.67	14.54	26.99	72.46	13.48	2.16	18.9	36.74
M1-D1	98	3.45	6.39	1.95	−15.48	14.08	3.08	4.25	0.97	−5.95	16.45	21.35	39.8	15.98	8.91	10.69	29.43
M2-D1	12	14.57	10.32	2.02	−11.52	38.49	0.35	6.3	1.02	−21.38	23.08	38.71	96.14	6.5	4.45	106.22	73.11
M2-D1	20	13.87	9.78	2.02	−12.08	37.47	−0.3	6	1	−18.88	21.04	38.45	102.99	7.29	4.7	96.28	65.78
M2-D1	40	12.16	8.4	1.82	−10.53	32.19	−0.93	5.6	0.89	−16.11	16.51	33.68	113.5	8.03	4.3	74.34	51.02
M2-D1	60	8.7	6.71	1.78	−9.48	26.68	−1.38	5.91	0.8	−14.42	17.02	27.08	99.95	11.96	3.16	38.77	39.98
M2-D1	80	3.61	4.11	0.95	−9.72	16.76	−2.06	6.16	0.88	−17.17	20.65	21.71	341.88	9.12	3.51	8.62	27.45
M2-D1	100	1.5	2.52	0.47	−13.73	7.36	−2.32	4.95	0.91	−15.52	14.62	19.91	316.8	5.8	5.74	3.81	15.43
M2-D1	102	1.68	2.83	0.55	−13.66	9.47	−2.05	4.49	0.82	−13.59	13.6	19.14	314.84	6.44	5.67	3.5	14.08
M3-D1	12	12.38	10.33	2.44	−14.75	35.89	−0.51	5.59	0.83	−16.84	18.07	36.65	107.17	9.55	3.81	76.76	68.92
M3-D1	20	11.46	9.55	2.25	−14.27	33	−0.82	5.19	0.77	−17.03	15.53	33.78	116.58	9.5	3.79	66	59.04
M3-D1	40	8.98	8.16	1.9	−11.41	30.08	−0.34	4.27	0.61	−12.81	14.14	30.84	68.86	9.24	3.45	40.35	42.42
M3-D1	60	4.72	8.11	1.66	−12.5	28.06	−0.1	4.73	0.62	−17.48	12.35	30.65	66.25	7.19	2.91	11.15	44.11
M3-D1	80	0.83	7.05	0.99	−16.92	22.2	−0.99	5.76	1.04	−20.67	12.53	25.33	60.95	3.39	5.61	0.83	41.45
M3-D1	100	−2.07	4.89	0.73	−14.83	13.69	−2.69	6.4	1.36	−22.78	13.49	24.34	200.66	3.81	7.76	5.77	32.42
M3-D1	120	−1.84	3.22	0.61	−10.7	6.61	−2.75	5.93	1.31	−21.1	14.64	22.68	201.55	6.08	8.34	5.47	22.75
M4-D1	12	12.68	9.99	2.16	−17.78	37.56	−1.38	5.56	0.81	−18.57	18.24	37.7	94.92	8.01	3.62	81.32	65.39
M4-D1	20	11.78	9.33	2.21	−17.32	36.41	−1.88	5.56	0.82	−18.3	15.44	36.6	95.94	9.59	3.74	71.19	58.99
M4-D1	40	11.35	8.48	2.65	−11.42	30.65	−2.47	4.69	0.92	−18.01	10.73	32.35	118.19	16.66	6.54	67.47	46.93
M4-D1	60	8.2	6.41	1.98	−8.3	28.32	−1.53	4.18	0.74	−13.35	9.01	28.79	100.77	16.28	5.39	34.81	29.31
M4-D1	80	1.69	4.69	1.02	−7.2	21.72	−0.84	5.08	0.76	−15.46	12.6	23.1	111.21	8.01	3.86	1.77	23.91
M4-D1	100	−1.29	1.57	0.19	−5.65	5.54	−0.7	4.68	0.8	−14.16	11.69	14.16	179.84	2.54	5.02	1.07	12.18
M4-D1	102	−1.08	1.53	0.17	−5.8	3.39	−0.74	4.32	0.76	−13.79	10.36	13.83	184.2	2.06	5.34	0.85	10.5
M5-D1	6	19.94	11.61	2.91	−8.36	45.79	2.34	4.49	0.85	−11.75	15.12	46.36	81	2.39	1.37	201.6	77.44
M5-D1	20	20.05	11.17	2.93	−7.75	45.65	0.02	3.98	0.73	−12.48	14.66	45.69	92.18	2.6	1.28	200.99	70.33
M5-D1	40	17.17	8.97	2.44	−6.42	37.16	1.02	3.06	0.57	−5.72	13.11	37.27	94.46	2.81	1.3	148	44.94
M5-D1	44	13.84	6.63	1.84	−4.61	28.9	2.23	2.69	0.54	−2.38	11.27	28.94	92.73	2.93	1.53	98.27	25.63
M1-D2	7	5.89	13.28	3.16	−35.76	41.82	1.32	8.39	1.21	−25.55	29.99	42.14	82.92	10.48	3.84	18.25	123.35
M1-D2	21	5.31	12.53	3.06	−37.29	36.70	−0.01	7.59	1.01	−23.24	28.96	38.43	254.42	11.07	3.26	14.12	107.26
M1-D2	41	3.93	11.50	3.08	−26.14	32.74	0.40	5.91	0.87	−15.40	23.30	32.95	83.36	13.34	3.98	7.80	83.65
M1-D2	61	2.99	9.96	1.72	−30.15	24.49	1.95	4.44	0.66	−13.35	13.91	30.18	272.57	5.54	4.16	6.37	59.44
M1-D2	81	1.55	7.43	1.01	−22.61	24.57	1.73	3.85	0.47	−11.52	15.73	28.22	59.43	3.40	2.74	2.71	35.02
M1-D2	91	0.80	5.96	0.78	−22.87	17.77	2.87	4.50	0.48	−10.39	24.92	30.57	35.46	3.22	2.15	4.44	27.87
M2-D2	10	7.10	12.99	3.76	−31.61	46.90	0.71	8.72	1.41	−20.88	33.94	47.31	70.16	15.72	4.92	25.48	122.36
M2-D2	20	6.14	12.88	3.97	−29.41	46.97	−0.12	8.42	1.33	−20.33	33.71	47.02	87.02	17.80	4.65	18.84	118.41
M2-D2	40	4.28	9.85	3.25	−26.79	35.51	0.35	7.03	1.09	−15.32	38.21	39.05	345.41	20.46	4.51	9.23	73.18
M2-D2	60	1.62	5.75	1.35	−23.01	17.44	0.88	6.21	1.07	−14.57	27.50	33.32	324.20	10.31	5.53	1.71	35.81
M2-D2	80	1.14	3.33	0.47	−11.24	8.93	−1.50	5.74	0.90	−12.86	17.31	19.68	331.23	3.78	4.65	1.76	22.01
M2-D2	100	1.69	1.73	0.20	−2.61	8.01	−1.33	2.61	0.31	−8.89	6.20	11.59	137.40	2.56	2.62	2.32	4.89
M3-D2	16	5.44	13.46	3.94	−30.68	52.89	−0.24	8.49	1.23	−20.47	34.75	59.21	63.13	16.02	3.95	14.82	126.61
M3-D2	20	5.11	13.42	4.00	−29.20	53.34	−0.37	8.34	1.21	−19.89	33.71	59.48	63.46	16.54	3.94	13.11	124.89
M3-D2	40	2.63	10.63	3.19	−24.58	40.17	−0.73	6.96	1.13	−16.16	28.35	40.19	88.47	16.83	4.95	3.73	80.75
M3-D2	60	−1.67	7.87	1.11	−20.36	27.18	−2.24	7.72	1.18	−23.84	25.27	28.61	214.30	3.71	4.37	3.92	60.82
M3-D2	80	−2.30	5.96	0.81	−14.42	18.17	−3.46	7.65	1.10	−25.31	14.75	28.29	206.65	3.43	3.83	8.63	46.99
M3-D2	100	−2.20	4.91	0.68	−15.44	11.11	−3.01	6.83	0.98	−25.92	16.71	30.14	210.70	3.56	3.82	6.97	35.35
M3-D2	116	−1.85	4.25	0.61	−17.29	13.29	−1.52	5.43	0.69	−27.08	20.35	32.12	212.54	3.81	3.04	2.86	23.78
M4-D2	11	5.11	12.05	3.13	−30.73	32.83	0.64	7.50	1.05	−18.46	34.33	35.78	116.02	12.61	3.65	13.27	100.69
M4-D2	21	5.20	12.01	3.31	−29.54	33.59	−0.13	7.31	1.02	−22.30	29.64	37.71	117.12	14.21	3.62	13.54	98.78
M4-D2	41	5.23	11.50	3.20	−24.41	32.78	−0.32	5.79	0.90	−17.40	25.51	32.93	95.49	14.42	4.50	13.74	82.90
M4-D2	61	2.92	5.90	0.82	−20.26	19.14	0.15	5.38	0.89	−15.15	21.67	22.62	342.77	3.61	5.14	4.28	31.84
M4-D2	81	−0.85	3.04	0.44	−9.63	10.43	0.67	4.32	0.58	−10.56	11.51	13.41	130.26	3.84	3.34	0.59	13.96
M4-D2	101	−1.33	1.22	0.15	−5.38	2.90	0.53	3.47	0.43	−9.57	13.26	13.52	348.67	2.74	2.81	1.02	6.76
M5-D2	6	6.95	13.64	2.29	−32.18	41.38	0.54	8.95	1.43	−27.93	40.85	46.15	118.25	5.26	4.75	24.31	133.04
M5-D2	20	5.60	12.65	3.58	−31.87	38.74	−0.99	7.85	1.22	−25.15	34.15	42.92	122.26	14.98	4.47	16.18	110.88
M5-D2	40	6.16	11.72	3.38	−26.40	32.03	1.42	6.47	1.10	−17.25	23.19	32.44	99.69	15.56	5.43	19.98	89.61
M5-D2	44	5.91	10.31	2.99	−19.09	29.16	2.91	5.47	1.07	−11.04	18.52	31.10	65.90	15.70	7.09	21.71	68.10

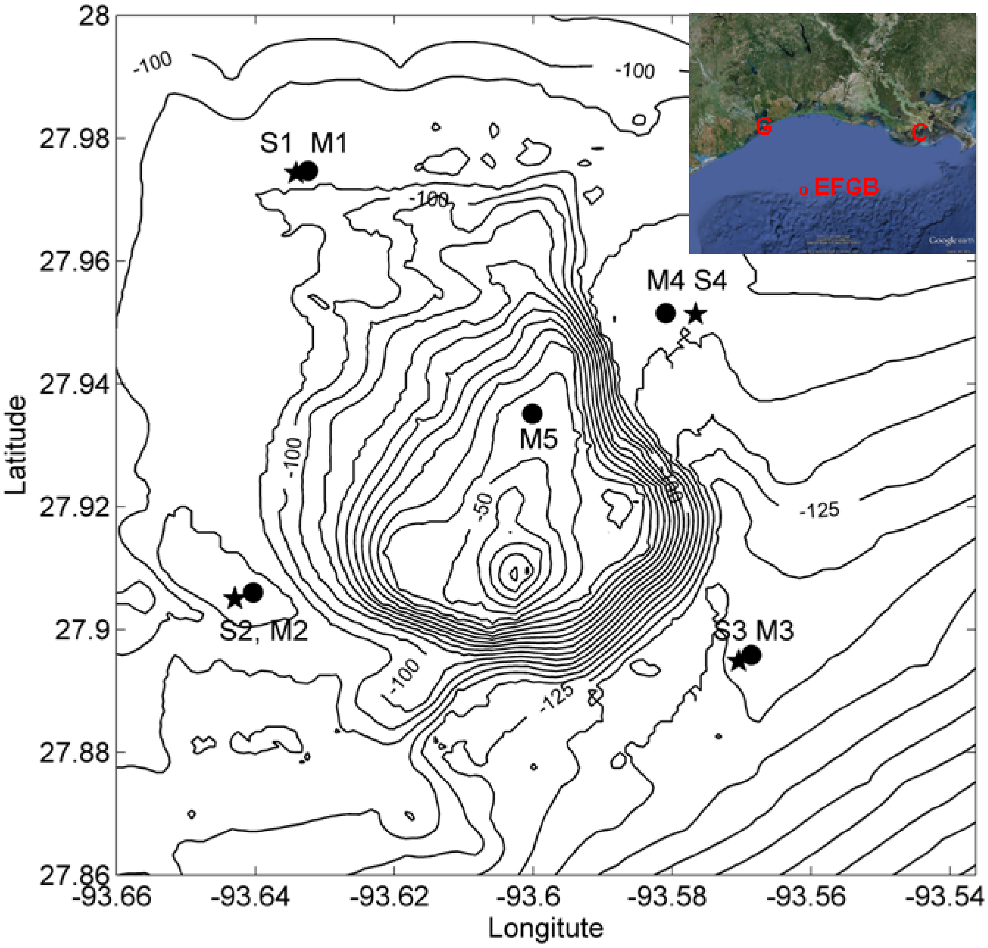

Figure 1. Locations of MORT ADCP moorings (M1-M5; dots) and temperature/salinity strings (S1-S4; stars) are shown along with bathymetry contours (in 5-m increments) at the East Flower Garden Bank (EFGB). The inset shows the location of the EFGB in the northwestern Gulf of Mexico in relation to Galveston (G), TX and Cocodrie (C), LA.

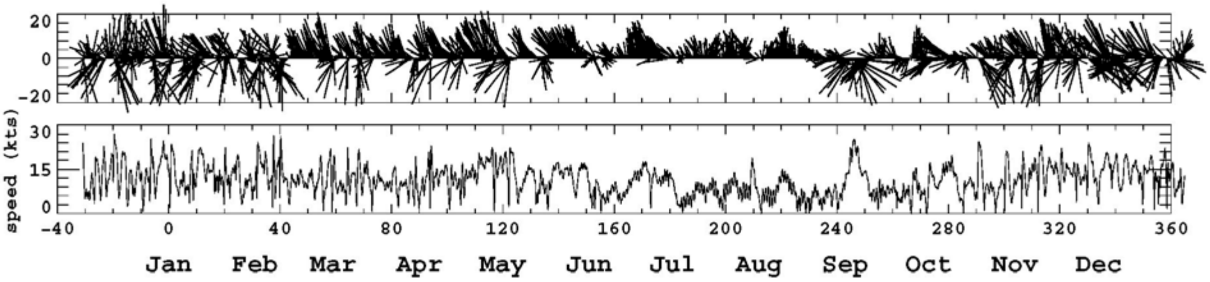

Figure 2. Vector stick plot of winds and wind speed time series. The velocity scale for the stick plots is indicated on the y-axis; northward component is up. X-axis shows days and months relative to 2011.

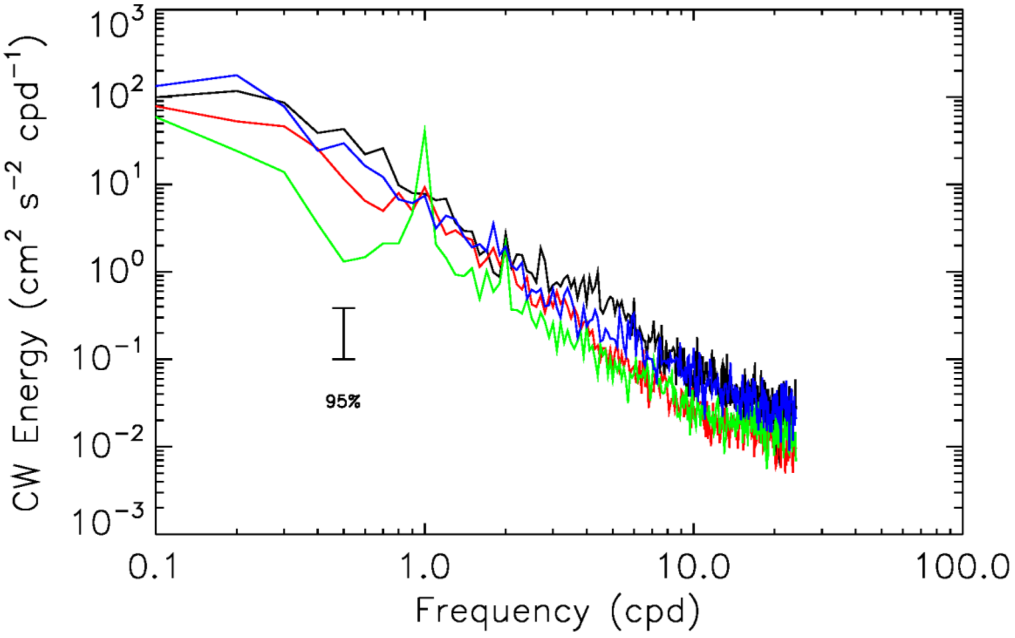

Figure 3. Clockwise (CW) rotary autospectra of the wind data for seasons (winter, spring, summer, and fall) of the year are shown. A significant diurnal peak (green curve) is present for the summer (July-September).

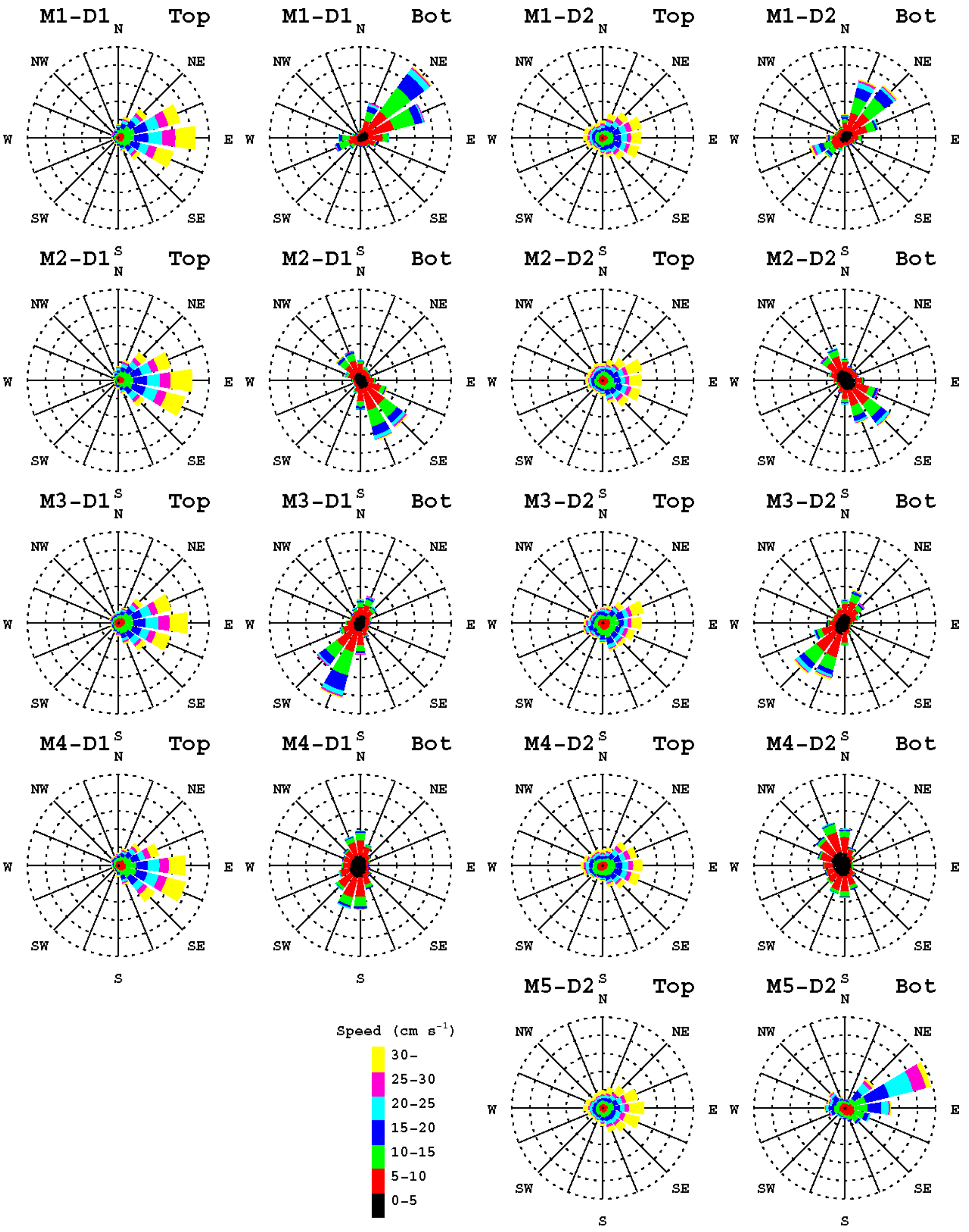

Figure 4. Compass rose diagrams for the near surface and near bottom currents are shown for each ADCP mooring except for M5-D1 (short record) for each deployment period (D1: deployment 1, winter-spring; D2: deployment 2, summer-fall). The current directions are distributed along the 16 compass points (every 22.5°) where the length of each bin provides the percentage of the number of observations in that direction and the color indicates the magnitude of the current. Dashed rings are every 5%, with the outermost ring representing 25%. Currents are plotted in the direction of the flow.

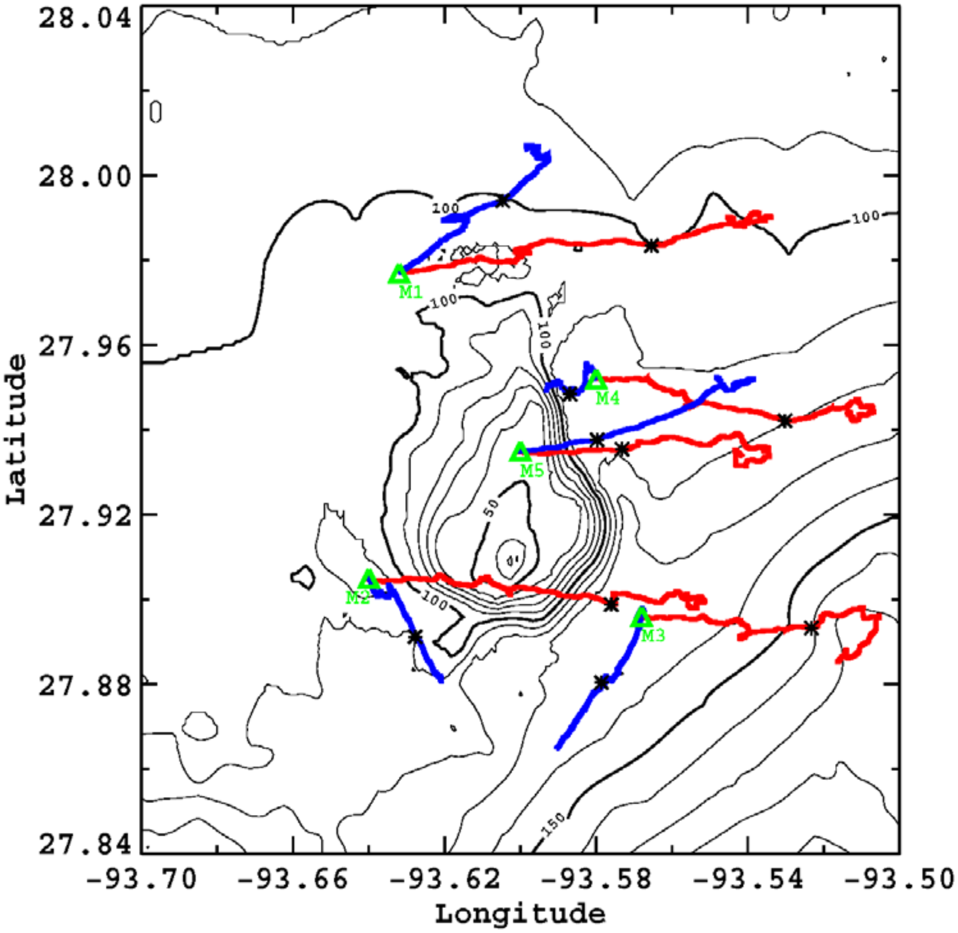

Figure 5. Progressive vector diagrams (pvds) for each ADCP mooring are shown for both the winter-spring period and for the summer-fall period. Red lines represent pvds for average velocities for the upper 80 m for M1-M4 and upper 40 m for M5. Blue lines represent the pvds for the lower layers above the bottom. Asterisks mark the end of the winter-spring period and start of the summer-fall period.

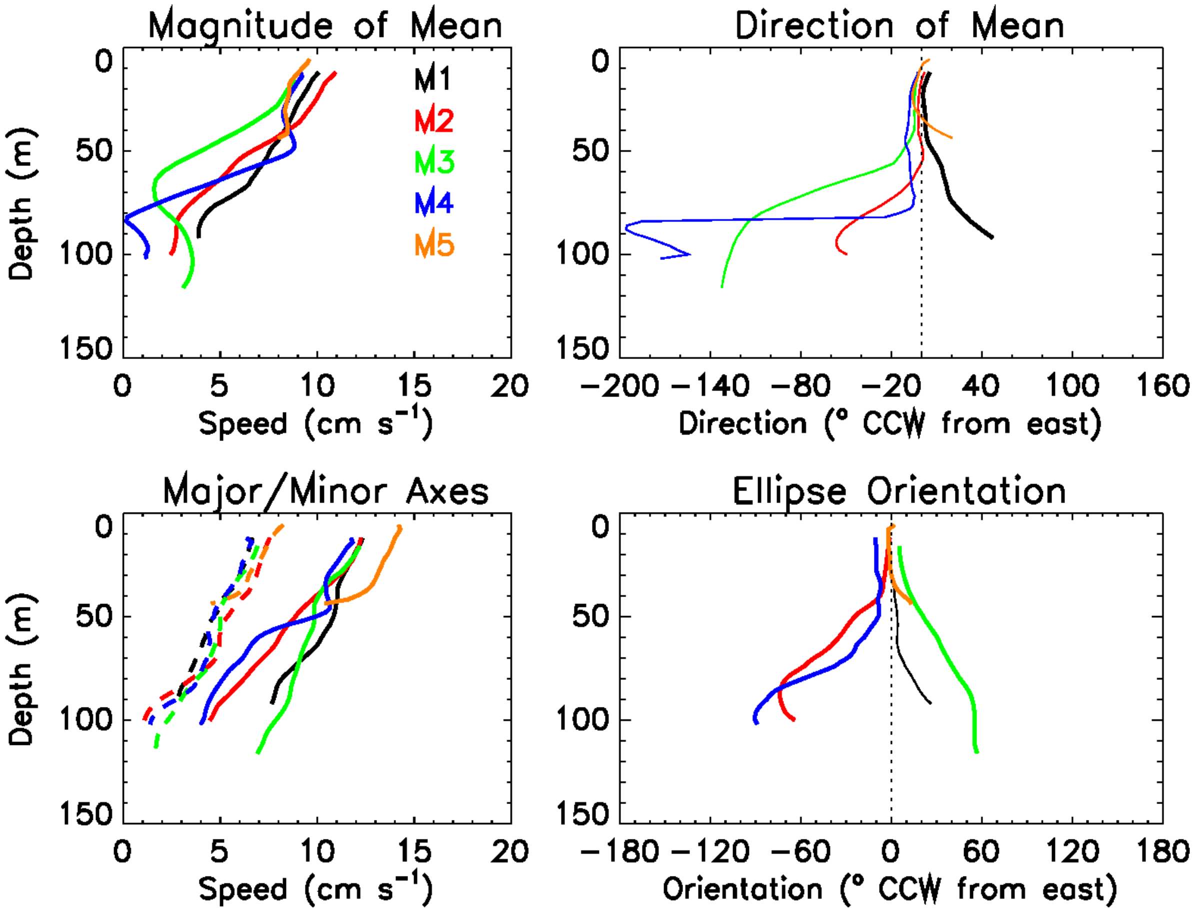

Figure 6. Magnitudes and directions of mean velocity (upper); major and minor (dashed) axes and orientations of principal ellipses (lower) for the entire deployment period.

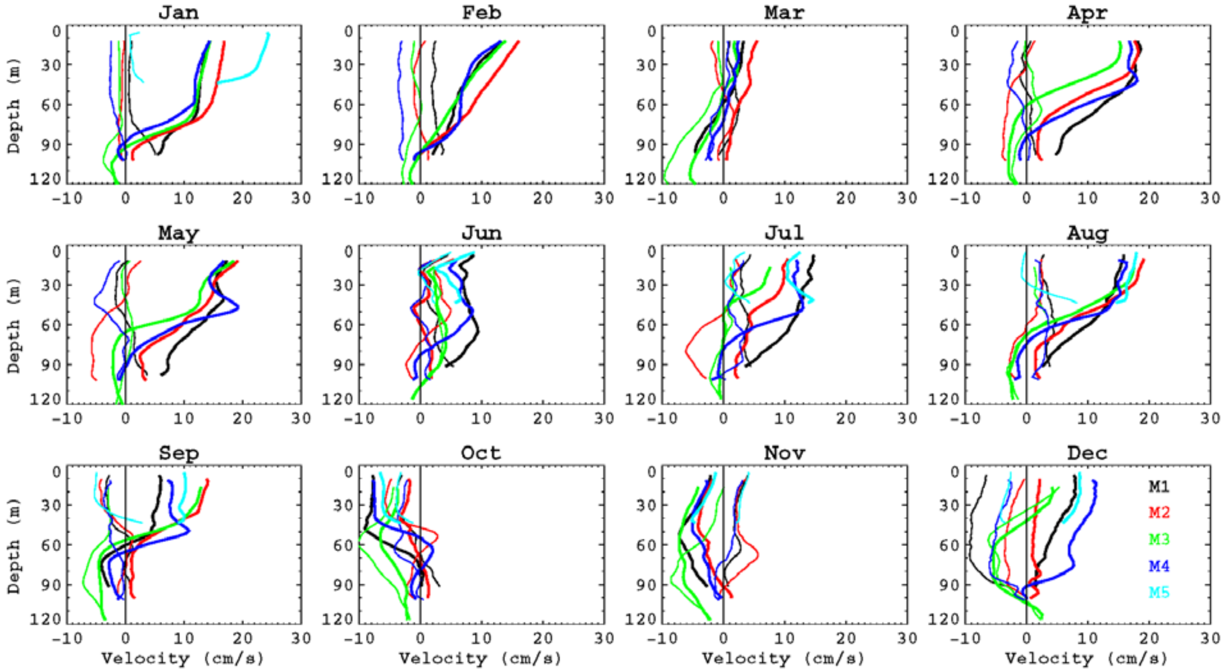

Figure 7. Average velocity profiles for U (thick lines) and V (thin lines) are shown for each month. Colors represent the individual ADCP moorings, indicated in the December frame.

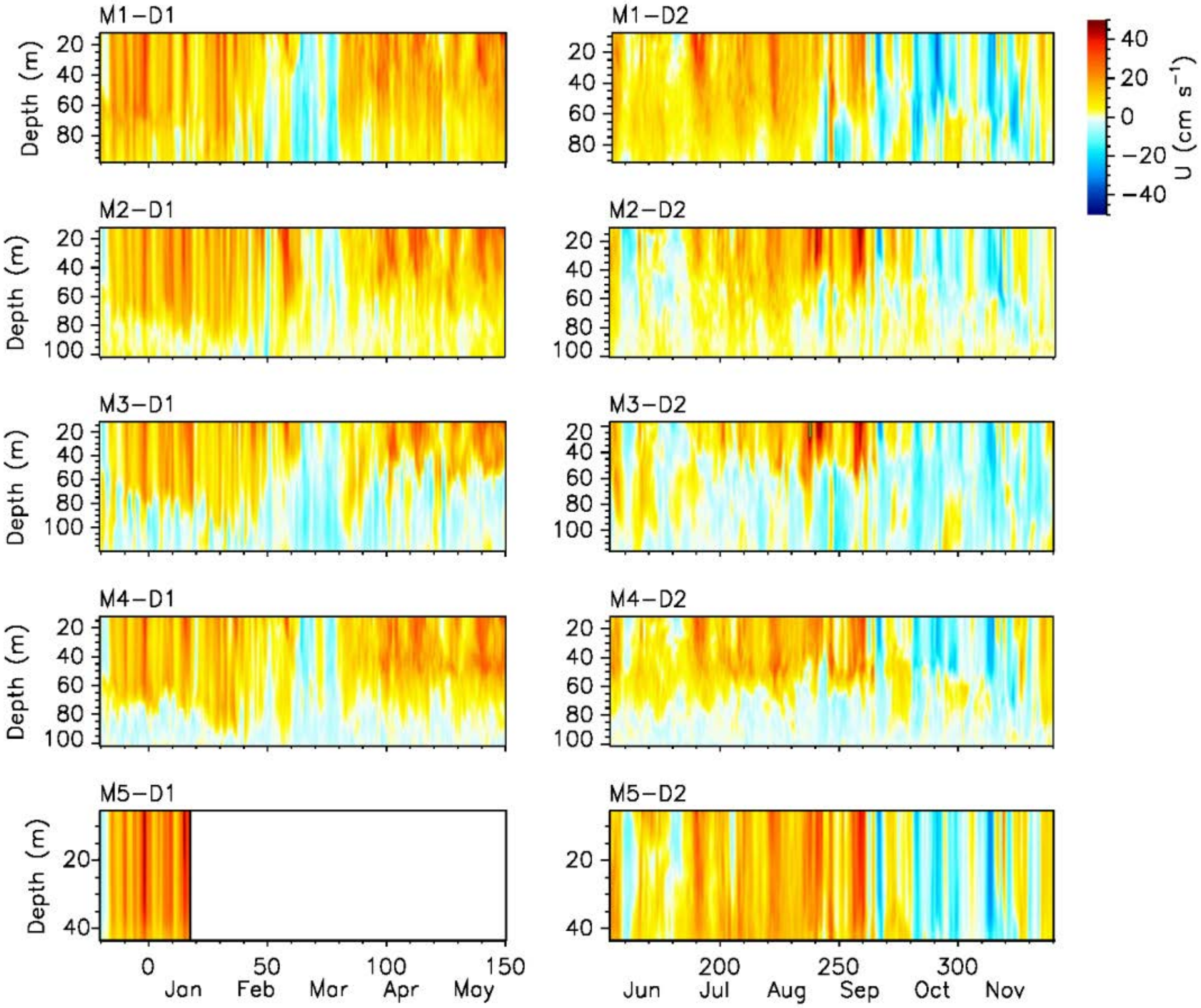

Figure 8. a. Velocity time series for the U (east-west component). Tides and inertial oscillations have been removed using a low-pass filter with a 40-h cutoff frequency. X-axis shows days and months relative to 2011.

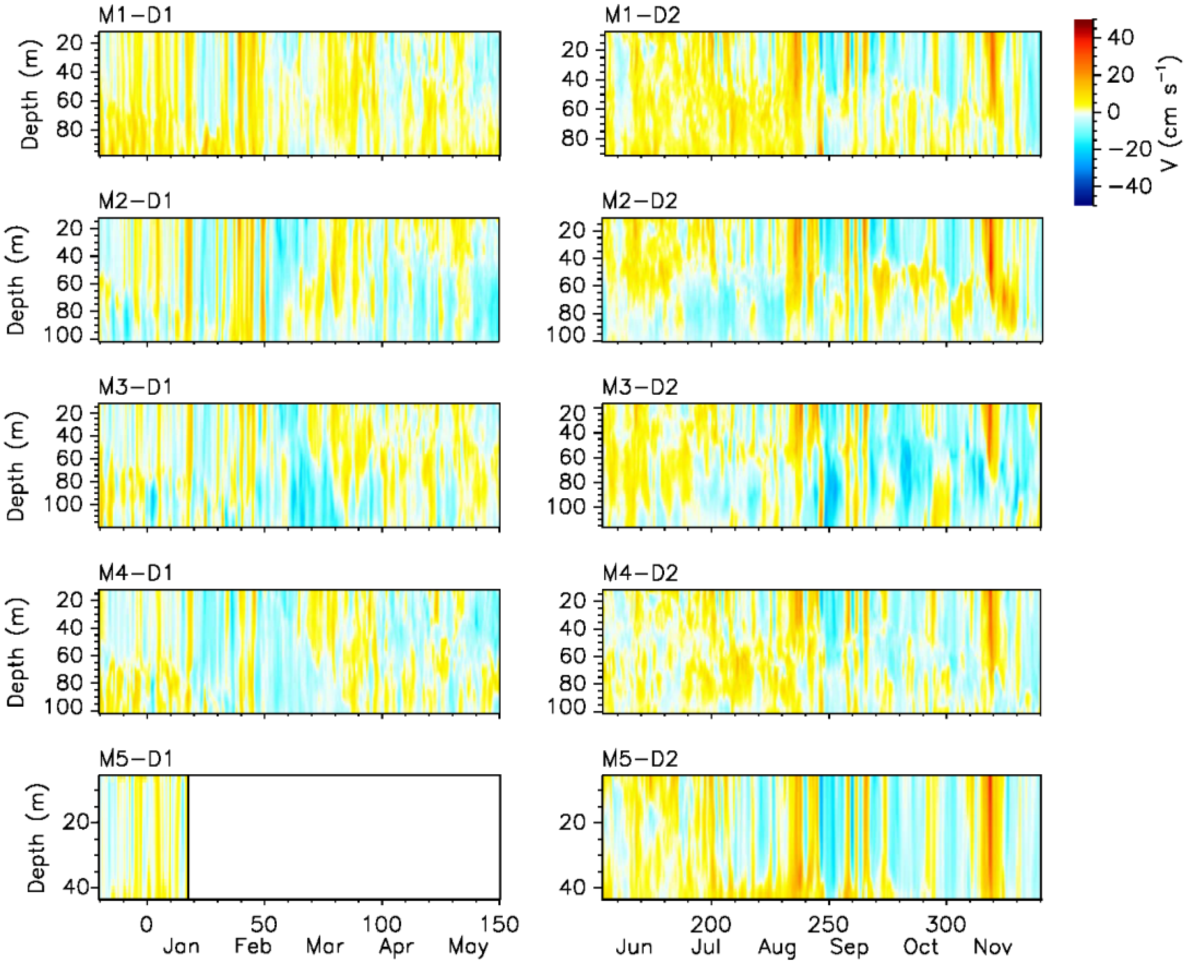

Figure 8. b. V (north-south) component. Tides and inertial oscillations have been removed using a low-pass filter with a 40-h cutoff frequency. X-axis shows days and months relative to 2011.

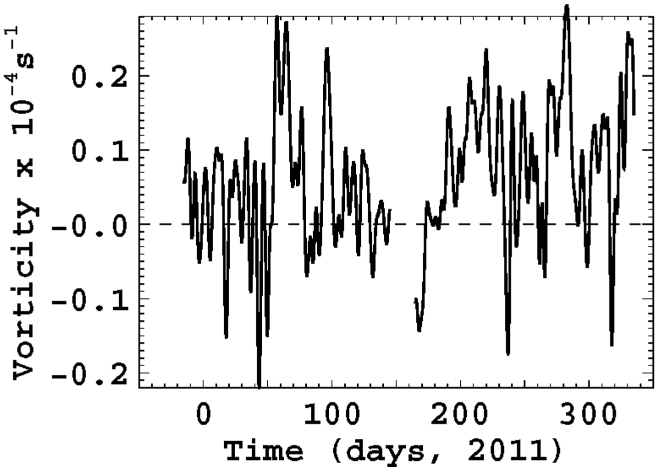

Figure 9. Current vorticity computed, with currents low-passed at 5 days, between current observations at M2, M3, and M4. Large positive vorticity values may be indicative of cyclonic eddy patterns.

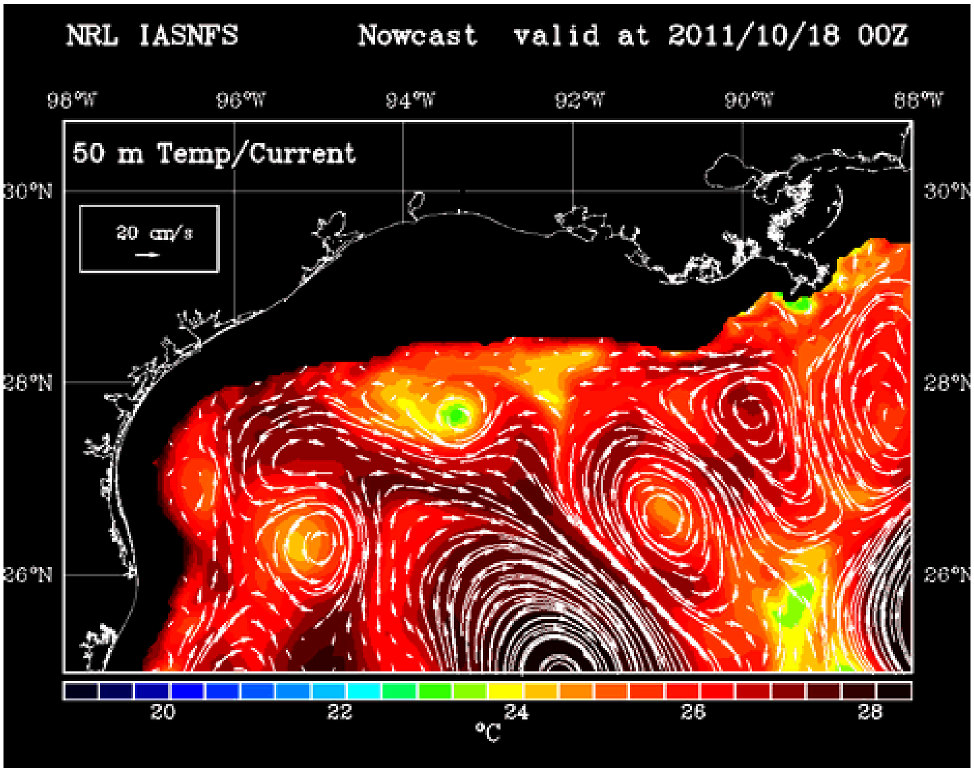

Figure 10. Snapshot of a possible current scenario from the Intra-Americas Sea Nowcast/Forecast System (IASNFS) for October 18, 2011. Arrows indicate the current velocity and direction and the colors indicate temperature, both for 50 m water depth. A LC ring is approximately at 25°N, 92°W and a cyclonic eddy, near the EFGB, is at 27.7°N, 93.5°W.

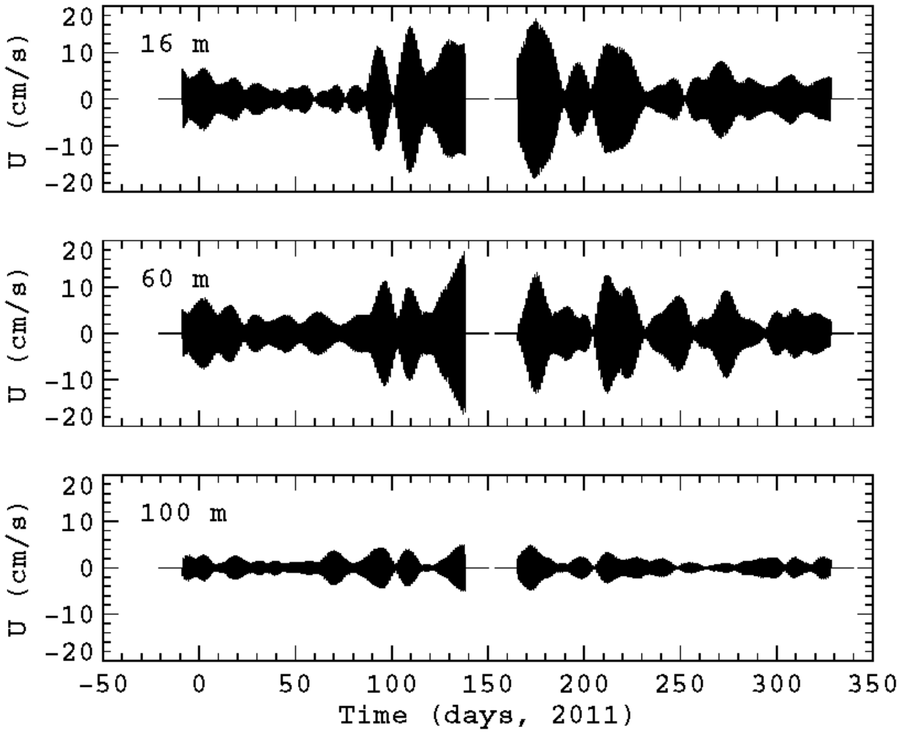

Figure 11. Inertial band currents (east-west) at M3 for 16 m, 60 m, and 100 m. The inertial period is 24.58 hours.

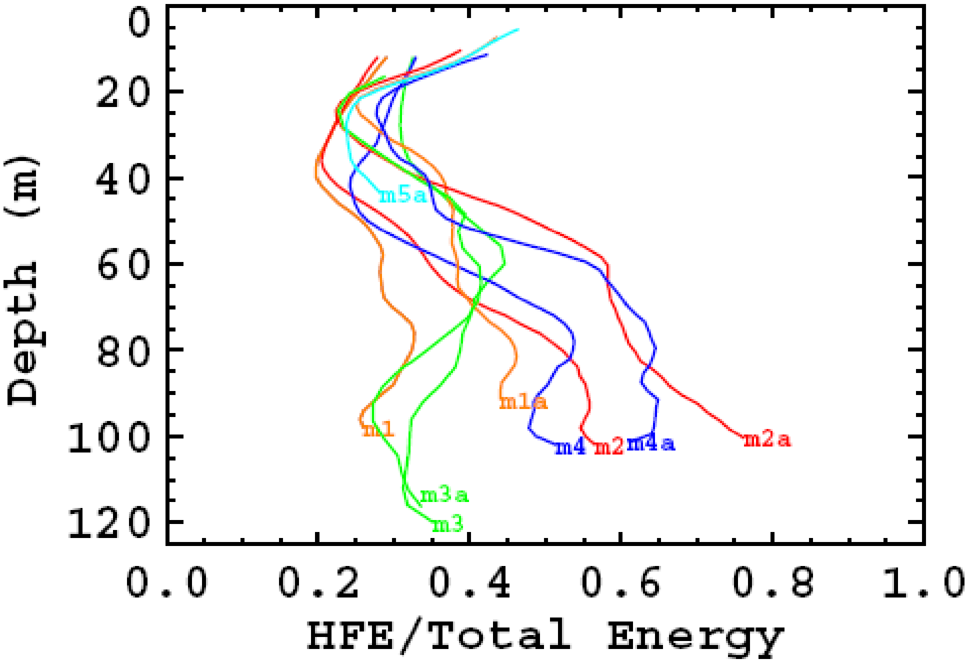

Figure 12. Vertical profiles of the ratio of higher frequency current energies (HFE; tidal, inertial, and higher frequencies) to the total current energy. Moorings for the winter-spring period are denoted by m1-m5 and for the summer-fall period by m1a-m5a.

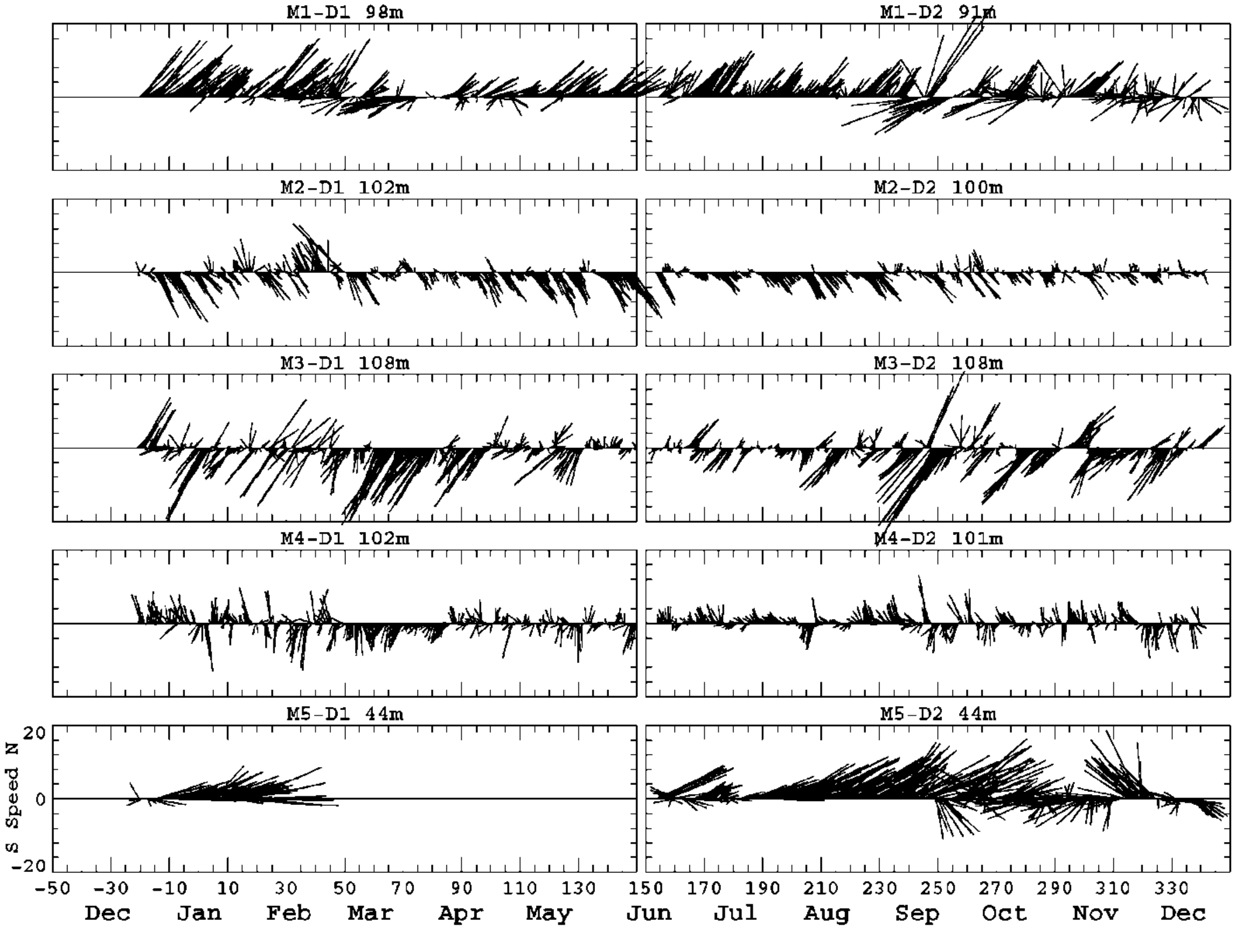

Figure 13. Current stick vectors for the near-bottom for each mooring. Northward is along the positive y-axis. X-axis shows days and months relative to 2011.

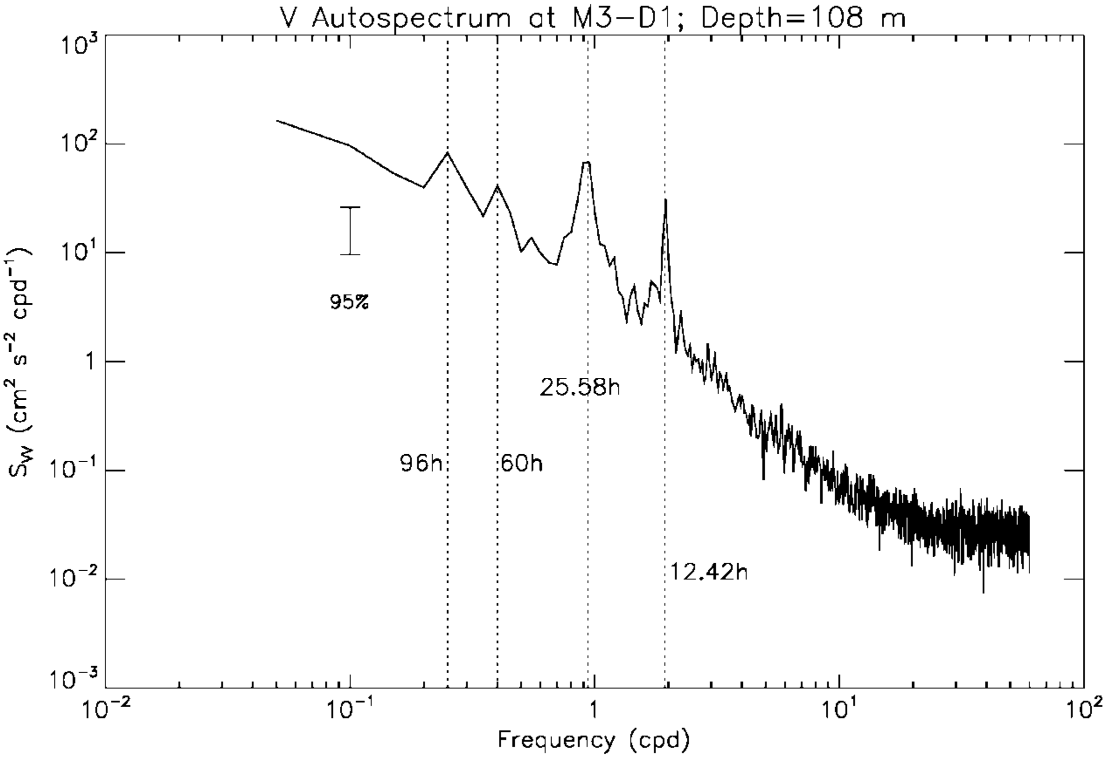

Figure 14. Autospectrum for the V velocity component near the bottom; 60 h and 96 h periods (typical for shelf waves), inertial (25.58 h), and the M2 tide period (12.42 h) are indicated by vertical dotted lines.

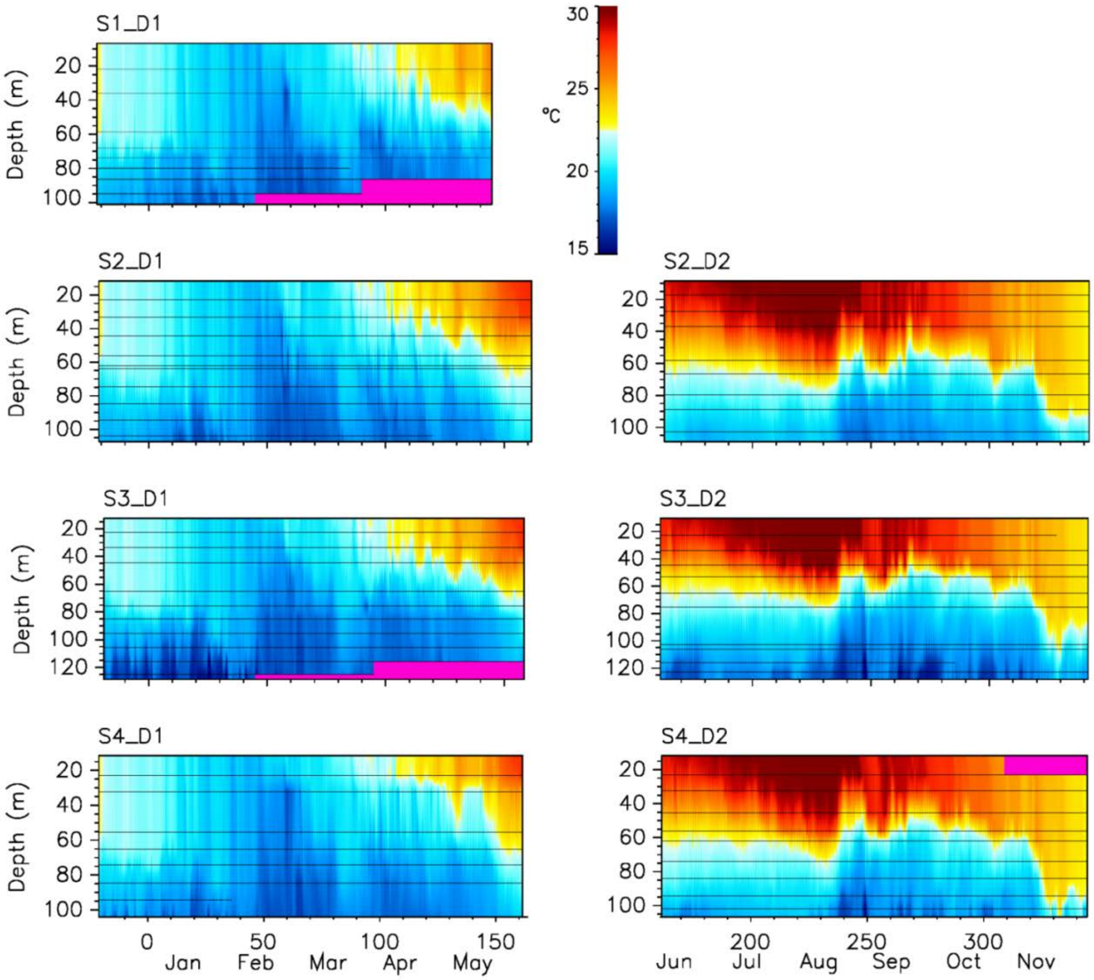

Figure 15. Temperature time series are shown for the four string moorings (S1-S4). Note that S2 was not redeployed for the summer-fall period. The pink color indicates no data. Horizontal lines indicate vertical positions of the sensors, using the average pressures. Truncated lines indicate bad or missing data, which have been vertically interpolated. X-axis shows days and months relative to 2011.

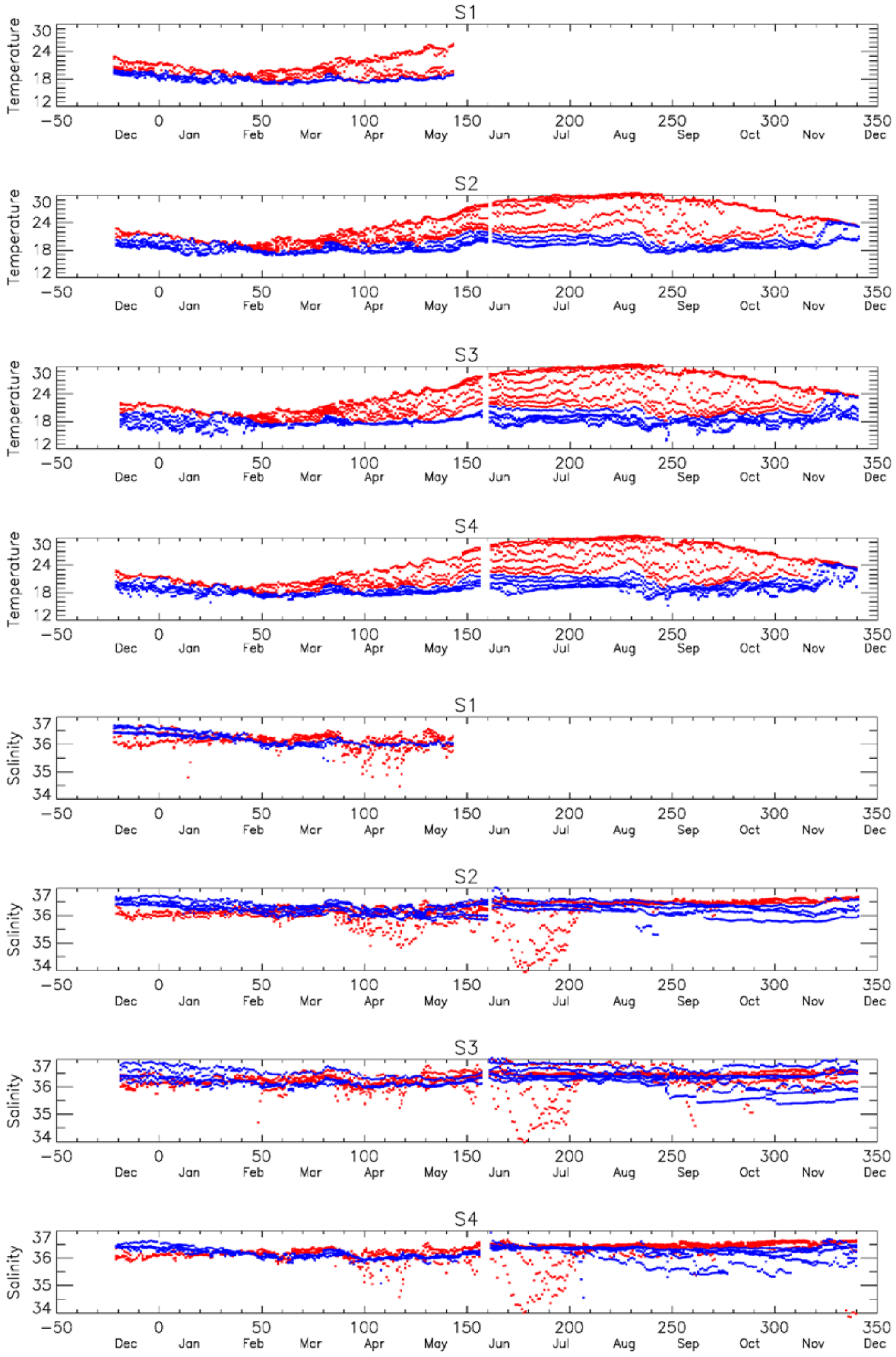

Figure 16. (a) Temperature time series for the 4 string moorings at one-day resolution. (b) Corresponding salinity time series. Above 75-80 m (red), below 75-80 m (blue). X-axis shows days and months relative to 2011.

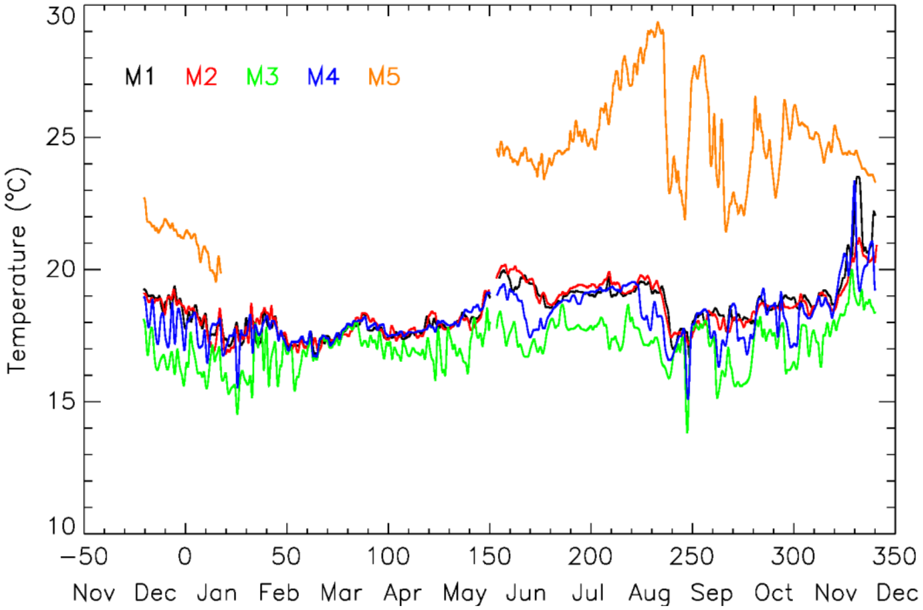

Figure 17. Bottom temperatures from the ADCP moorings (M1-M5). X-axis shows days and months relative to 2011.

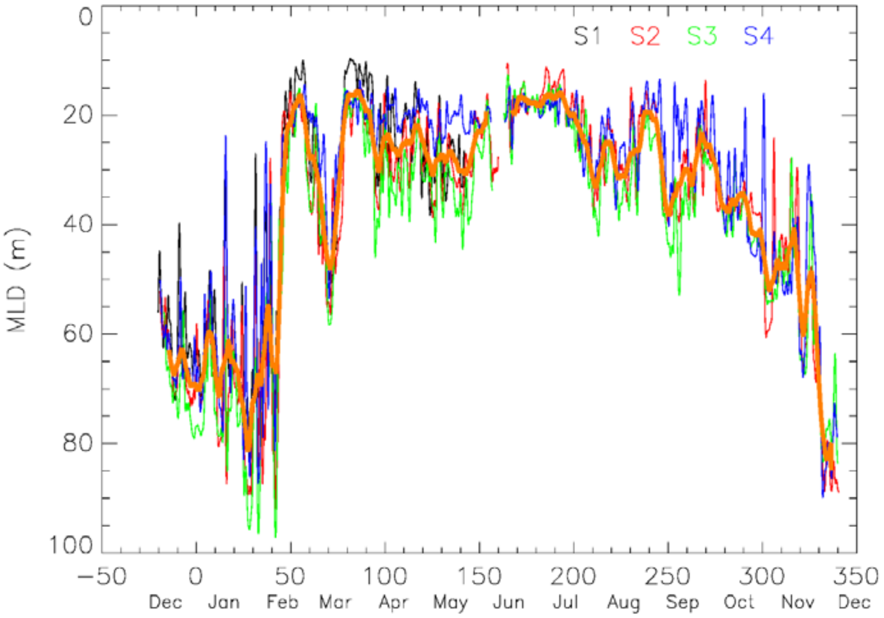

Figure 18. Mixed-layer depths computed from the string mooring temperature observations. Mixed-layer depths for each string (denoted by the color key in the upper right corner) were smoothed over a day. The orange curve is the 5-day average of the mixed-layer depths for the individual strings. X-axis shows days and months relative to 2011.

APPENDIX B

Surface Wave Effects on High-Frequency Currents over a Shelf Edge Bank

Surface Wave Effects on High-Frequency Currents over a Shelf Edge Bank

H. W. Wijesekera[1], D. W. Wang[1], W.J. Teague[1*], E. Jarosz[1], W. E. Rogers[1]
D.B. Fribance[2], and J. N. Moum[3]
[1]Naval Research Laboratory, Stennis Space Center, MS 39529, USA
[2]Coastal Carolina University, Conway, SC 29528, USA
[3]Oregon State University, OR 97330, USA

Journal Citation:
Wijesekera, H.W., D. Wang, W.J. Teague, E. Jarosz, E. Rogers, D.B. Fribance, and J.N. Moum, 2013. Surface wave effects on high-frequency currents over a shelf edge bank, Journal of Physical Oceanography, V43, 1627-1647, DOI: 10.1175/JPO-D-12-0197.1.

ABSTRACT

Several acoustic Doppler current profilers and vertical strings of temperature, conductivity, and pressure sensors, deployed on and around the East Flower Garden Bank (EFGB), were used to examine surface wave effects on high-frequency flows over the bank and to quantify spatial and temporal characteristic of these high-frequency flows. The EFGB, about 5 km wide and 10 km long, is located about 180 km southeast of Galveston, Texas and consists of steep slopes on southern and eastern sides that rise from water depths over 100 m to within 20 m of the surface. Three-dimensional flows with frequencies ranging from 0.2 to 2 cycles per hour were observed in the mixed layer when wind speed and Stokes drift at the surface were large. These motions were stronger over the bank than outside the perimeter. The squared vertical velocity, w^2, was strongest near the surface and decayed exponentially with depth, and the e-folding length of w^2 was two times larger than that of Stokes drift. The two-hour averaged w^2 in the mixed layer, scaled by the squared friction velocity, was largest when the turbulent Langmuir number was less than unity and the mixed layer was shallow. It is suggested that Langmuir circulation is responsible for the generation of vertical flows in the mixed layer, and that the increase in kinetic energy is due to enhancement of Stokes drift by wave focusing. The lack of agreement with open-ocean Langmuir scaling arguments is likely due to the enhanced kinetic energy by wave focusing.

---

[*] Corresponding Author: H.W. Wijesekera; Hemantha.Wijesekera@nrlssc.navy.mil; phone: 228-688-4845

1. Introduction

The oceanic surface layer is controlled by momentum and buoyancy fluxes near the surface and by entrainment fluxes at the base of the mixed layer. These fluxes generate a wide range of physical processes between the air-sea interface and thermocline, and play a vital role in climate variability, biological productivity, and marine pollution. In the highly unstable boundary layer, buoyancy production dominates in the production of turbulent kinetic energy (TKE) (e.g., Shay and Gregg 1986; Brubaker 1987; Lombardo and Gregg 1989). The production of TKE driven by surface cooling initially modifies the vertical velocity component and is then transferred by turbulent pressure forces into horizontal velocity components, thus generating coherent flows in geophysical boundary layers (see, e.g., Lumley and Panofsky 1964; Thorpe 2005). When the surface buoyancy flux is small and the boundary layer is near neutral, the production of TKE is dominated by shear production driven by surface wind stress (Dillon et al. 1981; Soloviev et al. 1988). Shear production modifies horizontal velocity fluctuations, especially in the downwind direction before transferring energy to the crosswind and vertical energy components via turbulent pressure fluctuations. These ideas have been used in turbulent closure schemes in the oceanic mixed layer (e.g., Mellor and Yamada 1982).

However, transfer of momentum and buoyancy at the air-sea interface is complicated by the presence of surface waves. Surface waves boost the vertical transport of surface fluxes through (i) enhancement of TKE dissipation by breaking, and (ii) generation of production-scale coherent structures in the mixed layer via wave-mean flow interactions. Several investigators (Agrawal et. al, 1992; Anis and Moum 1995; Drennan et al. 1996; Melville 1996; Terray et. al. 1996; Soloviev and Lukas 2003) report that the dissipation rate of TKE in the wave boundary layer is up to an order of magnitude larger than the predictions from wall-boundary layer scaling. The enhanced TKE dissipation rate by wave breaking is an important factor for momentum, heat and gas transfer rates at the air-sea interface.

As a response to the wind over the ocean, roll-vortices are formed roughly parallel to the wind direction. These circulation patterns can be recognized by the lines of convergence at the surface, as noted by Langmuir (1938), and they are referred as “Langmuir cells”. The orientation of these Langmuir cells is roughly opposed to the orientation of wind-driven/shear-driven turbulent eddies in the mixed layer. Craik and Leibovich (1976) describe a plausible theory for generation of these roll-vortices. The Craik-Leibovich mechanism requires interaction between surface waves and wind-driven shear flows to generate a forcing function governed by the wave-induced Stokes drift and vertical shear of mean currents. In Langmuir turbulence, the Stokes production term generates TKE in both crosswind and vertical directions. Detailed discussions of theory and relevant references are in Leibovich (1983) and Thorpe (2004).

Several investigators observed convergence zones on the surface layer and the associated cross-wind and vertical velocities in surface convergence zones (Weller and Price 1988; Smith et al. 1987; Pollard and Thomas 1989; Zedel and Farmer 1991; Smith 1992, 1998; Plueddemann et al. 1996). Weller and Price (1988) report three-dimensional structure in mixed-layer velocity and narrow regions of downwelling flow within the mixed layer, in coincidence with bands of convergent surface flow. They further report that the downwelling flow in the middle of the mixed layer was up to 0.2 m s^{-1}, and that the downwind, downwelling flow was jet-like in structure. Coherent vortices in the mixed layer have been studied using Doppler sonar techniques (e.g., Zedel and Farmer 1991; Plueddemann et al 1996; Smith 1992, 1998) and these investigators report the consistency of wind/wave forcing of Langmuir circulation. In the existing literature on Langmuir circulation studies, the majority of the observations is from deep water environments, and there are only a few references related to shallow water environments (e.g., Hunter and Hill 1980; Marmorino et al. 2005; Gargett and Wells 2007). In a shallow water environment, the physical set up is different since top and bottom boundary layers can merge under wind and buoyancy forcing, and thus bottom frictional effects can become a significant factor in mixed-layer dynamics. Gargett and Wells (2007) report that Langmuir circulation plays an important role in sediment transport in the shallow water environment.

There are numerous numerical modeling studies, mainly Large Eddy Simulations (LES), to examine, quantify, and scale Langmuir turbulence in the oceanic mixed layer (Skyllingstad and Denbo 1995; McWilliams et al. 1997; Skyllingstad et al. 1999; Li et al. 2005; Harcourt and D'Asaro, 2008; Grant and Belcher 2009). The papers cited here are just a few references out of many in the literature on this subject. In the majority of these models, Langmuir circulation is simulated by specifying Craik and Leibovich (1976) vortex-force parameters while specifying a Stokes drift corresponding to a monochromatic surface wave field. These studies describe the formation of Langmuir circulation, scaling of Langmuir turbulence, and the distinction among convection, shear-driven turbulence, and Langmuir flows in the upper ocean.

However, there are still unresolved issues such as quantitative understanding of the three-dimensional structure of Langmuir circulation and its interaction with convective- and shear-driven mixing and with internal waves in the thermocline, and scaling laws for Langmuir turbulence. The main objectives of this study are to examine surface wave effects on high-frequency flows over the East Flower Garden Bank (EFGB), to quantify spatial and temporal characteristic of these high-frequency flows, and to examine the scaling laws of vertical velocity based on Langmuir circulation theory. In this paper we describe measurements of high-frequency currents over the EFGB. The bank is located at the edge of Texas-Louisiana continental shelf, and it rises from depths of 100-150 m to about 20 m below the surface. When compared with previous observations from shallow water (e.g., Gargett and Wells 2007) and deep water (e.g., Smith 1998) our measurements represent both shallow- and deep-water conditions. The vertical velocity fluctuations described here show strong correlations with winds and surface-wave properties. We suspect these velocity fluctuations are manifestation of Stokes-drift induced wave-current interactions such as Langmuir circulations during wind events. Here we examine high-frequency velocity fluctuations including temporal, lateral, and vertical distributions, and characteristic vertical length scales for wide ranges of wind speeds and Stokes drifts. The paper is organized as follows. Section 2 describes platforms and measurements. Section 3 describes observations of winds, surface wave statistics, and background currents and hydrography. High-frequency velocity fluctuations and scaling of vertical velocity are described in section 4. Discussion is given in section 5. Finally, major findings are summarized in section 6.

2. Platforms and Measurements

Closely-spaced observations of velocity (u,v,w), temperature (T), conductivity (C), and pressure (P) were collected between December 2010 and December 2011 over the EFGB as part of projects sponsored by the Naval Research Laboratory (NRL) (Mixing Over Rough Topography (MORT)) and by the Bureau of Ocean Energy Management (BOEM) (Currents over Banks (COB)). The year-long observational program consists of two six-month mooring deployments (from December 2010 to June 2011, and from June 2011 to December 2011), and a two-week intensive experiment from May 26 to June 14, 2011. A detailed discussion of instrumentation, data collection, sampling methods, and data processing is in Teague et al. (2013), and therefore we just describe a subset of the data, relevant to this study which is mainly from measurements made during the second half of the experiment (June – December 2011).

Currents and hydrographic fields were collected from five trawl-resistant bottom-mounted ADCP moorings (M1-M5), referred to as "Barnys" due to their barnacle-shaped dome (Perkins et al. 2000), and four sub-surface string moorings (S1-S4), equipped with temperature, conductivity, and pressure (TCP) sensors. Bathymetry and locations of moorings at the EFGB are shown in Fig. 1. M1-M4 and S1-S4 were deployed at the four corners of the bank at water depths of 98 m, 105 m, 127 m, and 106 m, respectively, and M5 was deployed at a water of depth of 47 m, about 3 km north of the bank peak (about 20 m depth) (Fig. 1). The separations between Barnys and the associated string moorings were about 200 m. The moorings were equipped with Teledyne RD Instruments Workhorse ADCPs operating at 600 kHz (M5) and 300 kHz (M1-M4) with four transducers each with an incidence angle of 20 degrees. ADCPs recorded nearly full water-column current profiles every 15 minutes (an ensemble average of 120 realizations). The ADCPs at M1, M2, M4, and M5 had 2 m vertical resolution and the ADCP at M3 had 4 m vertical resolution. Shallowest ADCP depth-bins below the mean-water line at M1, M2, M3, M4, and M5 were 7.5m, 10.4 m, 16.4 m, 11.5 m, and 5.5 m, respectively, while the deepest depth-bins were off the bottom by 6.5 m, 4.6 m, 11 m, 4.5 m, and 3.5 m, respectively. The standard deviations for 15-minute averaged currents were less than 0.5% of the water velocity at the five mooring sites. Since moorings are bottom mounted, the platform motion is not a factor for velocity measurements. Apart from water column velocities at M5, surface wave parameters such as wave height spectra and directional wave spectra were collected from the ADCP (Strong et al. 2000). The spectral distribution of wave energy $E(f,\theta)$ in frequency f and direction θ was provided by a bottom-mounted upward-looking ADCP (600 kHz) based on the RDI's Wave Array Technique. It treats the ADCP depth cell bins as an array of independent sensors for acquiring wave orbital velocities. The frequency-direction spectrum, $E(f,\theta)$ is then derived using an array processing algorithm for velocities acquired every 2 hours for 5 minutes at a 2 Hz sampling rate. Three Barnys, at M2, M4, and M5, were also equipped with high-resolution pressure sensors (Ppods) developed by Moum and Nash (2008). The other two Barnys (M1, M3) contained SeaBird wave tide gauges. The sampling rates of the Ppods were 1 Hz and the resolutions were about 0.14 mm or 1 Pa (1Pa=1 N m^{-2}).

Four TCP string moorings were deployed at M1-M4 during the first half of the deployment and three were redeployed at M2-M4 during the second half. Each string mooring contained eight to twelve instruments that were approximately equally spaced between 7-12 m below the surface and 1 m above the bottom (Teague et al. 2013). Some of the instruments recorded only T and C while others recorded T, C, and P. The large majority of the instruments were Sea-Bird Electronics MicroCats (SBE37). A limited number of Aqua Trolls that recorded T, C, and P were distributed on each of the string moorings. The MicroCats sampled every 6 minutes with accuracies of ±0.002°C and 3 µS cm^{-1}. The Aqua Trolls sampled every 12 minutes with lower accuracies of ±0.1°C and ±0.5% of the data magnitude + 1 µS cm^{-1}. The conductivity sensors sometimes failed towards the ends of the records due to biofouling. We do not address processing and data quality issues here, since those topics are discussed in Teague et al. (2013).

3. Winds, Waves and Background Currents

a. Wind Field

Wind observations were collected hourly at the southern edge of the EFGB at the National Data Buoy Center (NDBC) station 42047 (Fig. 1), and at NDBC station 42046 located approximately 44 km west of the EFGB. Winds at 42046 were used when 42047 was out of service which was about half of the year-long mooring period. Winds at two buoy locations were similar when they were available. No wave data were available at these sites. For this study wind measurements were from 42046. The buoy provides wind velocity ($\vec{U}_4$) at 4 m (Z_4) above the sea surface. The standard 10-m (Z_{10}) wind velocity ($\vec{U}_{10}$) was estimated iteratively by assuming that the near surface atmospheric boundary layer was near neutral, where

$$\vec{U}_{10} \approx \vec{U}_4 + \vec{U}_* \kappa^{-1} \log(Z_{10}/Z_4), \qquad (1a)$$

$$\vec{U}_* = (\vec{\tau}/\rho_w). \qquad (1b)$$

$$\vec{\tau} = \rho_a C_D \vec{U}_{10} |\vec{U}_{10}|, \qquad (1c)$$

and $C_D = 10^{-4}(-0.016|\vec{U}_{10}|^2 + 0.967|\vec{U}_{10}| + 8.0558)$ (Hwang 2011). (1d)

$\vec{U}_*$ is the friction velocity, κ is the von Karman constant (0.4), $\vec{\tau}$ is the wind stress at the sea surface, C_D is the drag coefficient, ρ_w is the density of seawater, and ρ_a is the density of air. Winds (U_{10}) for September through December were dominated by north-south changes in direction caused by passages of numerous fronts (Fig. 2a). Winds from May through August were primarily out of the southeast. Wind events with magnitudes larger than 8 m s^{-1} lasted from 1 to 6 days. Wind events associated with passages of cold fronts were limited to 1-3 days.

b. Surface Waves and Stokes Drift

The wave-induced Stokes drift profile, $\vec{U}_S(z)$ for a random wave field, is calculated as an ensemble average of wave components (Kenyon, 1969), where

$$\vec{U}_S(z) = 4\pi \int_{f_{\min}}^{f_c} \int_0^{2\pi} f \vec{k} E(f,\theta) G(f,z)\, d\theta\, df \,. \qquad (2)$$

The function, $G(f,z)$, is expressed as $G(f,z) = \cosh(2k(H+z))[\sinh(2kH)]^{-1}$, where $k = |\vec{k}|$ is the wave number and $2\pi f = [gk\tanh(kH)]^{1/2}$. H is the water depth, g is the gravitational acceleration (9.81 m s^{-2}), and z is the vertical depth coordinate (negative downward) from the mean sea surface. The ADCP wave measurement system provides $E(f,\theta)$ for a frequency band varying from minimum frequency, $f_{\min}$, to cut-off frequency, f_c. This frequency band varies with environmental conditions, and during the experiment, $f_{\min} = 0.0098$ Hz, and f_c=0.3535 Hz. Stokes drift was computed at M5 where H=47 m.

Fig. 3 shows the ratio of surface Stokes drift, $U_{S0} = |\vec{U}_S(z=0)|$ to U_{10}, as a function of U_{10}. In general, the direction of estimated Stokes drift follows the direction of the wind closely. Data presented in Fig. 3 are within 15 degrees of the wind direction. The scatter plot shows two-hour estimates of the fractional Stokes drift, U_{S0}/U_{10}, and the bin-averaged U_{S0}/U_{10} over 1 m s^{-1} wind speed intervals with 95% confidence limits (circles with bars). As a reference, we also show U_{S0}/U_{10}, derived from directional wave spectra and wind speeds from a nearby NDBC directional wave buoy (42019) located 170 km east of the EFGB (Fig. 3). Earle et al. (1999) showed that the directional wave distribution can be derived from three different methods namely the directional Fourier series method, the Maximum Likelihood Method (MLM) and Maximum Entropy Method (MEM). In this study, the MLM was used to compute surface Stokes drift from the NDBC buoy data. We adapted this technique to be consistent with the Iterative Maximum Likelihood Method used for deriving ADCP directional wave spectra (Strong et al. 2000). We also computed surface Stokes drift from the Fourier method, and these results are plotted in Fig. 3. The fractional Stokes drift at M5 increases from about 0.1% to about 0.6% as wind speed increases from 5 m s^{-1} to 15 m s^{-1}. For winds greater than 10 m s^{-1}, the ratio U_{S0}/U_{10} at M5 is about 0.6, while that at the near by NDBC buoy is about 0.7 for the MLM, and is about 0.8 for the Fourier method (Fig. 3). Note: the cut off frequency of NDBC observation is 0.485 Hz.

Both wave measurement systems and wave-simulation models impose cutoff frequencies due to observational constraints and computational limitations. Therefore wave spectral components below this cutoff frequency (f_c) are available for the estimate of Stokes drift (Eq. 2). Contributions from high-frequency spectral components can be approximated by assuming a spectral tail shape and directional spreading function for frequencies higher than f_c (Webb and Fox-Kemper 2011; Rascle et al. 2008; Belcher et al. 2012). The spectral tail with f^{-5} contributes 30% to the surface Stokes drift compared to the truncated spectrum with f_c=0.41 Hz (Belcher et al., 2012). Rascle et al. (2008) show that the contribution can be about 0.4% of wind speed for simulated wave spectra with f^{-5} slope and a constant directional spreading at frequencies beyond f_c=0.41 Hz. The computation of the high-frequency contribution remains uncertain due to the lack of information about the high frequency directional wave spectrum.

It is noted that Stokes drift resulting from shorter waves penetrate into a very shallow depth near the ocean surface. While short-wave breaking in a shallow layer is important for mixing near the surface (e.g., McWilliams et al. 1997), the contribution of high-frequency (short) wave forcing to Langmuir turbulence is not clear (Belcher et al. 2012). Therefore, in the following analysis, we limit our computation of Stokes drift to the imposed cut-off frequency similar to Kukulka et al. (2011). A detailed discussion of cut-off frequency effects on the Stokes drift estimate is beyond the scope of this study.

As illustrated in Fig. 3, the ratio U_{S0}/U_{10} is a constant (= 0.0162) for the Pierson and Moskowitz (1964) spectral model (hereafter PM) (Li and Garrett 1993; Webb and Fox-Kemper

2011). The PM spectrum represents a fully developed and unidirectional wave field. However, the ratio U_{S0}/U_{10} is shown to be small compared with the PM spectral model and to vary with sea state development for spectral models of developing seas (Webb and Fox-Kemper 2011; Harcourt and D'Asaro 2008).

Time series of significant wave height (Hs), direction (θ_p) of dominant waves, and magnitude of Stokes drift at the surface (U_{S0}), derived from ADCP wave measurements are shown in Fig. 2b and c. During wind events, wave height was about 3 m over the bank, and the dominant wave period was about 8 s. Stokes drift was about 4-8 cm s^{-1}, which was a factor 2-4 times larger than the friction velocity induced by surface winds (Fig. 2a-c). In most cases, the dominant surface waves propagated in the direction of the wind. Surface-wave produced pressure at the bottom (Fig. 2d) was measured by the Ppod in the M5 Barny mooring (47 m depth). Surface waves with a dominant wave period of 8 s, measured from bottom-pressure measurements, are consistent with ADCP wave measurements (Fig. 2b). The timing and the duration of the wave signal, measured from both bottom pressure and ADCP surface wave measurements agreed remarkably well.

c. Mixed Layer Depth and Background Currents

The stratification was strong and mixed-layer depth (hereafter referred as MLD or subscript D) was shallow (~10-15 m) during the summer months (Fig. 4a). The stratification became weak and the mixed layer deepened during the passage of atmospheric fronts in fall of 2011. The MLD was estimated from moored temperature time series at S2-S4, since salinity had negligible impact here on the vertical structure of density (Teague et al. 2013). The MLD was computed as the depth at which temperature has decreased by 0.2°C from the shallowest temperature measurement. Estimates of MLD at M2-M4 are similar, and therefore the MLD at M2 is used for this analysis (Fig. 4a). Note: there was not a TCP string mooring at M5, and therefore MLD is inferred from the temperature records at M2-M4 (Fig. 4a). After October 28 (year day 300), the mixed layer around the bank deepened below 47 m, indicating that the water column over the bank was well mixed. A detailed discussion of MLD and its relationships with longer time-scale processes are described by Teague et al (2013). In the present study we will use MLD as a scaling parameter that controls the vertical distribution of high-frequency velocity fluctuations in the mixed layer.

Teague et al. (2013) described low-frequency flows around the bank for 2011. They note that background low-frequency motions were dominated by semi-diurnal tides (12.42 hour), near-inertial waves (25.58 hour), and 60 and 96 hour oscillations. In general, barotropic diurnal and semidiurnal tides were weak, and mean surface currents were eastward in the upper 80 m. Mean currents below approximately 20 m above the bottom followed the bottom topography. Figs. 4b and 4c show low-frequency horizontal currents at M5. Near-inertial currents were typically stronger and highly baroclinic during summer time when stratification was strong. Once the stratification was broken down during fall and winter seasons, the currents became nearly barotropic with relatively weak shear in the water column.

4. High Frequency Velocity Fluctuations

Vertical velocity (w) in the mixed layer over the bank was as large as 10 cm s^{-1} during wind events (Fig. 2e); w is based on 15-min averaged ADCP measurements. Vertical velocity became strongest when wind speed and Stokes drift velocity were largest (Fig. 2a-d). The squared vertical velocity averaged over water depth, $w^2{}_H$, clearly correlated with the occurrence of surface waves over the bank. Fig. 2d and 2e further illustrate the near perfect coincidence between the vertical velocity at 5.5 m and the surface wave signature, measured by the bottom mounted Ppod. A total of 12 wind events with significantly large $w^2{}_H$ were identified between June and December 2011 (Fig. 2f). In general, the production-scale turbulent flows in the mixed-layer have time scales varying from several minutes to hours. These time-scales are determined by the depth of the mixed layer and the dominant turbulent-eddies in the mixed layer. Therefore, the 15-min sampling rate may partially resolve production-scale turbulent flows in the mixed layer. We suspect that large vertical velocities over the bank were related to wave induced currents, such as Langmuir flows. According to the theory of Craik and Leibovich (1976), the combined effects of Stokes drift and background vorticity ($\vec{\Omega}$) of mean currents generates a vortex force $\vec{F}$, which drives the Langmuir circulation, where:

$$\vec{F} = \vec{U}_S(z) \times \vec{\Omega}. \qquad (3)$$

In the following we examine these high-frequency motions in the mixed layer and their relationships to winds and surface waves.

a. Three-Dimensional Velocity Structure

To examine strength and distribution of velocity variance at higher frequencies, velocity spectra were computed during several wind events. One example, shown in Fig. 5, is the variance-preserving velocity spectra for event #4. A spectrum for a given depth, was computed from 512 data points (or 5.33 day record) centered on the wind event. The spectra were multiplied by the corresponding frequencies to construct the variance-preserving spectra, which were then averaged into 32 frequency bands (Fig. 5). Depth-time series of horizontal and vertical velocities for event #4 are plotted in Fig. 6. Low-frequency currents and high-frequency velocity variances are illustrated separately. Low-frequency currents were constructed by removing velocities at higher than 0.08 cph, while high-frequency velocity currents were constructed by removing velocities at frequencies lower than 0.2 cph. A fourth-order Butterworth filter was used for filtering the velocity fields. Velocity spectra show distinct features: (i) spectral peak in horizontal velocity spectra at near-inertial frequency (0.041 cph), and (ii) elevated velocity variance at higher frequencies between 0.2 cph and the Nyquist frequency of 2 cph (Fig. 5). The high-frequency energy levels were largest near the Nyquist frequency, indicating that the 15-min sampling rate would resolve higher frequency motions partially.

During event #4, winds increased from 4 m s^{-1} to 15 m s^{-1}; the southerly winds rotated counter clockwise to form westerly winds in the middle part of event (days 246-247) before veering towards the south during the latter part of the event (Fig. 2). The mixed layer deepened from 20 to 40 m; and low-frequency currents (such as near-inertial waves) as large as 0.5 m s^{-1} were formed. $\langle u^2 \rangle$ was smaller than $\langle v^2 \rangle$, but the strongest values of $\langle u^2 \rangle$ and $\langle v^2 \rangle$ were in the cross-wind direction (Figs. 2, 6). $\langle w^2 \rangle$ varied with winds, but followed Stokes drift closely (not shown). The high-frequency velocity variances ($<u^2>$, $<v^2>$, and $<w^2>$) decreased with depth rapidly; for example, a couple of orders magnitude differences in variance of $<w^2>$ were found between 5.5 m and 40 m water depths (Fig. 6). $<w^2>$ penetrated to greater depths than $<u^2>$ and $<v^2>$. w must be zero at the sea surface and has a sub-surface maximum between the surface and 5.5 m, since w decays with depth starting at 5.5m depth. Furthermore, high-frequency motions were strong when near-inertial waves were large (Fig. 6). We suspect that the advection of high-frequency velocity variances by near-inertial currents might be an important term in the energy balance of high-frequency motions.

We further examined other wind events to understand the three-dimensional velocity structure in the mixed layer. Fig. 7 illustrates two examples of depth-time variability of $<u^2>$, $<v^2>$, and $<w^2>$, and magnitudes and directions of Stokes drift and surface currents. During the summer event (#2) the winds/Stokes drifts were approximately from the south and the mixed later was shallow (~20 m) (Fig. 7a-d); between year day 178 and 179, mixed-layer low-frequency currents were approximately 90^0 out of phase with Stokes drift; after year day 179, mixed-layer currents were dominated by clockwise-rotating, near-inertial motions and increasing mean flow (Fig. 7e). Stokes drift of about 3-5 cm s^{-1} was from the southwest, and reduced to below 2 cm s^{-1} after year day 181 (Fig. 7a). At the beginning of event #2, both the north-south (crosswind) velocity variance ($<u^2>$) and the east-west (downwind) velocity variance ($<v^2>$) were generated. The vertical velocities were strong and $<w^2>$ strengthened, penetrated below the MLD as the Stokes drift increased to above a threshold value (~2 cm s^{-1}) and diminished as Stokes drift decreased below the threshold (Fig. 7e). However, there is no apparent relationship between the magnitude of high-frequency motions and the direction of near-inertial currents (Fig. 7c,e,g,i). During the fall event (#5), the winds/Stokes drifts were approximately from the east and the mixed layer was deep (~40 m). The direction of the surface current was nearly 180^0 out of phase with the Stokes drift between year-day 278 and 281 and those currents became in phase during the later stages (Fig. 7d). At the beginning of event #5, winds/Stokes drift were small; Stokes drift opposed the surface current; and high-frequency velocity components were small. During the latter part of event #5, higher east-west (downwind) ($<u^2>$) and vertical velocity variances were generated as winds/Stokes drift increased and both Stokes drift and the surface-current were in the same direction (coming from the east) (Fig. 7d), but the north-south (crosswind) surface current component ($<v^2>$) remained low (Fig. 7j). For a typical Langmuir flow in the open ocean surface layer, we expect generation of crosswind surface currents, but here we observed a strong downwind surface current (Fig. 7h), perhaps similar to shear-driven turbulence. These examples show the generation of a three-dimensional complex flow field in the presence of wind events and background currents. However, the timing and the magnitude of velocity variances appear to depend on both strengths and directions of winds and waves over the bank. We further examine high wind events and their parameter dependence on $<w^2>$ in Section 4e.

b. Probability Distribution

As discussed above, high-frequency flows, observed during wind events were strongest near the surface, and decayed rapidly with depth. We also noted that magnitudes of upward and downward motions were comparable. Skewness of w for the 12 events between 5.5 m and 15.5 m is −0.34 with a standard deviation 0.36, and the corresponding kurtosis (or flatness) is 4.67

with a standard deviation 0.23. These statistics show that the probability distribution of *w* differs from the Gaussian distribution (in which skewness is 0 and kurtosis is 3). Fig. 8 shows cumulative probability distributions of normalized *u*, *v*, and *w* and the corresponding cumulative normal Gaussian distributions at 5.5 m depth for two wind events (#2 and #12), where the normalized variable $\phi = (\Phi - \overline{\Phi})/\sigma_{\Phi}$, Φ represents *u*, *v*, and *w*, σ_{Φ} is the standard deviation, and the over-bar denotes the mean of the data record. The events shown in Fig. 8 characterize two different background stratifications and wind/wave patterns (Figs. 2, 4). Cumulative distributions of *u*, *v*, and *w* are similar, and they all deviate from the Gaussian distribution when $\phi > \sigma_{\Phi}$, which is nearly 20% of the data record. We noted similar velocity distributions at different depths within the mixed layer. In a turbulent flow, the values of flatness are large compared with a Gaussian distribution if the probability distribution function has relatively large values in its tails (e.g. Fig. 8). The flatness occurs when the time series of the velocity field contains significant numbers of sharp peaks. We suspect that these high-frequency peaks represent production-scale wind-driven turbulent eddies and coherent structures such as Langmuir circulation cells.

c. Spatial Variability

Fig. 9 illustrates high-frequency kinetic energy at M1-M5 for three wind events (#2, #4, and #12). Vertical profiles of horizontal kinetic energy (HKE) and vertical kinetic energy (VKE) were computed from high-pass filtered ADCP velocity profiles. Kinetic energy profiles for these selected events were constructed by time averaging of squared high-pass filtered velocities (*u*,*v*,*w*), where VKE=0.5«w^2» and HKE=0.5(«u^2»+«v^2») and «» denotes a time average over wind events. Here the cut-off frequency was set to 0.2 cph. As we mentioned earlier, these events (Fig. 9) represent different background stratification and wind/wave patterns (Figs. 2, 4). In event #2, the MLD was shallow (~20 m) and winds were from the south - southeast at an average speed of about 8 m s^{-1}. During event #4, the MLD deepened from 20 m to 40 m and winds accelerated from 4 m s^{-1} to 15 m s^{-1} while wind and waves rotated clockwise from north to south. During event #12 there was a frontal passage and the water column was well mixed. The high-frequency kinetic energy at M5 was the largest of all mooring observations. The differences in energy were more pronounced in the vertical kinetic energy profiles than in the horizontal kinetic energy profiles. A significantly high energy level at M5 could be due to the intensification of surface-waves over the bank. M5 is located at 47 m water depth and 3 km north of the peak which is about 20 m below the sea surface. The region north of the peak is a plausible wave-focusing region for waves propagating from the south. We will discuss these wave focusing effects and their impacts on Stokes drift and vertical velocity in Section 5.

d. e-folding scales

The entrainment depth of vertical velocity can be examined from the e-folding length of w^2, since the e-folding length compares individual profiles independently of their magnitudes. The e-folding length (ζ) of w^2, was estimated by fitting the exponential profile between the shallowest depth (5.5m) and 30.5 m, provided that *w* at the shallowest depth was greater than 3 cm s^{-1}. This minimizes uncertainties of ζ by maintaining well-resolved vertical profiles for the computation. For the Craik and Leibovich (1976) theory, the Langmuir circulation is governed by the vortex force (Eq. 3), where the magnitude and vertical structure of w^2 depend strongly on

Stokes drift, $\vec{U}_S(z)$. Stokes drift decays exponentially with depth and is a function of horizontal wave length determined by wave period and water depth. The e-folding length (η) of $|\vec{U}_S(z)|$, was also determined by fitting an exponential profile between the surface and 15 m water depth, provided the magnitude of the Stokes drift at the surface (U_{S0}) is greater than 1 cm s^{-1}. The e-folding length of $|\vec{U}_S(z)|$ was also estimated by finding a depth at which, $|\vec{U}_S(z)|/U_{S0} = e^{-1}$ (e.g., Harcourt and D'Asaro 2008). Both methods produced comparable estimates of e-folding lengths. Note that w^2 profiles were available every 15 min while Stokes drift profiles were available every two hours.

Fig. 10 illustrates time series of e-folding lengths, ζ and η along with the mixed layer depth at S2. The e-folding length of w^2 varied between 3.5 m and 45 m (Fig. 10b) with average and standard deviation of 8.3 m and 3.9 m, respectively for the 12 events. Large values of ζ were found with deep MLD (Fig. 10a, b). Since the vertical scale of turbulent eddies depends strongly on the depth of the mixed layer, we can expect large values of ζ for deep mixed layers. The e-folding length of $\vec{U}_S(z)$ varied between 2 m and 9 m (Fig. 10c) with mean ($\overline{\eta}$) and standard deviation of 4.45 m and 1.02 m, respectively, and is much less than the mixed-layer depth (Fig. 10a). Therefore wave-forcing by the vortex force (Eq. 3) is limited to the upper 10 m or less. As shown in Fig. 10c, where k_p is the peak wavenumber, the vertical scale of dominant surface wave $(2k_p)^{-1}$ is comparable with η indicating that the vertical structure of the Stokes drift is controlled by the dominant wave. Mean and standard deviation of $(2k_p)^{-1}$ for the 12 events are 4.75 m and 1.37 m, respectively. The normalized $\overline{\eta}$ by the mean of $(2k_p)^{-1}$ is about 0.94, which is approximately a factor of 5 larger than the corresponding ratio for the PM spectral model (Li and Garrett 1993). Unlike ζ, η did not change with mixed layer depth but varied with wind speed (Figs. 2, 10). On average, the vertical kinetic energy penetrated approximately twice the average penetration depth of the Stokes drift. Our observations indicate that the penetration depth of w is determined by several factors, including U_{S0}, U_*, MLD, and mean currents, while the penetration of the vortex force is determined by the e-folding length of the Stokes drift.

e. Scaling Vertical Velocity

The relative importance of wind and wave forcing is described by the turbulent Langmuir number (McWilliams et al. 1997; Li et al. 2005; Harcourt and D'Asaro 2008),

$$La_t = \left[U_* / U_{S0}\right]^{1/2}. \qquad (4)$$

Fig. 11 shows La_t vs $\langle w^2_D \rangle / U_*^2$, where $\langle w^2_D \rangle$ was constructed by averaging w^2 over the MLD and then averaging temporally over a 2 hour segment before dividing by U_*^2. La_t is based on two-hourly estimates of U_{S0} and U_*. Almost all of the wind events had $La_t < 1$ although $\langle w^2_D \rangle / U_*^2$ varied between 0.1 and 60. Our estimate of averaged La_t for the 12 wind events is about 0.63 with a standard deviation of 0.17 (Fig. 11), and is comparable to the estimates of Kukulka et al. (2011) based on measured directional wave spectra with f_c= 0.4 Hz. For a fully develop wave field represented by the PM spectral model, La_t is about 0.3 (Li and Garrett 1993; Li et al. 2005). The turbulent Langmuir number is expected to be higher than 0.3 for developing seas under fetch-limited conditions due to weaker Stokes drift (Li et al. 2005; Harcourt and D'Asaro 2008).

Another important scaling parameter is the Hoennikker number (Li et al. 2005), which describes the relative importance of convection (unstable buoyancy forcing) and vortex force driving Langmuir circulation. However, we do not have the net surface buoyancy flux to evaluate the Hoennikker number. We examined day and night variability of $<w^2>$ for cases where $La_t < 1$ and $<w^2_D>/U_*^2 > 1$, but did not find significant differences during wind events.

The vertical velocity is examined within the framework of the wind/wave mechanism such as Langmuir circulation (Craik and Leibovich 1976). This framework is often used to describe the surface velocity variance observed from Doppler sonar systems (e.g., Plueddemann et al. 1996; Smith 1998) and the Large Eddy Simulation of the oceanic mixed layer, where the vortex forcing is added to mimic Langmuir circulation (Skyllingstad and Denbo 1995; McWilliams et al. 1997; Harcourt and D'Asaro 2008; Grant and Belcher 2009). D'Asaro and Dairiki (1997), and Tseng and D'Asaro (2004) compared MLD-averaged squared vertical velocity with squared friction velocity, and found that on average, $<w^2_D>$ was about a factor of 1.5-3.0 larger than U_*^2, showing the departure from the wall-boundary layer theory. Their empirical evidence is somewhat surprising due to lack of dependence on surface wave parameters. Plueddemann et al. (1996) suggest that surface velocity variance scales as U_*U_{S0}, while Smith (1998) reports that velocity variance follows U_{S0}^2 scaling once Langmuir circulation is established. Harcourt and D'Asaro (2008) suggest that turbulent vertical velocity scales as $U_*La_L^{-2/3}$, where $La_L=(U_*/<U_{SL}>)^{1/2}$ and U_{SL} is the averaged Stokes drift within the surface layer (L), which is taken as 20% of the height of the mixed layer. Based on LES studies, Grant and Belcher (2009) report that the velocity scale of Langmuir turbulence can be expressed as $(U_*^2U_{S0})^{1/3}$, similar to the scaling suggested by Smith (1996). The observations and modeling studies indicate that there is no consistent scaling for Langmuir cell velocities, even though all these scaling arguments are either related to U_{S0} or a combination of U_*, U_{S0}, and mixed layer depth. $<w^2>$ can vary with surface forcing such as Stokes drift, friction velocity, and surface buoyancy flux, and with upper ocean dynamics such as mixed layer depth and advection caused by mean currents.

We will apply some of the existing scaling methods to the observed vertical velocity in the mixed layer over the bank. We limit our analysis to 12 wind events shown in Fig. 2f where a significant number of good vertical velocity profiles can be found. These wind events occupied a total of about 41 days between June and December 2011. We used 3928, 15-min-averaged w profiles for the analysis. We note that the magnitude and vertical structure of w^2 and that magnitudes and directions of Stokes drifts and winds varied significantly within a wind event. Therefore the scaling of vertical profiles should be conducted by identifying profiles which have similar dynamical regimes or belong to similar parameter regimes defined by the underlying physical process. Fig. 12 shows spreading of $<w^2_D>/U_*^2$ as a function of D/H, where D/H is the fractional mixed layer depth. The segments cover a broad range of values where $<w^2_D>/U_*^2$ ranges from 0.1 to 60 and D/H from 0.2 to 1 (Fig. 12). The vertical velocity profiles were divided into three groups of ($<w^2_D>/U_*^2$) denoted by A, B and C (Fig. 12). These groups were selected by considering the mixed-layer vertical kinetic energy relative to the wall boundary-layer estimates; for example, ($<w^2_D>/U_*^2$) >1 represents regimes which depart from wall boundary scaling. As shown in Fig. 12, data belong to a wide range of mixed-layer depths, and therefore each group was divided into four subgroups representing four different segments of D/H (e.g. A1, A2, A3, and A4 in Fig. 12). For example, the subgroup A1 represents weak energy and shallow mixed-layer profiles whereas the group A4 represents weak energy and deep mixed-layer profiles. Profiles of $<w^2>$ in each subgroup were scaled by U_*^2, U_*U_{S0}, $(U_*^2U_{S0})^{2/3}$, and U_{S0}^2 before constructing averaged profiles.

Scaled $<w^2>$ profiles of all subgroups are compared as a function of scaled depth, z/D (Fig. 13). Here we compare near surface estimates and the vertical structure of scaled $<w^2>$ resulting from U_*^2, U_*U_{S0}, and U_{S0}^2, since the scaling by U_*U_{S0} and $(U_*^2U_{S0})^{2/3}$ produce relatively similar results. The averaged profiles of $<w^2>$, scaled by U_*^2, U_*U_{S0}, and U_{S0}^2 are plotted, respectively, in the left, middle, and right columns of Fig. 13. The top, middle, and bottom rows in Fig. 13 contain profiles from group-A, group-B, and group-C (Fig. 12), respectively. There is a fair qualitative agreement with U_*^2 scaling for group A (Fig. 13a). Here $<w^2>/U_*^2$ profiles in group A collapse to a single curve in the upper half of MLD. However, U_*^2 scaling fails for $(<w^2_D>/U_*^2) >1$ (Figs. 13b,c). The scaling of $<w^2>$ by U^*U_{S0} is also qualitatively consistent with group A even though near surface estimates are slightly smaller than the expected estimate of unity (Fig. 13d). U^*U_{S0} scaling over predicts slightly for B1, B3, and B4 (Fig. 13e). Like U_*^2 scaling, U_*U_{S0} does not provide a satisfactory agreement for group C, where $<w^2>/U_*U_{S0}$ near the surface is about 10. There is a wide range of values for $<w^2>/U_{S0}^2$ for groups A and B, but $<w^2>/U_{S0}^2$ near the surface is close to unity for subgroups A2, A4, B1, B2, and B4. None of the scaling methods works well for group C, nevertheless U_{S0}^2 scaling provides near surface estimates of $<w^2>/U_{S0}^2$ close to a factor of two. In most of the groups, the vertical structure of scaled profiles decays with varying e-folding scales. These results reflects the fact that there is no unique scaling of $<w^2>$ profiles in the mixed layer based on surface forcing parameters, although $<w^2>$ depends on U_*, U_{S0}, mixed layer depth, and e-folding scales of w^2.

Wind events generate near-inertial currents (e.g., Fig. 5), and the relative direction between winds and surface currents can make a difference in the vertical shear of horizontal currents which in turn can alter turbulence production in the mixed layer. This scenario could be a plausible explanation why our parameterizations were significantly different from previous publications. We examined the impact of low-frequency (near-inertial) currents on high-frequency vertical velocity by examining correlations between vertical velocity and directional difference between winds and near-surface currents. Relations among wind and surface current directions, wind speed, and variability of high-frequency flows for 12 events (Fig. 2) were examined. We did not find a clear relation between the angular difference of the mixed layer current and wind speed, and $<w^2>$ during different stages of wind events. The difference between wind and current directions were computed from 2-hour averaged current and wind fields. Here near-surface currents at M5 were constructed by depth-averaging low-pass filtered horizontal currents between 5.5 and 15.5 m.

5. Discussion

a. Vertical scaling

Scaling of $<w^2>$ by surface forcing parameters such as friction velocity and Stokes drift produced inconclusive results. We note that the e-folding scale of $<w^2>$ has a wider range and varies with the mixed-layer depth. For example, profiles in groups B and C have higher energy levels at depth than the rest of the profiles. The vertical distribution of $<w^2>$ should also be considered when scaling $<w^2>$ (e.g., D’Asaro and Dairiki 1997; Harcourt and D’Asaro, 2008), since individual profiles of w^2 have diverse e-folding scales and are associated with different mixed layer depths (Fig. 9). Therefore, we consider mixed-layer averaged statistics such as squared vertical velocity, $<w^2_D>$, as our variable to be scaled and then examine the variability of scaled $<w^2_D>$ as a function of the e-folding length scale of w^2 and the mixed layer depth. Fig. 14 illustrates $<w^2_D> /U_*^2$ vs ζ/D and $<w^2_D> /U_{S0}^2$ vs ζ/D where ζ/D is the fractional e-folding length. For $<w^2_D> /U_*^2 <1$, the scaling by U_*^2 provides a tighter relationship with ζ/D (Fig. 14a), which is consistent with Fig 13a, but U_*^2 scaling fails for $<w^2_D> /U_*^2 >1$. The scaling by U_{S0}^2 forces close-fitting between $<w^2_D> /U_{S0}^2$ and ζ/D. As shown in Fig. 14b, log($<w^2_D> /U_{S0}^2$) is approximately a linear function of ζ/D, and the least square fit to the data is

$$\frac{< w_D^2 >}{U_{S0}^2} = \alpha \; Exp\left[\beta \frac{\zeta}{D}\right], \qquad (5)$$

where $\alpha = 0.2$, $\beta = 3.75$.and $0 < \zeta / D \leq 1$. In general U_{S0}^2 scaling provides a better representation of data, when effects of the mixed layer depth and the penetration depth of the vertical velocity are included.

b. Wave focusing over the bank

We noted that high-frequency kinetic energy over the bank at M5 is significantly larger than the kinetic energy around the bank, and these differences can be clearly seen in the vertical kinetic energy, especially when winds were from the south-southeast (Fig. 8). We suspect that these higher velocity fluctuations are generated by wave-current interaction mechanisms defined by the vortex force (Eq. 3). The amplitude of the vertical component of the vortex force is: $F_v = | U_S(z) \partial \overline{U_m} / \partial z |$, where $|U_S(z)|$ is the amplitude of the Stokes drift and $\partial \overline{U}_m / \partial z$ is the vertical gradient of the mean current in the direction of the Stokes drift. To examine the influence of $\partial \overline{U}_m / \partial z$ on F_v, these gradients are compared at different sites. As shown in Fig. 15, all five moorings sites over and around the bank had similar profiles of vertical shear of the mean currents. Here components of vertical shear were computed from centered-differencing of low-pass filtered ADCP records, where, the squared shear of the mean current is: $Sh^2 = (\partial \overline{U}_m / \partial z)^2 = [(\partial U / \partial z)^2 + (\partial V / \partial z)^2]$ (Fig. 15). The low-frequency shear is dominated by near-inertial currents and is largest at the base of the mixed layer. Shear profiles vary with wind events and background stratification, but the magnitude and vertical structure of shear profiles are relatively similar for all mooring sites. Therefore, it is unlikely that $\partial \overline{U}_m / \partial z$ alone generates a larger vertical velocity over the bank than at other locations around the bank.

The propagation of surface waves over complex bottom bathymetric features may be associated with many processes including shoaling, refraction, energy dissipation and diffraction. We suspect that waves coming from the south (southwest to southeast) generate a focusing region behind the peak of the bank, while enhancing surface wave amplitudes and Stokes drift. To examine the plausibility of wave focusing, we apply a refraction and diffraction numerical wave model (REF/DIF1) developed by Kirby and Dalrymple (1994). REF/DIF1 is a phase-resolving parabolic refraction-diffraction model for ocean surface wave propagation.

We apply REF\DIF1 to a domain of 14 km (north-south) by 10 km (east-west) encompassing the EFGB (Fig. 1) with the x-axis as the offshore boundary for incoming waves. The surface Stokes drift for a monochromatic wave can be estimated as $U_{S0} = a^2 k\omega$, where a is the amplitude of the monochromatic wave, k is the wave number and ω is the radian frequency. Note the wave height is twice the wave amplitude.

Fig. 16 shows simulation results of wave height and Stokes drift for a representative monochromatic wave of 1 m amplitude (or 2 m wave height) and 8 s wave period, propagating from the southern boundary into the model domain. The selected wave statistics are similar to the waves statistics observed during event #2 (Fig. 2). The model results display the spatial variation of wave height and Stokes drift induced by the depth changes from the presence of the bank. The northward propagating wave focuses over a narrow area behind the peak of the bank while generating a much higher wave height and Stokes drift. The wave height in the focusing area reaches 3 m which is a 50% increase over the incoming wave. The surface Stokes drift increases to 12 cm s^{-1}, which is approximately a factor of 2.5 higher than that of the incoming wave. Several sensitivity REF\DIF1 simulations were also conducted by changing the incoming wave direction by ±15 degrees. Similar narrow band wave focusing zones were found. Out of five moorings, only one mooring (M5) is in the vicinity of the focusing zone. Our simulation is limited to a monochromatic wave train with a single direction and no background currents. Nevertheless this simulation demonstrates the underlining physical process. It is likely that the observations of high energy levels of kinetic energy at M5 would be a result of enhancement of Stokes drift caused by wave focusing induced by the bathymetric variation of the EFGB.

c. Impact of Vertical Motion on Corals

The EFGB marine sanctuary is a biologically diverse environment, and supports a large number of species including corals. Coral reefs are complex, dynamic, and sensitive eco-systems. Therefore understanding of the hydrodynamics, turbulence characteristics, mixing of water masses over banks and transport of suspended sediment are important for the coral reef system. Wave-current interactions and generation of deeply penetrating vertical motions can play an important role in mixing, rapid deepening of the mixed layer, and vertical transports of near-surface water toward coral habitats on the bottom. Vertical velocities intensify during wind events, while wave focusing can further enhance wave-driven Stokes drift thus providing an efficient mixing and transport mechanism over the bank.

6. Conclusions

The main objectives of this study are: (i) to examine surface wave effects on high-frequency flows over the EFGB, (ii) to quantify spatial and temporal characteristic of these high-frequency flows, and (iii) to examine the scaling laws of vertical velocity based on the Langmuir circulation theory. The major observational findings and inferences of this study are:

- High-frequency, three-dimensional flows with frequencies ranging from 0.2 to 2 (Nyquist frequency) cycles per hour were found in the mixed layer when wind speed and Stokes drift were large. It is suggested that Stokes drift and mean flow interactions such as Langmuir circulation are responsible for generating the observed velocity fluctuations.

- Stokes drift over the bank was estimated from two-dimensional directional wave spectra from a 600 kHz ADCP. The estimated Stokes drift at the surface (U_{S0}) varied with the wind speed and is about 0.6% of the wind speed for winds greater than 10 m s^{-1}. However, our estimates are a factor of two smaller than the estimates based on the PM spectral model.

- Vertical velocity fluctuations showed upward and downward motions with similar magnitudes. The probability distribution of velocity fluctuations (u, v, w) departs from the Gaussian distribution especially at the tail ends of the distribution.

- Squared vertical velocity w^2 was strongest near the surface and decayed exponentially with depth, and the associated e-folding length is a factor of two larger than the e-folding length associated with Stokes drift.

- The two-hour and mixed-layer averaged $<w^2_D>$, normalized by the squared friction velocity U_*^2, varied from 0.1 to 60. $<w^2_D>/ U_*^2$ was strongest when the turbulent Langmuir number was less than unity and the mixed layer was shallow.

- Scaling of squared vertical-velocity profiles was examined as functions of U_*^2, U_*U_{S0} and U_{S0}^2. Although w^2 is likely to be a function of Stokes drift, U_*, and mixed layer depth, a unique scaling for profiles of w^2 was not found. For $<w^2_D>/ U_*^2 < 5$, there is a qualitative agreement with different scaling for wide ranges of the fractional MLD. For $<w^2_D>/ U_*^2 >5$, all the scaling techniques under-predict near surface estimates of w^2. However, when we consider mixed-layer averaged statistics such as squared vertical velocity, $<w^2_D>$ as the scaling variable, the scaling by U_{S0}^2 forces tighter relationships between $<w^2_D> /U_{S0}^2$ and ζ/D, and $<w^2_D> /U_{S0}^2$ is approximately an exponential function of ζ/D. In general U_{S0}^2 scaling provides a better representation of $<w^2_D>$ data, when effects of the mixed layer depth and the penetration depth of the vertical velocity are included.

- Largest velocity variances were found over the bank at M5, located nearly 3 km north of the peak of the bank. It is suggested based on a wave refraction-diffraction model (REF/DIF1) that the increase in kinetic energy over the bank is due to enhancement of Stokes drift by topography-induced waves focusing.

- The lack of agreement with open-ocean parameterizations of vertical kinetic energy over the bank is likely due to the enhancement of kinetic energy resulting from localized focusing of surface waves.

Wave-driven velocity fluctuations play an important role in mixing and vertical transports and, in addition, can strongly impact coral habitats over the EFGB. Our study reveals that such velocity fluctuations over the bank are closely related to surface wave conditions that can have strong localized variability due to wave focusing over the bank. Our findings indicate that the scaling of wave-induced mixed-layer currents over a shelf edge bank differs from the open ocean. Recently, Belcher et al. (2012) examined the global perspective of Langmuir turbulence in the ocean surface boundary layer using LES and diagnostic analysis techniques. However, the lack of understanding of detailed physical process suggests that further studies are needed for the generalization of wave-driven mixing processes in the coastal environment.

Acknowledgements

This work was sponsored by the Office of Naval Research in a Naval Research Laboratory (NRL) project referred to as “Mixing over Rough Topography (MORT)” under program element 0601153N and by the Bureau of Ocean Energy Management (BOEM; formerly Minerals Management Service) in the project referred to as “Currents over Banks (COB)” through the Interagency Agreement No. M10PG0003. Support for James Moum was provided through ONR grant N00014-09-1-0280. The measurements were made in cooperation with the Flower Garden Banks National Marine Sanctuary, administered by the National Oceanic and Atmospheric Administration (NOAA). Supports provided by Alexis Lugo Fernandez of BOEM and Emma Hickerson of NOAA were greatly appreciated. We thank Mark Hulbert, Steve Sova, Andrew Quaid, and Justin Brodersen for their technical support in mooring preparations and successful deployments. We also thank the captain, crew, and marine technician of the R/V Pelican and crew of R/V Manta for their assistance. We thank the two anonymous reviewers for their thorough and careful review of the manuscript, and useful comments.

References:

Agrawal, Y. C., E.A. Terray, M. A. Donelan, P. A. Hwang, A. J. Williams III, W. M. Drennan, K. K. Kahma, and S. A. Kitaigorodskii, 1992: Enhanced dissipation of kinetic energy beneath surface waves. *Nature*, **359**, 219–220.

Anis, A., and J. N. Moum, 1995: Surface wave-turbulence interactions: Scaling $\varepsilon(z)$ near the sea surface. *J. Phys. Oceanogr*., **25**, 2025–2045.

Belcher, S. E., A. L. M. Grant, K. E. Hanley, B. Fox-Kemper, L. V. Roekel, P. P. Sullivan, W. G. Large, A. Brown, A. Hines, D. Calvert, A. Rutgersson, H. Pettersson, J-R Bidlot, P. A. E. Janssen, and J. Polton, 2012: A global perspective on Langmuir turbulence in the ocean surface boundary layer. *Geophys. Res. Lett.*, **39**, L18605, doi:10.1029/2012GL052932.

Brubaker, J. M., 1987: Similarity structure in the convective boundary layer of a lake. *Nature*, **330**, 742-745.

Craik, A. D. D. and Leibovich, S., 1976: A rational model for Langmuir circulations. *J. Fluid. Mech.*, **73**, 401–426.

D'Asaro, E. and G. Dairiki, 1997: Turbulence intensity measurements in a wind driven mixed layer. *J. Phys. Oceanogr.*, **27**, 2009-2022.

Dillon, T. M., J. G. Richman, C. G. Hansen, and M. D. Pearson,1981: Near-surface turbulence measurements in a lake. *Nature*, **290**, 390–392.

Donelan, M. A.,J. Hamilton, and W. H. Hui, 1985: Directional spectra of wind-generated waves. *Philos. Tans. Roy. Soc. London*, **A315**, 509-562.

Drennan, W.M., M.A. Donelan, K.B. Katsaros and E.A. Terray, 1996: Oceanic turbulence dissipation measurements in SWADE. *J. Phys. Oceanogr*., **26**, 808-815.

Earle, M.D., K. E. Steele, D. W. C. Wang, 1999: Use of advanced directional wave spectra analysis methods. *Ocean Engineering,* **26**, 1421–1434.

Gargett, A. N., and J. R. Wells, 2007: Langmuir turbulence in shallow water. Part 1. Observations. *J. Fluid. Mech.*, **576**, 27-61, doi:10.1017/S0022112006004575.

Grant, A. L. M., and S. E. Belcher, 2009: Characteristics of Langmuir turbulence in the ocean mixed layer. *J. Phys. Oceanogr.*, **39**, 1871–1887.

Harcourt, R. A., and E. A. D'Asaro, 2008: Large-Eddy simulation of Langmuir turbulence in pure wind sea. *J. Phys. Oceanogr.*, **38**, 1542-1562.

Hunter, R. E., and G. W. Hill, 1980: Near-shore current pattern off south Texas: an interpretation from aerial photographs. *Remote Sensing Environ*., **10**, 115–134.

Hwang, P. A., 2011: A note on the ocean surface roughness spectrum. *J. Atmos. Oceanic. Technol*., **28**, 436-443, DOI:10.1175/2010JTECHO812.1.

Kenyon, K. E., 1969: Stokes drift for random gravity waves. *J. Geophys. Res.,***74,** 6991–6994.

Kirby, J. T., and R. A. Dalrymple, 1994: Combined Refraction-Diffraction Model REF/DEF1, Version 2.5 Documentation and User's Manual, Report 94-22, Center for Applied Coastal Research, University of Delaware. http://chinacat.coastal.udel.edu/programs/nearcom/wave_module_refdif1.html.

Kukulka, T., A. J. Plueddemann, J. H. Trowbridge, and P. P. Sullivan, 2011: The influence of crosswind tidal currents on Langmuir circulation in a shallow ocean. *J. Geophys. Res.* **116**, C08005, doi:10.1029/2011JC006971.

Langmuir, I., 1938: Surface motion of water induced by wind. *Science*, **87**, 119–123.

Leibovich, S., 1983: The form and dynamics of Langmuir circulations. *Annu. Rev. Fluid Mech.,* **15**, 391–427.

Li, M., C. Garrett, and E. Sykllingstad, 2005: A regime diagram for classifying turbulent eddies in the upper ocean. *Deep-Sea Res.*, I **52**, 259–278. doi:10.1016/j.dsr.2004.09.004.

Li, M. and C. Garrett, 1993: Cell merging and jet/downwelling ratio in Langmuir circulation. *J. Mar. Res.,* **51**, 737-769.

Lombardo, C. P., and M. C. Gregg, 1989: Similarity scaling of viscous and thermal dissipation in a convecting surface boundary layer. *J. Geophys. Res*., **94**, 6273–6284.

Lumley, J. L., and H. A. Panofsky, 1964: The Structure of Atmospheric Turbulence. Wiley-Interscience, New York, 239 pp.

Marmorino, G. O., G. B. Smith, and G. J. Lindemann, 2005: Infrared imagery of large-aspect-ratio Langmuir circulation. *Cont. Shelf Res.*, **25**, 1–6. doi:10.1016/j.csr.2004.08.002.

McWilliams, J. C., P. P. Sullivan, and C.-H. Moeng, 1997: Langmuir turbulence in the ocean. *J. Fluid Mech.*, **334**, 1–30.

Mellor, G. L., and T. Yamada, 1982: Development of a turbulent closure models for planetary boundary layers, *J. Atmos. Sci.*, **31**, 1791-1806.

Melville, W. K., 1996: The role of surface-wave breaking in air-sea interaction. *Annu. Rev. Fluid Mech.*, **28**, 279–321.

Moum, J. N., and J. D. Nash, 2008: Seafloor pressure measurements of nonlinear internal waves. *J. Phys. Oceanogr.*, **38**, 481–491.

Perkins, H., F. De Strobel, and L. Gauldesi, 2000: The barny sentinal trawl-resistant ADCP bottom mount: design, testing, and application. *IEEE J. Ocean. Engr.*, **25**, 430–436.

Pierson, W. J., and L. Moscowitz, 1964: A proposed spectral form for fully developed wind seas based on the similarity theory of S A Kitaigorodskii. *J. Geophys. Res.*, **69** (24), 5181–5190.

Plueddemann, A. J., J. A. Smith, D. M. Farmer, R. A. Weller, W. R. Crawford, R. Pinkel, S. Vagle, and A. Gnanadesikan, 1996: Structure and variability of Langmuir circulation during the surface waves processes program. *J. Geophys. Res*., **101**, 3525–3543.

Pollard, R., and K. J. H. Thomas, 1989: Vertical circulation revealed diurnal heating of the upper ocean in late winter, part 1: Observations. *J. Phys. Oceanogr.*, **19**, 269-278.

Rascle. N, A. Fabrice, Q. Pierre, and C-F Denis, 2008: A global wave parameter database for geophysical applications. Part 1: Wave-current-turbulence interaction parameters for the open ocean based on traditional parameterizations. *Ocean Modelling*, **25**(3-4), 154-171.

Shay, T. J., and M. C. Gregg, 1986: Convectively driven turbulent mixing in the upper ocean, *J. Phys. Oceanogr.*,**16**, 1777-1798.

Skyllingstad, E. D., W. D. Smyth, J. N. Moum, and H. Wijesekera, 1999: Upper ocean turbulence during a westerly wind burst: A comparison of large-eddy simulation results and microstructure measurements. *J. Phys. Oceanogr.*, **29,** 5–28.

Skyllingstad, E. D., and D. W. Denbo, 1995: An ocean large-eddy simulation of Langmuir circulations and convection in the surface mixed layer. *J. Geophys. Res.*, **100**, 8501–8522.

Smith, J. A., R. Pinkel, and R. A. Weller, 1987: Velocity structure in the mixed layer during MILDEX. *J. Phys. Oceanogr.* **17**, 425–439.

Smith, J. A., 1992: Observed growth of Langmuir circulation. *J. Geophys. Res*. **97**, 5651–5664.

Smith, J. A, 1996: Observations of Langmuir circulation, waves, and the mixed layer, in *The Air Sea Interface: Radio and Acoustic Sensing, Turbulence, and Wave Dynamics*, edited by M. A. Donelan, W. H. Hui, and W. J. Plant, pp 613-622, Univ. of Toronto Press., Toronto, Ont., Canada.

Smith, J. A., 1998: Evolution of Langmuir circulation during a storm. *J. Geophys. Res.* **103**, 12,649-612,668.

Soloviev, A. V., N. V. Vershinsky, and V. A. Bezverchnii, 1988: Smallscale turbulence measurements in the thin surface layer of the ocean. *Deep Sea Res*., **35**, 1859–1874.

Soloviev, A. and R. Lukas, 2003: Observation of wave enhanced turbulence in the near surface layer of the ocean during TOGA COARE, *Deep-Sea Research*. Part I, **50**, 371-395.

Strong, B., B. Brumley, E, A. Terray, and G. W. Stone, 2000: The performance of ADCP-derived directional wave spectra and comparison with other independent measurements. *Proc. MTS/IEEE Oceans 2000 Conf.* Rhode Island, USA, Providence, 1195–1203.

Teague, W. J., H.W. Wijesekera, and E. Jarosz, D.B. Fribance, A. Lugo-Fernández, and Z.R. Hallock, 2013: Current and Hydrographic Conditions at the East Flower Bank in 2011. *Cont. Shelf Res.* (in revision).

Terray, E.A., M.A. Donelan, Y.C. Agrawal, W.M. Drennan, K.K. Kahma, A.J. Williams III, P.A Hwang, and S.A. Kitaigorodskii, 1996: Estimates of kinetic energy dissipation under breaking waves. *J. Phys. Oceanogr.* **26**, 792-807.

Tseng, R-S., and E. A. D'Asaro, 2004: Measurements of turbulent vertical kinetic energy in the ocean mixed layer from Lagrangian floats. *J. Phys. Oceanogr*., **34**, 1984–1990.

Thorpe, S. A., 2004: Langmuir circulation. *Annu. Rev. Fluid Mech*., **36**, 55–79.

Thorpe, S. A., 2005: *The Turbulent Ocean*. Cambridge University Press, Cambridge CB2 2RU, UK, 439pp.

Webb, A., and B. Fox-Kemper, 2011: Wave spectral moments and Stokes drift estimation, *Ocean Modelling*, **40**, 273-288.

Weller, R. A. and J. F. Price, 1988: Langmuir circulation within the oceanic mixed layer. *Deep-Sea Res.*, **35**, 711–747.

Zedel, L., and D. Farmer, 1991: Organized structures in subsurface bubble clouds – Langmuir circulation in the open ocean. *J. Geophys. Res.,* **96**, 8889-8900.

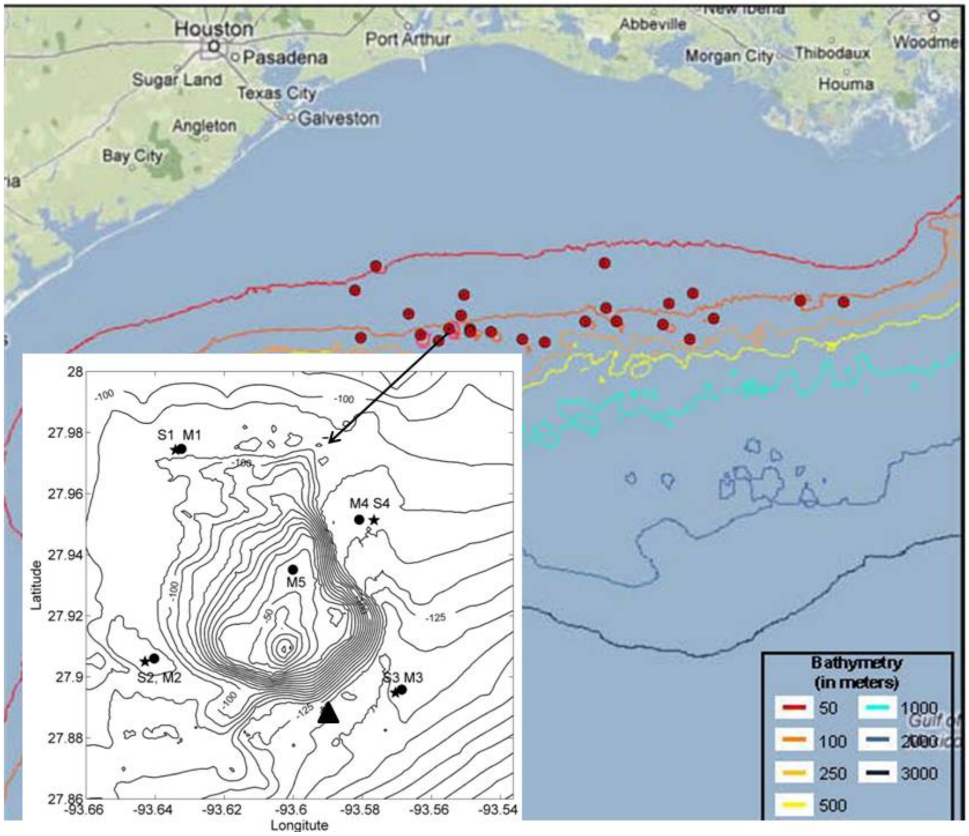

Figure 1**.** Color image shows the location of the Flower Garden Banks National Marine Sanctuary. Red circles represent salt domes or banks along with selected bathymetric contours. The black and white map illustrates the bathymetric contours of the East Flower Garden Bank (EGFB) and the locations of the five bottom mounted ADCP moorings (M1-M5) (filled circles) and four string moorings (S1-S4) (filled stars). The contour interval of bathymetry is 5 m. The solid triangle denotes the location of NDBC buoy 42047.

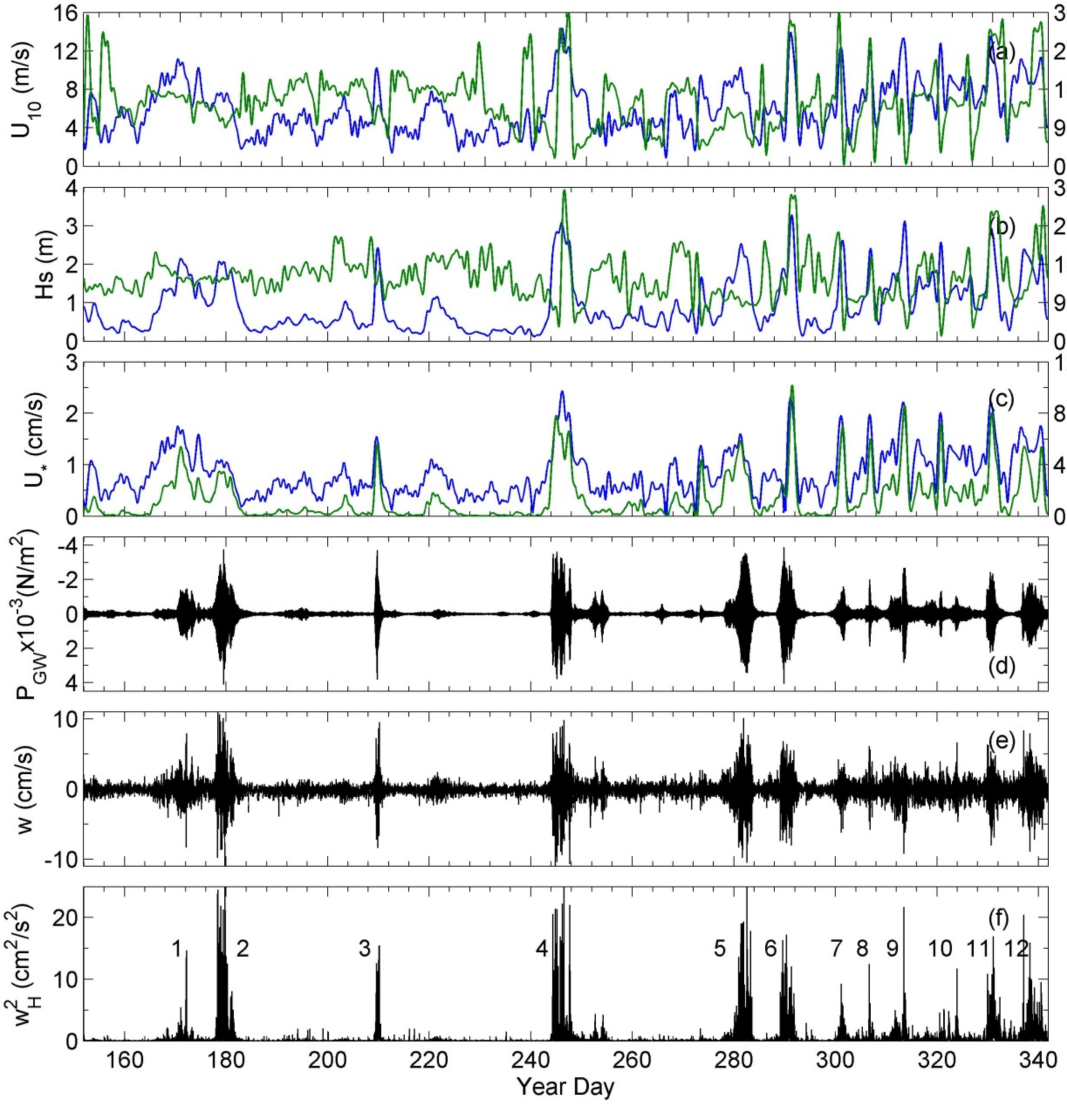

Figure 2. Time series between June 2 (Year Day 152) and December 8, 2011 (Year Day 342): (a) Wind speed, U_{10} (blue) and direction θ_{U10} (green). (b) Surface wave height, *Hs* (blue) and the direction of the wave corresponding to the peak wave energy θ_P (green). (c) Frictional velocity U_* (blue) and Stokes drift velocity at the surface U_{S0} (green). (d) High-pass filtered pressure (P_{GW}) at 47 m depth (bottom) from Ppod pressure sensor at M5; P_{GW}/1000 is plotted. (e) Time series of 15-min averaged vertical velocity at 5.5 m depth at M5, where water depth is 47 m. (f) Depth-averaged squared vertical velocity (w^2_H) at M5. Targeted wind events are numbered 1-12.

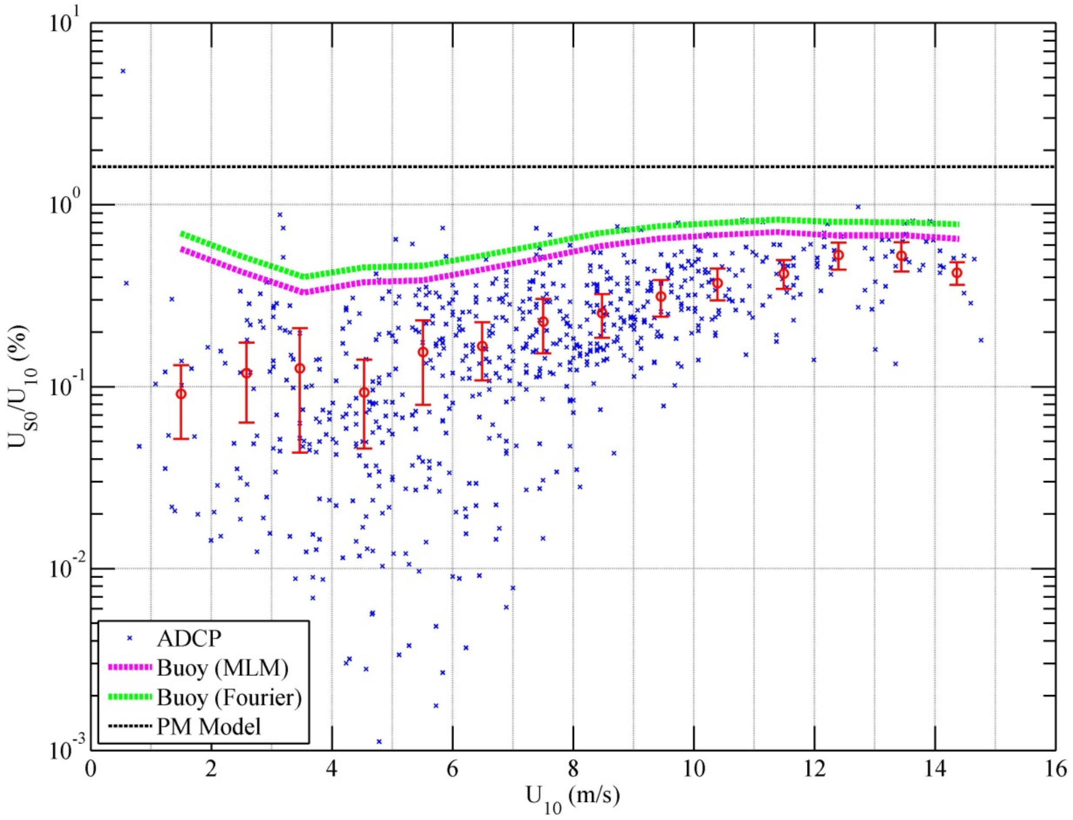

Figure 3. Ratio of surface Stokes drift to wind speed, U_{S0}/U_{10} versus U_{10}. Red circles are bin-averaged U_{S0}/U_{10} for 1 m s^{-1} wind speed intervals. The error-bars show one standarad deviation. The magenta and green dashed lines represent bin-averaged results from NDBC buoy 42019 for all of 2011 based on directional spectra derived from the MLM and Fourier series methods, respectively. The black dashed line represents a value of 1.62% derived from the PM spectral model.

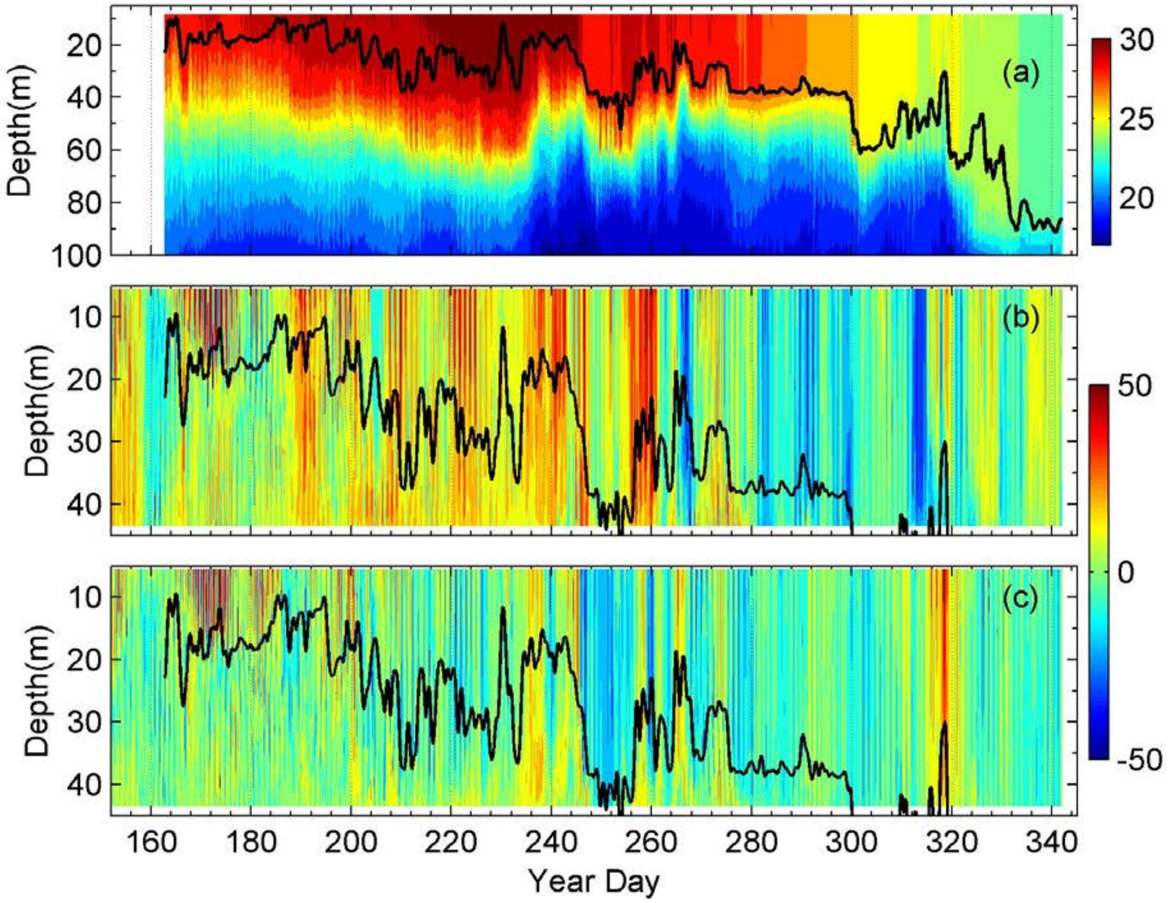

Figure 4. Top panel (a): The color image shows the time-depth series of temperature (in ^{o}C) at S2. The thick black line denotes the mixed layer depth. Middle and bottom panels: Low-pass filtered east-west (*U*) (b) and north-south (*V*) (c) velocity components at M5 where water depth is 47m. Units are cm s^{-1}. Cut off frequency of low-frequency currents is 0.08 cph. The black lines indicate the mixed layer depth at S2.

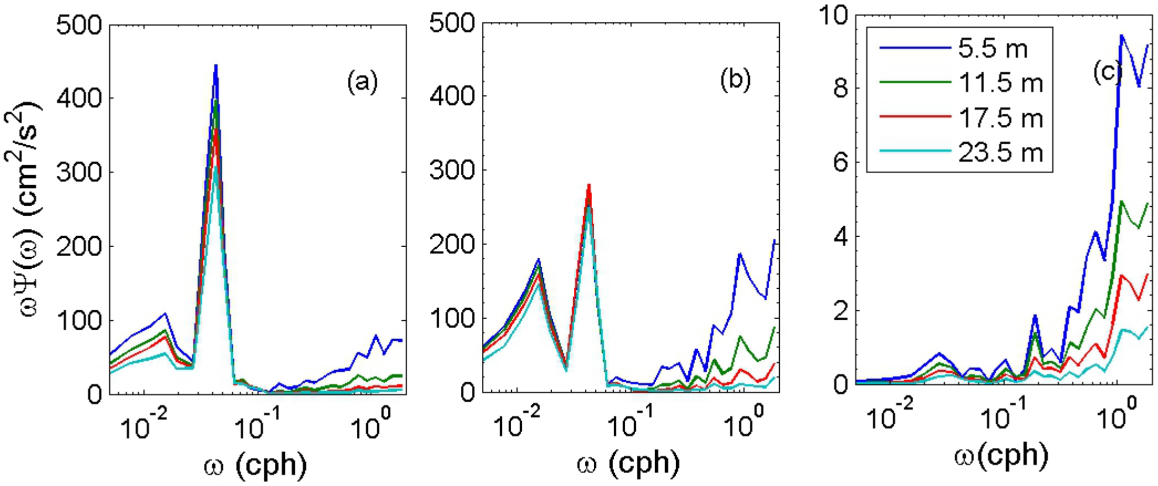

Figure 5. Variance-preserving frequency spectra: (a) east-west, (b) north-south, and (c) vertical components of velocity computed at 5.5, 11.5, 17.5, and 23.5 m water depths for the wind event #4. The inertial frequency is 0.041 cph.

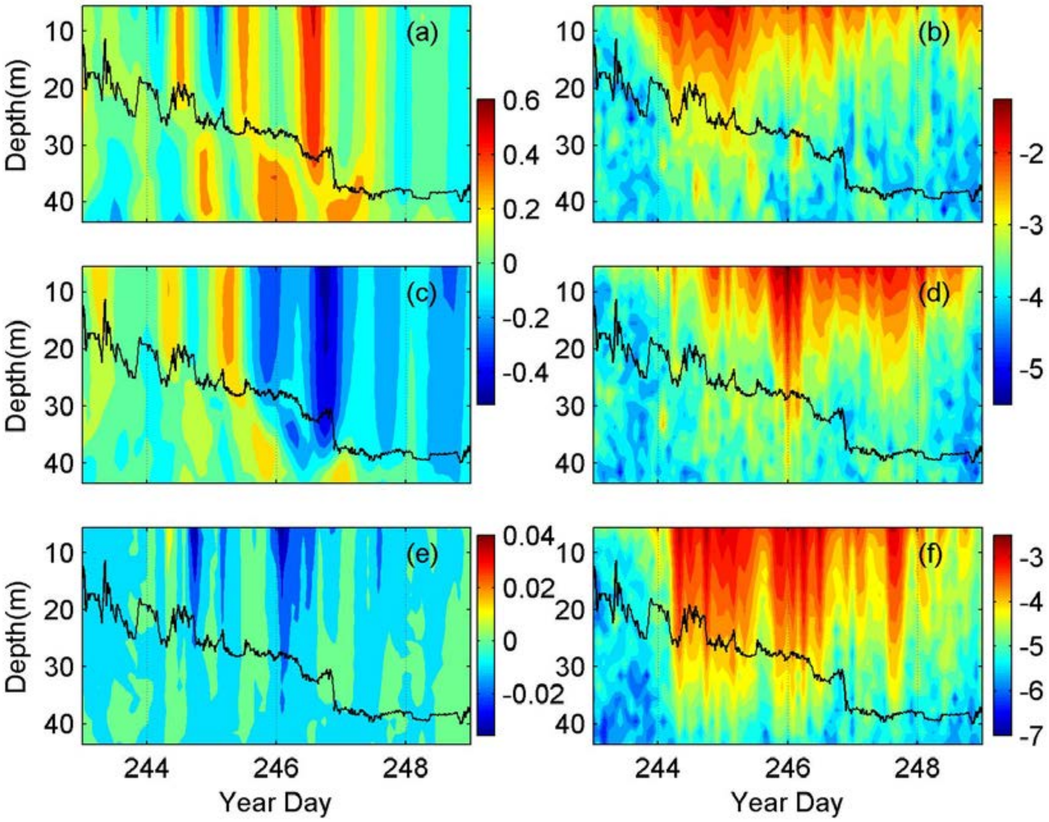

Figure 6. Depth-time sections of currents at M5 during wind event #4. Left Panel: Low-pass filtered currents (a) east-west (*U*), (c) north-south (*V*), and (e) vertical (*W*) in m s^{-1}. East, north, and upward directions are positive. Right Panel: log10 values of squared high-frequency currents (b) $\log_{10}(<u^2>)$, (d) $\log_{10}(<v^2>)$, and (f) $\log_{10}(<w^2>)$, where *u*, *v*, *w* are in m s^{-1}. The black lines denote the mixed layer depth. The cut off frequency for high-frequency fluctuations is set to 0.2 cph.

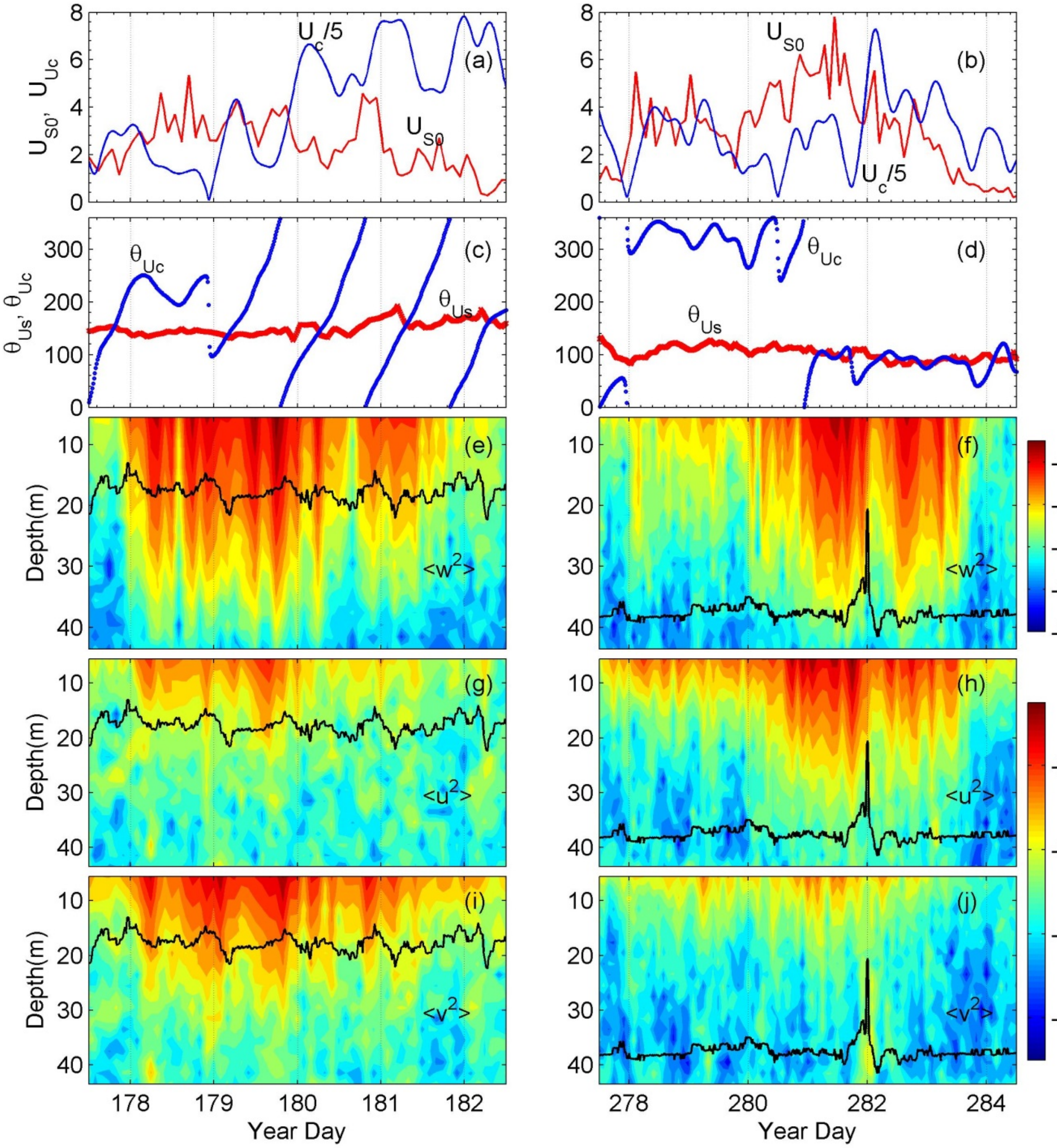

Figure 7. (a, b): The magnitude of the Stokes drift, U_{S0} (red) and surface current (U_C /5, blue) in the upper 15.5 m, both in cm s^{-1} at M5 during event #2 (left panel) and event #5 (right panel). (c, d): Corresponding directions of Stokes drift, θ_{Us} (red) and the surface current θ_{Uc} (blue) in degrees. (e-j) Corresponding depth-time sections of squared high-frequency currents <w^2>, <u^2>, and <v^2>. Log$_{10}$ values of velocity variances are plotted. Units of velocity are m s^{-1}. The thick black lines denote the MLD. The directions follow the convention used in meteorology and represent the direction from which the Stokes drift and currents originate.

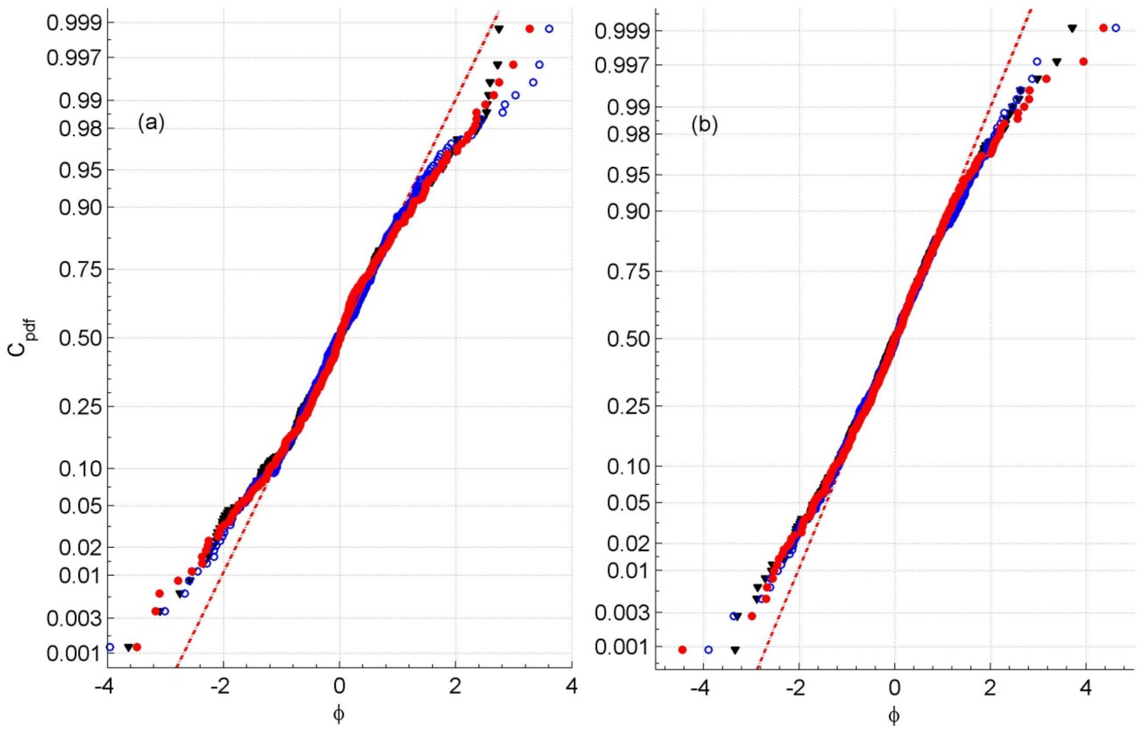

Figure 8. Cumulative probability distribution function (C_{pdf}) of high frequency velocity at 5.5 m depth is plotted against the normalized velocity, φ. (a) summer event #2, (b) fall-winter event #12. The black triangles, blue open circles and red dots denote *u*, *v*, and *w* velocity components, respectively. The red dashed line represents the Gaussian distribution function.

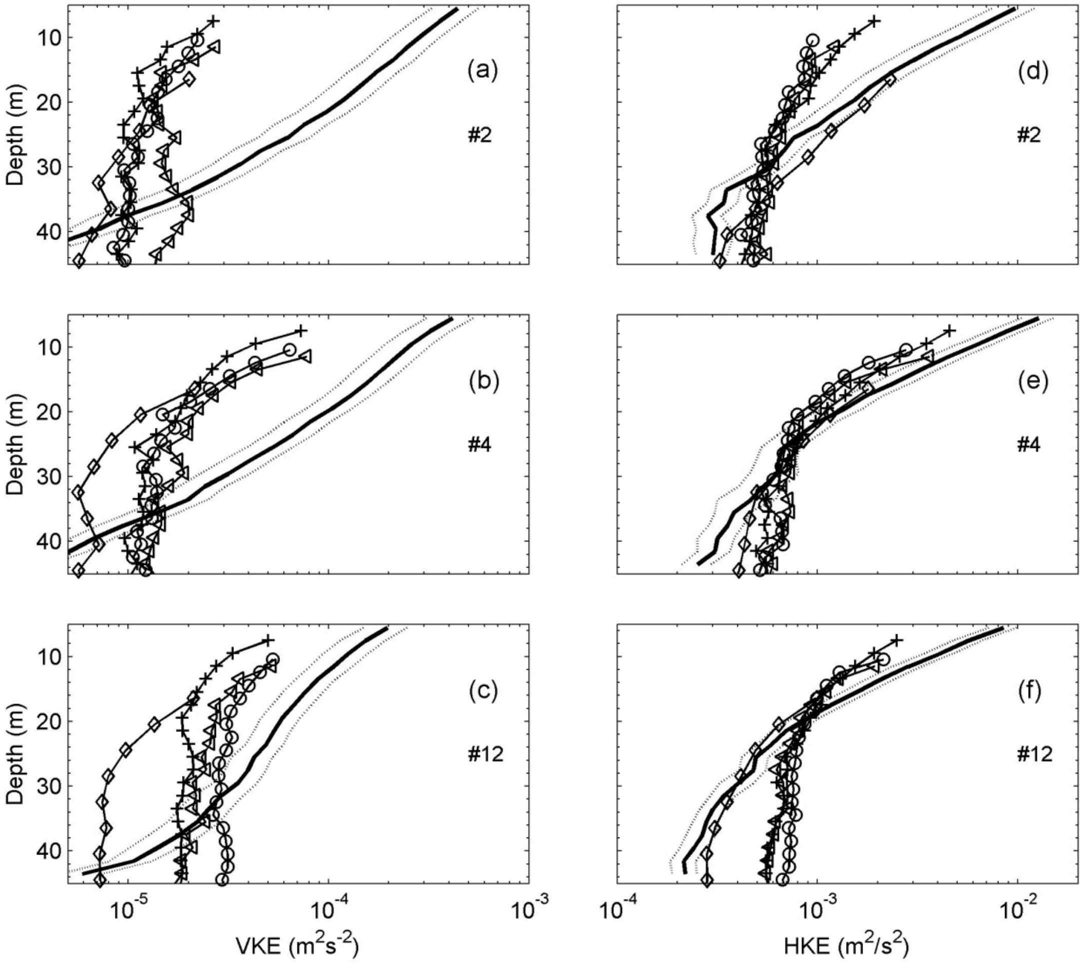

Figure 9. Vertical profiles of vertical kinetic energy (VKE; left panels – a,b,c) and horizontal kinetic energy (HKE; right panels – d,e,f) averaged over three wind events (#2, #4, and #12). The thick solid lines represent energy levels at M5 and the dashed lines show 95% confidence limits. The energy levels at M1, M2, M3, and M4 are marked in crosses (+), open circles (o), diamonds (◊), and triangles (Δ), respectively. Confidence limits of energy levels at M1-M4 are not plotted.

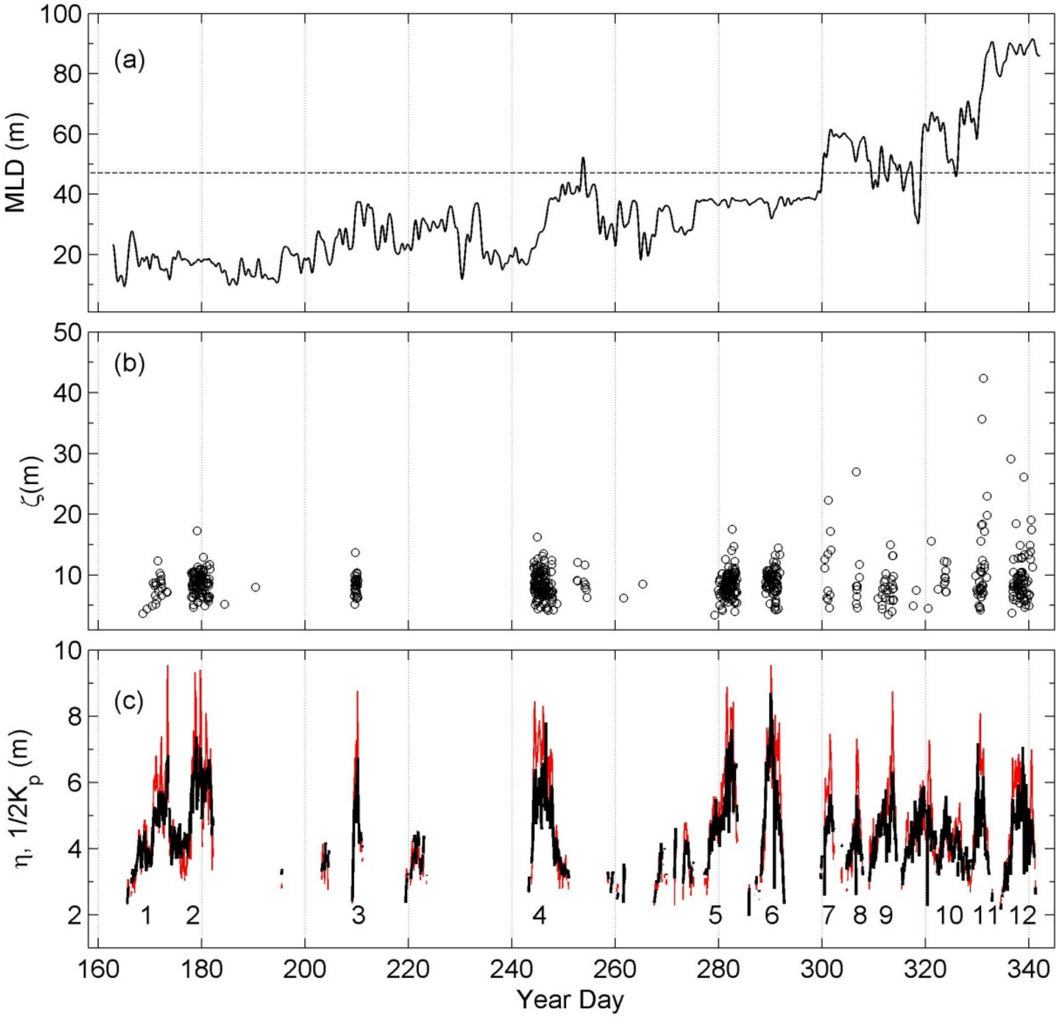

Figure 10. (a) Time series of mixed layer depth (referred as MLD or D) at S2. The black dashed line denotes the water depth (47 m) at M5. (b) e-folding length (ζ) of w^2 at M5 for individual profiles. (c) e-folding length of Stokes drift (η) (black lines), and vertical scale of the peak wave ($1/2k_p$), red lines, at M5. Numbers 1-12 are the wind events marked in Fig. 2.

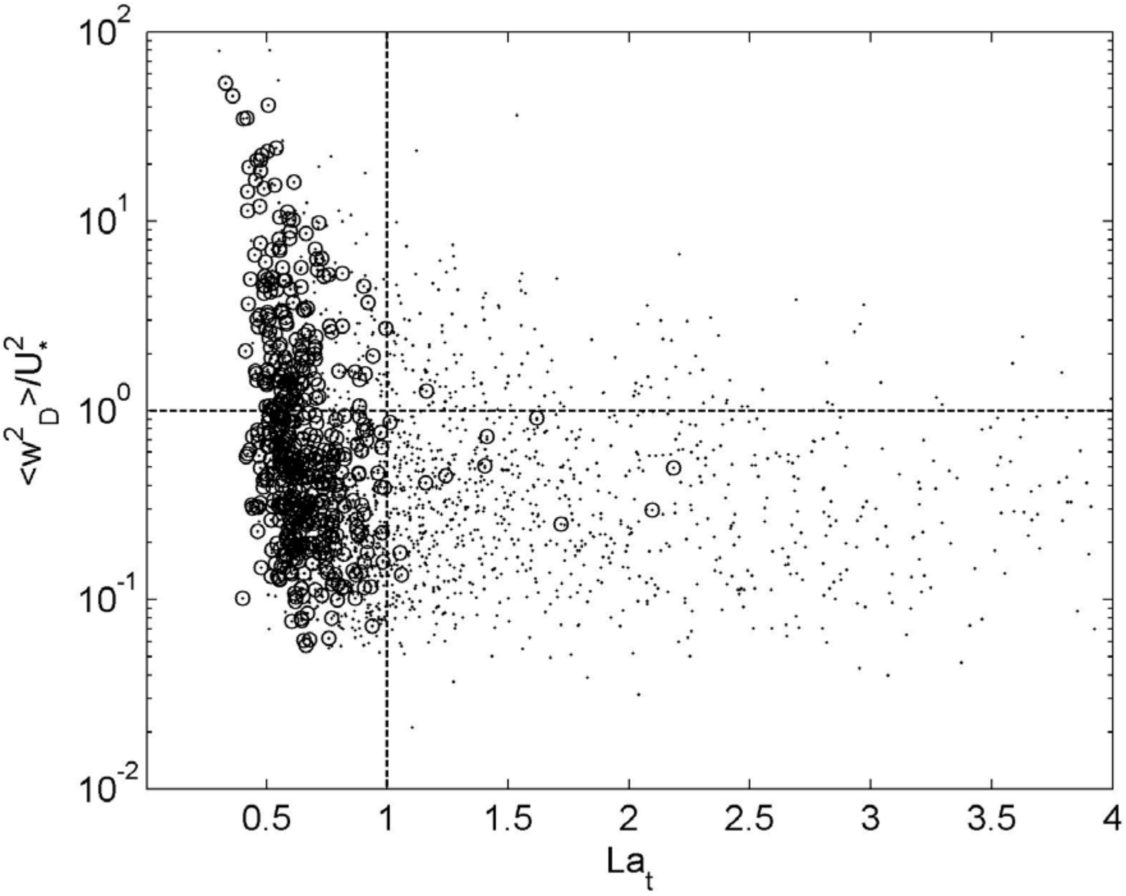

Figure 11. $<w^2_D>/ U_*^2$ vs turbulent Langmuir number (La_t). Black dots represent the entire data set and circles represent data from 12 wind events shown in Fig. 2.

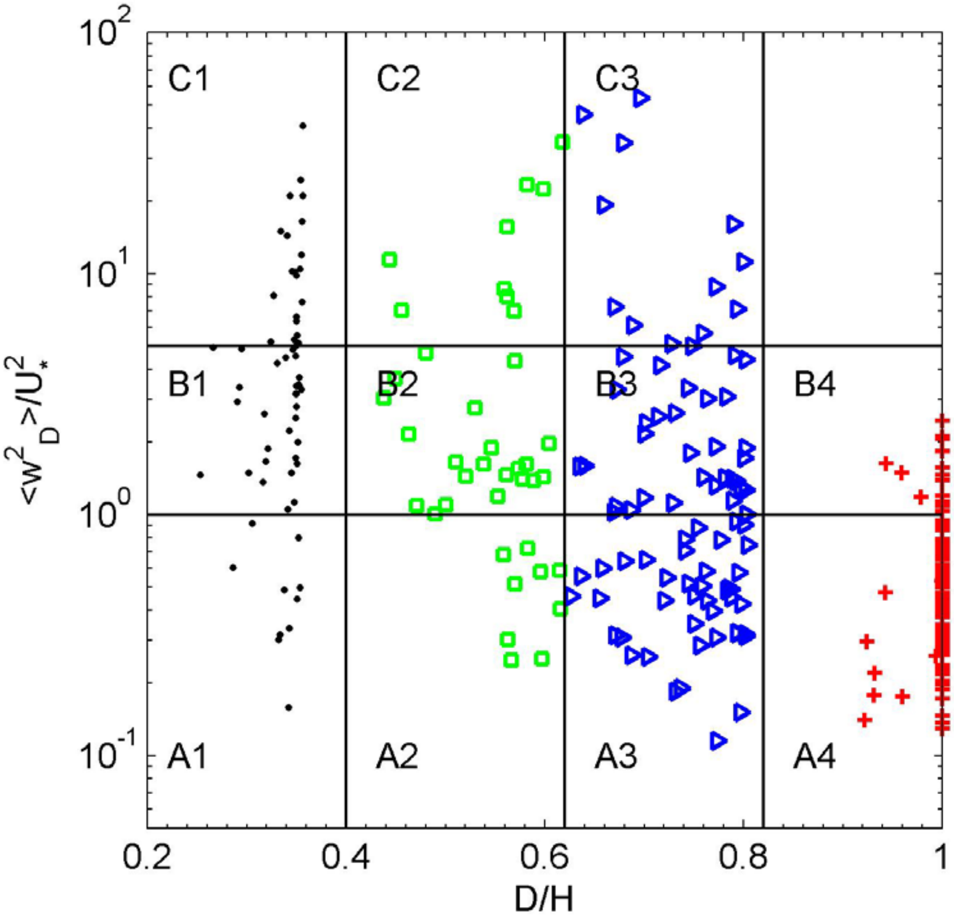

Figure 12. $<w^2_D>/ U_*^2$ vs fractional mixed layer depth, *D/H*. A, B, and C represent three groups of $<w^2_D>/ U_*^2$, and each group is divided into four sub-groups of *D/H* as indicated subcripts 1-4. The colors represent different *D/H* groups.

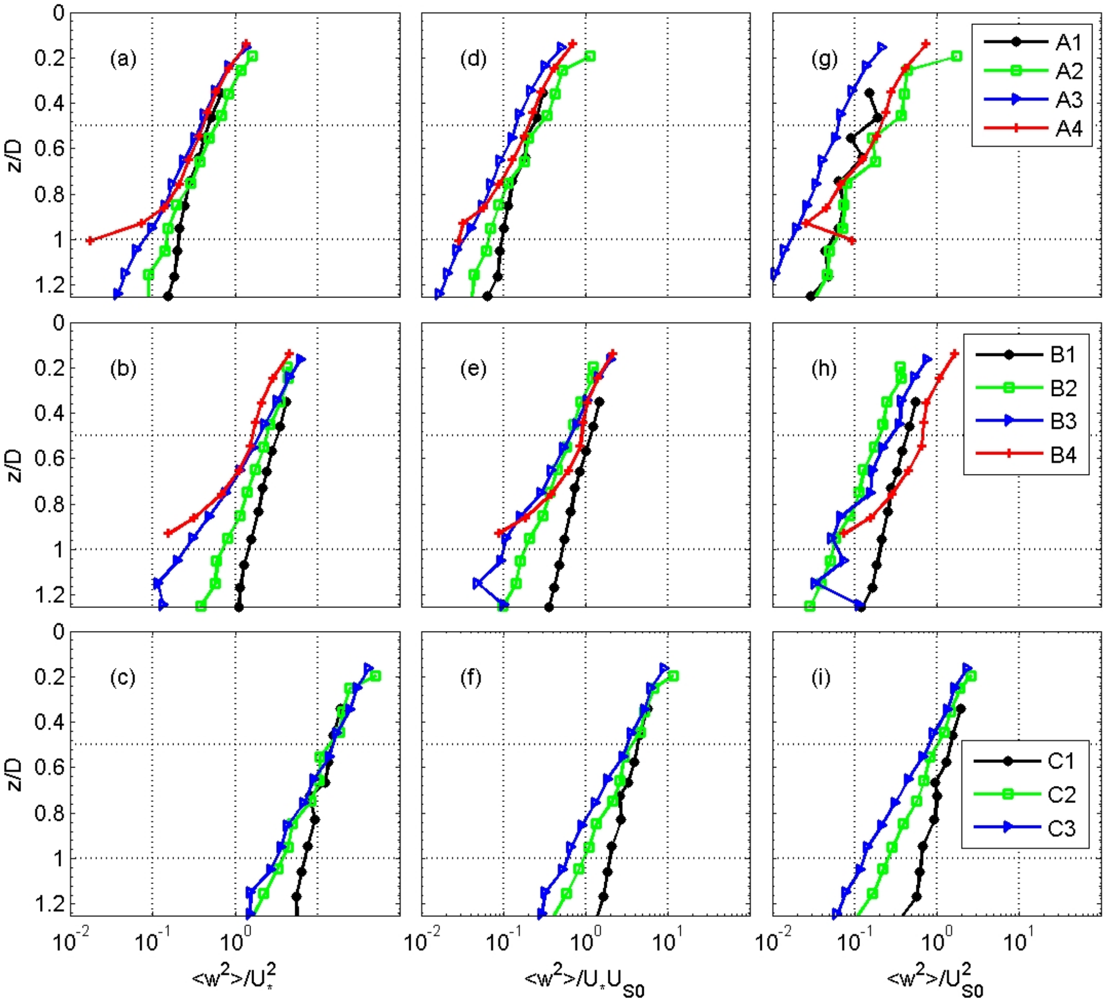

Figure 13. Scaled squared vertical velocity plotted as a function of scaled water depth (*z/D*). (a,b,c) represent U_*^2 scaling for groups A, B, and C, respectively, (d,e,f) represent $U_* U_{S0}$ scaling, and (g,h,i) represent U_{S0}^2 scaling. Colored symbols represent regions of *D/H* as marked in Fig. 12.

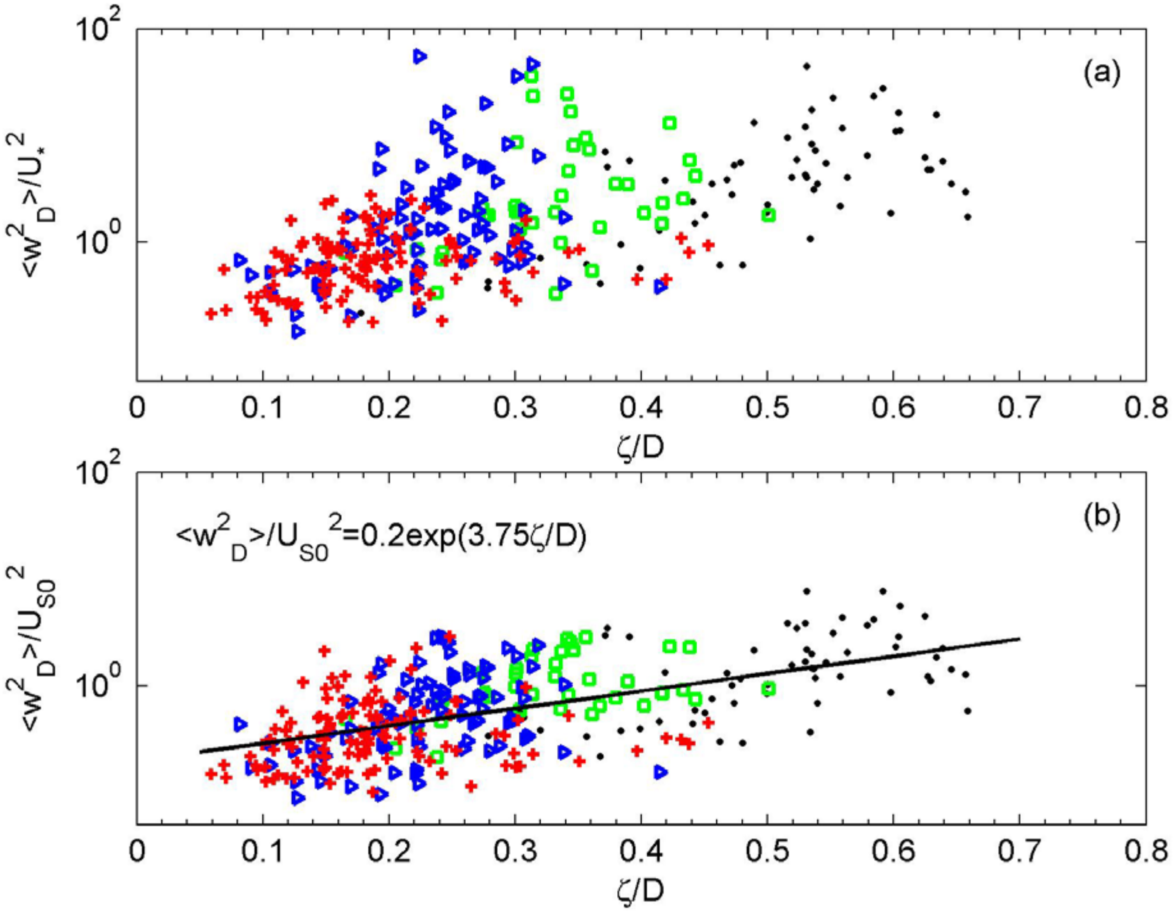

Figure 14. (a) $\langle w^2_D\rangle/U_*^2$ vs ζ/D (normalized e-folding length of $\langle w^2\rangle$ by mixed layer depth). (b) $\langle w^2_D\rangle/U_{S0}^2$ vs ζ/D. The colored symbols represent groups of fractional mixed layer depth D/H as marked in Fig. 12. The thick solid line in (b) represents the least square exponential fit.

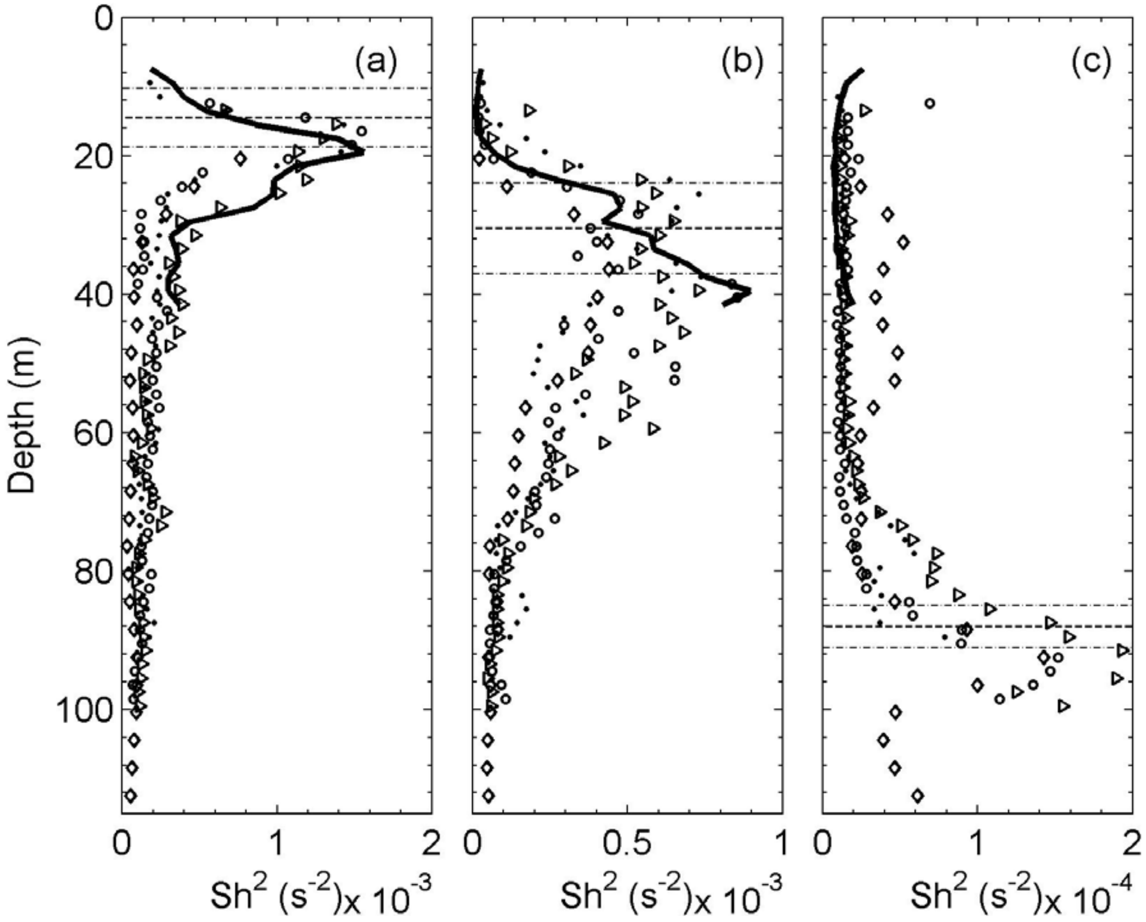

Figure 15**.** Squared vertical shear (Sh^2) of low-frequency horizontal currents at M1-M5 for three different wind events. (a) #2, (b)#4, and (c)#12. Bullets, open circles, diamonds, trangles, and thick solid line denotes M1, M2, M3, M4, and M5 respectively. Thick dashed lines denote mean MLD at M2 mooring and thin dashed lines denote one standard deviation from the mean.

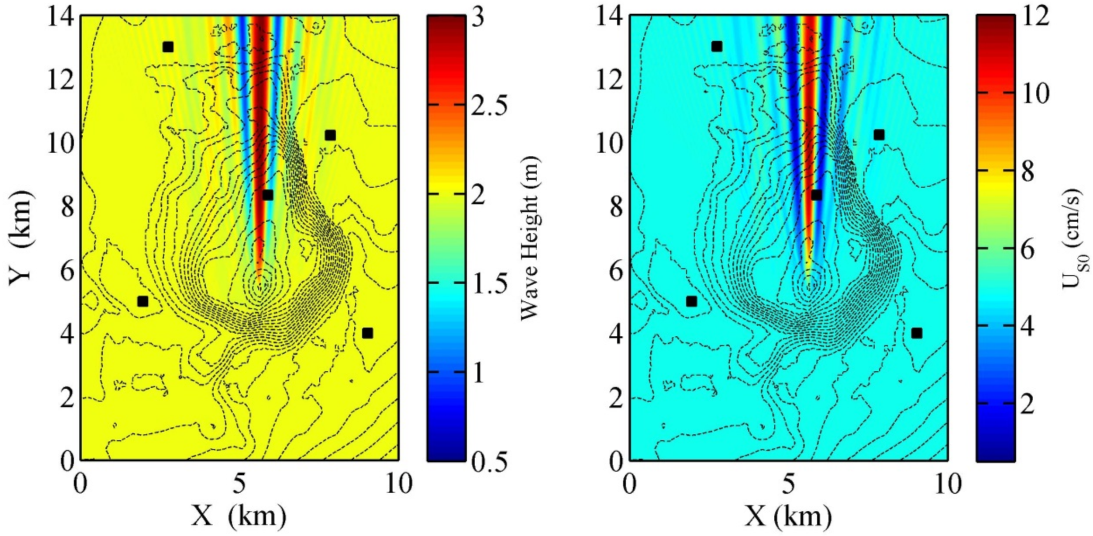

Figure 16. Color images show spatial variations of wave height (left) and Stokes drift (right) from REF/DRF 1 simulations. Thin dashed black contours show the bathymety of EFGB. The black squares are the locations of Barny moorings (M1-M5) and M5 is located over the bank (see also Fig. 1).

APPENDIX C

Measurements of Form and Frictional Drags over a Rough Topographic Bank

Measurements of Form and Frictional Drags over a Rough Topographic Bank

H. W. Wijesekera[1], E. Jarosz[1], W. J. Teague[1], D. W. Wang[1], D.B. Fribance[2],
J.N. Moum[3], and S.J. Warner[3]

[1]Naval Research Laboratory, Stennis Space Center, Mississippi
[2]Coastal Carolina University, Conway, South Carolina
[3]Oregon State University, Corvallis, Oregon

Journal Citation:

Wijesekera, H.W., E. Jarosz, Teague, W.J., and D.W. Wang, D.B. Fribance, J. N. Moum, and S. J. Warner, 2014. Measurements of form and frictional drags over a rough topographic bank, Journal of Physical Oceanography, submitted.

ABSTRACT

Pressure differences across the topography generate a form drag, which opposes the flow in the water column, and viscous and pressure forces acting on roughness elements of the topographic surface generate a frictional drag on the bottom. Form drag and bottom roughness lengths were estimated over the East Flower Garden Bank (EFGB) in the Gulf of Mexico by combining an array of bottom pressure measurements, and profiles of velocity and turbulent kinetic dissipation rates. The EFGB is a coral bank, about 6 km wide and 10 km long, located at the shelf edge; it rises from 100 m water depth to about 18 m below the sea surface. The average frictional drag coefficient over the entire bank was estimated as 0.006 using roughness lengths that ranged from 0.001 cm for relatively smooth portions of the bank to 1–10 cm for very rough portions over the corals. The measured form drag over the bank showed multiple time-scale variability. Diurnal tides and low-frequency motions with periods ranging from 4 to 17 days generated form drags of about 2000 N m^{-1}–3000 N m^{-1}, with average drag coefficients between 0.03 and 0.22, which are a factor of 5–35 times larger than the average frictional drag coefficient. Both linear wave drag and quadratic drag laws have similarities with the observed form drag. The form drag is an important flow retardation mechanism even in the presence of the large frictional drag associated with coral reefs, and requires parameterization.

1. Introduction

Roughness elements and rough bathymetric features generate resistance to flow through skin friction and pressure anomalies, which are referred to as frictional drag (or frictional skin drag) and pressure drag (or form drag), respectively. Frictional drag is a tangential stress on the surface caused by the molecular diffusion of momentum across a velocity interface (Schlichting 1962), and also applies to heat, salt, and other scalars. This is primarily true for hydro-dynamically smooth flows where the bulk of the force on the surface is by viscosity because pressure forces are negligible. However, in rough flows, where the roughness elements are larger than the molecular sub-layer, the force on the surface is transmitted mainly by the pressure forces on roughness elements and the force is parameterized as frictional drag (Schlichting 1962; Tennekes and Lumley 1972). The frictional drag depends strongly on the hydrodynamic roughness or the roughness Reynolds number (e.g., Nikuradse 1933). The parameterization of frictional drag is typically derived from inertial or wall-boundary-layer theory (e.g., Tennekes and Lumley 1972; Stull 1988) and has been applied in both atmosphere and ocean models (Blumberg and Mellor 1987; Hodur 1997).

Form drag is related to the dynamic pressure differences across an obstacle that arise from upstream blocking, and separation of flow, formation of eddies, hydraulic jumps, and lee-wave disturbances downstream of the obstacle (Gill 1982; Smith 1989; Baines 1995). The nature of the flow depends on the governing parameters such as Froude Number (*Fr*), non-dimensional obstacle height (h_n) and width (a_n), and mode number (*K*). For single-layer hydraulic flows, $Fr = U_0 / \sqrt{gD}$, where U_0 is the flow speed of the layer, *g* is the gravitational acceleration, and *D* is the flow depth.

In stratified depth-limited flows, the non-dimensional height of the bank or nonlinearity parameter (h_n), the non-dimensional width (a_n), the mode number (*K*), the aspect ratio of the bank (h_0 / L), and the height parameter (h_0 / D) are used as non-dimensional parameters to describe the nature of the flow, where $h_n = N_0 h_0 / U_0$, $a_n = N_0 a_0 / U_0$, and $K = N_0 D / (\pi U_0)$; N_0 and U_0 are characteristic scales of stratification and flow speed of the water column, h_0 is the height of the bank, *D* is the flow depth, *L* is the width of the bank , and a_0 is the half width scale (Hunt and Snyder 1980; Smith 1980; Durran 1986; Baines 1995; Vosper et al. 1999). For $h_n < 1$ and $K < 1$ the flow moves over the bank (non-blocked flow), and for $h_n > 1$ and $K > 1$, the flow moves around the bank (blocked flow) (e.g., Hunt and Snyder 1980). In the presence of background stratification, the flow over obstacles generates internal gravity waves, and in turn transports horizontal momentum vertically (when h_n<1). The resulting wave-momentum flux generates a form drag to the background flow which is also referred to as wave drag (e.g., Durran 1986, 1990; Smith 1989). Form drag is patchy in space due to the spatial variability of the bottom topography, unlike frictional drag that occurs on the entire bottom-surface.

Form drag for air flow over mountains has been studied extensively in both field observations and numerical simulations with special emphasis on improving the parameterization of mountain wave drag (Smith 1978, 1979, 1980; Bougeault et al. 1990; Durran 1990; Clark and Miller 1991;

Olafsson and Bougeault 1996; Doyle and Jiang 2006). Several decades of mountain wave studies were beneficial to the estimation of mountain wave drag based mainly on linear internal wave solutions. Such parameterizations have resulted in substantial improvements in current weather prediction models (e.g., Kim and Arakawa 1995; Wood et al. 2001; Kim et al. 2003). Form drag has been computed for both small and large atmospheric mountain ranges. On a smaller, scale Smith (1978) evaluated pressure drag in the Blue Ridge Mountains in the United States using several microbarographs across the ridge, resolving the pressure field over the ridge similar to the oceanic observations made by Warner et al. (2013). However in most atmospheric observations, the measurement of pressure over mountain terrains is quite sparse, as the instruments cannot cover the entire mountain range. Hafner and Smith (1984) used a limited number of microbarographs over the European Alps to evaluate the pressure drag by assuming lateral pressure gradients were constant; even though these observations do not resolve the entire pressure field over the complex terrains, a rough estimate of form drag was obtained. In recent mountain wave experiments such as T-REX (Grubisic et al. 2008) microbarographs measurements were used, but a few microbarographs measurements are not sufficient to compute the pressure drag directly. Instead, pressure measurements have been used to obtain information on internal lee waves.

In the ocean, observational studies of form drag are very limited (e.g., Nash and Moum 2001; Warner et al. 2013). Form drag acts on the entire water column over the topographic feature and leads to the generation of mixing and turbulence, eddies, and internal waves away from the bottom (e.g., Polzin et al. 1997; Jane and St. Laurent 2001; Pawlak et al. 2003; Garrett and Kunze 2007). Some aspects of topographic-tidal flow interaction and formation of lee waves have been studied analytically and numerically using non-hydrostatic models (Bell 1975; Nakamura et al 2000; Khatiwala 2003; Legg and Huijts 2006). Several numerical studies have been conducted to examine the dynamics of flows over small banks (e.g., Lamb 1994; Skyllingstad and Wijesekera 2004; Seim et al. 2012). Lamb (1994) and Skyllingstad and Wijesekera (2004) reported qualitatively comparable results to the theoretical and laboratory results of Long (1955) and Baines (1979) for a similar dynamical parameter range ($1<K<2$ and $a_n<10$). Skyllingstad and Wijesekera noted for $K < 1$, a substantial reduction in the wave drag compared to a no-slip boundary when bottom roughness was introduced. Ocean circulation models do not have form drag parameterizations (Blumberg and Mellor 1987; Oke et al. 2002), mainly due to lack of information on magnitude and spatial distribution of form drag although some attempts have been made to approximate wave drag from linear theory (Nikurashin and Ferrari 2011).

The total form drag consists of different components that involve isopycnal displacement (referred as “internal”) and surface tilt (referred as “external”) (e.g., McCabe et al. 2006). Different components of form drag over coastal banks and ridges were examined by several investigators (Moum and Nash 2000; Nash and Moum 2001; Edwards et al. 2004; McCabe et al. 2006). Warner et al. (2013) were first to measure the total form drag from high-precision pressure sensors (referred to as Ppods; Moum and Nash 2008) deployed over Three Tree Point (TTP), a headland in Puget Sound, Washington. Warner et al. (2013) reported that the form drag coefficient is at least one-order of magnitude greater than the frictional drag coefficient at the bottom.

In the following, we compute both form drag and frictional drag from in-situ measurements collected over the East Flower Garden Bank (EFGB) on the Texas–Louisiana shelf (Fig. 1) as part of projects sponsored by the Naval Research Laboratory (NRL) (Mixing Over Rough Topography [MORT]) and by the Bureau of Ocean Energy Management (BOEM)(Currents over Banks [COB]). As described below, the flow over the EFGB consists of h_n>>1, K>>1, and a_n ~O(100) along with large bottom-roughness lengths (z_0~1-10 cm). This parameter regime belongs to non-linear, hydrostatic, blocking flows, and there is no theoretical prediction of the form drag. The main objectives are to quantify the magnitude and temporal variability of the form drag through bottom pressure measurements collected from June through December, 2011, and to quantify roughness lengths and associated frictional drag coefficients from microstructure and velocity profiles collected during an intensive observational period in June 2011 and in August 2011.

The paper is organized as follows. Section 2 describes field observations. Section 3 describes form and frictional drag formulations. Estimates of form drags and roughness length scales are provided in section 4 and section 5, respectively. Discussion is given in section 6. A summary and major findings are in section 7. Finally, a sensitivity study of the estimated form drag based on numerical simulations is provided in the Appendix.

2. Observations

Sampling was conducted at the EFGB, located approximately 190 km southeast of Galveston, Texas in the northwestern Gulf of Mexico (GOM). The EFGB is part of the National Marine Sanctuary System, and is one of many banks formed by salt domes on the continental shelf. The EFGB is a biologically diverse coral reef consisting of brightly colored sponges, plants, and other marine life. The habitat map and an example of the size of a typical coral head are shown in Fig. 1. The EFGB is a pear-shape bathymetric feature rising from below 100-m water depth to 18 m below the surface (Figs. 1 and 2). The bank is about 10 km long and about 6 km wide; its projected area to the horizontal plane encompassed by the 100-m bathymetry contour is approximately 40 km^2. The EFGB has steep lateral slopes (~50 m height change within 500 m distance) at the eastern and southern boundaries. The top, located just off the southern peak, is nearly flat with more gentle slopes westward and northward but contains rough bathymetric elements such as corals (Figs. 1 and 2). The top of the bank is dominated by relatively large, head-forming corals; *Montastrea annularis* (boulder star corals), make up 30% of the total coverage between 18 and 36 m depth, and the species *Diploria strigosa*, *Colpophyllia natans*, *Montastrea cavernosa*, *Millepora alcicornis*, and *Porites astreoides* account for an additional 20% coverage (Fig. 1). The total coral coverage on the upper reef averages approximately 55% (Bright et al. 1984). Between 30–40 m depth algal ridges are common, and below 50 m algal nodules (rhodoliths) are dominant. In these deeper zones nodules can reach 1–2 m height, due to lower current velocities (Minnery 1990) (Fig. 1).

The observational program over the EFGB consisted of two six-month mooring deployments (from December 2010 to June 2011, and from June 2011 to December 2011), a two-week intensive observational period (IOP) from May 31 to June 14, 2011, and a week-long microstructure survey during a coral spawning event in August 2011 as a part of the MORT and COB projects. Two ships (R/V *Pelican* and R/V *Manta*) took measurements over the bank during the IOP. Microstructure surveys were conducted from the R/V *Manta*, while moorings were deployed from the R/V *Pelican*. Detailed discussions of instrumentation, data collection, sampling methods, and data processing for the long-term and short-term deployments are in Teague et al. (2013) and in Jarosz et al. (2014), respectively. Here we describe the subset of the data relevant to this study, i.e, measurements made during the IOP and in August 2011, and from the moorings deployed during the second half of the COB experiment (June–December 2011). Bathymetry and locations of these short and long-term moorings at the EFGB are shown in Figs. 1a and 2a.

a. Moorings: currents, pressure, and hydrography

A total of ten Teledyne RD Instruments (RDI) acoustic Doppler current profilers (ADCPs) were deployed in bottom-mounted, trawl-resistant housings, referred as "Barnys" (Perkins et al. 2000), at stations M1–M8, measuring east, north, and vertical velocities (Fig. 1 and 2a). The ADCP at M5 operated at 600 kHz, and all others at 300 kHz. Transducer heads were approximately 0.5 m above the sea floor. Year-long currents and hydrographic fields were collected from five ADCP moorings (M1–M5) and four sub-surface string moorings (S1-S4) equipped with temperature, conductivity, and pressure (TCP) sensors. ADCPs recorded nearly full water-column current profiles every 15 minutes (an ensemble average of 120 realizations) during long-term deployments. During the IOP, high-temporal resolution current and hydrographic data were collected from another five bottom-mounted ADCPs at stations M4a, M5a, M6, M7, and M8, and two string moorings at S5 and S8. Samples were averaged every minute at M4a, M5a, and M6, and every two minutes at M7 and M8. Vertical bin sizes were 1 m at M5a, 2 m at M4a, and 4 m at M6, M7, and M8. Accuracy for the ADCP measurements is 0.5% of the observed water velocity ± 0.5 cm s^{-1}.

Barny moorings were also equipped with Ppods (Moum and Nash 2008). Ppods are modified Paroscientific pressure sensors and have a precision of about 0.14 mm or 1 Pa (1Pa = 1 N m^{-2}). A total of five Ppods were deployed during MORT (Fig. 2a) at M2, M4, M5, M7, and M8; their pressure is referred to as P_{M2}, P_{M4}, P_{M5}, P_{M7}, and P_{M8}. Three Ppods (P_{M2}, P_{M4}, and P_{M5}) were deployed along a line over the bank for a period of nearly six months (between June and December 2011) and the other two (P_{M7} and P_{M8}) were deployed during the IOP for two weeks in June 2011. We noted mismatches in time stamps and non-uniform sampling rates in the long-term deployed Ppods. The first step was to obtain correct time stamps and sampling rates. The time stamps of P_{M2} and P_{M4} were accurate, but their sampling rates deviated from 1 Hz indicating drifts in the sampling clocks. Note: the average sampling rate was 0.97 Hz. To fix sampling rates caused by clock drifts, we resampled (i.e., interplolated) P_{M2} and P_{M4} data at 1 Hz sampling rates between accurate time stamps of starting and ending times. We noted that the accurate clock in P_{M5} was broken in August 2011, but the sampling clock had an accurate time stamp with a sampling rate of 1 Hz; when comparing the rest of the Ppods, the sampling clock in P_{M5} was consistent with the other accurate clocks in P_{M2} and P_{M4}. Therefore, we used the time stamp of the sampling clock as the accurate time stamp for P_{M5}.

Four TCP string moorings (S1–S4) were deployed close to M1–M4 during the first half of the deployment and only three (S2-S4) were redeployed near M2–M4 during the second half (Fig. 2a). Each string mooring contained eight to twelve TCP sensors that were approximately equally spaced between 7–12 m below the surface and 1 m above the bottom (Teague et al. 2013). We do not address processing and data quality issues here, since those topics were discussed in Teague et al. (2013).

For the current data, we used local coordinates with the *U* component oriented toward the axis of the M2–M4 mooring line and the *V* component oriented perpendicular to the mooring line. We rotated ADCP currents by19° counter clockwise to the horizontal direction to match with the direction of the form drag estimated in Section 4. Low-frequency east-west flow showed a two-layer structure around the bank (Teague et al. 2013). A similar flow pattern was found in *U*. Figure 3 shows the depth-averaged low-frequency (<0.02 cycles per hour (cph)) currents (U_U , V_U) in the upper 50-m layer. The U_U was nearly eastward during the first half of the record, and changed direction after year day 263 (Fig. 3a,b). Currents in the lower layer (U_L, V_L) were smaller than in the upper layer, and were highly influenced by the bank (Fig. 3c,d; Teague et al. 2013). Mean currents approximately 20 m above the bottom followed the bottom topography (Teague et al. 2013). Shipboard and moored velocity measurements made during the IOP (June 2–13, 2011) showed generation of sub-mesoscale and mesoscale motions and reversals of bottom currents in the lee-side of the bank (Jarosz et al. 2014). Based on all the ADCP velocity records, we noted that the currents in the upper 50-m layer at M1 were least affected by the bank. M1 was located at the northwest corner of the bank, where the bottom slope was less steep compared to slopes south and east side of the bank (Fig. 2). Near-surface intensified high-frequency currents (>0.2 cph) were observed over the top of the bank and were closely related with wind and surface waves (Wijesekera et al. 2013).

The spectra of U_U and V_U show several distinctive frequency bands associated with tidal/inertial waves and sub-tidal flows (Fig. 4). The near-inertial period (25.52 h) lies between the K_1 (23.93 h) and O_1 (25. 82 h) tidal periods. Teague et al. (2013) reported that near-inertial currents were as large as 20 cm s^{-1} especially during summer months, and that barotropic diurnal tides were less than about 4 cm s^{-1}. The tidal-inertial components of east-west and north-south directions had similar magnitudes, while the semidiurnal components in the north-south direction were stronger than the east-west components (Fig. 4). The sub-tidal band contains 4–6 day, 10–12 day, and 16–17 day fluctuations. There was no clear spring-neap tidal signal (period ~ 14 day) in the sub-tidal band (Fig. 4). In the northern GoM, the 4–6-day signal may relate to synoptic-scale weather systems (e.g., Donohue et al. 2006). Dohonue et al. (2006, 2008) observed 16- and 14-day oscillations in bottom pressure in the north central GoM, but these signals were unexplained. However, Donohue et al. (2008) further noted that the 16-day signal is in-phase with water level variations measured by coastal tide gauges on the west Florida shelf.

Near-surface temperature showed seasonal warming in summer and cooling in late fall (Fig. 3e). The advection of cold water, especially near the bottom, appeared after year-day 240 (lasting close to the end of the observational period [Fig. 3e]) and changed the vertical structure of temperature and density fields, which in turn altered bottom pressure across the bank in sub-seasonal to seasonal time scales. Teague et al. (2013) suggested a plausibility of advection of cold water by eddies in the region. In the following analysis, we focus on motions which can be well-resolved by our data, and therefore, we limit the computation of the form drag to tidal (12–25 h) and sub-tidal (4–17 day) motions.

b. Ship surveys: currents, hydrography, and microstructure

Ship surveys were conducted from the National Oceanic and Atmospheric Administration's R/V *Manta*, a 25-m catamaran vessel out of Galveston, Texas. A 300 kHz RDI ADCP was mounted on the side of the boat and recorded currents with a vertical bin size of 4 m. Velocities were processed using the University of Hawaii's CODAS system (Firing et al. 1995) to correct for ship motion, and were averaged over four-minute intervals. A Biosonics DT-X Digital Scientific Echosounder was used to acquire bathymetric data based on acoustic backscatter. The echosounder sampled at a rate of 3 Hz with a frequency of 123 Hz. The average horizontal sampling distance was approximately 25 cm.

Additionally, vertical profiles of small-scale velocity and temperature along with fine-scale T, C, and P fields were collected from a free-falling Rockland Scientific Vertical Microstructure Profiler (VMP), equipped with a pressure sensor, shear probes, a fast thermistor, micro-conductivity, and Sea Bird Electronics temperature and conductivity sensors (e.g., Wolk et al. 2002). These profiles were collected while the R/V Manta was drifting or steaming slowly along quasi-straight lines over the bank at speeds of 0.5 to 1 m s^{-1} (blue and green lines in Fig. 2a). The velocity shear accuracy was 5%, and the VMP probe had an average descent speed of 0.8 m s^{-1}, producing shear measurements approximately every 0.2 cm. Shear measurements were used to estimate turbulent kinetic energy (TKE) dissipation rates using $\varepsilon = 7.5\nu\overline{\left(\partial u/\partial z\right)^2}$, where ν is the kinematic viscosity of water estimated from concurrent temperature observations and $\partial u/\partial z$ is the velocity shear (Gregg 1987). The velocity shear variance was calculated by integrating the spectrum for the wave number range from 2 to 30 cpm (cycles per meter), and the spectrum was estimated in bins of 1024 shear data records, with a 512- record overlap. We noted that more than 90% of the spectral variance was between 2 and 30 cpm wavenumbers.

In this study we focus on the dissipation estimates near the bottom. A detailed discussion of dissipation estimates and their distribution during the IOP is given in Jarosz et al. (2014).

3. Form and Frictional Drags

a. Form Drag

The form drag is defined as the spatial integral of the product of the bottom pressure anomaly and the lateral slope of the bathymetry (e.g., Gill 1982, p. 145; Baines 1995). The form drag along a line of pressure measurements is (e.g., McCabe et al. 2006; Warner et al. 2013),

$$D_{form}(t) = -\int_{x_1}^{x_2} p_b'(x,y,t)h_x dx \qquad [\mathrm{N\ m^{-1}}], \tag{1}$$

where p_b' is the bottom pressure anomaly in N m^{-2}, h is the bottom height in meters, h_x is the lateral gradient of the bank in the direction where the drag is estimated, t is the time, x and y are the orthogonal co-ordinates over the bank, and x_1 and x_2 are points of the equal depth on either side of bank (Fig. 2). The power (P_{form}) associated with D_{form} or the rate of energy loss of the background flow due to the form drag is defined as the product of D_{form} and the free-stream velocity undisturbed by the topographic feature, U_m (Gill 1982, section 8.7; Warner et al. 2013), where

$$P_{form} = D_{form}U_m. \tag{2}$$

The drag coefficient, C_{DF} associated with the form drag (1) is defined as (e.g., Lott and Miller 1997; Vosper et al. 1999; Warner and MacCready 2009):

$$C_{DF} = \frac{D_{form} / h_0}{-1/2\rho_0 \, |U_m| U_m}, \qquad (3)$$

where ρ_0 is the sea-water density and h_0 is the topographic height. Here a minus sign is included because the drag and the velocity have opposite signs. C_{DF} is an O(1) quantity and is referred to as the bluff-body drag coefficient (Warner et al. 2013). C_{DF} is widely used in engineering applications. To give an oceanographic context, we also defined a bulk (form) drag coefficient, C_D, associated with D_{form} as an equivalent frictional drag coefficient based on mean flow velocity U_m (e.g., Warner et al. 2013), where

$$C_D = \frac{D_{form} / l_0}{-1/2\rho_0 \, |U_m| U_m}, \qquad (4)$$

and l_0 is the topographic length. Equation (4) defines the bulk drag coefficient in the same way as the frictional drag coefficient, although the near-bottom velocity is typically used in computing the frictional drag resulting from bottom roughness elements (see equation 13). The form drag coefficient, C_D, can be treated as an enhanced frictional drag coefficient from a numerical modeling perspective. From (3) and (4), $C_{DF}/C_D = l_0/h_0$, and for the EFGB (Fig. 2) with h_0~50 m, and l_0~9 km, C_{DF}/C_D ~180.

The first step in estimating the form drag is to determine p_b' from bottom pressure measurements. The bottom pressure sensors, deployed during MORT measured the total pressure at the seafloor (p_b), which includes atmospheric pressure, pressure resulting from surface elevation and water density, and non-hydrostatic pressure. Following Moum and Smyth (2006) and Warner et al. (2013), we express the total pressure ($p(X,t)$) at depth z by integrating the vertical momentum balance from z to the sea surface height $\eta(x,y,t)$:

$$p(X,t) = p_{Atm} + g\rho_0(\eta(x,y,t) - z) + g\int_z^{\eta} \overline{\rho}(z',t)dz' + g\int_z^{\eta} \rho'(X,t)dz' + \rho_0\int_z^{\eta} \frac{Dw}{Dt}dz', \qquad (5)$$

where $p(X,t)$ varies in all directions; $X = (x,y,z)$ represents a right-handed co-ordinate system with the x-axis parallel to the bottom pressure sensor array, the y-axis perpendicular to the sensor array, the z-axis positive upward, and $z = 0$ at the bottom**;** p_{Atm} is the atmospheric pressure at the surface and is assumed to be uniform over the domain; D/Dt is the material derivative; w is the vertical velocity; g is the gravitational acceleration (9.81 m s^{-2}). The density is expressed as $\rho(X,t) = \rho_0 + \overline{\rho}(z,t) + \rho'(X,t)$, where ρ_0 = constant, $\overline{\rho}(z,t)$ is the background stratification, and $\rho'(X,t)$ is the density fluctuation. The sea surface can be divided into four components:

$$\eta(x,y,t) = \overline{\eta}(t) + \eta_{Tf}(x,y,t) + \eta_{Ti}(x,y,t) + \eta'(x,y,t), \qquad (6)$$

where $\overline{\eta}(t)$ is the spatially averaged sea surface height; $\eta_{Tf}(x,y,t)$ is the contribution to sea surface height associated with the sea-surface slope resulting from rotational effects. Here barotropic pressure gradients associated with surface elevation are balanced by the Coriolis force; $\eta_{Ti}(x,y,t)$ is the surface elevation resulting from accelerations/decelerations of flow over the bank; and $\eta'(x,y,t)$ is the remaining sea-surface height anomaly (e.g., Warner et al. 2013). By combining (5) and (6) we obtain:

$$p(X,t) = p_{Atm} + g\rho_0\overline{\eta}(t) + g\rho_0\eta_{Tf}(x,y,t) + g\rho_0\eta_{Ti}(x,y,t) + g\rho_0\eta'(x,y,t) - g\rho_0 z + g\int_z^{\eta}\overline{\rho}(z',t)dz + g\int_z^{\eta}\rho'(X,t)dz' + \rho_0\int_z^{\eta}\frac{Dw}{Dt}dz' . \tag{7}$$

Pressure terms, which vary in the *x*-direction, contribute to the form drag given in (1). The pressure anomaly that is dynamically relevant to the flow over the bank is given by:

$$p'(X,t) = g\rho_0\eta_{Ti}(x,y,t) + g\rho_0\eta'(x,y,t) + g\int_z^{\eta}\rho'(X,t)dz' + \rho_0\int_z^{\eta}\frac{Dw}{Dt}dz' . \tag{8}$$

Rotational contributions to sea surface height are excluded because their associated velocity component is orthogonal to the direction of the form drag.

b. Frictional Drag

Frictional stress resulting from turbulence and viscous effects (Schlichting 1962; Tennekes and Lumley 1972) is:

$$F_m = \rho\langle uw\rangle - \rho\nu\frac{\partial\tilde{U}}{\partial z} \quad [\mathrm{N\,m^{-2}}] \tag{9}$$

where $\tilde{U}$ is the mean lateral velocity, *u* and *w* are the lateral and vertical velocity fluctuations, *v* is the kinematic viscosity, and *z* is the distance from the sea floor (positive upward) as defined above. The angle brackets denote the average over turbulence motions. In the presence of strong surface waves, the turbulent bottom stress, $-\rho\langle uw\rangle$ over the continental shelf and shallow banks may include a stress component from surface-wave induced oscillatory currents (e.g., Grant and Madsen 1982). The surface wave-driven stress is significantly larger over the shelf during severe storms (e.g., Wijesekera et al. 2010), but in the following analysis, we limit our bottom drag computations to mean currents, because hurricane strength winds were not present over the EFGB during the observational period. As discussed below, we estimated bottom roughness lengths and frictional drag coefficients when microstructure observations were available for 10 days in June and August 2011. Winds were less than 6 m s^{-1} and surface wave heights were 0.2–0.5 m (Wijesekera et al. 2013). Surface-wave induced bottom currents were negligible over the top of the bank. Therefore, the surface-wave induced bottom frictional effects or “the apparent roughness lengths” were not a significant factor. The wall-boundary-layer theory provides an estimate of the roughness length of bottom roughness elements.

Sufficiently far from the boundary, $z >> \nu/u$ or at sufficiently large Reynolds numbers $uz/\nu >> 1$, a layer (referred as the inertial layer) exists in which the overall dynamics of turbulence is independent of viscosity. In this layer $F_m = \rho\langle uw\rangle = -\tau$ where τ is the bottom stress. The flux term can be rewritten as a down-gradient flux, $F_m = -\rho K_m\frac{\partial\tilde{U}}{\partial z}$, where K_m is the turbulent transfer coefficient having dimensions of velocity and length and $\partial\tilde{U}/\partial z$ is the vertical gradient of the mean flow. For the inertial layer, $K_m = \kappa u_* z$, $|\tau| = \rho u_*^2$, and

$$\frac{\partial \tilde{U}}{\partial z} = \frac{u_*}{\kappa z}, \tag{10}$$

where κ is von Karman's constant (0.41) and u_* is the water friction velocity which is independent of *z*. The turbulent fluxes in the inertial layer are nearly independent (within 10-20%) of the distance from the boundary. By integrating (10), we can obtain a mean velocity profile,

$$\tilde{U} = \frac{u_*}{\kappa} \log\left(\frac{z}{z_0}\right), \tag{11}$$

where z_0 is the roughness length and is determined by the geometry of the surface. z_0 is a small fraction of the frictional-element heights; for example, for closely-packed sand grains of size λ, $z_0 = \lambda / 30$ (Nikuradse 1933).

Suppose we have observations in the inertial layer at $z = z_a$ where $\tilde{U}(z_a) = \tilde{U}_a$, then squaring equation (11), we solve for the magnitude of the bottom stress:

$$|\tau| = \rho\left(\kappa^2 \log(z_a / z_0)^{-2}\right)\tilde{U}_a^2 = \rho C_d \tilde{U}_a^2, \tag{12}$$

where

$$C_d = \left(\kappa / \log(z_a / z_0)\right)^2 \tag{13}$$

is the frictional drag coefficient. Within the inertial layer the production of TKE by sheared currents approximately balances the dissipation rate, and thus

$$u_* = \left(\varepsilon \kappa z\right)^{1/3}, \tag{14}$$

(e.g., Dewey and Crawford 1988), where ε is the TKE dissipation rate. The roughness length becomes,

$$z_0 = z_a \exp(-\kappa \tilde{U}_a / u_*). \tag{15}$$

In the following, we use velocity and TKE dissipation rate profiles to compute the roughness length and the associated frictional drag coefficient over the EFGB.

4. Evaluation of Form Drag

a. Bottom pressure anomaly from Ppods

Fig. 5 shows bottom pressure fluctuations at five mooring sites (Figs. 1 and 2) between June 2 (year-day 152) and June 13 (year-day163), 2011. The pressure fluctuations were constructed by removing the temporal mean for a given record length of 12 days. The demeaned pressure fluctuations show diurnal tides and a segment of the spring-neap cycle. Tides around and over the bank had similar phases (Fig. 5b, c) because the spatial scales of tidal motions are much larger than the lateral spacings between moorings. Unlike pressure, the depth-averaged velocities at M1–M5 were not always in phase, especially at the beginning of the records (Fig. 5b, c).

While pressure fluctuations were dominated by diurnal tides, velocity fluctuations contained combinations of tides and near-inertial waves.

Pressure spectra calculated at M2, M4, and M5 (Fig. 6) show several distinctive features including the surface-gravity wave band between 0.08Hz and 0.2 Hz, the infragravity wave band between 0.002 Hz and 0.08 Hz, the semi-diurnal M_2 tide (period = 12.42 h), and the diurnal tidal bands, K_1 (period = 23.93 h) and O_1 (period = 25.82 h). Our pressure spectra also indicate variability in the synoptic time scale (4–6 days) and in 10–17-day fluctuations, similar to velocity spectra shown in Fig. 4. The amplitude of a given tidal frequency was estimated as an amplitude from the variance of that peaks, $\left(\Phi_P(\omega)\omega\right)^{1/2} / \rho_0 g$, where $\Phi_P(\omega)$ is the pressure spectrum and ω is the frequency, and the amplitudes of O_1, K_1, and M_2 tides are 0.72 m, 0.78 m, and 0.27 m, respectively. The pressure spectrum (Fig. 6) has a slope of about -1.5 between 10^{-4} Hz and 10^{-3} Hz. Teague et al. (2013) examined velocity components of tides and near inertial waves (period=25.52 h). They reported that tidal velocities were smaller than near-inertial velocities and magnitudes of K_1 and O_1 were about 3–5 cm s^{-1}. The magnitude of the M2 tidal velocity, was about 2.5 cm s^{-1}.

We adopted the following procedure to compute pressure anomalies. First, high-frequency pressure fluctuations and spikes were removed by filtering raw pressure to remove frequencies higher than 10^{-3} Hz. Second, seasonal and sub-seasonal motions with time scales greater 30 days were filtered out since these motions are not well-resolved and our focus is on tidal and sub-tidal (4-17 day) oscillations. These band-pass filtered pressure fluctuations at M2, M4, and M5 are referred as $\tilde{P}_{M2}$, $\tilde{P}_{M4}$, and $\tilde{P}_{M5}$. The 30-day high-pass filter basically removed the largest term ($\rho_0 gz$) in (7). The sea-surface elevation, $\rho_0 g\overline{\eta}(t)$, was removed by subtracting the reference or the background pressure at a location away from the bank. Here we used $\tilde{P}_{M2}$ as the reference pressure record. This choice of the reference pressure does not affect the form drag calculation and any Ppod pressure could have been used as a background. $\rho_0 g\overline{\eta}(t)$ is spatially uniform and so does not affect the form drag calculation. Pressure anomalies at M4 (ΔP_{M4}) and at M5 (ΔP_{M5}) were obtained by removing $\tilde{P}_{M2}$ from $\tilde{P}_{M4}$ and $\tilde{P}_{M5}$, where $\Delta P_{M4} = \tilde{P}_{M4} - \tilde{P}_{M2}$ and $\Delta P_{M5} = \tilde{P}_{M5} - \tilde{P}_{M2}$ (Fig. 7). Note the pressure anomaly at M2, ΔP_{M2} became zero. The subtraction of the reference pressure also removed the atmospheric pressure p_{Atm} since p_{Atm} was assumed to be uniform over the bank. The background stratification term, $g\int_z^\eta \overline{\rho}(z',t)dz'$ was not computed because the time-dependent depth-averaged density was not well known. Time-depth series of hydrographic data from three TCP moorings at S2, S3, and S4 were available, but lateral and vertical resolutions of the density field were limited to make an accurate estimate of the background stratification term. This term is spatially uniform, and therefore the subtraction of the reference pressure, $\tilde{P}_{M2}$ removes the term $g\int_z^\eta \overline{\rho}(z',t)dz'$ from pressure anomalies at M4 and M5. The sea-surface tilt due to rotational effects was estimated from the geostrophic balance,

$g\frac{\partial \eta_{Tf}}{\partial x} = f\overline{V}$, where $\overline{V}$ is the low-pass filtered (periods greater than 48 hours), depth-averaged velocity perpendicular to the mooring line, and f is the Coriolis parameter. We noted that $\overline{V}$ was nearly uniform around the bank (not shown). Therefore, the pressure induced by the sea-surface height due to rotational effects at a given location along the mooring line was approximated from $g\rho_0\eta_{Tf} \approx \rho_0 f\overline{V}\,(x - x_{M2})$. For f = 6.84x10^{-5} s^{-1}, $\overline{V}$ = 0.1 m s^{-1}, ρ_0 = 1000 kg m^{-3}, and $x = x_{M4}$ with $[x_{M4}$-$x_{M2}]$ = 9 km, the resulting pressure anomaly at M4 is as large as 100 N m^{-2} (Fig. 7a).

As described above, the bottom pressure anomalies west of, east of, and in the middle of the bank (M2, M4, and M5, respectively) were obtained by (i) the band-pass filtering pressure between1000 s and 30 days, (ii) subtracting a selected reference pressure outside the bank (i.e., pressure at M2), and (iii) subtracting the pressure due to rotational effects. Bottom pressure anomalies at M2, M4, and M5 are, respectively, $p'_{bM2} = 0$, $p'_{bM4} = \Delta P_{M4} - \rho_0 f\overline{V}(x_{M4} - x_{M2})$, and $p'_{bM5} = \Delta P_{M5} - \rho_0 f\overline{V}(x_{M5} - x_{M2})$. The bottom pressure anomalies were dominated by the combined external, internal and inertial pressure anomalies (ΔP_{M4} and ΔP_{M5}). The rotational effect which depends on the relative distance from M2 is important especially at M4 but it is a smaller term at M5 (Fig. 7). Bottom pressure fluctuations (Fig. 7) show multiple time-scale variability in ΔP_{M4} and ΔP_{M5}. They were about 50–100 N m^{-2} at tidal frequencies and about 50–200 N m^{-2} for low-frequency motions (periods ~ 4–17 day).

b. Form Drag

We used three pressure sensors at M2, M5, and M4 (Fig. 2a) to compute the form drag over the bank. The drag was computed along the mooring line that was oriented about 19^{o} counterclockwise from the east-west direction (Fig. 2). The topographic section along the mooring line is close to “top hat” shaped bathymetry. In general, the EFGB has steeper slopes along the east and south boundaries and the significant portion of the bank top is relatively flat, except near the peak (Fig. 2).The major challenge is to evaluate the form drag (1) from only three pressure measurements. Hafner and Smith (1985) estimated the form drag over the European Alps using a limited number of pressure measurements. They transformed the surface integral (1) to the flux integral and evaluated the form drag as the product of the horizontal, locally constant pressure gradient and the volume of the mountain terrain. This is equivalent of assuming that the local pressure gradient is linear between two nearby observation sites. Hafner and Smith (1985) discussed the uncertainty of pressure that was determined by a linear formula based on their surface stations.

The form drag is large in regions where both bathymetric slopes and pressure anomalies are significant. Warner et al. (2013) examined the sensitivity of a number of pressure measurements by evaluating the integral (1) over a sloping headland, Three Tree Point (TTP) in Puget Sound, Washington, and found that four sensors (two on either slope of the ridge, Fig. A1) can provide an accurate estimate. We also examined sensitivity for our three-point measurement set-up (one on the top and one on either side of the ridge, Fig. A1) using Warner’s (2012) numerically generated pressure fields over the TTP ridge. As described by Warner (2012), at TTP, the large bottom pressure anomalies were found where the topography was the steep. The model was able to capture some, but not all of these pressure anomalies. The spatial resolution of the model and the required smoothing of the topography for the model to run were major factors for simulating an accurate pressure field over the bank (Warner 2012). Because the Ppods in MORT were not located on the sloping sections of the topography, some of the largest pressure anomalies could have been missed.

A sensitivity analysis described in the Appendix allows the examination of uncertainties in our computation based on three pressure measurements, although the geometrical and dynamical settings of this study and Warner et al.'s (2013) are not identical and the model results may not perfectly capture the distribution of bottom pressure anomalies due to numerical limitations. We compared form drag estimates based on multiple pressure measurements to three pressure measurements as described in the Appendix. We used three methods to compute the form drag over the bank. Method-I computes the form drag by approximating bottom pressure for a given slope as the mean pressure between the top and the outer edge of the ridge and then multiplying it by the mean slope. Method-II computes the form drag as a product of the observed slope and a linearly interpolated pressure between the outer edges and the top of the ridge. Method-III computes the form drag as a product of the mean pressure for a given slope and the maximum magnitude of that slope. The estimates from methods I and II were comparable, but their maximum magnitudes were a factor of two smaller than those obtained from the method-III and the fully resolved solution. Here we applied all three methods to compute the form drag along the M2–M4 mooring line, and results are illustrated in Fig. 8. Topographic gradients of the bank are small or near zero over the top and outside the 100-m bathymetry contour compared to the two major slopes of the bank (Figs. 1a and 2).Therefore we can expect major contributions to the form drag from sloping boundaries. The EFGB is asymmetric, especially toward the southern end, where the lateral slopes over the bank are not negligible. We may not compute the form drag completely since our computation is limited to the east-west direction. Drags estimated from linearly interpolated pressure and from mean pressure are comparable. The form drag estimated from method-III is twice as great as those that calculated from methods I and II, similar to the findings in the Appendix, indicating the sensitivity to the slope.

In the following analyses, we used the form drag computed from method-II similar to Hafner and Smith (1985), even though we may underestimate the expected value by a factor of two. To examine the time variability of the total form drag, we examine tidal and sub-tidal components (time scales greater than two days) separately. The corresponding drag estimates based on method-II are shown in Fig. 9a,b. The tidal band contains diurnal and semi-diurnal tides, and the sub-tidal band contains multiple time-scales (4–17 days). Frequency spectra of D_{form} were also computed to examine multiple time-scale processes related to the total form drag (Fig. 10). The semi-diurnal and diurnal tidal components, 4–6 day synoptic time-scale variability, and 10–17 day low-frequency variability are major contributors to the total form drag similar to the velocity spectrum shown in Fig. 3. The most dominant components of D_{form} are the diurnal and 4–17-day band with drag magnitudes in excess of 2000 N m^{-1} (Table 1; Figs. 9 and 10).

The total form drag (1,8) may contain inertial pressure exerted by the oscillatory nature of the flow (e.g., Warner and MacCready 2009; Warner et al. 2013). Due to tidal acceleration, such as during slack tides, the barotropic pressure gradient (i.e., sea-surface slope, $\partial \eta_{Ti} / \partial x$) is in the direction of the tidal acceleration ($\partial \overline{U} / \partial t$), which in turn generates an "inertial drag" or an "apparent form drag" without flow separation. We noted that the tendency term ($\partial \overline{U} / \partial t$) of the depth-averaged velocity was nearly uniform over and around the bank (not shown). Therefore, the pressure due to acceleration of the oscillatory flow is approximated as: $g\rho_0\eta_{Ti} \approx \rho_0 \frac{\partial \overline{U}}{\partial t}(x - x_{M2})$, where $\overline{U}$ is the depth averaged velocity along the M2-M4 line, and the corresponding inertial drags (D_{iner}) for tidal and sub-tidal bands are plotted in Fig. 9. For tidal motions, D_{iner} is a significant part of the total form drag (Fig. 9a), but for sub-tidal motions (Fig. 9b), D_{iner} is negligible.

c. Power: P_{form}

Both currents and the estimated form drag consist of non-stationary processes, and convectional Fourier co-spectrum analysis does not provide information about power variations within data records. Therefore, the power per unit length is estimated as a product of D_{form} and U_m (2), where U_m is the free-stream velocity in the direction of the form drag at an upstream location where the flow is undisturbed by the topographic feature. Unfortunately, our observations outside the bank were close to the walls of the bank. The flow below the height of the bank was impacted by the topography, and among those observations, the flow in the upper 50 m at M1 was the least affected. Therefore, we used the upper 50-m averaged velocity (U_U) at M1 as the undisturbed mean flow (U_m). A time series of P_{form} for the sub-tidal band is shown in Fig. 11. For most occasions, $-U_U$ and D_{form} were in phase, indicating kinetic energy loss of mean currents due to the form drag over the bank with negative P_{form}. Positive values of P_{form} may reflect phase differences between the drag and the velocity, but some differences may be attributed to uncertainties in D_{form}. The energy loss ($P_{form} < 0$) has a wide range variability with values as large as 800 W m^{-1} (Fig. 11). The six-month averaged energy loss ($P_{form} < 0$) was about 73 W m^{-1} with 95% confidence limits between 69 and 77 W m^{-1}. The power associated with the diurnal tidal components was not computed, since tidal velocities were heavily contaminated by inertial motions. The magnitude of average energy loss per unit area, P_{form}/l_0, at sub-tidal (4 to 17-day) bands is about 10^{-2} W m^{-2}. Energy loss over the bank can be expressed as $(P_{form}/l_0)A_0$, where A_0 is the projection of the bank to the horizontal plane. The long-term average energy losses for the 4–17 day band is about 0.32 MW, where $l_0 = 9$ km, and A_0 (= 40.76 km^2) is the projected bank area encompassed by the 100 m bathymetric contour.

d. Drag Coefficient

The bluff-body drag coefficient, C_{DF} (3), and the bulk drag coefficient, C_D (4) were computed, and the estimates of C_D are presented here since $C_{DF}/C_D = l_0/h_0$. The bulk drag coefficient was calculated from the observed relation between $F_D(= -1/2\rho_0|U_m|U_m)$ and D_{form}/l_0 for the sub-tidal band, where U_m was set to U_U at M1 (Figs. 3a, 4a). The relationships between D_{form}/l_0 and F_D were explored for sub-tidal flows at all five mooring sites, and the bin-averaged D_{form}/l_0 is plotted as a function of F_D for U_U values at M1-M5 (Fig. 12). As discussed earlier, U_U at M1 is the best approximation for an undisturbed velocity for estimating C_D, but observations at M2–M5 produced similar results. The slope of the scatter plots represents the bulk drag coefficient. The average C_D based on a least-square fit for $10 > F_D > -10$ is about $26\text{x}10^{-3}$. Individual estimates of C_D (i.e., the ratio, $D_{form}/l_0\, F_D$) vary between $5\text{x}10^{-3}$ and $180\text{x}10^{-3}$ with a mean, standard deviation, and standard error of about $36\text{x}10^{-3}$, $20\text{x}10^{-3}$, and $5\text{x}10^{-3}$, respectively. Here we excluded few data points for $F_D < -10$ at M1. For the tidal band we used (4) to evaluate C_D from the tidal drag based on the spectral peak of the form drag spectrum (Fig. 10), where the tidal drag was approximated as $\left(\omega\Phi_{drag}(\omega)\right)^{1/2}$ and mean tidal currents were from Teague et al. (2013) (Table 1); C_D was not computed as a function of time because it is difficult to generate a time series of accurate tidal flow without contamination by inertial currents. The estimated bulk drag coefficients for the tidal and low-frequency bands are about (26–226)x10^{-3} (Table 1).

e. Wave Drag from Linear Theory

The approximation, $D_{form}/l_0 \approx -1/2\rho_0 C_D|U_U|U_U$ with quasi-steady values of C_D (Fig. 12) suggests that the form drag can be a linear function of flow speed as found in the linear theory of lee waves generated by bottom topography (e.g., Baines 1995). A formation of hydrostatic lee waves and the associated form drag for the non-dimensional height of the bank, $h_n<1$, and the non-dimensional width, $a_n >> 1$, have been studied extensively (e.g., Baines 1995). Queney (1948) calculated the wave drag (D_{wave}) of a mountain terrain profile ("Witch of Agnesi") with constant stratification and constant background velocity provided $h_n<<1$. In the following, we computed D_{wave} as a function of time using the observed velocity (U_U) and the background stratification (N), where,

$$D_{wave} = -\pi\,\rho_0\,N\,h_0^2\,U_U/8\,. \tag{16}$$

The minus sign in (16) is consistent with the definition of the form drag given in (1). N was estimated between depths of 15 m and 65 m from density time series at S2, S3, and S4 (Fig. 13a). The h_0 was taken as the spatially averaged height of the bank above the 60-m bathymetry contour, and is about 46 m (±5 m standard deviation). Wave drag at M1 and M4 (Fig. 13c) were similar in magnitude. We did not have N at M1, so N at S2 was used (Fig. 13a). Surprisingly, sign and magnitudes of D_{wave} were comparable with D_{form} for most occasions (Fig. 13b). There were several instances where D_{wave} was significantly smaller than D_{form} and there was no apparent relation between the wave and form drags. The observed parameter range reflects a blocking flow ($h_n>>1$), which is significantly different from Queney's non-blocked-flow solution ($h_n<<1$). We discuss the applicability of linear theory in the discussion section.

5. Estimates of Frictional Drag

We compute the frictional drag coefficient (C_d) (13) and the roughness length (z_0) (15) over the bank by combining measured TKE dissipation rates and currents near the bottom. The spacing between VMP profiles is, on average, approximately 200 m, much larger than individual coral features. Hence, our measurements can be best used to estimate the range of roughness over the top of the bank rather than a precise value at an individual location. The measured values of velocity and TKE dissipation rate (ε) were interpolated to a grid with 0.5 m vertical spacing. The bottom boundary-layer depth at which density changed by 0.01 kg m^{-3} from the near bottom density was about 4 m from the bottom for nearly 75% of the VMP profiles collected over the bank. The inertial boundary layer is typically less than 20% of the boundary-layer depth and is expected to be less than 1 m. Dissipation measurements were averaged over the first 4 m from the bottom (or approximately over the bottom boundary layer), and 5 sequential profiles were combined, resulting in spacing on the order of 1 km. The maximum likelihood estimator method (Baker and Gibson 1987) was used to calculate the expected value and 95th percentile confidence limits. Velocities were also averaged in time using 5 adjacent profiles with any measurements more than 7.5 m above the bottom discarded. The frictional velocity, u_* (14), was calculated from ε as described above, and errors are propagated to the new term. The near-bottom mean velocity, $\tilde{U}$, was calculated in three different ways: (i) using the smoothed velocity at the deepest available depth (d_0), (ii) by fitting the measured velocity at d_0 to an exponentially decaying curve where $\tilde{U}(d_0) = \tilde{U}_1$ with the slope at 3 m above the bottom defined by the calculated u_* (where $\partial\tilde{U}_2 / \partial z = u_* / \kappa z_a$), and (iii) a linear extrapolation of velocities to 3 m above the bottom using the deepest two bins. These three methods are referred to as $\tilde{U}_1, \tilde{U}_2$, and $\tilde{U}_3$, respectively. The three techniques give a better sense of the range of $\tilde{U}$, as the ship ADCP typically did not measure velocities within the inertial layer, with the deepest bin typically 5–7 m above the bottom. All three versions of $\tilde{U}$ were applied to calculate three values of z_0, with errors in z_0 propagated from u_* and $\tilde{U}$. Calculations of C_d (13) are based on a reference height at z_a = 3 m above the bottom, which lies within the bottom boundary layer. The minimum for z_0 was set to 10^{-3} cm, as this is the value for a muddy bottom (Deacon 1953) and lower values are physically unrealistic.

Habitat composition maps show algal nodules covering most of the bank, with the coral reef zone (55% coverage) over the shallower regions (Fig. 1). The expectation is that the bank will contain a range of values, including both smooth areas and rough (coral coverage) regions. Previous estimates indicate that the roughness length over corals is expected to be several centimeters (Rosman and Hench 2011), much larger than what was seen at the moorings located just off and on top of the bank. The calculated roughness length (15), the measured dissipation rates, and bottom velocity along the two transects shown in Fig. 14 contain significant variability partly due to limited sampling in both space and time. Dissipation, velocity magnitude, and frictional velocity (multiplied by 10) are shown in the first two panels of Fig. 14 for T1 and T2 (the transects highlighted in Fig. 2a, c). The third panel shows two estimates of the roughness length z_0 with 95th percentile confidence levels calculated from the near-bottom velocity ($\tilde{U}$) alone (black line), and the mean and standard deviation of all three estimates of z_0 derived using $\tilde{U}_1$, $\tilde{U}_2$, and $\tilde{U}_3$ (red line). Along both T1 and T2, which pass over the shallow coral zone, the roughness lengths have values between 1 and 10 cm (Fig. 14), as expected over corals (Rosman and Hench 2011).

The calculated roughness lengths (15) and the associated drag coefficients (13) over the EFGB vary spatially (Fig. 15). Given the transect range of the ship ADCP, estimates of z_0 and C_d are exclusively over the top and sides of the bank. To get values over the sandy bottom next to the bank, estimates of z_0 at the long-term mooring locations were made using times when the dissipation transects came within approximately 500 m of a mooring. Measured $\tilde{U}$ was 1-5 m off the bottom, depending on the mooring configuration. M4, M5 and M6 had close transects and an ADCP bin within 5 m of the bottom. M5 is near the top the bank, but was placed in an area free of coral in order to avoid damage to the reef. Estimates for z_0 are 0.02 cm at two mooring locations (M4, M6), and 0.2 cm at the third (M5). Some uncertainty is expected because we do not have dissipation time series at these locations, but the values are consistent with other estimates over a sandy bottom (Reidenbach et al. 2006). Distribution functions of both z_0 and C_d deviate substantially from the Gaussian distribution, and are close to the log-normal distribution. The values of z_0 based on 243 estimates varied between 0.001 cm and 68 cm with an arithmetic mean of 3.62 cm (Figs. 14, 15, Table 2). The values of C_d varied between 1x10^{-3} and 75x10^{-3} with an arithmetic mean of 6.2x10^{-3} (Fig. 15, Table 2).

The range of frictional regimes over the bank can be seen in Fig. 16, which shows C_d and the roughness Reynolds number (Re_*), defined as $Re_* = z_0 u_* / \nu$. For pipe flows, Re_* shows hydraulically smooth regimes for $Re_* < 5$, and completely rough regimes for $Re_* > 70$ (e.g., Schlichting 1962). A drag coefficient of 2x10^{-3} is indicated by a black line, as this is the approximate value at the mooring locations and represents a hydraulically smooth bottom. The measurements make up both values typical for a smooth bottom as well as values similar to those measured previously over corals (i.e., values of 9x10^{-3}- 150x10^{-3} found by Reidenbach et al. 2006).

6. Discussion

a. Form Drag, Power, and Bulk Drag Coefficient

Analysis of a six-month long time series of pressure over the EFGB revealed that D_{form} was generated by multiple time-scale processes. The magnitude of D_{form} at the diurnal-tidal band is about 2800 N m^{-1} for tidal velocities of about 3-5 cm s^{-1} and the inertial drag was a significant component of the total form drag for this band. Apart from D_{form} at tidal oscillations, we found large form drags at sub-tidal bands with timescales 4–6 day, 10–11 day, and 16–17 day periods (Figs. 9 and 10) for depth averaged currents less than 10 cm s^{-1}. For these low-frequency bands, the inertial drag was negligible. Values of D_{form} for diurnal tides and 4–17 day oscillations were similar. Form drags resulting from semi-diurnal tides are well-documented in previous studies (Nash and Moum 2001; Warner et al. 2013), but there are no quantitative estimates of the form drag for sub-tidal motions such as 4–17 days oscillations observed in the GoM. Our analysis demonstrates that the form drag resulting from low-frequency currents is an important flow retardation mechanism even in the presence of the large frictional drag associated with coral reefs.

The six-months averaged power removed from the low-frequency motions by the form drag was 73W m^{-1}. Jarosz et al. (2014) computed along transect-depth integrated turbulent kinetic energy dissipation rate (E) over the bank (transects shown in Fig. 2a), where $E = \rho_0 \iint \varepsilon \, dz \, dx$. E varied between 6.5 W m^{-1} and 40 W m^{-1}, and the space-time averaged E over seven transects was about 23 W m^{-1}. The short-term estimates of TKE dissipation are a factor of 2–3 smaller than the six-month averaged P_{form}. These differences are not surprising, since winds and background currents were weak during the IOP. The six-month averaged bulk drag coefficient (C_D) over the bank can vary between 0.03 and 0.22, which is 3–35 times larger than the estimated frictional drag coefficient (C_d), apart from the fact that the frictional drag coefficient over the bank is also large due to the coral habitats (Tables 1, 2).

b. Parameter Dependence and Linear Theory

As described in the introduction, $h_n = N_0 h_0 / U_0$, $a_n = N_0 a_0 / U_0$, and $K = N_0 D/(\pi U_0)$, where N_0 and U_0 are characteristic scales of stratification and flow speed in the upper layer of the water column, h_0 is the height of the bank, D is the flow depth, L is the width of the bank (Fig. 2), and a_0 is the half width scale (Baines, 1995). We computed these non-dimensional parameters by replacing N_0 by N and U_0 by U_U. We noted for flow over the EFGB that h_n (Fig. 17) and K were greater than 1 for most occasions, except for when the stratification became weak and the mixed layer was deep as observed during late fall frontal passages. Here N is estimated from the 6-hr low-pass filtered potential density at 15 m and 65 m at S2, and U_U is the 6-h low-pass filtered, upper 50-m depth-averaged flow speed at M1. For h_0=46 m, D=100 m, L=6 km, and a_0=1 km, h_0/L=0.017, and h_0/D = 0.46. The non-dimensional parameters, h_n, K, and a_n calculated from the time averaged velocity U_U and the buoyancy frequency N are about 5.6 (±3.5), 3.8(±2.6), and 125(±78), respectively; where the time averaged U_U and N are 0.15(±0.07) m s^{-1}, and 0.023(±0.005) s^{-1}, respectively The standard deviations are given in parenthesis. The height parameter, h_0/D shows that the bank occupies nearly 50% of the water column, and values of non-dimensional parameters (a_n >> 1, h_n >>1, K>>1, and D/L<<1) suggest highly nonlinear, hydrostatic, high-drag state flow with upstream blocking (e.g., Baines 1979; Hunt and Snyder 1980; Vosper et al. 1999). The a_n >>1 indicates that the lateral scale of the bank is much larger than the distance traveled by the flow during a buoyancy period.

Garrett and Kunze (2007) have suggested extra parameters including a steepness parameter, $e_n = kh_0\left((\omega^2 - f^2)/(N^2 - \omega^2)\right)^{-1/2}$, and a tidal excursion, kU_U/ω, for oscillatory flows over the bank with frequency ($\omega > f$) and horizontal wave number (k). For flows over the EFGB, the steepness parameter exists for the K$_1$ tide with ω_{K1} (=7.29x10^{-5} s^{-1}) > f (=6.84x10^{-5} s^{-1}), e_n =10^4 and kU_U/ω_{K1} = 2.0 for $k = 1/a_0 =$ 1x10^{-3} m^{-1}. e_n >>1 suggests that the topographic slope is supercritical with respect to the tidal ray slope, and kU_U/ω =2 suggests that quasi-steady lee waves can be generated in the region.

Formation of hydrostatic lee waves and the associated form drag for a_n >> 1 and h_n < 1 have been studied extensively (e.g., Baines, 1995). As discussed in section 4*e*, D_{wave} from linear theory shows similarities with the observed D_{form}, but not all the time (Fig. 13b), even though dynamics of the blocking flow (h_n >>1) observed here was significantly different from Queney's (1948) non-blocked-flow solution. A theoretical description of the flow for a_n >> 1and h_n >>1 is not well established. If the wave drag (16) can be approximated as the form drag defined in (3) and (4), then drag coefficients are functions of non-dimensional parameters such as h_n and (h_0/l_0), i.e., $C_{DF} = \pi h_n/4$ and $C_D = \pi h_n/4(h_0/l_0)$. Vosper et al. (1999) show that the C_{DF} increases by a factor 3 as h_n increases from 1 to 4, and is consistent with $C_{DF} \approx \pi h_n/4$.

Numerical simulations of air flow over mountains show that horizontal flow becomes highly nonlinear, and moves around the mountain while forming closed vortices on the lee side of the mountain (Smolarkiewicz and Rotunno 1989). Similar lee vortices were observed in laboratory experiments (e.g., Baines 1979; Hunt and Snyder 1980; Vosper et al. 1999). Jarosz et al. (2014) reported upstream stagnation flow, flow around the bank, vortex formation and bottom flow reversals on the lee side of the EFGB. They noted that their findings were qualitatively similar to the laboratory experiments conducted by Baines (1979) and Hunt and Snyder (1980). The dynamical parameters ($a_n >> 1$, $h_n >> 1$, $K >> 1$, and $D/L << 1$) and Jarosz et al.'s observations suggest that at least part of the measured form drag was caused by pressure anomalies associated with flow separation and vortices generation on the lee side. The strongest flow over the bank was associated with near-inertial waves (Teague et al. 2013); hence, flow-separation and eddy shedding could occur within the inertial cycle on the lee side of the bank (especially over the steep slopes), apart from the low-frequency motions. The Rossby number, U_U/fL is about 0.35 (±0.14) for $U_U = 0.15$ m s^{-1}, $f = 6.84\text{x}10^{-5}$ s^{-1}, and $L = 6$ km, and therefore rotation can also be a factor in the local dynamics (e.g., Smith 1979).

c. Frictional Drag Coefficients associated with Corals

The frictional drag coefficient over the bank is large due to high-roughness elements associated with coral reefs. The observations, which were used to estimate this coefficient, were made when winds were weak and surface waves were small. Consequently surface-wave induced bottom currents could not influence the bottom TKE dissipation rate. The estimated roughness lengths reflect the true roughness lengths of small-scale bathymetric features over the EFGB. The coral coverage is not continuous over the bank, thus, z_0 had a range of values from those representing a smooth bottom with a roughness length of 0.001 cm to those for relatively rough regimes with z_0 as high as 68 cm. Nearly 1/3 of our estimates were greater than 1 cm, and the average drag was about 6 x10^{-3}. These higher roughness lengths correspond to high drag coefficients and large frictional Reynolds numbers. The impact of high bottom frictional forces can be important because the strength of the bottom boundary layer stress can change lee wave formation, decrease the form drag, and reduce the overall momentum loss to bottom obstacles or banks compared to a typically assumed free-slip boundary (Skyllingstad and Wijesekera 2002). Pratt (1986) reported that hydraulic controlled flows over straits and sills with friction can alter the dynamics of the flow such as shifting of control points from a sill to downstream locations. Although these modeling studies do not mimic the EFGB observations, the observed large bottom stress over the bank is a factor to consider in the parameterization of the form drag.

7. Summary and Conclusions

Hydrographic, velocity, microstructure, and bottom pressure measurements were used to quantify the magnitude and temporal variability of the form drag, roughness lengths and associated frictional drag coefficients over the EFGB bank. The EFGB is a rough topographic feature located on the Louisiana-Texas shelf approximately 190 km southeast of Galveston, Texas. The EFGB, about 6 km wide and 10 km long, is located at the shelf-edge in 100 m of water depth with a peak rising to about 18 m below the sea surface. The area encompassed by the 100-m bathymetric contour of the bank is about 40 km^2. The bank is one of the northernmost tropical coral reefs. The bank includes both coral coverage and sandy bottoms.

Nearly six-month-long bottom-pressure records (June–December 2011) showed significant semi-diurnal (M_2) tide, diurnal (K_1 and O_1) tides, synoptic scale (4–6 day), and 10–17 day variability over and around the bank. Based on the pressure spectra, tidal elevations of M_2, K_1 and O_1 were 0.27 m, 0.78 m, and 0.72 m, respectively. Note, tidal analysis conducted by Teague el (2013) showed that the barotropic tidal currents were small (K_1, O_1 speeds < 5 cm s^{-1}) compared to inertial currents that were over 15 cm s^{-1}. M_2 tidal currents were less than 3 cm s^{-1}, and the depth-averaged sub-tidal currents were about 4–9 cm s^{-1}.

The estimated form drag from bottom pressure anomalies across the bank showed variability on multiple time scales. Here, D_{form} was estimated from three pressure measurements over and around the bank while assuming that the local horizontal pressure gradient was a constant between two observational sites (e.g., Hafner and Smith 1985). It is likely that D_{form} was underestimated by a factor of two. Therefore, our estimate of D_{form} could be treated as a lower bound of the expected value. The drag resulting from diurnal tidal motions and 4–17 day oscillations had magnitudes of about 3000 N m^{-1} and 2000 N m^{-1}, respectively. Coefficients of the time-averaged bulk drag (C_D) ranged from 0.03 to 0.22, which was a factor of 5–35 larger than the averaged-frictional drag coefficient (Tables 1,2). P_{form} was estimated as a product of the velocity and the form drag for low-frequency motions. The enumerated power per unit length at sub-tidal motions was about 73 W m^{-1}. The total power over the bank, $P_{form} A_0 / l_0$ was ~ 0.3 MW, where $A_0 \approx 40\,\text{km}^2$ and l_0 = 9 km.

Physical parameters describing the dynamics of flows over the EFGB have a range of values representing a highly non-linear, hydrostatic flow regime with upstream blocking, where h_n>>1, K>>1, and a_n ~O(100). For these parameters, there is no theoretical prediction of the form drag. It is interesting to note, however, that the wave drag based on linear theory of the flow over a bank with h_n << 1 produces similar estimates of the measured drag for sub-tidal flows even though the flow observed here moved around the bank with h_n >> 1. Both linear wave drag and quadratic drag laws had similarities with the observed form drag, but no unique parameterization was found.

Using measurements of the velocity and estimated TKE dissipation rates along multiple transects crossing the bank, the range of roughness lengths (z_0) and bottom frictional drag coefficients (C_d) were computed (Table 2). These measurements of the velocity and dissipation over the bank provide the first estimates of frictional drag coefficients and roughness lengths over the EFGB. Over the top of the bank the bottom roughness lengths encompass those expected for a smooth bottom with z_0 of 0.001 cm and higher roughness values over corals. Given that the coral coverage is not continuous, a range of values representing smooth to relatively rough regimes was expected. The range of z_0 was from 0.001 cm to 68 cm, with mean and median values of 3.6 cm and 0.24 cm, respectively (Table 2). Nearly 1/3 of the roughness estimates were greater than 1 cm. The mean and median of the frictional drag coefficient were about 6×10^{-3} and 3×10^{-3}, respectively (Table 2). These findings are comparable with previous measurements over other coral reefs (e.g., Reidenbach et al. 2006).

Large roughness elements can impact the hydraulic flow control as well as coral reef ecology. Locations with coral coverage have increased drag, leading to more turbulence and mixing at these locations relative to regions without corals. This turbulence in turn increases the delivery of nutrients and particulates to the corals. Additionally, it helps to disperse larvae during spawning events, generating a positive feedback cycle that sustains the health of the coral community. The magnitude of the bottom stress over the bank can modify the separation of flow, lee wave structure and strength of the form drag; hence, it is a factor to consider in the parameterization of the form drag in numerical models. Consequently, our observations and analysis of the hydrographic, velocity, microstructure and pressure measurements suggest that the EFGB is a "hot spot" of mixing on the shelf of GoM. The analysis further demonstrates that the form drag resulting from low-frequency currents over an isolated bank on the continental shelf is an important physical process that must be parameterized to represent a wide range of flow states.

Acknowledgements: This work was sponsored by the Office of Naval Research in a NRL project referred to as "Mixing over Rough Topography (MORT)" and by BOEM in the project referred to as "Currents over Banks (COB)" through the Interagency Agreement No. M10PG00038. Support for James Moum was provided through ONR grant N00014-09-1-0280. The measurements were made in cooperation with the Flower Garden Banks National Marine Sanctuary, administered by the National Oceanic and Atmospheric Administration (NOAA). Assistance provided by Alexis Lugo-Fernandez of BOEM and Emma Hickerson of NOAA, and the crew of the R/V *Pelican* and R/V *Manta* was greatly appreciated.

APPENDIX

Estimation of the form drag based on numerical simulations: Sensitivity study

The form drag over an underwater topographic feature is estimated from bottom pressure fluctuations and a horizontal slope of the bathymetry as indicated in (1). The accuracy of the estimated drag depends on the number of pressure measurements and the location of the pressure measurements. A sensitivity study was conducted to examine the minimum number of pressure measurements required to calculate a reasonable estimate of the form drag. Here we used numerically simulated pressure fields over a sloping headland, Three Tree Point (TTP) in Puget Sound, Washington, developed by Warner (2012) as part of her PhD dissertation. The TTP model was based on the Regional Ocean Modeling System (ROMS) and details of the model set up is given by Warner (2012). The study helps us to quantify some uncertainties in an estimation of the form drag over the EFGB based on three pressure measurements. The ROMS results are an approximation to the real observations due to numerical limitations given by Warner (2012). It is also noted that the shape and size of TTP are different from the EFGB, and that the locations of Ppods during MORT might have missed large pressure fluctuations. Therefore, the results discussed below have more uncertainties than the model results alone.

A time series of modeled bottom-pressure anomalies along the TTP ridge was used to compute the form drag based on (1). The spatial resolution of the model was 50.5 m. The ridge is about 2 km wide and is nearly symmetrical (Fig. A1). Gradients of the ridge, perpendicular to the ridge axis are strongest on the mid-sections of the ridge with the maximum on the right side and the minimum on the left side. Total pressure anomalies (8) including external, internal, and inertial components at three different locations (near bottom and top of the ridge) are shown in Fig. A2.

We computed the form drag using the modeled pressure along the ridge and the measured slope with 50.5 m spatial resolution, and referred to it as the complete solution (D_0):

$$D_0 = -\sum_{i=1}^{I} (p_B)_i \left(\frac{\partial h}{\partial x}\right)_i \Delta x, \text{ and } \Delta x = 50.5 \text{ m}, \qquad \text{(A1)}$$

where I is the total number of pressure measurements used in the integration and X_3-X_1= $I\Delta x$ = 2.1 km (Fig. A1). We computed D_{form} by approximating the pressure field based on three pressure measurements at X_1, X_2, and X_3 while mimicking the observational set up over the EFGB during the MORT.

a. Method-I

The first estimate was made by using mean values of the pressure and slope over the bank, and the resulting drag is:

$$D_1 = -P_{m1}\left\langle\frac{\partial h}{\partial x}\right\rangle_1 [X_2 - X_1] - P_{m2}\left\langle\frac{\partial h}{\partial x}\right\rangle_2 [X_3 - X_2], \qquad \text{(A2)}$$

where $P_{m1} = \dfrac{p_B(X_1) + p_B(X_2)}{2}$ and $P_{m2} = \dfrac{p_B(X_2) + p_B(X_3)}{2}$. The angle brackets are the spatial means over the slope.

b. Method-II

The second approximation assumed that the pressure distribution was linear over the slopes. We interpolated pressure linearly between X_1 and X_2 representing the left side of the bank, and pressures between X_2 and X_3 representing the right side of the bank. The resulting drag based on the linearly interpolated bottom pressure p_I with fully resolved bathymetric slope, $\left(\frac{\partial h}{\partial x}\right)$ is :

$$D_2 = -\sum_{i=1}^{I} (p_I)_i \left(\frac{\partial h}{\partial x}\right)_i \Delta x\,. \tag{A3}$$

c. Method-III

Here the form drag was approximated by using a mean value of the pressure and the maximum slope over the bank, and the resulting drag is:

$$D_3 = -P_{m1}\left|\frac{\partial h}{\partial x}\right|_{\max 1}\left[X_2 - X_1\right] + P_{m2}\left|\frac{\partial h}{\partial x}\right|_{\max 2}\left[X_3 - X_2\right], \tag{A4}$$

where $\left|\frac{\partial h}{\partial x}\right|_{\max 1}$ and $\left|\frac{\partial h}{\partial x}\right|_{\max 2}$ are the maximum slopes of left and right sides of the bank (Fig. 2b).

The estimated drag over the ridge from the three different methods is illustrated in Fig. A3. The drag resulting from all three methods have the same sign, even though the magnitudes of the complete solution (D_0) and method-III (D_3) are larger than D_1 (A2) and D_2 (A3). D_1 and D_2 have similar magnitudes, but their maximum magnitudes are about 2 times smaller than the maximum of D_0 and D_3 (Fig. 3A). However, when averaged over the tidal cycle, both D_1 and D_2 are about 70% of the complete solution (D_0). There are large variations of the slope across the ridge, and it appears that the slope is an important factor in the computations.

REFERENCES

Baines, P. G., 1979: Observations of stratified flow over two-dimensional obstacles in fluid of finite depth. *Tellus*, **31**, 351-371.

Baines, P. G., 1979: Observations of stratified flow over two-dimensional barriers. *J. Geophys. Res*., **84**, 7834-7838.

Baines, P. G., 1995: *Topographic Effects in Stratified Flows*. Cambridge University Press, 482 pp.

Baker, M. A., and C. H. Gibson, 1987: Sampling Turbulence in the Stratified Ocean: Statistical Consequences of Strong Intermittency. *J. Phys Oceanogr*., **17**, 1817-1836.

Bell, T. H., 1975: Topographically generated internal waves in the open ocean. *J. Geophys. Res*., **80**, 320-327.

Blumberg, A. F., and G. L. Mellor, 1987: A description of a three-dimensional coastal ocean circulation model. *The Three Dimensional Coastal Ocean Models,* N. S. Heaps, Ed., Coastal and Estuarine Sciences Series. Vol 4, Amer. Geophys Union, 1-16.

Bougeault, P., B. Benech, B. Carissimo, J. Pelon, and E. Richard, 1990: Momentum budget over the Pyrenees: The PYREX experiment. *Bull. Amer. Meteor. Soc.*, **71**, 806-818.

Bright, T. J, G. P. Kraemer, G. A. Minnery, and S. T. Viada, 1984: Hermatypes of the Flower Garden Banks, Northwestern Gulf of Mexico: A comparison to other western Atlantic Reefs. *J. Mar. Sci.*, **34**, 491-476.

Clark, T. L., and M. J. Miller, 1991: Pressure drag and momentum fluxes due to the Alps. II: Representation in large scale models. *Quart. J. R. Met. Soc.*,**11**7, 527-552.

Deacon, E. L.,1953: Vertical profiles of mean wind in the surface layers of the atmosphere. *Geophys. Mem.*, **91**, Air Ministry Meteorol. Office, London.

Dewey, R. K., and W. R. Crawford, 1988: Bottom stress estimates from vertical dissipation rate profiles on the continental shelf. *J. Phys. Oceanogr*., **18,** 1167-1177.

Donohue, K., P. Hamilton, K. Leaman, R. Leben, M. Prater, D. R. Watts, and E. Waddell, 2006: Exploratory study of deep-water currents in the Gulf of Mexico, Volume II: Technical report. U.S. Dept. of Interior, Mineral Management Service, Gulf of Mexico, OCS Region, New Orleans, LA, OCS Study MMS 2006-074, 430 pp.

Donohue, K., P. Hamilton, R. R. Leben, D. R. Watts, and E. Waddell, 2008: Survey of Deep-water currents in the northwestern Gulf of Mexico. Volume II: Technical Report, U.S. Department of the Interior, Minerals Management Service, Gulf of Mexico OCS Region, New Orleans, LA, OCS Study MMS 2008-031, 364 pp.

Doyle, J. D., and Q. F. Jiang, 2006: Observations and numerical simulations of mountain waves in the presence of directional wind shear. *Q. J. R. Meteorol. Soc*., **132**, 1877-1905, doi: 10.1256/qj.05.140.

Durran, D. R., 1986: Another look at downslope wind storms. Part I: The development of analogs to supercritical flow in an infinitely deep, continuously stratified fluid. *J. Atmos. Sci*., **43**, 2527-2543.

Durran, D. R., 1990: Mountain waves and downslope winds. Atmospheric processes over complex terrain. *American Meteorological Society Meteorological Monographs*, **23**, 59-81.

Edwards, K. A., P. MacCready, J. N. Moum, G. Pawlak, J. Klymak, and A. Perlin, 2004: Form drag and mixing due to tidal ow past a sharp point. *J. Phys. Oceanogr.*, **34**, 1297-1312.

Firing, E., J. Ranada, P. Caldwell, 1995: Processing ADCP data with the CODAS software system version 3.1, User's manual (Manual and software available electronically at http://currents.soest.hawaii.edu/docs/doc/codas_doc/)

Garrett, C., and E. Kunze, 2007: Internal tide generation in the deep ocean. *Annu. Rev. Fluid Mech.*, **39**, 57-87.

Gill, A. E., 1982: *Atmosphere-Ocean Dynamics.* Academic Press, San Diego, CA.

Grant, W. D., and O. S. Madsen,1982: Movable bed roughness in unsteady oscillatory flow. *J. Geophys. Res.*, **87**, 469-481.

Gregg, M. C., 1987: Diapycnal Mixing in the Thermocline: A Review. *J. Geophys. Res.*, **92**, 5249-5286.

Grubisic, V., and co-authors, 2008: The terrain-induced rotor experiment: A field campaign overview including observational highlights, *BAMS, Amer. Met. Soc*.,1514-1533.

Hafner, T. A., and R. B. Smith, 1985: Pressure drag on the European Alps in relation to synoptic events. *J. Atmos. Sci.* **42 (6)**, 562-575.

Hodur, R.M., 1997: The Naval Research Laboratory's Coupled Ocean/Atmosphere Mesoscale Prediction System (COAMPS). *Mon. Wea. Rev.*, **135**, 1414-1430.

Hunt, J. C. R., and W. H. Snyder, 1980: Experiments on stably and neutrally stratified flow over a model three-dimensional hill. *J. Fluid Mech*., **96**, 671-704.

Jarosz, E., H. W. Wijesekera, W. J. Teague, D. B. Fribance, and M. Moline, 2014: Observations on stratified flow over a bank at low Froude Numbers, *J. Geophys. Res.* (submitted)

Jayne, S. R. and L. C. St. Laurent, 2001: Parameterizing tidal dissipation over rough topography. *Geophys. Res. Lett.*, **28**, 811-814.

Khatiwala, S., 2003: Generation of internal tides in an ocean of finite depth: Analytical and numerical calculations. *Deep-Sea Res. I*, **50**, 3-21.

Kim, Y.-J, and A. Arakawa, 1995: Improvement of orographic gravity parameterization using a mesoscale gravity wave model. *J. Atmos. Sci.*, **52**, 1875-1902.

Kim, Y.-J., S. D. Eckermann, and H.-Y. Chun, 2003: An overview of the past, present and future of gravity-wave drag parameterization for numerical climate and weather predictionmodels: Survey article. *Atmosphere-Ocean*, **41** (1), 65-98.

Lamb, K. G., 1994: Numerical experiments of internal wave generation by strong tidal flow across a finite amplitude bank edge. *J. Geophys. Res*., **99**, 843-864.

Legg, S. and K. M. H. Huijts, 2006: Preliminary simulations of internal waves and mixing generated by finite amplitude tidal flow over isolated topography. *Deep-Sea Res. II.*, **53**, 140-156.

Long, R. R., 1955: Some aspects of the flow of stratified fluids. III. Continuous density gradients. *Tellus*, **7**, 341-357.

Lott, F. and M. J. Miller, 1997: A new subgrid-scale orographic drag parameterization: Its formulation and testing. *Q. J. R. Meteorol. Soc.*, **123**, 101-127.

McCabe, R., P. MacCready, and G. Pawlak, 2006: Form drag due to flow separation at a headland. *J. Phys. Oceanogr*., **36**, 2136-2152.

Minnery, G. A., 1990: Crustose coralline algae from the Flower Garden Banks, northwestern Gulf of Mexico; controls on distribution and growth morphology. *J. Sediment. Res.*, **60**(6), 992-1007.

Moum, J. N. and J. D. Nash, 2000: Topographically induced drag and mixing at a small bank on the continental shelf. *J. Phys. Oceanogr*., **30**, 2049-2054.

Moum, J. N. and W. D. Smyth, 2006: The pressure disturbance of a nonlinear internal wave train. *J. Fluid Mech.*, **558**, 153-177, doi:10.1017/S0022112006000036.

Moum, J. N. and J. D. Nash, 2008: Seafloor pressure measurements of nonlinear internal waves. *J. Phys. Oceanogr.*, **38**, 481-491.

Nakamura, T., T. Awaji, T. Hatayama, K. Akitomo, and T. Takizawa, 2000: The generation of large-amplitude unsteady lee waves by subinertial K1 tidal flow: A possible mixing mechanism in the Kuril Straits. *J. Phys. Oceanogr*., **30**, 1601-1621.

Nash, J. D., and J. N. Moum, 2001: Internal hydraulic flows on the continental shelf: High drag states over a small bank. *J. Geophys. Res.*, **106**, 4593-4612.

Nikuradse, J.,1933: Stromungsgesetz in rauhren rohren, vdi-forschungsheft 361. (English translation: Laws of flow in rough pipes), 1950. Technical report, NACA Technical Memo 1292. National Advisory Commission for Aeronautics, Washington, DC.

Nikurashin, M. and R. Ferrari, 2011: Global energy conversion rate from geostropic flows into internal lee waves in the deep ocean. Geophys. Res. Lett., **38**, L08610, doi:10.1029/2011GL046576.

Olafsson, H., and P. Bougeault, 1996: Nonlinear flows past an elliptic mountain ridge. *J. Atmos. Sci.,* **53**, 2465-2489.

Oke, P. R., J. S. Allen, R. N. Miller, G. D. Egbert, and P. M. Kosro, 2002: Assimilation of surface velocity data into a primitive equation coastal ocean model. *J. Geophys. Res*.,**107** (C9), 3122-3147.

Pawlak, G., P. MacCready, K. A. Edwards, and R. McCabe, 2003: Observations on the evolution of tidal vorticiy at a stratified deep water headland. *Geophys. Res. Lett.*, **30** (24), 2234.

Perkins, H., F. De Strobel, and L. Gauldesi, 2000: The barny sentinal trawl-resistant ADCP bottom mount: design, testing, and application. *IEEE J. Ocean. Engr.* **25**, 430–436.

Polzin, K. L., J. M. Toole, J. R. Ledwell, and R. W. Schmitt, 1997: Spatial variability of turbulent mixing in the abyssal ocean. *Science*, **276** (5309), 93-96.

Pratt, L. J., 1986: Hydraulic control of sill flow with bottom friction. *J. Phys. Oceanogr*., **16**, 1970-1980.

Queney, P., 1948: The problem of air flow over mountains: A summary of theoretical studies,
Bull. Am. Meteorol. Soc., 29, 16-26.

Reidenbach, M. A., S. G. Monismith, J. R. Koseff, G. Yahel, and A. Genin, 2006: Boundary layer turbulence and flow structure over a fringing coral reef. *Limnol. Oceanogr.*, **51** (5), 1956-1968.

Rosman, J. H., and J. L. Hench, 2011: A framework for understanding drag parameterizations for coral reefs. *J. Geophys. Res*., **116**, C08025.

Schlichting, H., 1962: *Boundary Layer Theory*. 6th ed. McGraw-Hill, New York, 817pp.

Seim, K. S., I. Fer, and H. Avlesen, 2012: Stratified flow over complex topography: A model study of the bottom drag and associated mixing. *Cont. Shelf Res*., **34**, 41-52.

Smith, R. B., 1978: A measurement of mountain drag. *J. Atmos. Sci.*, **35**, 1644-1654.

Smith, R. B., 1979: The influence of the earth's rotation on mountain wave drag. *J. Atmos. Sci*., **36**, 177-180.

Smith, R. B., 1980: Linear theory of stratified hydrostatic flow past an isolated mountain. *Tellus*, **32**, 348-364.

Smith, R. B., 1989: Hydrostatic airflow over mountains, *Advances in Geophysics*, Academic Press, **31**, 1-41.

Skyllingstad, E. D., and H. W. Wijesekera, 2004: Large-eddy simulation of flow over two-dimensional obstacles: High drag states and mixing. *J. Phys. Oceanogr*., **34**, 94-112.

Smolarkiewicz, P. K., and R. Rotunno, 1989: Low Froude-number flow past 3-dimensional obstacles Part I: Baroclinically generated lee vorticies. *J. Atmos. Sci*., **46**, 1154-1164.

Stull, R.B., 1988: *An Introduction to Boundary Layer Meteorology*. Kluwer Academic Publishers, Dordrecht, the Netherlands, 666 pp.

Teague, W. J, H. W. Wijesekera, E. Jarosz, D. B. Fribance, A. Lugo-Fernández, and Z. R. Hallock, 2013: Current and Hydrographic Conditions at the East Flower Garden Bank in 2011. *Cont Shelf Res.*, doi: 10.1016/j.csr.2013.04.039.

Tennekes, H., and J. L. Lumley, 1972: *A first course in turbulence*. The MIT Press, Cambridge, Massachusetts, 300 pp.

Vosper, S. B., I. P. Castro, W. H. Snyder, and S. D. Mobbs, 1999: Experimental studies of strongly stratified flow past three-dimensional orography. *J. Fluid Mech*., **390**, 223-249.

Warner, S. J. and P. MacCready, 2009: Dissecting the pressure field in tidal flow past a headland: When is form drag “real"? *J. Phys. Oceanogr.*, **39** (11), 2971-2984.

Warner, S. J., 2012: Using bottom pressure to quantify tidal form drag on a sloping headland. Ph.D. thesis, University of Washington, Seattle, Washington, 131pp.

Warner, S. J., P. MacCready, J. N. Moum, and J. D. Nash, 2013: Measurement of tidal form drag using seafloor pressure sensors. *J. Phys. Oceanogr.*, **43**, 1150-1172.

Wijesekera, H. W., D. W. Wang, W. J. Teague, and E. Jarosz, 2010: High sea-floor stress induced by extreme hurricane waves. *Geophys. Res. Lett.*, **37**, L11604, doi:10.1029/2010GL043124.

Wijesekera, H. W., D. W. Wang, W. J. Teague, E. Jarosz, W. E. Rogers, D. B. Fribance, and J. N. Moum, 2013: Surface wave effects on high-frequency currents over a shelf edge bank. *J. Phys. Oceanogr*., **43**, 1627-1647.

Wolk, F, H. Yamazaki, L. Seuront, and R. G. Lueck, 2002: A New Free-Fall Profiler for Measuring Biophysical Microstructure. *J. Atmos. Oceanic Technol*., **19**, 780-793.

Wood, N., A. R. Brown, and F. E. Hewer, 2001: Parameterizing the effects of orography on the boundary layer: An alternative to effective roughness lengths. *Q. J. R. Meteorol. Soc*., **127**, 759-777.

Table 1. Averaged form drag, velocity, power, and bulk drag coefficient (4). Estimates of P_{form} were limited to low-frequency motions (Fig.11). The magnitudes of K_1 and O_1 tidal velocities estimated by Teague et al. (2013) are also included in the Table. The values inside the brackets are 95% confidence limits. C_D for the diurnal tides was computed from velocity estimates given in Teague et al. (2013). The estimated bulk drag coefficient for semi-diurnal tides by Warner et al. (2013) is given in the bottom row.

Variable	Diurnal Tides (K_1 & O_1)	Synoptic time scale (4-6 days)	10–17 day variability
D_{form} (N m^{-1}): $\left[\omega\Phi_{drag}(\omega)\right]^{1/2}$	2828 [2236, 4000]	1265 [1000, 2000]	2000 [1414, 3742]
U_U (cm s^{-1}) $\left[\omega\Phi_U(\omega)\right]^{1/2}$ Tidal analysis [Teague et al. 2013]	7–11.4 [may contain inertial motions] 3 –5	4.5–6.3	4.5–8.4
P_{form} (W m^{-1}): $D_{form} \times U_U$		-73 [-77 , -69]	
Bulk Drag Coefficient (4): C_D	$226\text{x}10^{-3}$ $\{(179 – 320)\ \text{x}10^{-3}\}$	$36\text{x}10^{-3}$ $[(21, 51)\ \text{x}10^{-3}]$ min and max: $\{(5 - 180)\text{x}10^{-3}\}$	
C_D from Fig. 12		$26\text{x}10^{-3}$	
C_D (Warner et al. 2013)	Semi-diurnal tides: $90\text{x}10^{-3}$		

Table 2. Bottom roughness (z_0) and frictional drag coefficient (C_d) estimated over the EFGB. Maximum, minimum, arithmetic-mean, and median were estimated from 243 observations. The maximum likelihood estimator (MLE) was computed by assuming log-normal distributions for z_0 and C_d, where $\text{MLE} = \exp(m + s^2/2)$; m and s are the arithmetic mean and standard deviation of *ln*(variable) (e.g., Baker and Gibson 1987).

Variable	Minimum	Maximum	Mean	Median	MLE
z_0 (cm)	0.001	68	3.6	0.24	22
C_d	0.001	0.075	0.0062	0.0032	0.0056

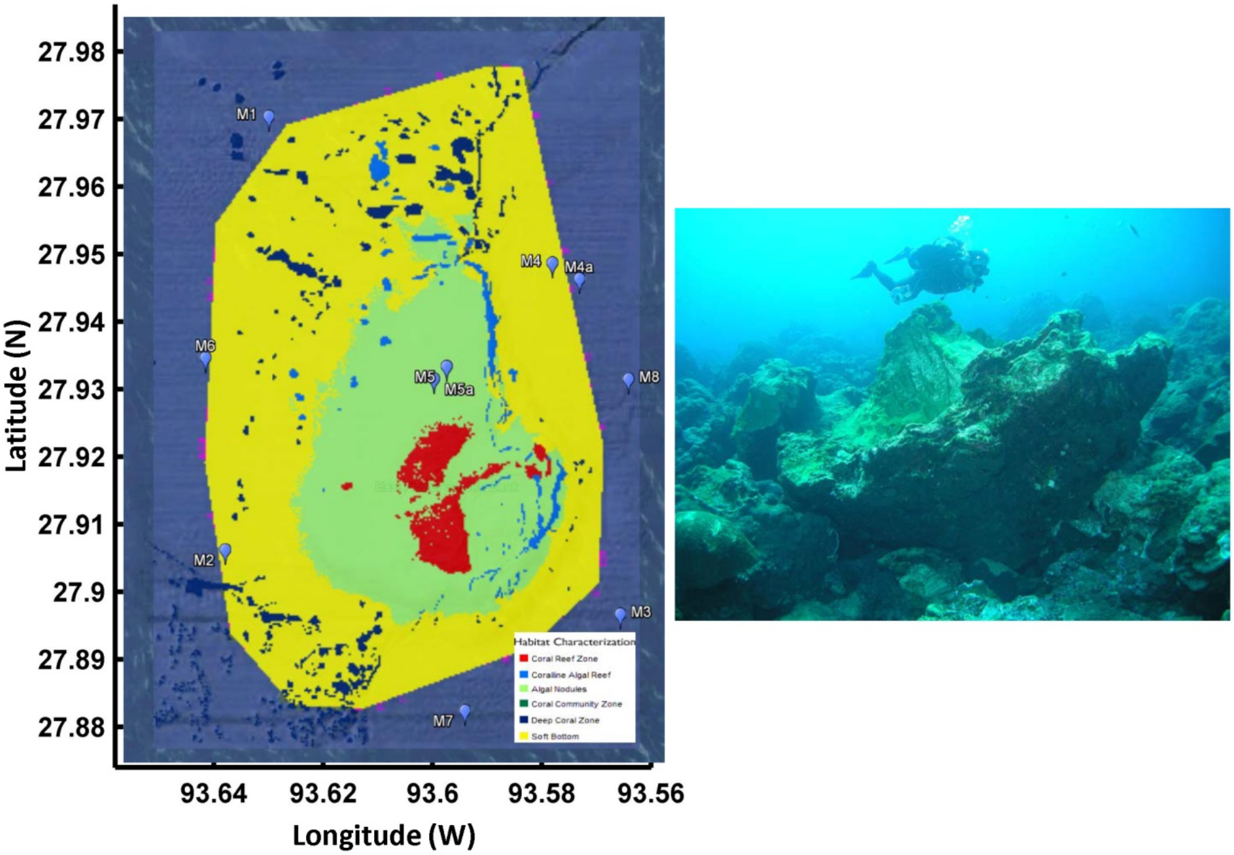

Fig. 1. Left panel: Habitat characterization map of the East Flower Garden Bank (EFGB), along with mooring locations. The edge of the habitat map is the boundary of the marine sanctuary. Habitat characterization was provided by NOAA. Red, blue, light green, green, dark blue, and yellow regions denote coral reefs, coralline algal reef, algal nodules, coral community zone, and soft bottom, respectively. Barny moorings (M1-M8, M4a, M5a) are also marked on the map. Right panel: Roughness elements associated with corals. A diver was examining the underside of a dislodged coral head after Hurricane Ike in September 2008. Photographer: E. Hickerson, Flower Garden Banks National Marine Sanctuary.

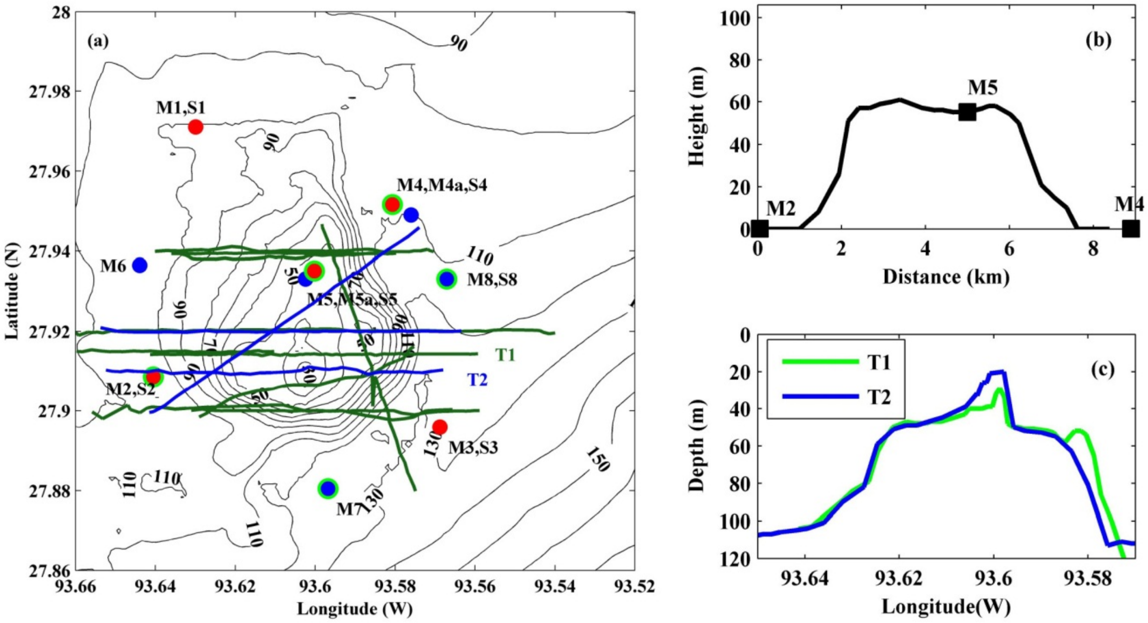

Fig. 2. (a) Bathymetric map of the bank with contours every 10 m. The red bullets are the long-term Barny mooring locations, and the blue bullets are the short-term mooring locations. The locations of Ppods are marked in green circles. Note: the string moorings (S1-S5, and S8) were located about 100–200 m from the Barny locations. The green lines are June transects and blue lines are August transects. (b) Cross-section of bathymetry along M2-M5-M4 line. Distance (positive eastward) is from M2 and the height of bank (positive upward) is from 106-m bathymetry contour. (c) Longitude-depth cross-sections of bathymetry along T1 and T2 transects.

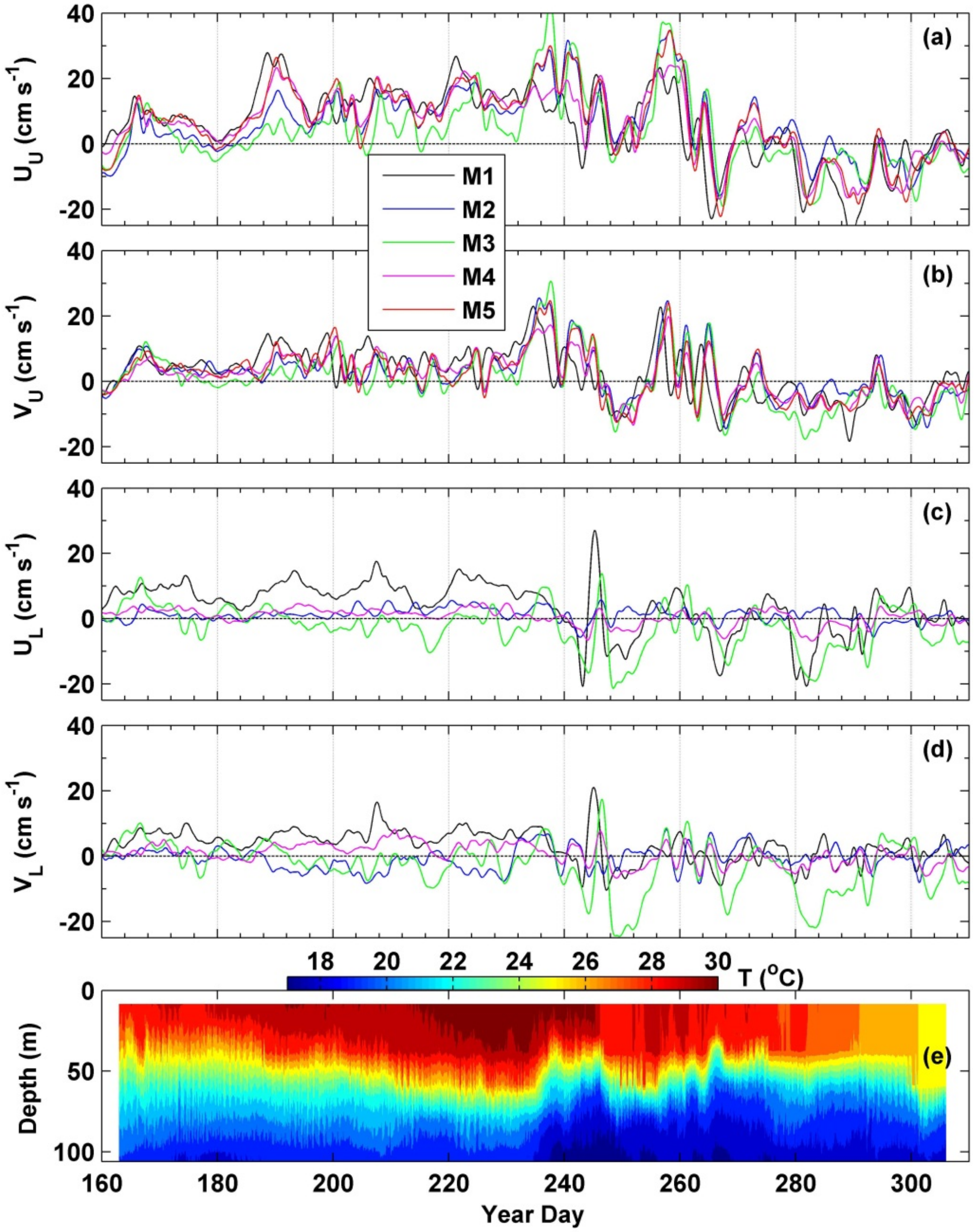

Fig. 3. Time series of 48-h low-passed filtered upper layer (above 50 m) and lower layer (below 50 m) velocities (in cm s^{-1}). (a) Upper layer velocity along the direction of the mooring axis M2-M4 (U_U). (b) Upper layer velocity perpendicular to the mooring axis (V_U). (c) Lower layer velocity along the direction of mooring axis M2-M4 (U_L). (d) Lower layer velocity perpendicular to the mooring axis (V_L). (e) Color image of depth-time series of 15-min averaged temperature (in °C) at S2.

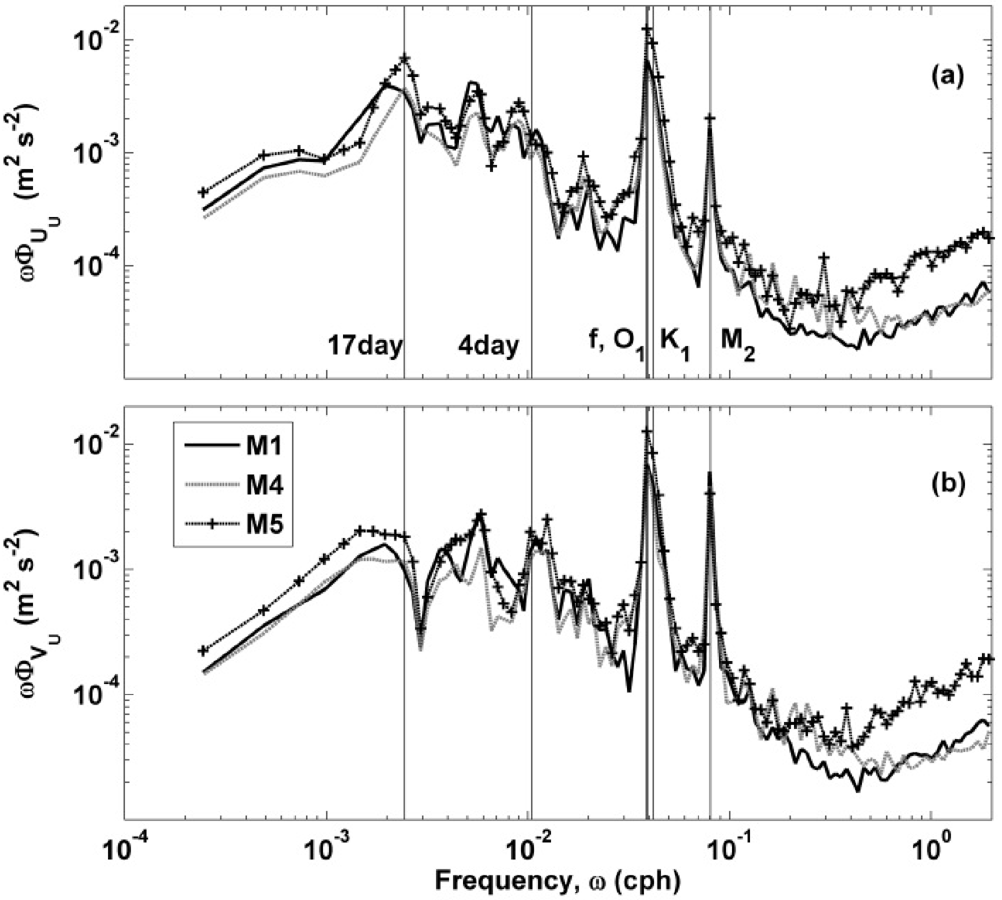

Fig. 4. Depth-averaged frequency weighted velocity spectra in the upper 50 m based on time-series of velocity shown in Fig. 3a and b. (a) U_U, and (b) V_U. Spectra at M1, M4, and M5 are plotted. Vertical lines denote periods of M2, K1, O1, f, 4 day, and 17 day motions.

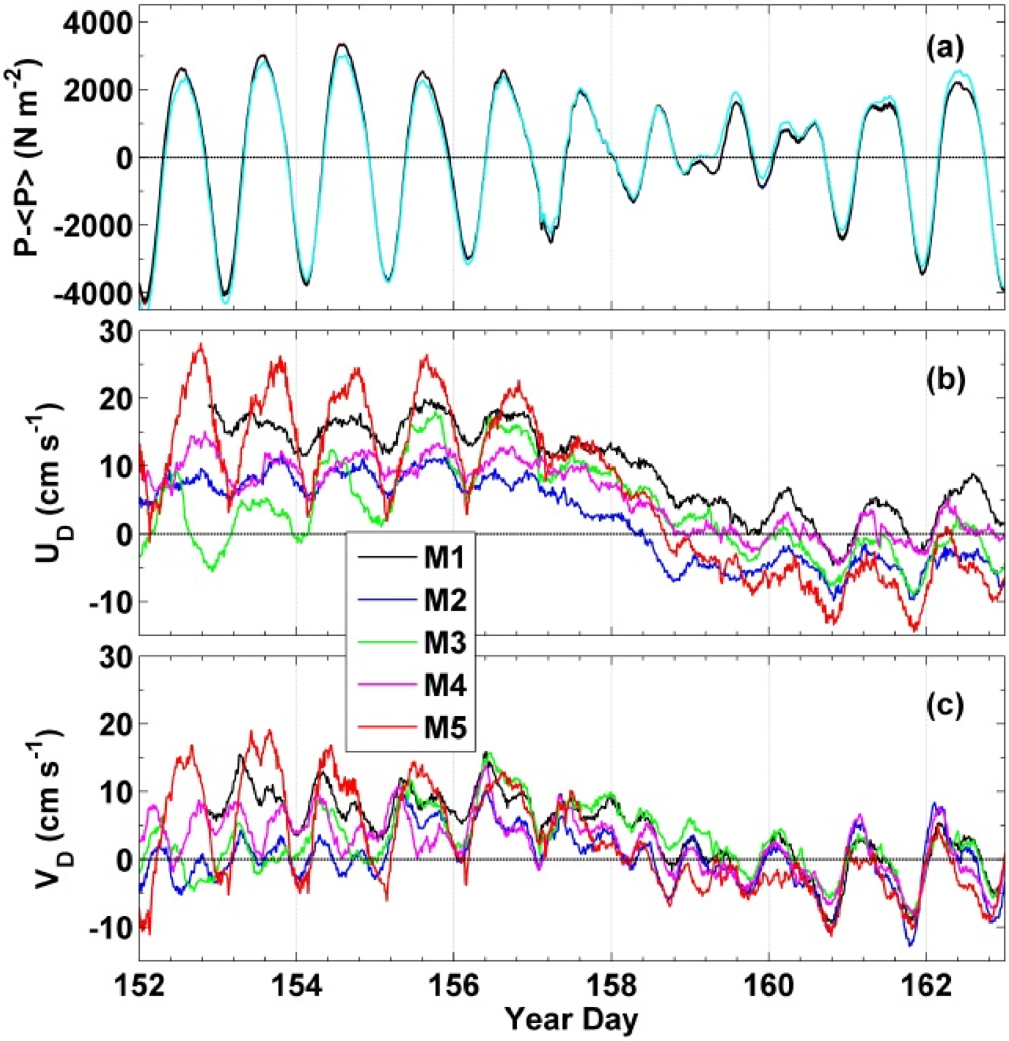

Fig. 5. (a) Demeaned bottom pressure (P-<P>) at M2, M4, M5, M7, and M8 between June 2 (year-day 152) and June 13 (year-day 163), 2011, where <P> is the time averaged pressure. Pressure at M7 (south of the bank, Fig. 2a), marked in cyan differs from the rest of the observations. Depth averaged velocity in the direction of the mooring axis (U_D) (b) and velocity perpendicular to the mooring axis (V_D) (c) at M1-M5.

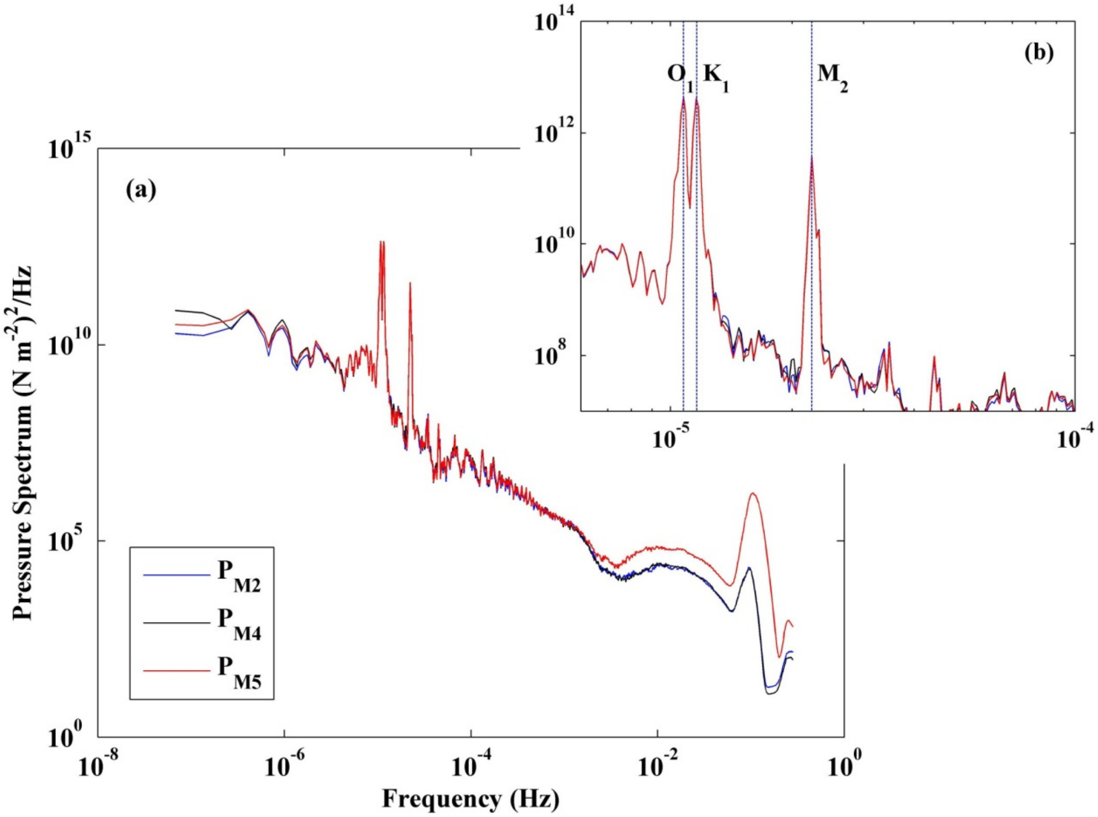

Fig. 6. (a) Frequency spectra of bottom pressure at M2, M4, and M5.The spectra were based on the entire pressure record with a sampling rate of 1 Hz. Spectra were averaged into 2^{10} frequency bins. (b) Enlarged plot showing diurnal tides, O_1 and K_1, and semidiurnal tide, M_2.

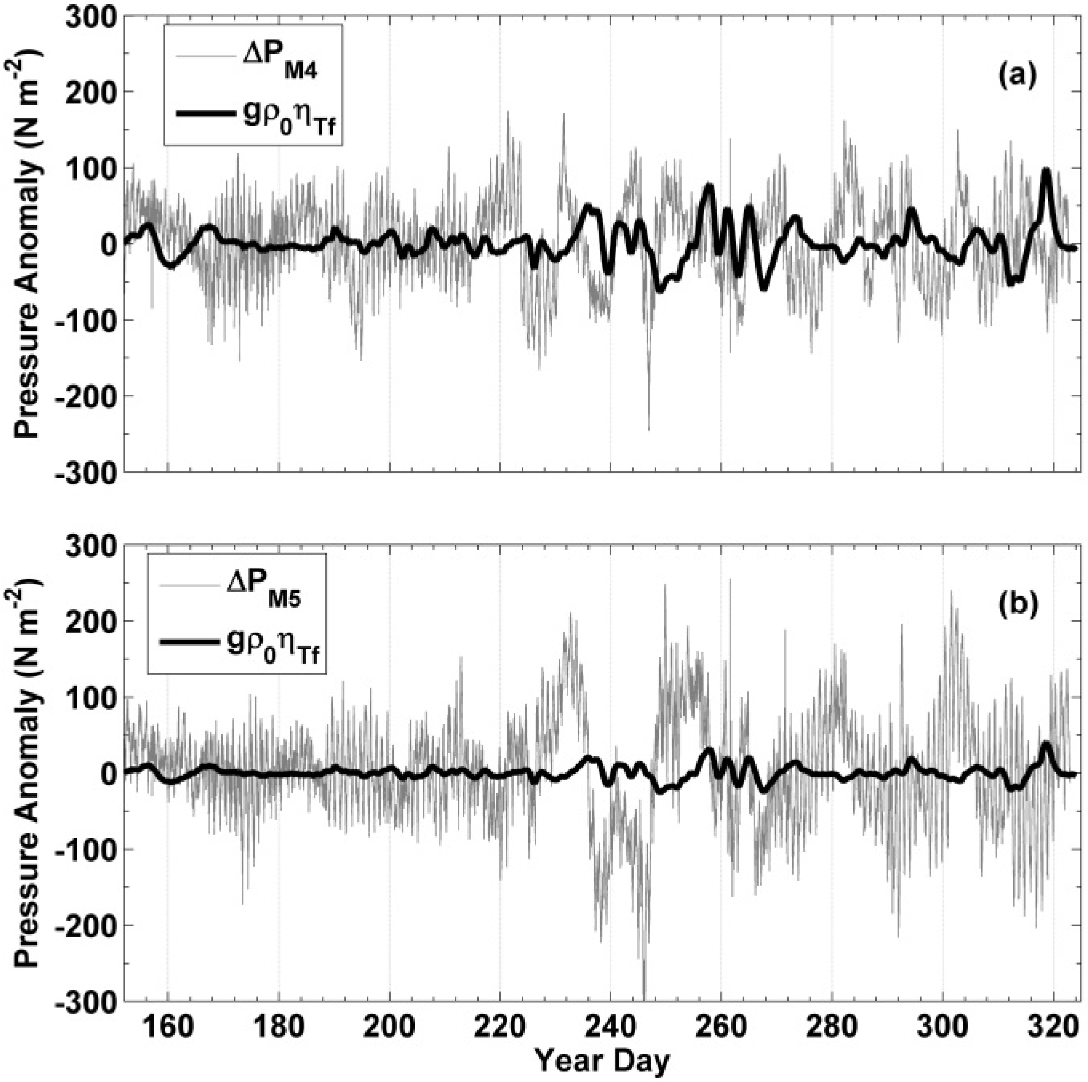

Fig. 7. Bottom pressure anomalies at M4 (a), $\Delta P_{M4} = \tilde{P}_{M4} - \tilde{P}_{M2}$ and M5 (b), $\Delta P_{M5} = \tilde{P}_{M5} - \tilde{P}_{M2}$ (thin gray lines). Barotropic pressure anomaly estimated from rotational effects, $g\rho_0\eta_{Tf} \approx \rho_0 f\overline{V}\ (x - x_{M2})$, are marked by thick black lines.

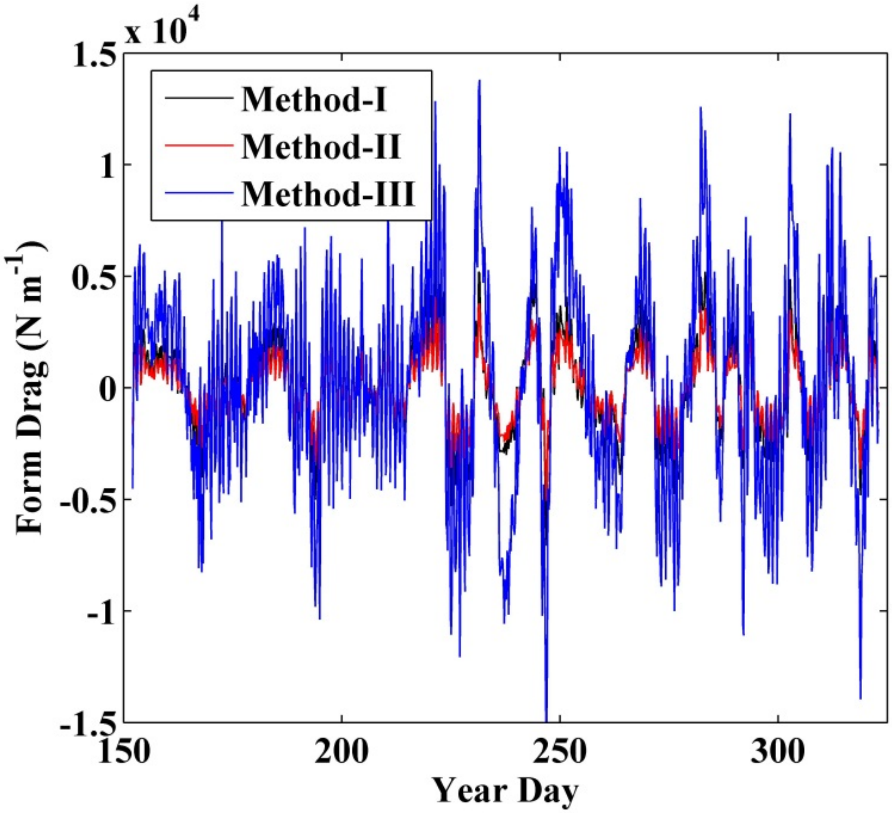

Fig. 8. Form drag estimated from three methods described in Appendix.

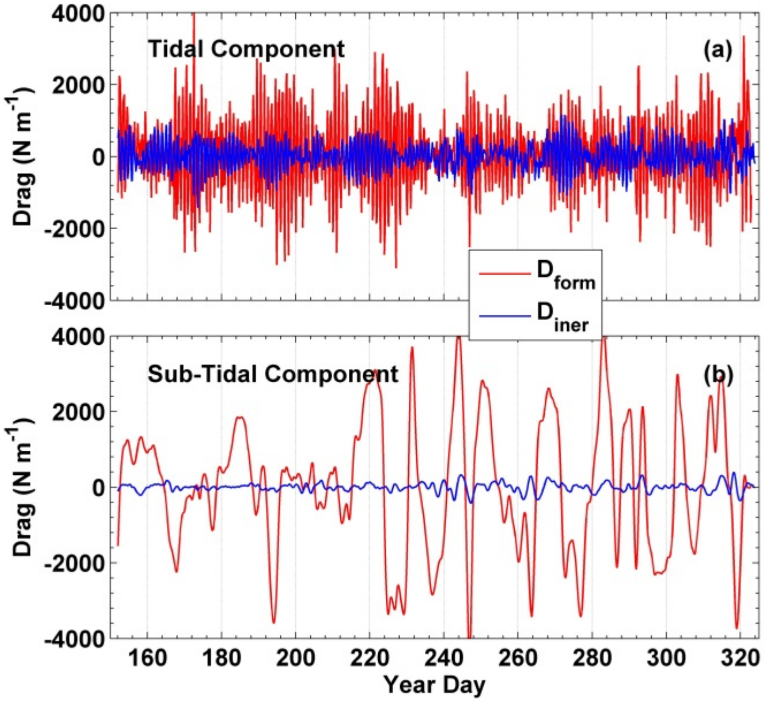

Fig. 9. Total form drag, D_{form} based on interpolated pressure fluctuations (method-II). (a) tidal band, and (b) sub-tidal bands (period >2 days). The blue line in (a) and (b) is the inertial component of the form drag, D_{iner} due to acceleration and deceleration of the flow.

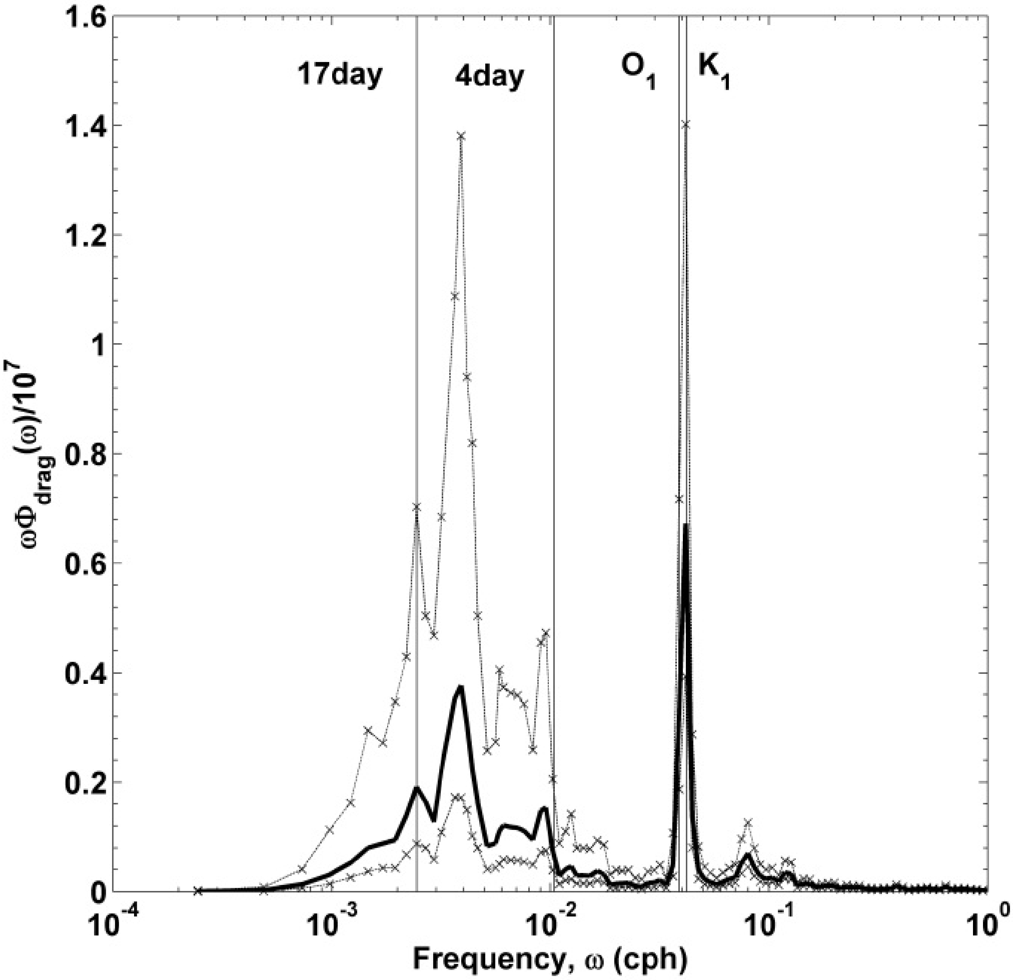

Fig. 10. Variance-preserving power spectra of the form drag in (N m^{-1})^2/10^7. Thin lines with crosses denote 95% confidence limits. Vertical lines denote periods of K1, O1, 4 day, and 17 day motions.

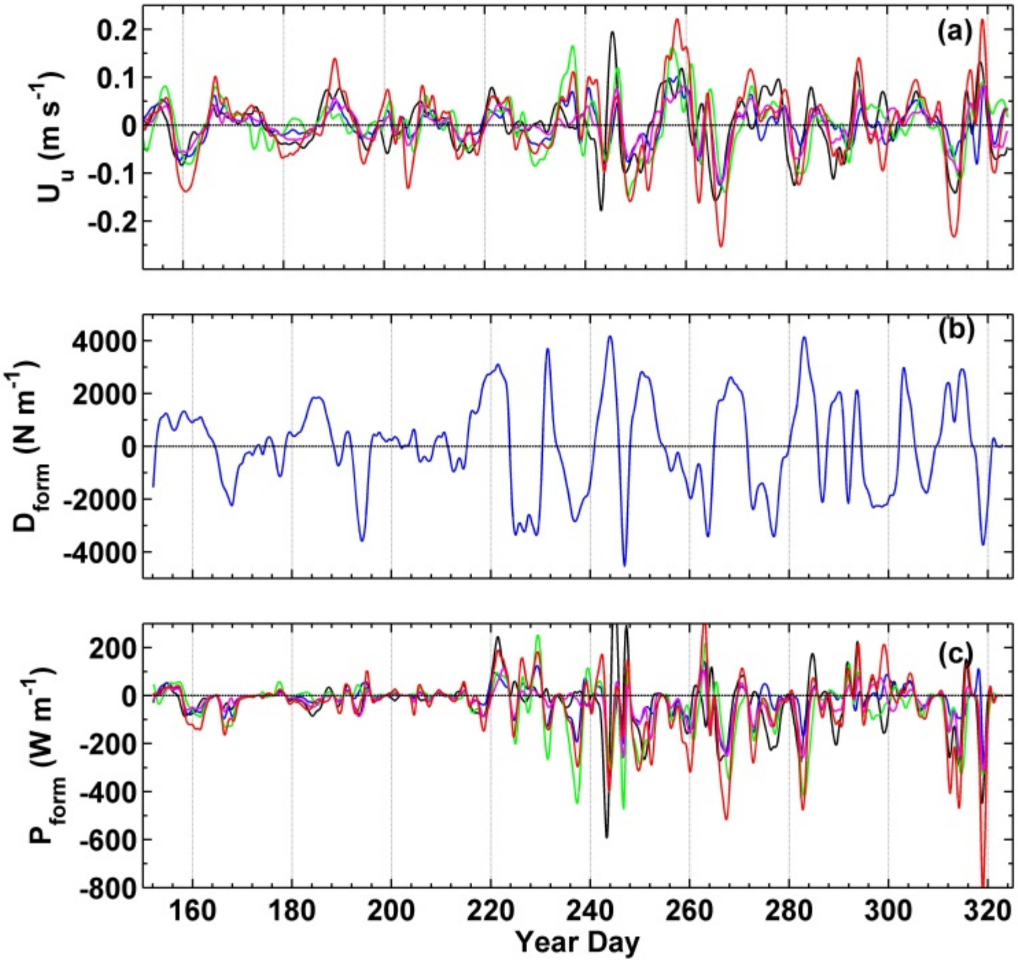

Fig. 11. Time series of (a) Upper 50-m layer velocity U_U at M1-M5, (b) D_{form} for sub-tidal band, and (c) Power (P_{form}) at M1-M5.

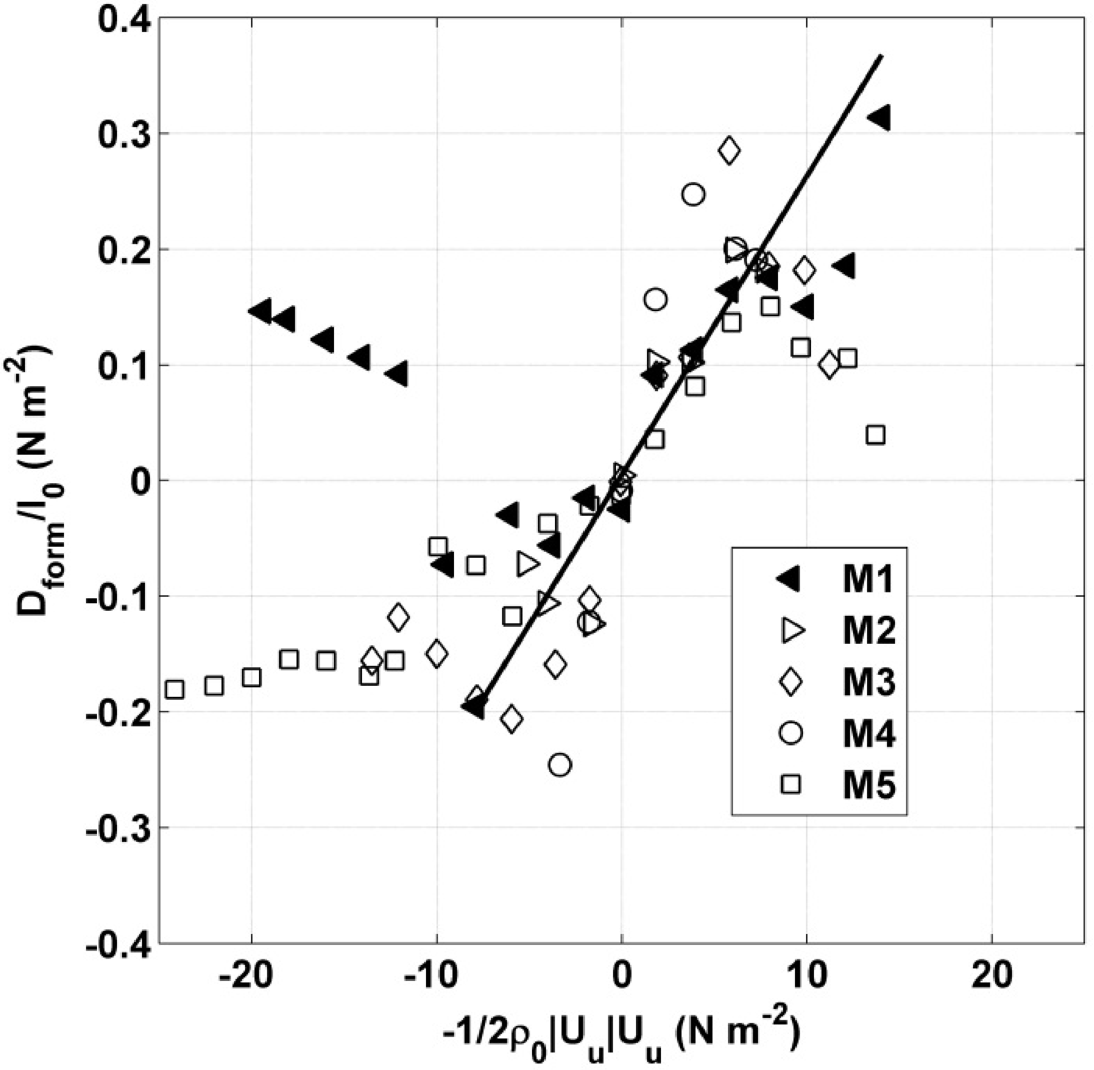

Fig. 12. Form drag per unit area D_{form}/l_0 plotted against F_D (= $-1/2\rho_0|U_U|U_U$) for velocities at M1–M5 . The thick solid line denotes least square fit for $F_D \geq -10$-. The slope of the line represents the bulk drag coefficient (4) and is about 26x10^{-3}.

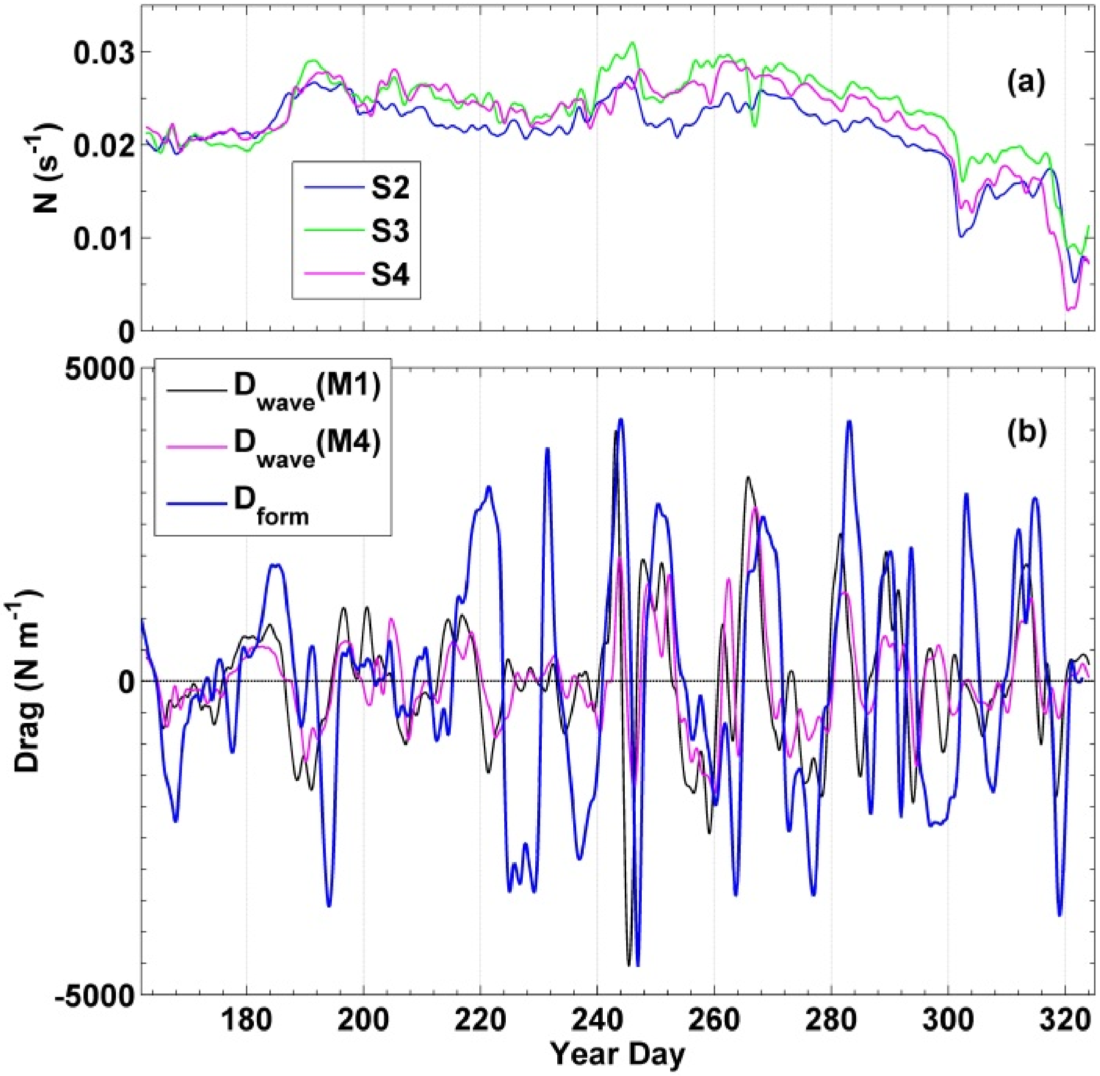

Fig. 13. (a) Buoyancy frequency (*N*) at S2, S3, and S4 mooring locations. (b) Observed form drag (D_{form}) for sub-tidal motions (blue line) and the estimated wave drag from linear theory (16) at M1 (black) and M4 (magenta).

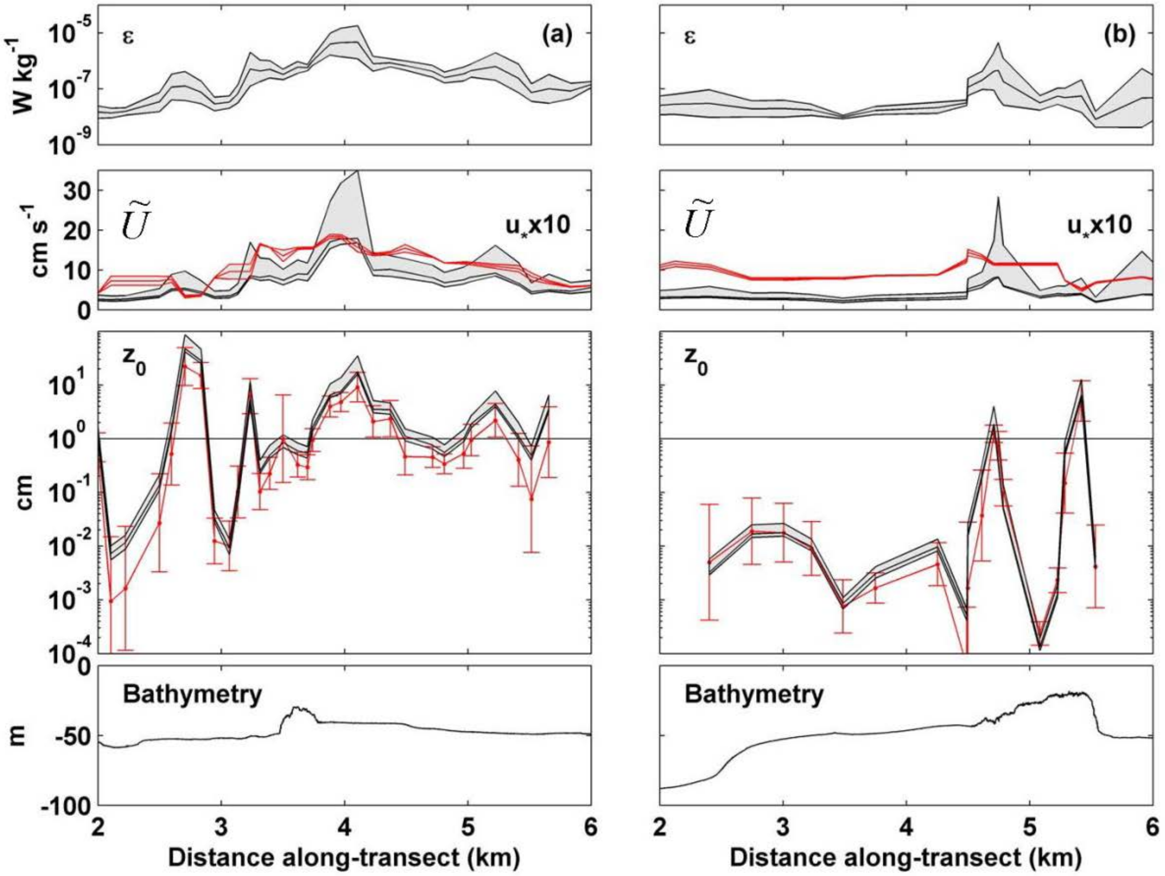

Fig. 14. Near-bottom TKE dissipation rate (ε), near-bottom velocity ($\tilde{U}$), friction velocity (u_*) multiplied by 10, roughness length (z_0), and bathymetry at transects T1 (a: left panels) and T2 (b: right panels). The shaded regions in the first three panels are the 95th percentile errors for each parameter. For z_0 both the value calculated using only the near-bottom velocity (black line) and the mean and standard deviation of the three z_0 values obtained using $\tilde{U}_1$, $\tilde{U}_2$, and $\tilde{U}_3$ (red line with error bars) are shown. The horizontal line is at 1 cm, the lowest reported value for coral roughness in prior studies (Rosman and Hench 2011).

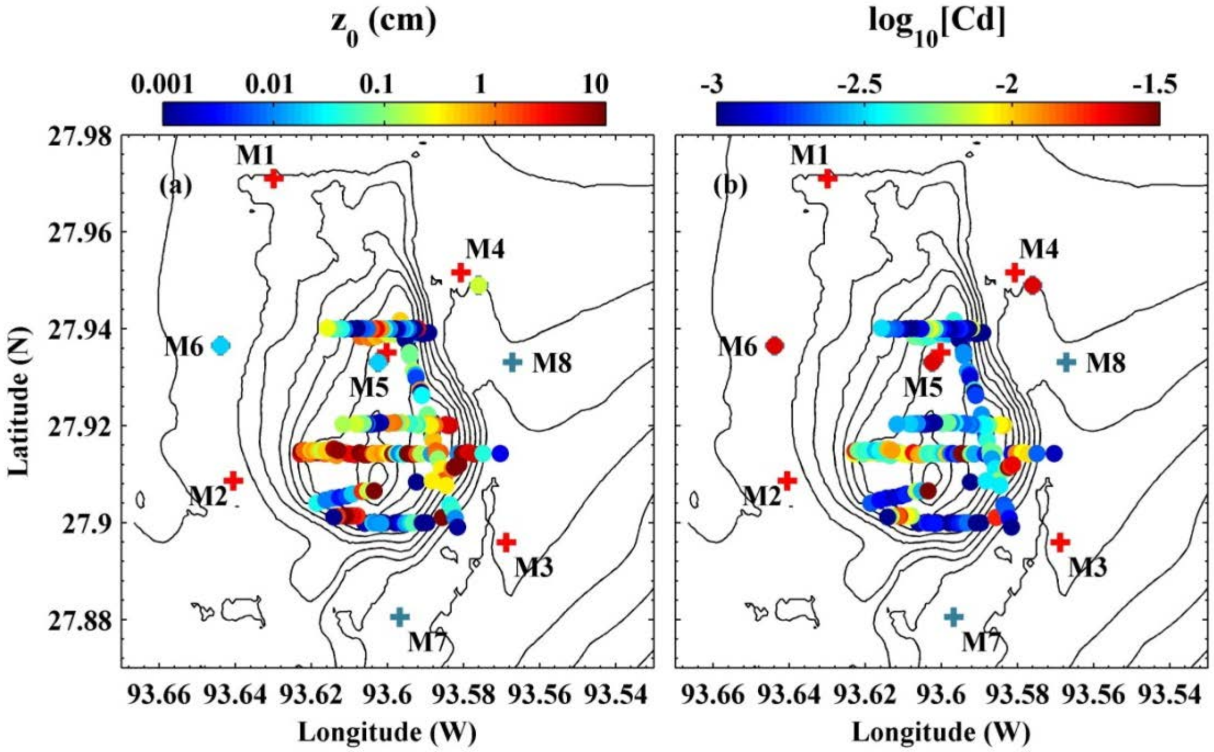

Fig. 15. All values of z_0 (cm) (a) and $\log_{10}$ values of bottom drag coefficient (C_d) (b) over the bank.

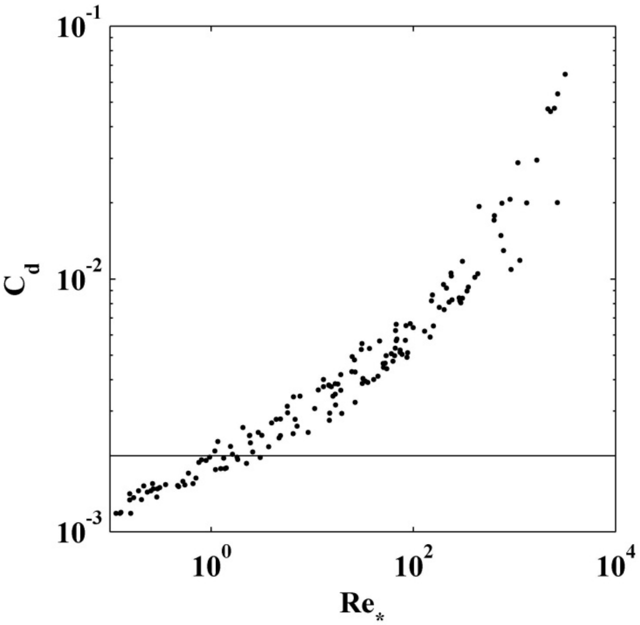

Fig. 16. C_d as a function of frictional Reynolds number (Re_*). The horizontal line is at 0.002, the approximate value of C_d at the mooring locations.

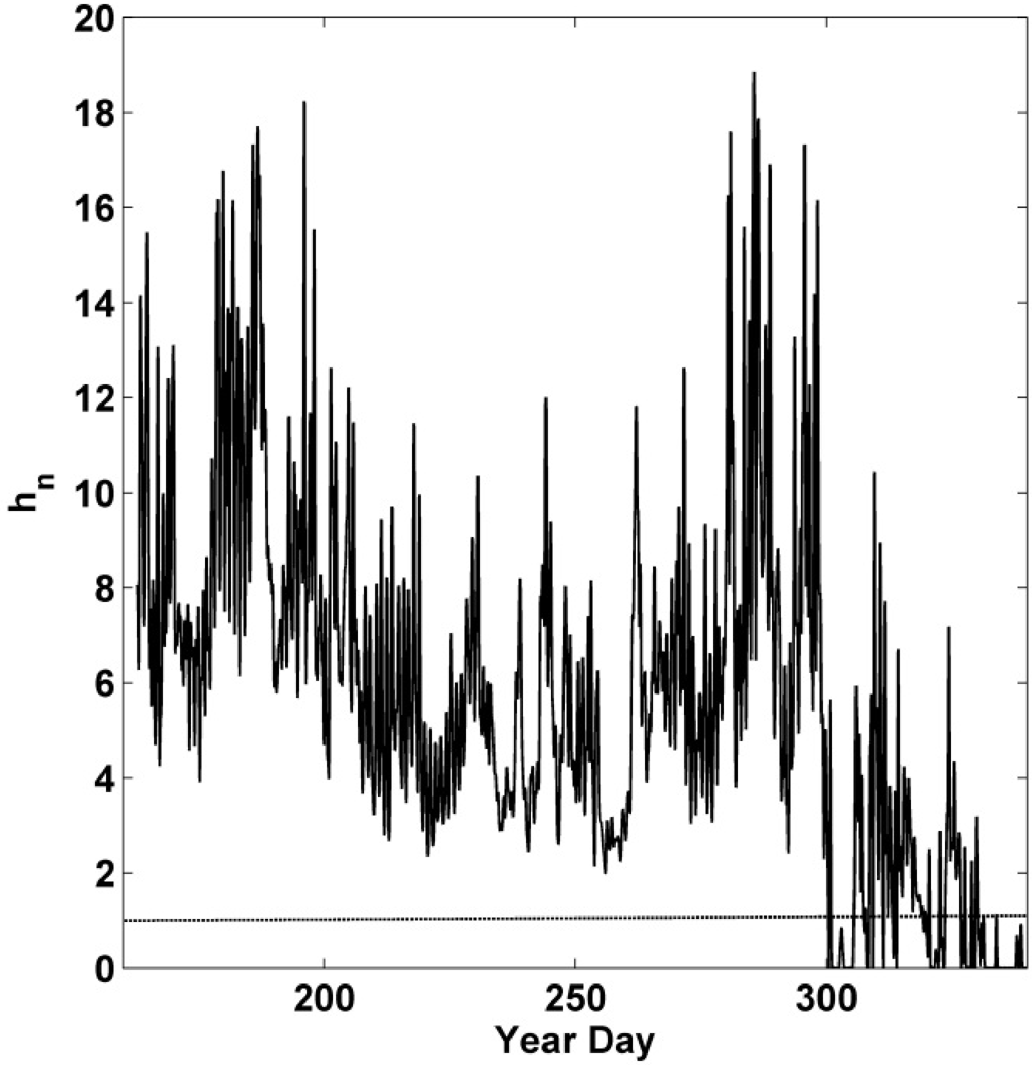

Fig. 17. Non-dimensional bank height, h_n at M1. Fluctuations less 10 hours were filtered out before plotting. The dashed line represents $h_n = 1$.

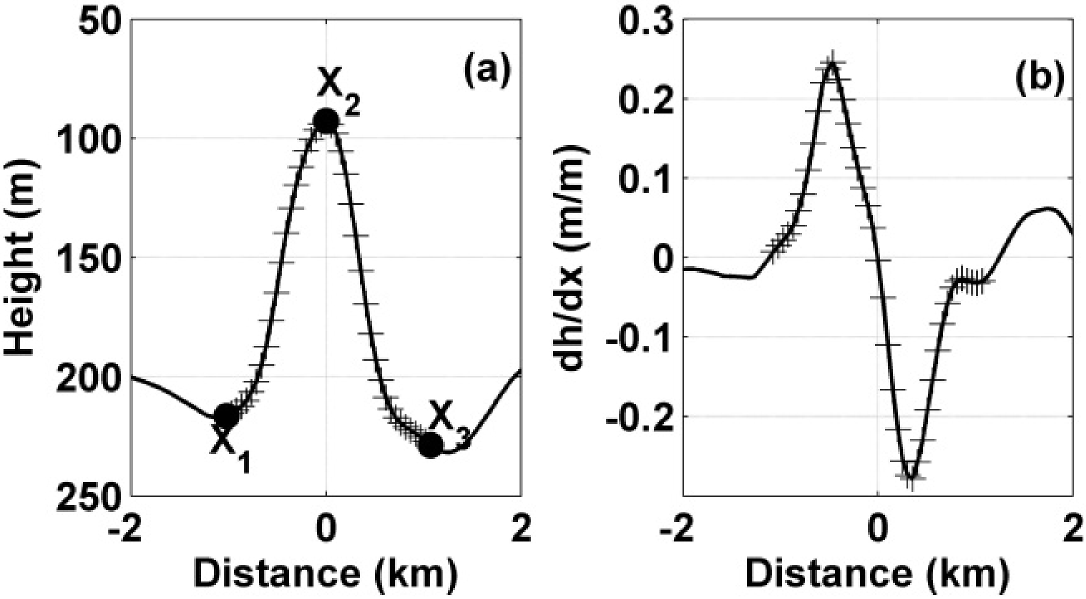

Fig. A1. (a) Cross section of the ridge transect based on the model bathymetry. Spatial resolution is 50.5 m. The crosses are the data points used in the analysis. The bullets represent locations of pressure time-series plotted in Fig. A2. (b) Horizontal gradient of ridge topography, dh/dx across the ridge (from Warner 2012).

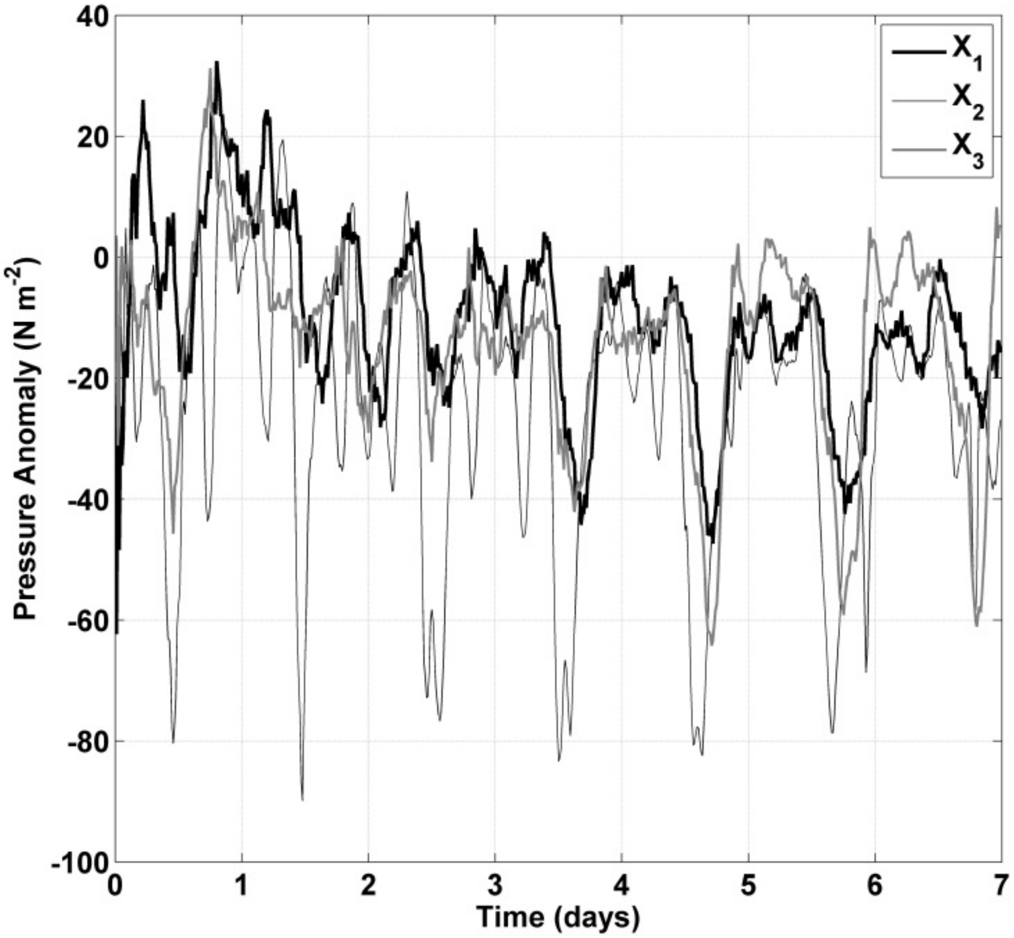

Fig. A2. Dynamic bottom pressure fluctuations at three different locations, X_1, X_2, and X_3. Locations of X_1, X_2, and X3 are marked in bullets in Fig. A1 (from Warner 2012).

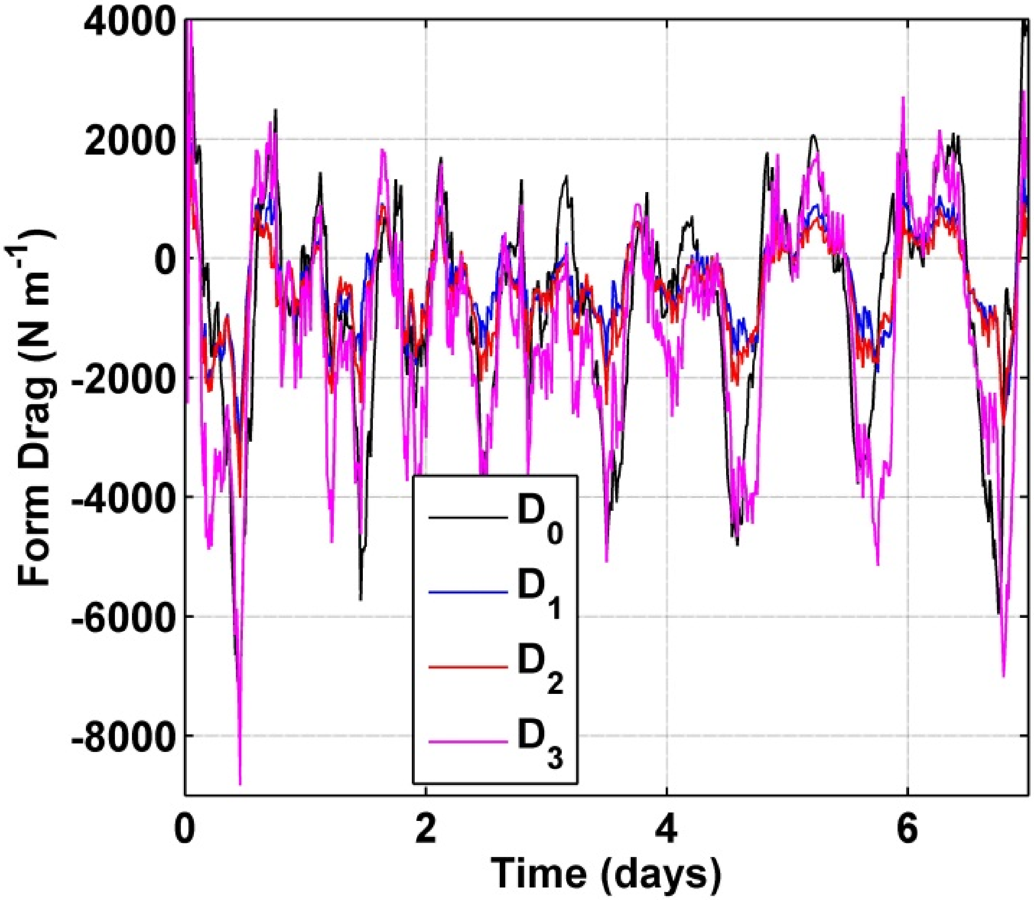

Fig. A3. Estimated pressure drag from four different methods: the complete integration, D_0 (A1), mean-pressure and mean-lateral gradient, D_1 (A2), linearly interpolated solution, D_2 (A3), and mean-pressure and maximum amplitude of lateral gradient, D_3 (A4).

APPENDIX D

Observations on Stratified Flow over a Bank at Low Froude Numbers

Observations on Stratified Flow over a Bank at Low Froude Numbers

Ewa Jarosz[1], Hemantha W. Wijesekera[1], William. Teague[1], Diane B. Fribance[2],
and Mark A. Moline[3]

[1]Naval Research Laboratory, Stennis Space Center, Mississippi, USA
[2]Coastal Carolina University, Conway, South Carolina, USA
[3]School of Marine Science and Policy, University of Delaware, Lewes, Delaware, USA

Journal Citation:
Jarosz, E., Wijesekera, H.W., Teague, W.J., D.B. Fribance, and Moline, M.A., 2014. Observations on stratified flow over a bank at low Froude numbers, Journal of Geophysical Research, submitted.

Abstract

In June 2011, a nine-day oceanographic survey was conducted over the East Flower Garden Bank, a coral reef located on the outer shelf in the northwestern Gulf of Mexico. Current, temperature, conductivity, and microstructure measurements were collected to characterize flow evolution, turbulence, and mixing over the bank. During the experiment, the flow was highly stratified, subcritical with the Froude number below 0.4, hydrostatic, and non-linear; rotational effects were not negligible. Observations showed that flow structure, turbulence, and mixing were highly dependent on the direction and strength of currents; thus, they varied spatially and temporarily. Responses resulting from interactions between the free-stream flow and the obstacle were significantly different on the upstream and downstream sides of the bank. Blocking and diverging of the flow just below the bank height was observed on the upstream side. On the downstream side, a wake with imbedded vortices developed. Moreover, turbulence was amplified over the bank top and on its downstream side. Turbulent dissipation rates were as high as 10^{-6} W kg^{-1} resulting in measured rates of energy dissipation and mixing by turbulence per unit width as high as 40 W m^{-1}. Mixing on the downstream side was also elevated; eddy diffusivities reached 10^{-3} m^2 s^{-1} well above a typical value of 10^{-5} m^2 s^{-1} commonly found in the ocean thermocline and over shelves with flat topography. On the upstream side, estimated eddy diffusivities were close to that for the ocean thermocline, i.e., they were generally less than $0.5 \cdot 10^{-4}$ m^2 s^{-1}.

1. Introduction

Substantial research efforts in past decades have been devoted to studying flows over rough bottom topography in the ocean. They have led to the conclusion that mixing is much greater there than the mixing observed over the gradually varying seabed or in the thermocline in the open ocean (e.g., Gregg, 1987; Dewey and Crawford, 1988; Ledwell et al., 1993; Lueck and Mudge, 1997). Significant bathymetric features, such as sills, canyons, banks, seamounts, ridges, underwater volcanos, and mountain ranges, are ubiquitous in the ocean. They impact flow patterns locally and they may even influence large-scale circulation (e.g., Kunze and Toole, 1997; Polzin et al., 1997; Nash and Moum, 2001; Rudnick et al., 2003; McCabe et al., 2006).

On continental shelves, small banks are fairly common features. Their spatial dimensions can vary greatly from a few hundred meters to several kilometers; however, they are often too small to be included in numerical modeling efforts developed for the coastal waters. As a result, flow stratification, mixing, and biochemical processes are not very well resolved by numerical simulations near such bathymetric structures. In situ observations have shown (e.g., Loder et al., 1992; Moum and Nash, 2000; Nash and Moum, 2001; Dewey et al., 2005) that underwater banks are able to significantly alter ambient flow, considerably increase density gradients, modify vertical current shear, and enhance turbulence. Stratified flow approaching an obstacle often accelerates and, to conserve momentum, mechanical energy is released that can be dissipated locally or radiated away through internal waves. As a result, lee waves, hydraulic jumps, and eddies are very common features near banks. Amplified turbulence over a bank usually accounts for a large fraction of the entire shelf mixing, exerts a larger bottom stress, and dissipates a significant amount of energy in a shelf region.

Stratified flows over an obstacle are often categorized as subcritical, critical, and supercritical in terms of a Froude number that is usually defined as a ratio of the flow speed to the buoyancy frequency and the total depth. Evolution of flows and their major features vary dramatically as a function of the Froude number. Past observational and modeling efforts in the ocean have often been focused on studying energetic flows with Froude numbers approaching or larger than 1, i.e., critical and supercritical flows going over rough topography with energy being released through, for instance, a hydraulic jump (e.g., Wesson and Gregg, 1994; Farmer and Armi, 1999; Hogg et al., 2001; Moum and Nash, 2000). Much of our understanding of flow dynamics for very low Froude numbers (much less than 1) comes from the atmospheric research done for subcritical air flows over a mountain (e.g. Hunt and Snyder, 1980; Smolarkiewicz and Rotunno, 1989; Smith and Grønås, 1993; Vosper et al., 1999; Dalziel et al., 2011). These air flows are usually characterized by blocking, splitting, and moving around on the upstream side of the obstacle. On its downstream side, a wake develops where enhanced turbulence and eddy shedding are commonly observed.

In this paper, recent current and hydrographic observations are analyzed to describe the evolution and main features of the subcritical highly-stratified flow over an isolated bank located on the outer northwestern Louisiana-Texas shelf in the Gulf of Mexico. Moreover, collected microstructure measurements allow an assessment of turbulence and mixing in this region.

The paper is organized as follows. In section 2, the bank, field experiment, and observations are described. Background meteorological and oceanographic conditions are discussed in section 3. Snapshots of flow patterns and stratification are presented in section 4. Turbulence and mixing conditions over the bank are characterized in section 5. In section 6, a discussion of the results in terms of non-dimensional parameters is presented. Finally, findings are summarized in section 7.

2. East Flower Garden Bank Experiment

The field experiment was a part of the MORT ("Mixing over Rough Topography") and COB ("Currents over Bank") projects funded by the Naval Research Laboratory (NRL) and the Bureau of Ocean Energy Management (BOEM), respectively. It took place from 31 May to 13 June 2013 over and around the East Flower Garden Bank (EFGB). The EFGB is located on the shelf edge in the northwestern Gulf of Mexico about 190 km southeast of Galveston, Texas (Figure 1). The bank is a thriving coral reef that is a part of the Flower Garden Banks National Marine Sanctuary managed by NOAA, and it is one of many banks formed by salt domes on the Louisiana-Texas shelf. The EFGB is asymmetric with rather steep slopes on its southern and eastern sides. It is about 10 km long and 6 km wide with major and minor axes approximately aligned in north-south and east-west directions, respectively. The bank top rises from water depths of 100 m–130 m to about 18 m below the sea surface. An ocean bottom area covered by the bank (within a 100-m isobath) is about 40.76 km^2.

Two research vessels, R/V *Pelican* and R/V *Manta*, occupied waters over the bank to measure currents, hydrography, and strength of mixing. Almost all data collected by instruments deployed from or towed by the ships were taken between 4 June and 12 June 2011. Both vessels were equipped with 300 kHz acoustic Doppler current profilers (ADCPs) to collect current velocity profiles with vertical resolution of 4 m. Velocity observations were processed using the University of Hawaii's CODAS system (Firing et al., 1995) to correct for ship motion and averaged over four minutes intervals. A towed undulating vehicle, ScanFish MK II, manufactured by EIVA of Denmark and equipped with a Sea-Bird Electronics SBE 49 FastCAT was used to sample hydrography from the R/V *Pelican*. Conductivity, temperature, and microstructure observations were collected with a Vertical Microstructure Profiler (VMP; the profiler was manufactured by Rockland Oceanographic Services Inc. and is similar to a profiler described by Wolk et al., (2002)) from the R/V *Manta*. The VMP profiler carried a thermistor (FP07), a micro-conductivity sensor (Sea-Bird Electronics SBE7-38), two velocity shear probes, a high-resolution pressure sensor, accelerometers, and fine-scale external conductivity (Sea-Bird Electronics SBE4) and temperature (Sea-Bird Electronics SBE3) sensors. VMP profiles extended from a few meters below the surface to near the bottom. Moreover, turbulent kinetic energy (TKE) dissipation rates (ε) were estimated from current velocity shear observations following a formula for isotropic turbulence (Oakey, 1982): $\varepsilon = \frac{15}{2}\nu\overline{\left(\frac{\partial u'}{\partial z}\right)^2}$, where ν is the kinematic viscosity, and $\overline{\left(\frac{\partial u'}{\partial z}\right)^2}$ is the variance of the current shear. The velocity shear variance was calculated by integrating the spectrum for the wave number range from 2 cpm to 30 cpm (cycles per meter), while the spectrum was estimated in bins of 1024 shear data records, with a 512-record overlap. Selected ScanFish sections and locations of VMP drops are displayed in Figure 1.

Additionally, two dye releases were conducted from the R/V *Pelican* to visualize flow patterns over and around the EFGB. The first release was on the western side of the bank around 21:00 UTC on 6 June 2011. The dye was released near the top of the thermocline (~ 30 m). The second dye patch was also released near the depth of ~ 30 m but on the eastern side of the bank at about 15:00 UTC on 9 June 2011. The dye used in the experiment was the water soluble fluorescein dye (Keyacid Uranine K Liquid) referred as Uranine. The density of the liquid Uranine (40% concentrate) was 1111 kg m^{-3}. To obtain a target density close to 1023.79 (±0.01) kg $m^{-3,}$ the dye concentration was reduced to 12% by adding 175 gallons of fresh water and 12 gallons of isopropyl alcohol. The dye was released into the sea through a diffuser (of about 1 meter length) attached to the end of a hose. The dye volume of ~270 gal was pumped at 10 gal min^{-1} while the R/V *Pelican* steamed at a speed of about 1 m s^{-1} in the north-south direction. The depressor undulated approximately ±2 m from the 30 m depth. We planned for a dye patch of 1 m wide, 2 m high and 1.1 km long with the initial dye concentration of 14 mg l^{-1} (or 14 ppm). The dye was sampled by fluorometers attached to the ScanFish and a REMUS Autonomous Underwater Vehicle (AUV) (e.g., Moline et al., 2005), and by a WETLabs ac-9 absorption and attenuation meter (a 490 nm absorption channel) installed on the ScanFish. Immediately after dye release, the Scanfish was deployed in a lawn mower pattern while undulating between 10 m and 40 m water depths to capture the dye distribution. Several hours later the REMUS AUV was deployed for a duration of 10 hours. The ScanFish fluorometer was calibrated to measure a maximum concentration up to 400 ppb with 0.05 ppb resolution so that it was initially out of scale since the dye concentration was greater than 400 ppb; hence, we used the observed linear correlation between the Uranine and chlorophyll to recapture the high values of the missing dye concentration.

Ten Barny (trawl-resistant pods) and six string moorings were in place around and on the EFGB during the field experiment (Figure 1). Five Barny (M1-M5) and four string (S1-S4) moorings were already deployed for the COB project and remained in the water for approximately one year (Teague et al., 2013). Another five Barny (M4a, M5a, M6, M7, and M8) and two string (S5 and S8) moorings were deployed just for two weeks specifically for the experiment as a part of the MORT project. All Barny moorings contained Teledyne RD Instruments workhorse acoustic Doppler current profilers and either wave-tide gauges (Sea-Bird Electronics SBE26) or high-resolution pressure sensors called Ppods (Moum and Nash, 2008). String moorings were equipped only with temperature/conductivity/pressure (TCP) sensors, except for S8 which also had a downward-looking ADCP. The number of TCP sensors on the string moorings varied between 5 and 12, and they were either Sea-Bird Electronics MicroCAT (SBE37) or In Situ Aqua Troll instruments. Detailed information such as deployment times and depths, sampling rates, ADCP frequency and bin depth resolutions for all moorings deployed for the COB program is in Teague et al. (2013). Similar details for the MORT moorings are given here in Table 1. ADCPs for the MORT project were 300 kHz Teledyne RDI units, except for moorings M5a and S8 which were furnished with 600 kHz Teledyne RDI current profilers.

3. Atmospheric and Oceanographic Settings

3.1. Atmospheric Conditions

Atmospheric pressure and winds from nearby NDBC buoy 42047 are shown in Figure 2. Atmospheric pressure (Figure 2a) began increasing on 31 May 2011and remained high with a maximum of 1022.5 hPa during the first part of the experiment. After 5 July 2011, it dropped below 1016 hPa. A few days before the experiment began the winds were fairly strong reaching 10 m s^{-1} (Figure 2b) and blew from the southern quadrant, i.e., from southeast, south, or southwest. Winds from the southern quadrant are very typical for summer months in the northwestern Gulf of Mexico (Gutierrez de Velasco and Winant, 1996). During the sampling period, winds weakened and dropped below 6 m s^{-1}. They also blew from variable directions until 8 July 2011. After that date they switched again to a summer pattern, i.e., to southeasterlies.

3.2. Oceanographic Conditions

Mean flow (frequency less than 0.6 cycles per day (cpd)) had two phases during the experiment (Figure 3). Until mid-day on 8 June 2011, mean currents were moderate (40 cm s^{-1} or less) and generally directed eastward. Afterwards, the mean currents weakened (30 cm s^{-1} or less) and reversed, flowing to the west. Note that mean flow was less impacted by the bank at the M1 mooring than at the M4 mooring. M4 was deployed closer to the EFGB and the currents just below the bank height were very weak, especially evident for the eastward flow phase (Figure 3). Higher frequency fluctuations including tides, inertial, and super-inertial oscillations are usually superimposed on the mean flow. Barotropic tidal currents are rather weak in the northwestern Gulf of Mexico (DiMarco and Reid, 1998). Teague et al. (2013) estimated amplitudes of major tidal constituents M_2, K_1, and O_1 from observations at the M1–M4 long-term moorings, and near the EFGB, tidal currents were between 3 cm s^{-1} and 5 cm s^{-1}. Near-inertial oscillations have a period of 25.58 h (close to the O_1 period), and they are generally more energetic than barotropic tides in the northwestern Gulf of Mexico (Chen et al., 1996). Near the EFGB, the inertial currents were about 15 cm s^{-1} or larger (Teague et al., 2013). During the experiment, measured currents comprised of the mean flow, tides, near-inertial currents, and higher frequency motions (frequency higher than 2.4 cpd) as displayed in Figure 4. Tidal currents showed a spring-neap cycle, and the inertial currents were likely produced by rotating winds at the beginning of June. In the upper 40 m, the currents were as high as 50 cm s^{-1} and 25 cm s^{-1}; 40-m depth/time averages were about 20 cm s^{-1} and 10 cm s^{-1} with standard errors of 1 cm s^{-1} and 0.5 cm s^{-1} for the eastward and westward mean flows, respectively. All velocity estimates were computed from current observations collected at M1, which seem to be the least impacted by a presence of the EFGB. Only 3.3 % of the EFGB area, located just in its southern part, rises above 40 m of the water depth so that the flow above 40 m should have been influenced the least by the bank. This assumption should be especially valid at the M1 mooring located approximately 7 km north of the highest part of the bank. Therefore, 40-m depth current velocity means calculated from M1 observations should be rather good estimates of the free-stream flow velocity and were used in further analyses and discussions.

Time series of temperature, salinity, and density from S8 are plotted in Figure 5. These observations encompassed almost the entire time period of the field experiment and showed that there was a very shallow mixed layer during this time as also indicated by Teague et al. (2013). Salinity at S8 varied little vertically with a range between 35.20 psu and 36.66 psu, while temperature showed more variability ranging from 18.10 ^{o}C near the bottom to 28.64 ^{o}C at about 6 m below the sea surface. Similar variability and ranges were found at the other TCP moorings. Such distributions of temperature and salinity around the bank generated a mean density that nearly linearly increased with depth as indicated in Figure 6a. Displayed mean densities were calculated from available TCP temperatures and salinities that were averaged over time separately for each mean flow phase, i.e. between 00:00 UTC 4 June and 12:00 UTC 8 June 2011 for the mean eastward flow and between 12:00 UTC 8 June and 23:00 UTC 12 June 2011 for the mean westward flow. The density profiles also implied that there was almost no difference in the mean stratification between the mean eastward and westward flows over the EFGB. Moreover, the mean density was used to estimate an average buoyancy frequency (N, the squared buoyancy frequency is defined as: $N^2 = -(g/\rho_o)(d\rho/dz)$, where g is the gravitational acceleration, ρ is the density, z is the depth in meters, and ρ_o is the reference density) shown in Figure 6b. The N profiles displayed some variations with depth and among TCP mooring locations, but very limited variability between the mean flow phases. The mean N values were generally less than 0.03 s^{-1} with the depth average of 0.018 s^{-1} and standard error of 0.001 s^{-1}. Equivalent values for the upper 40 m are 0.016 ± 0.001 s^{-1} and 0.018 ± 0.002 s^{-1} for the eastward and westward mean flows, respectively. These two 40-m N means were used in further analyses as representative numbers of the ambient stratification.

4. Flow Patterns and Stratification over the East Flower Garden Bank

Figures 7 and 8 show current observations from three transects (PT4, PT5, and T3) recorded by shipboard ADCPs between 12:15 UTC on 6 June and 2:30 UTC on 7 June 2011. Figure 8 also displays hourly current data at four depths from all moorings as well as means estimated from those data averaged over the duration of the survey time period. Moreover, Figure 7 shows density along the three transects. During these passes, the mean flow was eastward. The currents were generally directed towards the east above the bank height on both upstream and downstream (lee) EFGB sides (Figures 7 and 8a). Below the crest on the upstream side, the flow decelerated and diverged horizontally around the bank as indicated by current data shown in Figures 8b, 8c, and 8d. The flow was more complex on the downstream side of the bank. The north/south velocity structure for the PT4 and PT5 sections suggested a presence of a vortex on the lee side of the bank (Figures 7b and 7d). They also indicated that this vortex with speeds as high as 20 cm s^{-1} was cyclonic with a horizontal scale of about 4 km and a finite thickness of about 20 m. Current data along PT4 and PT5 transects were taken within 6 h and they were the most applicable to be used for computing a vertical component of the relative vorticity ($\zeta = \frac{\partial v}{\partial x} - \frac{\partial u}{\partial y}$, where u and v are horizontal east/west and north/south velocity components, respectively). Figure 9c shows layer-averaged ζ ($H < 40$ m, $40 \text{ m} \leq H \leq 60$ m, and $H > 60$ m, where H is the total depth). The vorticity on the upstream side was negligible and generally close to the noise level of the computations. However, a layer of positive vorticity exceeding 10^{-4} s^{-1} was found at depths between 40 m and 60 m on the lee side of the EFGB, where ζ was about a factor of two larger than the planetary vorticity, $f = 6.84 \cdot 10^{-5}$ s^{-1}. The velocity field close to the bank was not well resolved by the shipboard ADCP measurements, and therefore, estimates of negative vorticity found close to the bank on its lee side were not very reliable. Positive temperature (T') and negative potential density (σ_θ') fluctuations (Figure 9a and 9b) estimated from observations collected along the PT4 transect dominated between 40 m and 60 m on the lee side of the bank. These fluctuations may have been partially related to lee-side vortex as well as to internal waves and/or mixing. Fluctuations of T' and σ_θ' at a given depth along PT4 were computed by subtracting transect-averaged means. Similar temperature and density variations on the lee side were observed along PT5 (data not shown). Typically sub-mesoscale cyclonic eddies are associated with negative temperature anomalies, contrary to the positive temperature variations observed here. At this time, we are not able to explain these sub-mesoscale T' and σ_θ' variations around the bank. Observations along the T3 transect indicated highly variable currents on the lee side suggesting a plausible eddy-like feature below 40 m (Figures 7e, 7f, and 8d). Furthermore, the current observations shown in Figure 7 seem to imply that there was weak flow towards the bank beneath the vortex.

The flow pattern on the upstream side and over the EFGB was also captured by a dye-release survey conducted just after sections shown in Figures 7a – 7d were finished. The dye-patch was released approximately at a depth of 30 m (roughly between 23.8 kg m^{-3} and 24.1 kg m^{-3} isopycnals). It was sampled by the ScanFish and the REMUS AUV between 6 and 7 June 2011 (Figure 10a). The dye patch spread vertically between 25 m and 45 m depths but it was generally trapped within original density surfaces indicating weak diapycnal mixing. Figure 10b shows a horizontal spreading of the dye with the currents. The currents shown in Figure 10b (black arrows) are averages of those measured between 25 m and 45 m by shipboard ADCPs and by moored ADCPs for the time period between 20:00 UTC on 6 June and 14:00 UTC on 7 June 2011. The dye concentration was normalized by dividing by 0.05 ppb, which was the resolution of the fluorometer. The current and the dye concentration structure implied flow divergence on the upstream side with a dye patch being advected by the currents around the bank.

Figures 11 and 12 illustrate current and hydrographic fields when the mean flow was westward. Figure 11 displays currents from the shipboard ADCP instruments and density from T8, T9, and T10 transects collected between 13:30 UTC on 11 June and 03:30 UTC on 12 June 2011; Figure 12 shows velocity vectors along the transects and from the moored ADCPs at four different depths. There were similarities in flow patterns between both mean flow phases. On the upstream side of the bank, the flow decelerated and diverged near the bank. Similar to the eastward flow, the westward flow tended to generate eddy-like features near mooring M2 on the lee side of the bank (Figures 11c, 11d, 12c, and 12d). The second dye release at a depth of 30 m occurred on 10 June 2011 on the eastern (upstream) side of the EFGB. The vertical spreading of the dye was almost negligible, and the patch was yet again simply advected by the currents over the bank just north of its highest part (Figure 13). The dye experiment showed that there was once more very little vertical mixing, at least along the ScanFish and REMUS tracks and at the depths of the dye release.

Figures 7 and 11 also display examples of potential density (σ_θ) along the transects, while the buoyancy frequency along T4 and T10 is shown in Figure 14. It is obvious from the displayed density and N distributions that waters in the EFGB region were very highly stratified. The upper 40 meters of the water column contained a number of well-defined density gradients where the buoyancy frequency was also high (N was often larger than 0.03 s^{-1}). Around depths of 3 m to 5 m below the sea surface, there was a first pycnocline (see, for instance, near surface density in Figure 7e) partially related to a daily temperature cycle, which is quite pronounced in the Gulf of Mexico (Stommel et al., 1969), and partly associated with lower salinity near the sea surface. The next distinct density gradient, as that displayed in Figure 11, appeared to be associated with salinity variability and was generally at depths between 10 m and 15 m depending on a location. The main pycnocline, strongly related to the temperature gradient, was found at depths between 35 m and 40 m. These data suggest that during the experiment there was no mixed layer of significant thickness over the EFGB. An identical assessment was almost true for the bottom boundary layer because the density and N distributions showed that waters were also stratified near the bottom. A thickness of this layer was estimated using potential density. Only waters with $\sigma_\theta > (\sigma_{max} - \Delta\sigma)$ were considered within the bottom boundary layer, where σ_{max} is the maximum potential density of each VMP profile and $\Delta\sigma = 0.01$ kg m^{-3}. Estimates of this thickness from density data, which extended nearly to the bottom, showed that the bottom boundary layer was less than 4 m thick for 75% of the VMP profiles. On average, this layer thickness was about 2.3 m (standard deviation = 1.5 m and median = 1.4 m) and 3.1 m (standard deviation = 1.8 m and median = 2.5 m) for the eastward and westward mean flow phases, respectively.

5. Turbulence and Mixing

Rough topography on continental shelves is usually characterized by enhanced turbulence and mixing. During the June experiment, flow conditions over the EFGB were weak to moderate and stratification was strong. At the same time, however, observed turbulence and mixing over the bank and on its lee side were elevated. Figures 15 and 16 display selected transects showing turbulent kinetic energy dissipation rates (ε) for the eastward and westward mean flows, respectively. The upstream side of the bank was better sampled during the eastward mean flow phase by the microstructure measurements (Figure 15). Except very near the sea surface or the bottom, ε was generally less than $5\cdot10^{-8}$ W kg^{-1} on the upstream side with depth-averaged means and medians of ε below 10^{-8} W kg^{-1} for each profile. Away from the sea surface and bottom, spatial structures of the dissipations rates also indicate that turbulence was rather intermittent in the water column over the bank and on its downstream side. Some of those turbulent patches on the lee side may have been associated with possible vortices as, for instance, the patches found between depths of 40 m and 80 m starting at about 3 km on the lee side of T3 transect where ε was as high as 10^{-6} W kg^{-1} (Figure 15b). High values of ε, which easily reached 10^{-6} W kg^{-1}, were also found near the bottom of the EFGB as well as near the sea surface (above 10 m; Figures 15 and 16). Near-surface turbulence seemed to be partially related to the daily temperature cycle since at that time winds were rather weak and surface waves were small and not breaking (surface wave significant heights were less than 0.5 m (Wijesekera et al., 2013)).

Measured rates of energy dissipation and mixing by turbulence per unit width over the bank and on its downstream side were calculated from $\frac{dE}{dt} = \iint \rho(\varepsilon + J_b)dzdx$, where J_b is the irreversible buoyancy flux that is often approximated by $\Gamma\varepsilon$ (Γ is the mixing efficiency and it is often assumed to be 0.2 (Osborn, 1980)). They varied highly among transects. Integrations were done vertically between the first and last depth where energy dissipation rates were available and then horizontally between the foot of the bank on the upstream side to the last available VMP profile on the lee side of the EFGB. For those taken during the mean eastward flow and shown in Figure 15, they were 28.1 W m^{-1}, 28.5 W m^{-1}, and 6.5 W m^{-1} for T2, T3, and T4, respectively. Estimates for the T8, T9, and T10 transects displayed in Figure 16 were correspondingly 13.2 W

m^{-1}, 40.0 W m^{-1}, and 23.8 W m^{-1}. They also varied temporarily at the same location and for the same mean flow conditions. For instance, for the most northward transect (indicated as T10 in Figure 16), they were 23.8 W m^{-1} and 9.7 W m^{-1} as estimated from observations taken about 10 hours apart on 12 June 2011.

Following Osborn (1980), the eddy diffusivity (K_ρ) was estimated from $K_\rho = \Gamma\varepsilon N^{-2}$. It has been suggested that the mixing efficiency, Γ, may not be completely constant particularly when stratification is weak (Shih et al., 2005; Ivey et al., 2008). For eddy diffusivity estimates discussed here, $\Gamma = 0.2$ was used as presented in the vast majority of oceanographic mixing literature (see, for example, Osborn, 1980; Oakey, 1982; Moum, 1996; Nash and Moum, 2001). Gregg et al. (2012) also provide an extensive discussion and justification for this choice of Γ. Additionally, the eddy diffusivity was estimated only for $N^2 > 10^{-6}$ s^{-2} to avoid a bias towards large values of K_ρ at depths where stratification was very weak. Estimates of K_ρ spanned from $2.2 \cdot 10^{-7}$ m^2 s^{-1} to $1.1 \cdot 10^{-2}$ m^2 s^{-1} and they varied horizontally and vertically. The horizontal variations of the eddy diffusivity along with means and medians for individual profiles are shown in Figure 17 for the T3 and T9 transects. Upstream of the EFGB, the mixing was rather subdued with K_ρ generally less than $5 \cdot 10^{-5}$ m^2 s^{-1}. Such low values of the eddy diffusivity are representative for mixing over slowly varying topography in the ocean and in the open ocean thermocline. Higher K_ρ (> 10^{-4} m^2 s^{-1}), thus more vigorous mixing, was found over and downstream of the bank. Over the EFGB, estimates of the eddy diffusivity were 10^{-3} m^2 s^{-1} or higher, and elevated mixing was often found near the bottom. On the lee side, similar high K_ρ values were found at depths where the velocity observations implied a presence of vortices. Spatial variability of mixing in the EFGB region was also reflected in results of the dye experiment. For both releases, the dye patches barely spread vertically implying weak vertical mixing as indicated by rather low estimates of the eddy diffusivity, especially on the upstream side of the EFGB. The dye patches were advected horizontally by the currents generally at depths where they were injected.

Despite spatial variations of the eddy diffusivity, turbulent mixing was still more effective and stronger over the EFGB when compared to that over the flat or slowly varying bottom of the continental shelf. One way to compare mixing proficiency is to evaluate total diapycnal buoyancy fluxes over the bank and shelf areas, i.e., J_bA_b and J_sA_s where J_b, J_s are the fluxes and A_b, A_s are the areas of the bank and shelf, respectively. The fluxes are defined as $J_b = K_{\rho b}N_b^2$ and $J_s = K_{\rho s}N_s^2$, where $K_{\rho b}$, $K_{\rho s}$ are eddy diffusivities and N_b^2, N_s^2 are squared buoyancy frequencies for the bank and the shelf respectively. Following Lueck and Mudge (1997), an area of the shelf, which is required to perform as efficient mixing as that over the EFGB, can be estimated by setting $J_bA_b = J_sA_s$. The area of the EFGB within a 100 m isobath is about 40.76 km^2. Taking a typical value of the eddy diffusivity for the shelf, $K_{\rho s} = 10^{-5}$ m^2 s^{-1}, and those estimated for the EFGB, $K_{\rho b} = 10^{-4}$ m^2 s^{-1} – 10^{-3} m^2 s^{-1}, and assuming that $N_b^2 \sim N_s^2$, the shelf area has to be from 10 to 100 times larger than that of the bank, i.e., it should be between 407.6 km^2 and 4076 km^2.

The velocity and hydrographic observations taken by the shipboard ADCP and the VMP profiler were also used to calculate the Richardson number ($Ri = N^2 \left(\frac{dU}{dz}\right)^{-2}$, where $\frac{dU}{dz}$ is the horizontal current shear; estimates not shown) along transects shown in Figures 15 and 16. Values of Ri were rather underestimated due to coarse vertical resolution of the current velocity observations (4 m); thus, higher resolution current observations are required to obtain the more accurate spatial Ri distribution and to fully understand mixing over the EFGB. Additionally, the Richardson number was estimated only for the squared current shear and N^2 larger than 10^{-6} s^{-2} to avoid a bias towards very small values of Ri at depths where the current shear was low or/and stratification was weak. The distribution of Ri does not indicate that mixing in the EFGB region was mainly related to shear instabilities, i.e., the Richardson number was rarely found to be 0.25 or less. Ri was generally above 1 on the upstream side. The smaller values of the Richardson number at some depths, even as low as 0.25 or less, were mostly found on the downstream side and over the crest of the bank.

6. Discussion

Flows over obstacles are often described in terms of dimensionless parameters. Among those parameters, more common ones are: the Froude number ($F_o = \pi U/NH$), a quantity often referred to as the topographic Froude number ($F_h = U/Nh$), the Rossby number ($Ro = U/fL$), the non-dimensional obstacle width ($l_n = Nl/U$) and height ($h_n = h/H$) where h is the obstacle height, l is the half of the obstacle width (L), H is the finite upstream depth, U is the upstream flow speed, and f is the Coriolis parameter (see, for example, Hunt and Snyder, 1980; Baines, 1995, Vosper et al., 1999). Moreover, a ratio (a_n) of the flow depth (H = 100 m) to the obstacle width (L = 6000 m) is a good measure whether the flow is hydrostatic. If a_n is much less than one, i.e., for an obstacle with a long horizontal scale, the flow is assumed to be hydrostatic, which is a good approximation for the EFGB for which this ratio is ~ 10^{-2}. The rotational effects were also important in this region since Ro was 0.33 (the Ro standard error = 0.06; $f = 6.84\text{x}10^{-5}$ s^{-1}).

The non-dimensional obstacle width, which is larger than 100 for the EFGB, determines if the flow produces dispersive, non-hydrostatic waves ($l_n < 10$) or hydrostatic waves confined mostly to the region near the obstacle ($l_n > 10$). This number indicates that the latter scenario was a possibility in the EFGB region, and the density structures (e.g., Figure 7) seem to indicate that waves-like features were generated over the bank top. Additionally, the non-dimensional height (h_n) of the EFGB varies but in not larger than 0.82 (a h maximum ~ 82 m) and for a major part of the bank, i.e., for 82 % of the EFGB area, h_n is below 0.5. h_n is not likely to be important unless it is very close to 1 when the free surface may interact with an obstacle and generated disturbances will be confined vertically. For the EFGB, that may be the case only in its very small southern part where the bank is over 80 m high. Previous research of the flow over a 3-dimensional obstacle also has shown that a response, especially on a lee side of the obstacle, strongly depends on its shape and asymmetry (e.g., Baines (1995)). The observations presented here implying that interactions between the free-stream flow and the asymmetric EFGB were very complex during the field experiment.

The Froude number is generally used to classify flows over topography. In ocean science, the classically defined Froude number, which is based on the first-mode internal wave speed (c_o) (e.g. $F_o = U/c_o = \pi U/NH$, where $c_o = NH/\pi$) is used for flow descriptions. Lawrence (1993) has distinguished four basic flow regimes: subcritical, crest-controlled, approach-controlled, and supercritical. The flow is referred to as subcritical if F_o is very low (« 1). Transitional crest-controlled and approach-controlled flows occur in intermediate F_o (~ 1), while supercritical flows are characterized by $F_o > 1$. During the period (4–12 June 2011) of the extensive sampling over the EFGB, hourly estimates of F_o were always below 0.51. For the eastward mean flow, its average values (averaged over a time used to collect observations along a transect) and their standard errors (in parentheses) were 0.38 (± 0.02), 0.32 (± 0.01), and 0.25 (± 0.01) for T2, T3, and T4, respectively. All F_o were below 0.20 for the westward mean flow, e.g., the transect means were 0.11 (± 0.01), 0.09 (± 0.01), and 0.17 (± 0.02) for T8, T9, and T10, respectively. H was taken as 100 m and estimated 40-m depth averages of N and U were used in the F_o calculations. These transect-averaged Froude numbers were much less than 1 undoubtedly indicating that the flow was subcritical during the experiment in the EFGB region.

Estimated mean topographic Froude numbers, which are commonly used in the atmospheric research to study air flows over mountainous terrains, were less than 0.25 for all transects regardless of the mean flow phase, and those small numbers clearly imply that the flow was also subcritical and highly non-linear. It has been shown that highly stratified flows with small F_o and F_h numbers are more complex with nonlinear effects being important when compared, for instance, to weakly stratified flows with Froude numbers larger than 1 (e.g. Hunt and Snyder, 1980; Smith, 1988). Moreover, these subcritical-highly stratified flows are blocked on the upstream side of the obstacle and tend to move around it (e.g. Brighton, 1978; Baines, 1979; Hunt and Snyder, 1980). This is the case here, i.e., even though the observations were spatially very coarse they still were able to capture the decelerated and diverged flow on the upstream side of the EFGB (Figures 7, 8, 11, and 12). Sheppard (1956) postulated that fluid parcels originated at depth levels above that of $h(1 - F_h)$ would pass over the top. Unfortunately, the observations did not resolve exact depth levels where a separation between fluid parcels going over and those flowing around occurred for the entire EFGB during the experiment; however, applying this approach to T3 and PT4 transects, only fluid at depths above $0.8h$ (~ 44 m) would pass over the bank, while fluid at and below that depth would move around the bank (the bank height (h) ~ 70 m). The current velocity observations from these two transects clearly show that the flow was over the bank approximately to 40 m below the sea surface, i.e., just above the depth estimated from Sheppard's criterion, whereas the flow decelerated and began moving along the bank below 40 m.

Previous laboratory and numerical studies ((e.g., Hunt and Snyder, 1980; Smolarkiewicz and Rotunno, 1989; Schär and Durran, 1997; Vosper et al., 1999)) also have shown that a wake filled with vortices develops on the lee side of an obstacle for subcritical flows. The lee wake is usually characterized by elevated turbulence levels and mixing when compared to those observed on the upstream side of the obstacle. The studies also indicate that vortex shedding occurs generally when F_h falls below 0.4 (Vosper et al., 1999), and that shed vortices are considered to be a means of dissipating flow energy. Our current velocity measurements and estimated relative vorticity seem to indicate that there was a cyclonic vortex on the lee side (the near M4 and M4a moorings; see Figure 1 for their locations) of the EFGB during the mean eastward flow. An eddy-like structure emerging from the current observations was less clear for the mean westward flow; however, the data seem to imply that a vortex may have been generated on the lee side of the bank near the M2 mooring (see Figure 1 for the mooring location). Our observations are not sufficient to speculate whether vortices observed during the subcritical flow conditions in the EFGB area were consistent features that were generated by the mean currents, or if they were periodic features forced by tidal/inertial flows, or if they resulted from a combination of both motions. Moreover, the collected microstructure data clearly show that turbulence and mixing, as expected, were enhanced on the downstream side when compared to those on the upstream side of the EFGB for both mean flow phases (Figures 15, 16, and 17). Enhanced turbulence was patchy and was partly related to vortices.

Furthermore, recent analyses of pressure distribution by Wijesekera et al. (2014; submitted to J. Phys. Oceanogr.) have shown that the highly stratified, non-linear, hydrostatic flow was able to generate high form drag over the EFGB. The form drag occurs when currents flow over rough topography creating a pressure difference between the upstream and downstream sides of an obstacle, i.e. a force that opposes the flow. This drag ranged from about 2000 N m^{-1} to 3000 N m^{-1} and shows multiple time-scale variability over the EFGB. Similarly, estimated average frictional drag over the bank was also quite high (~ 0.006). These findings are in agreement with those reported for other underwater banks (e.g., Moum and Nash, 2000).

7. Conclusions and Summary

Beginning on 4 June 2011, a nine-day extensive oceanographic survey was conducted over the East Flower Garden Bank, a coral reef, located in the northwestern Gulf of Mexico about 190 km southeast of Galveston, Texas. The EFGB is considered a rough topographic feature. It is about 6 km wide, 10 km long, and is located at the shelf edge in 100 m of water depth with a peak rising to about 18 m below the sea surface. The field experiment involved two research vessels, the R/V *Manta* and the R/V *Pelican*. Observations were collected by shipboard (ADCP), ship-towed (ScanFish), ship-deployed (VMP), autonomous (AUV), and moored (TCP string and ADCP moorings) instrumentation. These data were then used to characterize the flow variability, stratification, turbulence and mixing over the surveyed bank.

During the experiment, the mean currents over the EFGB switched from eastward to westward on 8 June 2011. The measured flow was a combination of the sub-tidal, inertial, tidal and higher frequency motions with a maximum speed of about 50 cm s^{-1}. The waters were highly stratified throughout the entire water column with the depth mean buoyancy frequency of 0.016 s^{-1} and 0.018 s^{-1} for the eastward and westward mean flow phases, respectively. As a result, the mixed surface and bottom boundary layers were generally less than 4 m thick. Consequently, the flow conditions over the EFGB were classified as subcritical when transects were sampled since all estimated Froude numbers (F_o) were less 0.4. Based on computed non-dimensional parameters (a_n, l_n, F_h, h_n, and Ro), flow dynamics over the bank were also hydrostatic and non-linear, and rotational effects were not negligible.

Observations clearly showed that flow structure and mixing were highly dependent on the direction and strength of the currents in the EFGB region; thus, they varied spatially and temporarily. As past observational, laboratory, and numerical efforts (e.g., Baines, 1979; Hunt and Snyder, 1980; Smolarkiewicz and Rotunno, 1989; Vosper, 2000; Nash and Moum, 2001; Skyllingstad and Wijesekera, 2004; Dewey et al., 2005) have also indicated, responses resulting from interactions between the free-stream flow and the bank were significantly different on the upstream and lee sides of the EFGB. For highly-stratified, subcritical flows over an obstacle, blocking and diverging of the flow is expected on its upstream side, and these flow features were observed on the upstream side of the EFGB for both mean eastward and westward current phases. On the downstream side of the bank, a wake developed as identified by past studies of flows with low Froude numbers. The currents observations and estimated relative vorticity also implied that eddies developed on the lee side of the bank. Furthermore, turbulence was amplified over the EFGB top and on its lee side. Estimated TKE dissipation rates from current shear observations were as high as 10^{-6} W kg^{-1} resulting in measured rates of energy dissipation and mixing by turbulence per unit width over the bank as high as 40 W m^{-1}. Even for such weak flow conditions, mixing on the downstream side was also enhanced by a few orders of magnitude above the typical shelf value of 10^{-5} m^2 s^{-1}, and the eddy diffusivity there was as high as 10^{-3} m^2 s^{-1}. On the upstream side, its estimated values were close to that for continental shelf with gradually varying bathymetry and it was generally less than $0.5 \cdot 10^{-4}$ m^2 s^{-1}.

Significantly stronger flows over the EFGB were recorded by the year-long moorings (M1–M5) (Teague et. al, 2013). Turbulence and mixing are expected to be more elevated during the more extreme but commonly observed currents in the EFGB region than turbulence and mixing observed during our nine-day intense oceanographic survey. Hence, the coral reefs can be probably considered as “hot spots” for mixing on the shelf in the northwestern Gulf of Mexico.

Acknowledgements

This work was sponsored by the Office of Naval Research in a NRL project referred to as “Mixing over Rough Topography (MORT)” and by BOEM in the project referred to as “Currents over Banks (COB)” through the Interagency Agreement No. M10PG00038. Support for Mark Moline was provided through the ONR grant N00014-13-1-0223. The measurements were made in cooperation with the Flower Garden Banks National Marine Sanctuary, administered by the National Oceanic and Atmospheric Administration (NOAA). Assistance provided by Alexis Lugo-Fernandez of BOEM, Emma Hickerson of NOAA, and the crews of the R/V *Pelican* and the R/V *Manta* during the experiment were very much appreciated.

References

Baines, P.G. (1979), Observations of Stratified Flow Past Three-Dimensional Barriers, *J. Geophys. Res., 84*, 7834-7838.

Baines, P.G. (1995), *Topographic Effects in Stratified Flows*, Cambridge University Press, Cambridge, United Kingdom.

Brighton, P.W.M. (1978), Strongly stratified flow past three-dimensional obstacles, *Q. J. R. Met. Soc., 104*, 289-307.

Chen, C., R.O Reid, W.D. Nowlin (1996), Near-inertial oscillations over the Texas-Louisiana shelf, *J. Geophys. Res., 101*, 3509-3524.

McCabe, R., P. MacCready, and G. Pawlak (2006), Form drag due to flow separation at a headland, *J. Phys. Oceanogr., 36*, 2136-2152.

Dalziel, S.B., M.D. Patterson, C.P. Caulfield, and S. Le Brun (2011), The structure of low-Froude-number lee waves over an isolated obstacle, *J. Fluid Mech., 689*, 3-31.

Dewey, R.K., and W.R. Crawford (1988), Bottom Stress Estimates from Vertical Dissipation Rate Profiles on the Continental Shelf, *J. Phys. Oceanogr., 18*, 1167-1177.

Dewey, R., D. Richmond, and C. Garrett (2005), Stratified Tidal Flow over a Bump, *J. Phys. Oceanogr., 35*, 1911-1927.

DiMarco, S.F., and R.O. Reid (1998), Characterization of the principle tidal current constituents on the Texas-Louisiana shelf, *J. Geophys. Res., 103*, 3093-3109.

Farmer, D.M., and L. Armi (1999), The generation and trapping of solitary waves over topography, *Science, 283*, 188-190.

Firing, E., J. Ranada, and P. Caldwell (1995), Processing ADCP data with the CODAS software system version 3.1, User's manual. (Manual and software available electronically at http://currents.soest.hawaii.edu/docs/doc/codas_doc/).

Gregg, M.C. (1987), Diapycnal Mixing in the Thermocline: A Review, *J. Geophys. Res., 92*, 5249-5286.

Gregg, M.C., M.H. Alford, H. Kontoyiannis, V. Zervakis, and D. Winkel (2012), Mixing over the steep side of the Cycladic Plateau in the Aegean Sea, *J. Mar. Syst., 89*, 30 – 47, doi:10.1016/j.jmarsys.2011.07.009.

Gutierrez de Velasco, G., and C.D. Winant (1996), Seasonal patterns of wind stress and wind stress curl over the Gulf of Mexico, *J. Geophys. Res., 101*, 18,127-18,140.

Hogg, A.M., G.N. Ivey, and K.B. Winters (2001), Hydraulics and mixing in controlled exchange flows, *J. Geophys. Res., 108*, 959-972.

Hunt, J.C.R., and W.H. Snyder (1980), Experiments on stably and neutrally stratified flow over a model three-dimensional hill. *J. Fluid Mech*., *96*, 671-704.

Ivey, G.N., K.B. Winters, and J.R. Koseff (2008), Density stratification, turbulence, but how much mixing?, *Ann. Rev. Fluid Mech., 40*, 169-184.

Kunze, E., and J.M. Toole (1997), Tidally Driven Vorticity, Diurnal Shear, and Turbulence atop Fieberling Seamount, *J. Phys. Oceanogr., 27*, 2663-2693.

Lawrence, G.A. (1993), The hydraulics of steady two-layer flow over a fixed obstacle, *J. Fluid Mech., 254*, 605-633.

Ledwell, J.R., A.J. Watson, and C.S. Law (1993), Evidence for slow mixing across the pycnocline from an open-ocean tracer-release experiment, *Nature, 364*, 701-703.

Loder, J.W., D. Brickman, and E.P.W. Horne (1992), Detailed structure of currents and hydrography on the northern side of Gorges Bank, *J. Geophys. Res., 97,* 14,331-14,351.

Lueck, R.G., and T.D. Mudge (1997), Topographically induced mixing around a shallow seamount, *Science, 276*, 1831-1833.

McCabe, R.M., P. MacCready, and G. Pawlak (2006), Form Drag to Flow Separation at a Headland, *J. Phys. Oceanogr., 36*, 2136-2152.

Moline, M.A., S.M. Blackwell, C. von Alt, B. Allen, T. Austin, J. Case, N. Forrester, R. Goldsborough, M. Purcell, and R. Stokey (2005), Remote Environmental Monitoring Units: An Autonomous Vehicle Characterizing Coastal Environments, *J. Atm. Oceanic Tech., 22*, 1797-1808.

Moum, J.N. (1996), Efficiency of nixing in the main thermocline, *J. Geophys. Res., 101,* 12,057-12,069.

Moum, J.N., and J.D. Nash (2000), Topographically Induced Drag and Mixing at a Small Bank on the Continental Shelf, *J. Phys. Oceanogr., 30*, 2049-2054.

Moum, J.N., and J.D. Nash (2008), Seafloor pressure measurements of nonlinear internal waves, *J. Phys. Oceanogr., 38*, 481-491.

Nash, J.D., and J.N. Moum (2001), Internal hydraulic flows on the continental shelf: high drag states over a small bank, *J. Geophys. Res., 106*, 4593-4611.

Oakey, N.S. (1982), Determination of the rate of dissipation of turbulent energy from simultaneous temperature and velocity shear microstructure measurements, *J. Phys. Oceanogr., 12*, 256-271.

Osborn, T.R. (1980), Estimates of the local rate of vertical diffusion from dissipation measurements, *J. Phys. Oceanogr., 10*, 83-89.

Polzin, K.L., J.M. Toole, J.R. Ledwell, and R.W. Schmitt (1997), Spatial Variability of Turbulent Mixing in the Abyssal Ocean, *Science, 279*, 93-96.

Rudnick, D.L., et al. (2003), From Tides to Mixing along the Hawaiian Ridge, *Science, 301*, 355-357.

Schär, C., and D.R. Durran (1997), Vortex Formation and Vortex Shedding in Continuously Stratified Flows past Isolated Topography, *J. Atmos. Sci., 54*, 534-554.

Sheppard, P.A. (1956), Airflow over mountains, *Q. J. R. Met. Soc., 75*, 528-529.

Shih, L.H., J.R. Koseff, G.N. Ivey, and J.H. Ferziger (2005), Parameterization of turbulent fluxes and scales using homogeneous sheared stably stratified turbulence simulations, *J. Fluid Mech., 525*, 193-214.

Skyllingstad, E.D, and H.W. Wijesekera (2004), Large-Eddy Simulation of Flow over Two-Dimensional Obstacles: High Drag States and Mixing, *J. Phys. Oceanogr., 34*, 94-112.

Smith, R.B. (1988), Linear theory of stratified flow past an isolated mountain in isosteric coordinates, *J. Atmos. Sci., 45*, 3889-3896.

Smith, R.B, and S. Grønås (1993), Stagnation points and bifurcation in 3-D mountain flow, *Tellus, 45A*, 28-43.

Smolarkiewicz, P.K., and R. Rotunno (1989), Low Froude Number Flow Past Three-Dimensional Obstacles. Part I: Baroclinically Generated Lee Vortices, *J. Atmos. Sci., 46*, 1154-1164.

Stommel, H., K. Saunders. W. Simmons, and J. Cooper (1969), Observations of the diurnal thermocline, *Deep-Sea Res., 16*, suppl., 269-284.

Teague W.J., H.W. Wijesekera, E. Jarosz, D.B. Fribance, A. Lugo-Fernández, and Z.R. Hallock, (2013), Current and hydrographic conditions at the East Flower Garden Bank in 2011, *Cont. Shelf Res., 63*, 43-58.

Vosper, S.B., I.P. Castro, W.H. Snyder, and S. D. Mobbs (1999), Experimental studies of strongly stratified flow past three-dimensional orography. *J. Fluid Mech., 390*, 223-249.

Vosper, S.B. (2000), Three-Dimensional Numerical Simulations of Strongly Stratified Flow past Conical Orography, *J. Atmos. Sci.*, *57*, 3716-3739.

Wesson, J. C., and M. C. Gregg (1994), Mixing at Camarinal Sill in the Strait of Gibraltar, J. Geophys. Res., 99, 9847–9878, doi:10.1029/94JC00256.

Wijesekera, H.W., D.W. Wang, W.J. Teague, E. Jarosz, W.E. Rogers, D.B. Fribance, and J.N. Moum (2013), Surafce Wave Effects on High-Frequency Currents over a Shelf Edge Bank, *J. Phys. Oceanogr.*, *43*, 1627-1647.

Wijesekera, H.W., E. Jarosz, W.J. Teague, D.W. Wang, D.B. Fribance, J.N. Moum, and S.J. Warner (2014), Measurements of Form and Frictional Drags over Rough Topographic Bank, submitted to *J. Phys. Oceanogr.*

Wolk, F, H. Yamazaki, L. Seuront, and R. G. Lueck (2002), A New Free-Fall Profiler for Measuring Biophysical Microstructure, *J. Atmos. Oceanic Technol*., *19*, 780-793.

Table 1. Mooring Summary.

Mooring	Latitude (N)	Longitude (W)	Water Depth (m)	Start Date End Date	Sampling Rate (s) /Bin Size (m)[a]	Depth Range or Instrument Depth (m)[b]
Barny Moorings						
M4a	27° 56.942’	93° 34.563’	106	06/02/2011 06/13/2011	60/2	10–102
M5a	27° 55.983’	93° 36.146’	46	06/01/2011 06/12/2011	60/1	3.7–44.7
M6	27° 56.187’	93° 38.633’	101	05/31/2011 06/12/2011	60/4	12–96
M7	27° 52.830’	93° 35.806’	120	05/31/2011 06/12/2011	120/4	8–112
M8	27° 55.983’	93° 34.025’	112	05/31/2011 06/13/2011	120/4	8–104
TCP Moorings						
S5:	27° 56.013’	93° 36.059’	47	06/03/2011 06/11/2011		
MC1[c]					30	5.6
MC2					30	17.3
MC3					30	26.0
MC4					30	36.3
MC5					30	45.86
S8:	27° 55.998’	93° 33.953’	112	06/03/2011 06/11/2011		
MC1					30	6.4
MC2					30	16.7
MC3					30	38.5
MC4					30	49.7
MC5					30	60.7
MC6					30	71.7
MC7					30	78.7
MC8					30	87.7
MC9					30	96.7
MC10					30	110.0
ADCP[d]					60/1	75.7 – 111.7 73.6[e]

[a] Sampling Rate (s) – sampling rates for all sensors used for the MORT project; Bin Size (m) – vertical resolution for ADCP instruments only.

[b] Depth Range – depth ranges over which ADCP data were collected at Barny moorings and the downward looking ADCP on S8; Instrument Depth – depths for MicroCATS.

[c] MC – Sea-Bird MicroCAT SBE37 instruments.

[d] ADCP – the downward-looking RDI 600 kHz ADCP on S8.

[e] A depth of the downward-looking ADCP on S8.

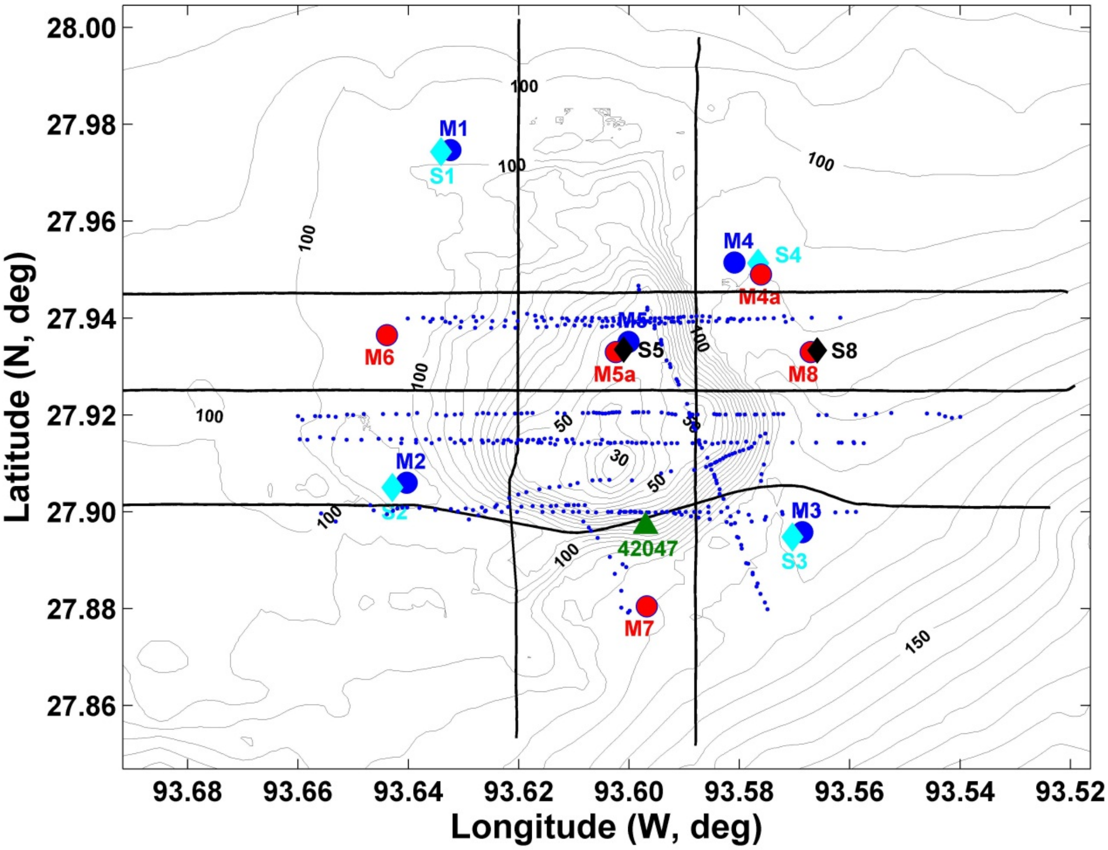

Figure 1. Map of the East Flower Garden Bank with depth contours (grey lines) every 5 m; also shown are locations of the long-term Barny (M1-M4; blue circles) and string (S1-S4; cyan diamonds) moorings~~-~~, short-term Barny (M4a, M5a, M6–M8; red circles) and string (S5 and S8; black diamonds) moorings, VMP drops (blue dots), selected ScanFish tows (black lines), and meteorological buoy 42047 (green triangle).

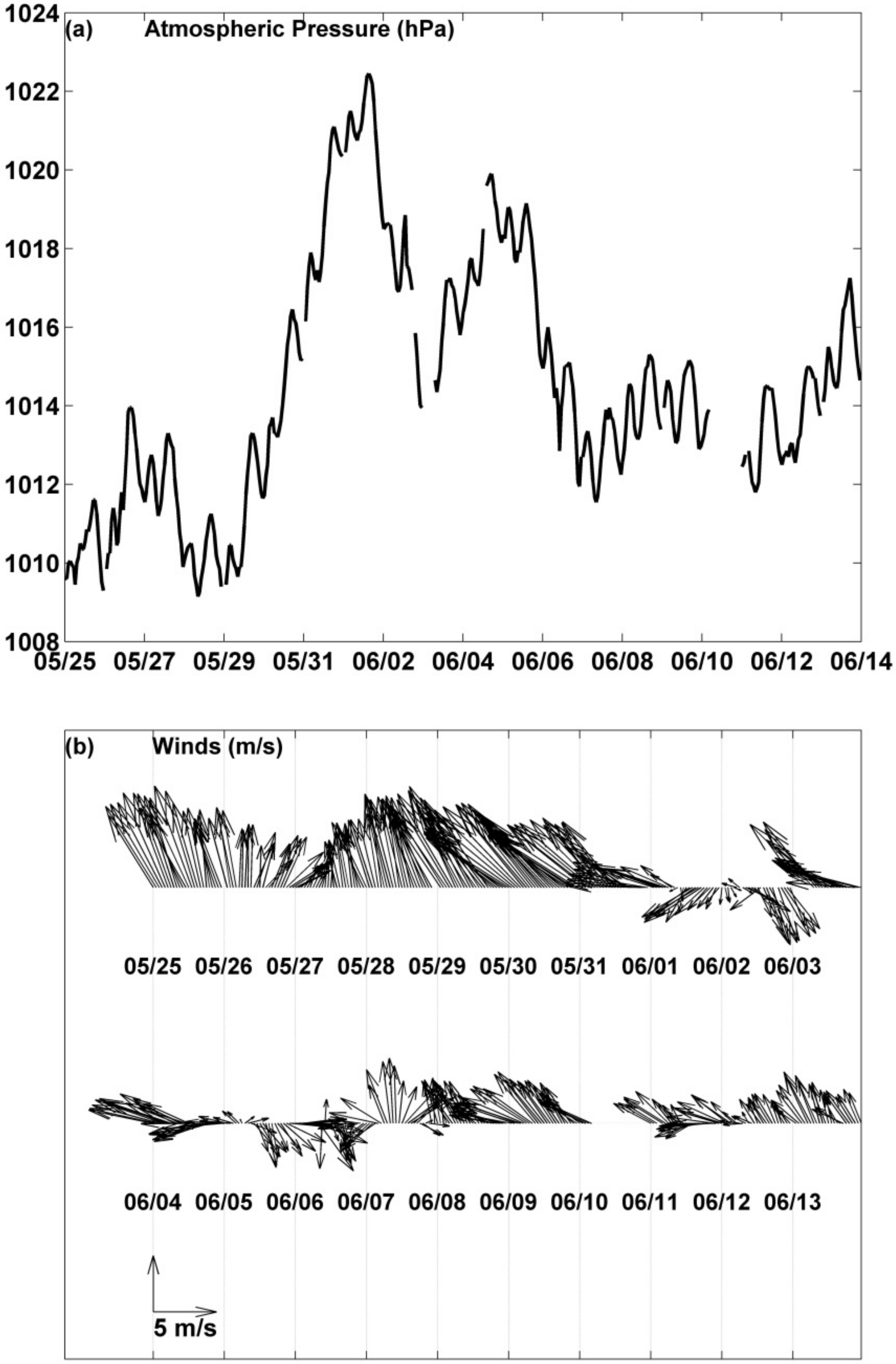

Figure 2. (a) Atmospheric pressure (hPa) and (b) winds (m s^{-1}) a few days before and during the field experiment.

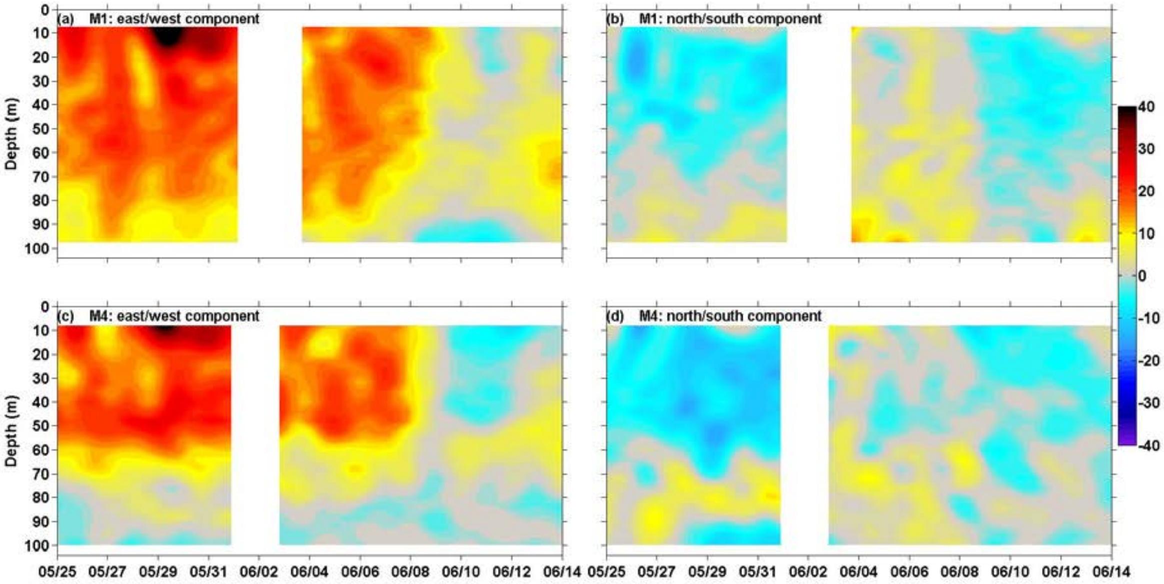

Figure 3. Mean flow at M1 (a, b) and M4 (c, d): east/west (a, c) and north/south (b, d) current components (cm s^{-1}); 40-hour low-passed data; positive values are towards east and north.

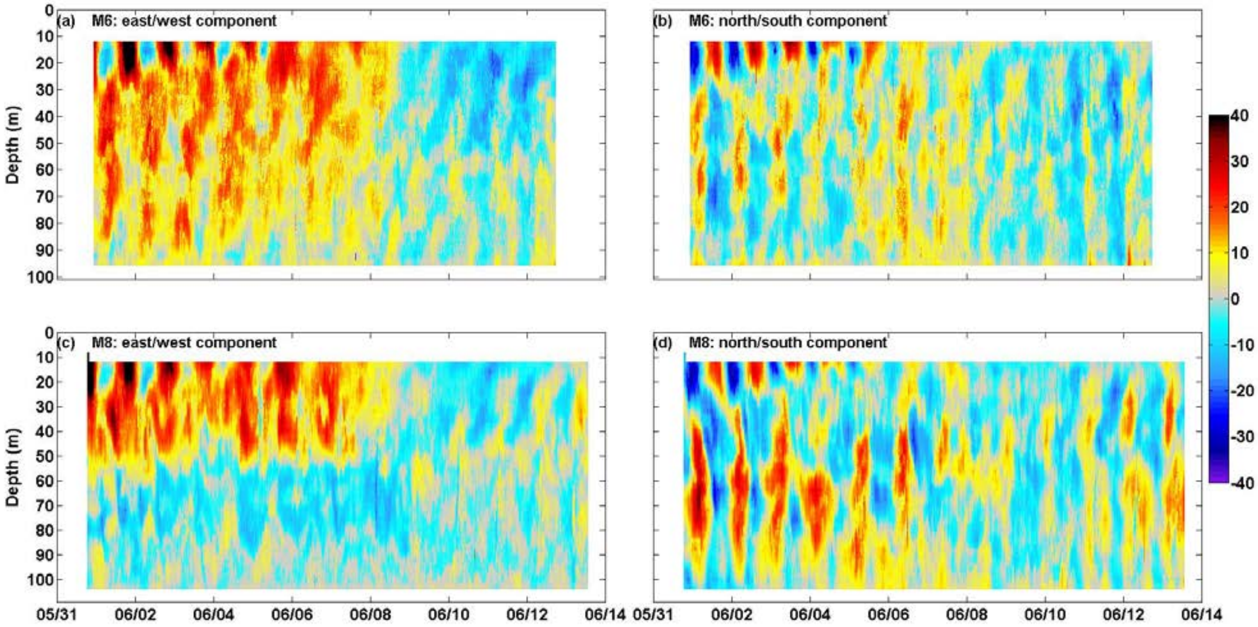

Figure 4. Current velocity components (cm s^{-1}): east/west at (a) M6 and (c) M8 and north/south at (b) M6 and (d) M8; positive values are towards east and north.

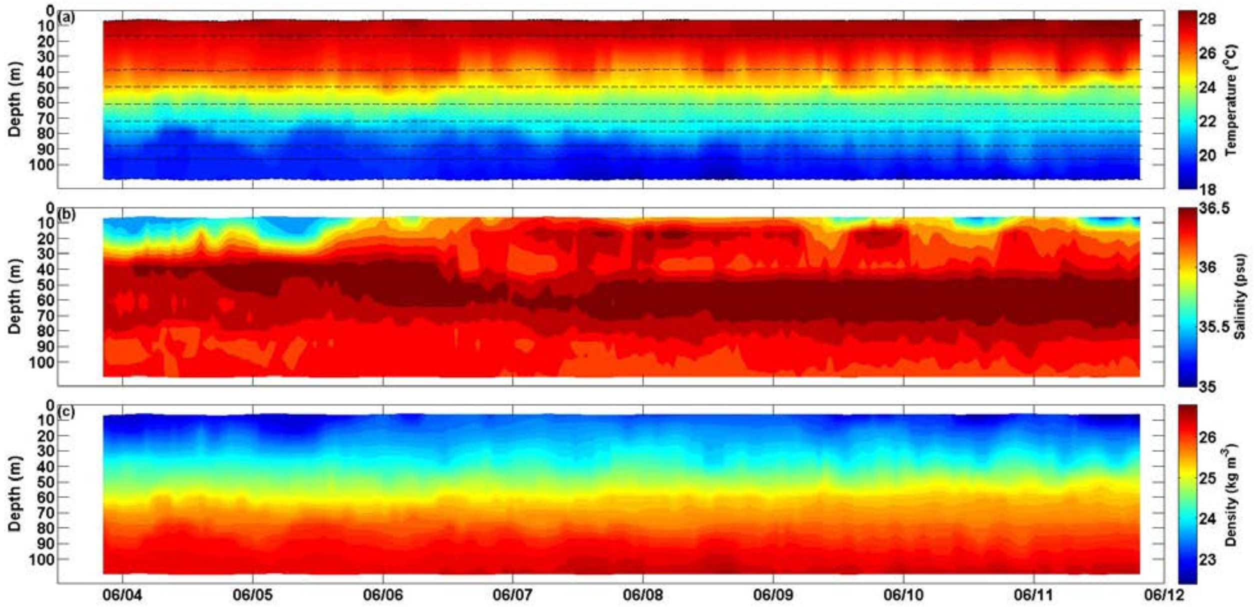

Figure 5. Time series of (a) temperature (^{o}C), (b) salinity (psu), and (c) density (kg m^{-3}) from the S8 mooring; black dashed lines in (a) indicate sensors depths.

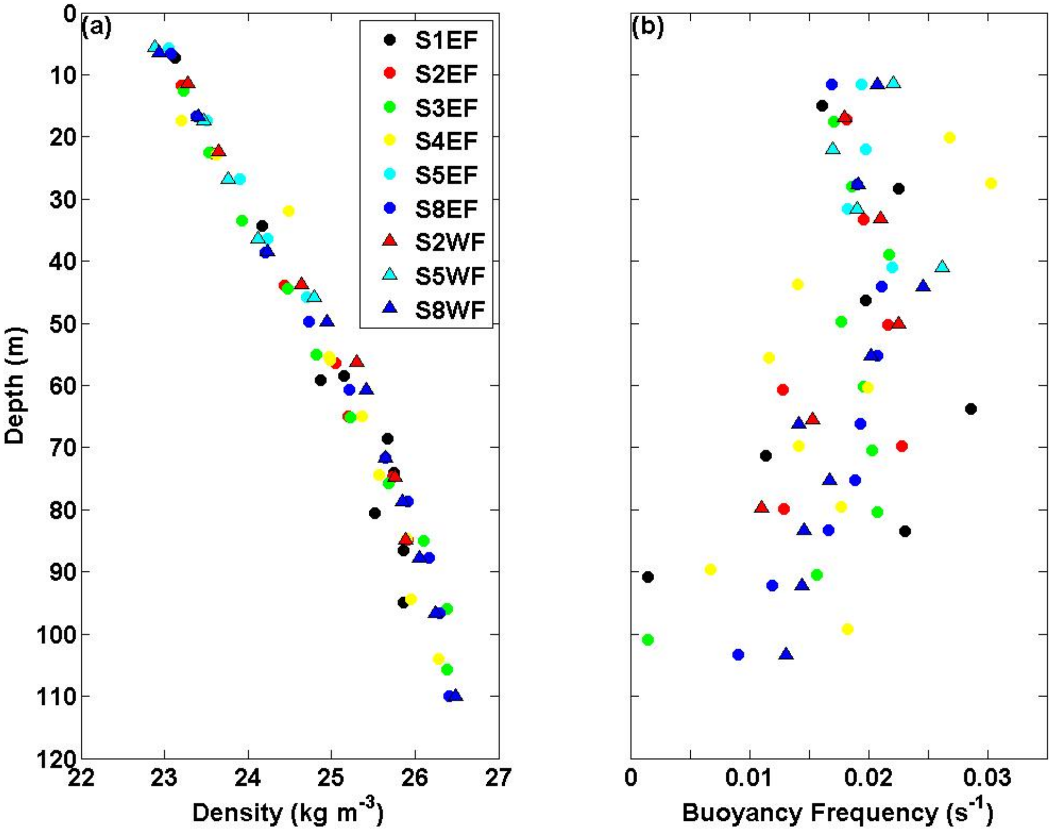

Figure 6. (a) Mean density (kg m^{-3}) and (b) mean buoyancy frequency (s^{-1}) profiles estimated from observations recorded at string moorings (S1–S8) for the mean eastward (EF, circles) and westward (WF, triangles) flow phases.

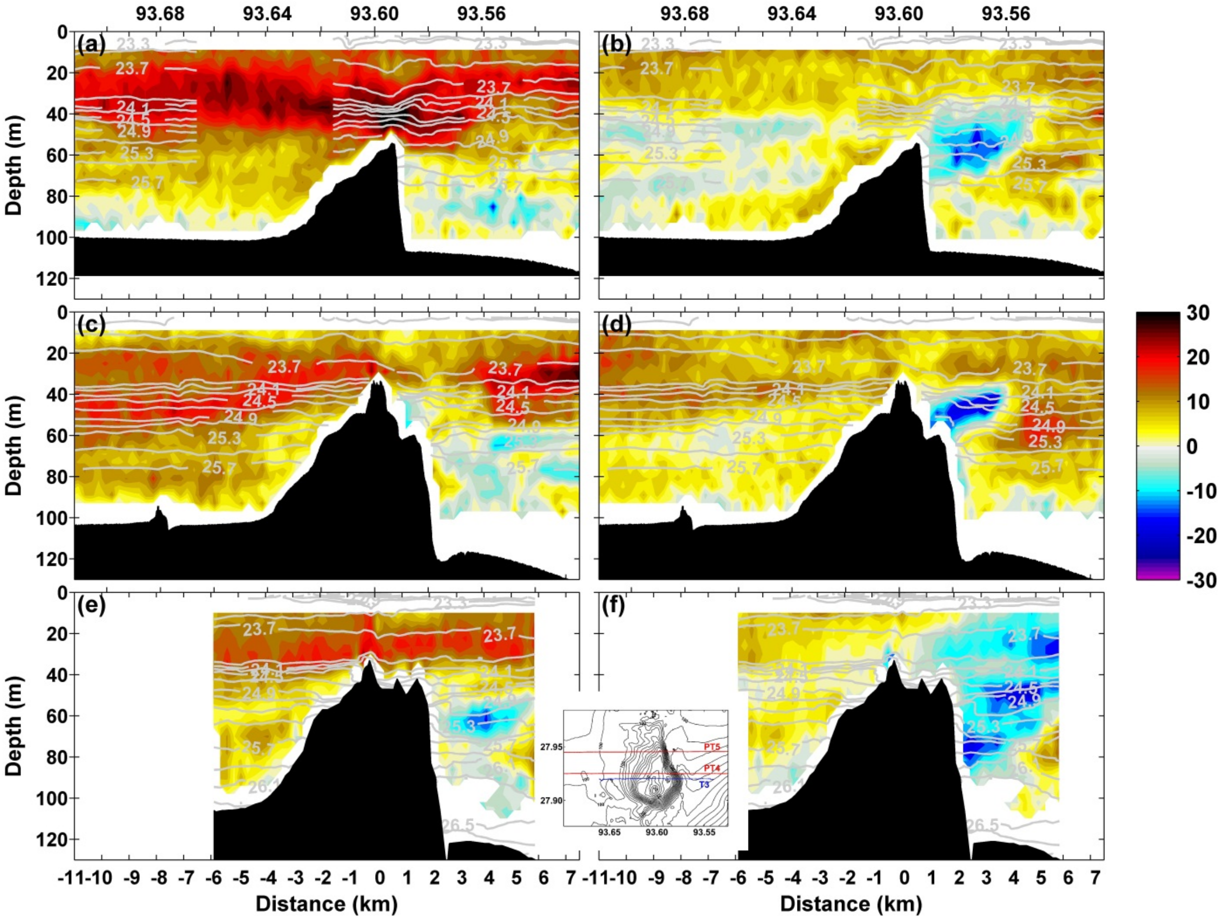

Figure 7. East/west (a, c, e) and north/south (b, d, f) current velocities (cm s^{-1}; color bar) from PT5 (a, b), PT4 (c, d), and T3 (e, f) sections taken between 12:15 UTC on 6 June and 2:30 UTC on 7 June 2011 during the mean eastward flow phase; density is also shown (kg m^{-3}; light grey lines plotted every 0.2 kg m^{-3}); top axes in (a) and (b) list longitudes (deg; W); an insert shows locations of the transects (measurements along PT4 and PT5 were taken from the R/V *Pelican*; T3 data were collected from the R/V *Manta*).

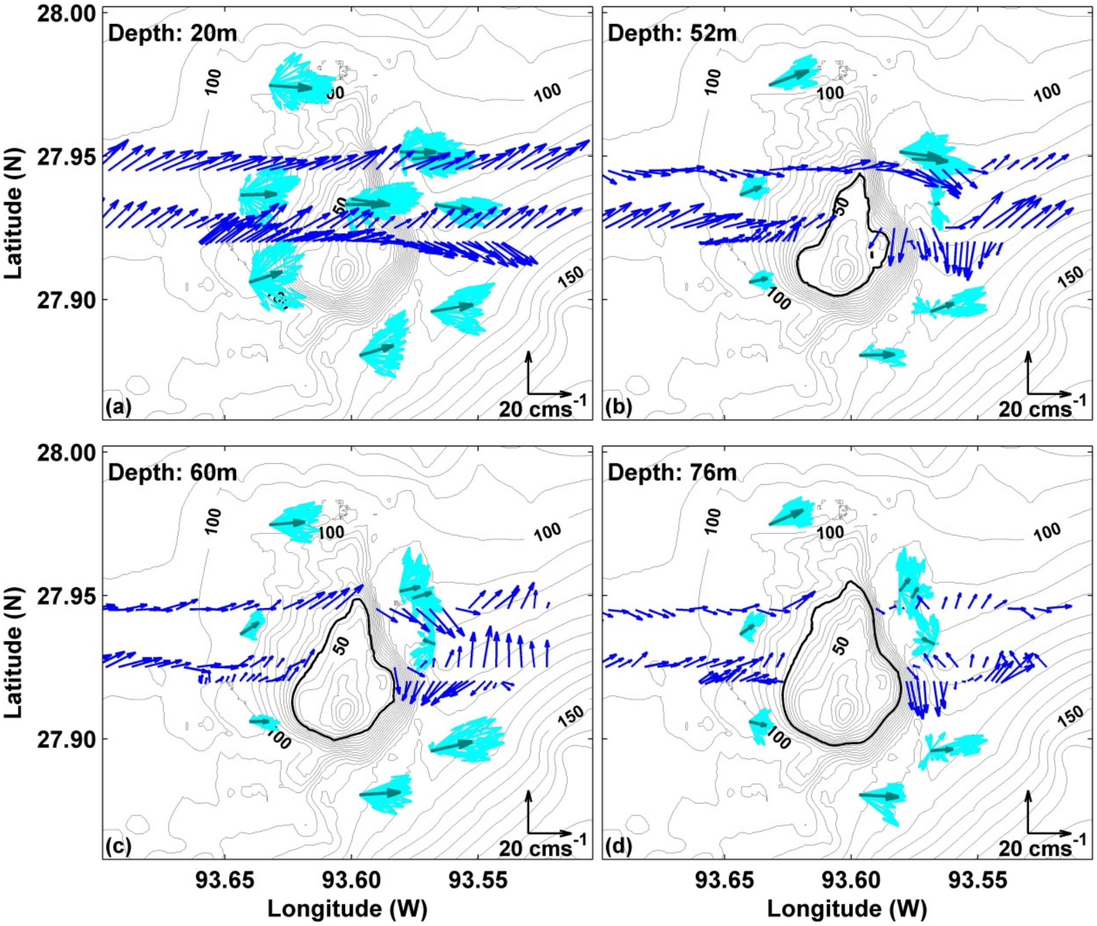

Figure 8. Current velocities (cm s^{-1}) along PT5, PT4, and T3 at (a) 20 m, (b) 52 m, (c) 60 m, and (d) 76 m as measured by shipboard (blue arrows) and moored (cyan arrows) ADCP instruments; also shown are time velocity means (12:15 UTC 6 June–2:30 UTC 7 June 2011; green arrows) estimated from mooring observations and depth contours for the chosen depth levels are highlighted by black contour lines.

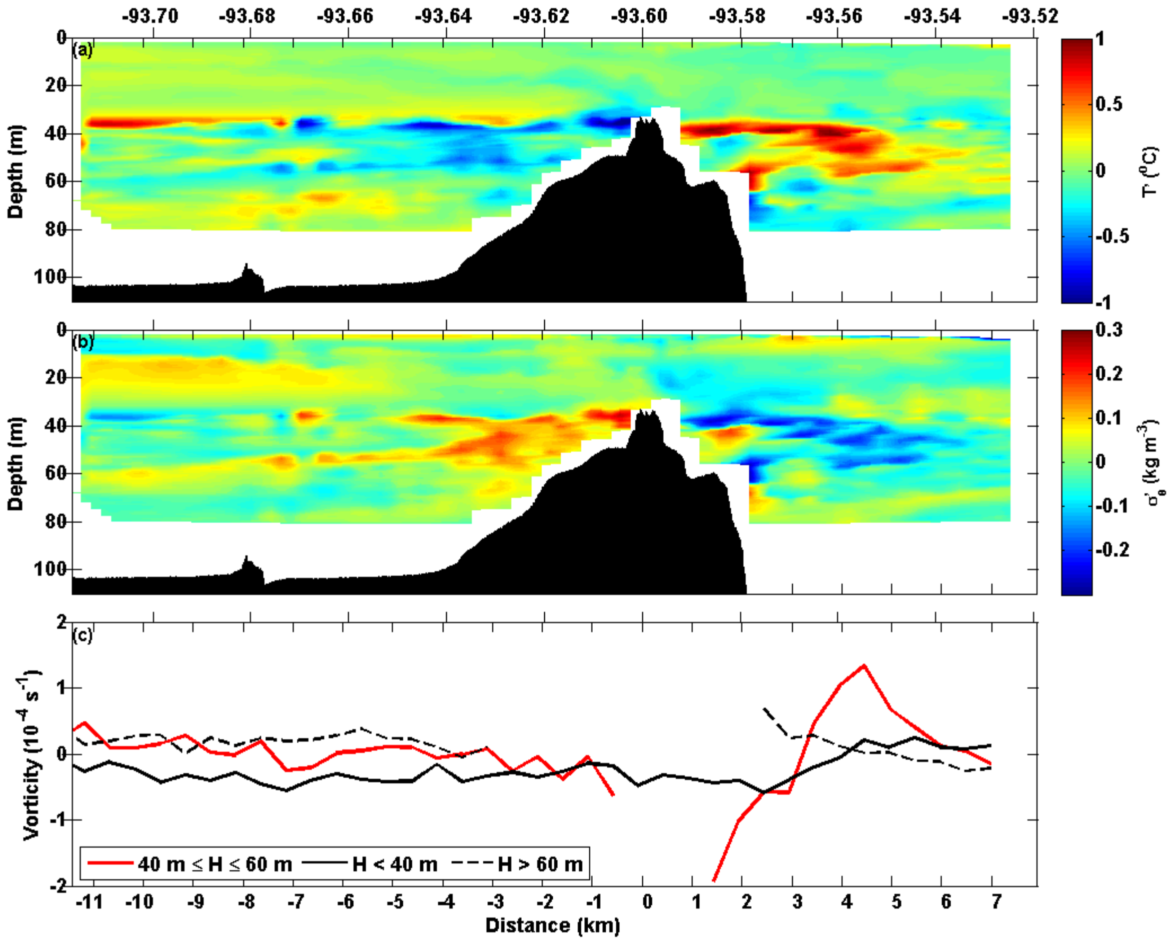

Figure 9. (a) Temperature (T'; ^{o}C) and (b) density (σ_{θ}'; kg m^{-3}) fluctuations along PT4, (c) relative vorticity (s^{-1}) estimated from velocity observations from PT4 and PT5.

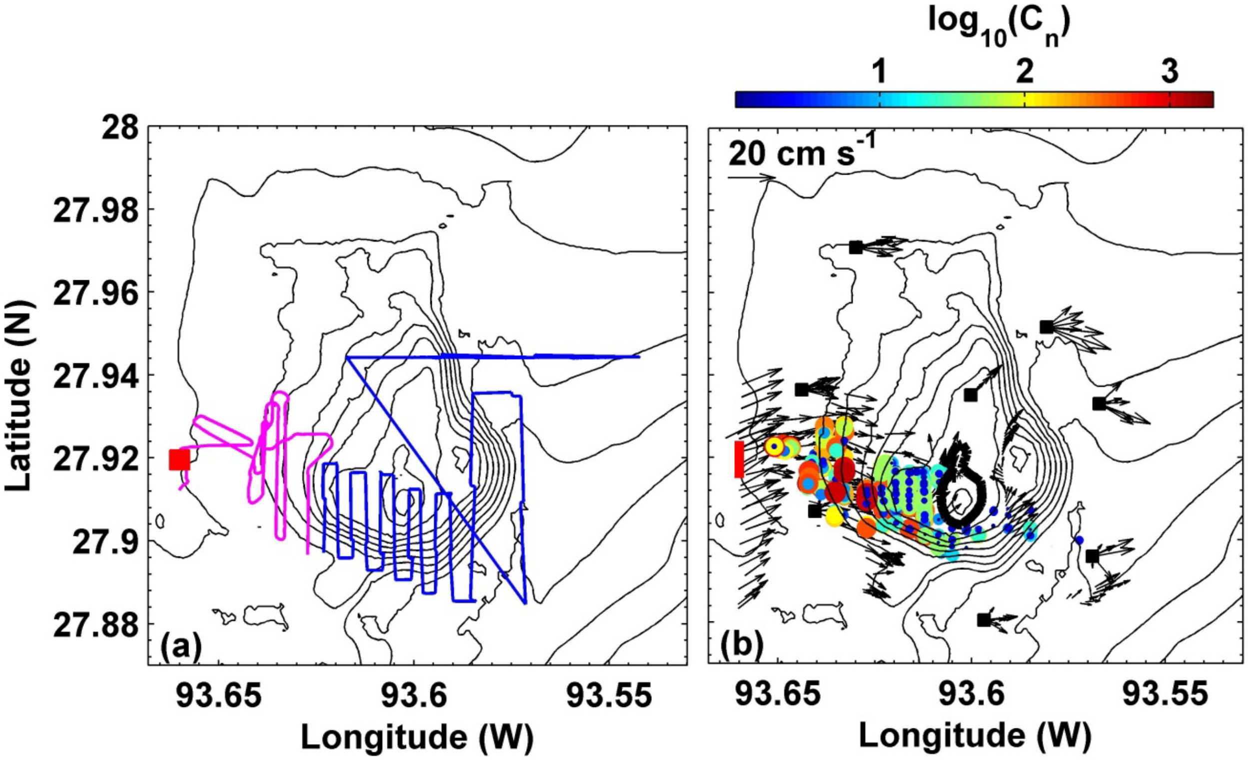

Figure 10. (a) The location (red square) of the dye release on 6 June 2011 and the REMUS (blue) and ScanFish (magenta) survey tracks from 6–7 June 2011; (b) normalized dye concentration (color bar) and currents (cm s^{-1}; black arrows).

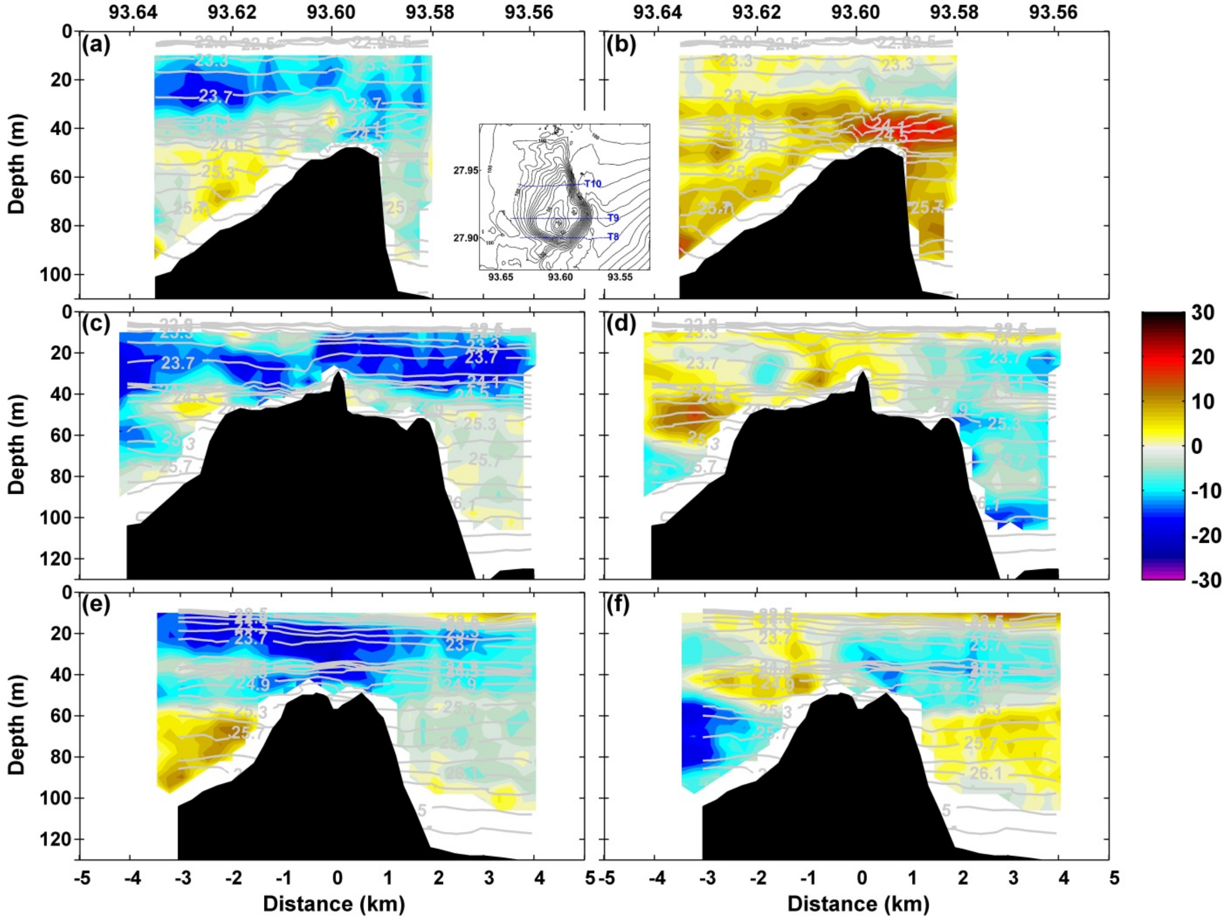

Figure 11. East/west (a, c, e) and north/south (b, d, f) current velocities (cm s^{-1}; color bar) from T10 (a, b), T9 (c, d), and T8 (e, f) sections taken between 13:45 UTC on 11 June and 3:30 UTC on 12 June 2011 during the mean westward flow phase; density is also shown (kg m^{-3}; light grey lines plotted every 0.2 kg m^{-3}); top axes in (a) and (b) list longitudes (deg; W); the insert shows locations of the transects (measurements along all transects were collected from the R/V *Manta*).

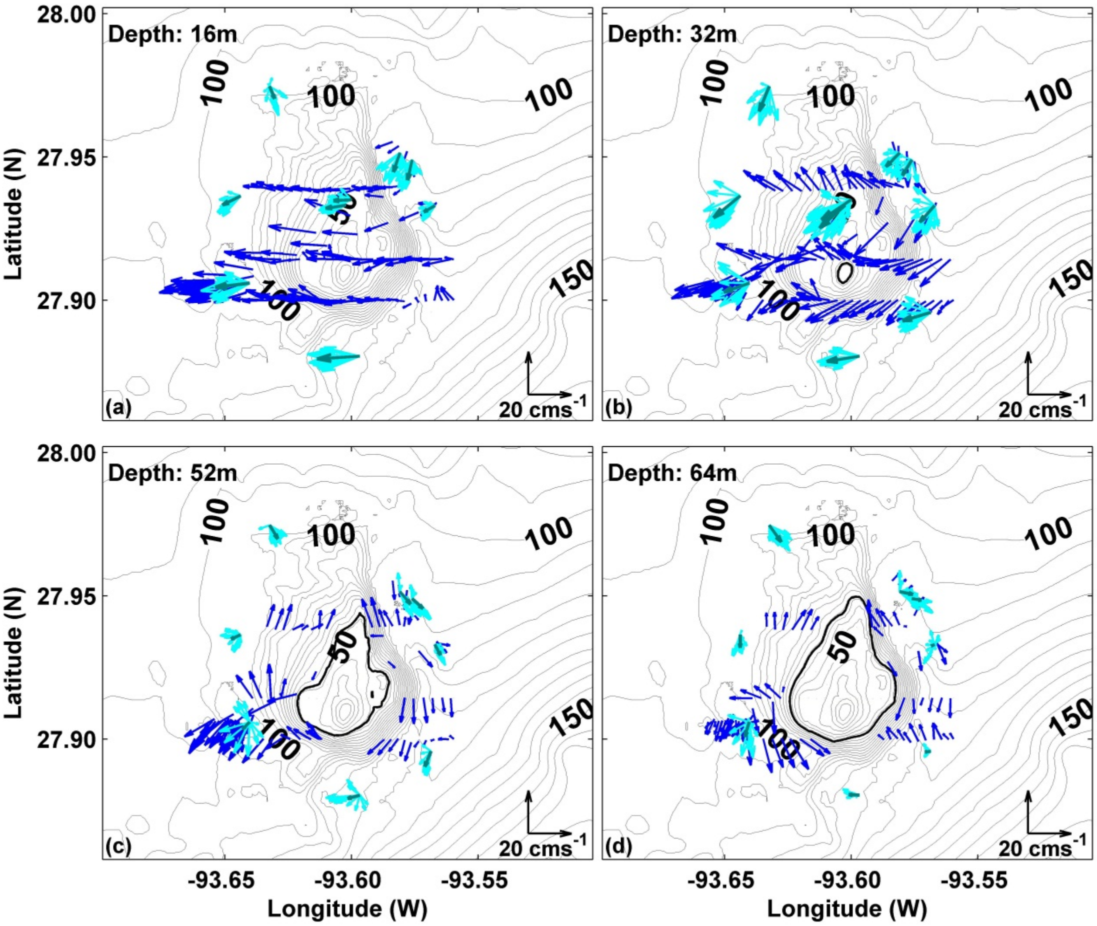

Figure 12. Current velocities (cm s^{-1}) along T8, T9, and T10 at (a) 16 m, (b) 32 m, (c) 52 m, and (d) 64 m as measured by shipboard (blue arrows) and moored (cyan arrows) ADCP instruments; also shown are time velocity means (13:45 UTC 11 June–3:30 UTC 12 June 2011; green arrows) estimated from mooring observations and depth contours for the chosen depth levels are highlighted by black contour lines.

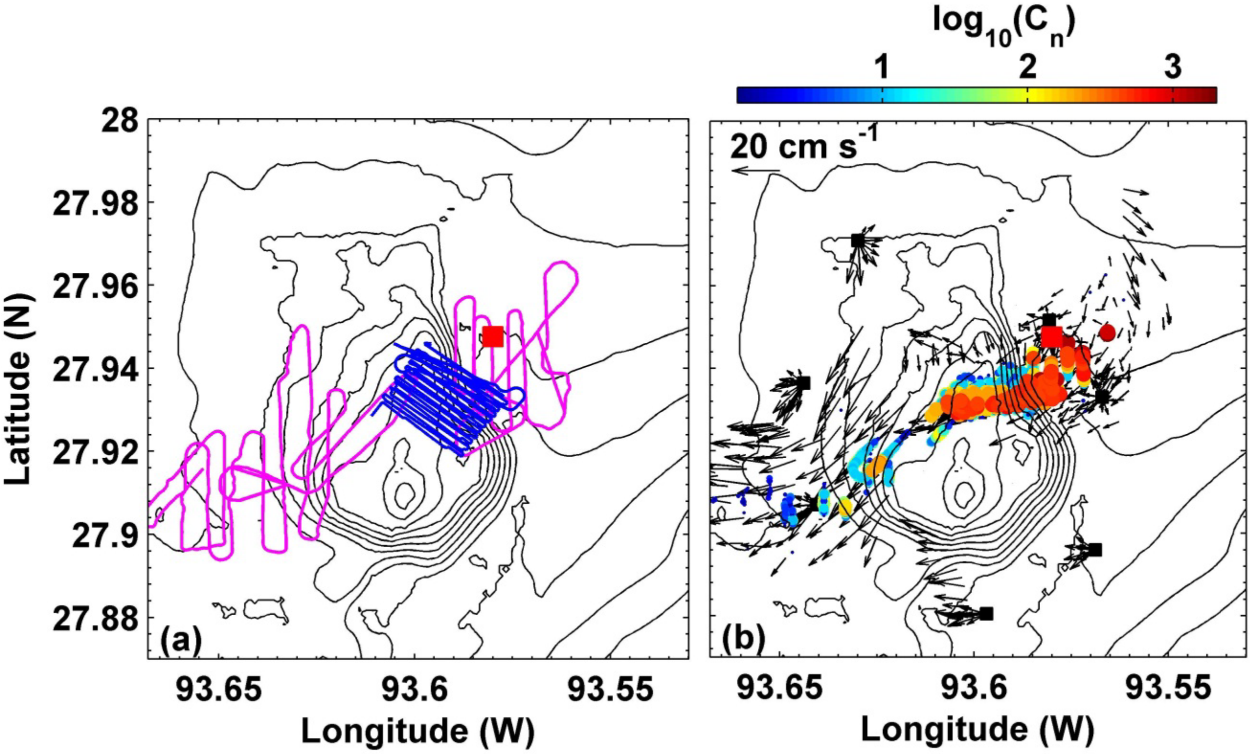

Figure 13. (a) The location (red square) of the dye release on 6 June 2011 and the REMUS (blue) and ScanFish (magenta) survey tracks from 10–11 June 2011; (b) normalized dye concentration (color bar) and currents (cm s^{-1}; black arrows).

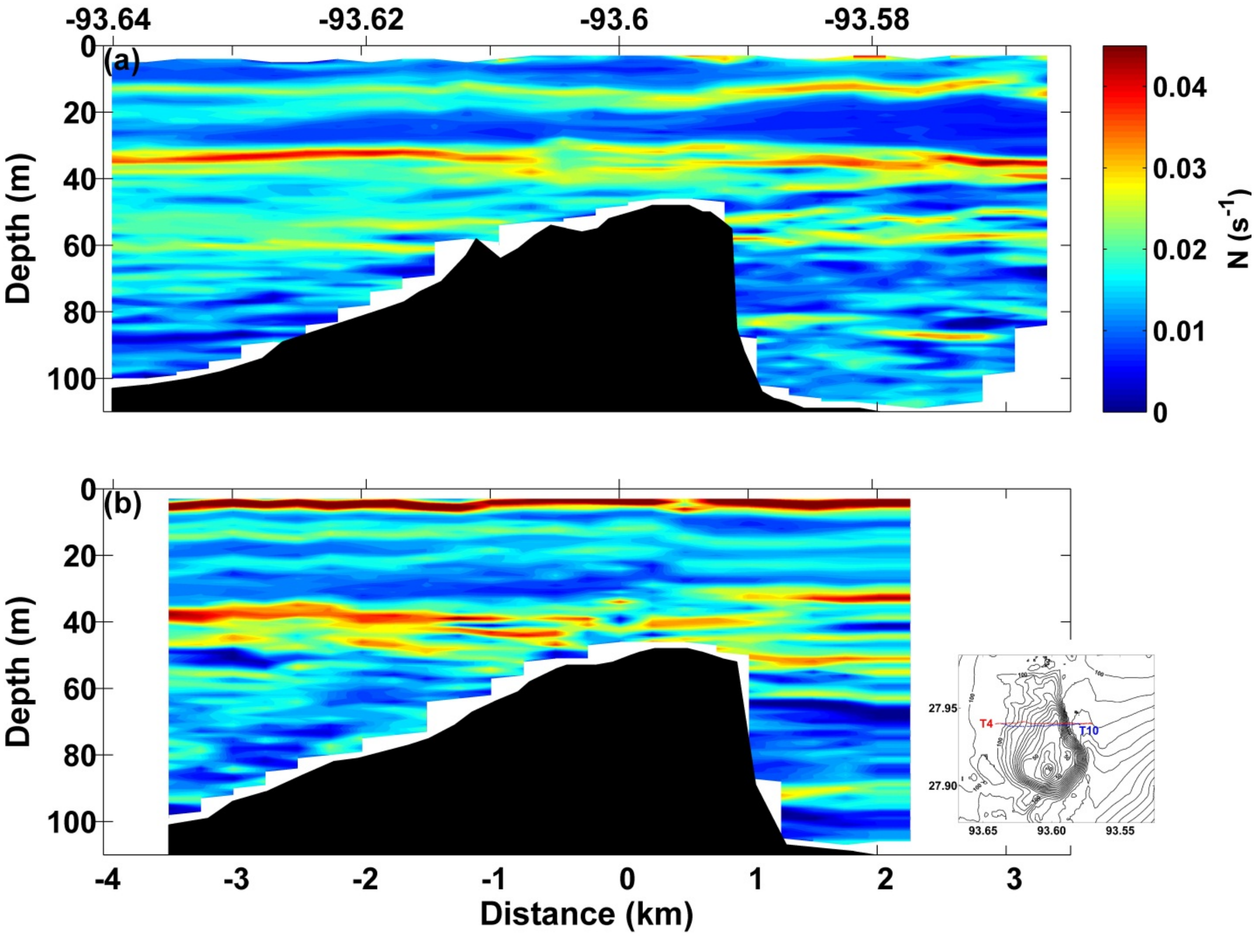

Figure 14. Buoyancy frequency (s^{-1}) along (a) T4 and (b) T10 transects; the insert shows locations of the transects.

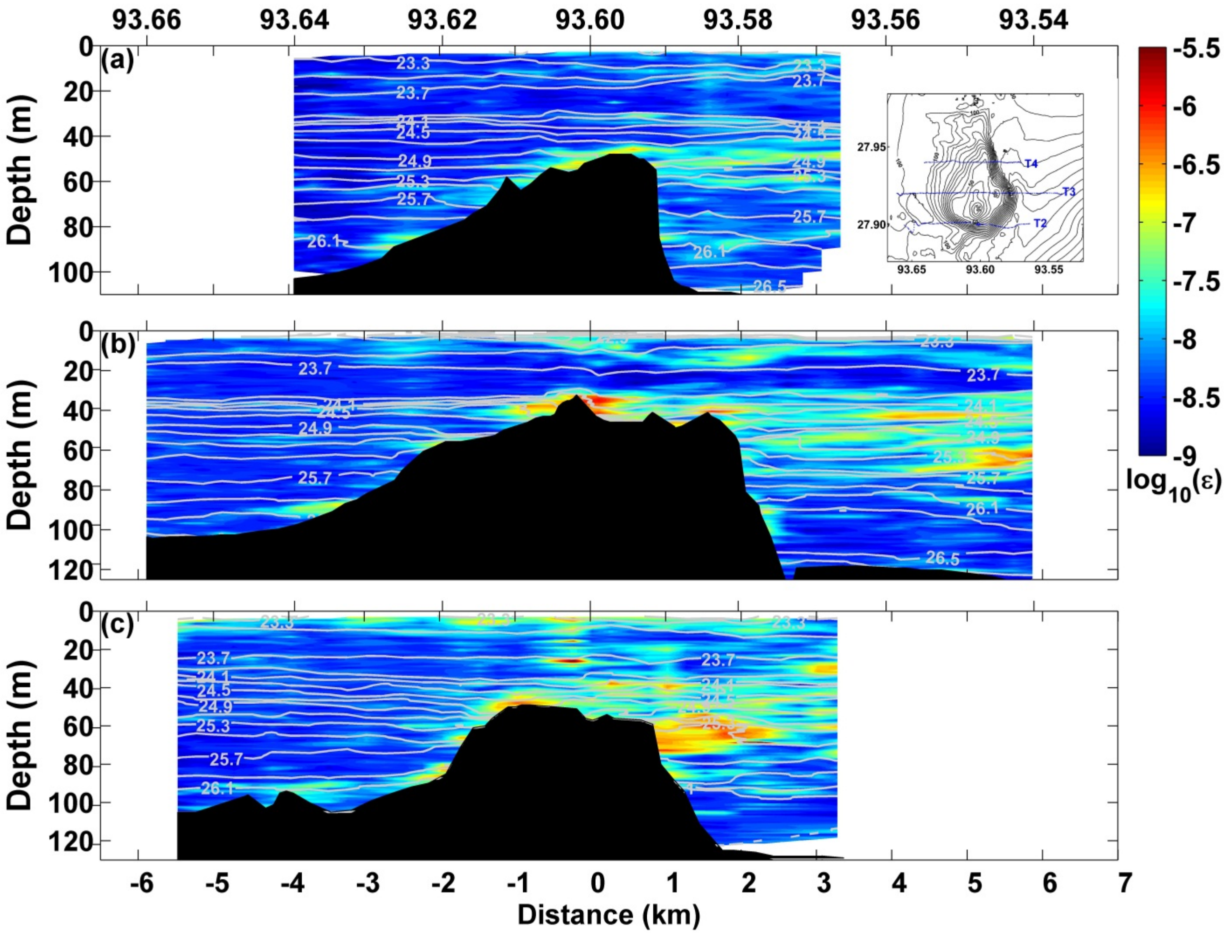

Figure 15. Turbulent kinetic energy (TKE) dissipation rates (*ε*; W kg^{-1}) along (a) T4, (b) T3, and (c) T2 transects; the top axis in (a) lists longitudes (deg; W); the insert shows locations of the transects; microstructure observations were taken between 21:00 UTC on 5 June and 00:30 UTC on 8 June 2011 from the R/V *Manta* during the mean eastward flow phase.

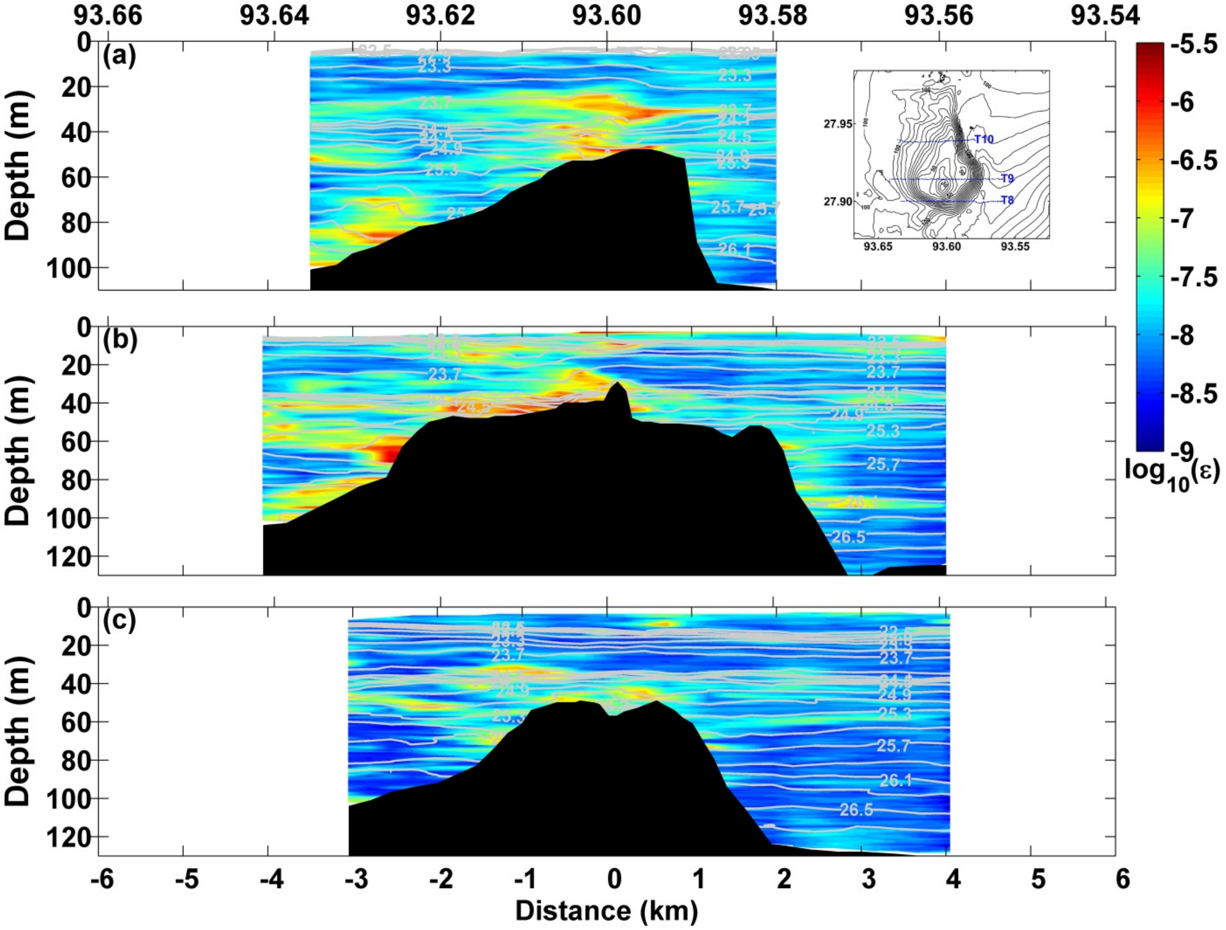

Figure 16. Turbulent kinetic energy (TKE) dissipation rates (ε; W kg^{-1}) along (a) T10, (b) T9, and (c) T8 transects; the top axis in (a) lists longitudes (deg; W); the insert shows locations of the transects; microstructure observations were taken between 13:45 UTC on 11 June and 3:30 UTC on 12 June 2011 from the R/V *Manta* during the mean westward flow phase.

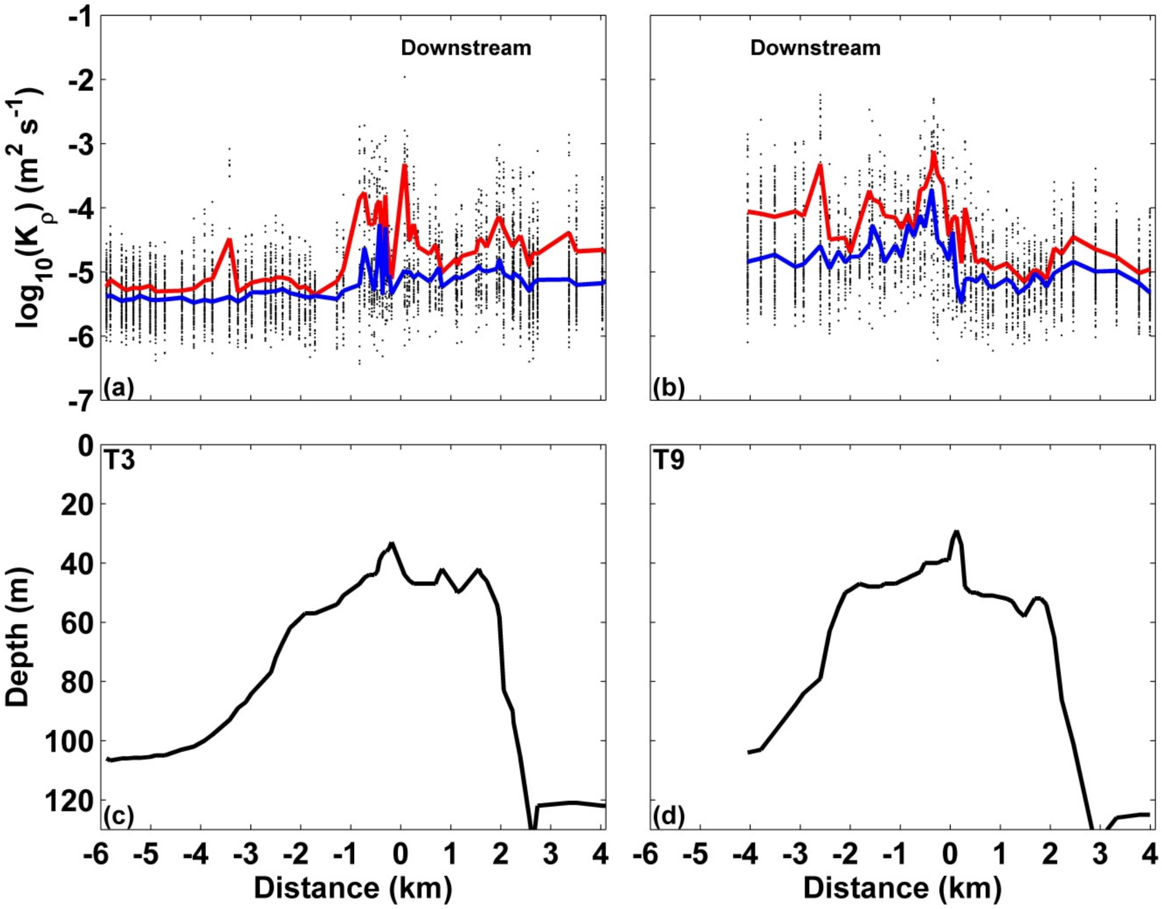

Figure 17. Eddy diffusivities (a, b; m^2 s^{-1}) and bathymetry (c, d) for T3 (a, c) and T9 (b, d) transects; means and medians of eddy diffusivities for each profile is marked by red and blue lines, respectively.

APPENDIX E

Wavelet Analysis of Near-Inertial Currents at the East Flower Garden Bank

Wavelet Analysis of Near-Inertial Currents at the East Flower Garden Bank

W.J. Teague[1], H.W. Wijesekera[1], E. Jarosz[1], A. Lugo- Fernández[2],
and Z.R. Hallock[3]

[1]Naval Research Laboratory, Stennis Space Center, MS, 39529, USA
[2]Bureau of Ocean Energy Management, New Orleans, LA, 70123, USA
[3]NVision Solutions, Inc., Bay St. Louis, MS, 39520, USA

Journal Citation:
Teague, W.J., H.W. Wijesekera, E. Jarosz, A. Lugo-Fernandez, and Z.R. Hallock, 2014. Wavelet analysis of near-inertial currents at the East Flower Garden Bank, Continental Shelf Research, submitted.

Abstract

Near-inertial currents (NICs) often dominate the mean circulation at the East Flower Garden Bank (EFGB), part of the Flower Garden Banks National Marine Sanctuary. The EFGB, one of several submerged coral reefs, is located in the northwestern Gulf of Mexico, about 190 km southeast of Galveston, Texas. The bank is about 6 km wide in the east-west direction and rises to within about 20 m from the surface. NICs near the EFGB are described using current data from five acoustic Doppler current profilers that were moored at the edges of the bank and on top of the bank for about a year. A wavelet analysis was used to better describe the nonstationarity of the NICs. NICs were strongest during spring and summer due to their near resonant response with sea breeze and the shallowness of the mixed layer, and exhibited a first-baroclinic-mode vertical structure. NICS were generally larger near the surface and extended to the bottom on the west side of the EFGB, but only to within about 20 m of the bottom on the eastern side of the bank. NIC ellipses were nearly circular and rotated clockwise above the top of the EFGB but became flatter and aligned with the bathymetry with increasing depth; occasionally, on the eastern side of the bank, the NIC vectors rotated counter-clockwise due to probable effects of lee vortices arising from the mean flow interacting with the bank. Both downward and upward energy propagations were observed below the mixed layer, but most energy input by the wind at the surface was likely transferred downward through divergence of the meridional flow against the coastal boundary. The inertial currents were at times more energetic that the mean flow, and often accounted for more than 50% of the total current energy.

Keywords: East Flower Garden Bank; Currents; Inertial Oscillations, Temperature/salinity; ADCP; Northwestern Gulf of Mexico; (27–28N; 93–94W)

1. Introduction

Near-inertial current (NIC) oscillations are common to the open ocean and to shelf regions (Webster, 1968). They are ubiquitous on the shelf in the northern Gulf of Mexico (Chen et al., 1996; DiMarco et al., 2000). NICs are characterized by clockwise (in the northern hemisphere) rotations of nearly circular horizontal currents at frequencies at or near the local inertial frequency (Pollard, 1970; Perkins, 1972; Kundu, 1976). NICs are forced by winds and most effectively by wind pulses on time scales of less than half of the local inertial period (Pollard, 1970; Perkins, 1972). Existing NICs can be enhanced by diurnal sea-breeze forcing if the currents and sea breeze are in phase (near-resonant conditions near 30º latitude) (Simpson et al., 2002; DiMarco et al., 2000; Jarosz et al., 2007). Inertial oscillations have been observed after the passage of hurricanes (Price, 1976; Brooks, 1983, Teague et al., 2007) and atmospheric cold fronts (Chen et al., 1996; Halper et al., 1988; Daddido et al., 1978). They can last from several days when generated by local winds and cold fronts to more than a week when generated by storms and hurricanes. NICs can generate the largest percentage of current variance, particularly where tides are weak, for periods of about a day. They commonly are of the order of magnitude of tidal variance in the northern Gulf of Mexico (Chen et al., 1996).

Long-term measurements of current velocity, temperature, and salinity were made at the East Flower Garden Bank (EFGB) from December 2010 to December 2011 (Figure 1). The EFGB is part of a marine sanctuary designated as the Flower Garden Banks National Marine Sanctuary, and are managed by the National Oceanic and Atmospheric Administration (NOAA). The Flower Gardens, the northern-most live coral reef in the Gulf of Mexico, are located near the edge of the Texas-Louisiana continental shelf in the northwestern Gulf of Mexico. The EFGB is about 6 km wide in the along shelf direction and 10 km in length, and peaks at about 20 m below the surface. The EFGB is quite steep on the eastern and southern sides and less so on the western and northern sides. All of the banks are surrounded by oil and gas activities. Interactions of the bank with the currents are important in processes over the bank. Protecting this natural habitat is very important to the ecology of the entire Gulf of Mexico. NICs are usually generated at the surface by the local winds, but circulation over rough bathymetric features at the edge of the shelf, such as the EFGB, may impact the structure and dynamics of the NICs and ultimately influence submesoscale mixing processes (Moum and Nash, 2000) at this bank, which may impact other nearby banks. The NICs can also contribute significantly to the overall current variability at the EFGB.

The objective of this work is to characterize the impact of a submerged bank near the shelf edge on the current flow, which is important for understanding of mixing and exchange mechanisms between the deep ocean and the shelf, and to describe the structure of near inertial currents over depth and time at locations surrounding and on top of EFGB under various wind forcing conditions. The effects of banks on inertial oscillations in modifying their structure and dynamics are not now well understood due to a scarcity of current measurements next to submerged banks. The structure of inertial oscillations at the EFGB has never been studied. The EFGB is large enough to alter the circulation at the shelf edge (Teague et al., 2013) and should have an effect on the inertial oscillations. The NICs can reverse the usual eastward mean flow over the bank when their amplitudes become large but these reversals may just last a few hours

(Teague et al., 2013). NICs can impact the dispersion of contaminants, biological organisms, and inorganic materials and hence may play a key role in bank habitats and oceanography.

The remainder of the paper is organized as follows. Current data are described in Section 2, and wind and pressure data are described in Section 3. The methodology for calculation of the mixed-layer depth and a brief description of the mixed layers are provided in Section 4. The wavelet analysis of the currents is described in Section 5. Similarly, a wavelet analysis is applied to the winds in Section 6. Results for the diurnal-inertial band, based on the wavelet analysis, of the currents are presented in section 7. Finally, some discussion and conclusions are given in Sections 8 and 9, respectively.

2. Current Data

From December 2010 to December 2011, four acoustic Doppler current profilers (ADCPs, M1-M4) were moored on the bottom at the edge and one ADCP (M5) was moored near the top of the EFGB. All moorings were recovered and redeployed in June 2011. Locations of the moorings and bathymetry are shown in Figure 1. M5 was located just to the north of the peak of the bank, at a depth of 47 m. M1–M4 were deployed just NW, SW, SE, and NE, respectively, of the EFGB, at depths ranging from 100 to 127 m.

RD Instruments Workhorse ADCPs, operating at 300 kH (M1-M4) and 600 kHz (M5), were mounted in trawl-resistant pods that rested on the bottom; these are referred to as Barnys due to their barnacle-like shape (Perkins et al., 2000). They recorded nearly full water column current profiles at 2 m vertical resolution except for 4 m vertical resolution at M3 every 12 or 15 minutes. ADCP accuracy is 0.5% of the water velocity. The usual naming conventions for the velocities are used: U positive towards the east, V positive towards the north, and W positive upwards. Further details on the data can be found in Teague et al. (2013). After initial processing and editing, ADCP data were resampled at even 30-minute times (compatible with wind data), and time-trimmed (at the series ends) so that all series from deployment 1 (D1) started and stopped at the same times (except for M5, which was short), and similarly for deployment 2 (D2).

Above the EFGB (shallower than about 40 m) horizontal velocities are significantly correlated. EOF analyses applied to U and V at 20 m and 40 m depths show that more than 80% of overall variance was in the first mode and less than 10% in mode 2 at 20 m. The mode 1 amplitudes are virtually constant for all moorings used (M1–M4 in deployment 1, M1-M5 in deployment 2), and mode 1 explained variance for each location is at least 75% at 20 m. Overall first-mode variance decreases with depth with an explained variance minimum of 60% at 40 m.

Inertial periods at the center, northern, and southern edges of the EFGB, using the 100 m isobath as the boundary, are approximately 25.55 h, 25.52 h, and 25.58 h, respectively. The three major tidal components are M2, K1, and O1 and have periods of 12.42 h, 23.93 h, and 25.82 h, respectively. The ADCP data were harmonically analyzed for four diurnal and four semidiurnal tidal constituents (K_1, O_1, P_1, Q_1, N_2, M_2, S_2, K_2). This analysis was done using depth-averaged currents at M1–M4; D1 and D2 records were concatenated yielding overall record lengths of nearly one year (363.8 days). The M5 records were excluded because M5–D1 was only 40 days long. The Rayleigh criteria for most combinations of the selected constituents are about 27 days or less; for K_1 and P_1, as well as K_2 and S_2, it is 182.6, well below the record length of 363 days; however, the year-long record is necessary for K_2 due to possible aliasing with a semiannual constituent. There were small variations of amplitudes among the mooring sites which may be due to shoaling effects near the shelf edge and the bank. The amplitudes for O_1, K_1 and M_2 were approximately 1.9 cm s^{-1}, 2.3 cm s^{-1} and 2.2 cm s^{-1}, respectively. The other five constituent amplitudes were small (< 1 cm s^{-1}). These amplitudes are somewhat smaller than those reported by DiMarco and Reid, (1998). Amplitudes of the inertial oscillations can exceed 15 cm/s and are often larger than tidal amplitudes. NICs can be modified by the diurnal tide, depending on the phase difference, but this effect is relatively small. Rotary autospectra for current velocity at 7.5 m depth from M1 are displayed in Figure 2 and show a strong clockwise peak near the diurnal-inertial as well as semi-diurnal periods. There is little energy at the diurnal frequency for the counter-clockwise component but some counterclockwise semi-diurnal energy is present but at a lower level than for the clockwise component. Removal of principal barotropic tidal constituents (also Figure 2) attenuates much of the semidiurnal energy but the clockwise diurnal-inertial peak is minimally affected.

Overall average squared vertical shear of horizontal currents ($S^2 = (\partial U / \partial z)^2 + (\partial V / \partial z)^2$) ranged from 0.005 s^{-2} to 0.011 s^{-2} at mooring sites. The squared shear combined with vertical density gradients (based on temperature and salinity data from string moorings, Section 4) were used to calculate gradient Richardson numbers ($R_i = N^2 / S^2$), where N^2 is the buoyancy frequency. With a few exceptions, some of which were likely spurious, R_i values were above 0.25 indicating vertical stability over most of the record. R_i values in the mixed layer were not included since both vertical shear and density gradients were small.

3. Wind and Pressure Data

Wind velocity and atmospheric pressure data were collected half-hourly at the southern edge of the EFGB at National Data Buoy Center Station 42047, and at Station 42046 located approximately 37 km west of the EFGB. Winds between these two stations were very similar for the concurrent recording periods. Winds at 42046 were used when 42047 was out of service which was about half of the year-long mooring period. Winds, during the deployment period, were typical for this region (de Velasco and Winant, 1996). Wind velocities and pressures are shown in Figure 3. Wind gusts are considerably larger than the 30-minute averaged velocities. The atmospheric pressure record shows numerous frontal passages from December 2010 to May (days -30 to 130) and from October 2011 through December 2011 (days 270 to 360). Winds were weakest mainly during summer (except for a wind event near day 245), and were generally southerly. Hurricanes or tropical storms did not impact the EFGB in 2011 and atmospheric pressure was almost always above 1000 mb (Figure 3). There is a significant peak in the clockwise (CW) rotary wind autospectrum (Figure 4) for the summer period that may be associated with sea-breeze effects (Zhang et al., 2009). The most intense inertial oscillations were found during spring and summer. These enhanced amplitudes are associated with a near-resonant response to sea-breeze effects (Teague et al., 2013; Zhang et al., 2009; Jarosz et al., 2007; Simpson et al., 2002; DiMarco et al., 2000). The EFGB is about 200 km off the Texas-Louisiana coastline and is considerably farther offshore than the 50 km range that Chen et al.

(1996) suggested that sea-breeze effects could be significant. However, Zhang et al. (2009) found that the sea breeze can extend to 300 km off the coast in this region.

4. Mixed-Layer Depths

Temperature data from string moorings located near (within several hundred meters) M–M4 were used to estimate the mixed-layer depth (MLD) (Teague et al., 2013). Temperature from string mooring instruments (typically 10) were interpolated to one-meter intervals, but not extrapolated to the surface. The MLD was defined as the depth where the temperature changed by at least 0.25°C from the shallowest temperature measurement. The MLDs computed from each string were smoothed over 24 hours to reduce the higher frequency variability. Finally, the average MLD over all the strings was computed and a five-day boxcar average was applied to reduce the daily variability. MLDs were deepest, 60 to 80m, during December and January. Throughout much of the year, MLDS ranged between 20 and 40 m. Rapid changes in the MLD may have been caused by eddy passages, such as the rapid decrease in MLD during March (Teague et al., 2013). The seasonal cycle in MLD at the EFGB is similar to that reported by McGrail (1983). The average MLD is shown in the upcoming wavelet plots (Figures 12–19).

5. Wavelet Analysis

Currents at the EFGB change quickly over time due to passing eddies, rapidly changing wind fields, and interaction with the bank. Hence the current patterns are not very predictable (Teague et al., 2013). These currents are not stationary and conventional Fourier spectrum analysis, which provides information about the average amplitude and phase for each harmonic and energy content for the entire time span of the data, presumes the data are stationary. This method, however, does not provide information about the energy levels and its variations within the time span of the data records. Wavelet analyses of ocean currents (Liu and Miller, 1996) can provide an effective way of obtaining time-frequency information of non-stationary processes, such as NICs. Wavelet analysis provides a complementary approach to the traditional Fourier spectrum analysis, and is used here to provide a description of the time evolution of NICs near the EFGB. Significant current fluctuation energy is present in the ADCP velocity series acquired near the EFGB. The objective here is to show the importance of variability in the diurnal-inertial band (DIB) relative to fluctuations at other frequencies, to describe the characteristics of variability in the DIB, to examine the relationship of DIB variability with local hydrographic conditions, and to calculate coherences between currents and wind velocity over the area.

Wavelet decomposition of a time series is essentially the systematic application of a set of band-pass filters whose bandwidths are proportional to the center periods of each (Torrence and Compo, 1998; Mallat, 1989). Here, we apply continuous wavelet transforms (CWTs) using a complex Morlet wavelet, with MATLAB software developed by Torrence and Compo (1998). The complex Morlet wavelet is essentially a cosine, sine wave with a Gaussian envelope for the real, imaginary parts, respectively; these functions are then convolved with the data to produce a set of band-passed complex series for each variable where the imaginary part is shifted by -90º form the real part. Wavelet decomposition was done with the half-hourly-sampled current series, and with the local wind data.

The wavelet analysis results in complex series of *U* and *V* velocity components which are functions of depth, time and frequency band, e.g.:

$$U(z,t) = \sum_k \tilde{U}(z,t,f_k) = \sum_k \left(\tilde{U}_r(z,t,f_k) + i\tilde{U}_i(z,t,f_k)\right), \qquad (1)$$

where the tilde indicates wavelet decomposition and *k* corresponds to a particular band. Following Gonella (1972), and Mooers (1973) band-limited velocities can be transformed to rotary components:

$$\begin{aligned} 2\tilde{U}^+ &= \tilde{U}_r - \tilde{V}_i, \\ 2V^+ &= \tilde{U}_i + \tilde{V}_r, \\ 2\tilde{U}^- &= \tilde{U}_r + \tilde{V}_i, \\ 2\tilde{V}^- &= \tilde{U}_i - \tilde{V}_r, \end{aligned} \qquad (2)$$

where the plus and minus superscripts indicate counter-clockwise and clockwise rotation, respectively, of the velocity vector. We calculate specific energy:

$$\tilde{S} = \left|\tilde{U}\right|^2 + \left|\tilde{V}\right|^2, \qquad (3)$$

for total velocity; energies for counterclockwise and clockwise currents, $\tilde{S}^+$ and $\tilde{S}^-$, are similarly defined. Plots of $\tilde{S}^-$ and $\tilde{S}^+$ for depths of 20 m (M1–M5), 40 m (for M5) and 70 m (M1–M4) appear as Figures 5-8. The y-axis shows the period instead of the frequency for easier visualization. The inertial oscillations will appear in the clockwise spectra at periods just greater than a day for the latitude of the EFGB. Because the inertial oscillations rotate clockwise, they are not evident in the counterclockwise spectra in the Northern Hemisphere.

The most prominent features in Figure 5 (~20 m) are the bursts of clockwise DIB energy, strongest between days 100 and 250, at all mooring locations. This should not be surprising given the diurnal peak, associated with the sea breeze, in the clockwise wind spectrum (Figure 4) during this time period. The high clockwise energy near the inertial period at day 245 is associated with a large north wind burst (Figure 3). Some bursts of semi-diurnal energy are also evident, especially near day 170 but, as indicated above, much of this may be tidal. Lower-frequency (LF) energy is also present, but is generally lower than that in the DIB. In particular, there are several bursts at periods of several days near times 250, 260 and 320 days. Also, between days 220 and 280 there is a persistent burst of ~17-day-period energy, primarily at M2, M3, and M5. DIB energy is essentially absent in plots of counterclockwise energy (Figure 6). The LF features, on the other hand, are more pronounced and also show up prominently at all mooring locations, with quite similar signatures, between days 230 and 280. LF counterclockwise features also appear near days 40–50, primarily at M2 and M3. These LF motions are likely to associated with passing eddies, as suggested during these time periods by Teague et al. (2013). Clockwise energies near 70 m (M1–M4) and 40 m (M5) (Figure 7) are quite similar to the shallower case (Figure 5), but show some attenuation of the DIB levels. Much of the ~17-day energy apparent at 20 m is gone at 70 m, but at M1 there is a significant burst of several-day energy near day 245 which also corresponds to the wind burst at the end of summer. Deeper counterclockwise energies (Figure 8) also show reduction in DIB intensity, but not as much as for the shallower level. Note the significant deep counterclockwise DIB energy bursts at M2 and particularly M4 which may be related to bathymetric effects of the EFGB.

6. Wind Forcing

Wavelet analysis also was applied to the wind velocities. Period-time plots of clockwise and counterclockwise (S_w) appear in Figure 9. Seasonal changes in the energy are evident with broadband frontal passages, primarily from late fall to early spring. Emergence and intensification of diurnal energy, mostly clockwise, are found during late spring and summer into late fall. Between days 170 and 270, the peak in energy for the DIB is well defined and is indicative of the strong sea breeze. Strong broadband summer events occur near days 170 and 210. There is some clockwise energy in the semidiurnal band during summer; it may be present at other times but is obscured by frontal passages and storms. We investigate possible wind forcing of the observed NICs with a wavelet coherence algorithm (Grinsted et al., 2004; Torrence and Compo, 1998). The cross-wavelet transform (C_{VVw}) for northward wind and current (at ~20 m) is defined by

$$C_{VVw} = \tilde{V}\tilde{V}_w^*, \qquad (4)$$

where the asterisk denotes complex conjugate. To properly calculate coherence (γ_{VVw}), smoothing over time and frequency (Grinsted et al., 2004), indicated by an overbar, is applied to C, $|\tilde{V}|^2$, and $|\tilde{V}_w|^2$, and

$$\gamma^2{}_{VVw}\ (f,t) = \frac{\left|\overline{C}_{VVw}(f,t)\right|^2}{\overline{\left|\tilde{V}\right|^2}(f,t)\ \overline{\left|\tilde{V}_w\right|^2}(f,t)}. \qquad (5)$$

The phase of the current relative to wind fluctuations is given by,

$$\phi_{VVw}(f,t) = \tan^{-1}\overline{C}_{VVw}(f,t), \qquad (6)$$

Coherences of noise series (using a Monte Carlo Method) yield a 5% significance level, $\gamma_5(f)$ (only 5% of coherences with random data rise above this level). This provides a measure of confidence for γ_{VVw}. γ_5 is a function of frequency and ranges from 0.84 to 0.86 between periods of 1.5 h and 40 days, For longer periods it increases nearly linearly, exceeding 0.90 at 60 days. γ_5 rises sharply for periods less than 1.5 h.

Figure 10 shows $\gamma^2{}_{VVw}$ at M1; the other locations are qualitatively similar, as are plots of $\gamma^2{}_{UUw}$ (not shown). The northward component was selected here to align with the principal direction (onshore-offshore) of the diurnal sea breeze, which is an important forcing agent. The similarities among locations should not be surprising, because correlations among 20 m current velocities from the moorings are quite high. Significant coherences (orange to red to brown) are most evident in the diurnal-inertial range and at several-day to several-week periods. The latter correspond to energetic meridional wind events, e.g., near day 250 (see Figures 9, 2b). Phases (Φ_{VVw}) for the 3 periods included in the DIB (Figure 11), plotted only where γ_{VVw} is significant, show periods of reinforcing ($-90^{\circ} < \Phi < 90^{\circ}$), particularly between days 120 and 270. There are also a few short periods consistent with attenuation ($|\Phi| > 90^{\circ}$), e.g., near day 230.

7. Diurnal-Inertial Band

Zhang et al. (2009) define the diurnal inertial band (DIB) containing energy at periods between 20 and 28 h. In this analysis, the wavelet band central periods include the following: […, 16.5290, 19.6560, 23.3750, 27.7980, 33.0570,…] h (out of a total of 53 bands), so we define our DIB as the 2nd–4th of the 5 periods shown. Hence, we sum currents for these three bands to form DIB velocity:

$$U_D(z,t) \equiv \sum_{k=18}^{20} \tilde{U}(z,t,f_k)\,; \qquad (7)$$

likewise for V_D and corresponding rotary components. It is useful to examine some time-dependent statistics of the DIB velocities. In the following, the statistics are 50%-overlapping two-day boxcar averages of respective quantities, yielding daily values. The time-smoothed quantities are denoted by overbars.

The smoothed energies, $\overline{S}_D$, $\overline{S}_D^+$, $\overline{S}_D^-$, can be interpreted as time and depth dependent spectra for the DIB. The CW spectral series, $\overline{S}_D^-(z,t)$, is shown in Figure 12 . The signature of $\overline{S}_D^-$ is nearly the same as that of $\overline{S}_D$ (not shown), indicating that CW energy dominates. The counterclockwise spectra, $\overline{S}_D^+(z,t)$, (Figure 13) show a much lower energy throughout most of the record. Notable exceptions include bursts near 70 m and day 170 at M2 and M3, and between day 140 and 230 at M4. There are other, CCW bursts of shorter extent in time and depth. Where the counterclockwise and clockwise energy are comparable, the currents are approximately rectilinear. The highest clockwise energy levels (Figure 12) occur primarily during the spring and summer (days 110 to 240), but there are other, more isolated, bursts outside this.

In general, the current vectors of band-limited rotary motions describe ellipses. These ellipses can range from circular to rectilinear in shape with either counterclockwise or clockwise rotation. Parameters of the ellipses, which here are functions of depth and time, can be derived from the spectra and other statistical series. The semi-major and semi-minor axes are given by:

$$X_{maj} = \sqrt{\overline{S}_D^+} + \sqrt{\overline{S}_D^-}\,,$$

$$(8)$$

$$X_{\min} = \sqrt{\overline{S}_D^+} - \sqrt{\overline{S}_D^-}\,.$$

A positive X_{min} indicates counterclockwise rotation; $X_{min} = 0$ results if the motion is rectilinear. If $X_{min} = \pm X_{maj}$ the motion is circular. When the magnitude of the ratio $R = X_{min} / X_{maj}$ is significantly less than unity, it is useful to calculate ellipse orientation:

$$\psi = \tan^{-1}\left(\frac{2\overline{U_D V_D}}{\overline{U_D^2} - \overline{V_D^2}}\right). \qquad (9)$$

Uncertainty in ψ increases as R approaches ±1. X_{maj} (plotted in Figure 14) represents the smoothed DIB current amplitude; the information here is similar to that shown in Figures 12, but is more directly comparable to current velocity. The ellipse axis ratios (R) (Figure 15) show the dominance of clockwise motions in the DIB and emphasize the counterclockwise periods, especially at M4 deeper than the top of the EFGB. The occurrences of counterclockwise energy at M4, which was located near the steep northeast side of the EFGB, may be associated with the generation of cyclonic vortices in the lee of the bank when mean currents are eastward (Jarosz et al., submitted). These counterclockwise periods in DIB energy roughly coincide with periods of eastward mean flow reported by Teague et al. (2013; their Figure 8a). At all locations, lighter colors (smaller magnitude of the ratio) indicate flatter ellipses, or more rectilinear fluctuations. These features suggest bathymetric effects on the flow. Ellipse orientations (or principal directions of variability) appear in Figure 16. Much of the plot shows green areas; these are where the ratio $|R| \sim 1$ and the uncertainty in calculated ψ is greater than about 30º, rendering it meaningless. At locations where useable orientations exist (deeper than about 60 m), they are about 30º to 45º at M1 and M3 and -45º to -80º at M2 and M4; these values align roughly with the bathymetry of the EFGB at these depths.

We can examine the ratio of energy in the DIB relative to total energy,

$$R_E(z,t) \equiv \frac{E_{DIB}}{E_{Tot}} = \frac{\overline{U_D^2} + \overline{V_D^2}}{\overline{U^2} + \overline{V^2}}, \qquad (10)$$

where the overbar, as above, represents a two-day, overlapping time average. R_E plotted in Figure 17 is generally highest during spring-summer, with the most pronounced event occurring between days 160 and 180. The DIB energy often exceeded 50% of the total current energy and sometimes even exceeded 70% of the total energy. These high energy contributions often extended from near surface to near bottom.

Complex correlations (recall that U_D and V_D are complex series) calculated (over each two-day segment, as above) between velocities at each depth relative to the shallowest depth yield series of magnitudes (ρ) and phases (Φ). The product ρ cos(Φ) yields zero-lag values for U_D and V_D. The zero-lag correlation for V_D is shown in Figure 18; the zero-lag correlation for U_D is quite similar; the main differences occurr where U values are lower, particularly at M4 below the depth of the top of the EFGB. The correlations are concentrated near 1 or -1, suggesting first-mode baroclinic motion. Also, estimates of mixed-layer depths (indicated on Figure 18) from moored strings of CTD recorders correspond roughly to the transition from positive to negative correlations. Phases (Φ) are shown in Figure 19. Because these results are quite noisy, the phases are assigned quadrants to provide estimates of gross changes over depth and time. In phase (315º–45º), leading (45º–135º), opposite phase (135º–225º) and lagging (225º–315º) are represented by white, red, green, blue, respectively. Above the mixed-layer depth, the current is roughly in phase with that at the shallowest depth. Below this, the current is primarily oppositely directed, but there are periods of leading and lagging fluctuations corresponding to upward and downward phase propagation (or downward and upward energy propagation), respectively. Overall, the vertical structure of DIB variability suggests a first baroclinic mode.

8. Discussion

Near-inertial currents are an important energy exchange mechanism between the winds and ocean and can be responsible for a substantial fraction of the kinetic energy throughout the water column. Our findings in the preceding sections, as well as the high horizontal coherence of currents above the bathymetry (Section 2), imply that NICs in the vicinity of the EFGB are primarily forced by winds acting on the mixed layer. Fluctuations at or near the inertial period (here, about 25.5 h) result from broadband excitation due to storms and frontal passages (Chen and Xie, 1997), and near-resonant diurnal (24 h) responses often occur when a significant sea breeze is present, mainly during late spring and summer months (DiMarco et al., 2000; Jarosz et al., 2007; Simpson et al., 2002, Rippeth et al., 2001). Furthermore, the response to wind forcing is enhanced when the mixed layer is shallow. DIB energy is input to the mixed layer as primarily clockwise currents with nearly circular ellipses. There is some evidence here of energy generated near the surface being propagated downward and energy generated near the bottom (by bathymetric interaction) being propagated upward (Kundu, 1976; Chant, 2001; Lerczak et al., 2001). However, the dominant mechanism in this case is likely due to the presence of the east-west boundary at the coast. This boundary allows a meridional pressure gradient to develop, associated with the north-south component of the NIC, which results in an oppositely-directed current below the pycnocline yielding a first baroclinic modal structure (Rippeth et al., 2001; Millot and Crepon, 1981; Pettigrew, 1981; Kundu et al., 1983; Tintore et al., 1995; Chen et al., 1996).

DIB energy penetrates most of the water column rather quickly (within about one day). Above the top of the EFGB, the NIC current vectors rotate clockwise and their ellipses are nearly circular. Below the mixed layer the velocities become anticorrelated with the mixed-layer velocities. The ellipses flatten as depths increase beyond about 50 m with their major axes aligning roughly with the nearby bathymetry, implying significant interaction with the bank. The interaction can cause the flow to become rectilinear. In some cases (mostly at M4) the ellipses exhibit the opposite vector rotation (counterclockwise) for extended periods; this occurs primarily when mean flow (see Figure 8a in Teague et al., 2013) is eastward over much of the water column at M1 and M2, during spring and summer, when DIB energy is highest. The lee side of the EFGB is very steep, but the west side slope is much less extreme. In the same figure, the eastward flow does not extend as deep at M3 and M4 due to the blocking effect of the EFGB. However, the presence of the bank in the eastward flow can produce cyclonic vortices (Jarosz et al., submitted) on the lee side of the bank which may further interact with the NICs resulting in the counterclockwise rotations seen at M4.

9. Conclusions

NICs at the EFGB occur in bursts throughout the year but are most concentrated during the spring and summer periods when they are enhanced by sea-breeze effects. The bank tends to modify NIC characteristics below the top of the bank. NICs can occasionally reverse the predominantly eastward mean flow on short time scales. Typically, the vertical structure of the NICs followed a first-baroclinic mode with a 180° phase shift between upper and lower layers but was more complicated when waters were weakly stratified. NICs were generally stronger at the surface but sometimes were largest at mid-depth. Barotropic tidal currents were small and generally less than the NICs. Above the bank, NICs were highly coherent. Below the top of the bank, the NIC ellipses tended to align with the bathymetry and become more rectilinear while flowing around the bank. Counterclockwise rotation of the ellipse vector was common on the lee or eastern side of the bank below the top. NICs were often a significant part of the total current and could account for more than 50% of the total current energy throughout the water column. NICs are likely to be partially responsible for enhanced mixing of physical, biological, and geological properties.

The Flower Garden Banks are very important to the ecosystems in the Gulf of Mexico. Characteristics of the near-inertial currents observed at the EFGB are expected to be similar at the other banks. In combination with the mean currents and passing eddies, in the vicinity of the banks, NICs probably play a significant role in the transport and mixing of physical and biochemical properties around the numerous banks at levels significantly greater than over most of the continental shelf. Hence, they may have a pronounced effect on the ecosystem of the Gulf of Mexico shelf region. In particular, NICs are most intense during spring and summer, the period of most active biological activity, such as the mass coral spawning event that happens annually 7–10 days after the full moon, typically in the month of August.

Acknowledgements

This work was sponsored by the Bureau of Ocean Energy Management (BOEM; formerly the Minerals Management Service) in the project referred to as “Currents over Banks (COB)” through Interagency Agreement No. M10PG00038 and by the Office of Naval Research in a Naval Research Laboratory (NRL) project referred to as “Mixing over Rough Topography (MORT)” under program element 0601153N. The measurements were made in cooperation with the Flower Garden Banks National Marine Sanctuary (administered by the National Oceanic and Atmospheric Administration [NOAA]).

References

Brooks, D.A., 1983. The wake of Hurricane Allen in the western Gulf of Mexico. Journal of Physical Oceanography 13, 117-129.

Chant, R. J. 2001. Evolution of near-inertial waves during an upwelling event on the New Jersey inner shelf. Journal of Physical Oceanography 31, 746 – 764.

Chen, C., Reid, R.O., Nowlin, W.D., Jr., 1996. Near-inertial oscillations over the Texas-Louisiana shelf. Journal of Geophysical Research 101, 3509-3524.

Chen, C. and Xie, L., 1997. A numerical study of wind-induced, near-inertial oscillations over the Texas-Louisiana shelf. Journal of Geophysical Research 102: doi: 10.1029/97JC00228. issn: 0148-0227.

Daddido, E., Wiseman, W.J., Murray, S.P., 1978. Inertial currents over the inner shelf near 30 N. Journal of Physical Oceanography 8, 728-733.

deVelasco, G. G., Winant ,C.D., 1996. Seasonal patterns of wind stress and wind stress curl over the Gulf of Mexico. Journal of Geophysical Research, 101(C8), 18127–18140, doi:10.1029/96JC01442.

DiMarco, S.F., Reid, R.O., 1998. Characterization of the Principal Tidal Current Constituents on the Texas-Louisiana Shelf. Journal of Geophysical Research 103, 3093-3109.

DiMarco, S.F., Howard, M.K., Reid, R.O., 2000. Seasonal variation of wind-driven current cycling on the Texas–Louisiana continental shelf. Geophysical Research Letters 27 (7), 1017–1020.

Halper, F.B., McGrail, D.W., Merrell, W.J., Jr., 1988. Seasonal variability in the currents on the outer Texas-Louisiana shelf. Estuarine, Coastal and Shelf Science 26, 33-50.

Gonella, J. 1972. A rotary-component method for analyzing meteorological and oceanographic vector time series. Deep Sea Research, 19, 833-846.

Grinsted, A., Moore, J.C., Jevrejeva, S., 2004. Application of the cross wavelet transform and wavelet coherence to geophysical time series. Nonlinear Processes in Geophysics, 11, 561–566, doi:10.5194/npg-11-561-2004.

Jarosz, E., Hallock, Z.R., Teague, W.J., 2007. Near-Inertial Currents in the DeSoto Canyon Region. Continental Shelf Research 27, 2407-2426.

Jarosz, E., Wijesekera, H.W., Teague, W.J., Fribance, D.B., Moline, M.A., 20xx. Observations on stratified flow over a bank at low Froude numbers. submitted.

Kundu, P.K., 1976. An analysis of inertial oscillations observed near the Oregon coast. Journal of Physical Oceanography 6, 879–893.

Kundu, P.K., S.-Y. Chao, J.P. McCreary, 1983. Transient coastal currents and inertio-gravity waves. Deep-Sea Research 30, 1059-1082.

Lerczak, J. A., Hendershott, M.C., Winant, C.D. ,2001. Observations and modeling of coastal internal waves driven by a diurnal sea breeze. Journal of Geophysical Research 106, 19,715 – 19,729.

Liu, P.C., Miller, G.S., 1996. Wavelet Transforms and Ocean Current Data Analysis. Journal of Atmospheric and Oceanic Technology 13, 1090-1099.

Mallat, S. G., 1989. A theory for multiresolution signal decomposition: the wavelet representation. IEEE Transactions on Pattern Analysis and Machine Intelligence 11 (7), 674-693.

McGrail, D. W.,1983. Flow, boundary layers, and suspended sediment at the Flower Garden Banks. In: Rezak, R., Bright, T.J,, McGrail, D.W. (Eds.).,Reefs and banks of the northwestern Gulf of Mexico: their geological, biological, and physical dynamics. Final Report,Technical Report no. 83-1-T. , U.S. Department of the Interior, Minerals Management Service, Gulf of Mexico OCS Regional Office, New Orleans, LA., pp 141–230.

Millot, C., Crépon, M., 1981. Inertial oscillations on the continental shelf of the Gulf of Lions—observations and theory. Journal of Physical Oceanography 11**,** 639–657.

Mooers, C.N.K., 1973. A technique for the cross spectrum analysis of pairs of complex-valued time series, with emphasis on properties of polarized components and rotational invariants. Deep-Sea Research and Oceanographic Abstracts, 20(12), 1129-1141, ISSN 0011-7471, http://dx.doi.org/10.1016/0011-7471(73)90027-2.

Moum, J.N., Nash, J.D., 2000. Topographically induced drag and mixing at a small bank on the continental shelf. Journal of Physical Oceanography 30, 2049-2054.

Perkins, H., 1972. Inertial oscillations in the Mediterranean. Deep-Sea Research 19, 289–296.

Perkins, H., De Strobel, F., Gauldesi, L., 2000. The barny sentinal trawl-resistant ADCP bottom mount: design, testing, and application. IEEE Journal of Oceanic Engineering 25, 430–436.

Pollard, R.T., 1970. On the generation by winds of inertial waves in the ocean. Deep-Sea Research 17, 795–812.

Pettigrew, N.R., 1981. The dynamics and kinematics of the coastal boundary layer off Long Island. Ph.D. thesis, Massachusetts Institute of Technology/Woods Hole Oceanographic Institution, WHOI-81-14, 262 p.

Price, J.F., 1976. Several aspects of the response of shelf waters to a cold front passage. Memoires Societe des Sciences de Liege, 6e series X, 201-208.

Rippeth, T. P., Simpson, J.H., Player, R.J., Garcia, M., 2001. Current oscillations in the diurnal-inertial band on the Catalonian Shelf in spring. Continental Shelf Research 22 (2), 247-265.

Simpson, J.H., Hyder, P., Rippeth, T.P., Lucas, I.M., 2002. Forced oscillations near the critical latitude for diurnal-inertial resonance. Journal of Physical Oceanography 32, 177-187.

Teague, W.J., Jarosz, E., Wang, D.W., Mitchell, D.A., 2007. Observed Oceanic Response over the Upper Continental Slope and Outer Shelf during Hurricane Ivan. Journal of Physical Oceanography **37**, 2181-2206.

Teague, W.J., Wijesekera, H.W., Jarosz, E., Fribance, D.B., Lugo-Fernandez, A., Hallock, Z.R., 2013. Current and hydrographic conditions at the East Flower Garden Bank in 2011. Continental Shelf Research 63, 43-58.

Tintore, J., Wang, D.-P., Garcia, E., Viudez, A., 1995. Near-inertial motions in the coastal ocean. Journal of Marine Systems 6, 301 – 312.

Torrence, C., Compo, G.P., 1998. A Practical Guide to Wavelet Analysis. Bulletin of the American Meteorological Society, 79, 61–78.
doi: http://dx.doi.org/10.1175/1520-0477(1998)079<0061:APGTWA>2.0.CO;2

Webster, F., 1968. Observations of inertial-period motions in the deep sea. Reviews of Geophysics 6, 473-490.

Zhang, X., DiMarco, S.F., Smith IV, D.C., Howard, M.K., Jochens, A.E., Hetland, R.D., 2009. Near-Resonant Ocean Response to Sea Breeze on a Stratified Continental Shelf. Journal of Physical Oceanography 39, 2137-2155.

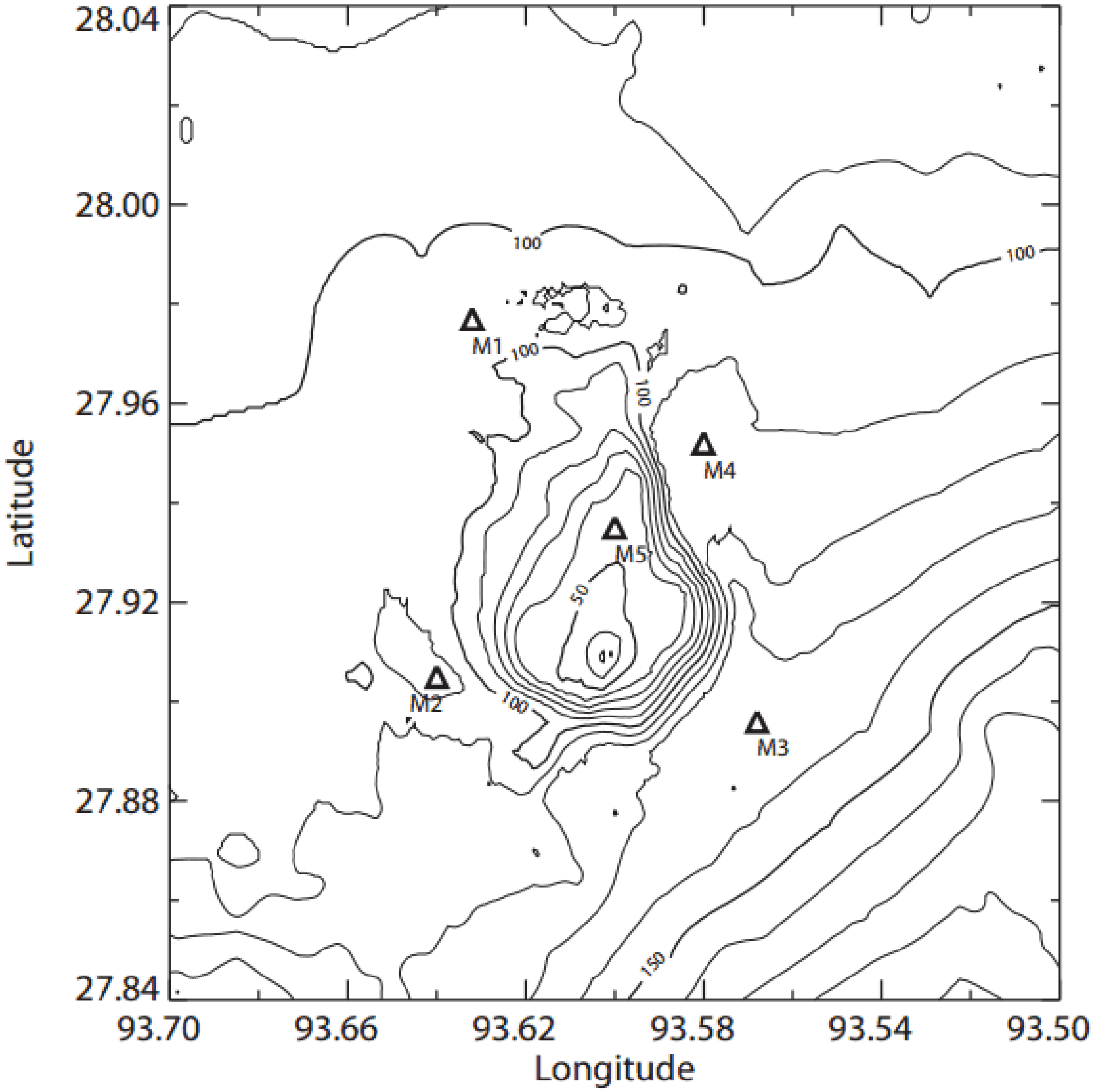

Figure 1. Locations of ADCP moorings (M1–M5) at the East Flower Garden Bank (EFGB) located near the shelf break in the northwestern Gulf of Mexico. Bathymetry contours are every 10 m. Temperature/salinity strings S1–S4 (not shown) were within about 200 m of corresponding M1-M4 ADCPs.

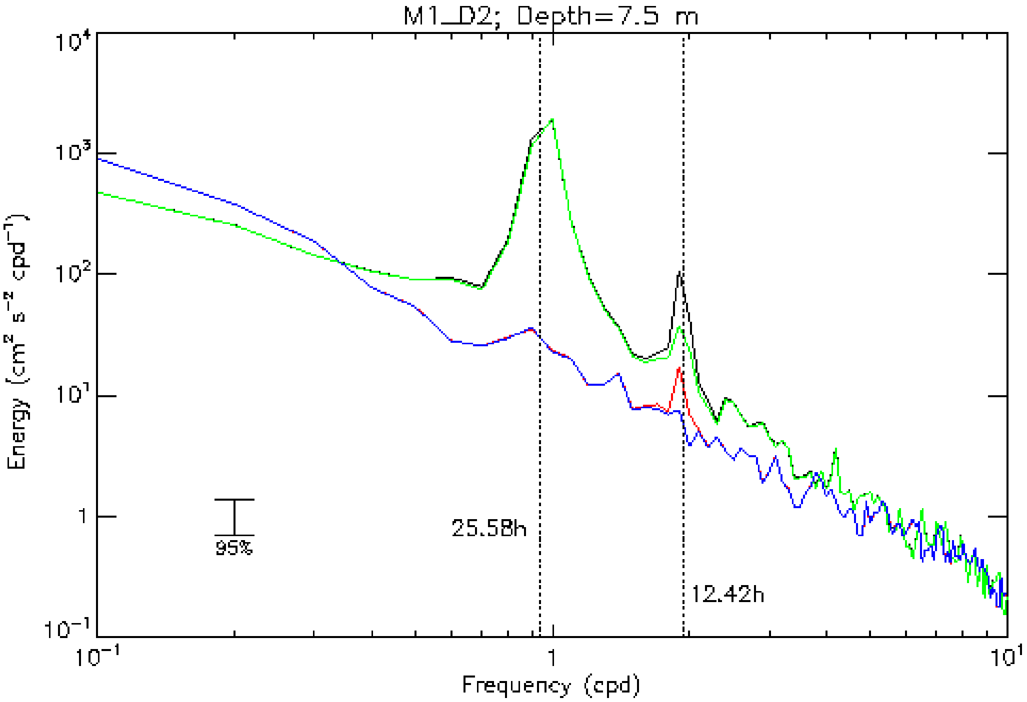

Figure 2. Rotary autospectra for ADCP M1–D2. Clockwise: with tides (black); barotropic tides removed (green). Counterclockwise: with tides (red); barotropic tides removed (blue).

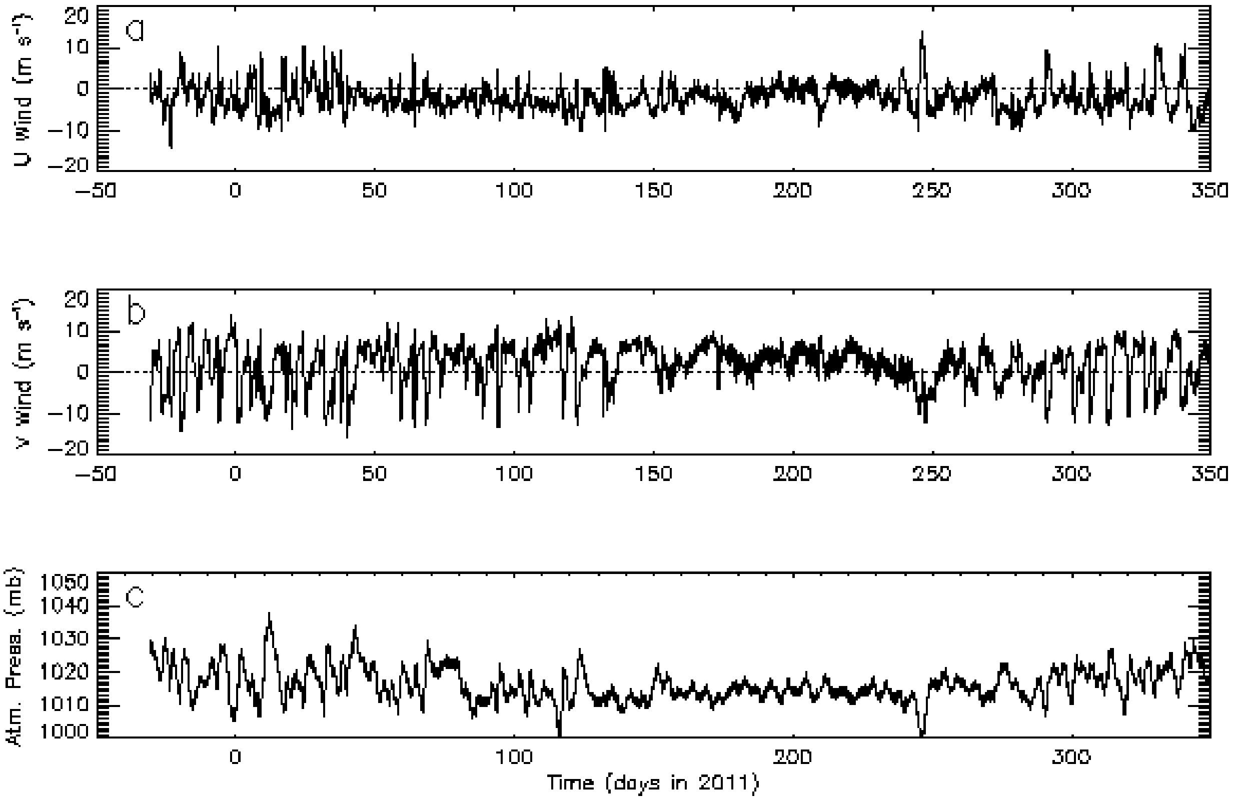

Figure 3. Eastward (a) and northward (b) components of wind velocity; atmospheric pressure (c), near the EFGB. First sample on 1 December 2010.

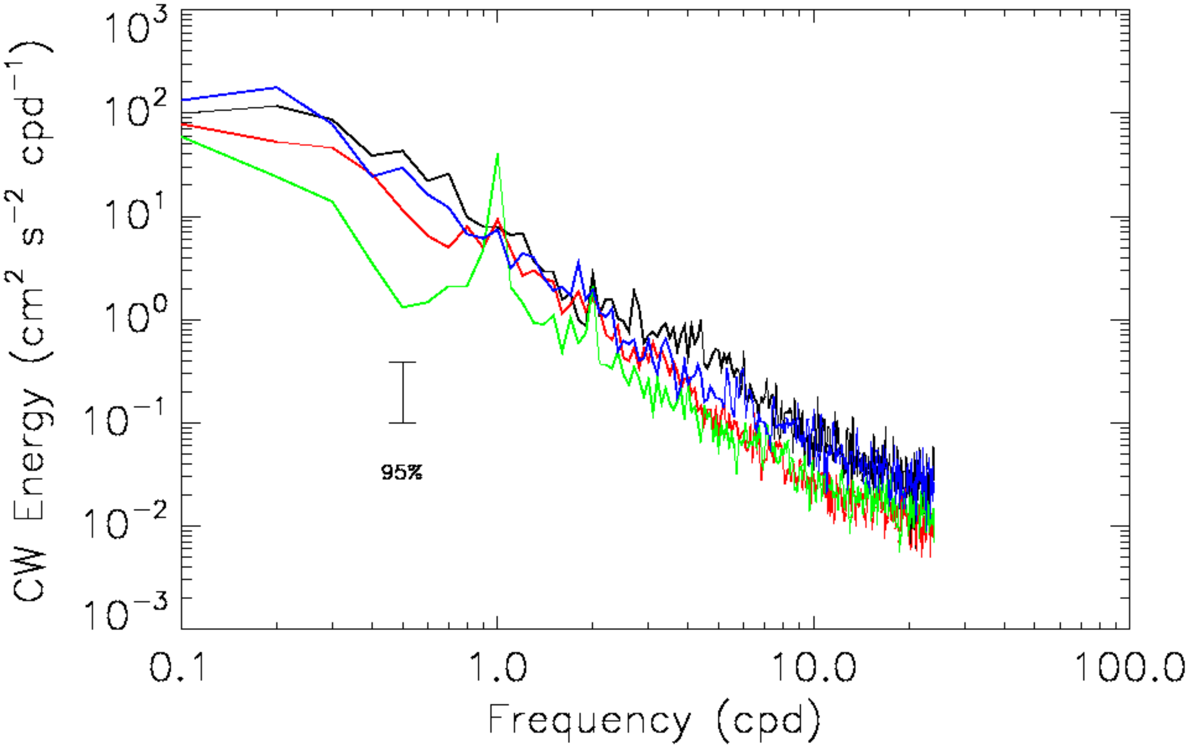

Figure 4. Clockwise rotary autospectra of the wind velocity for each season (black-winter, red-spring, summer-green, fall-blue) are shown. A significant diurnal peak is present for the summer (July–September). Counterclockwise spectra (not shown) are similar, but a diurnal peak is not present.

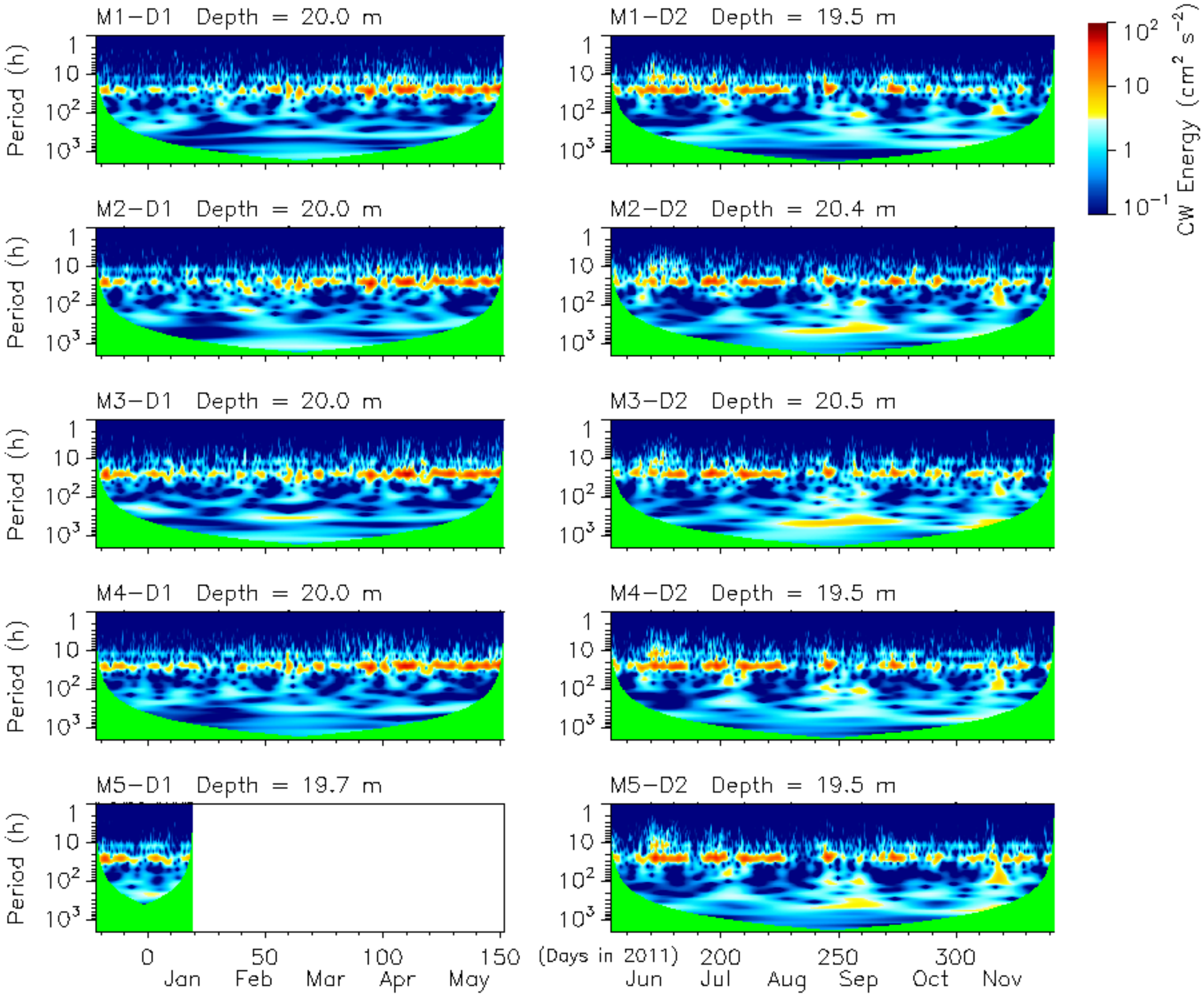

Figure 5. Clockwise energy for currents near depth = 20 m, as functions of period and time. Green areas indicate truncation limits, most evident for longer periods.

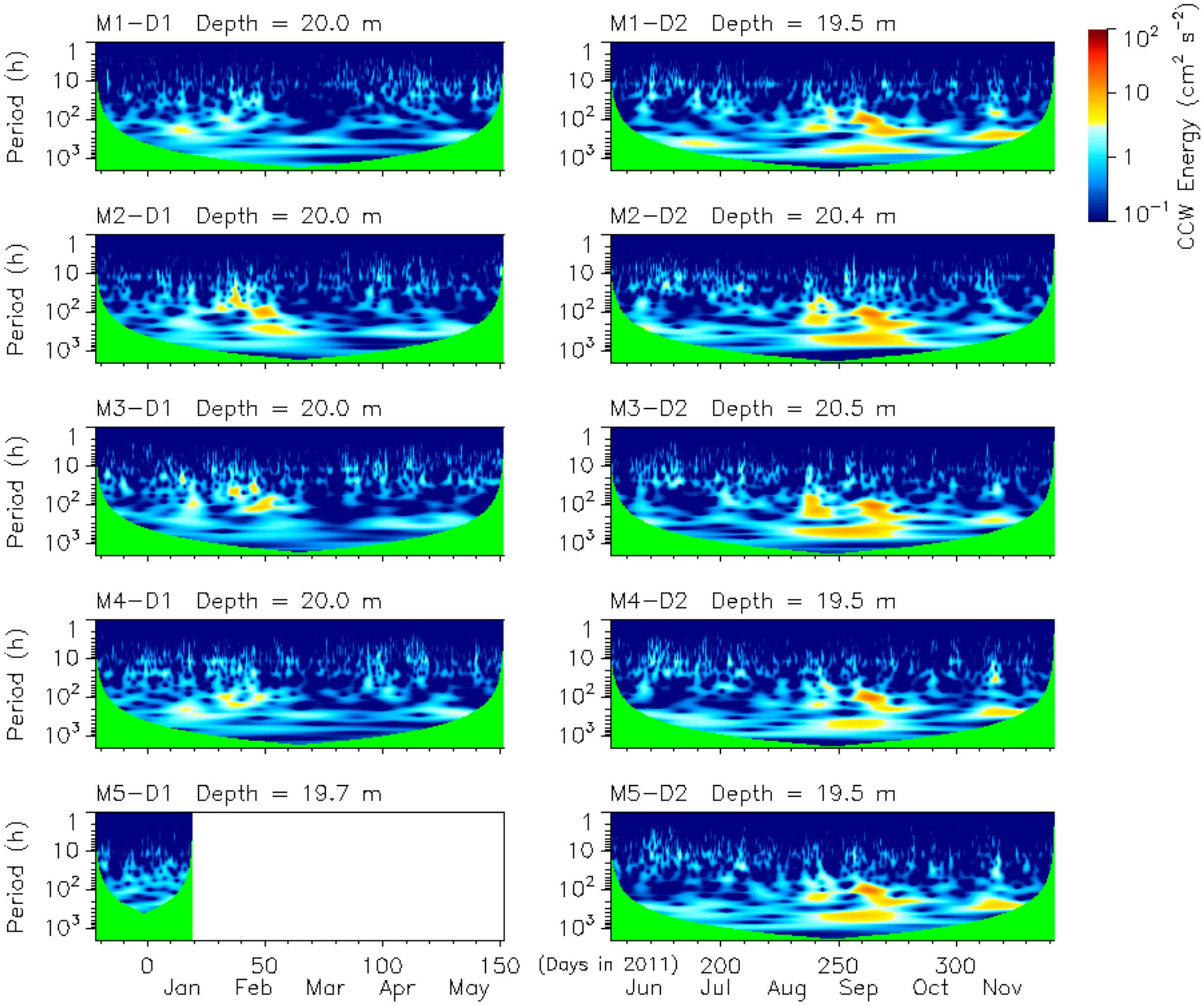

Figure 6. Counter-clockwise energy for currents near depth = 20 m, as functions of period and time. Green areas indicate truncation limits, most evident for longer periods.

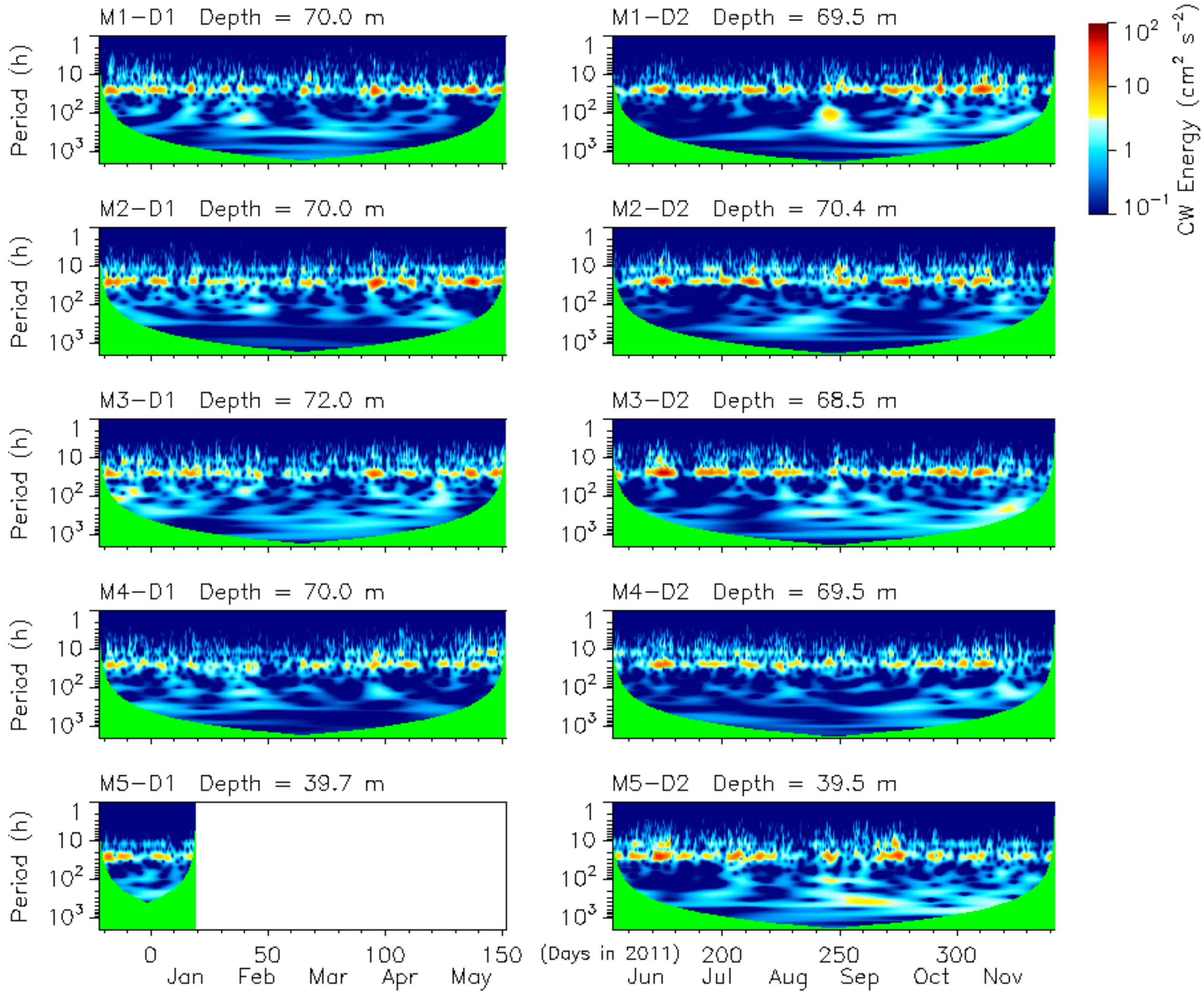

Figure 7. Clockwise energy for currents near depth = 70 m (M1–M4) and 40 m (M5), as functions of period and time. Green areas indicate truncation limits, most evident for longer periods.

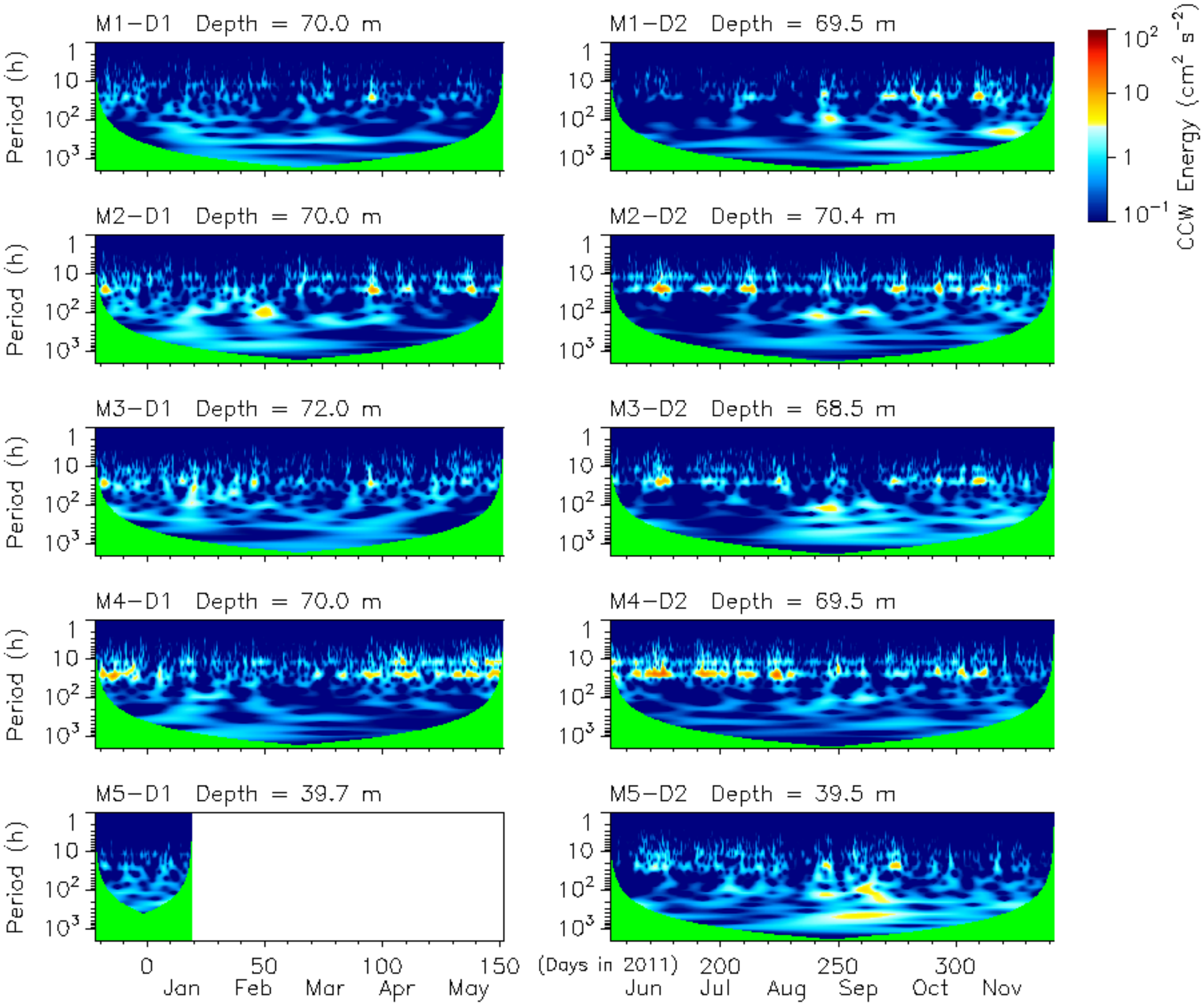

Figure 8. Counter-clockwise energy for currents near depth = 70 m (M1–M4) and 40 m (M5), as functions of period and time. Green areas indicate truncation limits, most evident for longer periods.

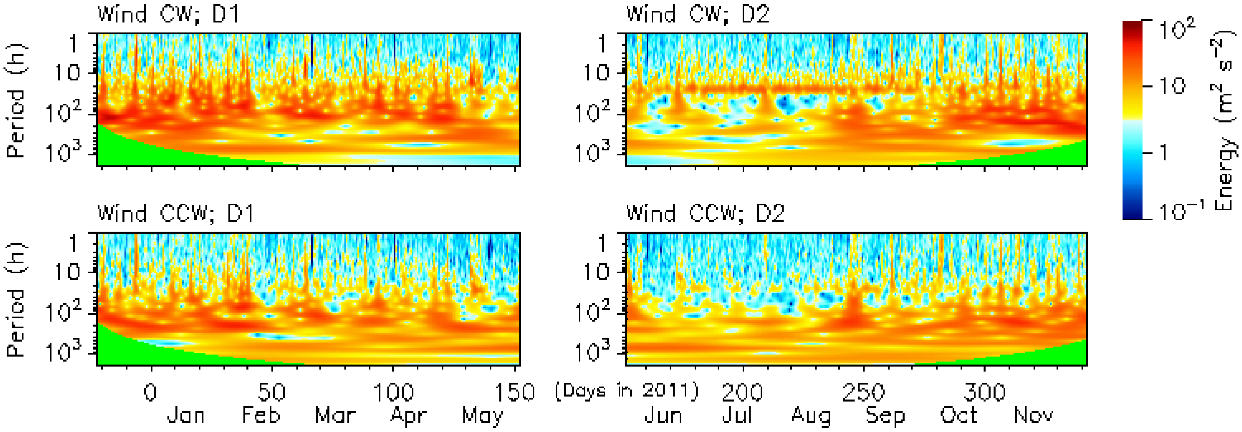

Figure 9. Clockwise and Counterclockwise wavelet wind energies. The time series was split to match the time intervals of the two ADCP deployments. Green areas indicate truncation limits, most evident for longer periods.

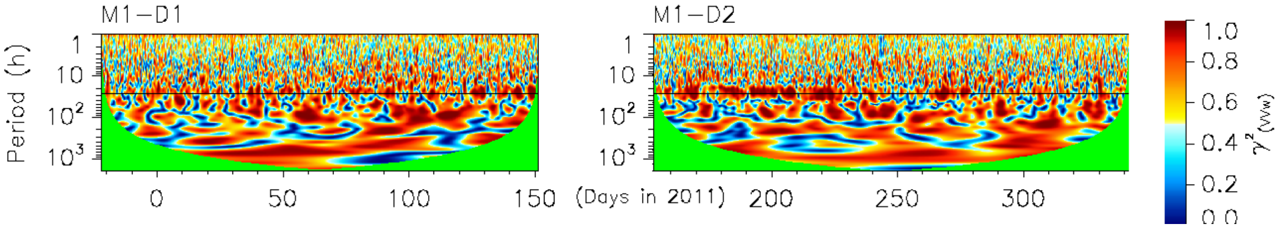

Figure 10. Coherence-squared between ~20 m northward current and northward wind at M1. The 5% significance level is about 0.85 for periods between 2 h and about 50 days, increasing gradually for longer periods. Green areas indicate truncation limits, most evident for longer periods. 24 h period is indicated by the black line.

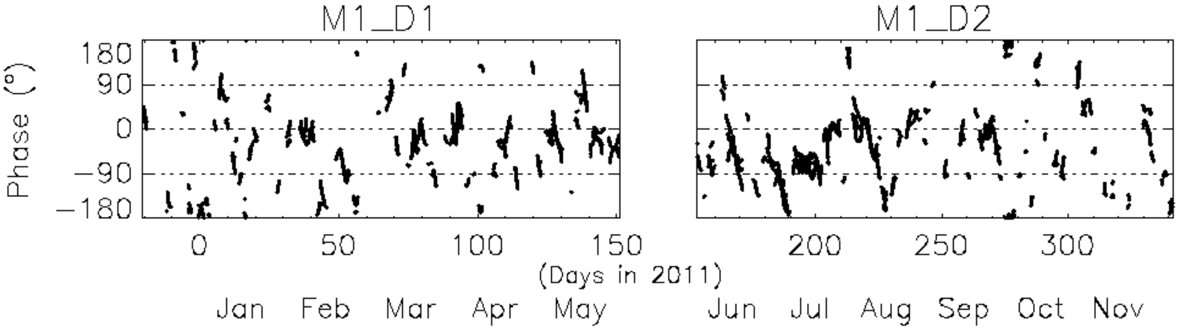

Figure 11. Temporal phase of ~20 m northward current relative to northward wind at M1, for three adjacent diurnal-inertial-band periods 19.656 h, 23.375 h, 27.798 h; positive phase indicates current leading wind.

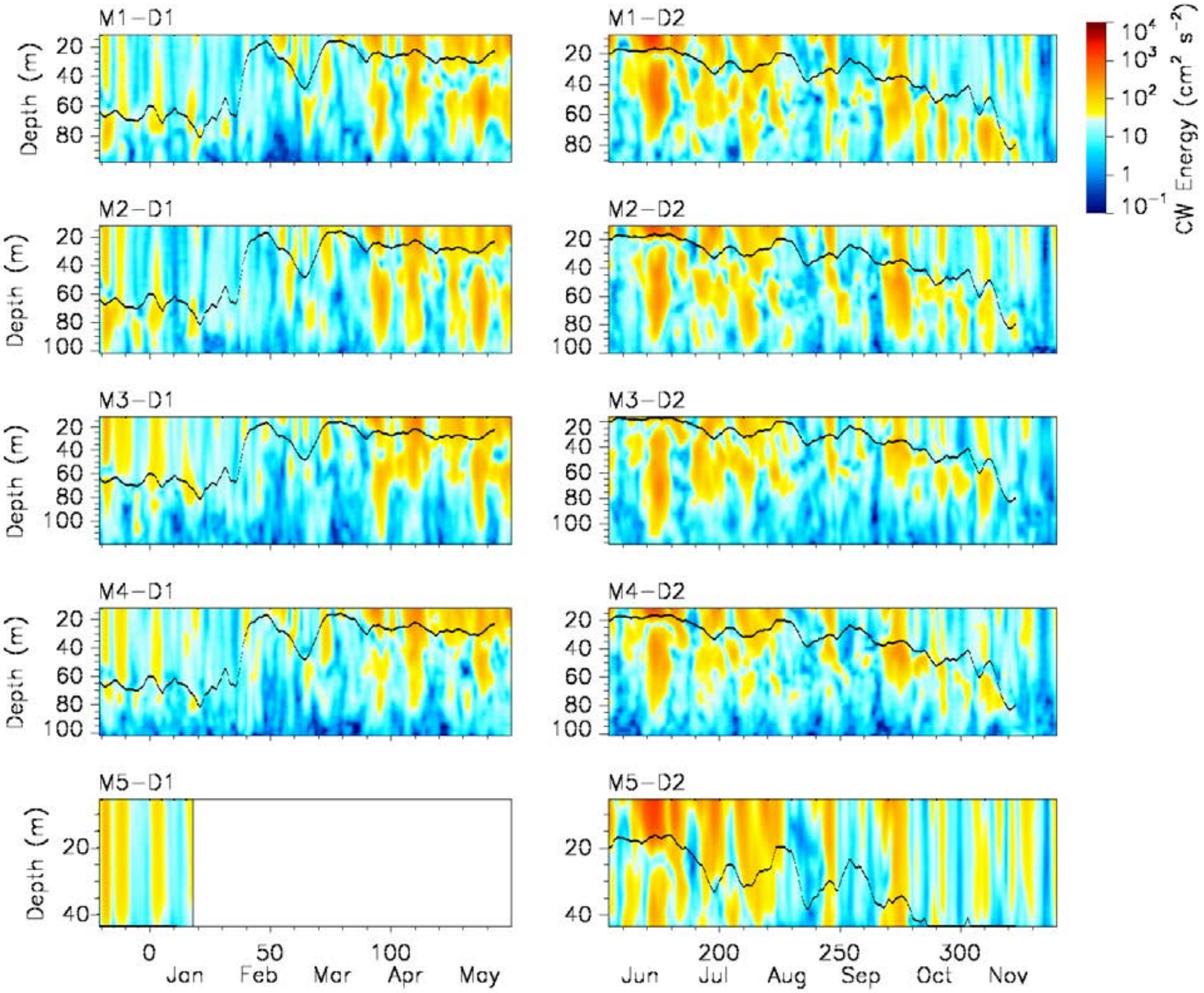

Figure 12. Clockwise spectra for diurnal-inertial-band (DIB) currents as functions of depth and time. Statistics averaged over two-day segments. The black curve represents mixed-layer depth.

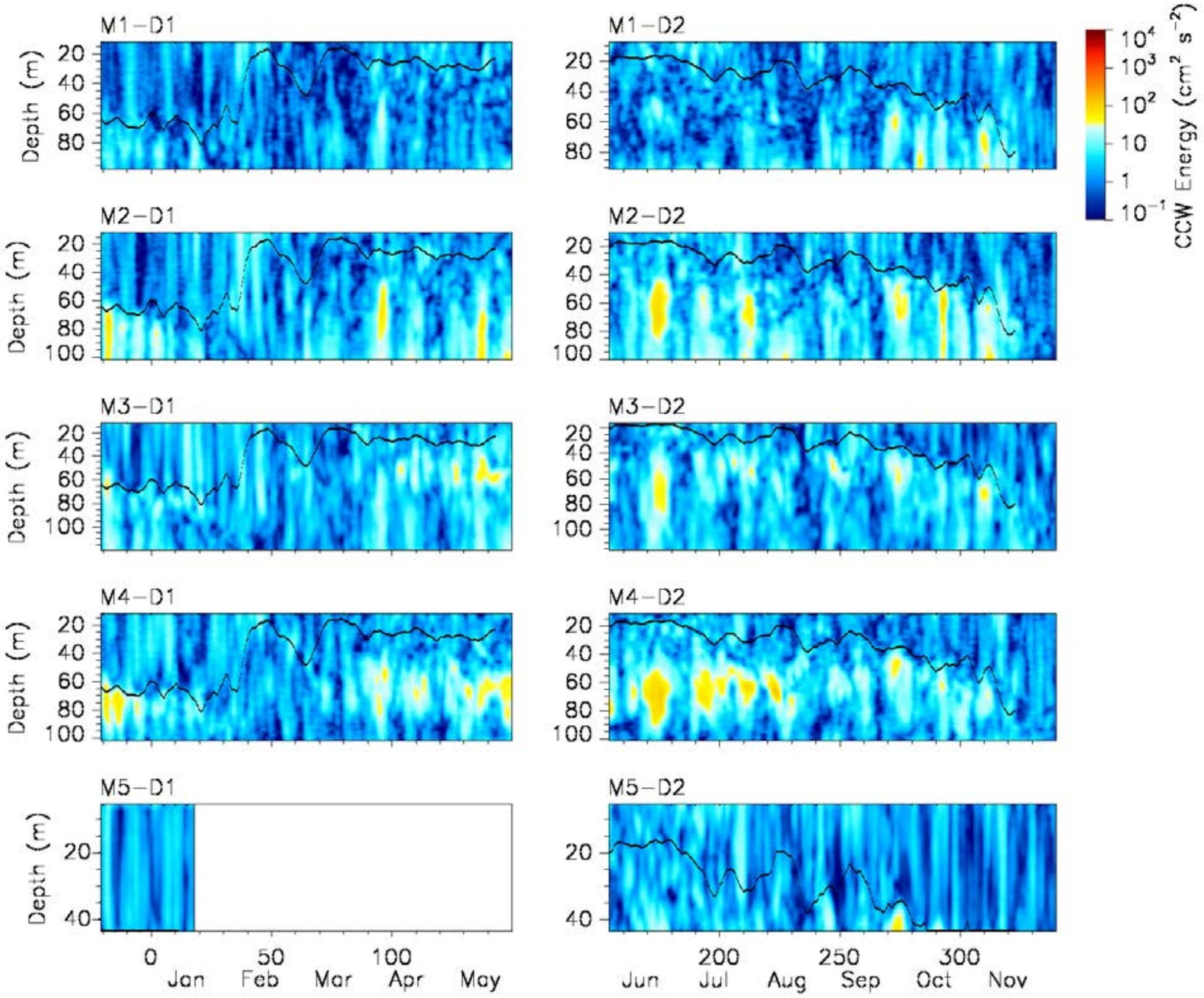

Figure 13. Counter-clockwise spectra for diurnal-inertial-band (DIB) currents as functions of depth and time. Statistics averaged over two-day segments. The black curve represents mixed-layer depth.

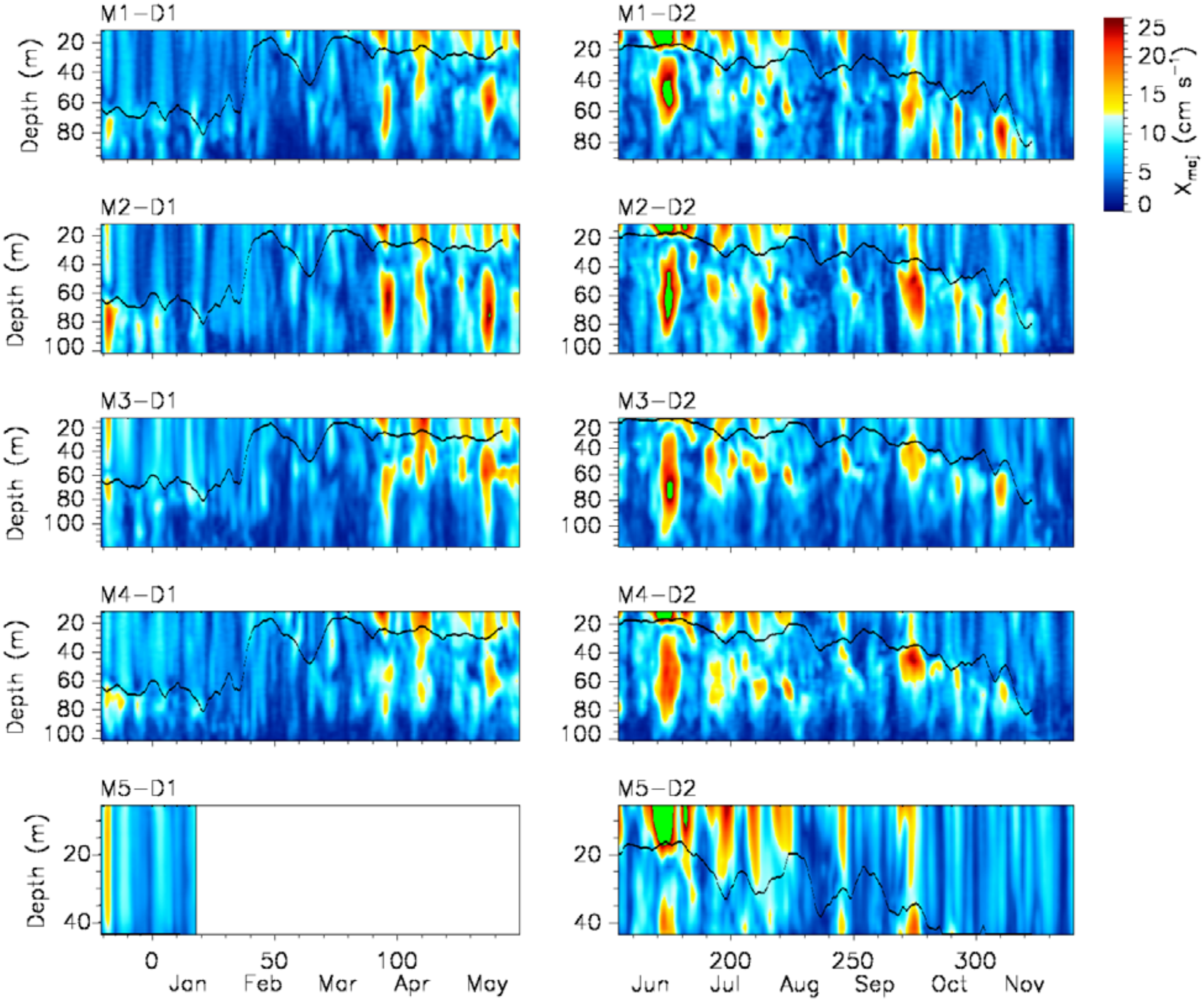

Figure 14. Semi-major axis length for DIB current ellipses. Green areas indicate values in excess of 25 cm s^{-1}. The black curve represents mixed-layer depth.

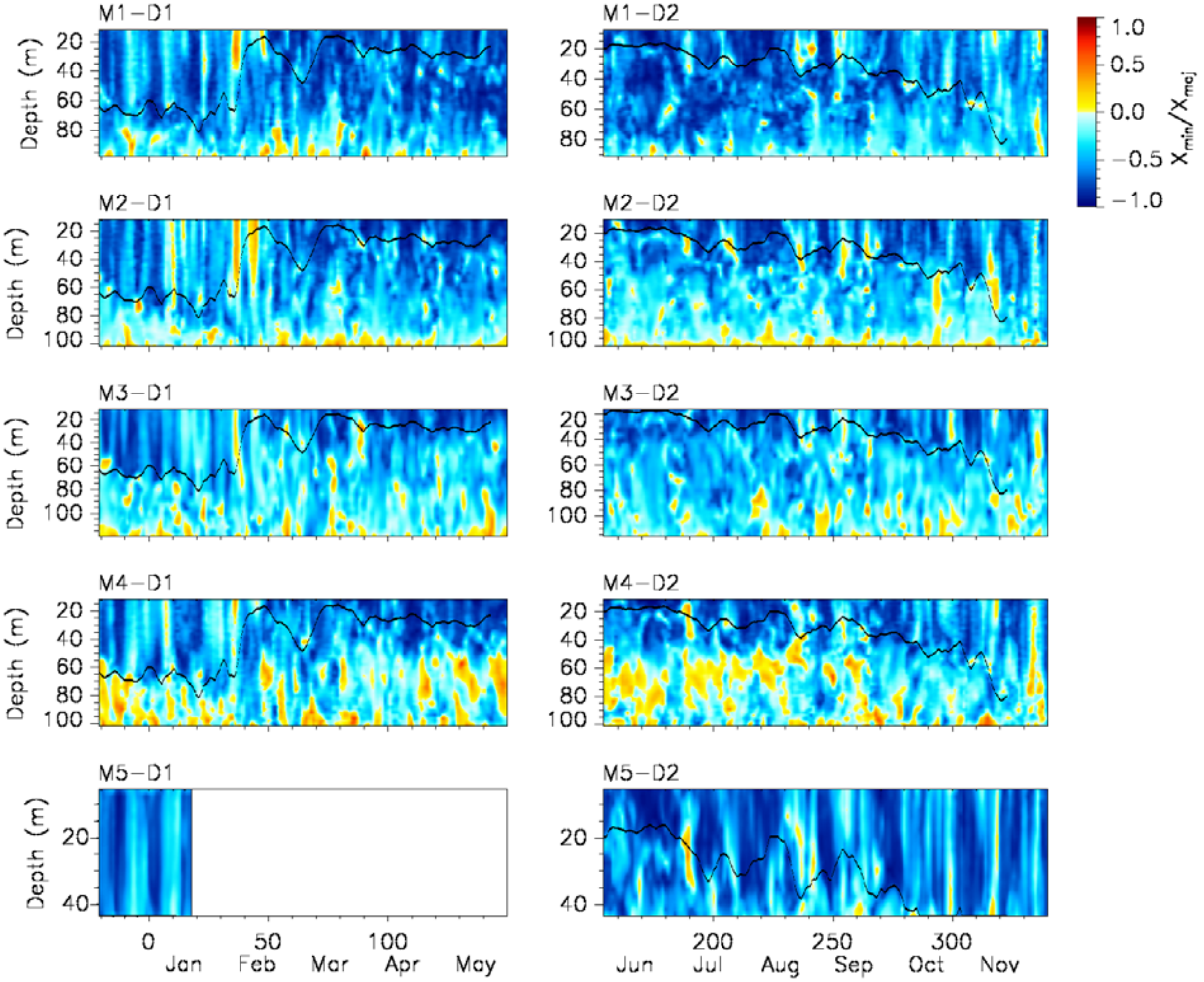

Figure 15. Ratio of minor to major axis for DIB current ellipses. Negative values indicate clockwise rotation of the current vector. The black curve represents mixed-layer depth.

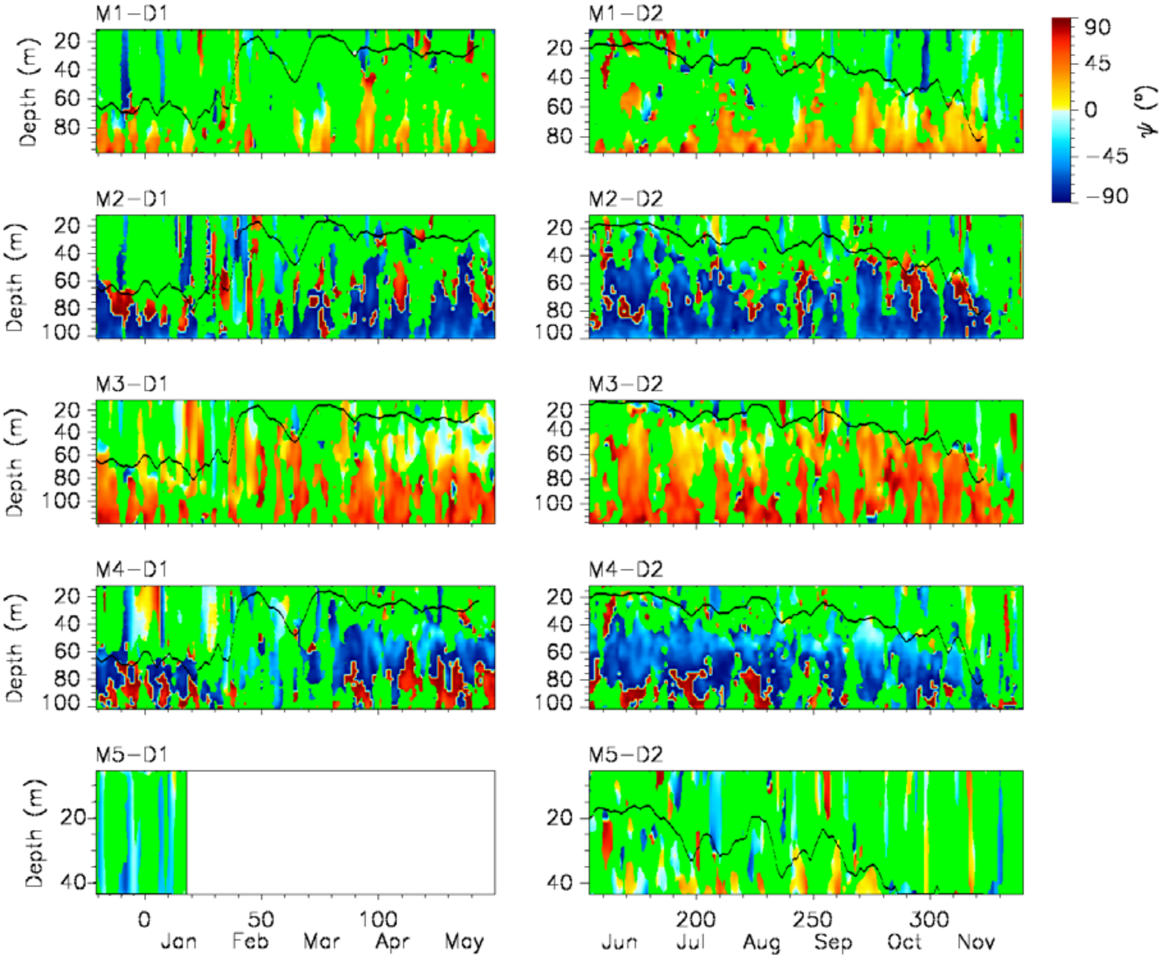

Figure 16. Orientations of DIB current ellipses. Positive values are counterclockwise from east-west. Green areas indicate orientations that are indeterminate due to uncertainties. The black curve represents mixed-layer depth.

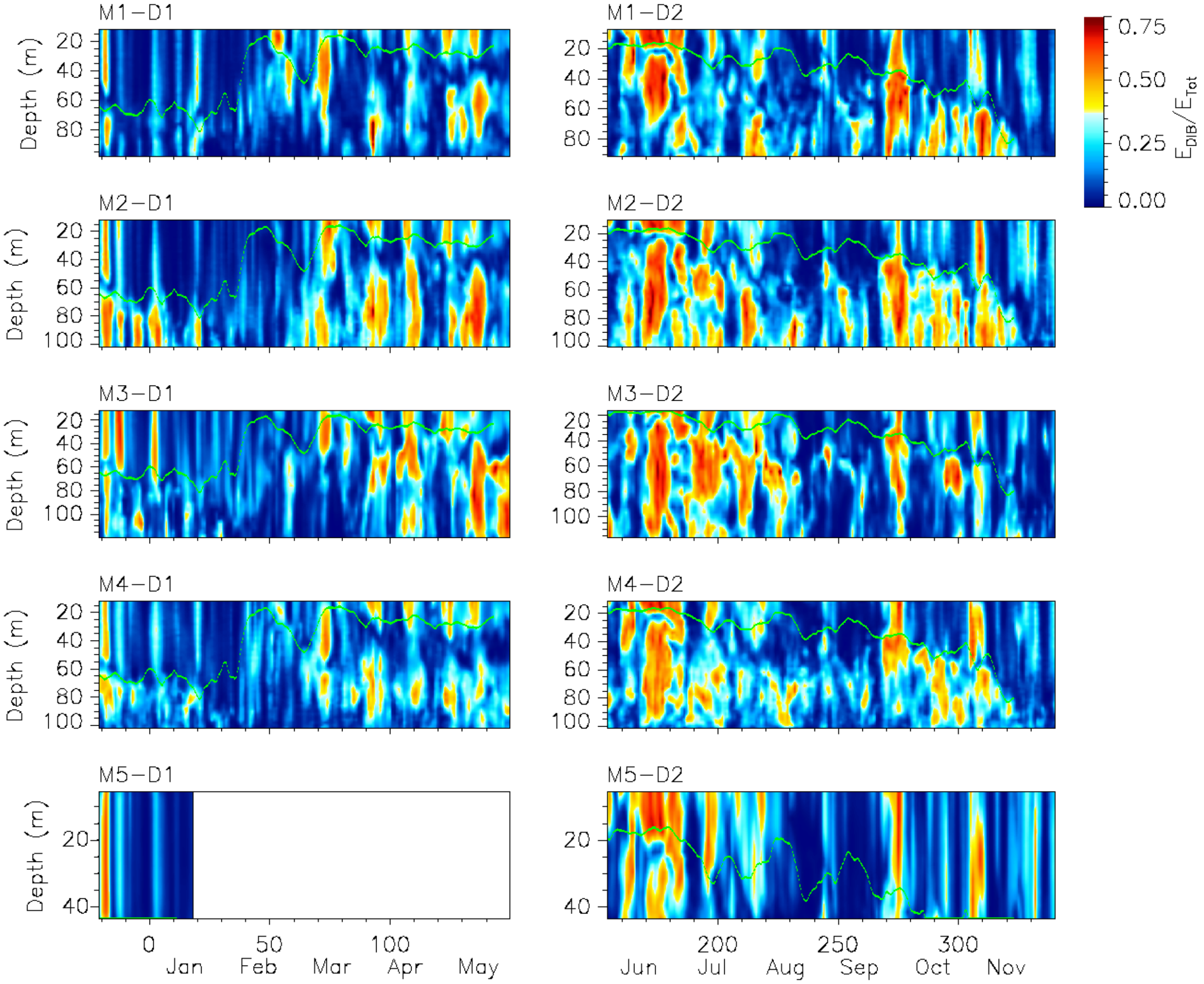

Figure 17. Ratio of DIB energy to total energy. The green curve represents mixed-layer depth.

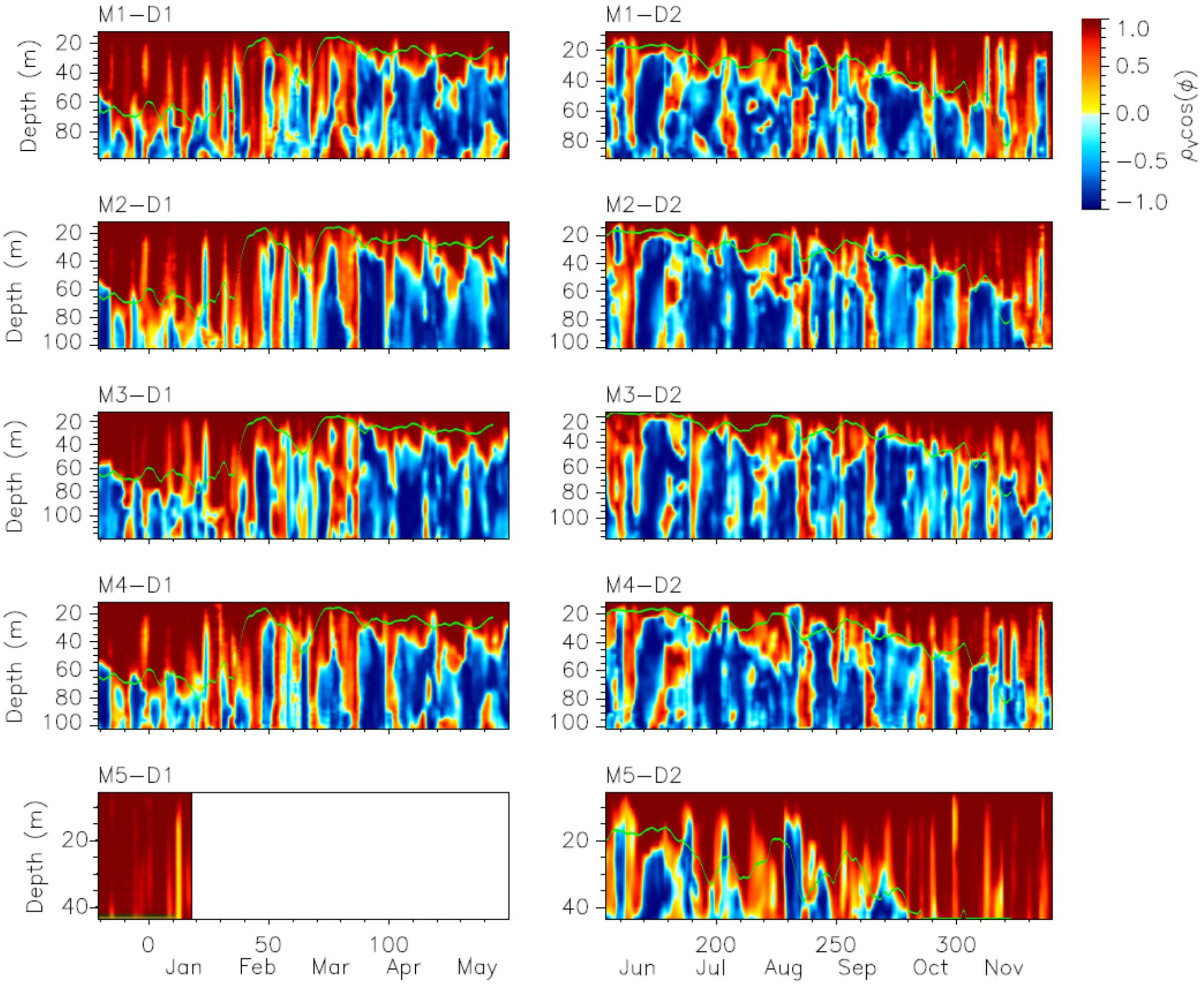

Figure 18. DIB zero-lag correlation for $V_D(z,t)$ relative to $V_D(z_0,t)$, where z_0 is the depth of the shallowest bin. The green curve represents mixed-layer depth.

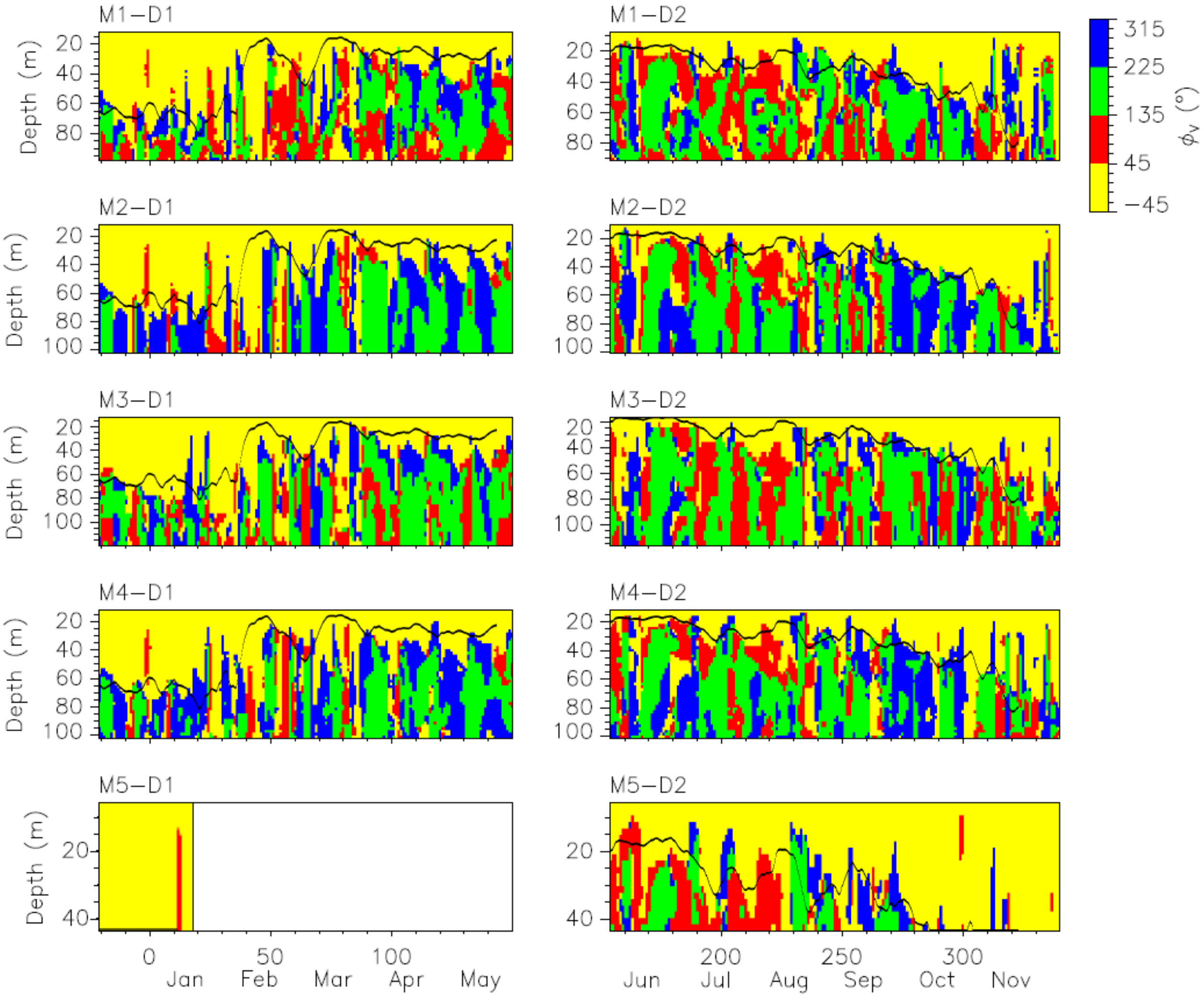

Figure 19. Lagged correlation phase (*Φ*) for V_D(z,t) relative to V_D(z_0,t), where z_0 is the depth of the shallowest bin. Phases are expressed in quadrants centered on 0º, 90º, 180º and 270º. The black curve represents mixed-layer depth. Currents are in roughly in phase for the -45º to 45º interval (yellow), have upward propagating phase for the 45º to 135º interval (red), have opposite phase for the 135º to 225º interval (green), and have downward propagating phase for the 225º to 315º interval (blue).

APPENDIX F

Mode-2 Hydraulic Control of Flow over a Small Ridge on a Continental Shelf

Mode-2 Hydraulic Control of Flow over a Small Ridge on a Continental Shelf

M.C. Gregg[1] and Jody M. Klymak[2]

[1]Applied Physics Laboratory, University of Washington, Seattle, Washington, USA
[2]School of Earth and Ocean Sciences, University of Victoria, British Columbia, Canada

Journal Citation:
Gregg, M.C. and J.M. Klymak, 2014. Mode-2 hydraulic control of flow over a small ridge on a continental shelf , Journal of Geophysical Research, submitted.

Abstract

Some of the most intense turbulence in the ocean has been found in hydraulic jumps found in the lee of sills where low internal modes are hydraulically controlled. Observations on the outer Texas-Louisiana continental shelf and modeling demonstrate hydraulic control of internal mode-2 over a 20-meter-high ridge on the 100-meter-deep continental shelf. Flow perturbations produced by the hydraulic response dominated the water column and included large vertical displacements in the weakly stratified surface layer overlaying the ridge. The mode-2 response differed in form from a hydraulic jump but produced turbulence one to two decades more intense than the local background.

Background and Introduction

Some of the most intense mixing found in the ocean occurs in hydraulic jumps found in the lee of sills lying across channels and straits when low internal modes are controlled over or near the sill crest (Farmer and Smith, 1980; Armi and Farmer , 1988; Wesson and Gregg , 1994; Ferron et al., 2003; Klymak and Gregg , 2004). More recent observations discovered hydraulic controls in the open ocean, specifically on the Hawaiian Ridge (Legg and Klymak , 2008; Alford et al., 2014) and over Stonewall Bank on the Oregon continental shelf (Moum and Nash, 2000; Nash and Moum, 2001). The former found intense mixing produced by high modes forced by barotropics tides crossing a large ridge rising from deep water, while the latter observed mode-1 controlled by episodic flows over a shallow bank. Here, we describe observations showing mode-2 control over a low ridge (h/D = 0.2) on the outer continental shelf in the Gulf of Mexico, where h is the height and D the water depth. Section 2 describes the bathymetry and sampling, and section 3 the stratification and flow. Observations of hydraulic control and its effects are presented in section 4, and modeling showing similar behavior is described in section 5. Results are summarized and their implications discussed in section 6.

Bathymetry and Sampling

East Flower Garden Bank is an exposed salt dome near the outer edge of the Texas-Louisiana continental shelf (Figure 1). Oriented roughly north-south, the bank is 6 km long and 4 km wide. Its summit lies 50 m below the surface and contains a small peak rising to 15 m. Northern and southern extensions of the bank form ridges rising above the surrounding shelf. Closely spaced profiles along lines 1 and 6 crossed these ridges with a depth-cycling towed body, revealing disturbed flow that was subsequently investigated more carefully with repeated transects along line 6 across the middle of the northern ridge. The northern ridge stands 20 m above the shelf, corresponding to h/D = 0.2 where D is the water depth (Table 1). It is relatively flat at 80 m depth for 1.4 km along and 1.4 km across line 6. Half a kilometer north of the line, the ridge descended to the shelf, and 800 m south of the line the bank rose steeply to 60 m depth. With a slope of 0.064, the east side descends to the shelf over 320 m, in contrast to the west side that requires 2,300 m to reach the shelf were is 5 m shallower than on the east side, giving a slope of 0.0073. For reference, the critical slope, $\alpha_c = \sqrt{(\omega^2 - f^2)/(N^2 - \omega^2)}$, is 0.0078 for M_2 tidal frequencies. Most of the energy, however, is close to $\omega_{K1} = 7.29 \times 10^{-5}\ s^{-1}$ which is slightly below the local inertial frequency of $f = 8.69 \times 10^{-5}\ s^{-1}$.

For a year beginning in December 2010, the Naval Research Laboratory (NRL) observed flow around and over the bank with an array of five Acoustic Doppler Current Profilers (ADCPs) mounted on the bottom (*Teague et al.*, 2013). The one on the bank, M5, was a 600 kHz Workhorse; the others, M1–M4, operated at 300 kHz. Between November 5 and 14, 2011, we sampled flows and scalar fields on and near the bank from R/V *Cape Hatteras*. Data from the M1 mooring provide background flows for this analysis and was used to force runs of the MITgcm.

SWIMS3, a depth-cycling towed body with upward and downward 300 kHz ADCPs was our primary instrument. In addition, the vehicle carried a Sea-Bird CTD with two sets of temperature and conductivity probes, sensors for dissolved oxygen and optical backscatter, and a fluorometer to detect chlorophyl. SWIMS3 data were taken in groups of related runs along tracks over the bank. This report focuses group 20, run between 0142 November 13 (year-day (yday) 316.0708) and 0339 November 14 (yday 317.152), where yday are elapsed days in 2011 starting at 0000 UTC on 1 January. The group consisted of 23 repeated SWIMS3 runs, termed subs, along line 6.

Background Stratification and Flow

Several days before group 20, a storm and cold air outbreak mixed the upper 60 m, with a strongly stratified interface, $\Delta\sigma = 1.2$ kg m^{-3}, separating the surface layer from the moderately stratified water just above the ridge (Figure 2). When group 20 began, the surface layer was also weakly stratified with an internal density step, $\Delta\sigma = 0.18$ kg m^{-3}, near 30 m. During group 20, the air was about 1°C cooler than the sea surface and wind stress was 0.15–0.02 Pa. Consequently, surface forcing was a minor factor in the evolution we observed in the upper layer.

As common in the Gulf of Mexico, daily tides were stronger than twice-daily ones (Figure 3). Sub-tidal currents dominated shallow flow at the M1 mooring, contributing about 80% of the current variance. The daily peak supplied the remainder and was dominant at greater depths, contributing about 75% of the variance. Analysis of the full record with T Tide (Pawlowicz et al., 2002) shows similar amplitudes for O1 and K1, but the short record during our cruise cannot distinguish between K1 (lunar-solar at $7.29 \times 10-5$ s^{-1}), O1 (lunar at 6.76×-5 s^{-1}), and near-inertial (f at $6.82 \times 10-5$ s^{-1}). The twice-daily tides, M2 and S2, contributed negligible variance.

SWIMS3 surveys over the entire bank usually found a net circulation around the bank below the interface. It was most commonly clockwise but reversed, apparently in response to the daily tide and low-frequency currents. During group 20 currents over the ridge were modest, rarely exceeding 0.25 ms^{-1} (Figure 4). Water below the interface flowed westward most of the time, reversing only after sub 16. Speeds above the interface were generally weaker than those below and also westward, except for two eastward bursts in the upper half. Progressive vector displacements (Figure 5) reveal that most water remained over the crest (3.8–4.0 km) during group 20. At the end of the group, water below 60 m ended 200 m west of where it began, and parcels between 20 and 40 m were displaced 400 m west and 200 m south.

A key parameter for flow over topography, $N\,h/U$ is sometimes interpreted as a Froude number or as a ratio of shear to stratification time scales (Klymak et al., 2010). Using N from upstream (eastward in most cases) at the depth of the ridge crest yields ratios of of about 2 (Table 2). This is well above the critical value for overturning over an asymmetric “Witch of Agnesi” profile (Baines, 1995). Although the ridge does not match this shape, the result is reasonably general, having also been found for other shapes. The very large values for NA/U, where A is the half-width, indicate that the flow should mostly be hydrostatic.

Hydraulic Responses to the Ridge

After estimating the hydraulic state of the flow over the ridge crest for each sub, sections of cross-ridge flow and density are used to examine structures associated with variations in control.

Hydraulic Control

Following the approach of Gregg and Pratt (2010), hydraulic control along line 6 was estimated using the Taylor-Goldstein equation written as

$$\frac{d^2\overline{w}}{dz^2} + \left[\frac{N^2}{(U-c)^2} - \frac{1}{(U-c)}\frac{d^2U}{dz^2}\right]\overline{w} = 0$$

where the eigenvalue c is the phase speed of the corresponding eigenfunction $\overline{w}(z)$. Because the ridge is aligned north-south, east-west velocity, U , was used.

Plotting speeds of the first 5 EOF modes in (Figure 4) shows that mode-1 was never close to being controlled, but mode-2 was controlled for eastward (positive) flow between subs 12 and 16, corresponding to yday of 316.66 to 316.85, an interval of almost 5 hours. Higher modes were controlled for slightly longer. Control occurred when the dominantly diurnal barotropic tide was at its peak westward flow. Near the end of the measurements, mode-5 was controlled for westward (negative) flow. Corresponding eigenfunctions are shown in Figure 6

Flow Structures

Even though none of the first five modes were controlled before sub 10, the interface was very active (Figure 7). Strong straining produced alternating regions of compression and extension from horizontal scales of several hundred meters to several kilometers. The structure in sub 6 suggests generation of a lee wave over the western side.

Mode-2 control developed when the entire water column over the ridge crest was flowing westward (Figure 4). West of the crest, however, the lower layer was beginning to flow eastward, finally ending control of mode-2 when it crossed the crest just before sub 17 (Figure 8). As increasing westward flow brought the profile close to mode-2 control, upward and downward bulges were found over the crest. When mode-2 was controlled, the lower part of the interface expanded just west of the crest, forming a weakly stratified wedge in the shear zone between oppositely directly flows above and below the interface. This is most evident in sub 16. Simultaneously, the density step within the upper layer descended east of the ridge.

As control was lost, bore-like features appeared above and below the center of the interface in sub 17. In the upper layer the top of this feature was formed by descent of the density step within the layer, leaving very weakly stratified water above 40 m. During subsequent subs, these features propagated eastward, forming a hydraulic response over the east side in the layer and a growing bulge in the top of the interface. During sub 19 a large trough and 20-m overturn formed in the upper layer at the leading end of this disturbance, as shown dramatically by fluorometer record (Figure 9). This is but one example of strong coupling of structures in the surface layer with flow over the ridge below the interface.

Mixing

Where overturns occur as local instabilities, the length scales of the overturns can be used to infer turbulent dissipation rates, ε (Dillon, 1982). In Knight Inlet, overturns were so large that ϱ from them compared favorably with direct measurements (Klymak and Gregg , 2004). Applying the same approach to overturns here and averaging across the subs, yields a cloud with 10^{-6} to 10^{-7} W kg^{-1} over the ridge from its eastern face to well down its western flank (Figure 10). Between 1 and 5 km, the group average below 60 m is 5.0×10^{-8} W kg^{-1}. On either end, dissipation rates several decades smaller are interspersed with weaker from more intermittent overturns.

The diapycnal diffusivity, $K_\rho = 0.2\,\varepsilon / N^2$, was computed for each overturn using the sorted monotonic density to compute N^2. Owing to the large variations in interface position and structure, it would not be representative to compute K_ρ using the group- average dissipation rates and stratification. The group-average (Figure 10, lower panel) exhibits the same pattern as ε with magnitudes of 10^{-4} to 10^{-3} m^2 s^{-1} in the cloud over the ridge. Although the dissipation rates were several decades smaller than those in the hydraulic response over Stonewall Bank, owing to the weaker stratification, diapycnal diffusivities were comparable.

Model Results

A hydrostatic MITgcm (Marshall et al., 1997) was set up with high-resolution bathymetry, initialized with observed farfield density profiles, and globally forced with upstream barotropic velocity profiles measured at NRL mooring M1. Because the forcing does not represent the full complexity of the flow, the purpose of the model runs is to test inferences of mode-2 control under conditions roughly similar to those observed.

Lateral resolution was refined near the ridge with $dx = 30$ m within 100 grid cells of the ridge crest and $dy = 50$ m within 160 grid cells. In a halo outside this region, resolution telescopes to $dx = 2500$ m and $dy = 3000$ m. Vertical resolution increased linearly from 1 m at 60-80 m depth, the depth of the ridge crest, to 7 m at the surface and bottom, set at 145 m. Vertical and lateral viscosity and diffusivity had background values of 10^{-5} m^{2}s^{-1} and 10^{-4} m^{2}s^{-1} which were enhanced in density overturns using Ozmidov and Osborn relations, as described in Klymak and Legg (2010). Advection used a non-linear Superbee scheme (van Leer , 1979), a technique to avoid spurious oscillations in high-resolution models.

Hydraulic analysis of modeled flow over the ridge crest, shows mode-2 control similar to that found using currents observed over the ridge (Figure 11). Control, however, began nearly half a day sooner (yday 316.1) than observed and lasted 16.8 hours (until yday 316.8), nearly three times as long as observed. This occurred because westward flow forcing the model was more uniform vertically than that observed over the ridge. In particular, the eastward flow that ended control in the observations was not included in model forcing.

Early during mode-2 control, the interface was depressed about 10 m over the center of the ridge, constricting and accelerating westward flow in the lower layer (Figure 12, upper left). The downward bulge was steeper and more diffuse on the west side than on the east. Simultaneously, isopycnals throughout the surface layer were elevated above, rising toward the east until being sharply depressed over the eastern end of the interface depression and rising again farther east. This wave, extending about 3 km horizontally and with a vertical amplitude of about 15 m, persisted in place with minor changes while mode-2 was controlled. The depression, however, thickened and broadened in response to mixing, while its lower part was carried westward by the flow in the lower layer (Figure 12, upper right). The upper layer response differed greatly from our observations, most likely because the density profile that initialized the model at the western side of the domain did not reflect the internal stratification of the layer found over the ridge. When control was lost, the interface depression relaxed as the disturbance began to propagate eastward (Figure 12, lower left). As it moved past the ridge, the leading edge evolved into bore-like structures above and below the interface that resembled those we observed (Figure 12, lower right).

Over the ridge the model produced strong dissipation with roughly the same pattern as that observed (Figure 13). Between -3 and 1 km in model coordinates (equivalent to 1-5 km in the observations) the average was 4.7×10^{-7} W kg^{-1}, nearly ten times the observed average. This is a larger discrepancy than expected, but we did not expect close agreement owing to contrasts between forcing and observed flows and the resulting difference in the duration of control.

Vertical diffusivities, K_v, were highest over the western slope, where stratification was weakest, with magnitudes exceeding 0.1 m^2 s^{-2} and averages above 10^{-3}. The diffusivity pattern is similar to that observed (Figure 10), but the magnitudes are also a decade larger. Time series of section averages demonstrate ε and K_v rising as mode-2 was controlled and falling when control was lost (Figure 14). The observations do not behave as regularly, which we also attribute to differences in real and model forcing.

Summary and Discussion

Our principal findings are:

- Flow across a 20-m-high ridge on a 100-m-deep continental shelf was critical to internal mode-2 for three hours while the water column flowed westward with maximum speeds somewhat less than -0.2 m s^{-1}. The profile was weakly stratified to 60 m, and internal mode-1 was never close to being controlled.

- During mode-2 control, the interface was depressed over the ridge crest, and overlying isopycnals were elevated throughout the weakly stratified surface layer. When control was lost the displacements propagated eastward, possibly as a bore along the interface that was related to large overturns were observed in the surface layer. These overturns carried fluid with high chlorophyll concentrations upward from the interface into most of the surface layer.

- Average dissipation rates below the interface and over the ridge were 10^{-8} to 10^{-7} W kg^{-1}, one to two decades larger than nearby background levels. Corresponding diapycnal diffusivities were 10^{-4} to 10^{-3} m^2 s^{-1}.

- A simulation with the MITgcm forced by barotropic currents measured at an NRL mooring captured the mode-2 control and eastward propagation of the disturbance after control was lost. Dissipation rates produced in the model were about one decade larger than those observed.

- With $h/D = 0.2$, the ridge is similar to Stonewall Bank on the Oregon shelf, but currents during our observations were relatively weak. Consequently, we observed mode-2 control rather than the mode-1 control found by Moum and Nash (2000) and Nash and Moum (2001) over Stonewall. Nonetheless, observed and modeled dissipation rates and diapycnal diffusivities rose by one to two decades over the primary region of control. These observations demonstrate that control of mode-2, and perhaps higher modes, can affect mixing over rough bottoms nearly as much as does mode-1 control. Moreover, this control can be simulated numerically, raising the prospect of being able to predict the dominant mixing once accurate energy balances are developed for the diverse set of hydraulic controls being found.

- The large responses observed in the surface layer over a ridge occupying only the bottom 20% of the water column demonstrate that mixed layer studies over continental shelves cannot be conducted without considering the effect of relatively small bottom roughness.

Acknowledgments

The Office of Naval Research (ONR) funded our measurements and analysis as part of their Mixing over Rough Topography (MORT) program. The Naval Research Laboratory was also funded by ONR and for the Currents over Banks project by the Bureau of Ocean Energy Management. We thank Bill Teague and Hemantha Wijesekera for including us in these programs and making data from their ADCP moorings available for our analysis. Captain Dale Master and the crew of the R/V *Cape Hatteras* provided excellent support that allowed us to collect the maximum amount of data, sometimes in difficult sea states. Steve Bayer, Tim McGinnis, Chris Siani, Dave Winkel, and Andrew Cookson from the Applied Physics Laboratory of the University of Washington ran our instruments with care and skill, and Jules Hummon (University of Hawaii) fixed problems with shipboard ADCP data.

References

Alford, M., J. Klymak, and G. Carter (2014), Breaking internal lee waves at Kaena Ridge, Hawaii, Geophys. Res. Lett., 41, 906–912, doi:10.1002/2013GL059070.

Armi, L., and D. M. Farmer (1988), The flow of Mediterranean water through the Strait of Gibraltar, in Progress in Oceanography, edited by M. V. Angel and R. L. Smith, pp. 1–105, Pergamon Press, Oxford.

Baines, P. (1995), Topographic effects in stratified flows, 1st ed., 482 pp., Cambridge, Cambridge, U.K.

Dillon, T. M. (1982), Vertical overturns: A comparison of Thorpe and Ozmidov length scales, J. Geophys. Res., 87, 9601-9613.

Farmer, D. M., and J. D. Smith (1980), Tidal interaction of stratified flow with a sill in Knight Inlet, *Deep-Sea Res.*, *27A*, 239–254.

Ferron, B., H. Mercier, K. Speer, A. Gargett, and K. Polzin (2003), Mixing in the Romanche Fracture Zone, J. Phys. Oceanogr., *28*, 1929–1945.

Gregg, M., and L. Pratt (2010), Flow and hydraulics near the sill of Hood Canal, a strongly sheared, continuously stratified fjord, J. Phys. Oceanogr., 40, 1087–1105, doi: 10.1175/2010JPO43121.

Klymak, J., and S. Legg (2010), A simple mixing scheme for models that resolve breaking internal waves, Ocean Modelling, 33 (3-4), 224–234.

Klymak, J., S. Legg, and R. Pinkel (2010), High-mode stationary waves in stratified flow over large obstacles, J. Fluid Mech., 664 (321-336), doi:10.1017/S0022112009992503.

Klymak, J. M., and M. C. Gregg (2004), Tidally generated turbulence over the Knight Inlet sill, J. Phys. Oceanogr., 34, 1135-1151.

Legg, S., and J. Klymak (2008), Internal hydraulic jumps and overturning generated by tidal flow over a tall steep ridge, J. Phys. Oceanogr., 38, 1949–1964, doi:10.1175/2008JPO03777.1.

Marshall, J., A. Adcroft, C. Hill, L. Perelman, and C. Heisey (1997), A finite-volume incom- pressible Navier-Stokes model for studies of the ocean on parallel computers, J. Geophys. Res., 102 (C3), 5753–5766.

Moum, J., and J. Nash (2000), Topographically induced drag and mixing at a small bank on the continental shelf, J. Phys. Oceanogr., 30 (8), 2049–2054.

Nash, J., and J. Moum (2001), Internal hydraulic flows on the continental shelf: High drag states over a small bank, J. Geophys. Res., 106 (C3), 4593–4612.

Pawlowicz, R., R. Beardsley, and S. Lentz (2002), Classical tidal harmonic analysis including error estimates in MATLAB using T TIDE, Computers & Geosciences, 28, 929–937.

Teague, W., H. Wijesekera, E. Jarosz, D. Fribance, A. Lugo-Fern´andez, and Z. Hallock (2013), Current and hydrographic conditions at the East Flower Garden Bank in 2011, Cont. Shelf Res., 63, 43-58.

van Leer, B. (1979), Towards the ultimate conservative difference scheme, J. Comput. Phys., 32, 101–136.

Wesson, J., and M. Gregg (1994), Mixing at Camarinal Sill in the Strait of Gibraltar, J. Geophys. Res., 99, 9847-9878.

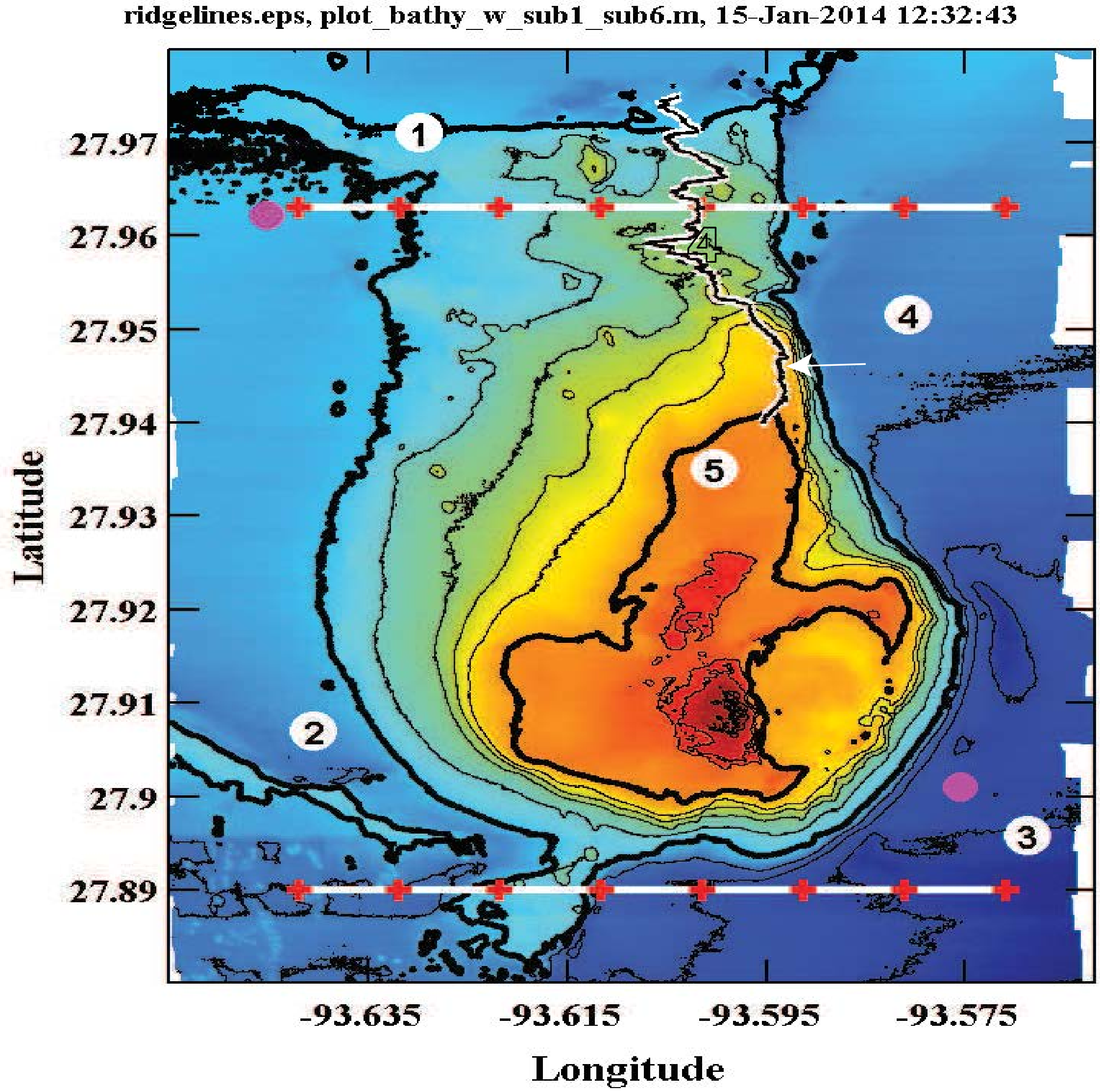

Figure 1. Bathymetry of East Flower Garden Bank, on the edge of the continental shelf. Contours have 10 m intervals and are thickened at 50 and 100 m. The black-over-white line marks the ridge crest north of the bank's top. Numbered white circles mark locations of NRL ADCPs M1 to M5, and pink circles indicate oil platforms. Repeated SWIMS runs were made across the ridge north of the bank along line 6, and occasional runs were made over the southern ridge along line 1. Both lines are marked at 1 km intervals.

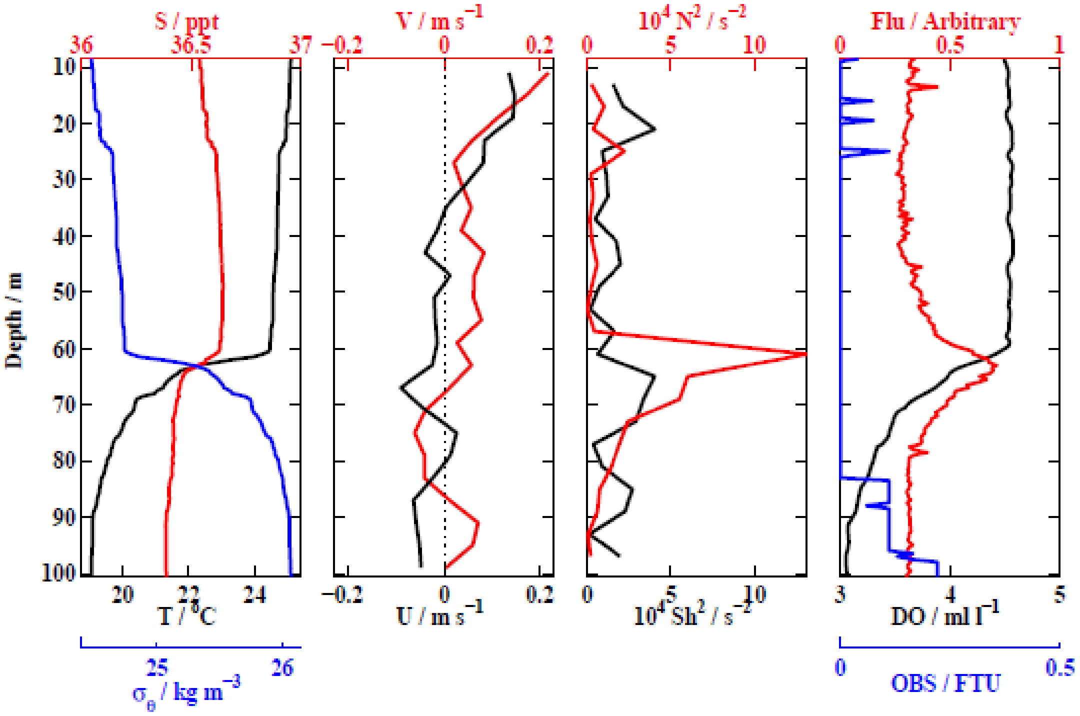

Figure 2. Stratification and flow near the east end of line 6 during group 20 sub 1, the first of the 25-hour time series along the line. In the rightmost panel, DO is dissolved oxygen, OBS is optical backscatter, proportional to particulate density, and Flu is the fluorometer signal, proportional to chlorophyll. The OBS signal is elevated at the bottom and extends slightly above the homogenous bottom boundary layer.

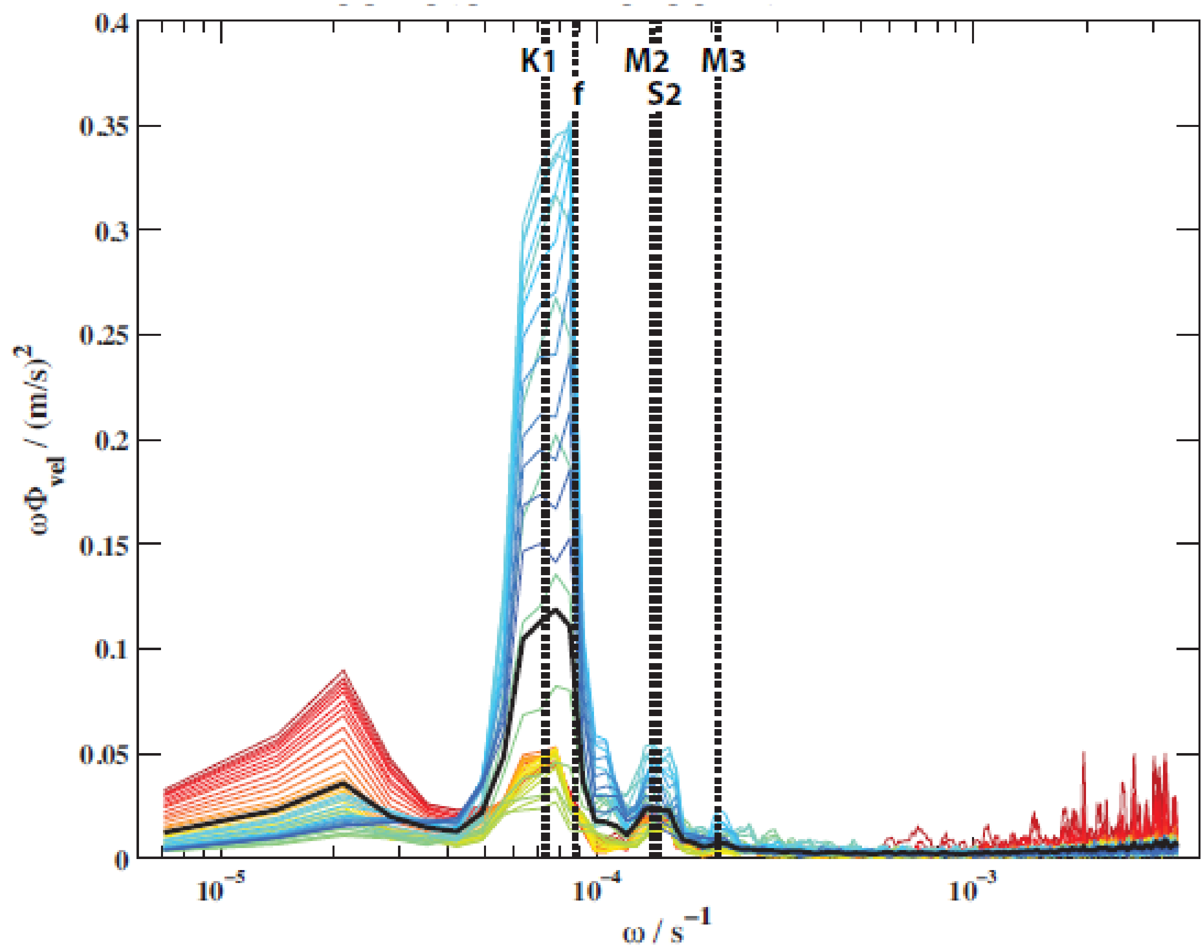

Figure 3. Variance-preserving frequency spectra of velocity at M1 during the 10 days of our cruise. Spectra are colored by depth, with red shallow and blue deep. The black line is the vertical average of the spectra. Sub-tidal frequencies dominate shallow depths, and the K1 is the major contributor at deeper depths. Variance in the twice-daily signal, M2 and S2, is negligible.

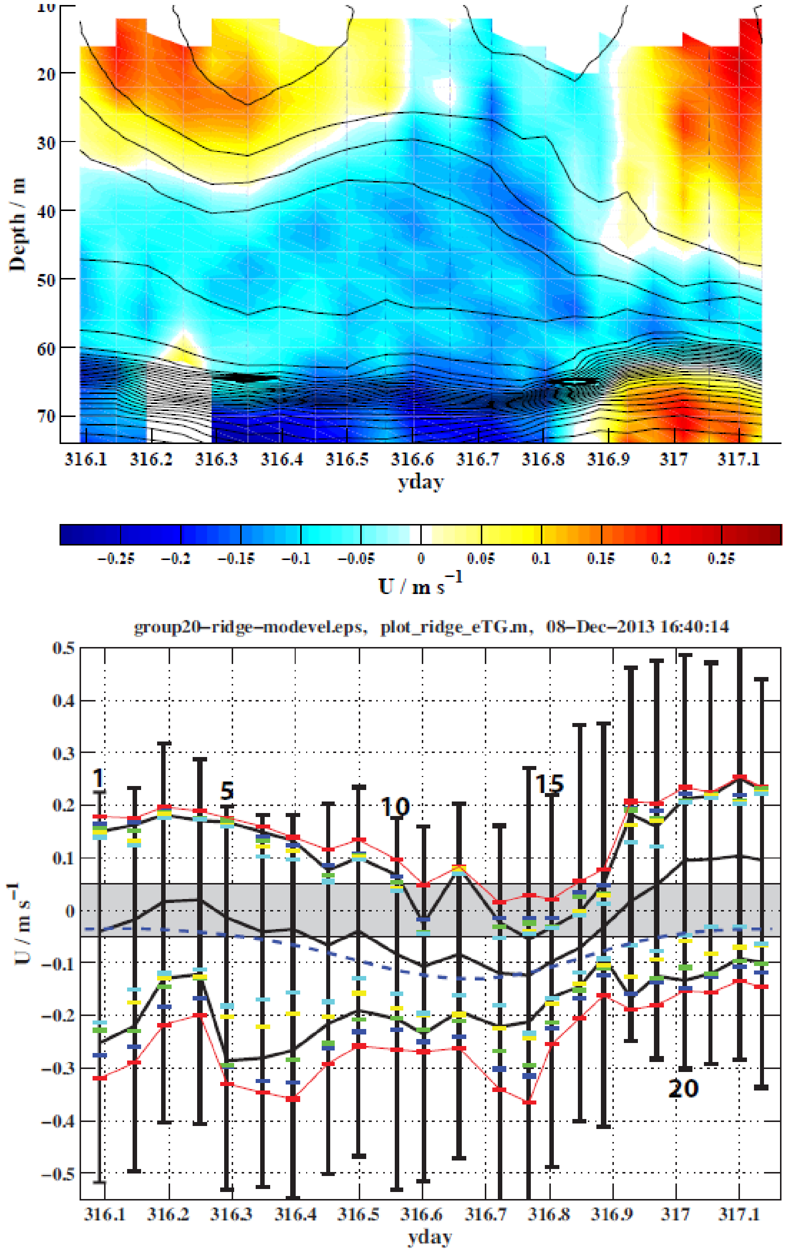

Figure 4. (Upper) East/west flow (colors) and σ_θ contours at intervals of 0.025 kg m^{-3}, over the ridge crest (3.8–4.0 km in Figure 1). (Lower) Speeds of internal EOF modes 1-5. Vertical lines in the upper panel mark positive (eastward) and negative (westward) speeds of the first EOF mode for each sub. Ticks on the lines are speeds of higher EOF modes: 2 (black), 3 (blue), 4 (yellow), and 5 (cyan). Modes are considered critical when within the shaded region of ±0.05 m s^{-1}. Thick black lines from left to right are the maximum, average, and minimum cross-ridge speeds. The blue dashed line is the tide computed using T TIDE (Pawlowicz et al., 2002). Mode-1 was never close to being critical, but mode-2 was controlled for eastward flow between 316.65 and 316.85, when the full water column was flowing westward.

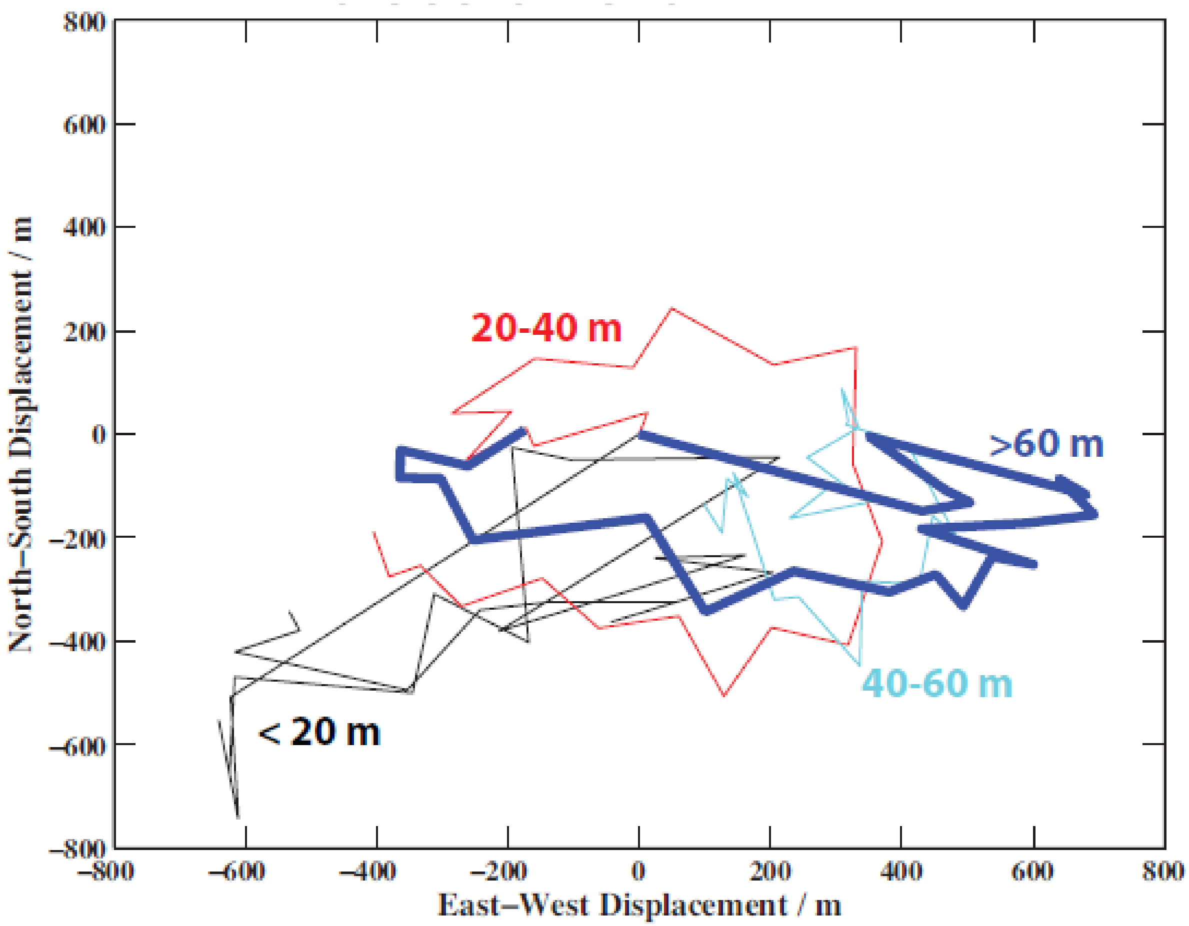

Figure 5. Cumulative displacements during group 20 estimated from velocities measured over the ridge crest, showing that none of the water moved off the ridge.

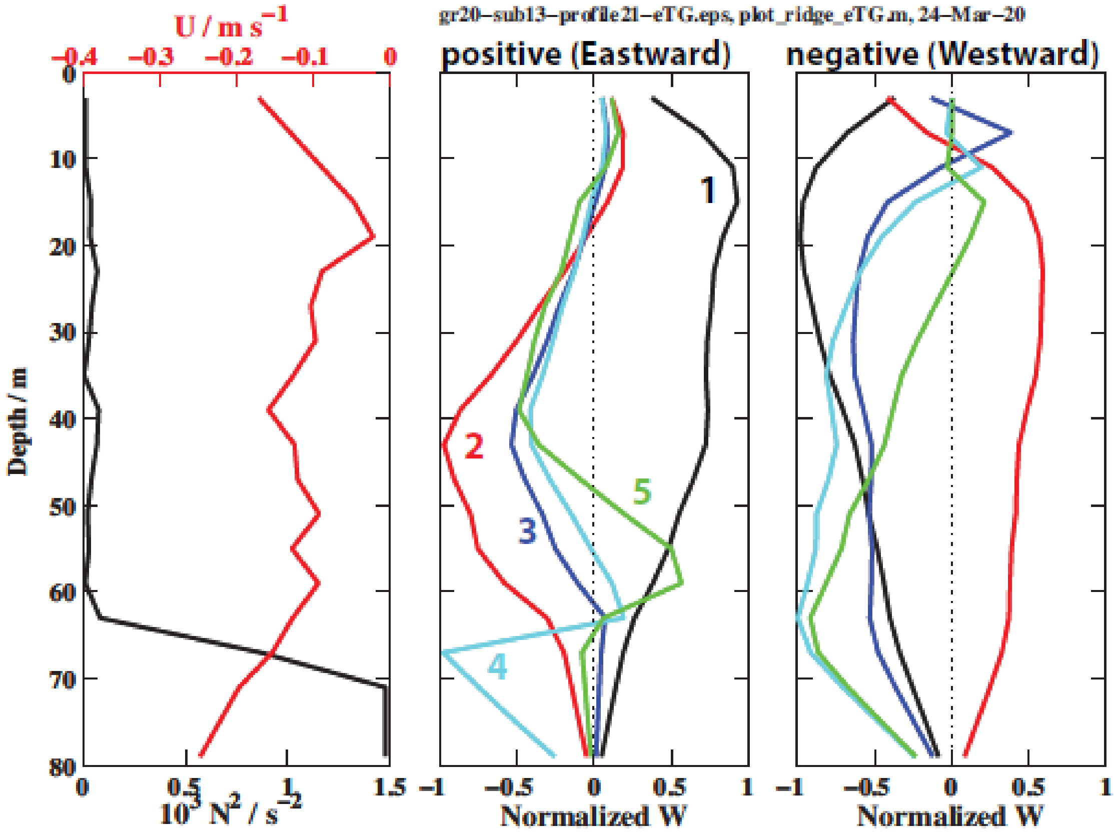

Figure 6. Potential density, σ_θ –and *u* over the ridge during sub 16 with the first 5 vertical modes.

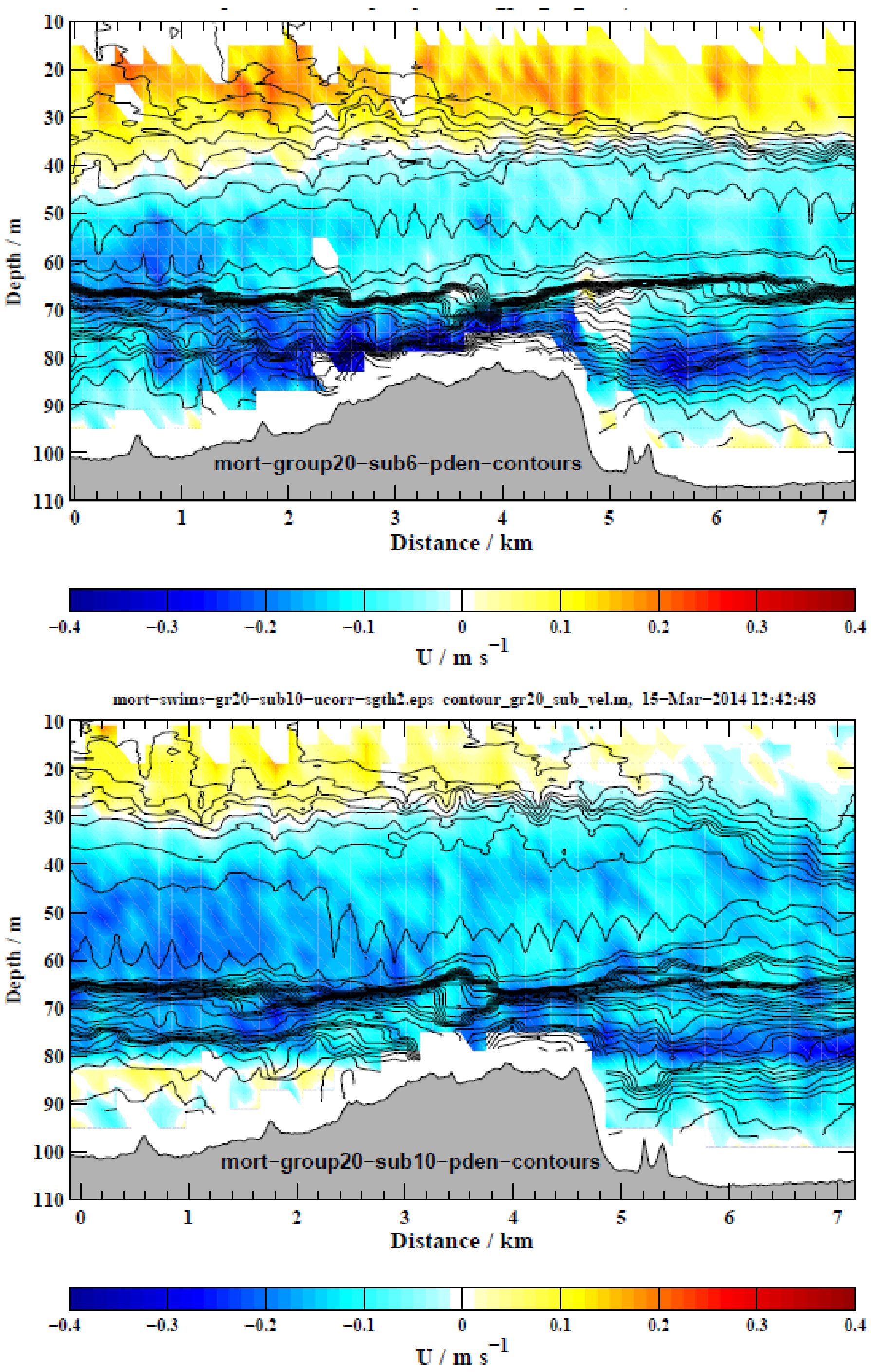

Figure 7. Eastward, *u*, velocity overlaid with σ_θ at intervals of 0.05 kg m^{-3} in the interface and half that above and below. Sub 6 (upper) contained 58 profiles and sub 10 (lower) had 54. intense activity of very high modes in the main interface. The first 5 modes were not controlled during sub 6, but modes 4 and higher were during sub 10.

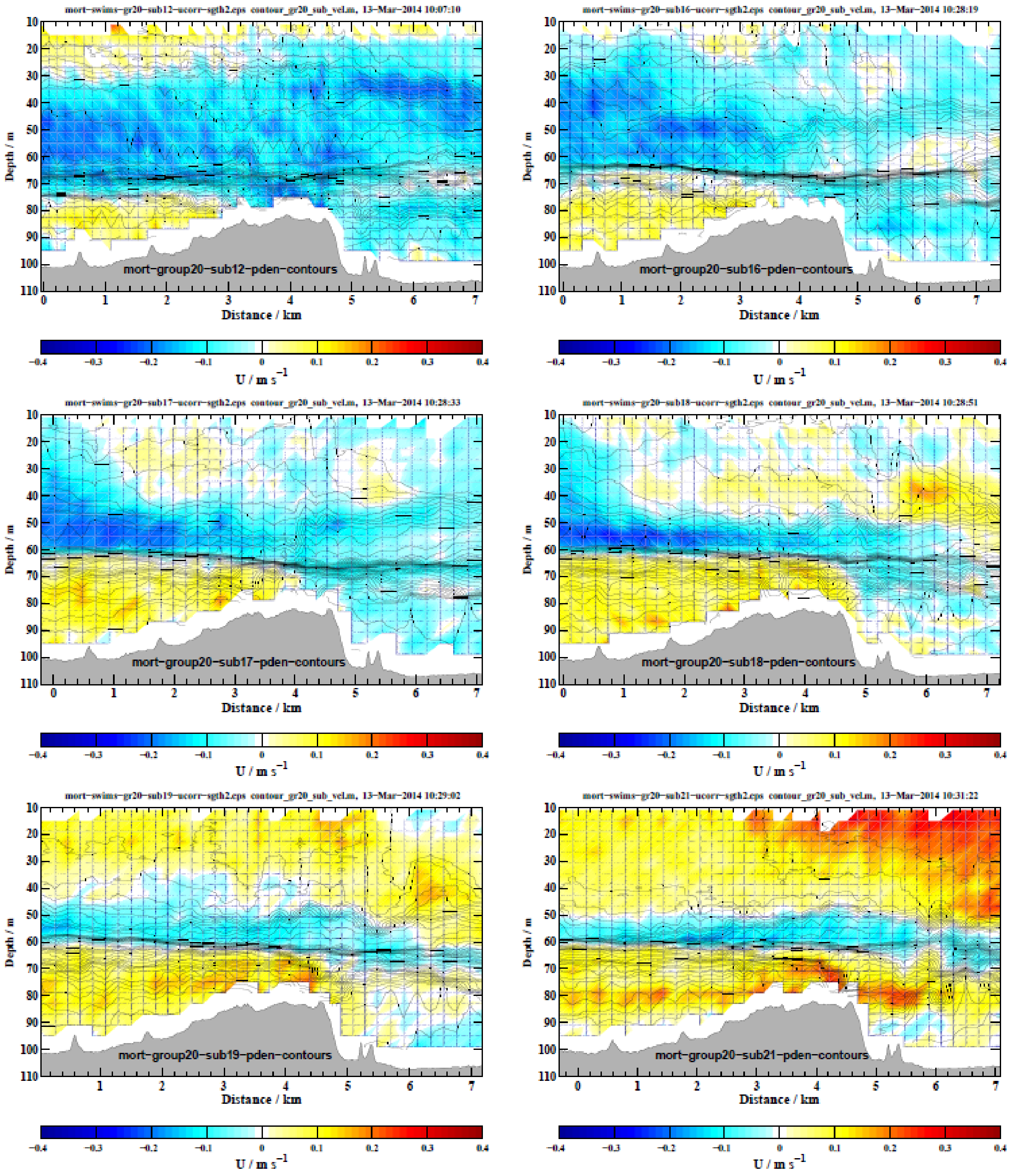

Figure 8. Before, during and after mode-2 control, east/west velocity overlaid with σ_θ with the same spacing as in the previous figure. Mode-2 phase speeds at 4 km, over the ridge, were: sub 12 (-0.071, 0.33), sub 16 (0.030, 0.25), sub 17 (-0.026, 0.47), sub 18 (-0.073, 0.22), sub 19 (-0.13, 0,23), sub 21 (-0.13, 0.31). Mode-2 control was unequivocal during sub 16, when both speeds were positive and was possible during sub 17 when the negative speeds were within the uncertainty band.

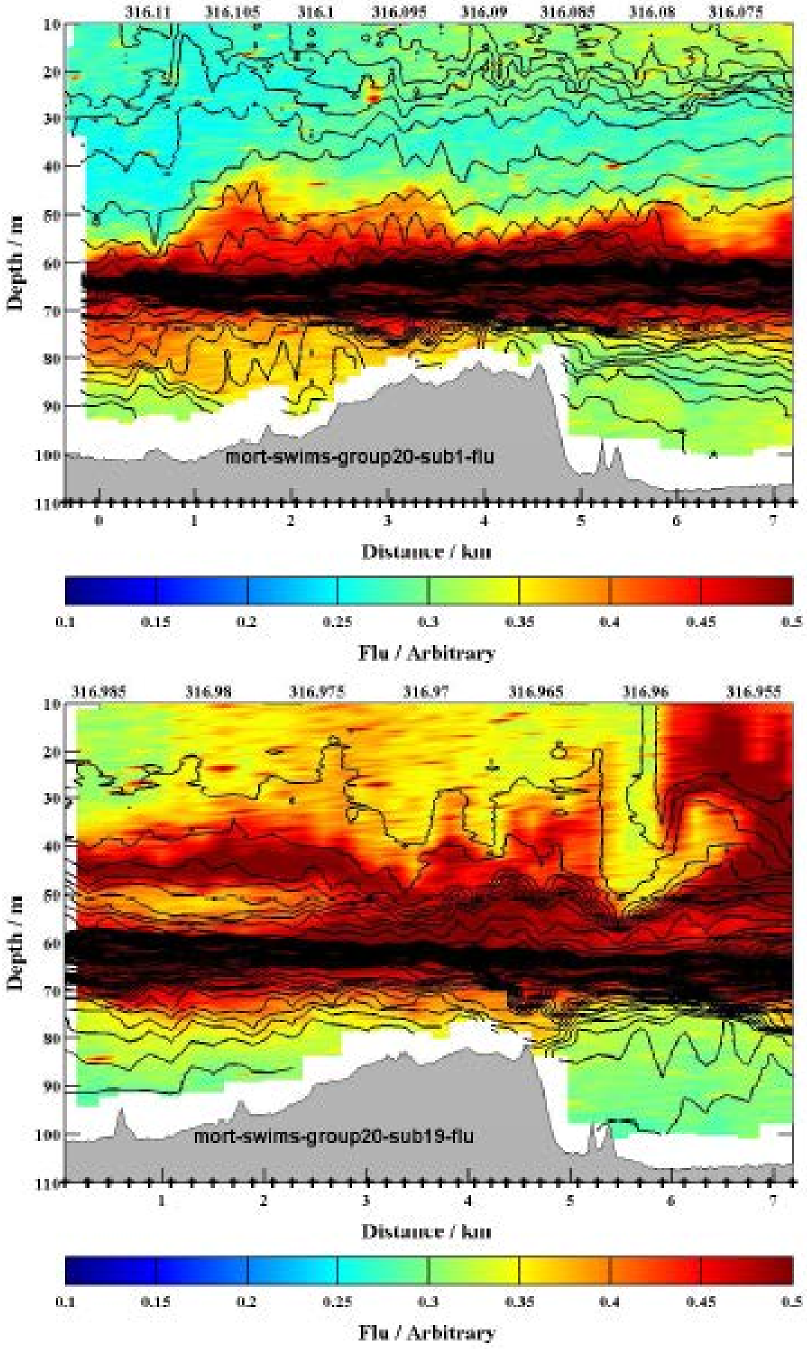

Figure 9. The fluorometer signal, in arbitrary units, overlaid with σ_θ contours, during the first sub (upper) contrasted with the large overturn (lower) after mode-2 control was lost.

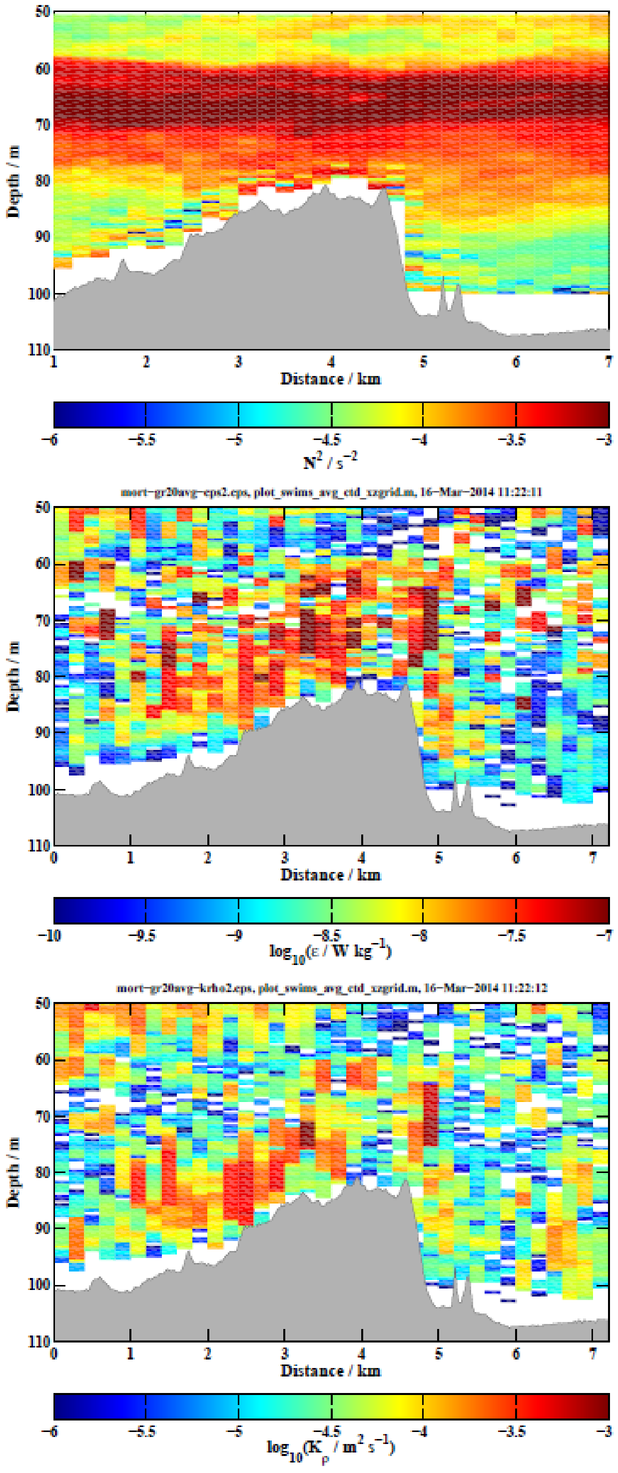
mort−gr20avg−eps2.eps, plot_swims_avg_ctd_xzgrid.m, 16−Mar−2014 11:22:11

mort−gr20avg−krho2.eps, plot_swims_avg_ctd_xzgrid.m, 16−Mar−2014 11:22:12

Figure 10. Group 20 average sections of N^2, ε, and $\overline{K}_\rho \equiv 0.2\,\varepsilon/N^2$. The interface was thicker over and east of the ridge compared to west of it. Most intense dissipation below the interface was over and west of the ridge, with many averages close to 10^{-7} W kg^{-1}. Corresponding diapycnal diffusivities close to the ridge were o10^{-4} to 10^{-3} m^2 s^{-1}.

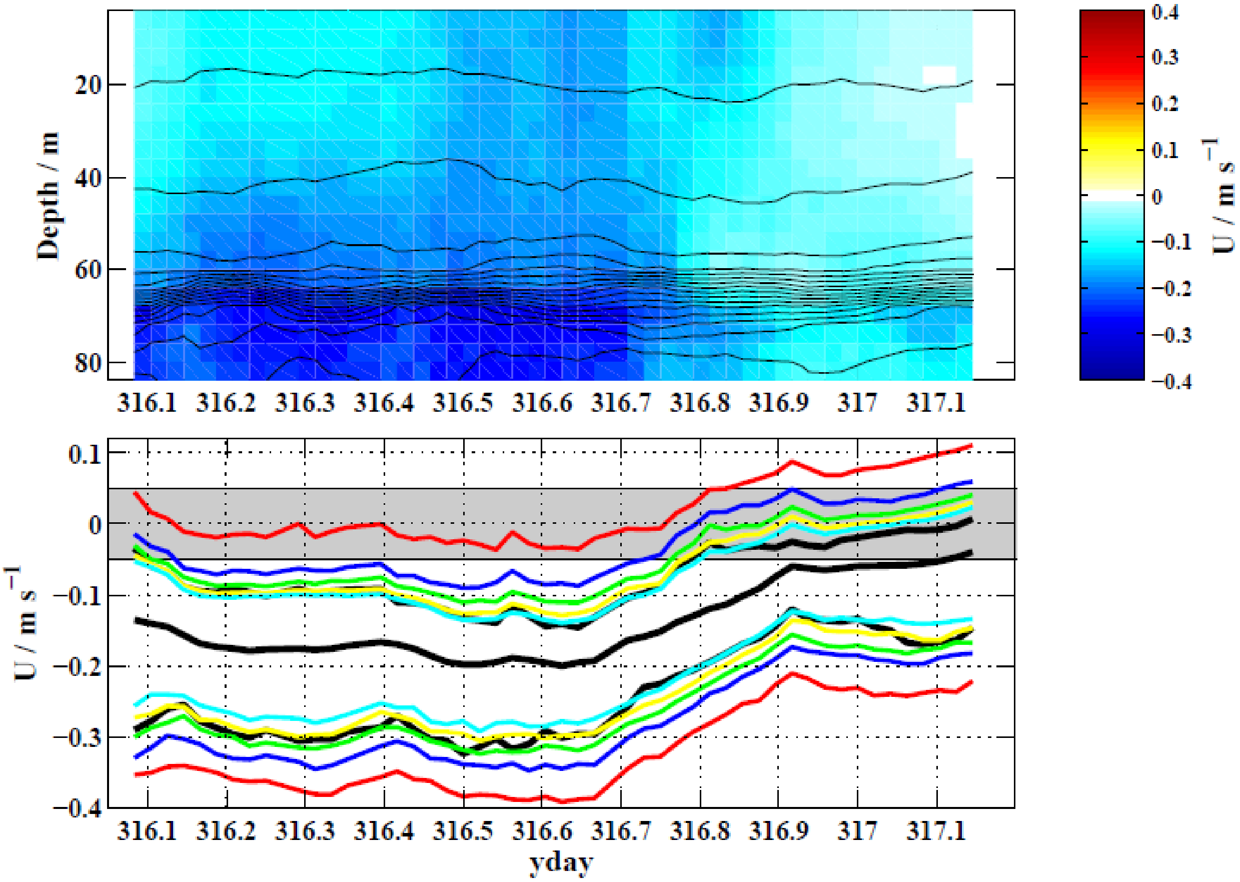

Figure 11. (Upper) Model-average velocity overlaid with temperature contours during group 20. (Lower) Speeds of internal EOF modes1-5 in the same format as Figure 4 but with the speeds connected with lines. EOF-2 was controlled for eastward flow between yday 316.1 and 316.8 when westward flow was most intense. Higher EOF was controlled the entire time, except at the end, when EOF-3 lost control. Forced from measurements at M1, model velocities lacked the observed deep eastward flow, resulting in control over a longer interval.

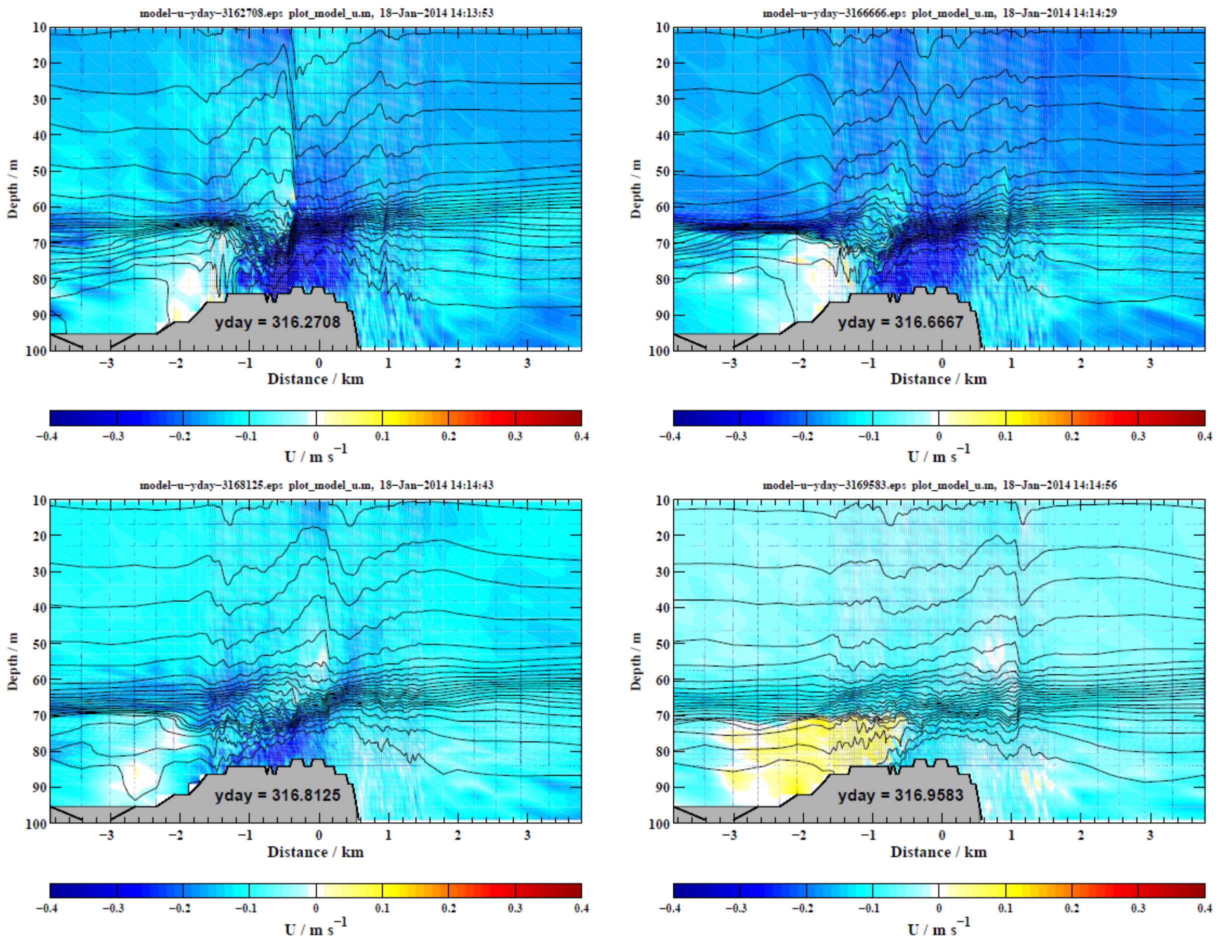

Figure 12. Eastward, u, velocity overlaid with σ_θ for model runs simulating group 20. Mode-2 was critical from yday 316.05 until yday 316.80. These model frames were taken during the turn between subs 4 and 5 (upper left) and during sub 12 (upper right), sub 15 (lower left), and sub 19 (lower right). Note the large vertical displacements above the interface and how they propagates eastward between the two bottom frames.

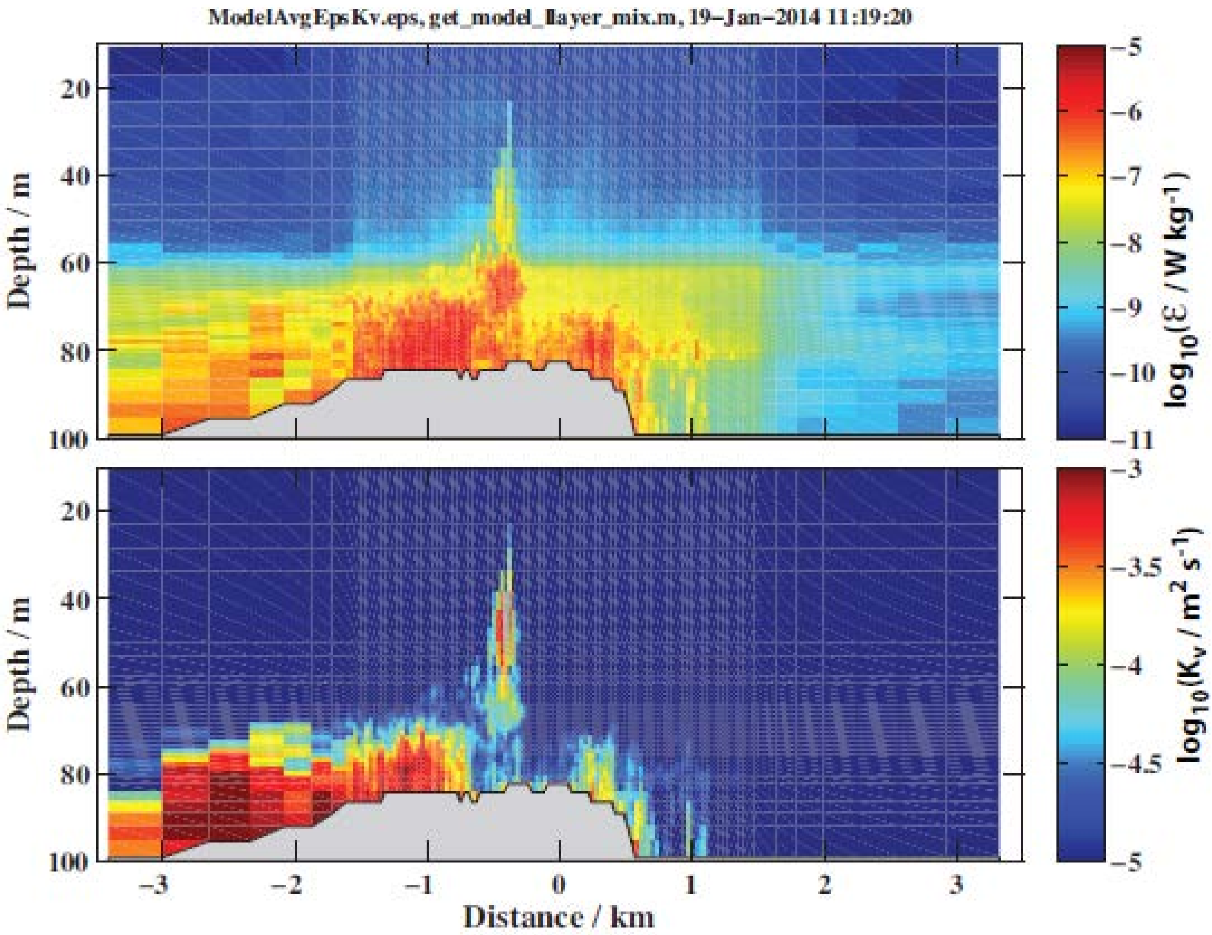

Figure 13. Average turbulent dissipation rate, ε, and vertical diffusivity, K_V, in the model during group 20.

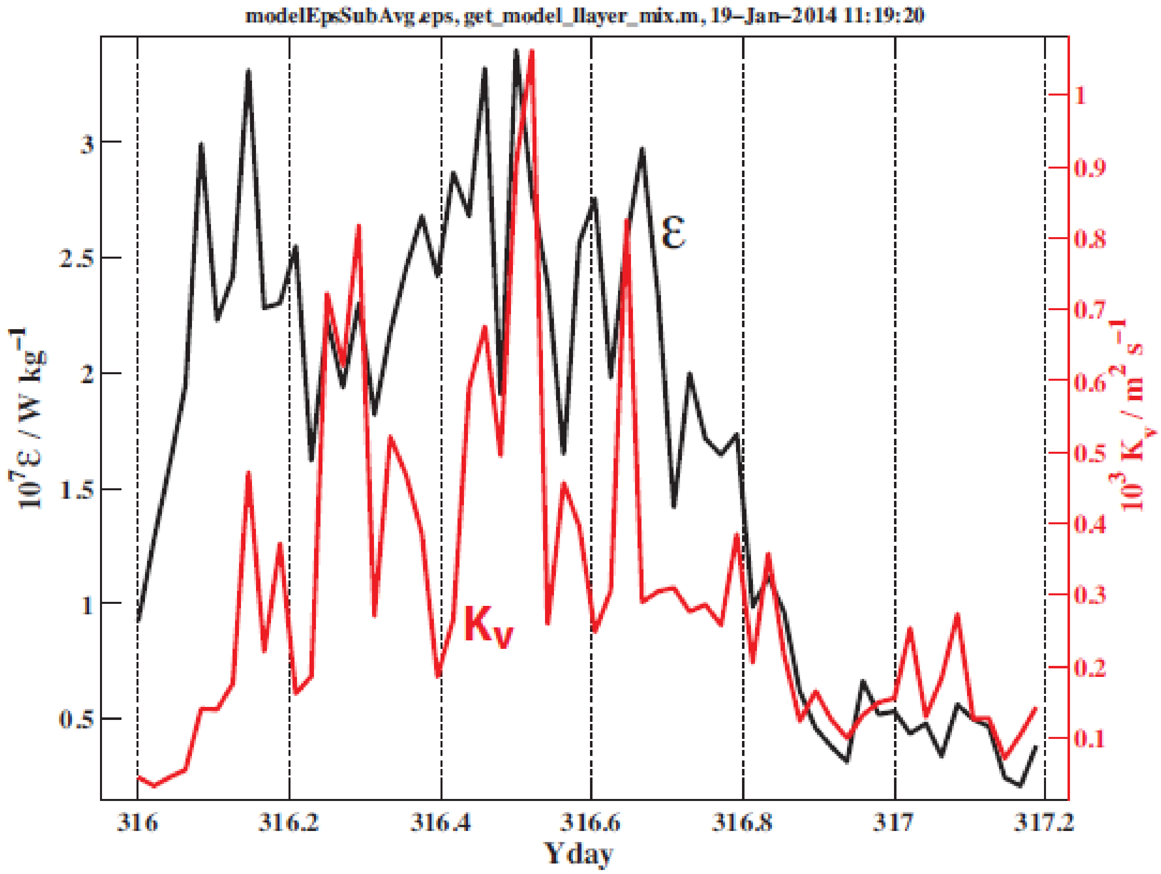

Figure 14. Section averages of ε and K_V in the model during group 20. Mode-2 was critical from yday 316.05 to 316.8.

Table 1. Ridge Characteristics. Parameters relevant to flow over the ridge. h is the height of the ridge above the adjacent continental shelf, and L is the horizontal length of ridge sides and crest. A is the half-width which is about half as long on the east side as on the west.

Location	h/m	L/m	Slope	A / m
East Side		320	0.064	860
Crest	20	1400		
West Side		2300	0.0073	1850

Table 2. Parameters Relevant to Flow Over the Ridge. Nh/U has been interpreted as a measure of non-linearity of flow over topography (Baines, 1995) and as a ratio of shear to stratification time scales (Klymak et al., 2010). NA/U relates to wave drag produced by the ridge, where A_e and A_w are half-width of the ridge on the east and west sides. Using parameters measured upstream at the depth of the crest, these ratios are evaluated using $h = 20$ m, $N = 0.013$ s^{-1} and $U = (0.1 - 0.2)$ ms^{-1}. Because these ratios are so high, the flow should have been hydrostatic in most places.

Nh/U	NA_e/U	NA_w/U
(2.6 - 1.3)	(112 - 56)	(240 - 120)

APPENDIX G

Bio-Physical Ocean Modeling in the Gulf of Mexico

Bio-Physical Ocean Modeling in the Gulf of Mexico

Sergio deRada, Robert A. Arnone, Stephanie Anderson

Naval Research Laboratory
Stennis Space Center, MS 39529

Details of the model used for East Flower Garden Bank appear in the following publication: deRada, S., R.A. Arnone, and S. Anderson, 2009. Bio-physical ocean modeling in the Gulf of Mexico, Oceans 2009, MTS/IEEE Biloxi–Marine Technology for Our Future: Global and Local Challenges, E-ISBN: 978-0-933957-38-1.

Abstract

The Naval Research Laboratory (NRL) Oceanography Division has implemented a 1/25º horizontal-resolution numerical ocean model for the Gulf of Mexico. The model domain encompasses the entire GOM extending from 18º to 31º North and from 77º to 98º West. The physical formulation is based on the Naval Coastal Ocean Model (NCOM) configured with a 40 level σ-z vertical structure: 19 terrain-following σ (sigma) levels at the top of the water column, and 21 z (depth) levels at the bottom. The terrain-following levels, reaching from the surface to about 137 meters, allow higher vertical resolutions for resolving mixed layer/shallow waters, while the z-levels are used in the stratified ocean. The ocean bathymetry is constructed from the NRL 2-minute database with the coastline set at a depth of two meters. The physical model is one-way coupled to a 13-component ecosystem (biogeochemical) model [Chai et. al., 2002, 2003, 2007] that includes nutrients, two classes of plankton, as well as O and CO2. The current configuration is tailored, but not limited to, real-time (RT) prediction; providing nowcasts (current state of the ocean) and up to 120-hour forecasts for the region. In this configuration, the model receives (initial) boundary information from the operational 1/8º Global NCOM, and it is forced by three-hourly 1/2º momentum and heat fluxes from the Naval Operational Global Prediction System (NOGAPS). The NCOMGOM model assimilates daily surface/subsurface temperature and salinity generated by the Modular Ocean Data Assimilation System (MODAS), which regresses satellite derived Sea Surface Temperature (SST) and Sea Surface Height (SSH) data to obtain T&S synthetic profiles. The model was initialized on January 1, 2009 from the operational 1/8º Global NCOM physical state and from the World Ocean Atlas 2005 and Carbon Dioxide Information Analysis Center (CDIAC) biogeochemical fields. Results from the real-time NCOMGOM nowcasting/forecasting ocean modeling system are compared and evaluated against in-situ and remotely sensed observations, which include bio-optical products processed by the NRL Ocean Color Section. Google Ocean™ is used as a platform for viewing the model results interactively and dynamically in real-time. Initial assessment of the model prediction skill is presented along with future plans for improvements and enhancements. The suitability of the system as a tool for decision management is discussed, outlining processes localized to particular areas such as hypoxia, dead zones, wetland loss and degradation, harmful algal blooms, as well as tropical storms and related issues that affect all coastal regions of the Gulf of Mexico.

I. MOTIVATION

The Gulf of Mexico (GOM) weather plays a significant role in the coastal areas of Florida, Alabama, Louisiana, Mississippi, Texas, and Mexico, with consequences that extend nationally and globally (e.g., oil and gas, fisheries, transportation, tourism, import-export). Accurate prediction of the oceanic, atmospheric, and coastal processes that govern this marginal sea is of the outmost importance in the socio-economic health of the region. Nothing has elucidated this more than the unprecedented events unleashed by Hurricane Katrina on August 29, 2005.

The Gulf Of Mexico Modeling System (GOMMS) has been implemented as a comprehensive interdisciplinary tool for oceanography research and for Forecasting and Weather Prediction (FWP). There are currently many tools and numerical models for the GOM and its estuaries, but they have specific realizations or are tailored to particular needs. The focus in this effort is creating an integrative modeling framework to address various scientific, managerial, and community needs. From the oligotrophic “blue waters” of the Yucatan Strait to the highly turbid and eutrophic waters of the Mississippi River plume, the GOM provides a wide range of rich and eclectic conditions and ecological habitats whereby many emerging scientific methodologies can be developed, tested, and ultimately be used in other regions of the world.

Major value added contribution from this effort, beyond that of the operational global NCOM, is the coupling of optical and biogeochemical models to the physical Ocean General Circulation Models (OGCMs). The scientific and applied objectives of this interdisciplinary effort will coherently address many of the processes and applications that impact the region: prediction of physical and optical conditions (e.g., turbidity), monitoring and preservation of flora, coral reefs and habitat (e.g., water quality), distribution and migration of ecological processes (e.g., fishery prediction and larval fish recruitment, hypoxia, productivity). Similarly, bio-optical and physical model forecasting is linked to naval requirements, such as diving operations, underwater laser performance, mine countermeasures, and expeditionary warfare. Optical responses are clearly characterized in satellite ocean color and provide the linkage to biological processes. Additionally, bio-optical modeling addresses the characterization of sound scattering layers, underwater acoustic propagation, ambient noise, and support for sonar testing. Thus, combining of physical, optical, and biological models into an integrative system coherently supports scientific objectives, naval requirements, and the needs of coastal managers who make decisions based on the “ocean bio-physical weather”. Monitoring and forecasting of the ocean conditions directly supports the decision-making capability used in operations and the effective planning in coastal zones.

Although multiple satellite remotely-sensed and in-situ ship, glider and mooring based observations of bio-optical properties are ubiquitous, they are still lacking the spatial and/or temporal density necessary to handle all regional processes. Furthermore, observations mostly cover surface or near-surface areas, so numerical models complement the observational data to create a fully comprehensive picture of the ocean environment. In mutual benefit, the numerical solution gains skill from the assimilation of observational data which are also used for the evaluation and validation of the model results.

The purpose of developing GOMMS is to optimally leverage the latest available resources and models to set forth a state-of-the-art system; as resources become available and better techniques are developed, the system will be continually improved to provide the best possible tool for research and FWP in the region.

II. THE GULF OF MEXICO MODELING SYSTEM

The foundation of the GOMMS is the integration of a vast array of components, data, and models that have been developed over the years at the Naval Research Laboratory; without these, the GOMMS would not be possible. The following section introduces the fundamentals of the NCOM model and describes the components that comprise the system; all summarized diagrammatically in Fig. 1. There are many configuration and parameterization options for each component, but the specific details are beyond the scope of this paper. In the context of the GOMMS configuration, a synopsis of each system component is mentioned here with the intent of providing overall background information. The reader is referred to the literature for detailed information on each component.

The NCOM Gulf of Mexico (NCOMGOM) model is implemented on a Mercator grid at 1/25° (equatorial) horizontal resolution, and a 40-level σ-z hybrid vertical structure (same as 1/8° Global NCOM). Computational resources at the United States Navy Department of Defense Supercomputing Resource Center (DSRC) have afforded higher horizontal –eddy resolving, and vertical –mixed layer resolving, resolutions, allowing this model to not only provide general circulation and oceanic state at interannual time scales, but also to resolve higher-order mesoscale and coastal dynamics critical to biogeochemical processes. The model incorporates a realistic bathymetry derived from the NRL 2-minute database with the coastline set at a depth of 2 meters, which, complemented by the high horizontal resolution, is capable of resolving shallow estuaries. The domain, illustrated in Fig. 2, extends from 18º to 31º north, and from 77º to 98º west. It covers the entire GOM, reaching farther east (and south) to encompass the entire state of Florida and to provide a smooth boundary transition.

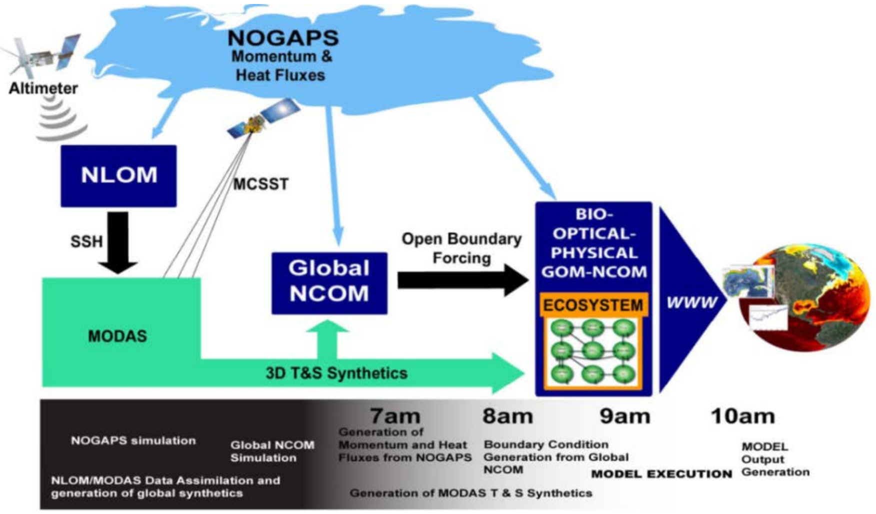

Fig. 1. Component diagram of the real-time Gulf of Mexico Modeling System describing system flow and integration. The timeline at the bottom of the figure represents the daily time at which input/output processing and model execution occur, starting with global prediction systems that run overnight and ending with the generation of the GOMMS model output and Web Portal update at around 10:30am CT.

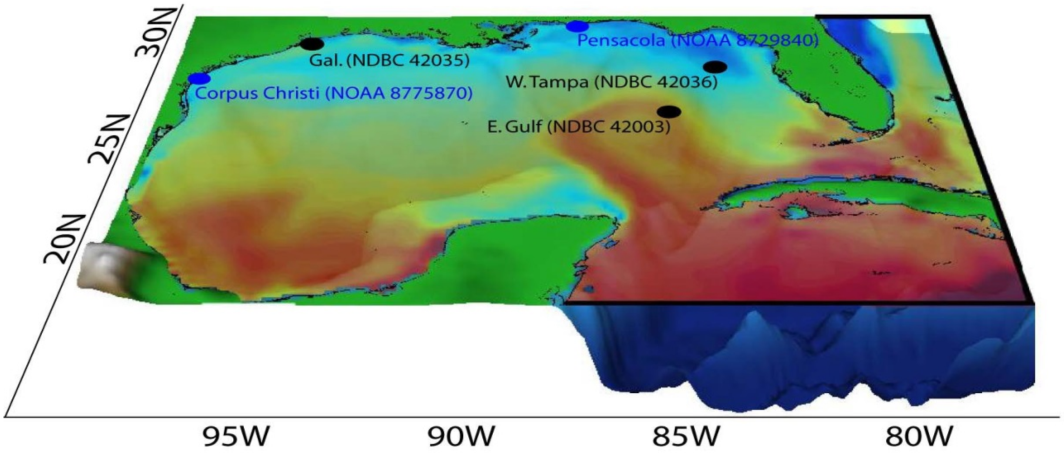

Fig. 2. The GOMMS domain, extending from 18º to 31º North and from 77º to 98º West, illustrates the open boundaries (bold black lines on south, east, and north-east of domain), and the NDBC buoys (black dots) and NOAA tide-gauge stations (blue dots) used for the evaluation of the model SST and SSH; respectively. The color surface field, semi-transparent to reveal the underlying bathymetry, represents the model SST for May 20, 2009.

In the current GOMMS context, NCOM is configured with Smagorinsky [6] horizontal mixing, and Mellor-Yamada Level 2.5 [7] turbulence closure scheme for vertical mixing. Density computation follows Mellor's [8] adaptation of the United Nations Educational Scientific and Cultural Organization (UNESCO) equation of state. Barotropic boundary conditions (surface elevation and normal velocity) use the Flather [9] radiation condition, and baroclinic information is exchanged via vertical structure distributions of temperature, salinity, and velocity fields; namely, tangential velocities use a zero-gradient condition, and normal velocities and tracers (including biology) use an advective scheme. Other formulations are being evaluated to further improve the model skill. River forcing is turned off for all but the Mississippi River and Evaporation-Precipitation (E-P) is not configured at this time. It is expected that salinity prediction will improve once E-P is implemented and all rivers are included.

The GOM ocean model physical state is initialized with and nested within the 1/8º Operational Global NCOM ocean prediction system [10,11,12]. Global NCOM is a Global Data Assimilation Experiment (GODAE) product used by researchers and forecasters around the world, and thus constitutes one of the primary global ocean prediction systems and a major provider of initial and boundary forcing for nested regional and coastal models. Down-scale nesting is not only essential for including oceanic signals, potentially generated far away, vital in modulating the general circulation of a region, but it is also necessary to resolve higher-order scales (in time and space) and localized processes (e.g., biogeochemistry) whose parameterization often requires explicit locale adjustments. The Global NCOM physical fields used for initialization and remote forcing in the GOMMS are Sea Surface Height (SSH), temperature, salinity, and ocean current velocity fields (Table 1). There is a trade-off between boundary updating frequency compared with global model feasibility to output data at higher rates, and as a result, regional/coastal models whose internal time-step is measured in the order of seconds inherently suffer from inaccuracies due to lower frequency boundary updating. For the initial configuration of the GOMMS, the boundaries are updated daily, but to minimize boundary forcing inaccuracies, and taking advantage of Global

NCOM 3-hourly output, this configuration will be changed to higher frequencies after the results are fully assessed.

The physical model is one-way coupled to either a 9-component or a 13-component ecosystem model [13,14,15,16]. The 9-component model includes three nutrients (silicate, nitrate and ammonia), two phytoplankton groups (diatoms and small- phytoplankton), two groups of zooplankton grazers (micro and meso), and two detrital pools (silica and nitrogen). Phosphate, oxygen, alkalinity, and carbon-dioxide are added in the 13-component model. Initial and boundary values for the ecosystem model are constructed from NOAA's World Ocean Atlas (WOA) [17,18] data and from the Oak Ridge National Laboratory (ORNL) Carbon Dioxide Information Analysis Center (CDIAC). Namely the fields: Silicate (SIO), Nitrate (NO_3), Phosphate (PO_4), and Oxygen (O) are constructed from the WOA-2005 monthly climatology [19,20], while Alkalinity (A_T) and Carbon Dioxide (CO_2) are constructed from the time-invariant CDIAC climate data. All other ecosystem constituents are initialized from analytical/literature based values as listed in Table 1.

The ocean model is forced with momentum and heat fluxes from Fleet Numerical Meteorology and Oceanography Center (FNMOC) 3-hourly 0.5º Navy Operational Global Atmospheric Prediction System (NOGAPS) [21,22]. The atmospheric surface forcing fields used are: shortwave radiation, longwave radiation, latent and sensible heat fluxes, and zonal and meridional surface wind stresses (Table 1). The atmospheric forcing forecast fields extend out to 120 hours facilitating forecasting up to five days, though climatologically adjusted persistence is used after 3 days because global NCOM only forecasts up to 72 hours.

Table 1. Fields used in initialization of surface and open boundary forcing in the GOOMS ocean model. The sources specify the data provider with the time frequency of each field in parenthesis. All fields are two-(SSH) or three-dimensional and time-varying except those indicated as constants or time-invariant.

Ocean Fields	**Source/Value**
SSH	Global NCOM (24-hr)
Temperature, Salinity	Global NCOM (24-hr)
Ocean Current Velocity U_x,V_y	Global NCOM (24-hr)
Nitrate (NO3)	WOA 2005 (monthly climatology)
Silicate (SO3)	WOA 2005 (monthly climatology)
Phosphate (PO4)	WOA 2005 (monthly climatology)
Oxygen (O)	WOA 2005 (monthly climatology)
Carbon Dioxide (CO2)	CDIAC (time-invariant)
Alkalinity (A_T)	CDIAC (time-invariant)
Phytoplankton, Diatoms	0.1 (constant)
Ammonium	0.0 (constant)
Detritus, Detritus Silicate	0.0 (constant)
Meso Zooplankton, Micro Zooplankton	0.01 (constant)

Atmospheric Fields	
Surface Wind Stress (τ_x,τ_y)	NOGAPS (3-hr)
Shortwave and Longwave Radiation	NOGAPS (3-hr)
Latent and Sensible Heat Flux	NOGAPS (3-hr)

The ocean model indirectly assimilates satellite derived SSH and SST through the Modular Ocean Data Assimilation System (MODAS) [23, 24]. MODAS uses SSH from the 1/32° (1/16° until March 2008) Navy Layer Ocean Model (NLOM) [25,26,27] to take advantage of the improved resolution and dynamics of the NLOM model over that of the statistical based MODAS. NLOM assimilates altimeter-derived SSH using optimal interpolation and an incremental updating scheme. Multi-Channel SST (MCSST) derived from the Advanced Very High Resolution Radiometer (AVHRR) is ingested by MODAS, along with NLOM SSH, to construct temperature and salinity 3D synthetics by regressing SST and SSH towards climatology whose covariance matrices were constructed from historical observations. Salinity is computed by climatologically-based temperature-salinity relationships. The 3D temperature and salinity synthetics (output from MODAS) are then used to relax (constrain) the model to the data using a slow incremental adjustment technique and a 3D time-scale weighting function representing the relative confidence between model and data. For the GOMMS, this function was constructed to account for NLOM SSH not extending over regions shallower than 200 meters, and to take into consideration the inherent near-land inaccuracies of satellite measurements. Specifically, a continuous function of stronger relaxation (shorter time scales) is imposed at the boundary zones and deeper ocean; smoothly tapers off (longer time scales) in shallower areas, and has minimal or no relaxation scales in the near-land coastal zone. This process allows confidence based adjustments to be made and minimizes dynamical disruption.

The model is configured to run once daily at the DSRC on an IBM SP6 computer using 64 processor. The model execution, including pre/post processing, takes about 42 minutes to run a seven-day simulation consisting of two hindcasts, one nowcast, and five forecasts. The model outputs all prognostic variables (see Table 1: Ocean Fields) at six-hourly frequency. Higher frequency output and other prognostic and diagnostic variables, including inherent and apparent optical properties, are available as needed.

III. EVALUATION

Several developmental experiments were run to test the robustness, cost, and performance of the model, including the optimization of the time-step and fine-tuning of the parallelization and scalability. The first production simulation was conducted in July 2009. This simulation was initialized on January 1, 2009 and run into the beginning of July 2009. At the time of this writing, the evaluation of the results is preliminary, but initial examination indicates that the model is correctly representing the general features of the region. Using higher spatial resolution should not effectively improve the overall physical skill of the model since the atmospheric forcing and data assimilation products used are the same as in Global NCOM, but noticeable differences over Global NCOM, largely accounted for localized parameterization and coastline affinity, have been identified. Future analysis will quantify the improvements that the regional model has over global NCOM.

The major added value of the GOM Ocean Model over that of Global NCOM is the addition of the optical and ecosystem models, which are validated against ocean-color observations, namely Chlorophyll from satellite. Fig. 3 shows a qualitative comparison of the GOMMS model computed chlorophyll (diatoms + small-phytoplankton) field compared with MODAS-AQUA observations.

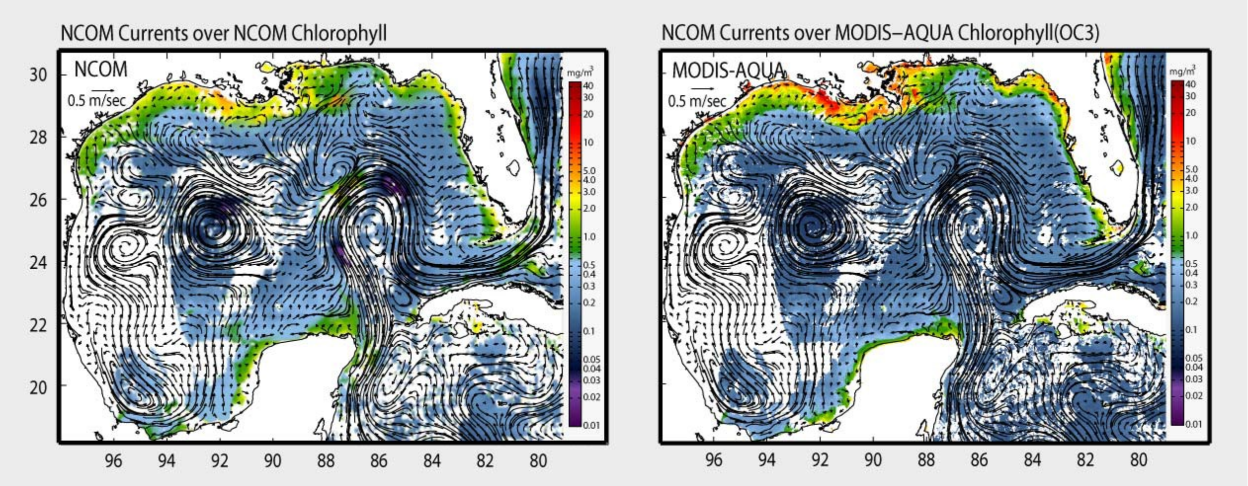

Fig. 3. An 8-day composite (May 25-June 1, 2009) of the Gulf of Mexico region is used as a general qualitative comparison of the model computed chlorophyll (left) to the imagery derived from satellite (MODAS-AQUA) by the OC3 algorithm (right). To provide a better visual comparison, the model data was interpolated to the satellite grid and cloud-masked, and the model currents were overlaid on both plots. Although finer coastal features and intensity have not been accurately represented, the general mesoscale structure of the bio-mass is well captured.

The qualitative comparison in Fig. 3 provides an important quality control step to assure that the GOMMS results are representative of expectations. The Chlorophyll comparison to satellite (an independent data source not assimilated into the system) demonstrates model skill and constitutes an important milestone in the initial evaluation process.

For a more quantitative assessment of the results, the model is validated against independent (not assimilated into the model) surface observations from NOAA’s National Oceanographic Data Center (NODC) and National Data Buoy Center (NDBC). Two coastal and one open ocean buoys were selected for the SST comparison, and two tide-gauge stations for the SSH comparison. The buoy locations (black dots) and the tide-gauge stations (blue dots) are depicted in Fig. 2. Model data was skipped when the observations were missing and a three-day filter was applied to both data sets before plotting and computing the statistics. Fig. 4 shows time-series of modeled SST and buoy observations, and model SSH and tide-gauge observations whose data was de-tided and corrected for atmospheric pressure. Each panel represents a model-data comparison at each location with the statistical metrics represented by the correlation (r) and the dimensionless skill score (ss) which demonstrate exceptional model skill.

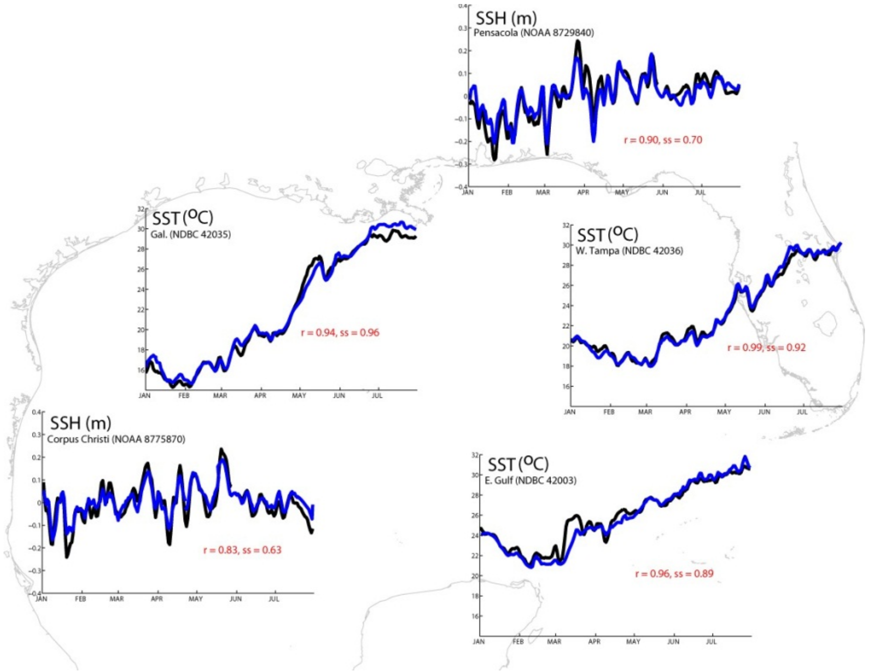

Fig. 4. The correlation (r) and dimensionless skill score (ss) provide a quantitative metric for the performance of the system. Model (blue) SSH anomaly and model SST are evaluated against observations (black) in different areas around the Gulf. Tide-gauge observations have been de-tided and pressure corrected.

IV. SUMMARY AND PLANS

A real-time GOMMS capable of forecasting biological, optical, and physical properties up to 120 hours has been developed. This new capability advances community efforts in the Gulf of Mexico by coupling the Navy's state of the art physical model (NCOM) with a 9 and a 13-component ecological model providing coastal managers and researchers advanced knowledge of bio-physical processes in both the coastal zone and the open ocean. This capability will help predict the influence that large mesoscale processes, such as the Loop Current and the Warm Core rings, have on localized coastal environments, estuaries, and embayment areas like Tampa, Mobile, and Houston. "Bio-Optical-Physical Ocean Weather Forecasting" is a new capability and falls behind present capabilities of Meteorological Weather Forecasting. However, the GOMMS framework augments "OCEAN" weather prediction and brings it to the coastal community by providing real-time access through web portals and programs like Google Earth™.

GOMMS is fully modularized whereas all the system components are coupled in a modular "swappable" fashion, with the vision of having a system where other models and tools can be incorporated without major redevelopment. The system is already capable of using initial and boundary forcing from any global ocean model (e.g., HYCOM –HYbrid Coordinate Ocean Model) as well as atmospheric forcing from any atmospheric model (e.g., COAMPS – Coupled Ocean/Atmosphere Mesoscale Prediction System [28]) or observational product (e.g., SeaWinds). Similarly, more sophisticated data assimilation systems, capable of assimilating biogeochemical and optical data, can be incorporated (e.g., NCODA --Navy Coupled Ocean Data Assimilation [29]).

This initial implementation presents an interdisciplinary Ocean Modeling Framework for the Gulf of Mexico complemented with a set of preliminary simulations to demonstrate skill and feasibility. The results presented here show evidence of a successful system implementation. The validation metrics, though not exhaustive, are of reasonable accuracy and provide the motivation to continue the development and enhancement of the system. As the model development progresses, relocatable finer-resolution (sub-kilometer) nests forced by high-resolution COAMPS flluxes will be implemented as 2-way air/sea coupled systems within the GOMMS.

An interactive web portal is being constructed as the central point for all activities relating to GOMMS. The site will house the model results in near-real-time, including up to 120 hour of forecasts. As research efforts progress, a comprehensive archive of observational, modeled data, and scientific studies will be available to collaborators, researchers, and government agencies.

REFERENCES

[1] Martin, P. J. (2000): Description of the Navy Coastal Ocean Model Version 1.0. NRL Report No. NRL/FR/7322/00/9962, 45 pp. Naval Research Laboratory, Stennis Space Center, MS.

[2] Martin, P. J., G. Peggion, K.J. Yip (1998): A comparison of several coastal ocean models. NRL Report No. NRL/FR/7322/97/9692, 96 pp. Naval Research Laboratory, Stennis Space Center, MS.

[3] Blumberg, A.F. and G.L. Mellor (1983): Diagnostic and prognostic numerical circulation studies of the South Atlantic Bight. *J. Geophys. Res.*, 88, 4579- 4592

[4] Blumberg, A.F. and G.L. Mellor (1987): A description of a three-dimensional coastal ocean circulation model. In: Three-Dimensional Coastal Models. N. Heaps, Ed., American Geophysical Union, New York, N.Y., 208 pp.

[5] deRada, S., S. Anderson, J.C. Kindle, B. Penta, I. Shulman (2005): Implementation of a high resolution Real-Time Naval Coastal Ocean Model for the California Current System, TOS International Research Conference, Paris, France June 2005. (*http://www.tos.org/2005_iorc/2005orc_program.pdf)*

[6] Smagorinsky, J. (1963): General circulation experiments with the primitive equations. I: The basic experiment. *Mon. Wea. Rev.,* 91, 99-164

[7] Mellor, G. L. and T. Yamada (1982): Development of a turbulence closure model for geophysical fluid problems. *Rev. Geophys. Space Phys.*, 20, 851-875

[8] Mellor, G. L. (1991): An equation of state for numerical models of oceans and estuaries. *J. Atmos. Oceanic Technol.,* 8, 609-611

[9] Flather, R. A., (1976): A tidal model of the northwest European continental shelf. Mem. Soc. Roy. Sci. Liege 6 (10), 141-164

[10] Barron, C.N., A.B. Kara, P.J. Martin, R.C. Rhodes and L.F. Smedstad, 2006: Formulation, implementation and examination of vertical coordinate choices in the Global Navy Coastal Ocean Model (NCOM). *Ocean Modeling*, 11(3-4), 347-375

[11] Barron, C.N., A. B. Kara, R. C. Rhodes, C. Rowley and L. F. Smedstad, 2007: Validation Test Report for the 1/8º Global Navy Coastal Ocean Model Nowcast/Forecast System. *NRL Tech Report* NRL/MR/7320--07-9019

[12] Rhodes, R.C., H.E. Hurlburt, A.J. Wallcraft, C.N. Barron, P.J. Martin, O.M. Smedstad, S.L. Cross, E.J. Metzger, J.F. Shriver, A.B. Kara and D.S. Ko (2002): Navy real-time global modeling systems, *Oceanography, 15(1), 29-43*

[13] Chai, F., R. C. Dugdale, T-H Peng, F. P. Wilkerson, and R. T. Barber (2002): One Dimensional Ecosystem Model of the Equatorial Pacific Upwelling System, Part I: Model Development and Silicon and Nitrogen Cycle. *Deep-Sea Res. II*, Vol. 49, No. 13-14, 2713-2745

[14] Chai, F., M. Jiang, R.T. Barber, R.C. Dugdale, and Y. Chao (2003): Interdecadal Variation of the Transition Zone Chlorophyll Front, A Physical-Biological Model Simulation between 1960 and 1990. *Journal of Oceanography*, Vol. 59, 461-475

[15] Chai, F., M-S Jiang, Y. Chao, R.C. Dugdale, F. Chavez, and R.T. Barber (2007): Modeling Responses of Diatom Productivity and Biogenic Silica Export to Iron Enrichment in the Equatorial Pacific Ocean. *Global Biogeochemical Cycle*, Vol. 21, GB3S90, doi:10.1029/2006GB002804

[16] Fujii, M., E. Boss, and F. Chai (2007): The value of adding optics to ecosystem models: a case study. Biogeosciences 4, 1585-1631

[17] Levitus, S., Climatological atlas of the world ocean (1982): *NOAA Prof. Pap., 13*, U.S. Govt. Printing Office, Washington, D.C., 173 pp. [18] Levitus, S., and T. Boyer, Temperature. Vol. 4, World Ocean Atlas 1994 (1994): *NOAA Atlas NESDIS 4, 150 pp.*

[18] Levitus, S., and T. Boyer, Temperature. Vol. 4, World Ocean Atlas 1994 (1994): *NOAA Atlas NESDIS 4, 150 pp.*

[19] Garcia, H. E., R. A. Locarnini, T. P. Boyer, and J. I. Antonov (2006): *World Ocean Atlas 2005, Volume 3: Dissolved Oxygen, Apparent Oxygen Utilization, and Oxygen Saturation.* S. Levitus, Ed. NOAA Atlas NESDIS 63, U.S. Government Printing Office, Washington, D.C., 342 pp.

[20] Garcia, H. E., R. A. Locarnini, T. P. Boyer, and J. I. Antonov (2006): *World Ocean Atlas 2005, Volume 4: Nutrients (phosphate, nitrate, silicate).* S. Levitus, Ed. NOAA Atlas NESDIS 64, U.S. Government Printing Office, Washington, D.C., 396 pp.

[21] Hogan, T. F. and T. E. Rosmond (1991): The description of the U.S. Navy Operational Global

Atmospheric Prediction System's spectral forecast model. *Mon. Wea. Rev., 119, 1786-1815*

[22] Rosmond, T. E., J. Teixeira, M. Peng, T. F. Hogan, and R. Pauley (2002): Navy Operational Global Atmospheric Prediction System (NOGAPS): Forcing for ocean models. *Oceanography, 15, 99-108*

[23] Fox, D.N., W.J. Teague, C.N. Barron, M.R. Carnes and C.M. Lee, (2001): The Modular Ocean Data Assimilation System (MODAS). *J. Atmos. Oceanic Technol., 19, 240-252*

[24] Fox, D.N., C.N. Barron, M.R. Carnes, G. Peggion, J. Van Gurley, (2002): The Modular Ocean Data Assimilation System, Oceanography, 15, 22-28

[25] Moore, D. R. and A. J. Wallcraft (1998): Formulation of the NRL Layered Ocean Model in spherical coordinates. NRL Report No. NRL/CR/7323/96/0005, 24 pp. Naval Research Laboratory, Stennis Space Center, MS.

[26] Wallcraft, A.J. and D. R. Moore (1997): The NRL Layered Ocean Model, *Parallel Comput.*, 23, 2227-2242

[27] Wallcraft, A.J., A.B. Kara, H.E. Hurlburt, and P.A. Rochford, (2003): NRL Layered Ocean Model (NLOM) with an embedded mixed layer sub-model: formulation and tuning. *J. Atmos. Oceanic Technol. 20, 1601-1615*

[28] Hodur, R.M., (1997): The Naval Research Laboratory's coupled ocean/atmosphere mesoscale prediction system (COAMPS). *Mon. Wea. Rev., 125 (7), 1414-1430*

[29] Cummings, J.A., (2005): Operational multivariate ocean data assimilation. *Quart. J. Royal Met. Soc., 131, 3583-3604*

APPENDIX
NCOMGOM COMPARISONS WITH MORT OBSERVATIONS

The Navy Coastal Ocean Model (NCOM) was configured at 1/25º (4-km) horizontal resolution for the Gulf of Mexico (GOM; NCOMGOM) (Figure 1). A 1-km high-resolution nest for the Flower Garden Banks Marine Sanctuary (FGBMS; Figures 1 and 2) is nested within NCOM. The physical formulation is based on the Naval Coastal Ocean Model (NCOM) configured with a 40-level σ-z vertical structure: 19 terrain-following σ (sigma) levels at the top of the water column, and 21 z (depth) levels at the bottom. The terrain-following levels, reaching from the surface to about 137 meters, allow higher vertical resolutions for resolving mixed layer/shallow waters, while the z-levels are used in the stratified ocean. The ocean bathymetry for the GOM domain is constructed from the NRL 2-minute database (DBDB2), while the coastline for the FGBMS nest is constructed from the 30-arc-second bathymetry from the General Bathymetric Chart of the Oceans (GEBCO). The GOM-FGBMS nested model was run from January 1, 2000 to December 31, 2010 using (initial) boundary information from the operational 1/8º Global NCOM and hourly atmospheric forcing from the 2/3º (longitude) x 1/2º (latitude) NASA's Modern Era Retrospective-analysis for Research and Applications (MERRA) dataset. The model assimilates daily surface/subsurface temperature and salinity generated by the Modular Ocean Data Assimilation System (MODAS), which regresses satellite derived Sea Surface Temperature (SST) and Sea Surface Height (SSH) data to obtain T&S synthetic profiles. The results from this reanalysis simulation, with focus on the FGBMS 1 km nest, follow.

The model is validated in multiple ways. First, the model bathymetry (1 km resolution) is compared to observed high-resolution bathymetry at the East Flower Garden Bank (EFGB; Figure 3) and West Flower Garden Bank (Figure 4). The lower-resolution model bathymetry captures the general shape of the banks well. Next, qualitative comparisons of model temperature and salinity fields were made from selected CTD casts (Figures 5 and 6) taken during the field experiment that was part of MORT (Mixing over Rough Topography) in June 2011 in the FGBMS. In general, the model reproduces the vertical temperature gradient well, but it is slightly cold biased and does not capture the small scale structure clearly present in the observations. It is visually evident that the higher horizontal resolution (both GOM and its inner nest have the same vertical structure) has better skill metrics computed using 1km nest. Bottom temperatures measured at the MORT moorings (M1–M5) were also compared with the model bottom temperatures in Figures 7 and 8 and the overall trend in bottom temperature was captured by the model. In addition, NCOMGOM sea-surface temperatures for the FGBMS banks for years 2000 to 2010 are shown in Figure 9; NCOMGOM depth-averaged temperatures in Figure 10; NCOMGOM bottom boundary-layer temperatures in Figure 11; NCOMGOM 3-D temperatures in Figure 12; NCOMGOM sea-surface salinities in Figure 13; NCOMGOM depth-averaged salinities in Figure 14; NCOMGOM bottom boundary-layer salinities in Figure 15; NCOMGOM 3-D salinities in Figure 16; NCOMGOM area-mean depth-averaged temperatures and salinities in Figure 17; and NCOMGOM area-mean depth-averaged temperatures and salinities in Figure 18. Skill scores (ss; deRada et al., 2009; Murphy, 1988; 1989; and 1995) based on the mean square error and their relationships to the correlation coefficient are included for Figures 5–8.

This research is responsive to studies dealing with climate change and adaptation in the Gulf of Mexico. The results so far are consistent with the literature. The GOMMS model simulated reanalysis results show excellent ability in hindcasting temperature measurements and therefore provide a baseline before attempting extended projections which will require further scrutiny and investigation. However, given the model's skill, these results confidently suggest that seasonal extremes are becoming more vigorous (i.e., colder winters, hotter summers). Extended projections of SST and upper ocean temperatures in the Gulf will then be possible with a higher degree of certainty and closure.

REFERENCES

deRada, S., Arnone, R., and Anderson, S., 2009. Biological-Physical Ocean Modeling in the Gulf of Mexico, OCEANS 2009, MTS/IEEE Biloxi – Marine Technology for Our Future: Global and Local Challenges, 26-29 October 2009.

Murphy, A.H., 1988. Skill scores based on the mean square error and their relationships to the correlation coefficient, Mon. Weather Rev., 116, 2417-2424.

Murphy, A.H., and E. S. Epstein, 1989. Skill scores and correlation coefficients in model verification, Mon.Weather Rev., 117, 572-581.

Murphy, A.H., 1995.The coefficients of correlation and determination as measures of performance in forecast verification, Weather Forecasting, 10, 681-688.

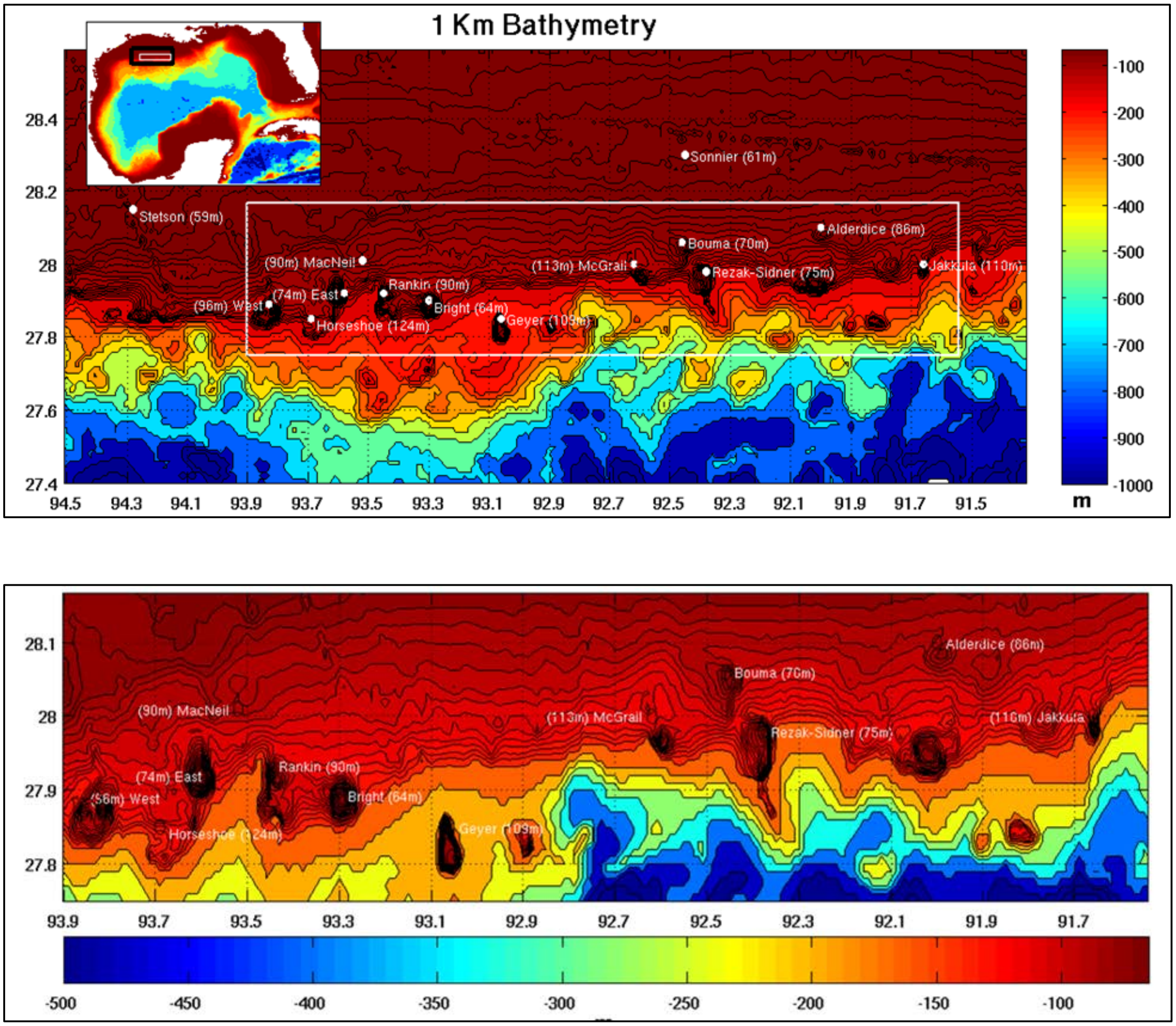

Figure 1. A 1 km resolution model (lower panel) configured for the FGBMS is nested within a 1/25º (4 km) horizontal-resolution numerical ocean model (upper panel) for the Gulf of Mexico (NCOMGOM). Bathymetry at 1 km resolution is shown.

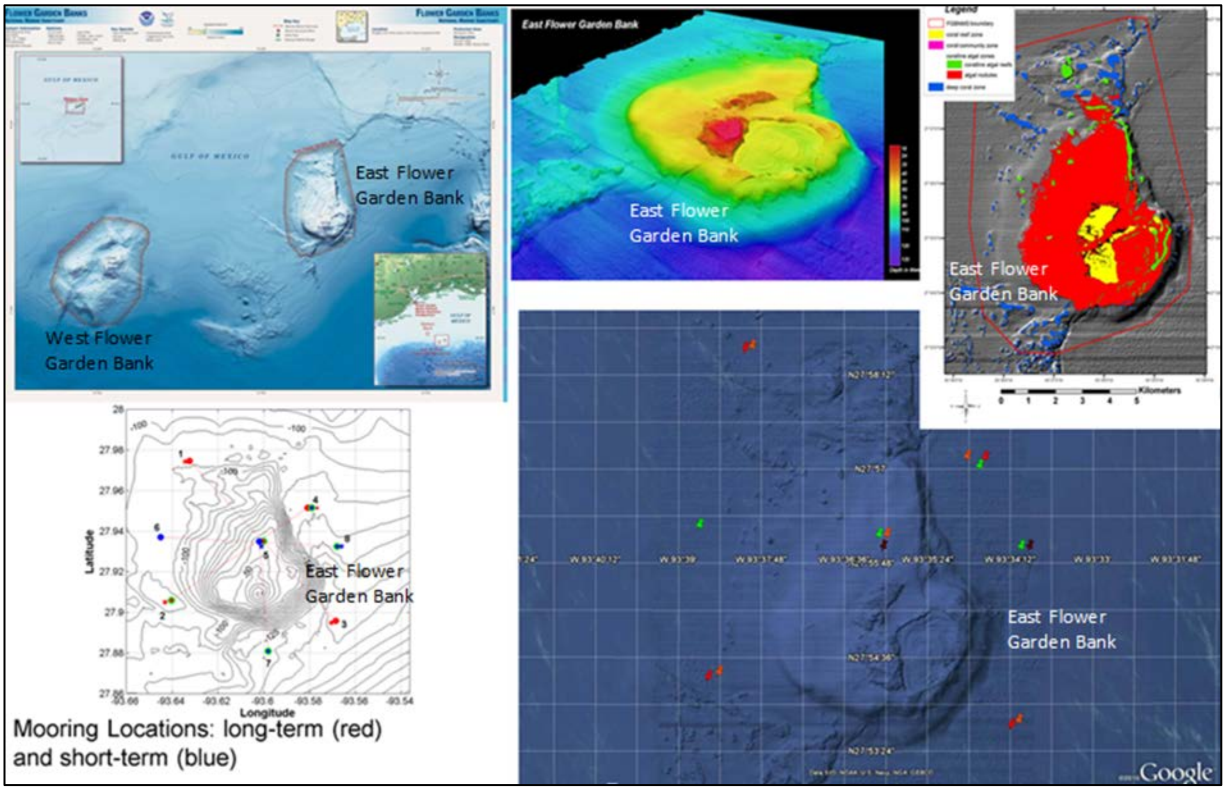

Figure 2. East and West Flower Garden Banks are located in the northwestern Gulf of Mexico. Bathymetry, mooring locations, topography, and coral habitats are shown.

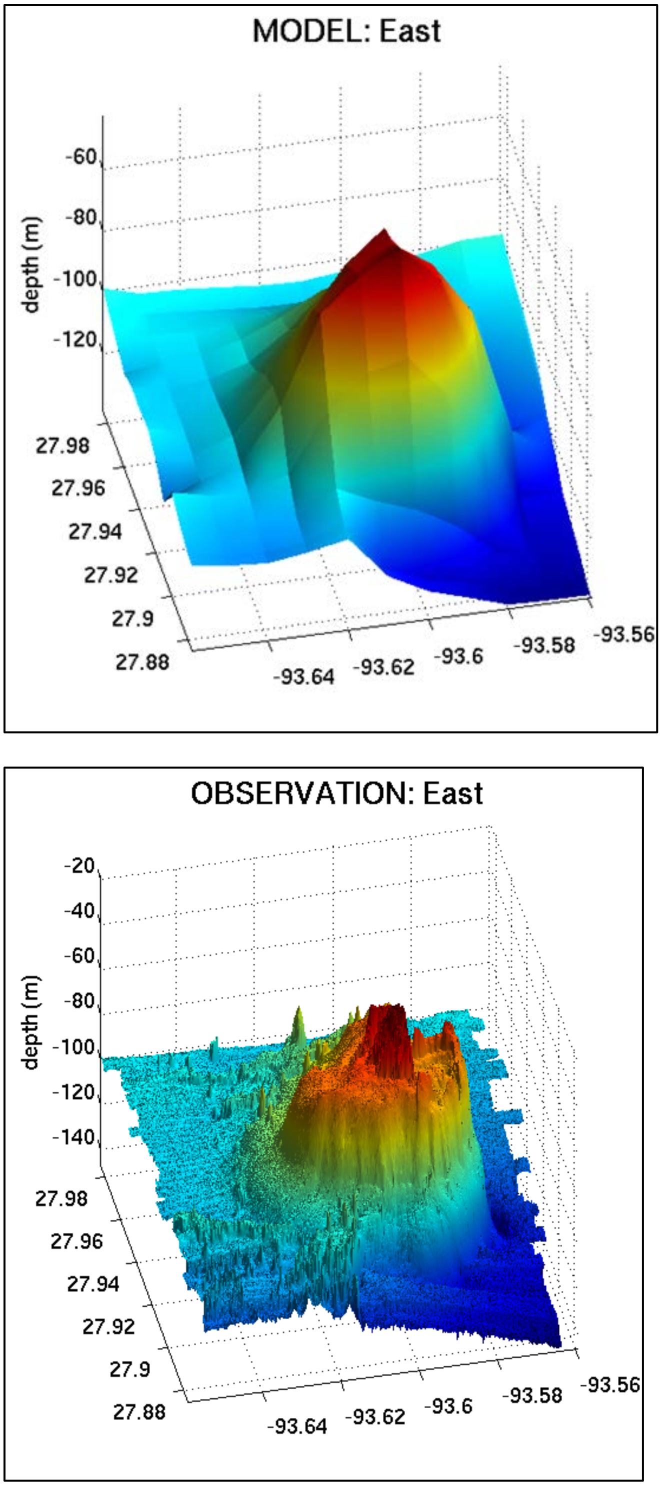

Figure 3a. Model bathymetry (3-D top panel; cross section across shallowest point, bottom panel) for the East Flower Garden Bank.

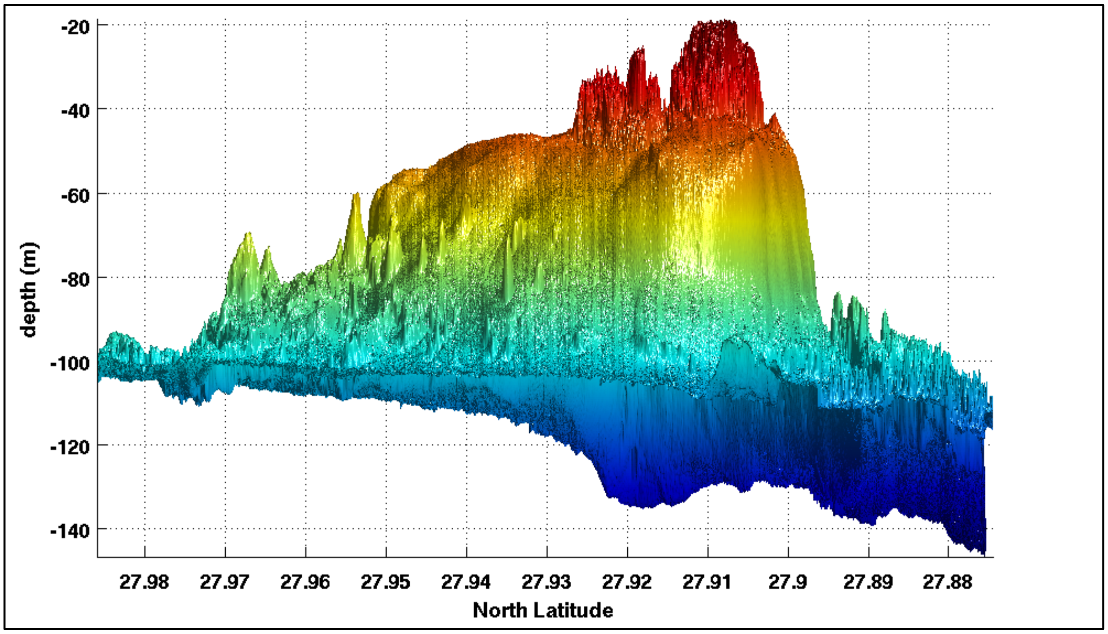

Figure 3b. Observed bathymetry (3-D top panel; cross section across shallowest point, bottom panel) for the East Flower Garden Bank.

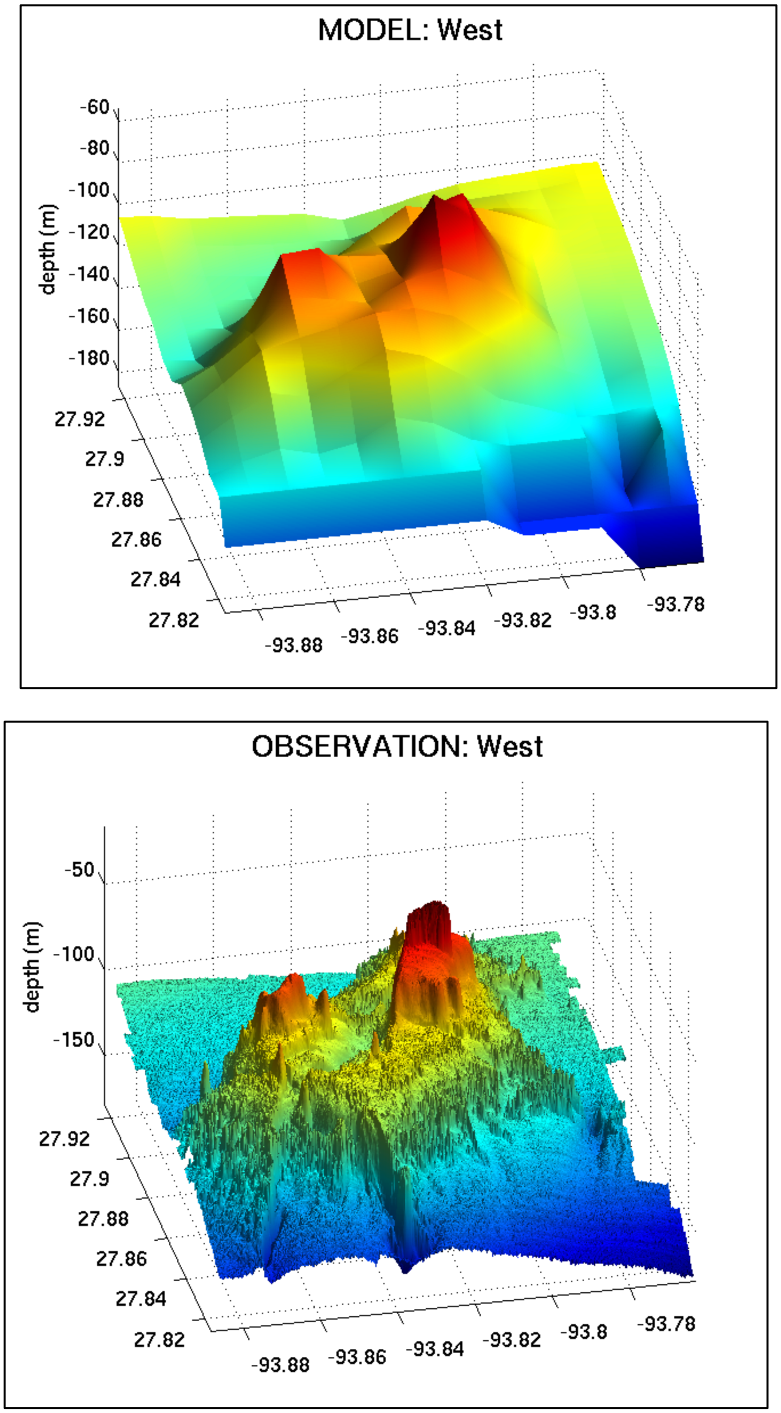

Figure 4. Model bathymetry (top), observed bathymetry (bottom) for the West Flower Garden Bank.

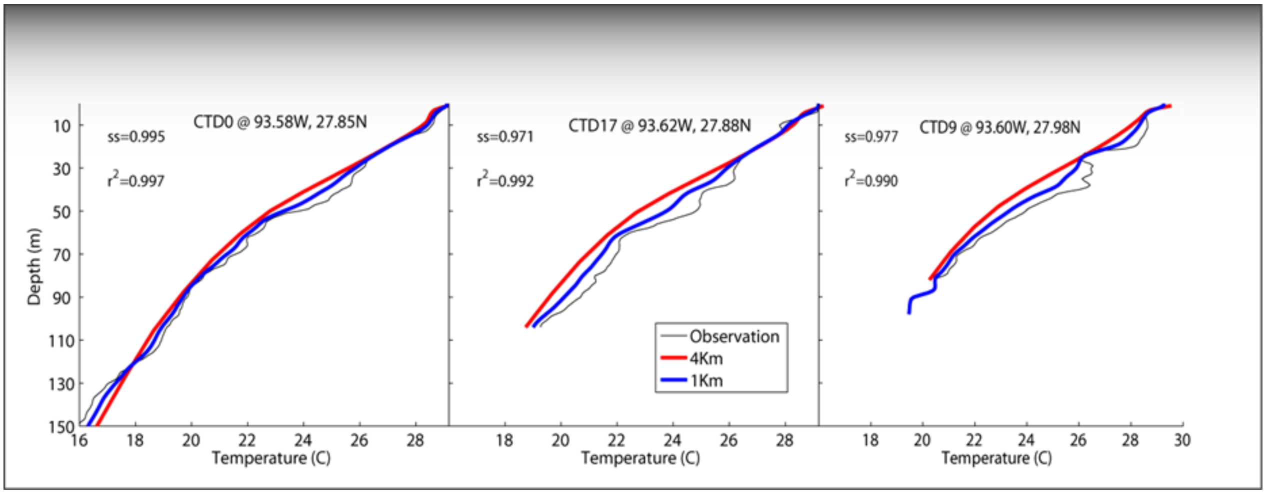

Figure 5. A qualitative comparison of the model fields (red=4 km GOM, blue=1 km inner nest) to selected CTD casts (black) taken during the MORT June 2011 field program in the FGBMS. In general, the model reproduces the vertical temperature gradient well, but it is slightly cold biased and does not capture the small scale structure clearly present in the observations. Correlation (r^2) and skill score (ss) are inset.

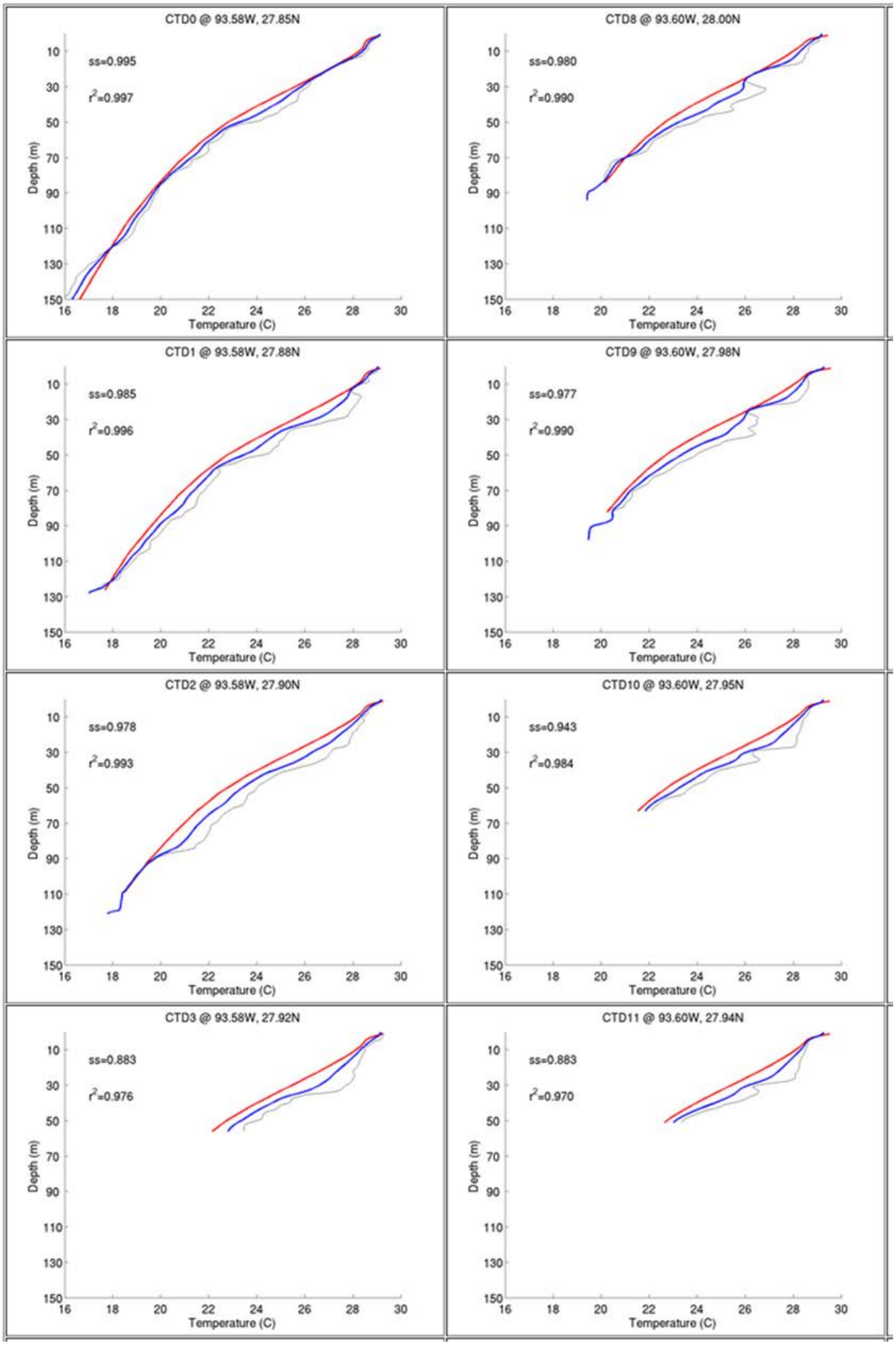

Figure 6a. Comparisons with MORT CTD data.

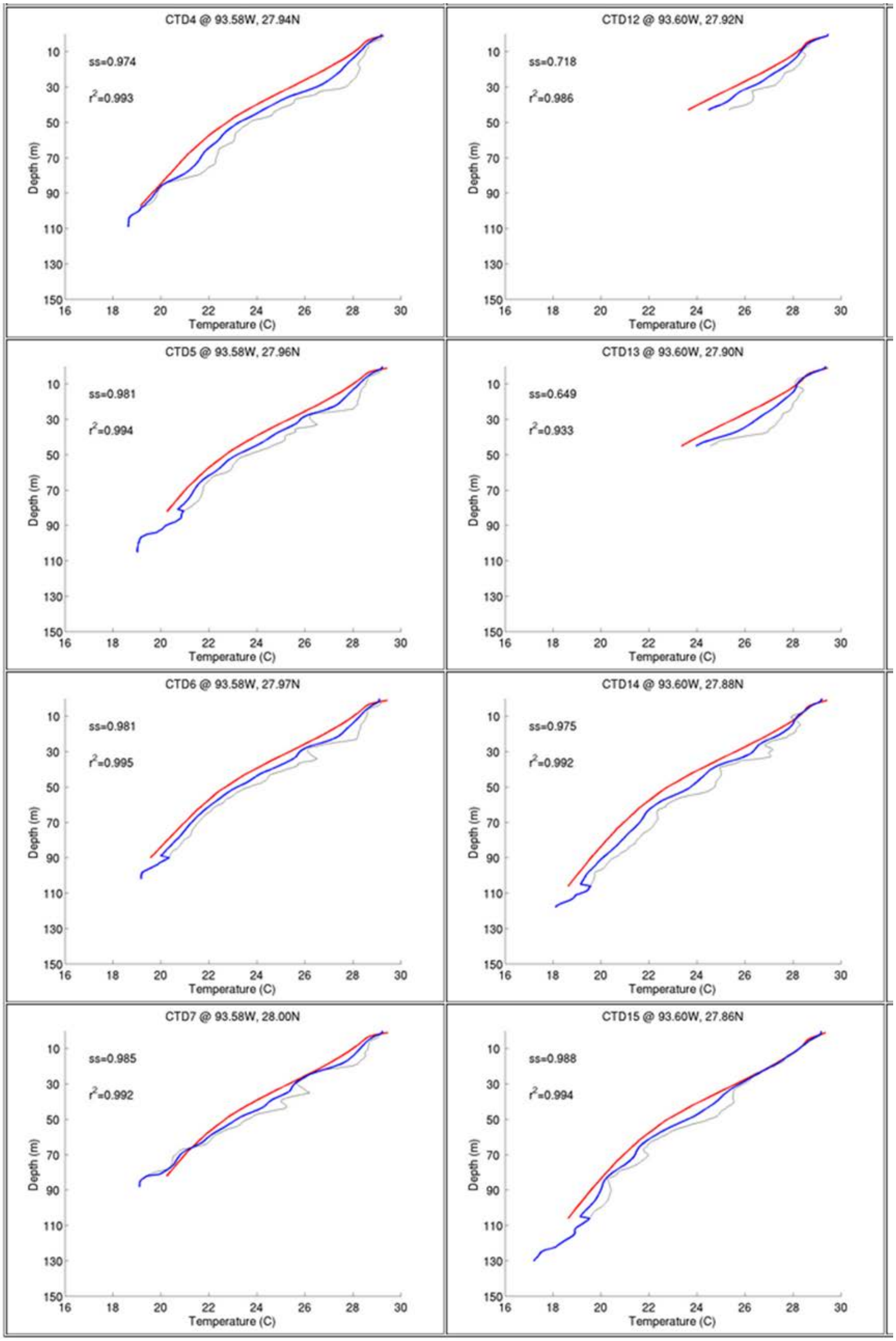

Figure 6b. Comparisons with MORT CTD data.

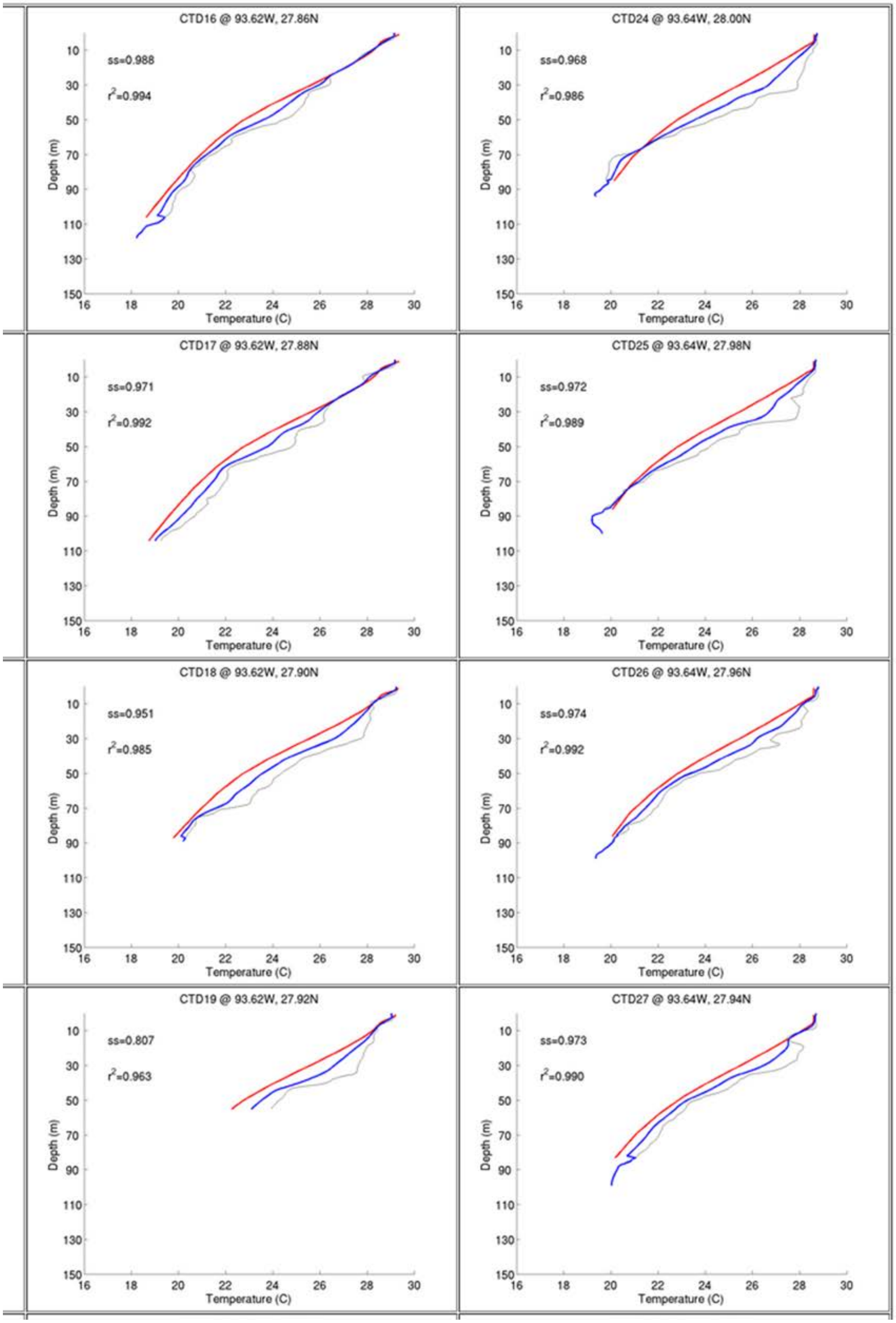

Figure 6c. Comparisons with MORT CTD data.

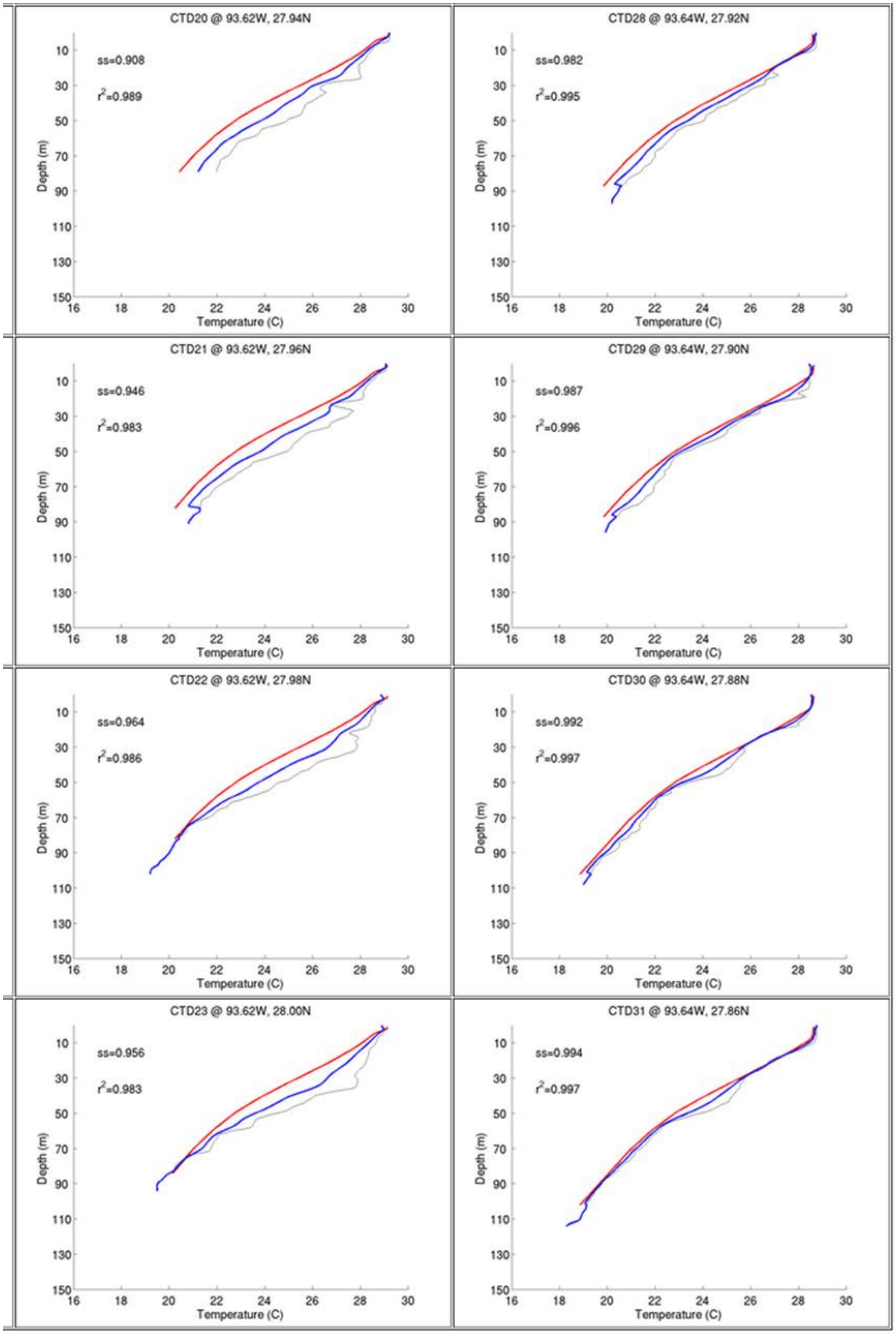

Figure 6d. Comparisons with MORT CTD data.

Mooring	Bottom Temp LT1 (Dec 2010 - Jun 2011)	Bottom Temp LT2 (Jun 2011 - Dec 2011)
M1	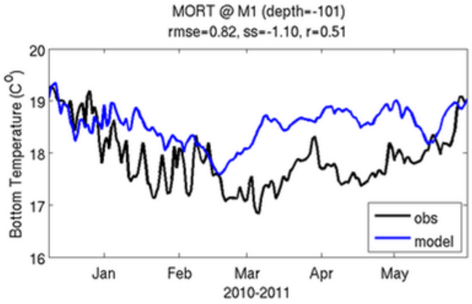 MORT @ M1 (depth=-101) rmse=0.82, ss=-1.10, r=0.51	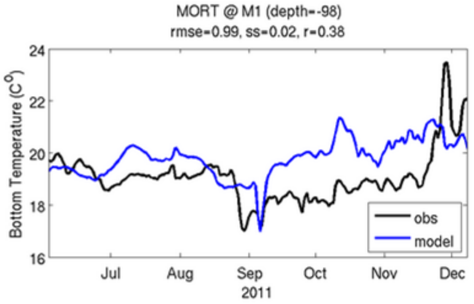 MORT @ M1 (depth=-98) rmse=0.99, ss=0.02, r=0.38
M2	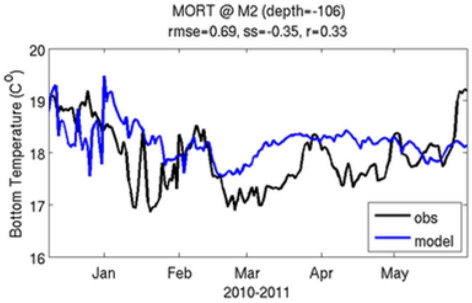 MORT @ M2 (depth=-106) rmse=0.69, ss=-0.35, r=0.33	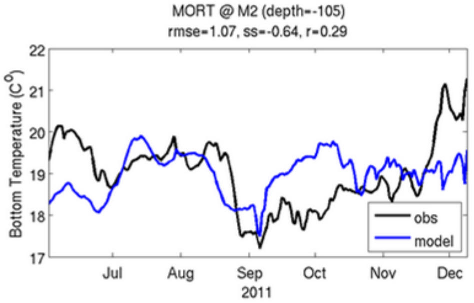 MORT @ M2 (depth=-105) rmse=1.07, ss=-0.64, r=0.29

Figure 7. Comparisons of MORT observed bottom temperatures at moorings M1 and M2 to bottom temperatures from NCOMGOM. In-situ data were binned at 1-day intervals. Correlation (r), skill score (ss), root-mean-square error (rmse) are inset.

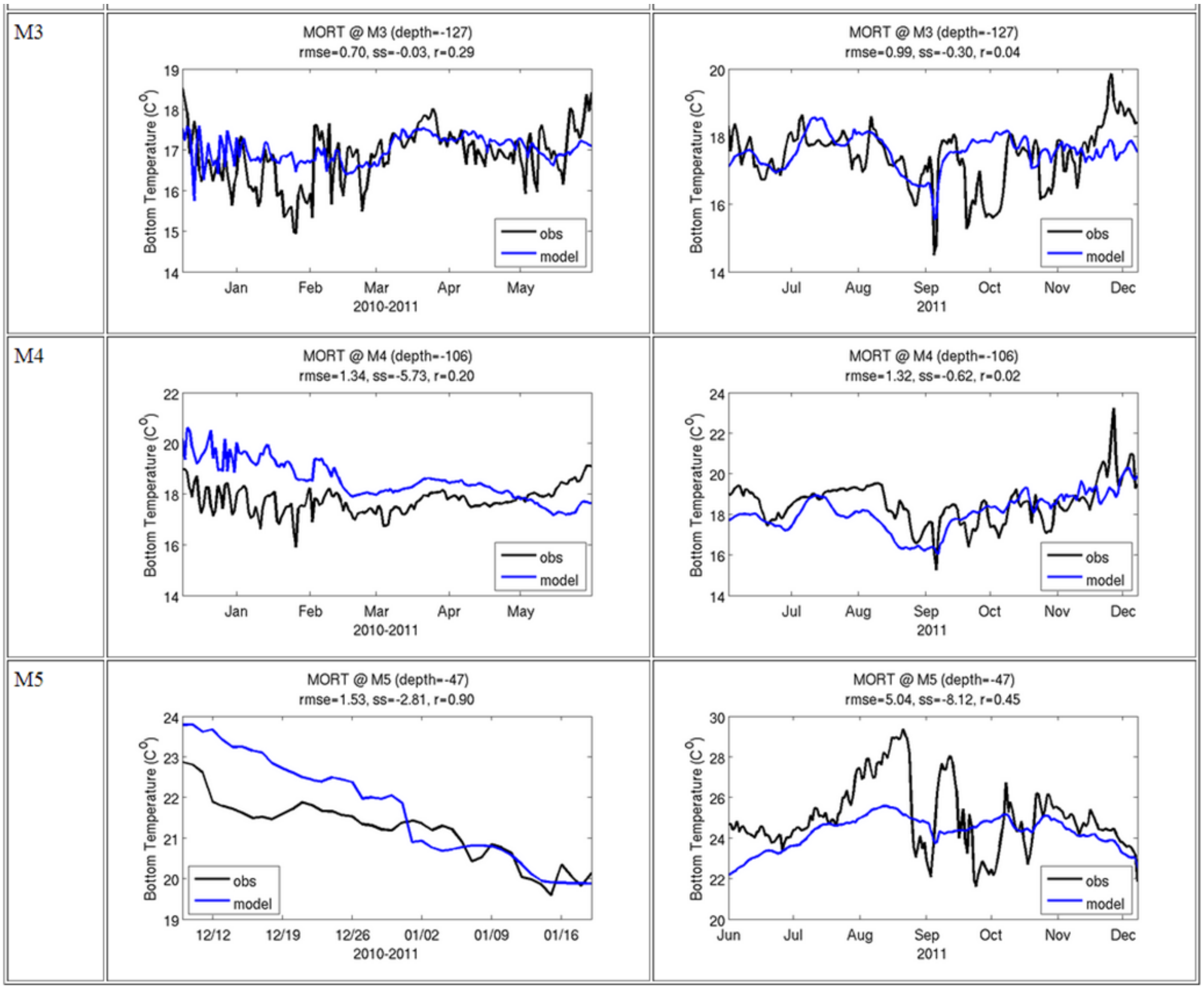

MORT @ M3 (depth=-127)
rmse=0.70, ss=-0.03, r=0.29

MORT @ M3 (depth=-127)
rmse=0.99, ss=-0.30, r=0.04

MORT @ M4 (depth=-106)
rmse=1.34, ss=-5.73, r=0.20

MORT @ M4 (depth=-106)
rmse=1.32, ss=-0.62, r=0.02

MORT @ M5 (depth=-47)
rmse=1.53, ss=-2.81, r=0.90

MORT @ M5 (depth=-47)
rmse=5.04, ss=-8.12, r=0.45

Figure 8. Comparisons of MORT observed bottom temperatures at moorings M3–M5 to bottom temperatures from NCOMGOM. In-situ data were binned at 1-day intervals. Correlation (r), skill score (ss), root-mean-square error (rmse) are inset.

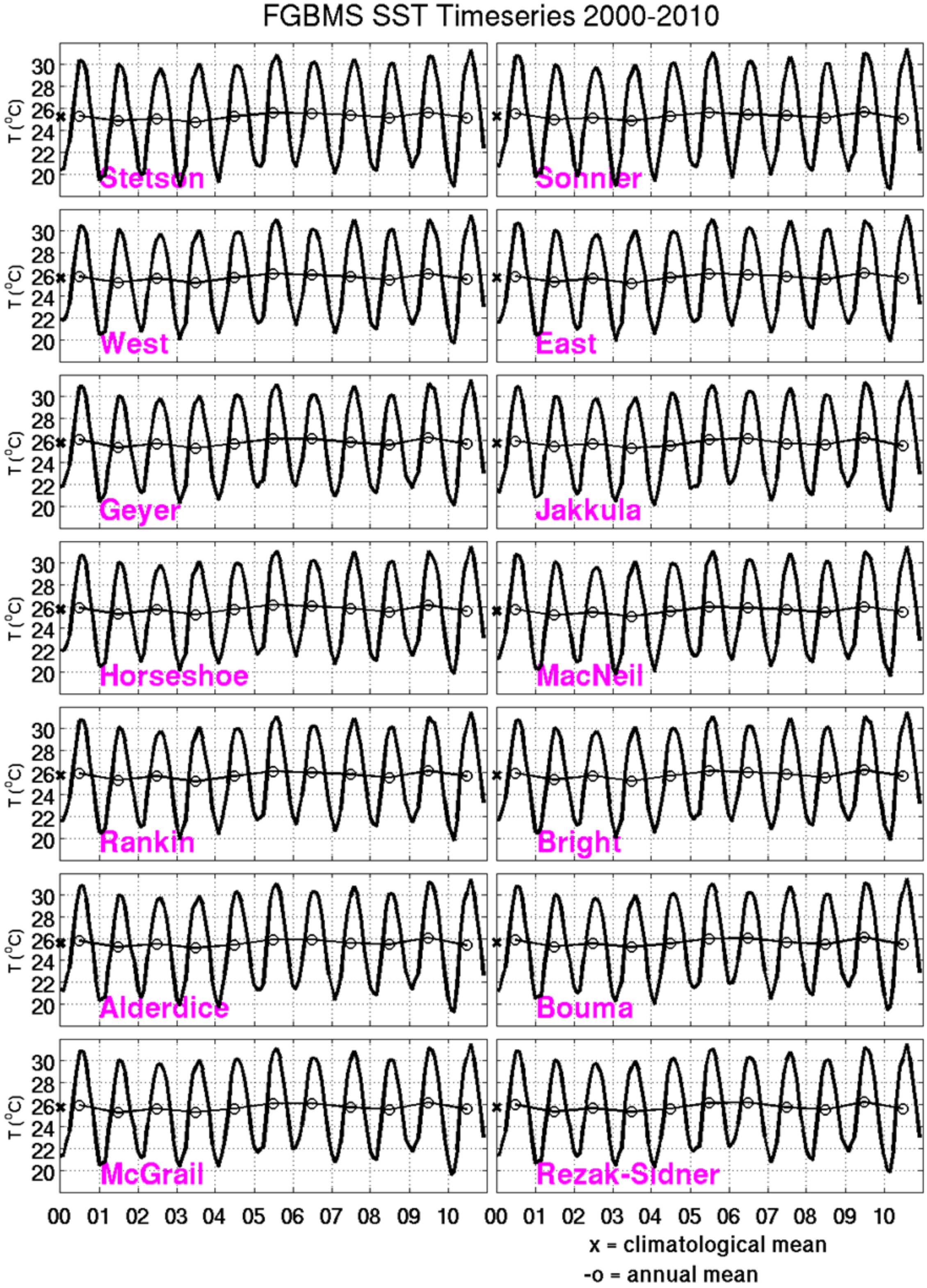

Figure 9. NCOMGOM sea-surface temperatures for the FGBMS banks for years 2000 to 2010.

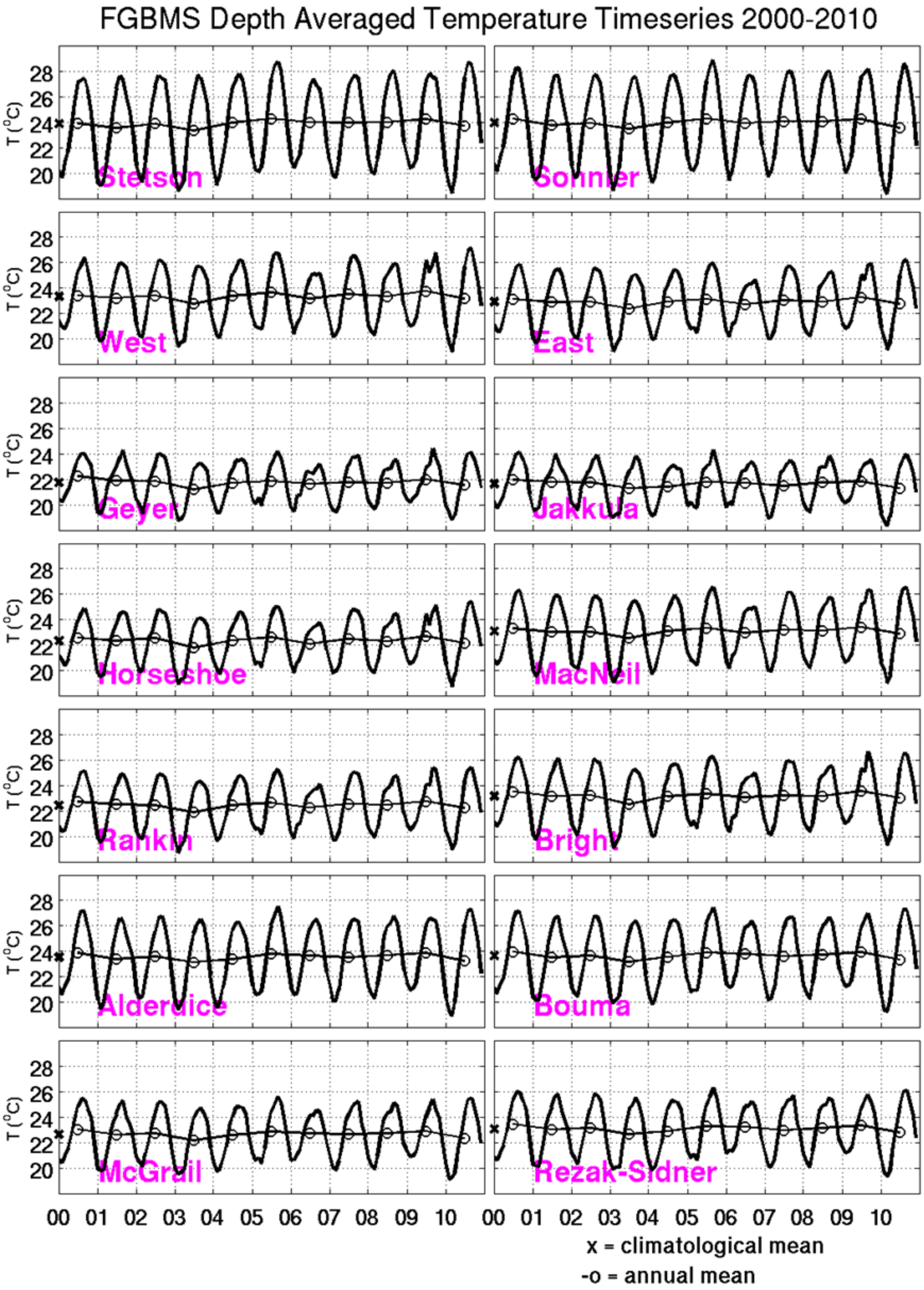

Figure 10. NCOMGOM depth-averaged temperatures for the FGBMS banks for years 2000 to 2010.

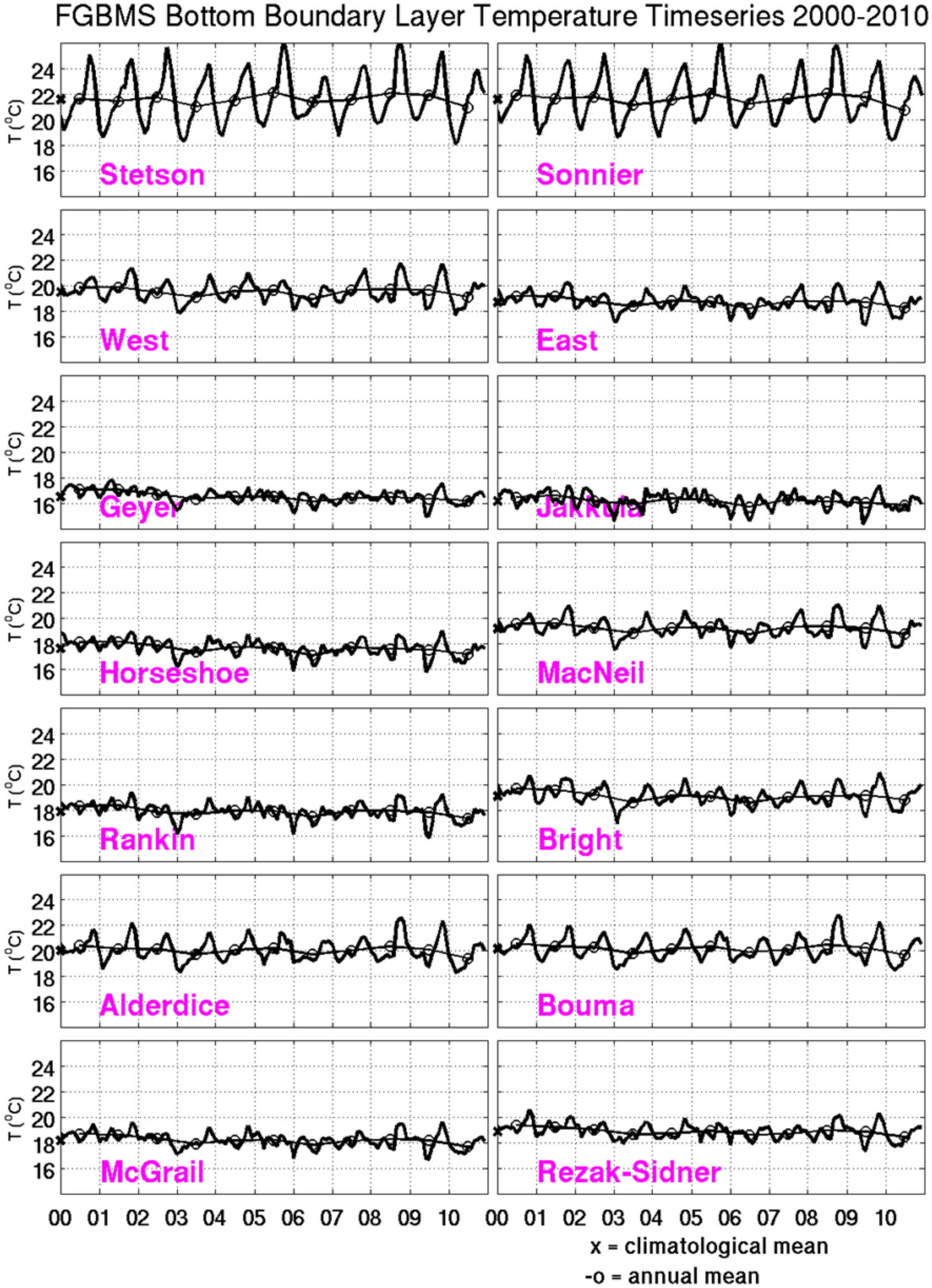

Figure 11. NCOMGOM bottom boundary-layer temperatures for the FGBMS banks for years 2000 to 2010.

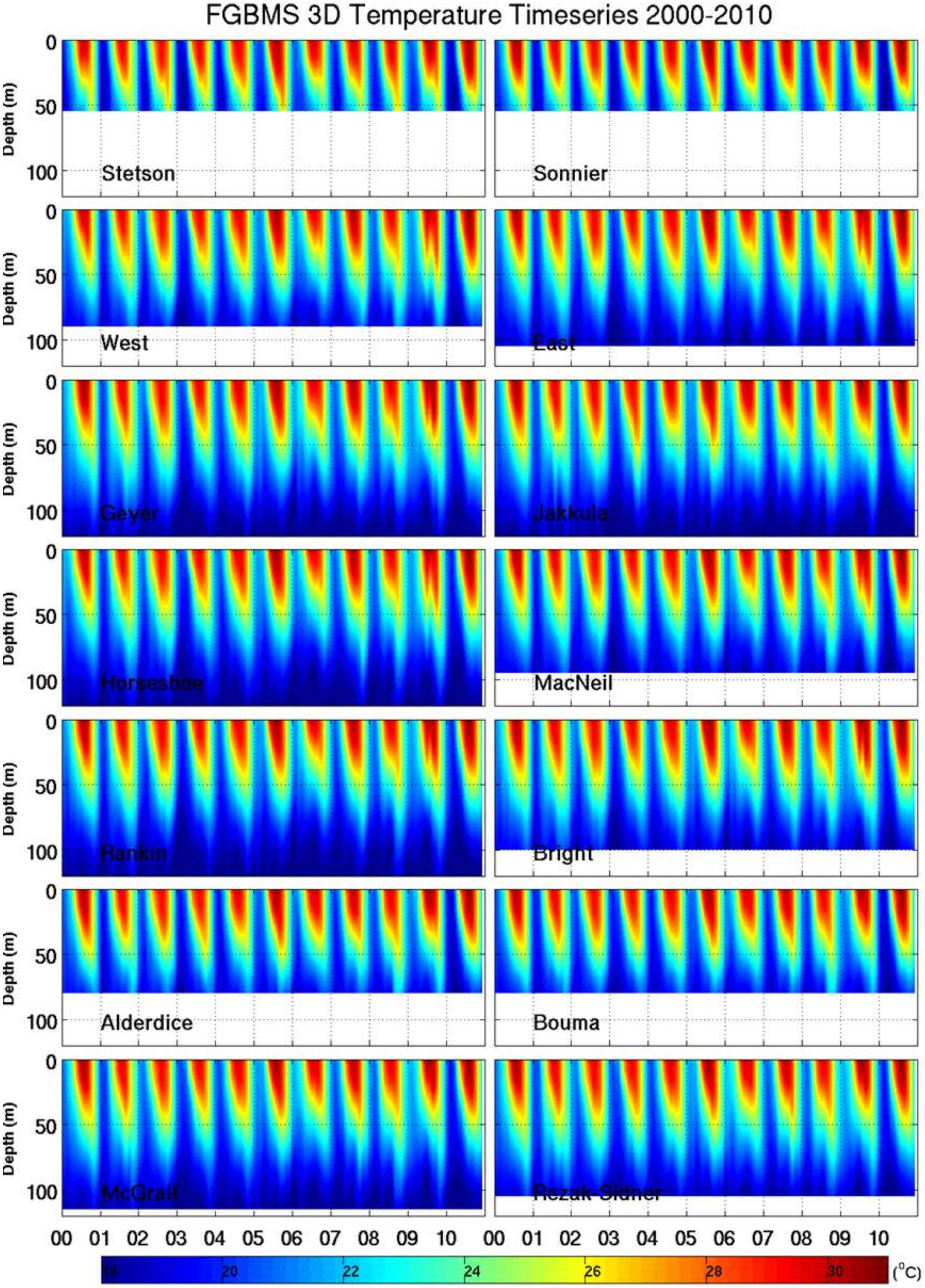

Figure 12. NCOMGOM 3-D temperatures for the FGBMS banks for years 2000 to 2010.

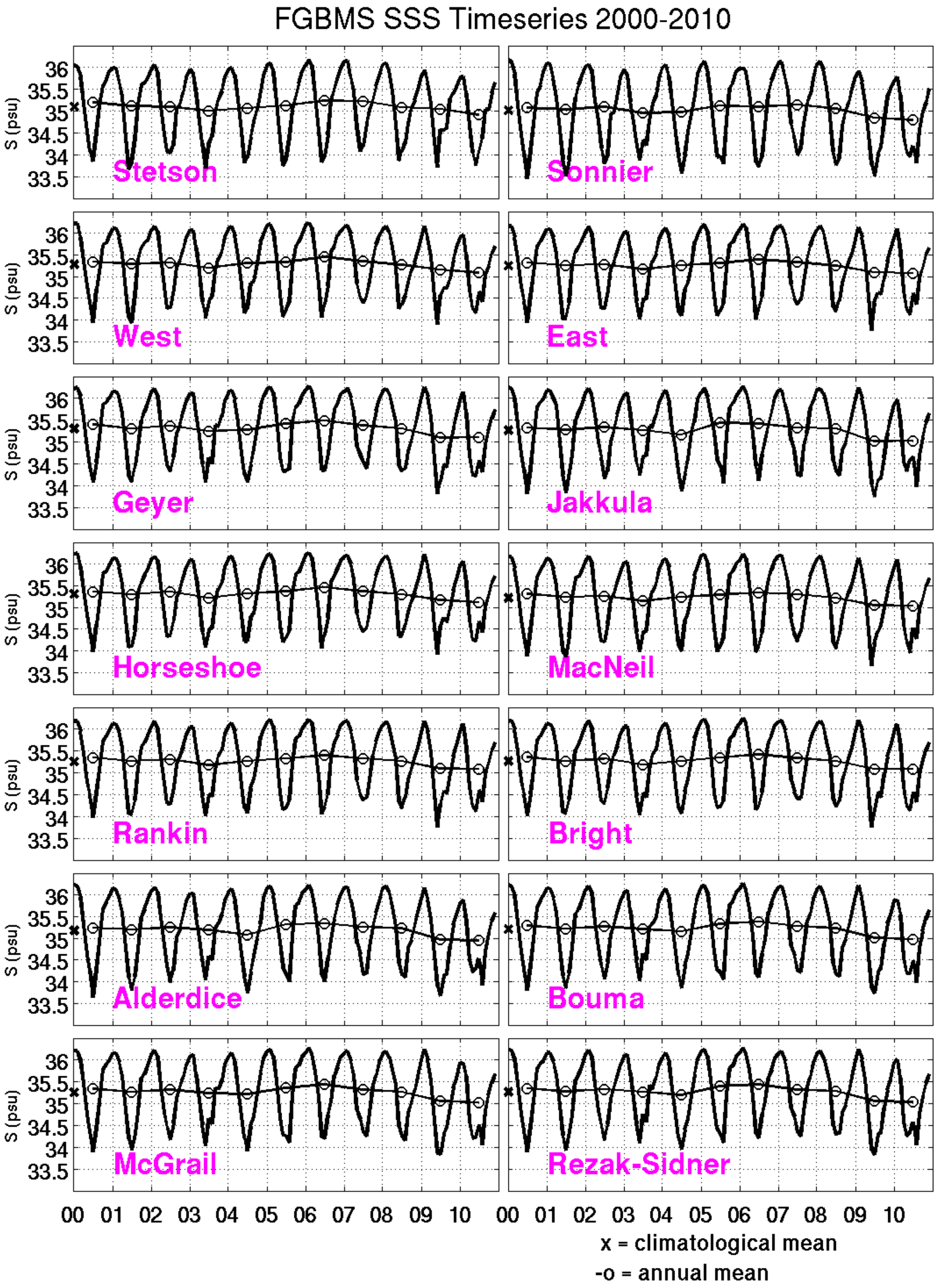

Figure 13. NCOMGOM sea-surface salinities for the FGBMS banks for years 2000 to 2010.

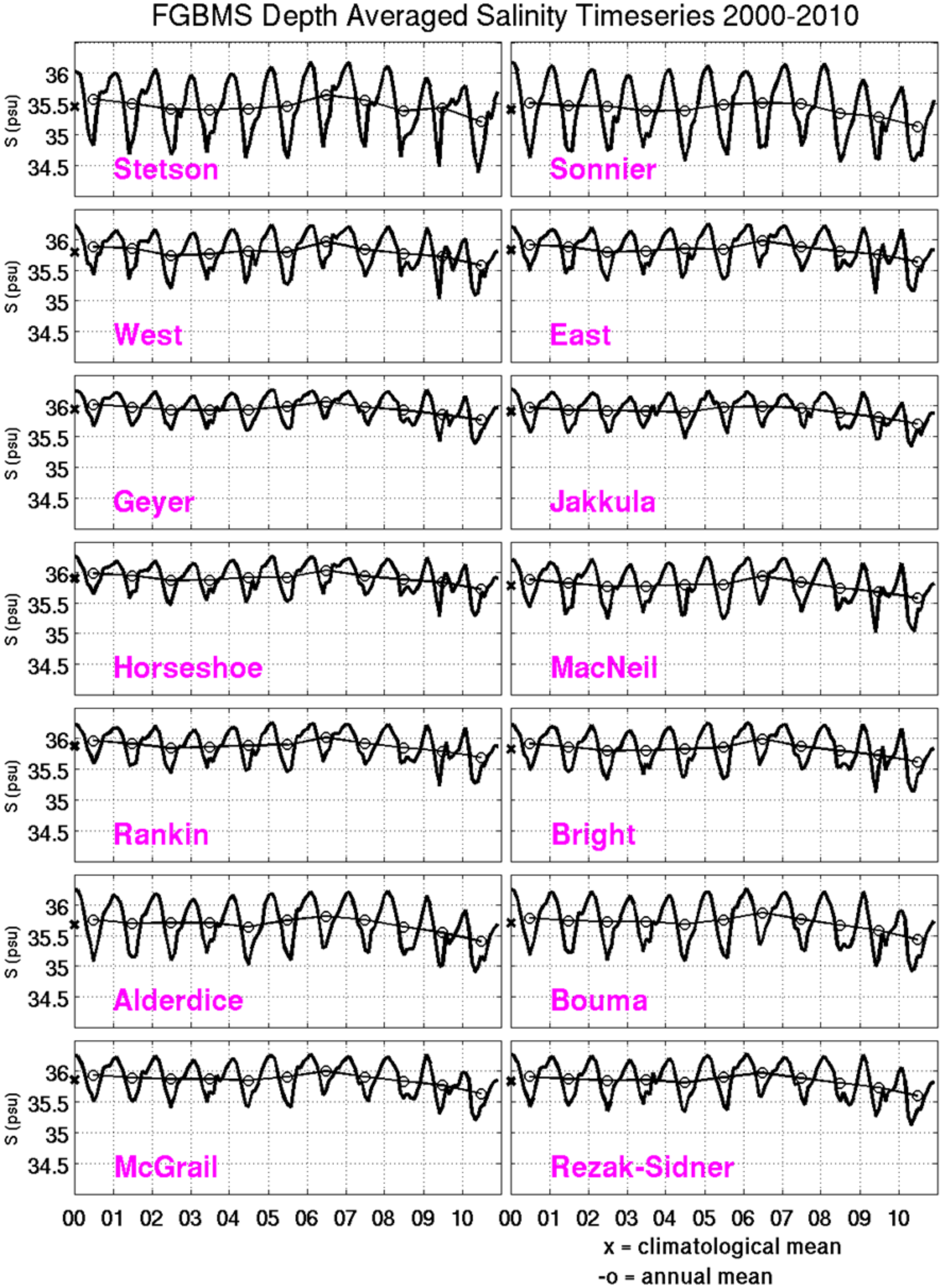

Figure 14. NCOMGOM depth-averaged salinities for the FGBMS banks for years 2000 to 2010.

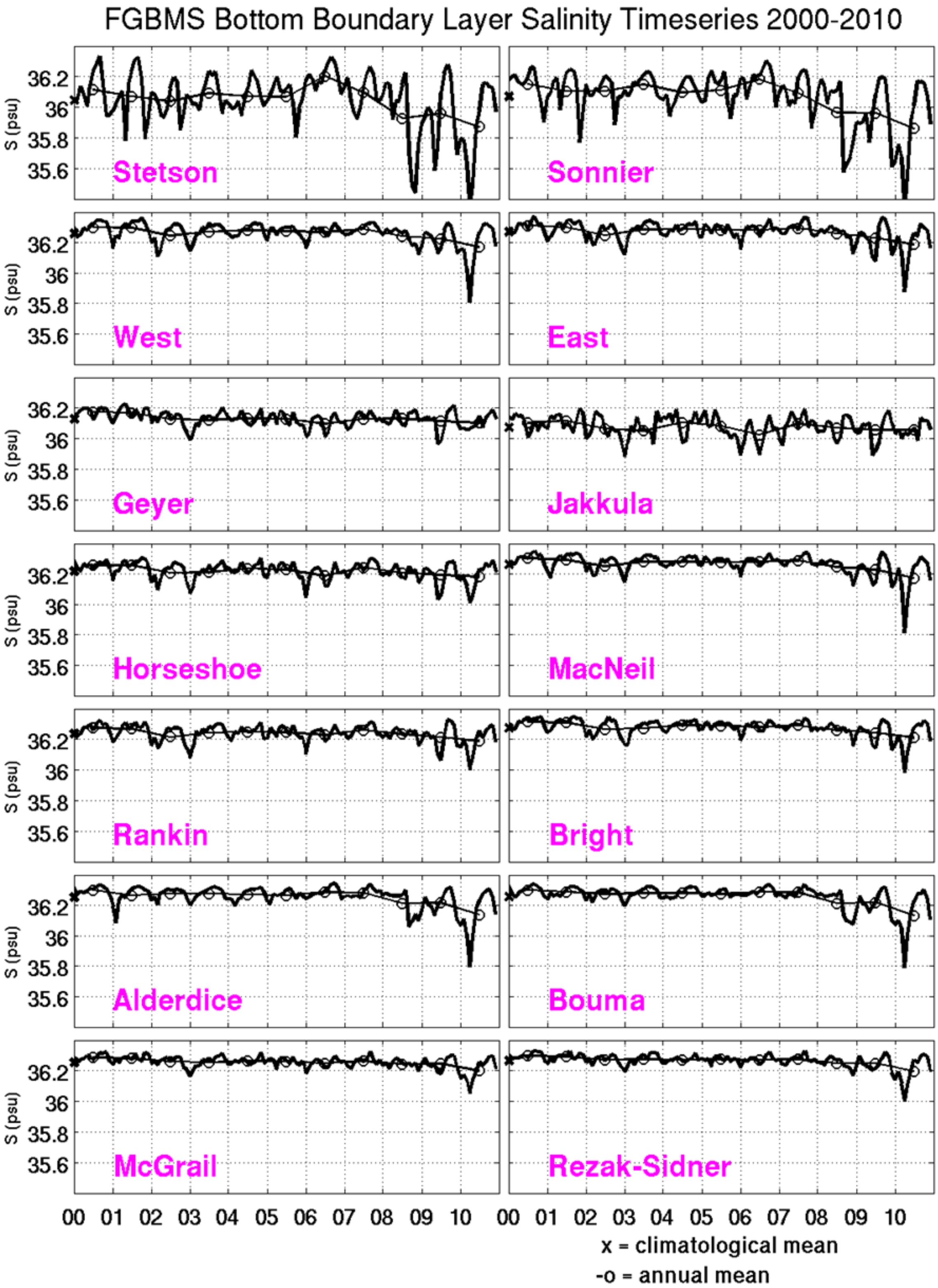

Figure 15. NCOMGOM bottom boundary-layer salinities for the FGBMS banks for years 2000 to 2010.

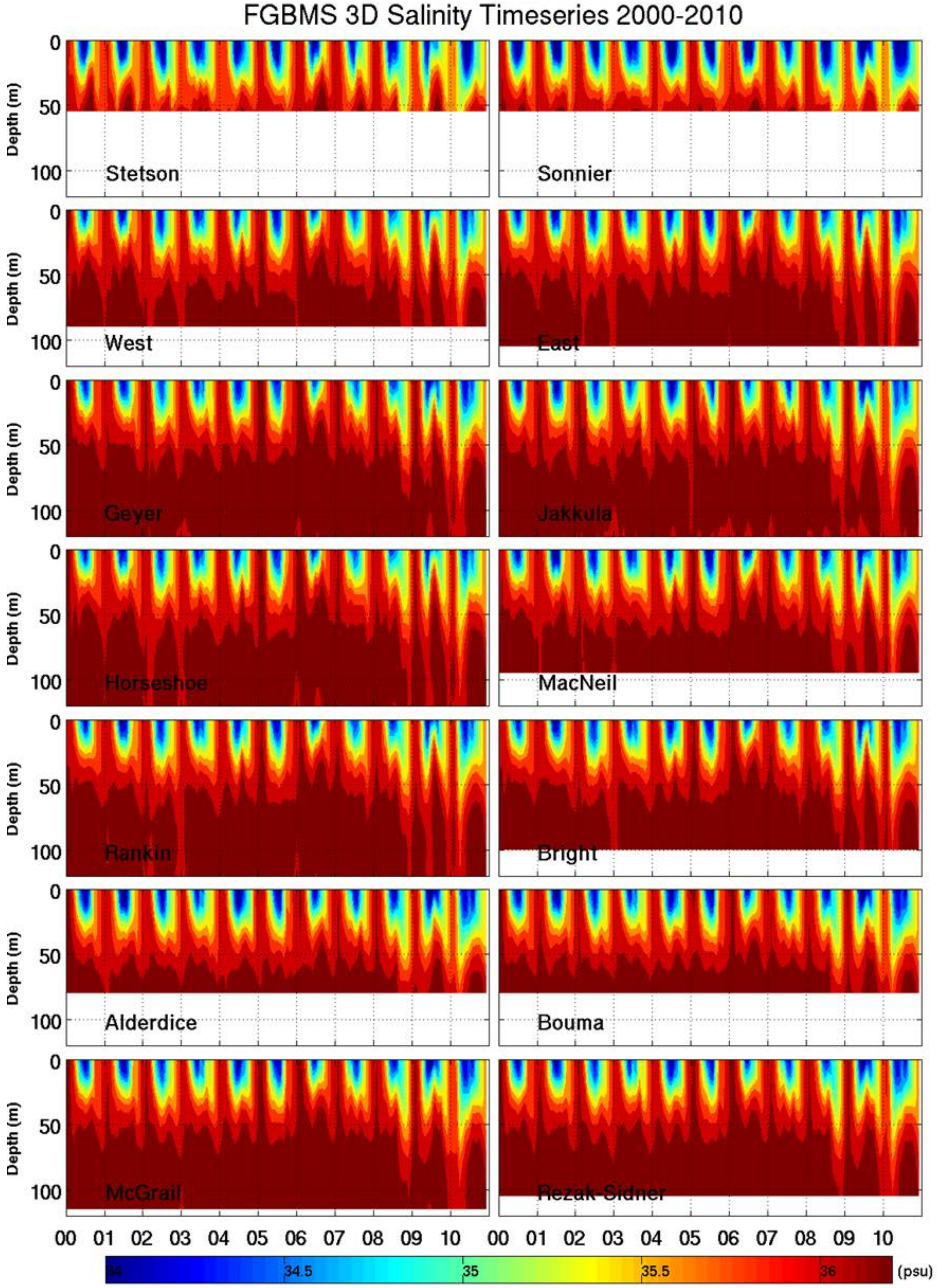

Figure 16. NCOMGOM 3-D salinities for the FGBMS banks for years 2000 to 2010.

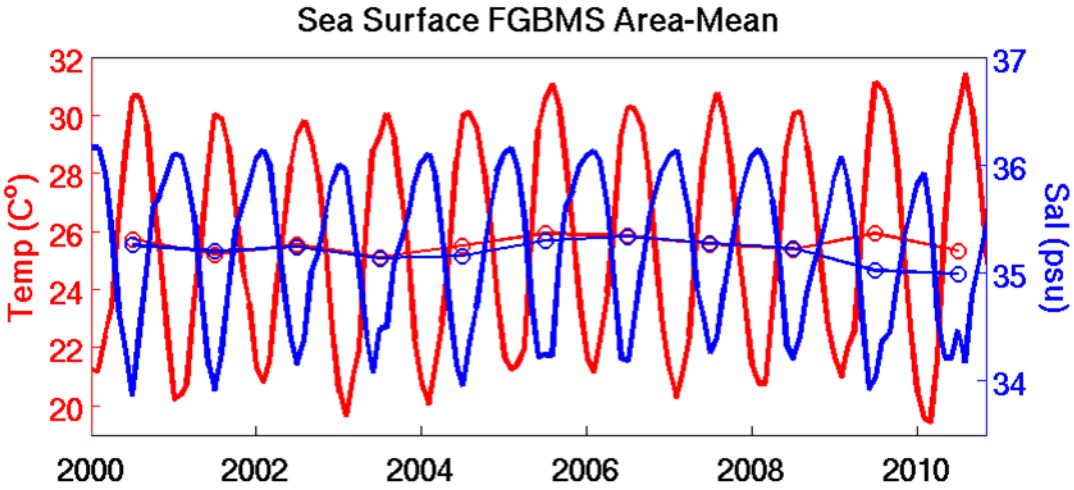

Figure 17. NCOMGOM area-mean sea-surface temperatures and salinities for the FGBMS banks for years 2000 to 2010.

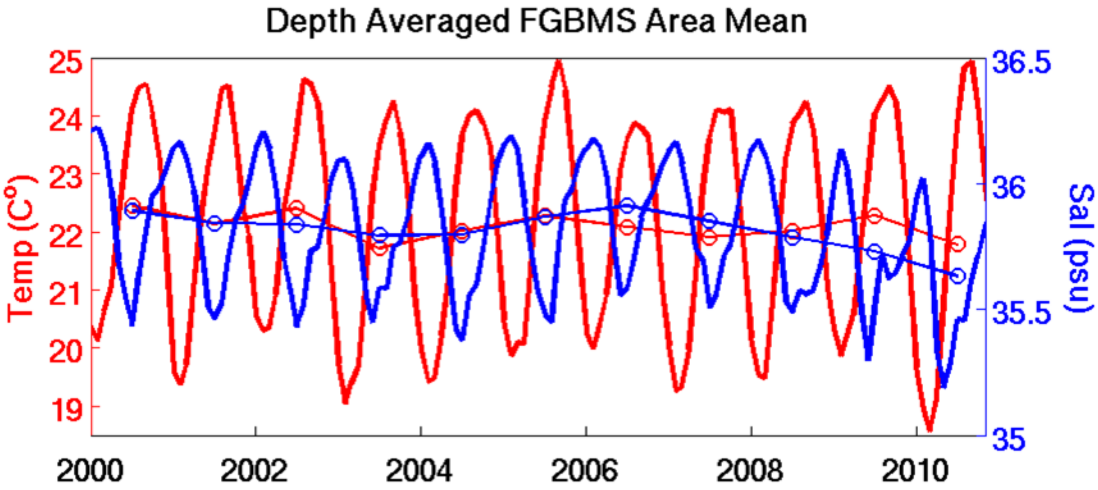

Figure 18. NCOMGOM area-mean depth-averaged temperatures and salinities for the FGBMS banks for years 2000 to 2010.

APPENDIX H

Stochastic Plume Forecasting of Larvae and Suspended Coral over the Flower Garden National Marine Sanctuary– An Early Demonstration

Stochastic Plume Forecasting of Larvae and Suspended Coral over the Flower Garden National Marine Sanctuary– An Early Demonstration

Emanuel Coelho and Germana Peggion

University of New Orleans, Naval Research Laboratory

These results were included in the following publication:

Coelho, E., G. Peggion, P. Hogan, P. Thoppil, C. Rowley, 2014. Long range stochastic plume simulations in the Gulf of Mexico, contribution 044/3-34, 2014 Gulf of Mexico Oil Spill and Ecosystem Science Conference, Mobile, AL, USA.

1. OBJECTIVE: To demonstrate simplified coral and larvae stochastic plume forecasts as applied to the Flower Garden National Marine Sanctuary (FGBNMS) echo system using passive tracers. The method that was used on this demonstration uses continuous source terms and includes the uncertainty on the dispersion depth as well as the estimated errors on the water velocities through an extended forecast range ocean model ensemble (60 days) in development by other related projects. The resulting maps from the system provide likely areas where possible existent larvae and suspended coral might be dispersed in the water column as well as the sources of water arriving to the FGBNMS along specific schedules.

2. MOTIVATION: The Naval Research Laboratory tide resolving, high resolution regional version of the Navy Coastal Ocean Model (NCOM) assimilates local observations, processed independently through the Navy Coupled Ocean Data Assimilation (NCODA) system (Cummings, 2005). The evolving forecast fields have levels of uncertainty determined by the errors at the initial states and given by the NCODA analysis and from other sources of error (e.g., model parameterizations, boundary conditions, bathymetry, etc). These errors will impact differently the information being delivered as forecast and future analysis. Typically, forecast errors have been studied using three different approaches: Proper Orthogonal Decomposition (e.g., Lumley-Stochastic tools in Turbulence, 1971); Polynomial Chaos Expansions (e.g., Meecham & Siegel, Phys. Fluids, 1964); and Error Sub-Space Monte-Carlo Analysis (e.g., Lermusiaux & Robinson, MWR-1999, Deep Sea Research-2001). Each of these techniques has advantages and disadvantages. In short, the proper orthogonal decomposition (POD) will be less expensive but will not account for the full error space or for non-stationary error growth as those errors due to instabilities developing during the forecast phase; the polynomial chaos expansions can address the full error space as detected in prior distributions, but will not account for error growth into the null-space as can occur when instabilities grow (i.e., will not properly extrapolate error growth on orthogonal spaces); the error sub-space approach will address only a small portion of the detected error space (as in the POD), but will use the full non-linear evolution of the error fields and that allows innovation to grow on an orthogonal dimension relative to the prior error space. The Naval Research Laboratory has been using an error sub-space approach with ensemble runs of the NCOM (e.g., Coelho et al., 2009a, Coelho et al., 2009b). In this approach, prior populations of ensemble runs are constrained by the new observations at each initialization step, using the Ensemble Transform (ET) method that shifts and re-scales perturbations at each analysis time following Mclay et al., 2008. The ET uses the best available estimate of analysis error covariance to transform forecast perturbations into analysis perturbations by finding K distinct linear combinations of K forecast perturbations that (a) are equally likely (b) lie within the vector subspace of forecast perturbations (c) are quasi-orthogonal although they sum to zero, and (d) have expected squared amplitudes equal to the trace of the best available estimate of the analysis error covariance matrix. The NCOM model is then run independently for each perturbed initial state. During the forecast runs, the atmosphere forcing terms are further perturbed using a space-time deformation of the surface winds and atmospheric pressure. Work is now under way to include also the perturbations of physics parameterizations, boundary conditions and the inclusion of stochastic forcing to account of the unconstrained and unresolved physics. These ensembles can predict uncertainties of the ocean currents and provide the input into diffusion-advection plume simulations. The ensemble populations of these advected plumes can provide estimates of joint distribution functions of concentrations or near-range presence of specific tracers or substances and used to compute the likelihoods of jointly reaching critical thresholds, motivating some awareness status or monitoring actions. The information can be conveyed in terms of stochastic plumes (e.g., Coelho et al. 2012a,b) defined through the Risk Assessment Codes (RAC) that associate numbers 1 to 6 to each geographical location on a grid. These codes use the likelihood (0.1, 0.25, 0.5, 0.75) of having the variables or criteria within prescribed threshold ranges (critical impact, severe impact, moderate impact, low impact), such that a code 1 will correspond to likelihood above 0.75 of impacts above the "critical impact", and a code 6 to likelihoods below 0.1 of "low impacts".

3. PROJECT SCHEDULE: The work included the following four tasks:

- TASK 1: Set-up and verification of Ocean Ensemble runs
- TASK 2: Lagrangian advection plumes and Risk Assessment Code Analysis
- TASK 3: KMZ generation and display of real-time fields
- TASK 4: Testing and Validation
-

Task 1: This task consisted of the set-up and tests of NCOM ensemble runs at 1km and 3km resolution and the adaptation of existent software to provide 4D velocity fields for ocean currents. Results showed the 3km system developed through other leveraging projects would be capable to provide the most consistent flow fields for this analysis.

Task 2: This task consisted of the usage of the 4D velocity fields from the ensembles to run lagrangian plumes and to compute probability distribution functions for the tracer distances relative to each grid point and at each forecast step. These functions were then used to produce Risk Assessment Code maps representing the tracer distributions.

Task 3: Through this task, we ran and maintained the system in real-time mode and displayed results on a web site, for external use, during several periods in March 31, 2013 to August 18, 2013. The system was also demonstrated with the long range prediction system in December 2013 for the production of a poster presentation and used to produce the examples in section 4 of this report.

Task 4: Overall system testing and validation was included in other projects and showed the NCOM ensemble system maintains a performance above persistency through the full 60 days forecast range and was capable of accurately predicting several occurrences of Loop Current detachment.

Project schedule

Task	Jul–Aug 2012	Sep–Oct 2012	Nov–Dec 2012	Jan–Feb 2013
Oc. Ensembles setup	▨	▨		
Risk Codes setup		▨		
System demonstration			▨	▨
Testing & Validation				▨

4. RESULTS: Major issues in characterizing and predicting the extent of the affected or sensitive regions in real-time during oil spills or other dispersive events in the ocean are a poor knowledge of the actual source functions and the fact that coastal dynamics may not be predictable in a deterministic sense. This demonstration presented a methodology that allows assessing the fate of larvae spawning events and the identification of water sources that will be present in the FGBNMS during the most sensitive periods for the several habitats in the region and allow for efficient planning of monitoring tasks and mitigation in the case of accidents at sea. The approach uses a 32-member ensemble of extended range forecasts (60 days) of high resolution runs of the Navy Coastal Ocean Model (NCOM) configured over the Gulf of Mexico. The ensemble runs are assumed to represent the uncertainty in larger scale dispersion and each run is assumed as a reference state for Lagrangian Gaussian stochastic models that take into account the smaller scale dispersion. The ensemble information is integrated as stochastic plumes by defining probability distribution functions for tracer distributions relative to each point on the model grid. Results are displayed using a Risk Assessment Code (RAC) analysis by associating a number from 1 to 5 to each grid point, determined by the likelihood of having tracers within the vicinity of each grid node. The threshold ranges can characterize the expected total dispersion from the ensemble runs and be tuned to represent levels of concentration relative to the source.

The ensembles are based on perturbation of model initial conditions and atmospheric forcing as schematized in Figure 1.

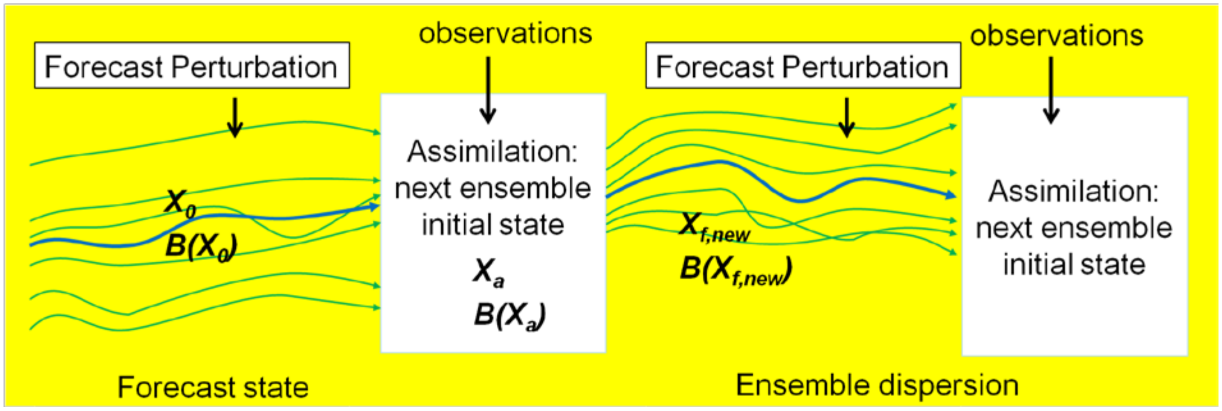

Figure 1: Schematic of the NCOM ensembles. Ocean ensembles are multiple runs of an ocean model representing a domain of likely alternatives: each run uses different parameters; parameter options are bootstrapped from distributions; distributions are determined by the error sources. The modeling system was set with 60 days long forecast runs, every week, using a 3 km horizontal resolution, 49 levels in the vertical and bathymetry from the NRL DBDB2' database. Forcing was taken from the atmospheric model COAMPS (surface forcing) and Ocean Forecasting System GOFS (lateral boundary condition) during the first 96 hours and then from a high resolution (3hr) climatology based on the previous five years. The system also included tidal forcing.

The several estimates provided by the ensembles are used to construct the probability distribution functions describing the distribution of tracers relative to each grid point in the model grid and used as inputs to Operational Risk Management (RAC's). The RACs weigh the probability of an occurrence of specific distributions versus the severity of the distributions taken as proxies of possible concentrations used the convention summarized in Figure 2.

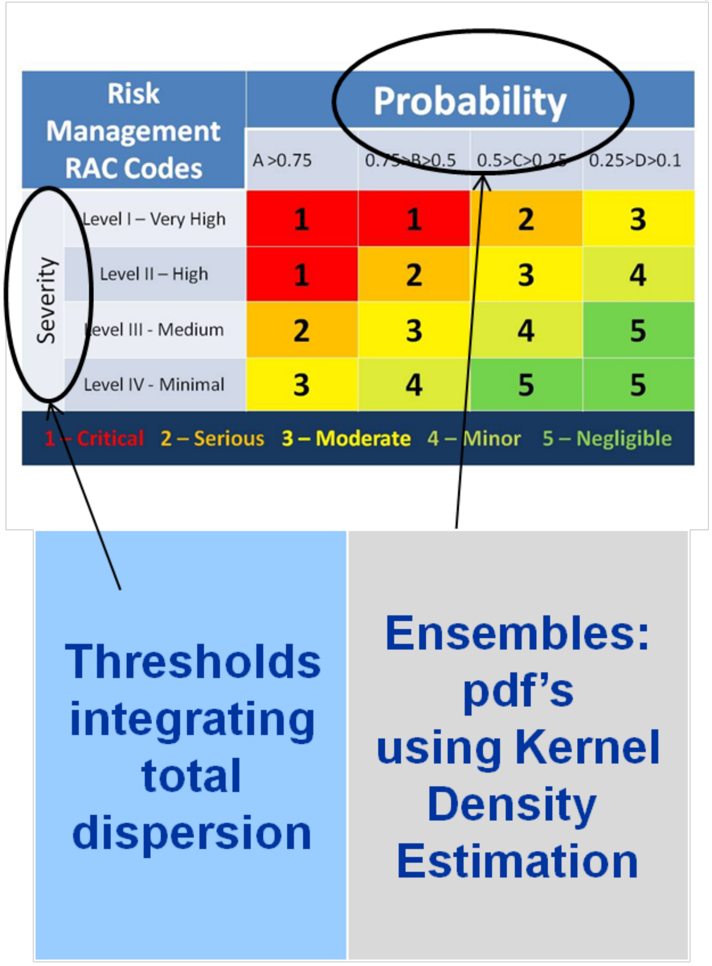

Risk Management RAC Codes		Probability			
		A >0.75	0.75>B>0.5	0.5>C>0.25	0.25>D>0.1
Severity	Level I – Very High	1	1	2	3
	Level II – High	1	2	3	4
	Level III - Medium	2	3	4	5
	Level IV - Minimal	3	4	5	5

1 – Critical 2 – Serious 3 – Moderate 4 – Minor 5 – Negligible

Figure 2: Risk Assessment Codes (RAC) used for plume or larvae concentration description. The severity levels were set as "very high" when tracers were present within 5km of a grid point, "high" when tracers were within 10km, "medium" when within 15km and as "minimal" if within 20km. This approach allows identifying areas in the ocean where traceable amounts of inputs can be found in the ocean given the uncertainty in the released substance/object, release times and locations.

Examples of RACs generated by the system are shown in Figures 3–6. These examples were taken from the run made December 15, 2013; they are summarized in Figure 3, which shows the temperature and velocity fields and the standard deviation of the 32 ensemble runs.

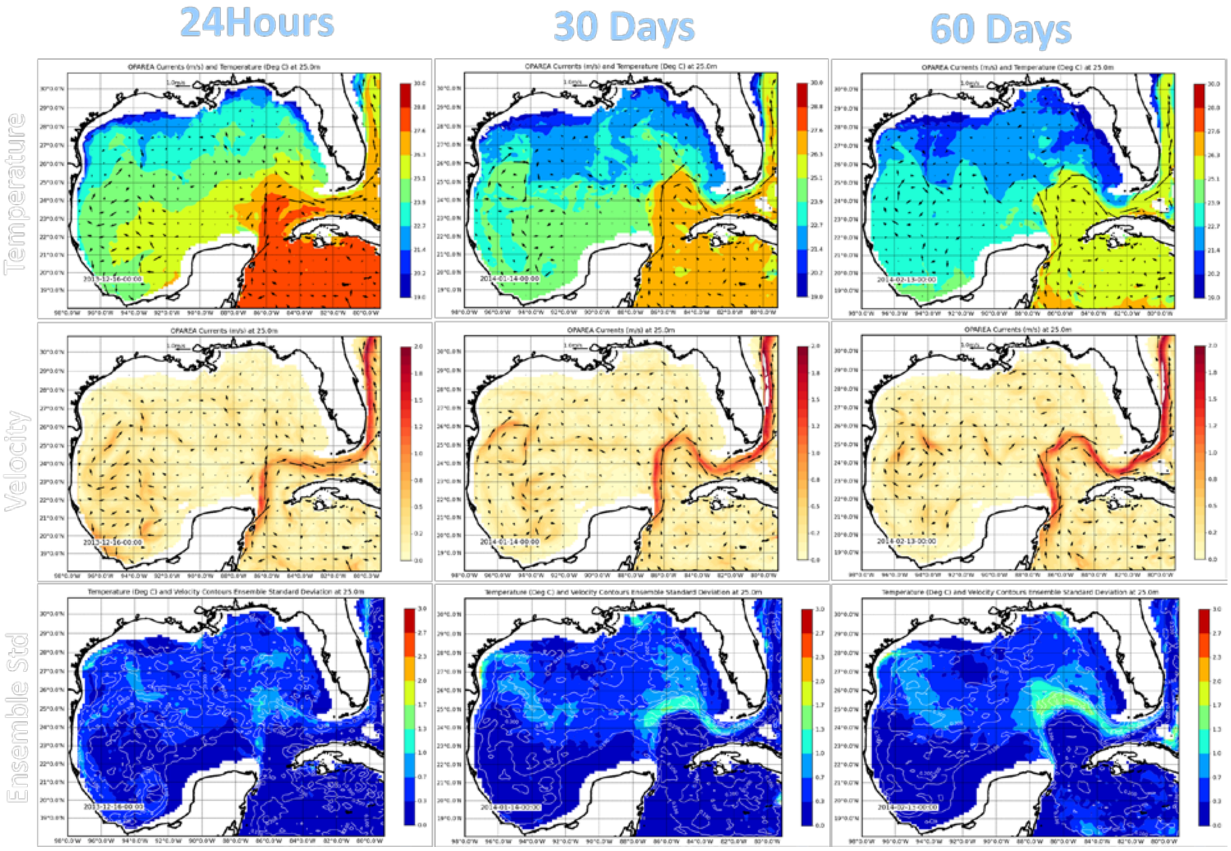

Figure 3: Long range ensemble forecast run on December 15, 2013. The upper plots show the surface temperature fields, the middle plots the surface currents, and the lower plots the temperature ensemble standard deviation (color) and velocity standard deviation (contours). The columns correspond to the 24 hour, 30 days, and 60 days forecasts, respectively.

The RAC code numbers 1 to 5 are assigned to each geographical location on a grid describing the trade-off between probabilities of occurrence vs. proximity of tracers. The probabilities are computed from the probability distribution functions defined from the tracer population using non-parametric methods. The tracer ranges with the likelihoods less than 0.1, between 0.1 and 0.25, between 0.25 and 0.5 or above 0.75, are then computed and compared against the severity levels to assign a risk code such that a code 1 will correspond to likelihood above 0.75 of tracers within the “high” range or above 0.5 for “very high”, and a code 5 to likelihoods below 0.1 for “medium” or below 0.25 for “minimum”. These distributions will depend on the initial release and concentration of tracers. For the system demonstration three scenarios were considered. The first case, shown in Figure 4, is the release of tracers along a route and analysis can be made into evaluating the probability or risk of their arrival towards the FGBNMS region. The second case, shown in Figure 5, is the evaluation of the potential connection between a continuous sources offshore a major harbor and urban area and the marine sanctuary. The third scenario, shown in Figure 6, looks into the general water sources likely advecting towards the sanctuary region during the 60 days period.

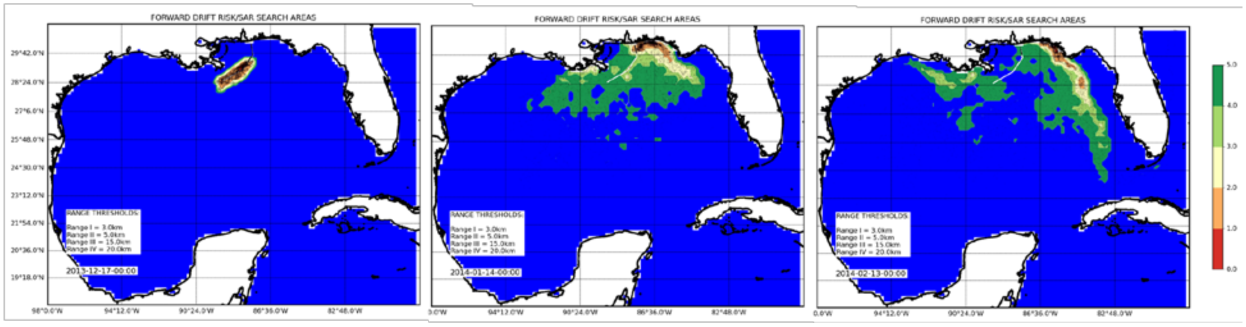

Figure 4: Example demonstrating a sequential release of tracers during three days along a route approaching Mobile Bay. The left panel shows the distribution of tracers mapped through the RAC codes after three days. The panel in the middle shows the RAC codes after 30 days and the right panel the RAC code distribution after 60 days. One can see the bi-model separation of tracers showing the likelihood of tracers to go East (and eventually arriving to the Marine Sanctuary), although the most likely scenario would be a westward dominant propagation of higher concentrations.

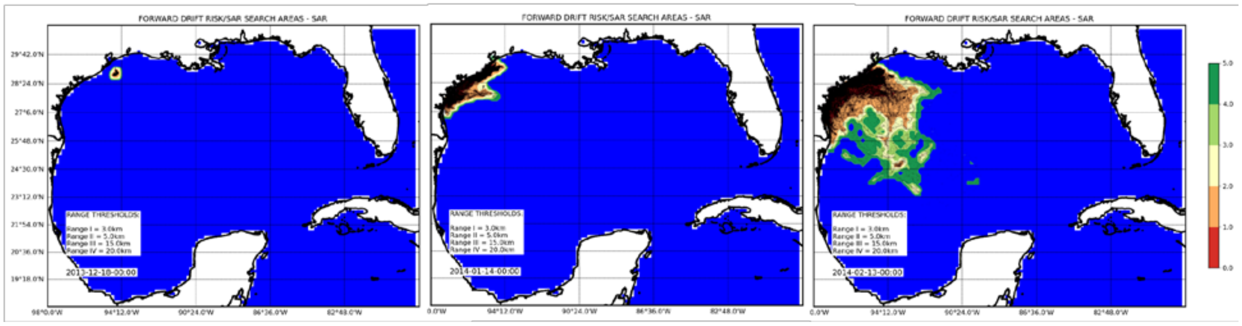

Figure 5: Example demonstrating a continuous release of tracers during the 60 days forecast from a position just off-shore Houston harbor. The left panel shows the distribution of tracers mapped through the RAC codes after three days. The panel in the middle shows the RAC codes after 30 days and the right panel the RAC code distribution after 60 days. One can see the bi-model separation of tracers showing the likelihood of tracers to go along-shore and off-shore to the East and eventually arriving to the FGBNMS within the 60 days period.

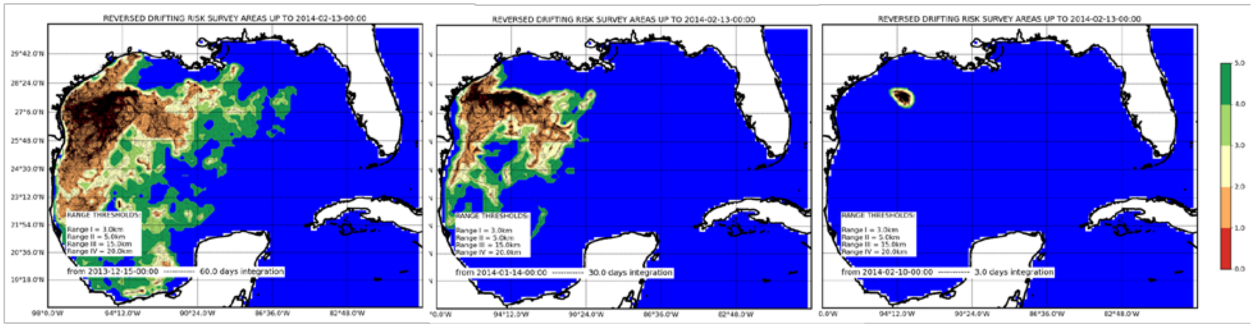

Figure 6: Example demonstrating the likelihood of the sources of water moving to the sanctuary by the end of the forecast period on February, 14 2014. The left panel shows the risk distribution in the 60 days period suggesting most of the water would be moving likely from the coastal regions of western Texas. The middle panel shows the sensitive regions within a 30 days period suggesting water arriving either from the southeast or southwest (or both). The plot on the right corresponds to the three days period, just before the end of the forecast, suggesting a larger sensitivity relative to a west-north-west advection route.

The demonstration products were delivered in a password protected website as Google-Earth™ kmz layers and associated source data in NetCDF format. The kmz-layers consisted of model fields (temperature, salinity, water level, currents) and lagrangian plume estimates, conveyed using the RAC codes.

7. REFERENCES:

Allard, R., T. Campbell, T. Smith, T. Jensen, S. Chen, J. Cummings, J. Doyle, X. Hong, R. Small, S. Carroll, 2010. Validation test report for the Coupled Ocean/Atmosphere Mesoscale Prediction System (COAMPS) Version 5.0., NRL Memorandum Report 7320-9283, 1-173.

Bishop, C. and D. Hodyss, 2009. Ensemble covariances adaptively localized with ECO-RAP, Part 1: Tests on simple error models, Tellus, 61, 84–96.

Coelho, E.F., C. Rowley, and G. Jacobs, 2009. Ocean data assimilation guidance using uncertainty forecasts, MTS/IEEE Oceans’09, 090611-014.

Coelho, E.,G. Peggion, C. Rowley, G. Jacobs, R. Allard, and E. Rodriguez, 2009. A note on NCOM temperature error calibration using the ensemble transform, Journal Marine Systems , Rapid Environmental Assessment special issue, 78, S272-S281.

Cummings, J., 2005. Operational multivariate ocean data assimilation, Quarterly Journal of the Royal Meteorological Society 131, 3583–3604.

Daley, R., and E. Barker, 2001. NAVDAS: Formulation and diagnostics, Mon. Wea. Rev., 129, 869-883.

Lorenc, A. C., 2003. The potential of the ensemble Kalman filter for NWP—A comparison with 4D-VAR, Quart. J. Roy. Meteor. Soc., 129, 3183–3203.

March 3, 1849

The Department of the Interior Mission

As the Nation's principal conservation agency, the Department of the Interior has responsibility for most of our nationally owned public lands and natural resources. This includes fostering the sound use of our land and water resources; protecting our fish, wildlife, and biological diversity; preserving the environmental and cultural values of our national parks and historical places; and providing for the enjoyment of life through outdoor recreation. The Department assesses our energy and mineral resources and works to ensure that their development is in the best interests of all our people by encouraging stewardship and citizen participation in their care. The Department also has a major responsibility for American Indian reservation communities and for people who live in island communities.

The Bureau of Ocean Energy Management Mission

The Bureau of Ocean Energy Management (BOEM) works to manage the exploration and development of the nation's offshore resources in a way that appropriately balances economic development, energy independence, and environmental protection through oil and gas leases, renewable energy development and environmental reviews and studies.